

# **Investigating disturbances of brain 5-HT systems by experimental MRI and SPECT neuroimaging**

Torsten Ruest, Diplom-Biologe (Dipl. Biol.)

A thesis submitted for the degree of Doctor of Philosophy to the Faculty of Medicine, University of Glasgow.

Wellcome Surgical Institute, Division of Clinical Neuroscience, University of Glasgow, Garscube Estate, Bearsden Road, Glasgow, G61 1QH.

© Torsten Ruest, April 2009

## **Acknowledgements.**

First I would like to thank Jim "Scotty" Mullin who always had a helping hand when it came to solve technical problems, regardless whether private or professional in nature. Dr. Stuart Cain who showed me to operate Fury (micro-SPECT), and Linda Carberry, who gave me a helping hand with the animal preparation for Fury and for covering time on the beast so that I would not starve. Also Dr. Sally Pimlott contributed a lot by providing the fuel (radioligands) for Fury. Joan Stewart, Drs. Rosie Spike and Souad Messahel for their time cutting my brains. Thanks also to Margaret Stewart who always sorted out problems with the temperamental cryostats when they went on strike, and to Ann Marie Colquhoun for the prompt drug orders. I wish to thank Dr. Chris McCabe and Lindsay Gallagher for their expert advice on animal procedures, including fixation and injections. Next I want to thank Dr. Mark Ansorge who supplied the "biological material" for the serotonin transporter knock-out study, and to Sheonagh Law who was involved in some of the image analysis in this study. I am deeply grateful for the invaluable collaboration with Dr. Julia Edgar who supported me with mice for the *Plp1* overexpression studies and her friends in high places so that we could use the MRI for FREE. In addition, she freed her technical staff and student for the preparation and analyses of histology data. Without, this thesis would only be half as thick. Therefore I am indebted for the work done by Jennifer Barrie, who did stain the sections and quantified the data, and Dr. Fredrik Gruenfelder who helped with the analyses and who always had a couple of minutes for valuable discussions. I also would like to thank Dr. Mark McLaughlin for his assistance and fruitful discussions on tissue preparation for NMR spectroscopy, even though it did not survive into this thesis. The help of Dr. Brian Smith was also highly appreciated, who ran some of the NMR samples on his spectrometer. Dr. William Holmes I would to thank for entrusting me with driving his baby (MRI) every now and so often, and for his fair and useful comments concerning MRI and suggestions for the write-up of this thesis (any complaints will be redirected to him). Then I am thankful for the advice and supervision provided by Prof Mhairi Macrae and Dr. Barrie Condon. I am greatly indebted by the close supervision by Dr. Debbie Dewar who (almost) always had an open door for constructive criticism ("I've tried to advise him but he just won't listen"). Her continuing patience through more than the last 3 years deserves credit, especially for all her time spent to make this thesis readable. I would like to thank my fellow PhD students who shared the experience of 3 years of suffering, namely Andrew Crawford, Kerrie Mulloy, and Dr. Tracy Farr who managed to go away early enough. I would also like to acknowledge the support by Tenovus Scotland that involved studies using the MCID image analysis system.

**Declaration.**

I hereby declare that this thesis comprises my own work, unless stated otherwise. In addition, this thesis has not been submitted for awarding any other degree at any other University.

## Summary.

Depression is one of the most common causes of periods of disability. There is evidence suggesting that the serotonin system is involved in the pathophysiology of depression. It has been suggested that synaptic serotonin levels are reduced in depressed patients, and that pharmacological blockade with antidepressants of the serotonin transporter (SERT) would result in alleviated symptoms of depression by enhancing serotonin neurotransmission. Since depression can be treated with antidepressants that target SERT, and a recently discovered 5-HTT gene-linked polymorphic region (5-HTTLPR) of the SERT gene has been shown to predispose to depression, the SERT assumes a key role in depression. Traditionally, depression severity was assessed using psychological testing of patients. However in the last 20 years, neuroimaging techniques using magnetic resonance imaging (MRI) of brain structures and molecular single photon emission computed tomography (SPECT) evolved which appear promising to better understand the pathophysiology at the tissue level. However, preclinical data on abnormalities that involve the serotonin system are limited.

The studies presented in this thesis attempt to shed more light on the feasibility of using the novel MRI technique diffusion tensor imaging (DTI), and SPECT to detect disturbances of the serotonin system. Firstly, in order to elucidate the capabilities of DTI as a research tool in the detection of conceivably mild changes in white matter involving the serotonin system, a mouse model of life-long SERT deficiency was studied. Secondly, in order to validate DTI image processing methodology, a mouse model with reportedly profound myelin dysfunction was examined. Histology techniques were applied to the same mouse brains in order to explore the tissue correlate of the DTI signal changes. Thirdly, as myelin was hypothesised to interact with the serotonin system, *in vitro* autoradiography of SERT in mice with widespread hypomyelination was conducted in order to test this hypothesis. Lastly, in a rat model of SERT depletion, the relative abilities of a well established SPECT radioligand, [<sup>125</sup>I]βCIT (2β-carbomethoxy-3β-(4-iodophenyl)tropane), and a relatively novel SERT tracer, [<sup>123</sup>I]ADAM (2-((2-((dimethylamino)methyl)phenyl)thio)-5-iodophenylamine) were examined using micro-SPECT.

The data demonstrate that DTI did not detect any changes in white matter organisation in SERT-deficient mice. Surprisingly, subtle changes in white matter microstructure were detected in mice that were haploinsufficient for SERT, i.e. heterozygous null mice, displaying a 50 % SERT reduction compared to WT as detected using DTI. On the other

hand, profound hypomyelination was detected using DTI in another mouse model with white matter pathology, and correlations between DTI and histopathological markers were present, indicating that this technology provides good indications of severe pathology, while small changes, if present, may be missed. In addition, the SERT availability appeared not to be affected in mice with widespread hypomyelination. While *post mortem* autoradiography of SERT-depleted rats showed widespread reductions in SERT binding using dedicated specific SERT ligands, micro-SPECT using [<sup>125</sup>I]βCIT and [<sup>123</sup>I]ADAM did not show any differences. [<sup>125</sup>I]βCIT delivered good quality brain SPECT images, however analysis of [<sup>123</sup>I]ADAM scans was hampered by the poor definition of structures.

Thus this thesis provides important information on the feasibility, and sensitivity of current neuroimaging modalities. In addition, methodological flaws and uncertainties in the current literature were identified, which underpins the need for improving and standardising methodological approaches, particularly in SPECT imaging.

## List of publications.

**T. Ruest**, J. M. Edgar, W. Holmes, J.A. Barrie, K.-A. Nave, T. J. Anderson, D. Dewar, "DTI of a mouse model of Pelizaeus-Merzbacher Disease: correlating MR measures with morphometric analyses." 17<sup>th</sup> Scientific Meeting & Exhibition, **International Society for Magnetic Resonance in Medicine**, Honolulu, HI, USA, April 18-24<sup>th</sup>, 2009

Stuart M Cain, **Torsten Ruest**, Sally Pimlott, Jim Patterson, Rod Duncan, Debbie Dewar and Graeme J Sills, "High resolution micro-SPECT scanning in rats using <sup>125</sup>I β-CIT: effects of chronic treatment with carbamazepine" **Epilepsia in press** (2009)

S Cain, **T Ruest**, S Pimlott, D Wyper, J Patterson, D Dewar and G Sills, "SPECT Imaging of Rat Brain Serotonin and Dopamine Transporters *In Vivo*" **Scottish Neuroscience Group Meeting**, Glasgow, UK, August 29<sup>th</sup>, 2008

S Cain, **T Ruest**, S Pimlott, D Wyper, J Patterson, D Dewar and G Sills, "High Resolution micro-SPECT Scanning in Rats Using <sup>125</sup>I β-CIT: Effects of Chronic Treatment with Carbamazepine and Acute Administration of Serotonin and Dopamine Reuptake Inhibitors." What do we want see in brain imaging? **The New York Academy of Sciences Meeting**, London, UK, December 3-4<sup>th</sup>, 2007

**T. Ruest**, J. M. Edgar, W. Holmes, T. J. Anderson, D. Dewar, "Diffusion-Tensor Imaging of a mouse model of Pelizaeus-Merzbacher Disease reveals widespread changes in major white matter tracts" **Scottish Society for Experimental Medicine Meeting**, Glasgow, UK, November 23<sup>rd</sup>, 2007

**T. Ruest**, J. M. Edgar, W. Holmes, T. J. Anderson, D. Dewar, "Diffusion-Tensor Imaging of a mouse model of Pelizaeus-Merzbacher Disease reveals widespread changes in major white matter tracts" **Scottish Neuroscience Group Meeting**, Edinburgh, UK, August 31<sup>st</sup>, 2007

## List of abbreviations.

5-HTTLPR	5-HTT gene-linked polymorphic region
ADAM	2-((2-((dimethylamino)methyl)phenyl)thio)-5-iodophenylamine
AIR	automated image registration
ANOVA	analysis of variance
APP	amyloid $\beta$ -precursor protein
b0	T2-weighted image with little diffusion weighting
Citalopram (R/S) / escitalopram (S)	1-[3-(dimethylamino)propyl]-1-(4-fluorophenyl)-1,3-dihydro-5- isobenzofurancarbonitrile
DAT	dopamine transporter
DTI	diffusion tensor imaging
DWI	diffusion-weighted imaging
EAE	experimental autoimmune encephalomyelitis
EM	electron microscopy
FA	fractional anisotropy
Fluoxetine	( $\pm$ )-n-methyl- $\gamma$ -[4-(trifluoromethyl)phenoxy]benzenepropanamine
Fomblin	perfluoropolyether
FSL	FMRIB software library
GFAP	glial fibrillary acidic protein
i. v.	intravenously
KO	knockout
MAO	monoamine oxidase
Mazindol	5-(4-chlorophenyl)-3,5-dihydro-2h-imidazo[2,1- <i>a</i> ]isoindol-5-ol
MBP	myelin basic protein
MD	mean diffusivity
MDMA	$\pm$ 3,4-methylenedioxymethamphetamine
MRI	magnetic resonance imaging
MS	multiple sclerosis
Multihance	(4RS)-[4-carboxy-5,8,11-tris(carboxymethyl)-1-phenyl-2-oxa-5,8,11- triazatridecan-13-oato(5-)] gadolinate(2-) dihydrogen compound with 1-deoxy-1-(methylamino)-D-glucitol (1:2).
Nomifensine	1,2,3,4-tetrahydro-2-methyl-4-phenyl-8-isoquinolinamine
P	postnatal day
p. i.	post injection

Paroxetine	(3S-trans)-3-[(1,3-benzodioxol-5-yloxy)methyl]-4-(4-fluorophenyl)piperidine
PBS	phosphate buffered saline
PFA	paraformaldehyde
PLP	proteolipid protein
PLPOVR	PLP overexpresser
PMD	Pelizaeus-Merzbacher disease
RA	relative anisotropy
RD	radial diffusivity
ROI	region-of-interest
RT	room temperature
S0	T2-weighted image with no diffusion weighting
SD	standard deviation
SERT	serotonin transporter
SPECT	single photon emission computed tomography
SSRI	selective serotonin reuptake inhibitor
TBSS	tract-based spatial statistics
Tr	diffusion trace
WIN 35, 428	2 $\beta$ -carbomethoxy-3 $\beta$ -(4-fluorophenyl)tropane
WT	wild-type
$\beta$ CIT	2 $\beta$ -carbomethoxy-3 $\beta$ -(4-iodophenyl)tropane
$\varepsilon_i$	$i$ th eigenvector
$\lambda_i$	$i$ th eigenvalue

## Table of contents.

<b>Acknowledgements.....</b>	<b>II</b>
<b>Declaration.....</b>	<b>III</b>
<b>Summary.....</b>	<b>IV</b>
<b>List of publications.....</b>	<b>VI</b>
<b>List of abbreviations. ....</b>	<b>VII</b>
<b>Table of contents. ....</b>	<b>IX</b>
<b>Table of figures.....</b>	<b>XII</b>
<b>Table of tables.....</b>	<b>XX</b>
<b>Chapter 1 - General introduction.....</b>	<b>2</b>
1.1 MRI and DTI.....	3
1.1.1 DTI in studies of brain development.....	10
1.1.2 DTI in studies of white matter pathology. ....	12
1.1.3 DTI in studies of psychiatric and developmental disorders.....	16
1.2 Serotonin.....	19
1.2.1 Events at the serotonergic synapse.....	22
1.2.2 The hippocampus and depression.....	23
1.2.3 Resistance to antidepressants.....	25
1.2.4 SERT in brain development.....	27
1.3 SPECT.....	28
1.3.1 [ <sup>123</sup> I]βCIT SPECT imaging.....	29
1.3.2 [ <sup>123</sup> I]ADAM SPECT imaging.....	34
1.4 Aims of the thesis.....	37
<b>Chapter 2 - Material and methods. ....</b>	<b>40</b>
2.1 DTI.....	40
2.2 Histology on mice with white matter pathology.....	48
2.3 Pilot study to establish a rat model of SERT depletion using MDMA.....	53
2.4 Pilot study to develop protocol for in vitro [ <sup>125</sup> I]ADAM autoradiography.....	70
2.5 In vivo micro-SPECT imaging and ex vivo autoradiography of SERT-depleted rats using the radioligands [ <sup>125</sup> I]βCIT and [ <sup>125</sup> I]ADAM.....	84
2.6 Statistics.....	97
<b>Chapter 3 - DTI of the brain in mice deficient in SERT. ....</b>	<b>99</b>
3.1 Introduction.....	99
3.2 Aims of the study.....	101
3.3 Material and methods.....	102

3.4	Results.....	103
3.4.1	DTI.....	103
3.4.2	Structural analyses.....	139
3.5	Discussion.....	143
3.5.1	Technical considerations.....	144
3.5.2	Callosal length.....	147
3.5.3	DTI data.....	149
3.5.4	Structural analyses.....	155
3.6	Final conclusions.....	156
<b>Chapter 4 - Investigating the structural correlates of DTI measures in the PMD mouse model of white matter pathology. ....159</b>		
4.1	Introduction.....	159
4.2	Aims of the study.....	160
4.3	Material and methods.....	161
4.4	Results.....	161
4.4.1	DTI.....	161
4.4.2	Structural analysis.....	180
4.4.3	Analysis of brain tissue.....	181
4.4.4	Comparison of DTI measures to histopathology.....	194
4.5	Discussion.....	211
4.5.1	DTI data.....	212
4.5.2	Histopathology.....	215
4.6	Final conclusions.....	223
<b>Chapter 5 - Autoradiographic measurements of SERT and DAT densities in a mouse model of PMD.....225</b>		
5.1	Introduction.....	225
5.2	Aim of the study.....	226
5.3	Material and methods.....	227
5.4	Results.....	228
5.5	Discussion.....	237
5.6	Final conclusions.....	239
<b>Chapter 6 - Autoradiographic and micro-SPECT imaging of SERT depletion in rats using the radioligands [<sup>125</sup>I]BCIT and [<sup>125</sup>I]ADAM. ....242</b>		
6.1	Introduction.....	242
6.2	Aims of the study.....	245
6.3	Material and methods.....	246

6.4	Results.....	246
6.4.1	<i>In vivo</i> [ <sup>125</sup> I]βCIT SPECT imaging and <i>ex vivo</i> autoradiography.....	248
6.4.2	<i>In vivo</i> [ <sup>125</sup> I]ADAM SPECT imaging and <i>ex vivo</i> autoradiography. ....	257
6.4.3	<i>In vitro</i> autoradiography.....	272
6.5	Discussion.....	302
6.5.1	<i>In vitro</i> autoradiography.....	303
6.5.2	<i>In vivo</i> SPECT imaging and <i>ex vivo</i> autoradiography. ....	305
6.5.3	Technical considerations.....	309
6.6	Final conclusions.....	313
	<b>Chapter 7 - General discussion.....</b>	<b>315</b>
	<b>References.....</b>	<b>321</b>
	<b>Appendices.....</b>	<b>A</b>

## Table of figures.

Fig. 1-1. Behaviour of spins in a static external magnetic field.....	4
Fig. 1-2. Stejskal-Tanner sequence. ....	5
Fig. 1-3. Illustration of the 3 eigenvalues ( $\lambda_1 - \lambda_3$ ) representing the diffusion coefficients along the 3 eigenvectors ( $\varepsilon_1 - \varepsilon_3$ , pictured as white arrows). ....	7
Fig. 1-4. Illustration of $\lambda_1$ , $\lambda_2$ , $\lambda_3$ , and RD overlaid onto the optic nerve. ....	8
Fig. 1-5. Diffusivity and FA may help to determine changes in the number, size and myelination of fibres, whereas only FA provides information about directionality.....	10
Fig. 1-6. Origin and projection fields of serotonergic fibres.....	20
Fig. 1-7. Different innervation patterns of serotonergic fibres originating from the dorsal and median raphe nuclei.....	22
Fig. 1-8. Mechanisms by which the storage, release, reuptake, and the degradation can be modulated.....	23
Fig. 1-9. Influence of fluoxetine treatment on plasticity and neurogenesis in the hippocampus. ....	24
Fig. 1-10. The human SERT. ....	26
Fig. 1-11. Effects of SERT polymorphism on [ $^{123}\text{I}$ ] $\beta\text{CIT}$ binding to the raphe in abstinent alcoholics and controls.....	33
Fig. 1-12. Example of [ $^{123}\text{I}$ ] $\beta\text{CIT}$ scan in humans. ....	34
Fig. 1-13. Example of [ $^{123}\text{I}$ ] $\text{ADAM}$ scan in humans.....	37
Fig. 2-1. Illustration of the WT FA template creation, coregistration of individual FA maps, generation of group averages and subtraction maps.....	46
Fig. 2-2. TBSS-generated skeleton is used to compensate for mis-registration. ....	47
Fig. 2-3. Determination of axon density on EM images.....	51
Fig. 2-4. Determination of percentage of myelinated axons on EM images.....	52
Fig. 2-5. Rat MDMA treatment paradigm. ....	53
Fig. 2-6. MDMA treatment reduces body weight of treated rats. ....	57
Fig. 2-7. Nonspecific <i>in vitro</i> [ $^3\text{H}$ ]citalopram binding is low. ....	58
Fig. 2-8. Nonspecific <i>in vitro</i> [ $^3\text{H}$ ]WIN 35, 428 binding is low. ....	60
Fig. 2-9. Nonspecific <i>in vitro</i> [ $^{125}\text{I}$ ] $\beta\text{CIT}$ binding is low in SERT-rich, but high in DAT-rich regions.....	63
Fig. 2-10. Nonspecific <i>in vitro</i> [ $^{125}\text{I}$ ] $\beta\text{CIT}$ binding is low in SERT-rich, but high in DAT-rich regions.....	66
Fig. 2-11. Initial results for <i>in vitro</i> [ $^{125}\text{I}$ ] $\text{ADAM}$ pilot autoradiography do suggest specific binding to SERT-rich regions. ....	73

Fig. 2-12. Varying washing times for <i>in vitro</i> [ <sup>125</sup> I]ADAM pilot autoradiography do not show specific binding to SERT-rich regions (1 dip in dH <sub>2</sub> O).	75
Fig. 2-13. Varying washing times for <i>in vitro</i> [ <sup>125</sup> I]ADAM pilot autoradiography do not show specific binding to SERT-rich regions (3 x 30 s in buffer).	76
Fig. 2-14. Varying washing times for <i>in vitro</i> [ <sup>125</sup> I]ADAM pilot autoradiography do not show specific binding to SERT-rich regions (4 x 2 min in buffer).	77
Fig. 2-15. Varying washing times for <i>in vitro</i> [ <sup>125</sup> I]ADAM pilot autoradiography do not show specific binding to SERT-rich regions (2 x 10 min in buffer).	78
Fig. 2-16. Varying washing times for <i>in vitro</i> [ <sup>125</sup> I]ADAM pilot autoradiography do not show specific binding to SERT-rich regions (1 x 1 min followed by 2 x 20 min in buffer).	79
Fig. 2-17. <i>In vitro</i> [ <sup>125</sup> I]ADAM pilot autoradiography does not show specific binding to SERT-rich regions in vehicle-treated rats.	80
Fig. 2-18. <i>In vitro</i> [ <sup>125</sup> I]ADAM pilot autoradiography does not show specific binding to SERT-rich regions in MDMA-treated rats.	81
Fig. 2-19. <i>In vitro</i> [ <sup>125</sup> I]ADAM pilot autoradiography does not show specific binding to SERT-rich regions, nor differences in the level binding in vehicle- vs. MDMA-treated rats.	82
Fig. 2-20. MDMA treatment paradigm.	85
Fig. 2-21. SPECT scanning paradigm.	86
Fig. 2-22. Illustration of voxel intensity and calibration to obtain the activity detected.	87
Fig. 2-23. Alignment of [ <sup>125</sup> I]βCIT SPECT image to an MRI scan.	88
Fig. 2-24. Definition of ROIs on coronal T2-weighted rat MRI and extraction of data from [ <sup>125</sup> I]βCIT SPECT scan.	90
Fig. 2-25. Initial [ <sup>125</sup> I]ADAM SPECT scan coregistration to T2-weighted rat MRI image.	91
Fig. 2-26. Illustration of reconstruction problem using [ <sup>125</sup> I]ADAM.	92
Fig. 2-27. Final [ <sup>125</sup> I]ADAM SPECT to T2-weighted MRI coregistration.	94
Fig. 2-28. Definition of ROIs on coronal T2-weighted rat MRI and extraction of data from [ <sup>125</sup> I]ADAM SPECT scan.	95
Fig. 3-1. Representative slices of individual FA images suggest no visually obvious differences between groups.	104
Fig. 3-2. Representative slices of individual eigenvalue images suggest no visually obvious differences between groups.	105

Fig. 3-3. Representative slices of the FA subtraction map derived from coregistered and group-wise averaged WT and SERT-KO FA images suggest differences in the corpus callosum of SERT-KO mice. ....	106
Fig. 3-4. Representative slices of individual coregistered WT vs. “aberrant” SERT-KO FA maps show structural abnormalities in the corpus callosum of some SERT-KO mice. ....	107
Fig. 3-5. Line intensity profile through the corpus callosum (CC) and external capsule (EC) shows differences in FA between WT, SERT-HT and SERT-KO in the CC.....	108
Fig. 3-6. Measuring the anterioposterior extent of the corpus callosum on individual, unregistered FA images.....	109
Fig. 3-7. The anterioposterior extent of the corpus callosum is abnormally short (< 1 mm) in 1 WT, and 3 SERT-KO mice as measured on individual, unregistered FA images.....	110
Fig. 3-8. Measuring the brain length on individual, unregistered S0 images. ....	111
Fig. 3-9. Brain length is not different between groups as measured on individual, unregistered S0 images. ....	111
Fig. 3-10. Ratio of corpus callosal length to brain length shows low ratios for 2 SERT-KO mice.....	112
Fig. 3-11. Representative slices of the subtraction map derived from coregistered and group-wise averaged FA images suggest no major group differences. ....	114
Fig. 3-12. Representative slices of the subtraction map derived from coregistered and group-wise averaged eigenvalue images suggest no major differences between WT and SERT-KO.....	116
Fig. 3-13. Representative slices of the subtraction map derived from coregistered and group-wise averaged eigenvalue images suggest no major differences between WT and SERT-HT. ....	117
Fig. 3-14. Representative slices of the subtraction map derived from coregistered and group-wise averaged MD images suggest no major differences. ....	119
Fig. 3-15. Representative slices of the subtraction map derived from coregistered and group-wise averaged RD images suggest no major differences. ....	121
Fig. 3-16. Segmentation of corpus callosum on unregistered S0 images. ....	122
Fig. 3-17. Segmentation of hippocampal and anterior commissures, and internal capsule on coregistered S0 images.....	123
Fig. 3-18. FA is unaltered in selected white matter tracts.....	124
Fig. 3-19. $\lambda_1$ is unaltered in selected white matter tracts. ....	125
Fig. 3-20. $\lambda_2$ is reduced in the corpus callosum and anterior commissure of SERT-HT mice.....	126
Fig. 3-21. $\lambda_3$ is unaltered in selected white matter tracts. ....	127

Fig. 3-22. MD is reduced in the corpus callosum of SERT-HT mice.....	128
Fig. 3-23. RD is reduced in the corpus callosum and anterior commissure of SERT-HT mice.....	129
Fig. 3-24. TBSS statistical analysis shows no significant differences in FA (WT vs. SERT-KO).....	130
Fig. 3-25. TBSS statistical analysis shows no significant differences in $\lambda_1$ (WT vs. SERT-KO).....	130
Fig. 3-26. TBSS statistical analysis shows no significant differences in $\lambda_2$ (WT vs. SERT-KO).....	131
Fig. 3-27. TBSS statistical analysis shows no significant differences in $\lambda_3$ (WT vs. SERT-KO).....	131
Fig. 3-28. TBSS statistical analysis shows no significant differences in MD (WT vs. SERT-KO). .....	132
Fig. 3-29. TBSS statistical analysis shows no significant differences in RD (WT vs. SERT-KO).....	132
Fig. 3-30. TBSS statistical analysis shows no significant differences in FA (WT vs. SERT-HT).....	133
Fig. 3-31. TBSS statistical analysis shows significant differences in $\lambda_1$ (blue clusters; WT vs. SERT-HT). .....	134
Fig. 3-32. TBSS statistical analysis shows significant differences in $\lambda_2$ (green clusters; WT vs. SERT-HT). .....	135
Fig. 3-33. TBSS statistical analysis shows no significant differences in $\lambda_3$ (WT vs. SERT-HT).....	136
Fig. 3-34. TBSS statistical analysis shows significant differences in MD (blue clusters; WT vs. SERT-HT). .....	137
Fig. 3-35. TBSS statistical analysis shows no significant differences in RD (WT vs. SERT-HT).....	138
Fig. 3-36. No group differences in whole brain volume were detected.....	140
Fig. 3-37. Volumetric assessment of the hippocampus on unregistered S0 images. ....	141
Fig. 3-38. Volumetric assessment of the caudate-putamen on unregistered S0 images. ...	142
Fig. 3-39. No group differences in the volumes of the caudate-putamen and hippocampus were detected.....	143
Fig. 3-40. Exclusion of DTI data from 1 SERT-HT mouse because of signal abnormalities. ....	148
Fig. 4-1. Representative slices of individual FA images suggest visual differences between groups.....	162

Fig. 4-2. Representative slices of individual eigenvalue images suggest visual differences between groups. ....	163
Fig. 4-3. Representative slices of individual MD and RD images suggest visual differences between groups. ....	164
Fig. 4-4. Representative slices of the subtraction map derived from coregistered and group-wise averaged FA images suggest large group differences between WT and PLPOVR mice. ....	166
Fig. 4-5. Representative slices of the subtraction map derived from coregistered and group-wise averaged eigenvalue images suggest large widespread differences between WT and PLPOVR mice. ....	167
Fig. 4-6. Representative slices of the subtraction map derived from coregistered and group-wise averaged MD images suggest large widespread differences between WT and PLPOVR mice. ....	168
Fig. 4-7. Representative slices of the subtraction map derived from coregistered and group-wise averaged RD images suggest large widespread differences between WT and PLPOVR mice. ....	169
Fig. 4-8. TBSS statistical analysis shows significant differences in FA (blue clusters; WT vs. PLPOVR). ....	170
Fig. 4-9. TBSS statistical analysis shows significant differences in all 3 eigenvalues (blue clusters; WT vs. PLPOVR). ....	171
Fig. 4-10. TBSS statistical analysis shows significant differences in MD and RD (blue cluster; WT vs. PLPOVR). ....	172
Fig. 4-11. Defining ROIs on individual coregistered FA images. ....	173
Fig. 4-12. FA is reduced in all selected white matter tracts of PLPOVR mice. ....	175
Fig. 4-13. $\lambda_1$ is increased in all selected white matter tracts of PLPOVR mice. ....	176
Fig. 4-14. $\lambda_2$ is increased in all selected white matter tracts of PLPOVR mice. ....	177
Fig. 4-15. $\lambda_3$ is increased in all selected white matter tracts of PLPOVR mice. ....	178
Fig. 4-16. MD is increased in all selected white matter tracts of PLPOVR mice. ....	179
Fig. 4-17. RD is increased in all selected white matter tracts of PLPOVR mice. ....	180
Fig. 4-18. No group differences in whole brain volume were detected. ....	181
Fig. 4-19. MBP immunoreactivity is reduced in the corpus callosum of PLPOVR mice. ....	183
Fig. 4-20. MBP immunoreactivity is reduced in all selected white matter tracts of PLPOVR mice. ....	184
Fig. 4-21. APP immunoreactivity is increased in the corpus callosum of PLPOVR mice. ....	185

Fig. 4-22. APP immunoreactivity is increased in all selected white matter tracts of PLPOVR mice.....	186
Fig. 4-23. GFAP immunoreactivity is increased in the corpus callosum of PLPOVR mice. ....	187
Fig. 4-24. GFAP immunoreactivity is increased in all selected white matter tracts of PLPOVR mice.....	188
Fig. 4-25. Haematoxylin-stained cell nuclei density is unaltered in the corpus callosum of PLPOVR mice.....	189
Fig. 4-26. Haematoxylin-stained cell nuclei density is increased in the anterior commissure of PLPOVR mice. ....	189
Fig. 4-27. Haematoxylin-stained cell nuclei density is increased only in the anterior commissure of PLPOVR mice.....	190
Fig. 4-28. Light microscopy reveals astrocyte hypertrophy (black arrows) in the corpus callosum of PLPOVR mice.....	192
Fig. 4-29. Electron microscopy shows almost completely demyelinated axons in the corpus callosum of PLPOVR mice.....	193
Fig. 4-30. Axonal density is increased, while the percentage of myelinated fibres is reduced in PLPOVR mice. ....	194
Fig. 4-31. Comparison of FA index (A) to MBP immunoreactivity (B). ....	196
Fig. 4-32. Scatter plot of diffusion parameter values (FA, $\lambda_1$ , $\lambda_2$ , $\lambda_3$ , MD, RD) vs. MBP immunohistochemistry on individual animals at the level of the anterior commissure (Bregma 0.14 mm). ....	197
Fig. 4-33. Scatter plot of diffusion parameter values (FA, $\lambda_1$ , $\lambda_2$ , $\lambda_3$ , MD, RD) vs. MBP immunohistochemistry on individual animals at the level of the hippocampal fimbria (Bregma -1.46 mm). ....	198
Fig. 4-34. Scatter plot of diffusion parameter values (FA, $\lambda_1$ , $\lambda_2$ , $\lambda_3$ , MD, RD) vs. APP immunohistochemistry on individual animals at the level of the anterior commissure (Bregma 0.14 mm). ....	202
Fig. 4-35. Scatter plot of diffusion parameter values (FA, $\lambda_1$ , $\lambda_2$ , $\lambda_3$ , MD, RD) vs. APP immunohistochemistry on individual animals at the level of the hippocampal fimbria (Bregma -1.46 mm). ....	203
Fig. 4-36. Scatter plot of diffusion parameter values (FA, $\lambda_1$ , $\lambda_2$ , $\lambda_3$ , MD, RD) vs. GFAP immunohistochemistry on individual animals at the level of the anterior commissure (Bregma 0.14 mm). ....	205

Fig. 4-37. Scatter plot of diffusion parameter values (FA, $\lambda_1$ , $\lambda_2$ , $\lambda_3$ , MD, RD) vs. GFAP immunohistochemistry on individual animals at the level of the hippocampal fimbria (Bregma -1.46 mm).....	206
Fig. 4-38. Scatter plot of diffusion parameter values (FA, $\lambda_1$ , $\lambda_2$ , $\lambda_3$ , MD, RD) vs. haematoxylin histology on individual animals at the level of the anterior commissure (Bregma 0.14 mm). .....	209
Fig. 4-39. Scatter plot of diffusion parameter values (FA, $\lambda_1$ , $\lambda_2$ , $\lambda_3$ , MD, RD) vs. haematoxylin histology on individual animals at the level of the hippocampal fimbria (Bregma -1.46 mm).....	210
Fig. 5-1. Nonspecific <i>in vitro</i> [ <sup>3</sup> H]citalopram binding is low. ....	228
Fig. 5-2. Representative sections demonstrate that overall <i>in vitro</i> [ <sup>3</sup> H]citalopram binding to SERT is unaffected in PLPOVR mice (right).....	229
Fig. 5-3. Nonspecific <i>in vitro</i> [ <sup>3</sup> H]WIN 35, 428 binding is low. ....	232
Fig. 5-4. Representative sections demonstrate that overall <i>in vitro</i> [ <sup>3</sup> H]WIN 35, 428 binding to DAT is unaffected in PLPOVR mice (right). ....	233
Fig. 5-5. Haematoxylin staining shows abnormalities in a PLPOVR animal at Bregma -2.80 mm. ....	236
Fig. 5-6. Haematoxylin staining shows abnormalities in a WT animal at Bregma -2.80 mm. ....	236
Fig. 5-7. [ <sup>3</sup> H]WIN 35, 428 autoradiography shows abnormalities in a PLPOVR animal at Bregma 1.10 mm.....	237
Fig. 5-8. [ <sup>3</sup> H]citalopram autoradiography shows abnormalities in a PLPOVR animal at Bregma 1.10 mm.....	237
Fig. 6-1. MDMA treatment reduces body weight of treated rats. ....	247
Fig. 6-2. Representative <i>in vivo</i> [ <sup>125</sup> I] $\beta$ CIT SPECT images of vehicle- (middle) and MDMA-treated animals (right) do not appear different. ....	249
Fig. 6-3. MDMA treatment does not affect <i>in vivo</i> [ <sup>125</sup> I] $\beta$ CIT SPECT-derived binding ratios.....	250
Fig. 6-4. Representative <i>ex vivo</i> sections demonstrate that MDMA treatment (right) causes subtle reductions in [ <sup>125</sup> I] $\beta$ CIT binding.....	252
Fig. 6-5. <i>In vivo</i> [ <sup>125</sup> I] $\beta$ CIT SPECT correlates with <i>ex vivo</i> [ <sup>125</sup> I] $\beta$ CIT autoradiography. ....	256
Fig. 6-6. Representative <i>in vivo</i> [ <sup>125</sup> I]ADAM SPECT images of vehicle- (middle) and MDMA-treated animals (right) after 10 days of maintenance do not appear different, and are of poor quality. ....	257
Fig. 6-7. MDMA treatment does not affect <i>in vivo</i> [ <sup>125</sup> I]ADAM SPECT-derived binding ratios after a 10 day maintenance period.....	258

Fig. 6-8. Representative <i>ex vivo</i> sections demonstrate that overall [ <sup>125</sup> I]ADAM binding is unaffected by MDMA treatment (right) in animals of 10 day maintenance.....	260
Fig. 6-9. Representative <i>in vivo</i> [ <sup>125</sup> I]ADAM SPECT images of vehicle- (middle) and MDMA-treated animals (right) after 30 days of maintenance do not appear different, and are of poor quality. ....	264
Fig. 6-10. MDMA treatment does not affect <i>in vivo</i> [ <sup>125</sup> I]ADAM SPECT-derived binding ratios after a 30 day maintenance period.....	265
Fig. 6-11. Representative <i>ex vivo</i> sections demonstrate that overall [ <sup>125</sup> I]ADAM binding is unaffected by MDMA treatment (right) in animals of 30 day maintenance.....	266
Fig. 6-12. [ <sup>125</sup> I]ADAM batch (2) in vehicle-treated animals demonstrates reasonable binding to SERT-rich regions. ....	270
Fig. 6-13. [ <sup>125</sup> I]ADAM batch (2) in MDMA-treated animals demonstrates weak binding to SERT-rich regions.....	271
Fig. 6-14. Nonspecific <i>in vitro</i> [ <sup>3</sup> H]citalopram binding is low. ....	272
Fig. 6-15. Representative sections demonstrate that MDMA treatment (right) causes widespread reductions in <i>in vitro</i> [ <sup>3</sup> H]citalopram binding to SERT.....	274
Fig. 6-16. Nonspecific <i>in vitro</i> [ <sup>3</sup> H]WIN 35, 428 binding is low. ....	279
Fig. 6-17. Representative sections demonstrate that overall <i>in vitro</i> [ <sup>3</sup> H]WIN 35, 428 binding to DAT is unaffected by MDMA treatment (right). ....	281
Fig. 6-18. Nonspecific <i>in vitro</i> [ <sup>125</sup> I]βCIT binding is low in SERT-rich, but high in DAT-rich regions.....	284
Fig. 6-19. Representative sections demonstrate that MDMA treatment (right) causes widespread reductions in <i>in vitro</i> SERT-specific [ <sup>125</sup> I]βCIT binding (in the presence of mazindol). ....	285
Fig. 6-20. <i>In vitro</i> SERT-specific [ <sup>125</sup> I]βCIT binding correlates with [ <sup>3</sup> H]citalopram binding. ....	289
Fig. 6-21. Nonspecific <i>in vitro</i> [ <sup>125</sup> I]βCIT binding is low in SERT-rich, but high in DAT-rich regions.....	290
Fig. 6-22. Representative sections demonstrate that MDMA treatment (right) causes widespread reductions in <i>in vitro</i> DAT-specific [ <sup>125</sup> I]βCIT binding (in the presence of fluoxetine). ....	291
Fig. 6-23. <i>In vitro</i> DAT-specific [ <sup>125</sup> I]βCIT binding correlates with [ <sup>3</sup> H]WIN 35, 428 binding. ....	295
Fig. 6-24. Representative sections demonstrate that MDMA treatment (right) causes widespread reductions in <i>in vitro</i> [ <sup>125</sup> I]βCIT binding (in the absence of any displacers)..	296
Fig. 6-25. <i>In vitro</i> [ <sup>125</sup> I]βCIT binding correlates with [ <sup>3</sup> H]citalopram binding.....	301

Fig. 6-26. <i>In vitro</i> SERT-specific [ <sup>125</sup> I]βCIT binding ratios correlate with [ <sup>3</sup> H]citalopram binding ratios.....	302
Fig. 6-27. Evaluation of [ <sup>125</sup> I]ADAM batch (3) in vehicle-treated animals of 30 day maintenance. ....	311

## Table of tables.

Table 2-1. Details on mouse tissue processing for DTI image acquisition.....	41
Table 2-2. <i>In vitro</i> autoradiography protocols for [ <sup>125</sup> I]βCIT, [ <sup>3</sup> H]citalopram and [ <sup>3</sup> H]WIN 35, 428.....	55
Table 2-3. MDMA treatment causes widespread reductions in <i>in vitro</i> [ <sup>3</sup> H]citalopram binding to SERT.....	59
Table 2-4. Overall <i>in vitro</i> [ <sup>3</sup> H]WIN 35, 428 binding to DAT is unaffected by MDMA treatment.....	62
Table 2-5. MDMA treatment causes widespread reductions in <i>in vitro</i> SERT-specific [ <sup>125</sup> I]βCIT binding.....	64
Table 2-6. MDMA treatment causes widespread reductions in <i>in vitro</i> DAT-specific [ <sup>125</sup> I]βCIT binding.....	67
Table 2-7. MDMA treatment causes widespread reductions in <i>in vitro</i> [ <sup>125</sup> I]βCIT binding.....	69
Table 2-8. Experimental conditions to develop protocol for [ <sup>125</sup> I]ADAM autoradiography.....	71
Table 2-9. Initial results for <i>in vitro</i> [ <sup>125</sup> I]ADAM pilot autoradiography do suggest specific binding to SERT-rich regions.....	74
Table 3-1. Group comparison of experimental conditions suggests only significant differences between WT and SERT-HT for the period of brain equilibration to RT.....	103
Table 3-2. Agreement between ROI-based approach and TBSS data derived from the statistical analyses between WT vs. SERT-HT.....	139
Table 4-1. Correlation after Spearman of MBP vs. DTI measures (FA, λ <sub>i</sub> , MD, and RD) in the anterior commissure and hippocampal fimbria (sampled at Bregma levels given).....	199
Table 4-2. Correlation after Spearman of APP vs. DTI measures (FA, λ <sub>i</sub> , MD, and RD) in the anterior commissure and hippocampal fimbria (sampled at Bregma levels given).....	204
Table 4-3. Correlation after Spearman of GFAP vs. DTI measures (FA, λ <sub>i</sub> , MD, and RD) in the anterior commissure and hippocampal fimbria (sampled at Bregma levels given).....	207
Table 4-4. Correlation after Spearman of haematoxylin vs. DTI measures (FA, λ <sub>i</sub> , MD, and RD) in the anterior commissure and hippocampal fimbria (sampled at Bregma levels given).....	211
Table 5-1. Overall <i>in vitro</i> [ <sup>3</sup> H]citalopram binding to SERT is unaffected in PLPOVR mice.....	231
Table 5-2. Overall <i>in vitro</i> [ <sup>3</sup> H]WIN 35, 428 binding to DAT is unaffected in PLPOVR mice.....	235

Table 6-1. MDMA treatment causes widespread reductions in <i>ex vivo</i> [ <sup>125</sup> I]βCIT autoradiography. Expressed as ratio region/cerebellum. ....	255
Table 6-2. Overall <i>ex vivo</i> [ <sup>125</sup> I]ADAM autoradiography is unaffected by MDMA treatment in animals of 10 day maintenance. Expressed as ratio region/cerebellum.....	262
Table 6-3. Overall <i>ex vivo</i> [ <sup>125</sup> I]ADAM autoradiography is unaffected by MDMA treatment in animals of 30 day maintenance. Expressed as ratio region/cerebellum.....	268
Table 6-4. MDMA treatment causes widespread reductions in <i>in vitro</i> [ <sup>3</sup> H]citalopram binding to SERT.....	277
Table 6-5. MDMA treatment causes widespread reductions in <i>in vitro</i> [ <sup>3</sup> H]citalopram binding to SERT. Expressed as ratio region/cerebellum. ....	278
Table 6-6. Overall <i>in vitro</i> [ <sup>3</sup> H]WIN 35, 428 binding to DAT is unaffected by MDMA treatment.....	283
Table 6-7. MDMA treatment causes widespread reductions in <i>in vitro</i> SERT-specific [ <sup>125</sup> I]βCIT binding. ....	288
Table 6-8. MDMA treatment causes widespread reductions in <i>in vitro</i> DAT-specific [ <sup>125</sup> I]βCIT binding. ....	294
Table 6-9. MDMA treatment causes widespread reductions in <i>in vitro</i> [ <sup>125</sup> I]βCIT binding. ....	299
Table 6-10. MDMA treatment causes widespread reductions in <i>in vitro</i> [ <sup>125</sup> I]βCIT binding. Expressed as ratio region/cerebellum.....	300

**Chapter 1 - General introduction.**

## **Chapter 1 - General introduction.**

In the past two decades, the ability for early diagnosis of disease processes in the human body has advanced tremendously. In large part, imaging techniques have contributed to this effect by opening a window to the normal and abnormal structure and functioning of the human body, including the brain. Using molecular imaging techniques, like SPECT, diseases like Alzheimer's can be evaluated before structural changes, detectable through MRI, may occur. This is desirable, as early treatment of diseases may positively influence the outcome. In SPECT, a radioactively labelled tracer, i.e. a compound mimicking the naturally occurring compound whose function is to be evaluated, will be injected in, or inhaled by, the subject. Just like the natural compound, the tracer will interact with receptive molecules in the brain, allowing insights into its functioning, without interfering with metabolic processes.

In contrast to molecular imaging, MRI has proved to give insights in structures within the body at spatial resolutions of below 1 mm. Taking advantage of naturally occurring isotopes of certain atoms, such as  $^1\text{H}$ , and  $^{13}\text{C}$ , these nuclei can be detected, and their relaxation properties converted into a signal and subsequently into an image. Furthermore, since different tissues have different physical properties, like water content, they can clearly be distinguished from adjacent structures. MRI is also very versatile, so that modifications of standard scanning protocols allow, for instance, measuring the diffusion of water molecules within a sample by a system equipped with diffusion sensitising gradients. This method, DTI, takes advantage of physical barriers within the central nervous system, usually comprising myelinated white matter, restricting the diffusion of these water molecules.

Both, SPECT and MRI imaging technologies have advanced with respect to the resolution that can be achieved, making it feasible to scan small animals such as rodents. In addition, genetic tools have emerged that allow to modify gene expression in the living animal. For instance, certain genes can be deleted, or transgenes inserted that cause absence of a protein, or, for example, its overexpression, respectively. Thus, the pathology including its progression over time, in which a certain protein is involved, can be studied in detail using SPECT and MRI neuroimaging. The presented thesis applied both DTI and SPECT to elucidate abnormalities in the rodent brain that particularly involved the serotonin system. In a mouse model of depression (chapter 3, page 98), we aimed to elucidate the effects of

genetic deletion of the SERT gene on white matter maturation including its connectivity using DTI. DTI methodology was then evaluated in a mouse model of diffuse hypomyelination (chapter 4, page 158). Subsequently, the mouse model of hypomyelination was evaluated for differences in monoaminergic terminal densities using SERT and DAT autoradiography (chapter 5, page 224). Lastly, using SPECT imaging in a rat model of neurotoxin-induced SERT depletion, the relative capabilities of 2 SERT ligands to measure these induced changes in SERT were evaluated (chapter 6, page 242).

The following introduces MRI and DTI, and its application in human pathology, but also its use in preclinical studies. Following this, the serotonergic system and its role in disease, particularly in depression, is reviewed. Subsequently relevant literature on SPECT, with special emphasis on imaging SERT in humans and animals with the ligands used in this study, is summarised.

### **1.1 MRI and DTI.**

Proton MR imaging takes advantage of a property of hydrogen atoms within water molecules of tissues, called spin. These spins may act as a miniature magnet. After placing a sample in an MRI scanner, the individual spins within that sample, and therefore the net magnetisation vector, align with the static magnetic field generated by the MRI system (Fig. 1-1, a). After, for example, the application of a 90° excitation pulse as it occurs in a Stejskal-Tanner diffusion weighted spin echo imaging sequence (see below) (Stejskal and Tanner, 1965), the net magnetisation vector flips (Fig. 1-1, b) into the x, y plane (Fig. 1-1, c), and precesses about the direction of the static external magnetic field (Fig. 1-1, d). Subsequently, the spins dephase and recover with an exponential transverse T2 time constant (Fig. 1-1, e), whereas a slower longitudinal T1 time constant relative to T2 can be measured during the process of realignment of the spins with the static external magnetic field (Fig. 1-1, f). T2 decay occurs because of the varying magnetic field that individual spins experience causing them to dephase so that eventually no magnetisation is detectable longitudinally (for review of MRI basics see Hornak *et al.* <http://www.cis.rit.edu/htbooks/mri> (Hornak, 1996-2008)).

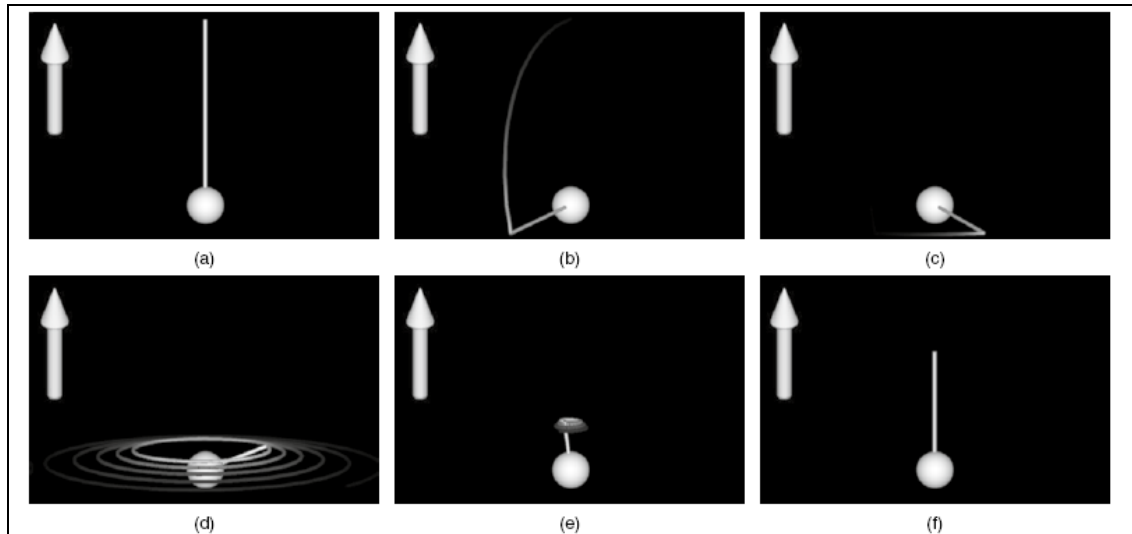


**Fig. 1-1. Behaviour of spins in a static external magnetic field.**

The direction of the external magnetic field is shown in each individual image (a-f) on the left side as a white arrow. The net magnetisation vector is depicted as a line originating from a sphere, representing the hydrogen atoms.

- a) The net magnetisation vector (i.e. all spins) of a sample is aligned with the static external magnetic field generated by the MRI system.
- b) Net magnetisation vector is flipped in the x, y plane after application of a  $90^\circ$  excitation pulse.
- c) Net magnetisation vector precesses about the direction of the static external magnetic field.
- d) The individual spins dephase because of the different magnetic field they experience causing transverse T2 decay.
- e, f) The net magnetisation vector recovers longitudinally with a T1 time constant to align again with the static external magnetic field.

Taken from Johansen-Berg *et al.* (Johansen-Berg and Behrens, 2009).

Using a spin echo sequence that has been modified to be sensitive to the diffusion of water by the addition of 2 diffusion sensitising gradients flanking the  $180^\circ$  refocusing pulse, the net magnetisation vector is first flipped to the x, y plane in the scanner reference frame using a  $90^\circ$  excitation pulse. Subsequently, the first diffusion sensitising gradient with magnitude G is switched on for a diffusion duration  $\delta$  causing the individual spins to dephase. This is followed by a  $180^\circ$  refocusing pulse at TE/2 (TE = echo time) and the application of another diffusion sensitising gradient of identical duration  $\delta$  and magnitude G to the first causing a reversal of the dephasing. In the case that no water molecules were diffusing in the diffusion separation time  $\Delta$ , i.e. the time between the onsets of the 2 diffusion sensitising gradients, the signal obtained will be identical because all spins will have the same phase at TE, i.e. no signal is lost. However if water molecules diffused in the time  $\Delta$ , the phase of their spins will not accrue with the spins of the water molecules that did not move, thus leading to an attenuation of the total signal obtained at TE. The difference in signal is the quantitative measure of diffusion along that particular diffusion direction. This is called the Stejskal-Tanner sequence and is depicted in Fig. 1-2. In order

to fully reconstruct the diffusion tensor, the diffusion along at least 6 directions needs to be sampled (Johansen-Berg and Behrens, 2009).

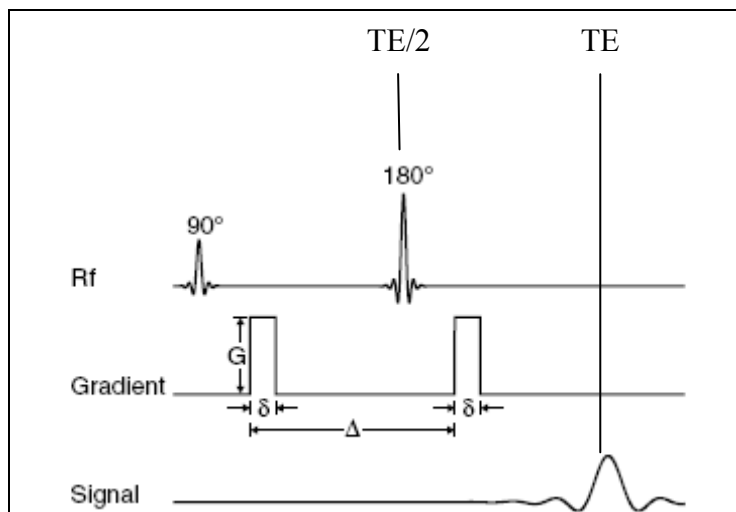


**Fig. 1-2. Stejskal-Tanner sequence.**

A spin echo sequence is defined as flipping the net magnetisation vector by 90° excitation pulse with a subsequent 180° refocusing pulse. This sequence has been made sensitive to diffusion by adding 2 gradients flanking the 180° refocusing pulse. The 90° excitation pulse flips the net magnetisation vector into the x, y plane, and the subsequent application of a gradient of magnitude G and duration  $\delta$  causes spin dephasing. After a duration TE/2 (TE = echo time), 180° refocusing pulse is applied followed by a gradient of identical magnitude and duration as the first one. This causes a reversal of the dephasing with an expected spin echo at exactly TE. In case that no water molecules diffused during the diffusion separation time  $\Delta$ , all spins accrue in phase and no signal is lost at TE. However if water molecules were diffusing in  $\Delta$ , not all spins will be in phase at TE causing a loss of signal. The difference in signal is the quantitative measure of diffusion along that particular diffusion direction.

Adapted from Johansen-Berg *et al.* (Johansen-Berg and Behrens, 2009).

DTI is a relatively novel MRI technique designed to measure the diffusion of water in samples. Due to its unique structural properties within the brain, white matter and its integrity can be measured and assessed using parameters derived from DTI. The measures that can be extracted from the DTI dataset consist of the 3 eigenvalues ( $\lambda_1 - \lambda_3$ ) that represent the diffusion coefficients measured along the 3 eigenvectors ( $\varepsilon_1, \varepsilon_2,$  and  $\varepsilon_3$ ). In grey matter, these 3 eigenvalues are of similar magnitude ( $\lambda_1 \approx \lambda_2 \approx \lambda_3$ ) indicating that the diffusion of water is not preferred in any direction. However, in case of white matter tracts, water diffusion within the tract is restricted along the axon. The first eigenvalues, also known as the axial diffusivity, describes the diffusion coefficient along the direction with the least restriction, i.e. parallel to the direction of axons, and the other 2 eigenvalues diffusion that perpendicular to the tract (Fig. 1-3). This restriction of water diffusion gives rise to diffusion anisotropy, which can be quantified by the fractional anisotropy (FA). FA can be computed (formula see below) as the ratio of the 3 eigenvalues, and reflects the degree of directionality within one given tract.

$$FA = \sqrt{\frac{3}{2} \left( \frac{(\lambda_1 - MD)^2 + (\lambda_2 - MD)^2 + (\lambda_3 - MD)^2}{\lambda_1^2 + \lambda_2^2 + \lambda_3^2} \right)},$$

where the mean diffusivity (MD) is defined as the average of all 3 eigenvalues. The sum of the 3 eigenvalues is referred to as the diffusion trace (Tr) (Basser and Pierpaoli, 1996).

$$MD = \frac{\lambda_1 + \lambda_2 + \lambda_3}{3} = \frac{Tr}{3}.$$

Similar to FA, the relative anisotropy (RA) is an indicator of diffusion anisotropy that is preferred by some groups over FA (Song et al., 2002). As this parameter is referred to in other publications cited in this thesis, it is necessary to introduce this parameter here. However as signal-to-noise is reported to be superior in FA images (Hasan et al., 2004), the FA is used in this thesis to quantify diffusion anisotropy.

$$RA = \sqrt{\left( \frac{(\lambda_1 - MD)^2 + (\lambda_2 - MD)^2 + (\lambda_3 - MD)^2}{3 * MD} \right)}.$$

In grey matter, where limited diffusion anisotropy is present, an FA value close to 0 is expected, while in white matter the FA values are expected to be nearer to 1 indicating a preferred direction of water diffusion.

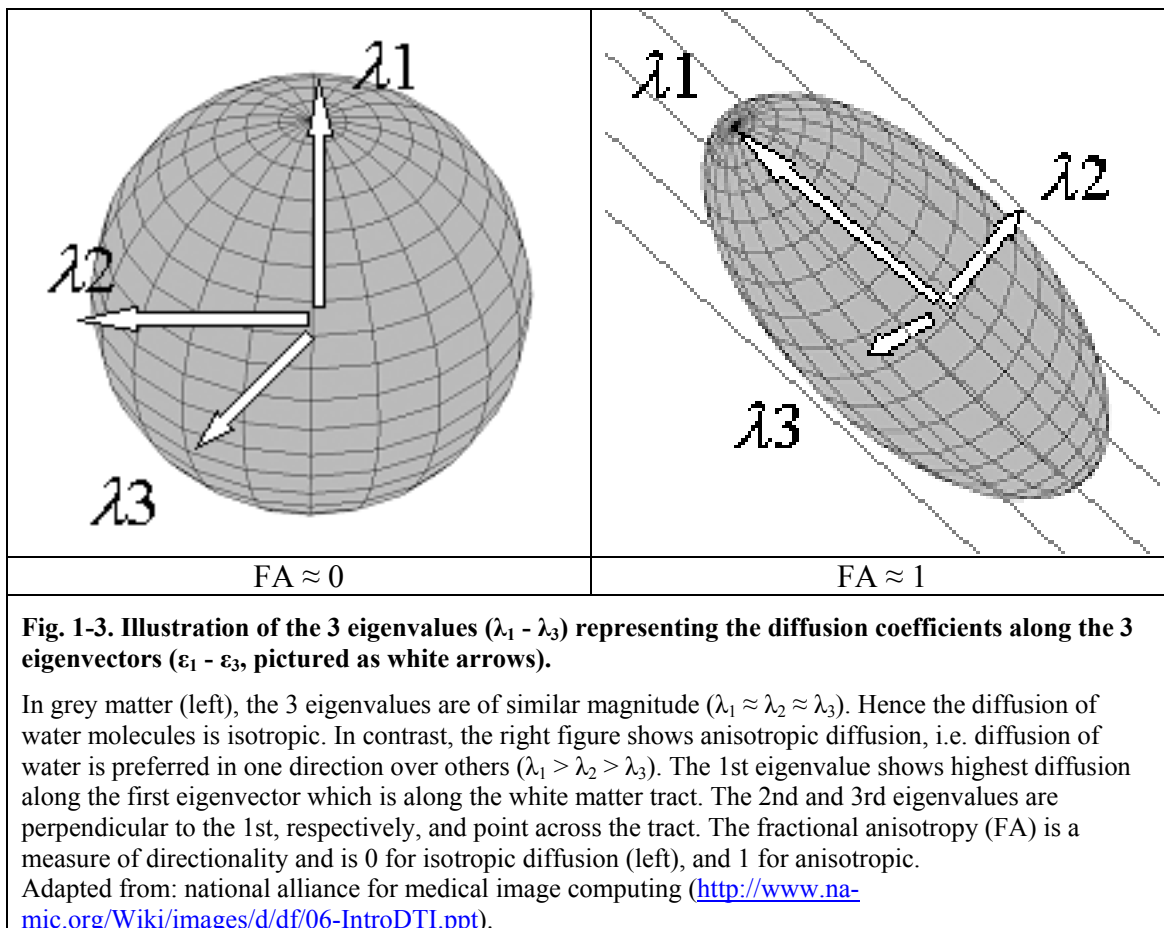
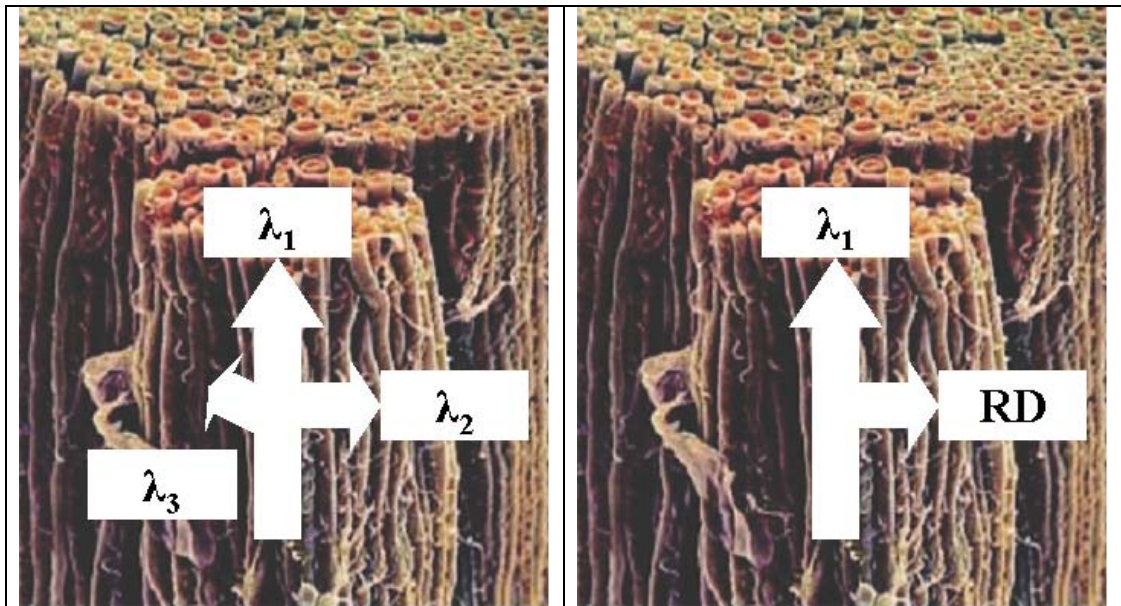


Fig. 1-4 highlights the relationship between the 3 eigenvalues overlaid onto a high magnification image of myelinated axons of the optic nerve. The perpendicular diffusivities can be pooled to generate a value for the radial diffusivity (RD), which is the average of  $\lambda_2$  and  $\lambda_3$  (Song et al., 2002):

$$RD = \frac{(\lambda_2 + \lambda_3)}{2}.$$



**Fig. 1-4. Illustration of  $\lambda_1$ ,  $\lambda_2$ ,  $\lambda_3$ , and RD overlaid onto the optic nerve.**

Left: 1st eigenvalue is measured along the tract, while  $\lambda_2$  and  $\lambda_3$  are the diffusion coefficients perpendicular to  $\lambda_1$ .

Right:  $\lambda_2$  and  $\lambda_3$  eigenvalue were averaged to form RD.

Adapted from Brian Wandell (<http://white.stanford.edu/~brian/papers/mri/2007-Wandell-HBM-Keynote.pdf>).

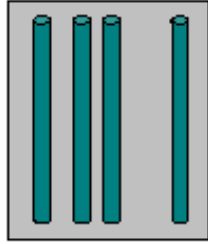
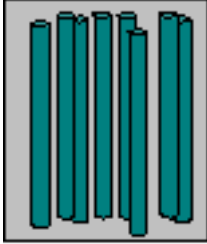
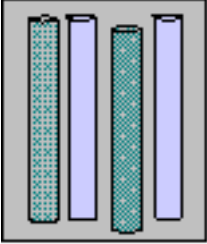
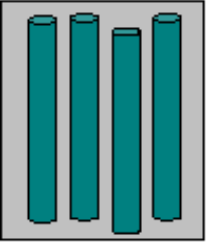
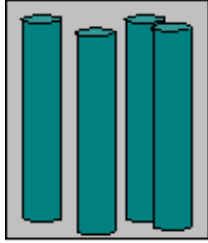
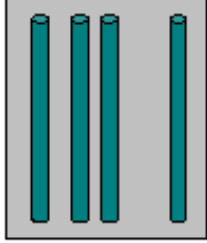
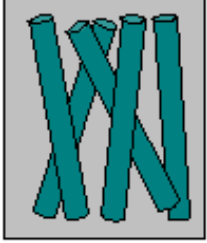
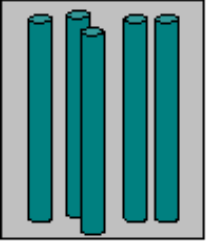
Fig. 1-5 summarises the influence of axon counts (A), fibre calibre (B), myelin (C), and fibre coherence (D) on FA and diffusivity. Increasing the number of fibres is reducing the diffusivity and increasing the FA. The mechanism by which this occurs appears to be through the reduction of the extracellular matrix, higher parallel organisation and higher axon packing. In support of this, it has been reported that in the pathology of multiple sclerosis, axon count strongly correlated with FA and MD (Schmierer et al., 2007). In addition, during brain development the extracellular space decreases that is associated with FA increases and MD reductions (Jito et al., 2008). However in both cases it is worth mentioning that myelin plays a role as well, whose effects cannot be easily separated from that of the fibre counts.

In addition, the axon diameter (excluding the myelin sheath) has been identified to correlate with  $\lambda_1$  (from DWI) suggestive of faster diffusion along the axon in larger calibre fibres. Perpendicular diffusion (from DWI) appeared not to be associated with axon diameter (Schwartz et al., 2005). Further support for higher anisotropy in smaller calibre fibres comes from a DWI study using giant squid axons, in which the FA was 0.11, with rapid perpendicular and longitudinal diffusivities indicating almost isotropic diffusion (Beaulieu and Allen, 1994). In the lamprey spinal cord using DWI, regions can be

identified with increasing anisotropy that corresponded to small mean diameter axons which are associated with denser axon packing (Takahashi et al., 2002).

Several developmental studies suggest that the appearance of myelin during brain development has a modulatory effect on FA and diffusivity. In the premyelination period, i.e. the period just before myelination takes place, significant anisotropy can be measured in the rat corpus callosum, while the subsequent appearance of myelin goes along with increasing FA and reductions in MD (Jito et al., 2008). Likewise, the myelin-deficient shiverer mice displayed lower FA and greater MD, however after receiving neuronal precursor cell transplants displayed increasing FA in the corpus callosum as these precursor cells developed into myelin producing oligodendrocytes (Nair et al., 2005). Finally along this line, mice treated with cuprizone causing selective demyelination of the corpus callosum, displayed decreasing anisotropy and increasing Tr, both of which normalised after ceasing the drug treatment coinciding with ongoing remyelination (Song et al., 2005).

There is some evidence indicating that the fractional anisotropy is sensitive to axonal alignment, or the coherence of fibres – a condition where diffusivity fails to distinguish between highly coherent fibres and disorganised axons. The mean diffusivity (in fact Tr), with exception of the cortical grey matter relative to other brain regions, is homogeneous across grey and white matter (Pierpaoli and Basser, 1996). However anisotropy measures were reported to be lower in white matter regions, where fibres merge (Pierpaoli et al., 1996), or cross (Pierpaoli et al., 2001).

A) Number of fibres		C) Myelination of fibres	
			
High diffusivity Low FA	High FA Low diffusivity	High diffusivity Low FA	High FA Low diffusivity
B) Size of fibres		D) Directionality of fibres	
			
High diffusivity Low FA	High FA Low diffusivity	Low FA Same diffusivity	High FA Same diffusivity
<p><b>Fig. 1-5. Diffusivity and FA may help to determine changes in the number, size and myelination of fibres, whereas only FA provides information about directionality.</b></p> <p>A) Axonal count correlates with FA and diffusivity, so that axonal degeneration causes a reduction of FA and an increase in diffusivity by increasing extracellular space and less dense axonal packing.</p> <p>B) Larger calibre fibres reduce the probability of water molecules to diffuse anisotropically within a given diffusion time, thus reducing FA and increasing the diffusivity compared to small calibre fibres.</p> <p>C) Myelin has a modulatory role with regard to FA causing an increase, while the diffusivity decreases, i.e. by reducing extracellular spacing and reducing diffusion perpendicular to the tract because of the myelin lamellae.</p> <p>D) Coherence of fibres can be detected by FA, while diffusivity remains the same. This is the case where fibres cross or merge, causing a reduction in FA.</p> <p>Adapted from: national alliance for medical image computing (<a href="http://www.na-mic.org/Wiki/images/d/df/06-IntroDTI.ppt">http://www.na-mic.org/Wiki/images/d/df/06-IntroDTI.ppt</a>).</p>			

### 1.1.1 DTI in studies of brain development.

DTI is proving to be a valuable tool in order to assess white matter integrity, for instance in neuropathologies that will be discussed later, but is also used to observe changes in tissue composition in cortical grey matter during brain development. DTI can be applied either *in vivo* or *ex vivo* to *post mortem* samples. For instance, DTI was used to study the development of the cerebral cortex in humans, where diffusion anisotropy was observed to increase up to the 26 - 28th week of gestation. This was suggested to reflect the radial organisation of glial cells along which neurons migrate from the ventricular zone to their

## Chapter 1 - General introduction.

target tissue (Gupta et al., 2005, McKinstry et al., 2002). Following the migration period, the radial glial cells transform into different cell types, for instance astrocytes (Voigt, 1989), and thereby tissue anisotropy decreases. Likewise in rats, development of deep cortical layers was associated with a decrease in FA from postnatal day 3 (P3) to P6. In addition, MD also decreased within this time frame in deep, and superficial cortical layers. These findings were paralleled with increases in microtubule-associated protein 2 immunoreactivity indicative of an increase in the number of neurons, and a decrease in radial glial cells as identified by nestin immunofluorescence (Sizonenko et al., 2007).

In the cerebellum of freshly aborted human foetuses, FA values increased and reached its maximum at 28 weeks of gestation and decreased thereafter. This process was associated with an increase in glial fibrillary acidic protein (GFAP) immunoreactivity, a marker for radial glial cells (but also activated astrocytes). The middle cerebellar peduncles showed increasing FA values over the whole study period (up to 37 weeks of gestational age) that was accompanied by increases in myelin basic protein (MBP) expression. MBP is a marker for compact myelin therefore suggesting that increases in diffusion anisotropy may be due to increasing myelin content ensheathing the axon as brain development progresses (Saksena et al., 2008). More evidence for the involvement of myelin in diffusion anisotropy came from rat DTI studies. Rat brain development was examined over the first 10 postnatal weeks, in which an increase in myelin content was correlated with increases in FA. In turn, increases in FA were paralleled with decreases in MD (Jito et al., 2008). That FA is a marker that reflects white matter maturation is supported by a recent study in mice that explored the magnitude of change in FA in several tracts including the corpus callosum. Compared to young mice (< P10), adolescent mice (P10 - P45) showed an increase in anisotropy of 54 %, and relative to the adolescent mice, old mice (> P45) displayed another increase in FA of 82 %. This study also highlights the sensitivity of DTI to maturational processes in the brain such as the transformation of radial glial into other cell types, which was indicated by a loss of anisotropy (52 %) in cortical areas of adolescent compared to young mice (Verma et al., 2005).

Based on the observation that increased anisotropy in human cerebral white matter exists before the onset of myelination, it was hypothesised that not only myelin, but also increases in fibre diameter, and decreases in extracellular space between fibres could contribute to diffusion anisotropy during brain development (Huppi et al., 1998). In support of this, the corpus callosum of the developing rat brain already displays modest FA

values in the absence of myelin, as shown by the lack of MBP immunoreactivity (0.37 on P1 compared to 0.54 on P10). Furthermore, an increase in anisotropy was negatively correlated with extracellular space, suggesting denser axon packaging, and a positive correlation was found between FA and the number of unmyelinated fibres. However, overall the factor making the largest contribution to tissue anisotropy in development was identified to be the area occupied by the myelin sheath (Jito et al., 2008).

### 1.1.2 DTI in studies of white matter pathology.

#### Multiple sclerosis.

Studies of brain development have tremendously improved our understanding of what DTI measures reflect at the level of brain tissue. However, the power of this imaging technique in the characterisation of white matter diseases combined with the possibility to assess intervention as disease progresses has raised interest in its therapeutic application. The prime example of diseases that involve white matter degeneration is that of multiple sclerosis (MS). Susceptibility to MS is inherited and involves parts of the immune system, however the exact cause of how MS evolves is unknown. It is thought that MS may be induced by an infection of microorganisms that are associated with agents mimicking myelin components, hence the immune system fails to distinguish between self and foreign causing myelin to be destroyed (Purves et al., 2001, Trapp and Nave, 2008). Axonal pathology in MS is suggested to be the key pathological feature leading to long-term disability, with smaller calibre axons, such as they are in the optic nerve, being more vulnerable to the autoimmune attack than larger fibres (Evangelou et al., 2001). As disease progression is initially asymptomatic, neuroimaging may provide the only means to monitor disease and treatment outcome (Trapp and Nave, 2008).

Early signs of MS include optic neuritis that was shown to influence DTI parameters in the optic nerve. The most affected parameter early in the disease (within 30 days of optic neuritis onset) was  $\lambda_1$ , which displayed a reduction indicating changes in this parameter to be a potential marker for early disease features. This was in contrast to changes in MD and RD, which only became abnormal after later in the disease (1 year after onset), when all three parameter,  $\lambda_1$ , MD, and RD, increased (Naismith et al., 2009). Four years after presentation of patients with acute optic neuritis, MD and RD were significantly increased, while FA was decreased, when compared to normal controls. However,  $\lambda_1$  remained unchanged, which suggests that this parameter is more useful in the early phase of the disease (Kolbe et al., 2009). In patients with optic neuritis, the FA in the normal appearing

corpus callosum was followed longitudinally over a period of several years (> 3 years, mean duration). All patients displayed lower FA values in the splenium of the corpus callosum compared to controls, however only those patients who went on to definitely develop clinical MS displayed further reductions in FA over time. MD was not sensitive enough to detect any differences between patients and controls (Bester et al., 2008). In a separate study of MS patients with less than 4 years disease duration, parts of the corpus callosum were found to have significantly elevated  $\lambda_1$  and RD values, while FA was decreased (Roosendaal et al., 2009), which indicates a degree of consistency between different clinics in DTI measurements in MS.

The most commonly used animal model of MS is experimental autoimmune encephalomyelitis (EAE), which is induced by immunisation of the animal with agents containing myelin, or its proteins. As in the human condition this model also displays axonal pathology and a higher vulnerability of small calibre optic nerve axons over others. Three months post-immunisation, mice had symptoms of disease and displayed reductions in RA and  $\lambda_1$ , and RD was increased only in the optic nerve and optic tract compared to control animals. Other tracts, including the corpus callosum and anterior commissure, remained unaffected (Sun et al., 2007).

Changes in DTI parameters in the rodent brain following induction of EAE appear to be somewhat limited to the optic nerve and tract (Sun et al., 2007, Wu et al., 2007). However, numerous studies have used DTI to assess white matter changes in the spinal cord following induction of EAE. In all of these studies, the RD was increased, while  $\lambda_1$  and FA (or RA where appropriate), were reduced thus indicating a high level of consistency between different studies and laboratories when applying DTI to assessing spinal cord pathology in the EAE model (Budde et al., 2008, DeBoy et al., 2007, Kim et al., 2006).

Interestingly in the light of changes in the corpus callosum being an early predictor for human MS, callosal changes are observed in another model of demyelination induced by cuprizone treatment. Mice fed on a cuprizone-rich diet, a toxin that selectively leads to demyelination of the corpus callosum, showed increases in RD and decreases in RA but unchanged  $\lambda_1$ . Remyelination, as it occurs in early (relapsing remitting) human MS, is achieved when cuprizone treatment is ceased. In parallel, abnormal DTI parameters normalise again (Song et al., 2005).

### **Pelizaeus-Merzbacher disease.**

While considerable efforts have been applied to elucidating DTI parameter changes in MS and animal models of this disease, only a few studies have used DTI to investigate other white matter diseases and in particular the corresponding animal models. Work on an animal model of human Pelizaeus-Merzbacher disease (PMD) is presented later in this thesis, however this disease has received minimal attention in DTI studies. PMD is an X-chromosome-linked disease that affects the proteolipid protein gene (*PLP1*) located on this chromosome (for review see Griffiths *et al.* (Griffiths et al., 1998)). PLP is the most abundant myelin protein constituting about 50 % of total myelin protein (Karim et al., 2007). The disease is characterised by diffuse hypomyelination, and may be caused by mutations such as missense mutations in or deletions of the *PLP1* gene. The most common cause however is the duplication of the *PLP1* gene leading to overexpression. The variety of causes is reflected by the different phenotype severities in humans. A commonly used mouse model of PMD is the *jimpy* mouse, in which a mutation leads to the deletion of an exon (exon 5) of the *Plp1* gene (Griffiths et al., 1998). Other mouse models have been generated that overexpress *Plp1*. Homozygous transgene carriers in the #66 strain carry additional 14 copies, while the #72 mice, used in this thesis (PLPOVR), carry 6 additional *Plp1* transgenes. The *Plp1* gene dosage appears to influence the phenotype severity. Thus, while the #72 mouse strain survives for 4 months, #66 strain mice die earlier at 2 months (Readhead et al., 1994).

Early studies of PMD involved the use of conventional T2-weighted MRI, where a tigroid pattern, resembling the skin of a leopard, was observed. This described the patches of normal-appearing white matter which alternated with patches of high signal intensity indicative of abnormal white matter (Caro and Marks, 1990, Nezu et al., 1998). Longitudinal studies of a single human case using conventional MRI (T1-, and T2-weighted imaging), conducted annually between the age of 7 and 9 (thus 3 conventional scans), confirmed the non-progressive nature of initially observed lesions, which is indicative of hypomyelination. A diffusion-weighted imaging (DWI, not DTI) study followed, which detected diffusion anisotropy in fibre tracts of the brain in this PMD patient that raised the question as to the source of the diffusion signal as it was believed that the white matter in these patients was disrupted (as determined by T1- and T2-weighted imaging). In addition, it was thought that this novel technique, DWI, might help to distinguish de- from dysmyelination (Ono et al., 1994). In mouse models of demyelination (the *twitcher* mouse modelling Krabbe's disease) and dysmyelination (the

*jimpy* mouse modelling PMD), diffusion anisotropy in the optic nerve seemed to be unaffected in the *jimpy* mouse, but reduced in the *twitcher* mouse relative to controls (Ono et al., 1995). A clinical case study followed that compared a PMD patient to a patient with Krabbe's disease using DWI that confirmed the distinct diffusion anisotropy characteristics between demyelination and dysmyelination (Ono et al., 1997). Surprisingly, apart from a report in poster form, there is no peer-review published article on the use of DTI in PMD patients. However this preliminary report demonstrated a loss of contrast between white and grey matter of PMD patients compared to controls using T2-weighted MRI. In addition, there were marked reductions in FA and MD in the internal capsule of PMD patients (Laukka et al., 2006). In *jimpy* mice, the  $\lambda_1$ , MD, and RD were increased, while reduced FA indicated loss of myelin compared to wild-type (WT) (Harsan et al., 2007). Another indication that DTI might have value in distinguishing between different forms of white matter pathology was suggested by comparing the results from *jimpy* mice to those of oligo-TKK mice. Oligo-TKK mice express an enzyme that, upon injection of the appropriate substrate, catalyse the reaction to produce an oligodendrocytic toxin, which results in demyelination (Harsan et al., 2006). Male oligo-TKK mice exhibited a reduction in  $\lambda_1$  in the corpus callosum, however, in male *jimpy* mice this parameter was increased compared to controls. Oligo-TKK mice did exhibit only little astrocytosis, while in *jimpy* mice it was massive, so the authors concluded that astrocyte hypertrophy could explain the contrasting changes in  $\lambda_1$  observed in the 2 different mouse models. Aquaporin, a water channel that may facilitate water exchange, was found to be increased in *jimpy* mice, and was mainly located at the extensions of astrocytes. Thus this may indicate an astrocytic contribution (through aquaporin expression) to the  $\lambda_1$  diffusion coefficient (Harsan et al., 2007).

### **The *shiverer* mouse model of demyelination.**

The *shiverer* mouse model of dysmyelination has severe hypomyelination due to deletion of the gene for MBP (Griffiths et al., 1998), but increased gliosis and numbers of macrophages are not present compared to controls (Bird et al., 1978). MBP is the second most abundant myelin protein, constituting about 30 % of total myelin protein (Karim et al., 2007) At least until the age of 3 months, loss of axons in the spinal cord and inflammation appear to be absent, however the mice die at about 4 months of age (Andrews et al., 2006). The *shiverer* mouse is therefore a good model to study the effect of myelin-deficiency per se on DTI-derived parameters. The loss of myelin integrity in this mouse model was indicated by reductions in values of FA or RA, and increased RD (or increased perpendicular diffusion coefficients  $\lambda_2$  and  $\lambda_3$ ) consistent with greater diffusivity

of water molecules perpendicular to the tract (Nair et al., 2005, Song et al., 2002, Tyszka et al., 2006). *Shiverer* mice do not display axonal pathology therefore the unchanged  $\lambda_1$ , observed in these mice, was hypothesized to identify axonal injury, while the changes in RD reflect the loss of myelin (Song et al., 2002). However in a study of *shiverer* mice by another group,  $\lambda_1$  was increased and therefore the interpretation of  $\lambda_1$  needs further clarification (Tyszka et al., 2006).

### 1.1.3 DTI in studies of psychiatric and developmental disorders.

#### Substance abuse.

Studies of brain development and white matter disease indicate that DTI appears to be sensitive enough to detect rapid changes during brain maturation, and diseases with profound effects on the integrity of white matter. However is the technique able to provide insight into subtle changes in the assembly of fibres that may occur in psychiatric disorders or substance abuse? There is accumulating evidence in humans that drug abuse, including heroin, cocaine, ecstasy and alcohol lead to reductions in diffusion anisotropy, thus suggesting a detrimental effect of these drugs on various brain regions. In heroin dependence, frontal cortical areas displayed a loss in FA, which in the right frontal subgyral white matter was negatively associated with duration of dependency (Liu et al., 2008). Differences in FA between short-term ecstasy users and ecstasy naïve controls were found in the frontoparietal white matter (de Win et al., 2008). Axonal injury was suggested in ecstasy users compared to naïve controls in anterior parts of the corpus callosum due to reductions in  $\lambda_1$ , while all other parameters were unaltered (FA, MD, RD). In addition, reductions in  $\lambda_1$  in the corpus callosum correlated with behavioural test results in a decision-making paradigm, in which ecstasy users performed worse than controls. These fibres project to the medial prefrontal cortex, and the frontal cortex is implicated in decision-making (Moeller et al., 2007).

Cocaine abuse has been studied using DTI and in similarity to heroin, the duration of abuse was associated with reductions in FA in the anterior parts of the corpus callosum. Moreover, this loss of white matter integrity was correlated with several cognitive tests, i.e. negatively with impulsivity, and positively with measures of the ability to distinguish between 2 very similar stimuli, again implying compromised function in prefrontal cortex (Moeller et al., 2005). The susceptibility of white matter to cocaine dependence is further supported by reductions in frontal white matter volume (as measured by T1-weighted imaging) that correlated with the duration of abuse. Not surprisingly, apart from

compromised callosal and fibres of the internal capsule, frontal cortical areas showed significant reductions in FA (Lim et al., 2008). While in humans it is difficult to assess whether changes in white matter integrity are the cause or the consequence of cocaine dependence, inbred animal models to study the consequences of drug exposure on fibre integrity provide a means by which to address this issue. Rats that were treated with cocaine for 28 days displayed reductions in FA and  $\lambda_1$  in the corpus callosum, in addition to increases in RD in the same structure compared to control animals. Cocaine blood plasma levels indicated different concentrations between animals despite the fact that treatment (through an osmotic pump) was identical. However the cocaine plasma concentration correlated negatively with the level of callosal damage as measured with FA,  $\lambda_1$ , and MD. No association was found between blood plasma cocaine levels and RD. Interestingly, neurofilament immunoreactivity, which provides a measure of axonal integrity, was increased in the corpus callosum, while MBP immunoreactivity, a measure of myelin integrity, was decreased in cocaine-treated animals relative to controls (Narayana et al., 2009).

### **Autism.**

Autism is a so-called pervasive developmental disorder that is characterised by impairments in social interaction as well as showing problems in verbal communication, along with repetitive, stereotypic behaviour (American Psychiatric Association, 2000). There is evidence that the serotonergic system is involved, as indicated by elevated blood serotonin levels in a high proportion of autistic children. It has been suggested that these high blood serotonin levels may enter the brains of developing embryos while the blood-brain barrier has not been fully established, thus interfering with normal brain development (Whitaker-Azmitia, 2005). A volumetric MRI study performed on autistic babies compared to healthy controls with an age of up to 2 years showed both increased white and grey matter volumes suggestive of abnormal dendritic arborisation or failed apoptosis, i.e. pruning (Hazlett et al., 2005). In autistic children up to 4 years old, DTI showed increased anisotropy in several white matter tracts, including the corpus callosum and the internal capsule, and this was attributed to faster brain maturation compared to normal children. This was suggested to be due to the reasons mentioned above, i.e. denser axon packing because of failed apoptosis or dendritic pruning, but myelin status or axonal size were also discussed as potential factors (Ben Bashat et al., 2007). Compared to healthy control subjects within an age range between 10 - 35 years, autistic participants clearly displayed lower FA values in several fibre tracts, such as the corpus callosum and internal capsule, that were positively correlated with age. Interestingly increases of FA with increasing age

were also observed in other tracts of control subjects, while in the corpus callosum FA remained unaltered in the range of 10 - 35 year olds, and in the internal capsule there was a decrease with increasing age in controls (Keller et al., 2007). From adolescence onwards autists and healthy subjects appear not differ in brain size (Courchesne and Pierce, 2005). Although not investigated, this may indicate that in autistic babies high FA values are associated with higher than normal brain volumes, while in older autistic people (adolescence - adult), FA is below normal while brain volumes are similar to healthy people.

### **Depression.**

In the last 50 years, the age of onset of depression has decreased (from 35 to 28), and more people are likely to suffer from depression than before 1940 (Kandel et al., 2000). There is clear evidence for a genetic disposition to depression, and environmental factors such as increased stress levels may be associated with the expression of the depressive phenotype. According to the world health organisation, approximately 121 million people worldwide suffer from depression, where 5.8 % of men, and 9.5 % of women are estimated to go through a depressive episode every year. Depression is the major reason for periods lived with disability ((World Health Organisation, 2001); <http://www.who.int/>). Besides having a tremendous impact on the personal every day live of patients living with depression, major depression has also a great impact on the economy with patients being unable to pursue their work, and constituting a burden to the health care system (Judd et al., 1996). Despite the fact that depression can be treated pharmacologically and by cognitive behavioural therapy, affected patients usually delay seeking help and importantly, a significant proportion of patients do not respond effectively to treatment (see page 25).

Depression is a psychiatric condition in which the person is unable to experience any pleasure, so-called anhedonia, leading to social withdrawal with the inability to lead a normal life, including the pursuit of employment. In severe cases, the patients may attempt to commit suicide ((World Health Organisation, 2001); <http://www.who.int/>), thus having even lost the evolutionary drive to survive. The brain monoamine systems, particularly the serotonin system, appear to be involved in the pathology of depression (see below). While links between psychological and biological phenomena were initially regarded critically, but appreciated in the early 20th century (Carhart-Harris et al., 2008), evidence using conventional MRI now suggests that subcortical structures, e.g. the hippocampus (Sheline et al., 1996), and the caudate nucleus (Hickie et al., 2007) are altered in psychiatric dysfunction of depression. Recently, the integrity of white matter was examined using DTI

in order to elucidate whether there may be altered connectivities between different regions in the brains of depressed individuals. The most consistent findings are reductions in FA in frontal cortical white matter areas in geriatric depression (Bae et al., 2006, Nobuhara et al., 2006, Yang et al., 2007a), and in younger patients compared to healthy controls (Li et al., 2007a, Li et al., 2007b, Ma et al., 2007). The severity of depressive symptoms was found to be associated with frontal cortical reductions in FA in the elderly (Nobuhara et al., 2006), but not in younger patients (Li et al., 2007). In addition, a correlation between FA and results from psychological testing (Stroop test) has been suggested to indicate executive dysfunction in the frontal cortex of elderly depressed (Murphy et al., 2007). There is some evidence that patients not responding to antidepressant treatment have lower FA in several brain regions including the prefrontal cortex, corpus callosum, and anterior cingulate cortex in geriatric depression when compared to patients that do respond (Alexopoulos et al., 2008). However, in contrast Taylor *et al.* reported an association of higher FA in frontal areas in elderly patients that did not respond to antidepressants compared to those who do (Taylor et al., 2008).

### **1.2 Serotonin.**

Despite being one of the most common diseases in modern society, the aetiology of depression is not yet fully understood, but evidence suggests the involvement of the serotonergic system. During brain development, serotonin appears to act as a growth factor, and can regulate its serotonin fibre outgrowth through the inhibitory autoreceptor 5-HT<sub>1A</sub> allowing fine tuning of the initial crude innervation (negative feedback loop) (Whitaker-Azmitia, 2005). Synaptic serotonin concentrations are mainly controlled by SERT (Hirano et al., 2005), and disturbances during development in the serotonin system may cause malformations in the brain (see autism above for instance) (Whitaker-Azmitia, 2005). There are multiple ways in which serotonin may influence the development of the brain, including the modulation of synaptogenesis, neurogenesis and dendritic architecture (Duman et al., 2001, Hajszan et al., 2005). The soma of serotonergic neurons lie in the raphe nuclei, which are constituted of the raphe pallidus, raphe obscurus, and raphe magnus (B1 - B3) in the caudal medulla, the raphe paragigantocellularis (B4) at the level of the rostral medulla, and of the midbrain nuclei, including the dorsal and median raphe (B5 - B9) (Cordes, 2005, Kandel et al., 2000). The dorsal and the median raphe nuclei provide the majority of serotonergic neurons (Beck et al., 2004). While the raphe nuclei that are located more rostrally (B5 - B9) project to forebrain structures including the hypothalamus, thalamus, hippocampus, caudate-putamen and the cerebral cortex, the

serotonergic neurons that lie more caudally (B1 - B4) descend to the brainstem and spinal cord (Fig. 1-6, (Kandel et al., 2000)).

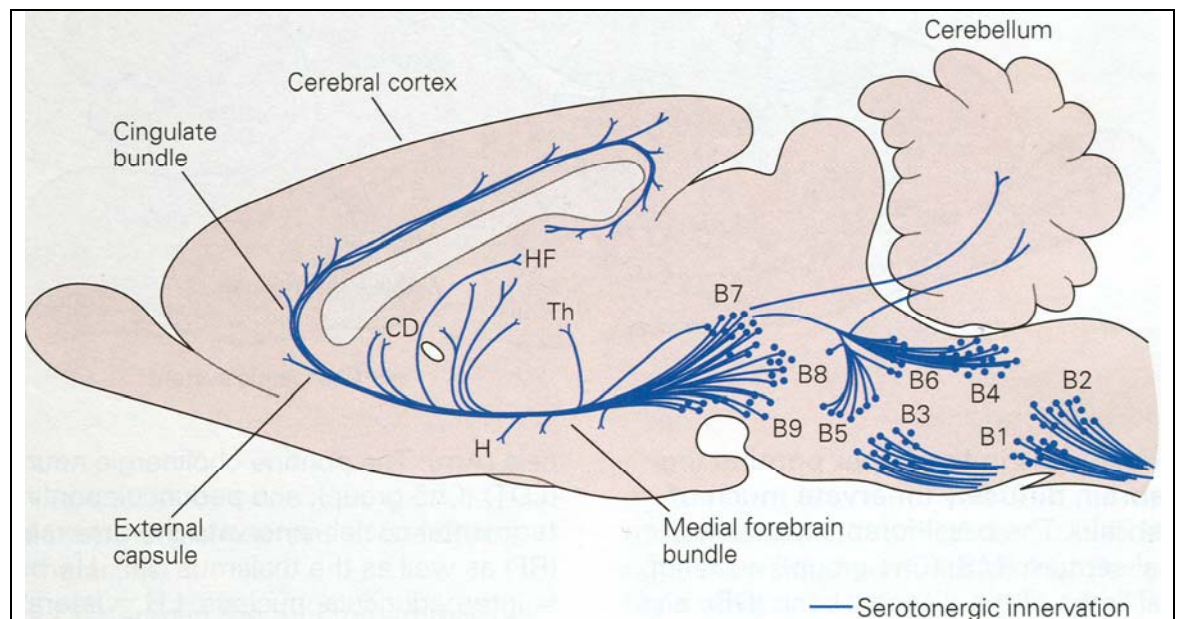


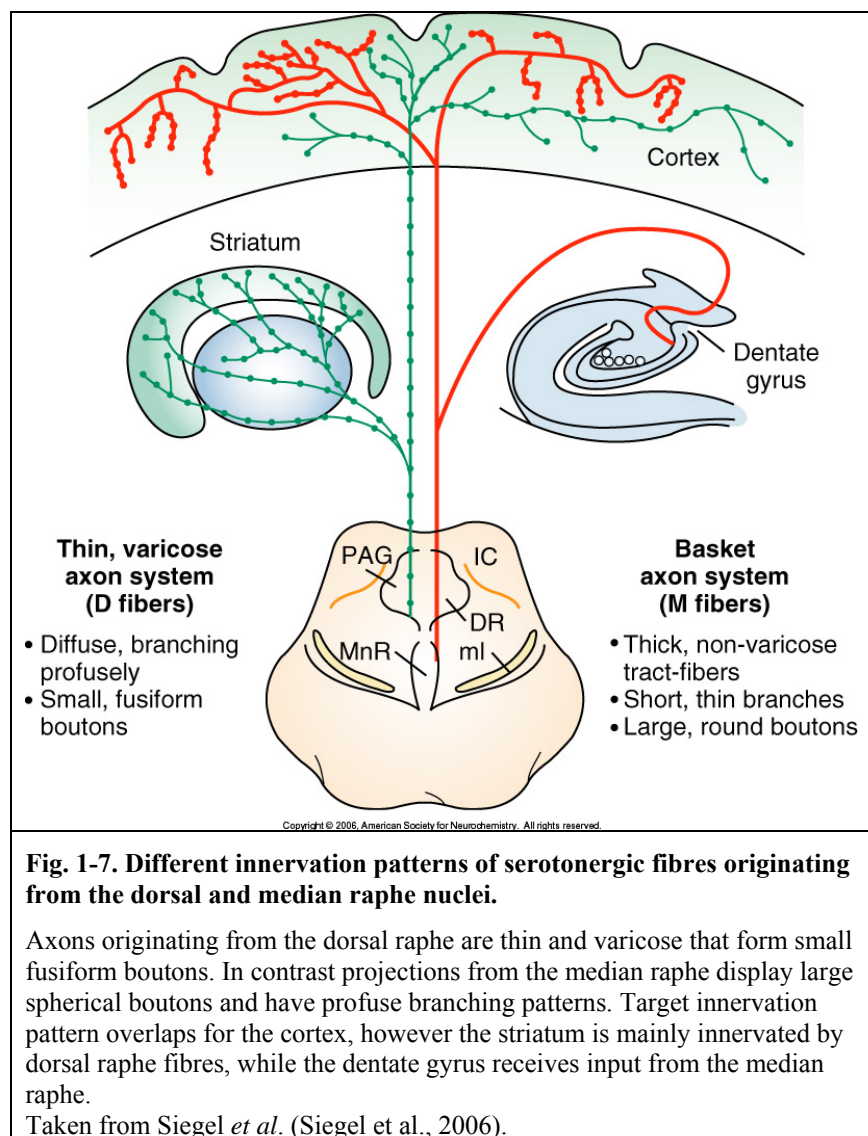
**Fig. 1-6. Origin and projection fields of serotonergic fibres.**

Caudally located nuclei, i.e. raphe pallidus, raphe obscurus, raphe magnus, and raphe paragigantocellularis (B1 - B4), project to the brainstem and spinal cord. In contrast, rostral serotonergic nuclei, including the dorsal and median raphe, and raphe pontis (B5 - B9), innervate structures such as the thalamus, hypothalamus, caudate-putamen and hippocampus in the forebrain as well as the entire cerebral cortex.

Taken from Kandel *et al.* (Kandel et al., 2000).

Ascending serotonergic fibres travel to the forebrain via the medial forebrain bundle, where they are predominantly unmyelinated. In the rat, the percentage of myelinated fibres in the medial forebrain bundle has been reported to be below 1 %, while in the monkey the percentage appears to be around 25 % (Azmitia and Gannon, 1983). In addition, in the rat, the fibres ascending from the dorsal raphe and the median raphe have been described to have a distinct morphology. Axons arising from the median raphe are characterised by large spherical varicosities with varying axonal diameter. In contrast, dorsal raphe axons are rather fine, and have granular or fusiform shaped small pleomorphic varicosities (Fig. 1-7). In addition, a distinct innervation pattern was found, with fibres originating from the median raphe projecting to limbic structures like the dentate gyrus, while the dorsal raphe, for instance, projects to the striatum (Kosofsky and Molliver, 1987). Moreover, the nucleus accumbens appears to be innervated by two distinguishable species of serotonergic neurons. When rats were either injected with para-chloroamphetamine or methamphetamine, the dorsal striatum and the nucleus accumbens core were completely devoid of serotonin-containing axons, whereas the control animals showed substantial

innervation of serotonin neurons. However, the nucleus accumbens shell in the treated animals still contained serotonin-containing axons comparable to that of the control animals. It was concluded that the neurotoxicity of para-chloroamphetamine or methamphetamine is dependant on the expression of SERT, whereas SERT-negative axons seemed to be resistant to either toxin. Interestingly, the SERT containing axons were described to have the same morphology as the dorsal raphe axons, i.e. fine and smooth. In contrast, the nucleus accumbens shell innervating neurons lacking SERT were described to be large in diameter, and highly varicose (Brown and Molliver, 2000), however raphe origins were not determined.



### 1.2.1 Events at the serotonergic synapse.

Mechanisms by which different classes of antidepressants interact with the serotonin system are depicted in Fig. 1-8. Synthesis and axonal transport of serotonin to the synaptic terminal are followed by the storage into vesicles. Upon activation of the serotonergic neuron leading to an action potential that propagates along the serotonergic fibre, vesicles containing serotonin fuse with the presynaptic membrane and serotonin is released into the synaptic cleft. This causes activation of the postsynaptic neuron, which is terminated by the reuptake of serotonin by SERT. Serotonin will then either be degraded by the monoamine oxidase (MAO), or stored in vesicles for further release. Antidepressants increase serotonin levels within the synapse, either by blockade of SERT with selective serotonin reuptake inhibitors (SSRIs) or tricyclic antidepressants. Another way to increase synaptic serotonin is by the inhibition of MAO, thus inhibiting the degradation of serotonin (see Kandel *et al.* for review, (Kandel *et al.*, 2000)).

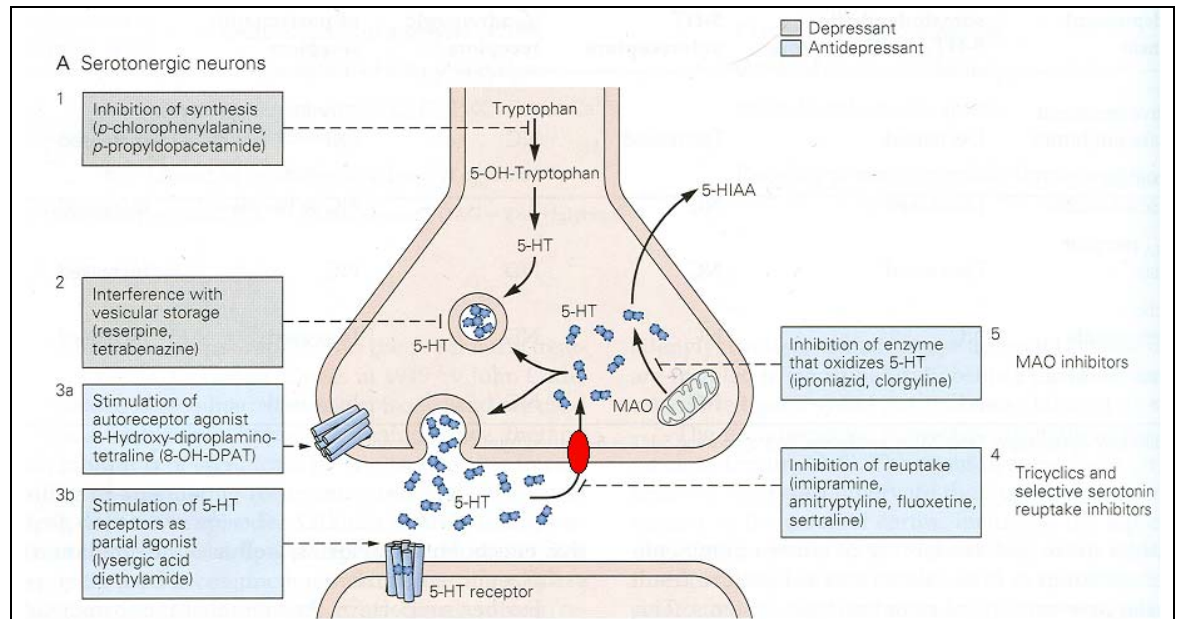


**Fig. 1-8. Mechanisms by which the storage, release, reuptake, and the degradation can be modulated.**

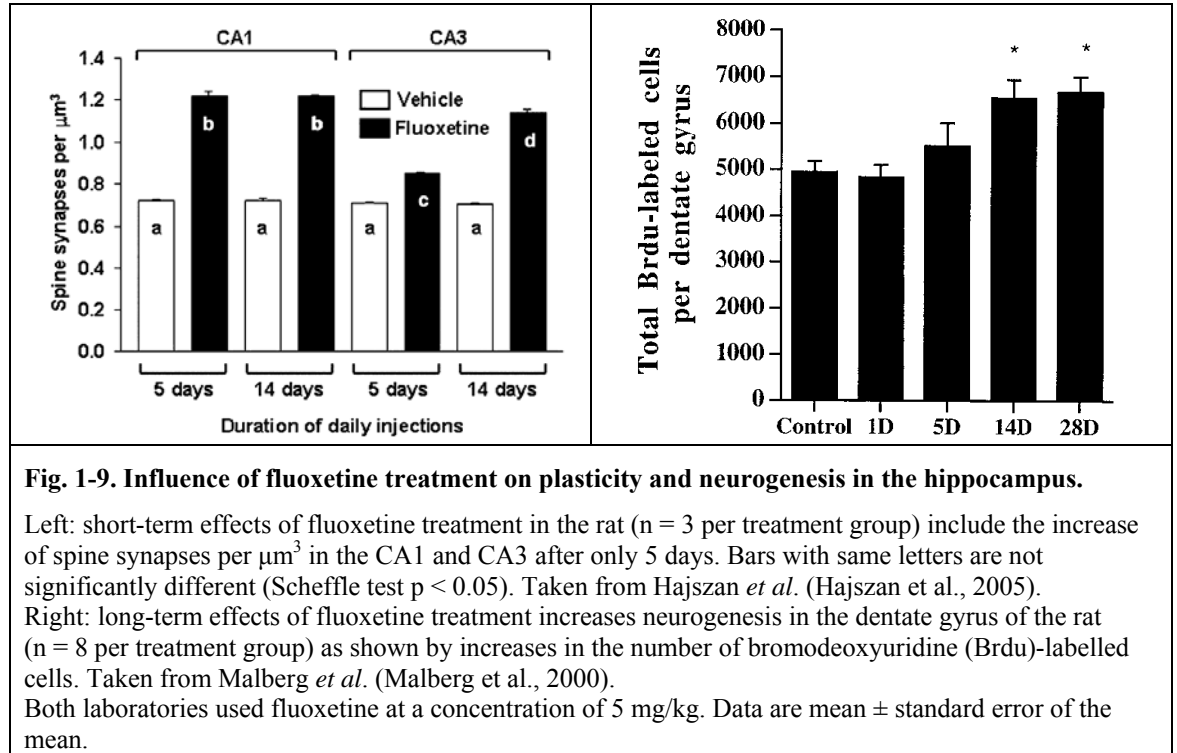
Serotonin is stored in vesicles, which fuse with the presynaptic membrane upon stimulation causing serotonin to be released into the synaptic cleft. Serotonin acts upon the serotonin receptors located post- or presynaptically to convey information. The SERT (red ellipse) terminates the action of serotonin by shunting the neurotransmitter back into the presynaptic terminal. Once shuffled back, the fate of serotonin is either the degradation by the MAO, or the recycling into vesicles for further release. Antidepressants aim to increase synaptic serotonin by either blockade of the SERT (SSRIs, or tricyclic antidepressants), or by inhibition of the MAO.

Adapted from Kandel *et al.* (Kandel *et al.*, 2000).

### 1.2.2 The hippocampus and depression.

The mechanisms of how elevated serotonin could help to ameliorate symptoms of depression are not yet fully understood. In particular, antidepressant intake leads to an immediate blockade of SERT, however symptoms alleviate only after several weeks of continuous administration (Quitkin *et al.*, 1996). Events taking place in the hippocampus are believed to be central to the positive outcome of antidepressant treatment. Rats that were treated with the SSRI fluoxetine ((±)-n-methyl-γ-[4-(trifluoromethyl)phenoxy]benzenepropanamine) showed a maximally increased spine synapse density in the CA1 as early as 5 days of treatment compared to control animals. Similarly, in the CA3 of the hippocampus, pyramidal neurons formed new dendritic spines after 5 days of fluoxetine treatment, and this was maximal after 14 days of treatment (Hajszan *et al.*, 2005). The subgranular zone in the hippocampus is one of 2 regions in the brain where neurogenesis is retained even in adulthood and these newborn cells can be incorporated into the local circuitry of the hippocampus (Lledo *et al.*, 2006). By labelling dividing cells with the marker bromodeoxyuridine, newborn neurons that were generated through the influence of antidepressant treatment could be quantified. Compared to control

rats, fluoxetine-treated rats displayed an increase in neurons in the dentate gyrus of the hippocampus after 14 days of treatment (Malberg et al., 2000). Thus this could explain the delayed response to antidepressants in humans, as neuronal remodelling needs to take place first. The effects of fluoxetine on spine density and neurogenesis in the hippocampus are summarised in Fig. 1-9.



Depressed patients were reported to have smaller hippocampi (Sheline et al., 1996, Videbech and Ravnkilde, 2004, Campbell et al., 2004, Sheline et al., 1999). In addition, the size of the hippocampus in depressed patients is negatively associated with the duration of depression (Sheline et al., 1999, Sheline et al., 1996). There is evidence supporting that stress, which raises corticosteroid levels in the brain, is associated with hippocampal atrophy. For example, rats that underwent a stress paradigm in which they were restrained on a daily basis for 14 days showed reductions in CA3 apical dendrite length and branching points, plus massive elevations in corticosteroid plasma levels (Watanabe et al., 1992). Interestingly, tree shrews that were subjected to psychosocial stress constituting of the presence of a dominant tree shrew in the cage, showed elevated urinary corticosteroid levels, and hippocampal shrinkage. When subdued animals were treated with the tricyclic antidepressant tianeptine, urinary corticosteroid levels were still elevated. However antidepressant treatment reversed hippocampal volume to normal and normalised the rate of neurogenesis, as measured with bromodeoxyuridine (Czeh et al., 2001).

### 1.2.3 Resistance to antidepressants.

Despite the positive effects of antidepressants, only 20 - 40 % of treated patients with depression are estimated to show remission. According to Sackeim, reasons for not responding to antidepressant treatment may include: inadequate antidepressant doses that failed to achieve significant levels of SERT occupancy; treatment cessation before beneficial outcome would have been achieved; lack of compliance of the patient, or inappropriate evaluation of the outcome (Sackeim, 2001).

Despite the fact that these issues exist, which can be summarised with the term "pseudo-resistance", there is growing evidence for the involvement of genetic predisposition factors that could lead not only into treatment resistance, but also into depression itself. Recently, a polymorphism in the promoter region of SERT has been identified (Heils et al., 1996), which was associated with anxiety-like traits (Lesch et al., 1996). In this polymorphism, the transcription-regulating region upstream of the transcription start carries repetitive elements of varying length, the 5-HTTLPR (Lesch et al., 1996). The 5-HTTLPR is only present in humans and non-human primates, and the alleles consist of either 14 (short, s), or 16 (long, l) repetitive elements (Murphy et al., 2004). In lymphocyte membrane preparations derived from humans, up to 30 - 40 % more [<sup>125</sup>I]βCIT binding was observed in the l/l carrying cells compared to l/s or s/s cells. In addition, [<sup>3</sup>H]serotonin uptake was about twice (1.9 - 2.2 fold) as much in the l-variant compared to cells carrying one or two s-alleles (Lesch et al., 1996). Over the past decade, more variations present within the SERT gene, and its regulatory elements, have been identified (for review see Murphy *et al.* (Murphy and Lesch, 2008)). Like the 5-HTTLPR, two single nucleotide polymorphisms, rs25531 and rs25532, are within the transcription regulating element of SERT and have been associated with obsessive-compulsive behaviour (rs25531 polymorphism became non-significant after correction for multiple comparison) (Wendland et al., 2007, Wendland et al., 2008). A glycine-to-alanine missense mutation at residue 56 was suggested to represent genetic susceptibility, particularly in males, to autism (Sutcliffe et al., 2005). In addition, isoleucine-to-valine substitution at residue 425 showed genetic predisposition to obsessive-compulsive disorder (Delorme et al., 2005). A variable number of tandem repeats (9, 10 or 12 repeats) in intron 2 was reported, in which a meta-analysis study provided compelling evidence for the association of the 12 repeat variant with schizophrenia (Fan and Sklar, 2005). Fig. 1-10 depicts the SERT gene (a) with the above-mentioned mutations highlighted, the SERT protein (c) *in situ*, and combinations of certain polymorphisms and their influence on SERT function (b). A theoretical maximal gain-of-

function, as measured *in vitro*, was observed for the 12 repeat variant in intron 2 in l/l allele carriers that was in the order of 4.65 fold higher than of those carrying the s/s alleles (in the presence of rs25531) (Murphy and Lesch, 2008).

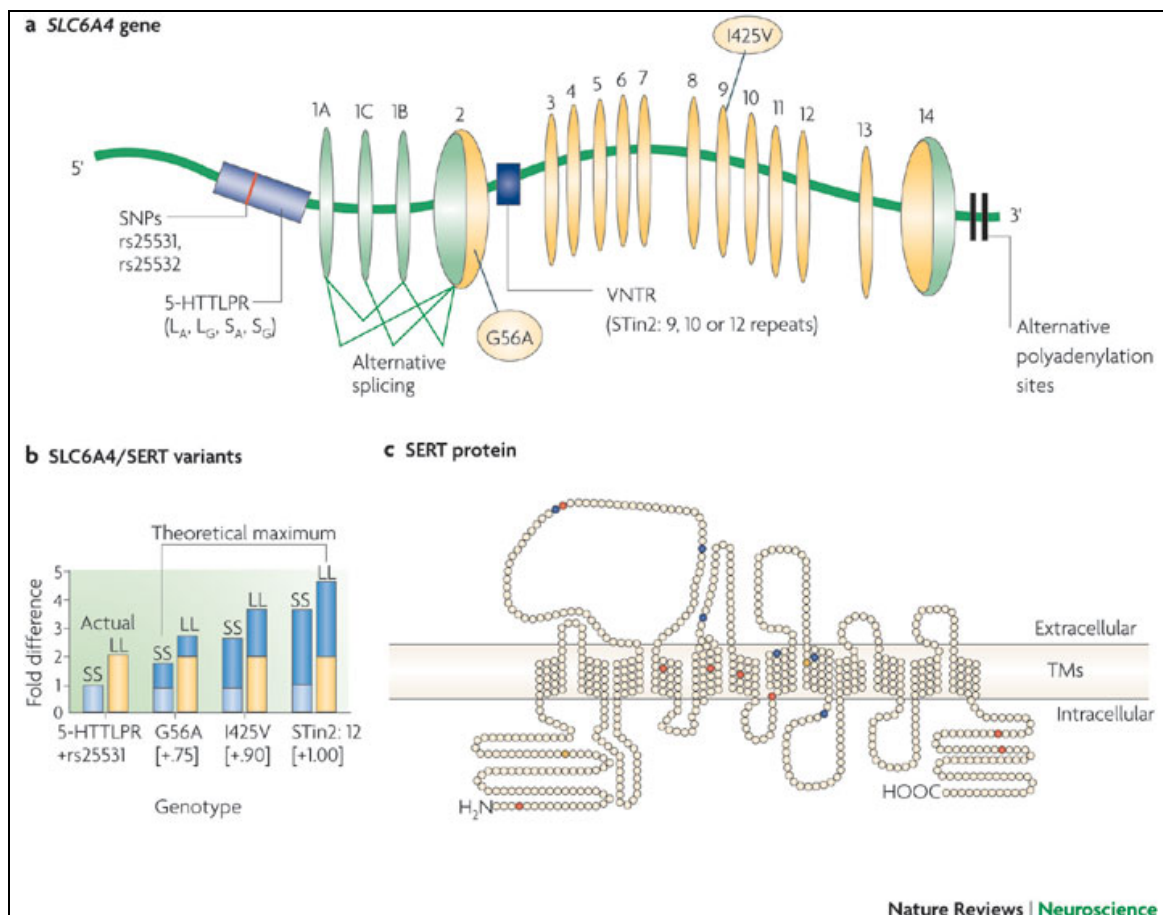


**Fig. 1-10. The human SERT.**

a) the SERT gene (SLC6A4):

Mutations in the SERT gene that cause functional differences include the promoter region polymorphism (5-HTTLPR), the single nucleotide polymorphisms in the promoter region (SNP), and the variable number of tandem repeats (VNTR) in intron 2 (STin2).

b) Relative functional differences of SERT associated with variations in the SERT gene:

Most 2 left bars: in the presence of the mutation rs25531 in the promoter region, long allele carriers (5-HTTLPR) display a 2 fold increase in SERT function and expression compared to short allele carriers. 6 bars on the right indicate the theoretical gain-of-function (predicted from *in vitro* experiments, depicted in dark blue) associated with G56A, I425V, and STin2 (12 repeats) mutations. Between the lowest expression/function condition as actually observed in short allele carriers in the presence of the rs25531 mutation, and the theoretical maximum (STin2 with 12 repeats in long allele carriers) there is a gain-of-function of 4.65 fold expression/function.

c) SERT protein:

The SERT contains 12 transmembrane spanning segments (TMs), with intracellularly located amino- and carboxy-terminals. SNPs that cause silent mutations are depicted with blue circles, while missense mutations are shown in yellow (causing functional abnormalities) and red (untranslated).

Taken from Murphy *et al.* (Murphy and Lesch, 2008).

The presence of the 5-HTTLPR polymorphism can have an important impact on the treatment of depression. 5-HTTLPR genotype distribution was found to be 32 % l/l, 49 % l/s, and 19 % s/s (Lesch *et al.*, 1996). Patients carrying the s/s variant were reported to have

a delay in responding to the SSRIs paroxetine ((3S-trans)-3-[(1,3-benzodioxol-5-yloxy)methyl]-4-(4-fluorophenyl)piperidine) (Pollock et al., 2000), and fluvoxamine (Smeraldi et al., 1998), compared to homozygous long allele carriers as identified with rating scales for depression. Similarly, after 4 weeks of fluoxetine treatment, the majority of depressed responders were found in the l/l group (Yu et al., 2002), which, if not taken into account, could result in premature termination of the treatment (Sackeim, 2001).

### 1.2.4 SERT in brain development.

As outlined above, depression is thought to be treated in the adult by elevation of synaptic serotonin levels. Paradoxically in brain development, serotonin levels that deviate from the norm can cause abnormalities in the adult (Cabrera-Vera and Battaglia, 1998, Cabrera-Vera et al., 1997, Feenstra et al., 1996). For instance, autistic children show high blood levels of serotonin (Anderson et al., 1990, Hoshino et al., 1984). In addition, an intriguing high incidence of autism of 11.4 % has been observed in cases where mothers took cocaine during pregnancy (Davis et al., 1992). Cocaine is known to be a potent blocker of SERT (Satel et al., 1995).

In the rat, effects of prenatal exposure to fluoxetine on SERT density included increases in the CA2 and CA3 of the hippocampus, in the amygdala, and in the lateral hypothalamus of prepubescent rats compared to controls, while serotonin levels were reduced in the frontal cortex. Reductions in SERT density were found in the dorsolateral hypothalamus, and substantia nigra. In adult rats treated prenatally with fluoxetine, no differences in SERT density were found, however midbrain serotonin levels were markedly reduced (Cabrera-Vera and Battaglia, 1998, Cabrera-Vera et al., 1997). Despite the fact that during brain development SERT levels normalise after prenatal exposure to SSRIs into adulthood, more subtle differences may be present, for example, the innervation of target structures could have changed and this might lead to behavioural deficits.

There is evidence that antidepressant treatment can predispose to depression as previously shown in behavioural studies in the mouse. Genetically modified mice deficient in SERT (SERT-KO; SERT knockout) displayed anxiety-like traits indicated by an increased latency to feed when in a novel environment, and reduced exploratory drive compared to control mice as assessed by the number of arm entries in the elevated plus maze (Lira et al., 2003). Subsequently, the same group studied mice that were treated during P4 and P21 with the SSRI fluoxetine, and their behaviour when adult was compared to that of SERT-

KO mice, as it was hypothesised that the behavioural abnormalities of the SERT-KO mice would be replicated in the fluoxetine-treated mice. Indeed, the behaviour of the fluoxetine-treated animals mimicked the behaviour of the SERT-KO mice (Ansorge et al., 2004). However, it was unclear from these studies what type of changes in brain structure caused by either gene deletion or postnatal fluoxetine treatment might underlie the behavioural abnormalities. Structural abnormalities in these SERT-KO mice using DTI were investigated in the study described in chapter 3 (page 98).

There is some evidence that indeed morphological abnormalities exist in SERT-KO mice. For instance, 50 % less serotonergic neurons were found in the dorsal raphe (Lira et al., 2003). In addition, the barrel field in the somatosensory cortex was absent (Persico et al., 2001), and whisker stimulation resulted in an attenuated response within the whisker-to-barrel field pathway. The barrel field in the rodent cortex is a direct representation of whiskers (1 barrel = 1 whisker) (Esaki et al., 2005). Reduced apoptosis has been shown in SERT-KO mice, suggesting, however not shown in this study, abnormal innervation patterns (Persico et al., 2003). This has been demonstrated in MAO-deficient (MAO-KO) mice that also display enhanced serotonin neurotransmission. In these mice, abnormal retinal projections were present that were attributed to the elevated serotonin compared to control mice (Upton et al., 1999).

### **1.3 SPECT.**

SPECT imaging has been widely used to study a variety of diseases, such as Parkinson's (Innis et al., 1993), Alzheimer's (Johnson et al., 1998, Jones et al., 1998), schizophrenia (Laruelle et al., 2000), and depression (Malison et al., 1998c). SPECT has been used in the early detection of diseases, such as Alzheimer's disease using [ $^{99m}\text{Tc}$ ]HMPAO to measure cerebral blood flow, which changes in Alzheimer's disease before structural changes occur (Johnson et al., 1998, Jones et al., 1998). This may help to initiate treatment early in the disease process. Despite the added dimension SPECT imaging brings to investigations of brain function in disease, it is limited by the availability of suitable radioligands. The first suitable SPECT tracer to image SERT *in vivo* using SPECT was [ $^{123}\text{I}$ ]βCIT (Laruelle et al., 1993), and its widespread application continues to date. Nevertheless, because of its binding to other monoamine transporters including dopamine transporter (DAT) and norepinephrine transporter (Neumeyer et al., 1996), there are obvious issues in the interpretation of the data. [ $^{123}\text{I}$ ]ADAM was recently introduced as a novel SPECT tracer for SERT, and is reported to be highly selective towards SERT, and superior to [ $^{123}\text{I}$ ]βCIT

(Sacher et al., 2007). Below, some of the applications are reviewed, in which [ $^{123}\text{I}$ ] $\beta\text{CIT}$  and [ $^{123}\text{I}$ ]ADAM were applied. Particular emphasis is placed on depression, and pharmacologically altered SERT availabilities induced by antidepressants, or the serotonin neurotoxin  $\pm$ 3,4-methylenedioxymethamphetamine (MDMA).

### 1.3.1 [ $^{123}\text{I}$ ] $\beta\text{CIT}$ SPECT imaging.

#### [ $^{123}\text{I}$ ] $\beta\text{CIT}$ SPECT imaging of DAT.

In clinical studies, [ $^{123}\text{I}$ ] $\beta\text{CIT}$  has proved to be a very successful tracer for measurements of DAT, especially in examining patients with Parkinson's disease (Halldin et al., 2001). In Parkinson's, a neurodegenerative disease affecting dopaminergic neurons, [ $^{123}\text{I}$ ] $\beta\text{CIT}$  measurements of DAT levels were shown to be highly reproducible, both in disease and healthy state (Seibyl et al., 1997). In addition, cell counts in the substantia nigra in a rat model of parkinsonism correlated with the SPECT signal obtained from the caudate-putamen, supporting the use of [ $^{123}\text{I}$ ] $\beta\text{CIT}$  as a valuable diagnostic tool in Parkinson's disease (Scherfler et al., 2002). SPECT and [ $^{123}\text{I}$ ] $\beta\text{CIT}$  were also employed to investigate treatments in cocaine addiction. Mazindol (5-(4-chlorophenyl)-3,5-dihydro-2H-imidazo[2,1-*a*]isoindol-5-ol), a reuptake inhibitor for catecholaminergic neurons, was thought to be a candidate in cocaine addiction treatment. However its therapeutic use was rejected because presumably intolerable doses of mazindol were estimated with [ $^{123}\text{I}$ ] $\beta\text{CIT}$  SPECT to be needed to block 50 % of DAT, an occupancy that was thought to be a prerequisite for effective treatment (Malison et al., 1998). In addition, acutely withdrawing cocaine addicts were shown to have a huge increase in striatal DAT binding of [ $^{123}\text{I}$ ] $\beta\text{CIT}$ , as measured with SPECT, that correlated with the severity of post-cocaine depression the subjects experienced (Malison et al., 1998a). Being a cocaine-derivate in itself, [ $^{123}\text{I}$ ] $\beta\text{CIT}$  shares some of its properties, i.e. the binding to SERT. Thus the advantage of this characteristic of [ $^{123}\text{I}$ ] $\beta\text{CIT}$  SPECT imaging has been used to examine diseases and conditions SERT is involved in. Because of the different kinetics DAT in the striatum, and SERT-rich regions such as the thalamus and the brainstem display, imaging paradigms can be adjusted to image these 2 monoamine transporters specifically when either of them reaches equilibrium. For instance [ $^{123}\text{I}$ ] $\beta\text{CIT}$  binding to the thalamus is reported to be stable 4 - 10 h post injection (p. i.), while a decline of binding in the brainstem was shown to occur 4 h p. i.. In contrast, it appears that striatal uptake is stable between 20 - 24 h p. i. (Pirker et al., 2000), thus making it possible to image DAT- and SERT-rich regions separately.

**[<sup>123</sup>I]βCIT SPECT in MDMA-induced neurotoxicity.**

Despite the fact that MDMA has been shown to be neurotoxic in rats, such that it destroys serotonergic terminals, its toxicity in humans is still under debate. Strong evidence that it could indeed be neurotoxic in humans was first demonstrated in a [<sup>123</sup>I]βCIT SPECT study in rhesus monkeys, where MDMA was shown to reduce [<sup>123</sup>I]βCIT binding in hypothalamic and midbrain regions compared to control animals (Reneman et al., 2002). Gender and the doses of MDMA taken also appear to influence neurotoxicity: in men overall reduction in SERT density was non-significant while in women it was significant. In addition, female ex-MDMA users showed recovery of [<sup>123</sup>I]βCIT SERT binding that was not statistically different from controls, and this may have contributed to the neurotoxicity of MDMA debate. Cortical [<sup>123</sup>I]βCIT binding levels were only lower in recent MDMA users, while ex-users did not show differences compared to controls (Reneman et al., 2001). In a thorough longitudinal study, short-term MDMA users did not show any differences in [<sup>123</sup>I]βCIT binding compared to drug-naïves (de Win et al., 2008). This was in contrast to heavy, long-term users of MDMA, where reduced thalamic [<sup>123</sup>I]βCIT binding was observed (de Win et al., 2008). In rats that were treated with neurotoxic doses of MDMA, the reduction of [<sup>123</sup>I]βCIT binding to thalamic SERT was in the order of 21 % compared to controls, providing evidence for MDMA being neurotoxic to serotonergic neurons (de Win et al., 2004).

**[<sup>123</sup>I]βCIT SPECT in psychiatric disorders.**

**Obsessive-compulsive disorder.**

In addition to being a sensitive measure in drug-induced changes in DAT and SERT, [<sup>123</sup>I]βCIT SPECT was also successfully applied in a variety of psychiatric disorders, including obsessive-compulsive disorder and depression. In obsessive-compulsive disorder, for example, the severity of the disease, as measured by means of standardised psychological tests, correlated negatively with [<sup>123</sup>I]βCIT binding to SERT in the thalamus and hypothalamus. In these structures, the binding was reduced compared to healthy controls. In addition, the [<sup>123</sup>I]βCIT binding positively correlated with the duration of the illness, giving this ligand a prognostic value in the evaluation of the disease (Zitterl et al., 2007). Interestingly, in an alternative, non-invasive measure of serotonin system function, i.e. the loudness dependence of the audio-evoked potentials, these measurements correlated positively with [<sup>123</sup>I]βCIT binding to DAT in the caudate nucleus, and to SERT in the midbrain/pons area of patients with obsessive-compulsive disorder, highlighting the

usefulness of [ $^{123}\text{I}$ ] $\beta\text{CIT}$ 's capabilities to bind to both, SERT and DAT (Pogarell et al., 2004).

### **Depression.**

The psychiatric condition, in which [ $^{123}\text{I}$ ] $\beta\text{CIT}$  has probably been studied the most, is depression. One of the earlier studies using [ $^{123}\text{I}$ ] $\beta\text{CIT}$  showed that SERT availability in the brainstem is reduced in the drug-naïve depressed compared to healthy controls (Malison et al., 1998c). Some other contributions to our current knowledge of depression include the higher binding of [ $^{123}\text{I}$ ] $\beta\text{CIT}$  to striatal DAT in depressed patients indicating an upregulation of DAT (Laasonen-Balk et al., 1999). Gender differences in depression were also reported, where depressed females show less [ $^{123}\text{I}$ ] $\beta\text{CIT}$  binding to SERT in the diencephalon compared to male subjects (Staley et al., 2006). Following this, the effects of antidepressant treatment were studied. In a 6 months follow-up study, in which depressed patients had a baseline scan before treatment, and 6 months later another [ $^{123}\text{I}$ ] $\beta\text{CIT}$  scan (patients were drug-free one month before the second scan) to test efficiency of the treatment. Patients that had a better score at the end of the experiment in the depression evaluation test also showed higher SERT [ $^{123}\text{I}$ ] $\beta\text{CIT}$  uptake in the midbrain, compared to those who had lower scores (Laasonen-Balk et al., 2004). Interestingly, in healthy subjects, as well as in depressed patients, that were treated with antidepressants, both showed increased [ $^{123}\text{I}$ ] $\beta\text{CIT}$  binding to striatal DAT, while SERT in brainstem and diencephalon was reduced. These findings indicated the predictive value of [ $^{123}\text{I}$ ] $\beta\text{CIT}$  in depression and its treatment; in addition it revealed some possible side effects associated with the pharmacological treatment of this psychiatric disorder (Kugaya et al., 2003).

### **Occupancy.**

In order to establish therapeutically efficient dose paradigms for the treatment of depression, antidepressant occupancy of SERT were studied with [ $^{123}\text{I}$ ] $\beta\text{CIT}$ . Antidepressant treatment of patients using various doses of citalopram (1-[3-(dimethylamino)propyl]-1-(4-fluorophenyl)-1,3-dihydro-5-isobenzofurancarbonitrile; 20 - 60 mg) did not lead to any higher SERT occupancy (~50 % compared to control group) in the hypothalamic/midbrain area as measured with [ $^{123}\text{I}$ ] $\beta\text{CIT}$  when the high dose was compared to the low (Pirker et al., 1995). Compared to normal controls, a case study of a single patient suffering from depression and bulimia nervosa showed reductions (~41 %) in SERT [ $^{123}\text{I}$ ] $\beta\text{CIT}$  binding in hypothalamic/midbrain regions after treatment with fluoxetine (60 mg) (Tauscher et al., 1999). Also in a follow-up study of obsessive-compulsive disorder, citalopram (40 mg) reduced [ $^{123}\text{I}$ ] $\beta\text{CIT}$  binding in the same order in midbrain-

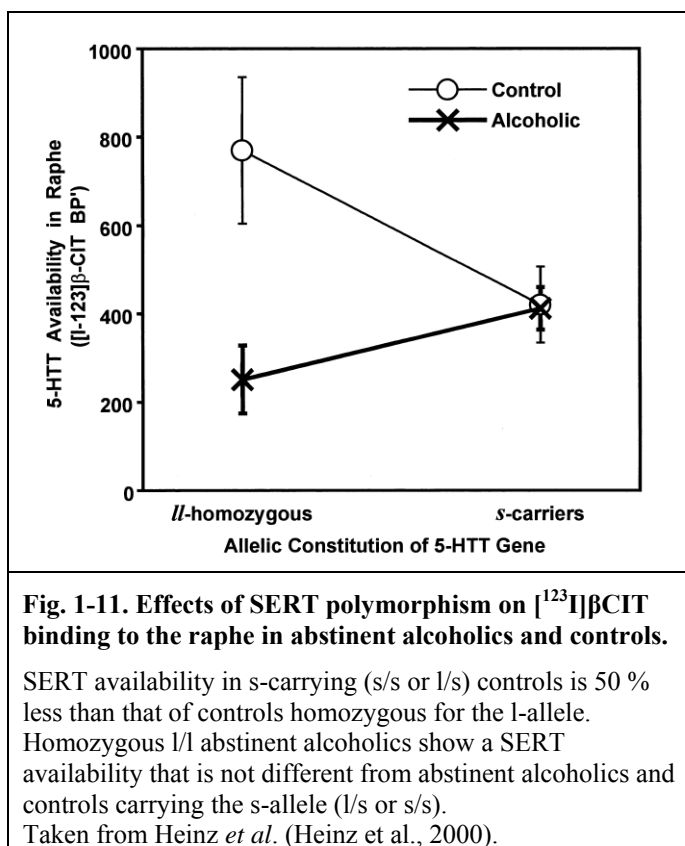
pons area, while DAT density in the striatum increased by 40 % (Pogarell et al., 2005). Acute citalopram (20 mg) treatment in healthy subjects showed a reduction of [ $^{123}\text{I}$ ]βCIT binding to SERT in the midbrain and thalamic area of 72 and 58 %, respectively, compared to baseline. In addition, [ $^{123}\text{I}$ ]βCIT was able to detect a cortical reduction in SERT in the presence of the SSRI citalopram (de Win et al., 2005). Finally along this line, SPECT scanning of healthy volunteers using the serotonin-norepinephrine reuptake inhibitor venlafaxine (75 - 150 mg) reduced [ $^{123}\text{I}$ ]βCIT binding to SERT in brainstem and diencephalon (~55 %), while striatal DAT binding was increased (~10 %) (Shang et al., 2007). Interestingly, a study performed in Glasgow comparing responders to non-responders during antidepressant drug treatment showed no difference between the two groups of patients in brainstem SERT availability using [ $^{123}\text{I}$ ]βCIT (Cavanagh et al., 2006).

The available reports considering occupancy studies in animals are limited. Acute treatment of dogs with citalopram (1 mg/kg) confirmed findings observed in humans, where striatal DAT binding ratios using [ $^{123}\text{I}$ ]βCIT were increased (44 - 160 %), and cortical (64 - 75 %) and midbrain binding (78 - 95 %) ratios (normalised to the cerebellum) as a measure of SERT were decreased compared to baseline (Peremans et al., 2006). Of particular relevance is an acute [ $^{123}\text{I}$ ]βCIT SPECT displacement study, which has been done in Glasgow with the micro-SPECT scanner in which administration to rats of 10 mg/kg fluoxetine prior to, and following [ $^{125}\text{I}$ ]βCIT injection reduced [ $^{125}\text{I}$ ]βCIT SERT binding in the thalamus by approximately 40 % (Cain et al., 2009).

### 5-HTTLPR.

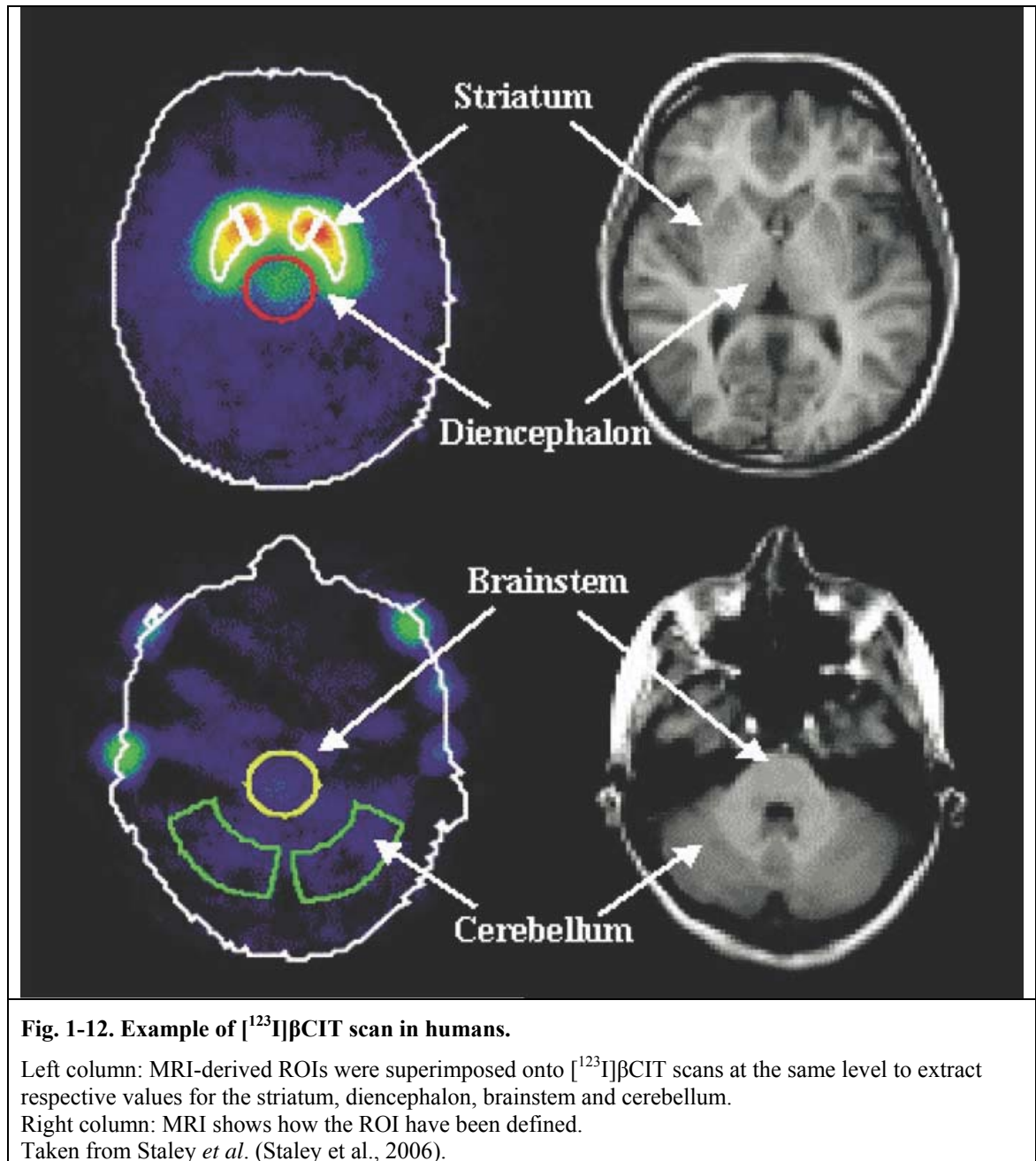
Recently, a polymorphism in the SERT gene, which concerns the length of the regulative element upstream of the SERT coding region, 5-HTTLPR, has been discovered and anxiety-related traits were postulated to be associated with the presence of the short alleles (page 25, Lesch *et al.* (Lesch et al., 1996)). In abstinent alcoholics that were homozygous l/l carriers, SERT [ $^{123}\text{I}$ ]βCIT binding in the raphe nucleus as detected with SPECT was reduced compared to the control subjects, while abstinent alcoholic and control subjects both carrying the short allele (pooled l/s and s/s) did not differ (Fig. 1-11). In addition, control l/l carriers had significantly higher [ $^{123}\text{I}$ ]βCIT binding to SERT in the raphe nucleus compared to control s allele (pooled l/s and s/s) carriers. Abstinent alcoholic s allele (pooled l/s and s/s) and l/l carriers did not differ in [ $^{123}\text{I}$ ]βCIT binding. This meant that not only that control s allele (pooled l/s and s/s) carriers appeared to have a 50 % reduction in SERT compared to l/l controls, as expected by Lesch *et al.* (Lesch et al., 1996), but also

that chronic excessive alcohol consumption in l/l carriers leads to a reduction in SERT availability not being different to those of s-allele carriers (l/s and s/s) (Heinz et al., 2000).



Similarly, suicide attempters carrying one or two short allele(s) have reduced SERT availabilities, as measured with [<sup>123</sup>I]βCIT binding in cortical areas compared to suicide attempters that were homozygous for the l-allele (Bah et al., 2008). However the contribution of the 5-HTTLPR polymorphism to SERT availability as measured with [<sup>123</sup>I]βCIT SPECT is not clear at all, as in a large sample of healthy human subjects, SERT availabilities did not differ between homozygous s-carriers and l-carriers. Even more surprising, s/s carriers showed higher SERT availability than those being heterozygous (l/s) for the 5-HTTLPR polymorphism (van Dyck et al., 2004).

A representative SPECT image of [<sup>123</sup>I]βCIT binding in the human brain is shown in Fig. 1-12 (Staley et al., 2006).



### 1.3.2 $[^{123}\text{I}]\text{ADAM}$ SPECT imaging.

Despite its success in reliably assessing a wide range of diseases and pharmacological treatments, the inability of  $[^{123}\text{I}]\beta\text{CIT}$  to specifically label SERT led to the development of a more specific SERT ligand. With  $[^{123}\text{I}]\text{ADAM}$ , a promising novel SERT ligand for SPECT imaging was found that appears to overcome the above mentioned problems observed with  $[^{123}\text{I}]\beta\text{CIT}$ .

Because  $[^{123}\text{I}]\text{ADAM}$  has only been available for a short period of time, it has not been as widely used as  $[^{123}\text{I}]\beta\text{CIT}$ , however the number of reports concerning this more specific SERT radioligand are steadily increasing. For instance,  $[^{123}\text{I}]\text{ADAM}$  binding in the

midbrain was shown to be negatively correlated with hostility scores (Yang et al., 2007). In addition, patients suffering from migraine showed higher SERT availability in the brainstem compared to controls, while thalamic [ $^{123}\text{I}$ ]ADAM binding was not altered (Schuh-Hofer et al., 2007). Interestingly, the same group that studied the loudness dependence of the audio-evoked potentials in obsessive-compulsive disorder using [ $^{123}\text{I}$ ]βCIT (page 30), repeated this experiment in healthy volunteers using [ $^{123}\text{I}$ ]ADAM, but showed a negative correlation (instead of positive as shown in the [ $^{123}\text{I}$ ]βCIT study) between the alternative, non-invasive, physiological measure of serotonin system function and [ $^{123}\text{I}$ ]ADAM binding in the brainstem (Pogarell et al., 2008).

### **[ $^{123}\text{I}$ ]ADAM SPECT in psychiatric disorders.**

#### **Depression.**

Similarly to the effects of depression on [ $^{123}\text{I}$ ]βCIT binding, midbrain SERT binding using [ $^{123}\text{I}$ ]ADAM in drug-free depressed patients was reduced compared to healthy controls. Reductions in [ $^{123}\text{I}$ ]ADAM binding correlated negatively with depression rating scores in depressed subjects, while [ $^{123}\text{I}$ ]ADAM binding correlated negatively with age in healthy controls (Newberg et al., 2005). This is in contrast to other reports that showed no differences between drug-naïve depressed patients and controls (Catafau et al., 2006, Herold et al., 2006), where thus the [ $^{123}\text{I}$ ]ADAM binding did not correlate with depression rating scores (Herold et al., 2006).

#### **Occupancy.**

A therapeutically relevant SERT blockade of 80 % was suggested previously to be effective in the treatment of depression (Meyer et al., 2001). In order to assess a dose-response relationship of antidepressant treatment, SERT occupancy using [ $^{123}\text{I}$ ]ADAM in healthy volunteers was measured before and after antidepressant treatment with the SSRI citalopram. Estimation of SERT occupancy in relation to citalopram blood plasma concentration suggested an 84 % ( $E_{\text{max}}$ ) blockade (Erlandsson et al., 2005, Klein et al., 2006). The  $E_{\text{max}}$  model is a widely used model that relates drug concentrations to its effects:  $E_{\text{max}}$  is the estimated maximal effect predicted by the model in response to a certain concentration of a drug (Schoemaker et al., 1998). A blockade of 65 %, and 70 % was calculated for 10 mg, and 20 mg single doses of citalopram, respectively (Klein et al., 2006), thus giving valuable information about patient dosing. In addition, SPECT imaging allows comparisons of the clinical effectiveness of antidepressants relative to the occupancy levels reached within the brain. For instance, citalopram contains the S- and R-

enantiomer, of which only the S-enantiomer is therapeutically active. Comparison of citalopram treatment (20 mg for 10 days) to escitalopram treatment (which is the S-enantiomer only; 10 mg for 10 days) showed a marked difference in [ $^{123}$ I]ADAM binding after treatment of healthy volunteers. While escitalopram yielded an occupancy of 82 %, only 64 % occupancy was shown for citalopram compared to baseline (Klein et al., 2007). This may be important in the case of adverse effects of the therapeutically inactive compound. Moreover, single doses of citalopram and escitalopram did not show any differences in [ $^{123}$ I]ADAM binding levels (Klein et al., 2006), indicating that these 2 compounds behave differently in long-term, but not in acute treatment. While these studies were performed in healthy volunteers, antidepressant response may be different in depressed persons because of various reasons, such as lower [ $^{123}$ I]ADAM binding in the drug-free state, and polymorphisms of SERT (which could also be present in non-depressed subjects). In depressed patients that were treated for 7 days with 10 mg citalopram daily, an occupancy of 61 % was observed using [ $^{123}$ I]ADAM to label SERT (Herold et al., 2006), which is in the same order as described above for a single dose in healthy subjects (Klein et al., 2006). Similarly, 20 mg paroxetine daily for 4 - 6 weeks showed a 66 % SERT reduction of [ $^{123}$ I]ADAM binding in the midbrain of depressed subjects compared to their baseline scan (Catafau et al., 2006).

To date [ $^{123}$ I]ADAM SPECT studies on small animals are relatively scarce including one study in rabbits and one in rats. Compared to untreated controls, rabbits pre-treated with fluoxetine before administration of [ $^{123}$ I]ADAM showed a reduction of [ $^{123}$ I]ADAM binding in the midbrain to levels indistinguishable from background levels. Likewise in the same study, the administration of the neurotoxin para-chloroamphetamine to rabbits, which destroys serotonin-containing neurons and leads to long-lasting serotonin depletion, showed SERT reductions in the midbrain region similar to background or fluoxetine treatment (Ye et al., 2004). In [ $^{123}$ I]ADAM SPECT of rats that had a baseline, and a scan after citalopram treatment, a SERT occupancy of 96 % was observed in the midbrain (Hwang et al., 2007).

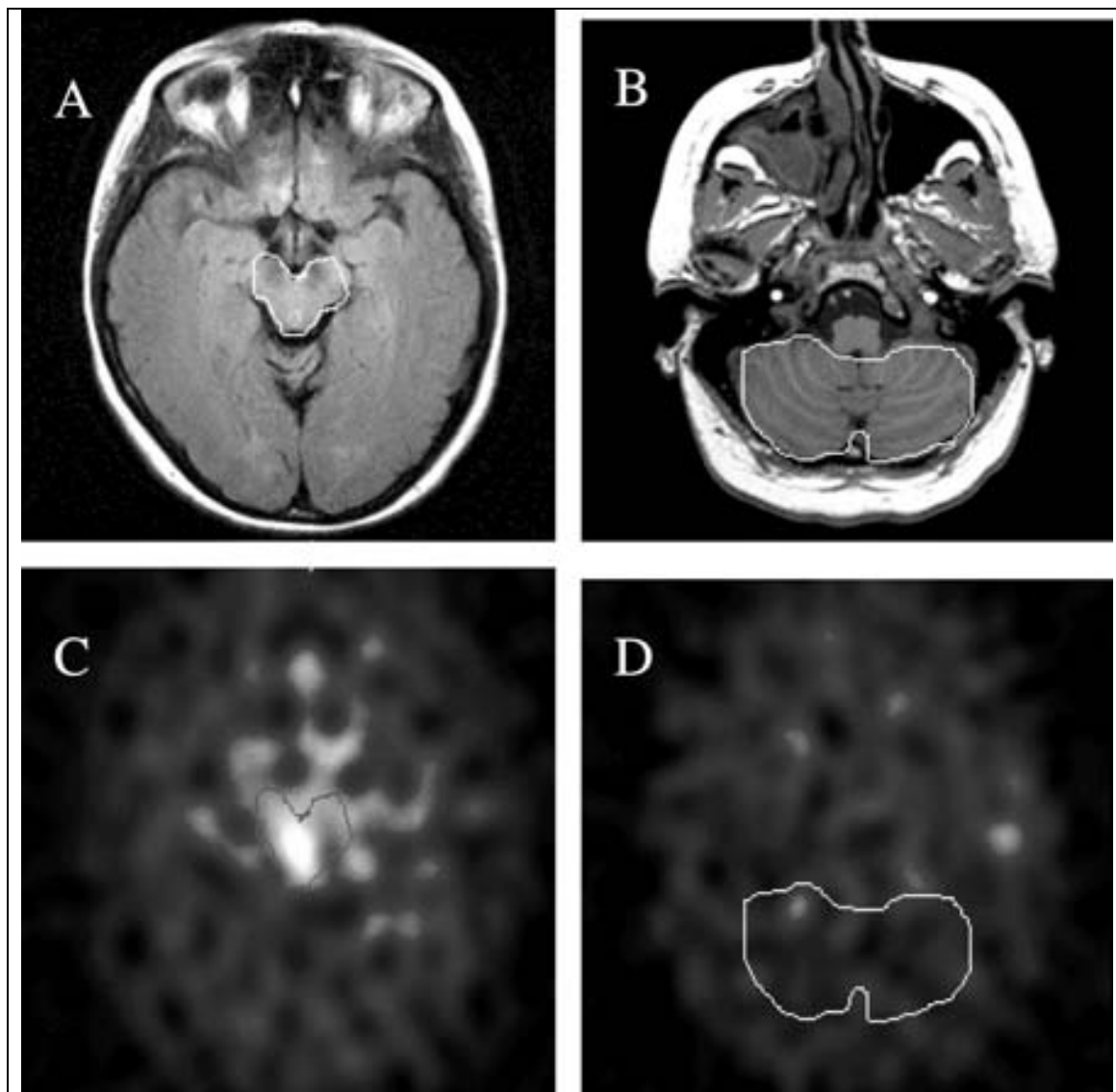


**Fig. 1-13. Example of [<sup>123</sup>I]ADAM scan in humans.**

A, B: MRI shows the ROI definitions of the midbrain (A) and the cerebellum (B).

C, D: MRI-derived ROIs were superimposed onto [<sup>123</sup>I]ADAM scans at the same level to extract respective values.

Taken from Herold *et al.* (Herold *et al.*, 2006).

#### **1.4 Aims of the thesis.**

SPECT imaging, in clinical but also preclinical research, is increasingly being used to study the abilities of new ligands using, in case of SERT ligands, neurotoxins and antidepressants to diminish, or block, binding of these ligands to SERT. DTI, in contrast, found its way into clinical and preclinical research through studies that investigate pathophysiology involving myelin. However, particularly in clinical research, DTI now provides another dimension into structural abnormalities present in psychiatric disorders such as depression and substance abuse. Despite this, advances in structural and molecular imaging in humans, and preclinical studies are limited that assess advantages and

disadvantages of certain SERT SPECT tracers in less confounding, i.e. inbred, animal models. In addition, to the author's knowledge, there is only one DTI study that deals with structural white matter abnormalities involved in substance abuse. Therefore, to contribute filling the gap in preclinical research, the following 4 aims/studies were addressed/employed.

- I. Investigation of a behavioural mouse model of depression (SERT-KO) using DTI to identify effects of life-long lasting, excessive synaptic serotonin levels on white matter integrity and arborisation. In order to do so, *ex vivo* tissue preparation of fixed mouse brains for DTI had to be established. In addition, DTI image analysis methodology had to be developed (chapter 3, page 98).
- II. The DTI image analysis methodology developed in chapter 3 (page 98) was validated in a mouse model of severe hypomyelination (PMD), with subsequent *ex vivo* tissue analysis to identify correlations between DTI measures and histopathology indicative of myelin, axon, and astrocyte changes in response to disease (chapter 4, page 158).
- III. Using the defined mouse model of hypomyelination described in chapter 4 (page 158), we aimed to identify whether severe hypomyelination would have any influence on serotonergic and dopaminergic systems by conducting autoradiographic studies to assess densities of SERT and DAT as markers for these monoaminergic systems (chapter 5, page 224).
- IV. Investigation of relative abilities of 2 different SPECT ligands to study SERT function in a rat model of SERT depletion. This involved the development of this model through neurotoxin administration, and the confirmation of binding patterns using specific ligands for SERT and DAT in an *in vitro* autoradiography experiment (chapter 6, page 242).

**Chapter 2 - Material and methods.**

## Chapter 2 - Material and methods.

### 2.1 DTI.

General tissue processing and image analyses for DTI imaging are described below, while the respective chapters that make use of DTI, i.e. chapter 3 (page 98) and chapter 4 (page 158), contain details concerning the respective studies.

#### Tissue processing for DTI.

Mice were killed according to the description given in the respective chapters. Tissue collection and preparation for DTI was performed using a protocol described by Tyszka *et al.* (Tyszka *et al.*, 2006), with slight modifications. The mice for the studies described in chapter 3 (page 98) and chapter 4 (page 158) underwent transcardiac perfusion. After perfusion, the heads were removed from the carcasses and the mouse heads were stored under constant agitation overnight in 4 % PFA (paraformaldehyde) at 4 °C. The next step included the storage of the heads in a solution of phosphate buffered saline (PBS) in order to wash out the fixative. Interstitial PFA in tissue may reduce T2 relaxation that reduces overall signal-to-noise ratio without benefitting T2 contrast (Dr. J. M. Tyszka, personal communication). Then the heads were stored in a solution containing the MRI contrast agent multihance ((4RS)-[4-carboxy-5,8,11-tris(carboxymethyl)-1-phenyl-2-oxa-5,8,11-triazatridecan-13-oato(5-)] gadolinate(2-) dihydrogen compound with 1-deoxy-1-(methylamino)-D-glucitol (1:2)) (Bracco Diagnostics, Inc.). An MRI contrast agent reduces T1 relaxation, hence reducing overall scanning time for a given resolution and signal-to-noise ratio (Tyszka *et al.*, 2006). Prior to scanning, the heads were allowed to equilibrate to room temperature, and then the deskulled brains (chapter 3, page 98), or intact heads (chapter 4, page 158), were transferred into a container filled with fomblin (perfluoropolyether). Fomblin is a near-ideal embedding medium, because it does not contain any protons that would cause a detectable signal (Benveniste and Blackband, 2002). The brains / heads in fomblin were degassed under vacuum to minimise bubbles forming in the sample during MRI scanning. Formed bubbles may give rise to susceptibility artefacts obscuring anatomical regions of interest (Benveniste and Blackband, 2002). Details on the procedure for the 2 studies are given in Table 2-1.

	<b>1) Study on SERT-deficiency (chapter 3, page 98).</b>	<b>2) Study on white matter pathology (chapter 4, page 158).</b>
<b>Transcardiac perfusion</b>	30 ml 1 % heparinised PBS, followed by 30 ml of 4 % PFA both at RT.	20 ml 1 % heparinised PBS, followed by 30 ml of 4 % PFA, both at RT.
<b>Postfixation</b>	stored at 4 °C in 20 ml 4 % PFA overnight.	stored at 4 °C in 4 % PFA for $1.11 \pm 0.33$ days. Then washed twice in 50 ml sterile PBS.
<b>Wash off fixative</b>	stored in 20 ml PBS with 0.01 % sodium azide at 4 °C for $17.3 \pm 2.0$ days.	stored in 50 ml of sterile PBS for $10.44 \pm 1.94$ days.
<b>Contrast agent incubation</b>	200 ml PBS with 0.01 % sodium azide containing 0.5 % multihance for $12.2 \pm 0.5$ days at 4 °C.	50 ml sterile PBS containing 0.5 % multihance for $20 \pm 1.5$ days at 4 °C.
<b>RT equilibration</b>	$11.5 \pm 5.3$ h.	$2.12 \pm 0.17$ h.
<b>Time spent in fomblin.</b>	skulls were removed, then stored in fomblin for $4.1 \pm 6.6$ h prior to acquisition.	heads were stored in fomblin for $8.15 \pm 8.06$ h prior to acquisition.
<p><b>Table 2-1. Details on mouse tissue processing for DTI image acquisition.</b></p> <p>Data are mean <math>\pm</math> SD.            For column 1): n = 8 for WT, n = 7 for SERT-KO, and n = 5 for SERT-HT (total n = 20).            For column 2): n = 5 for both, WT and PLPOVR, respectively (total n = 10).            RT: room temperature.            PBS: phosphate buffered saline.            PFA: paraformaldehyde.            Heparinised PBS was prepared using heparin from a stock concentration of 1000 units per ml.</p>		

In contrast to the chapter 3 (page 98), the brains in chapter 4 (page 158) were kept in the skull to avoid damage to the brains on removal. It was also anticipated that this would improve the coregistration as the brains would be in their natural *in situ* environment without any deformation and damage that could result from removing them from the skull.

### **DTI image acquisition.**

DWIs of fixed mouse brains were acquired on a 7T Bruker Biospin Biospec 70/30 MRI system. For scanning, the brain / head was spatially restrained in a container filled with fomblin, and placed in a 35 mm Bruker (B-G6) birdcage gradient coil. The echo time (TE) was set to 14.4 ms, the repetition time (TR) was 350 ms (chapter 3, page 98), or 500 ms (chapter 4, page 158), and the diffusion gradient separation ( $\Delta$ ) was 6.6 ms. The diffusion gradient duration ( $\delta$ ) was 3 ms, with a b-value of  $1450 \text{ s/mm}^2$ , and one b0 image (T2-weighted image with little diffusion weighting). The field-of-view was fixed to  $2 \times 1.2 \times 1 \text{ cm}^3$ , with voxel dimensions of  $0.13 \times 0.13 \times 0.13 \text{ mm}^3$ .

## Chapter 2 - Material and methods.

The total scanning time acquiring 2 averages along 6 diffusion directions, ( $[G_x, G_y, G_z] = [0.707107 \ 0.707107 \ 0], [0.707107 \ 0 \ 0.707107], [0 \ 0.707107 \ 0.707107] [-0.707107 \ 0.707107 \ 0] [0 \ -0.707107 \ 0.707107] [0.707107 \ 0 \ -0.707107]$ ), took 9 h 38 min (chapter 3, page 98), or 13 h 46 min (chapter 4, page 158).

Note the different TR in chapter 4 (TR = 500 ms, page 158) and chapter 3 (TR = 350 ms, page 98), which was because the original scanning protocol had been changed for a different study and overwritten in error.

### DTI image analysis.

The DTI image processing was performed as described by Tyszka *et al.* with modifications (Tyszka *et al.*, 2006).

### Software packages.

Paravision <sup>®</sup>	Bruker BioSpin MRI GmbH, Ettlingen, Germany
Xmedcon, (Nolf, 2003)	Freeware, available at <a href="http://xmedcon.sourceforge.net/">http://xmedcon.sourceforge.net/</a>
Medical Image Processing, Analysis and Visualization (MIPAV), (J. McAuliffe <i>et al.</i> , 2001).	Freeware, available at <a href="http://mipav.cit.nih.gov/">http://mipav.cit.nih.gov/</a>
FMRIB Software Library (FSL), (Smith <i>et al.</i> , 2004)	Freeware, available at <a href="http://www.fmrib.ox.ac.uk/fsl/">http://www.fmrib.ox.ac.uk/fsl/</a>
Automated image registration (AIR), (Woods <i>et al.</i> , 1998).	Freeware, available at <a href="http://bishopw.loni.ucla.edu/AIR5/index.html">http://bishopw.loni.ucla.edu/AIR5/index.html</a>
MRicro, (Rorden and Brett, 2000)	Freeware, available at <a href="http://www.sph.sc.edu/comd/rorden/mricro.html">http://www.sph.sc.edu/comd/rorden/mricro.html</a>
MRIConvert	Freeware, available at <a href="http://lcn.uoregon.edu/~jolinda/MRIConvert">http://lcn.uoregon.edu/~jolinda/MRIConvert</a>
ImageJ, (Abramoff <i>et al.</i> , 2004)	Freeware, available at <a href="http://rsb.info.nih.gov/ij/">http://rsb.info.nih.gov/ij/</a>

### Preparation of images for analysis.

The 6 DWIs and the b0 image for each animal were exported from Bruker's Paravision software (Ettlingen, Germany) in DICOM format, and converted to ANALYZE format using MRIConvert (<http://lcn.uoregon.edu/~jolinda/MRIConvert>). For the study described in chapter 4 (page 158), where the entire head was DTI scanned, the DWIs and the b0 image were averaged using Roger Woods' image registration software automated image registration (AIR) to produce a high signal-to-noise image (Woods *et al.*, 1998). To avoid possible mis-registrations because of different lengths of the spinal cord segments attached to the brains, the average images generated for chapter 4 (page 158), or the b0 images of the mouse brains for chapter 3 (page 98), were flipped and brought into an appropriate orientation using xmedcon, a medical image converter (Nolf, 2003), and the spinal cords in

images of individual animals were removed using the image processing software MIPAV (J. McAuliffe et al., 2001). As mouse tissue described in chapter 3 (page 98) consisted of deskulled brains, while the whole head was scanned in chapter 4 (page 158), the generation of the brain mask was performed differently (see below).

### **Brain mask generation for study on SERT-deficiency (chapter 3, page 98).**

In order to extract the invariants of the diffusion tensor using the diffusion toolbox (FDT) included in the FMRIB software library (FSL, a software library dedicated to MRI analyses) (Behrens et al., 2003b, Smith et al., 2004), a binary mask of the brain needed to be constructed to restrict calculations to this mask. First, the b0 image was median filtered using a 3 x 3-squared kernel in MIPAV, and subsequently, the mean and standard deviation (SD) were calculated for this image using the image processing software ImageJ (Abramoff et al., 2004). In MIPAV, the mean served as the threshold level to threshold the median filtered image (Ma et al., 2005). At this point, a preliminary mask was available.

### **Brain mask generation for study on white matter pathology (chapter 4, page 158).**

To extract the brain from the skull within the images and to create a mask for the following reconstruction of the diffusion tensor invariants, Otsu's thresholding method implemented in MIPAV was applied to the brainstem cut-off average (see above, page 42). This provided a preliminary mask which was processed the same way as the one obtained from the brain mask generation step in chapter 3 (page 98) described above.

Subsequently, a morphological opening operation with a 5 x 5 x 5 kernel was performed to remove disconnected tissue from the brain and remaining noise artefacts. In this operation, all the structures smaller than the kernel consisting of 5 x 5 x 5 voxels will be removed. This is followed by a morphological filling operation of the holes in the masks (Tyszka et al., 2006). The mask was then stored as an 8 bit image after manual editing in MRICro, where appropriate. Blank slices in the mask were removed using AIR, and the same cropping rule was applied to the 6 DWIs and the b0 image before feeding them into the DTI reconstruction tool.

### **Calculation of diffusion tensor invariants.**

Using the DTI reconstruction software dtifit in FSL (Behrens et al., 2003), the images were corrected for eddy currents, and then the metrics of the tensor, i.e. FA, MD, the three eigenvalues ( $\lambda_i$ ), and the three eigenvectors ( $\epsilon_i$ ), were computed. In addition, a T2-weighted

image (S0), free from diffusion weighting, was computed from the b0 and the 6 DWIs using FSL.

### **Creation of WT FA registration template.**

For the study performed in chapter 3 (page 98), a representative FA image was then chosen from the WT mice according to its orientation in space, with the brain being aligned with the x-, y- and z-axis. Following this, the FA images from individual WT mice were coregistered to the representative FA map using an optimised nonlinear registration routine performed with the image registration software AIR. Once all WT FA images were coregistered to the representative FA map, the WT FA template was created by using AIR's softmean script to average the individual FA maps. This FA template of WT animals provided a better representation of the normal variation within the respective mouse population used (Kovacevic et al., 2005).

When the tract-based spatial statistics (TBSS) package (a set of DTI analysis tools) became available within FSL (Smith et al., 2006), the registration routine (IRTK) (Schnabel et al., 2001), and the image calculator included therein were used for simplicity to calculate subtraction maps for all DTI extracted parameters, and subsequently perform statistical analyses. This also included the creation of another WT FA template in FSL, which was done the same way as described above using AIR. In order to differentiate whether the coregistration of images was done with FSL or AIR, the abbreviations AIR, or FSL, respectively, are given in the section's heading.

The WT FA template for the study described in chapter 4 (page 158) was entirely done using FSL. Minor corrections in the orientation of this template, where appropriate, were then performed using the AMIDE manual registration software (Loening and Gambhir, 2003).

### **Coregistration of all individual FA images to the WT FA template.**

Once the WT FA template was created, all individual WT, as well as the FA images of the transgenic animals were coregistered to this template. Group-wise averaging was performed using either AIR, or FSL, respectively, as described below.

### **Generation of RD images (FSL analyses only, see above).**

In order to generate RD subtraction maps, the second and third eigenvalue maps of individual images were averaged.

$$RD = \frac{\lambda_2 + \lambda_3}{2}.$$

### **Coregistration of individual non-FA images to WT FA template space.**

The transformation matrix obtained through the coregistration of the individual FA images to the WT FA template was applied to the non-FA images to bring them into coregistered standard space by feeding it either into AIR (for S0,  $\lambda_1$ ,  $\lambda_2$ ,  $\lambda_3$ ) or FSL (for  $\lambda_1$ ,  $\lambda_2$ ,  $\lambda_3$ , MD and RD).

### **Creation of subtraction maps.**

Once all FA and non-FA images (FA,  $\lambda_1$ ,  $\lambda_2$ ,  $\lambda_3$ , MD and RD) were in standard WT FA template space, group averages (WT, SERT-KO, SERT-HT, PLPOVR, respectively) for subtraction map analysis using AIR or FSL were generated, e.g.:

$$\text{mean } n = (n_1 + n_2 + \dots + n_i) / i$$

where  $n$  is the DTI parameter (FA,  $\lambda_1$ ,  $\lambda_2$ ,  $\lambda_3$ , MD and RD), and  $i$  the number of images included in the respective group.

Group-averaged DTI parameter maps for SERT-KO, SERT-HT, and PLPOVR, i.e. FA,  $\lambda_1$ ,  $\lambda_2$ ,  $\lambda_3$ , MD and RD, were then subtracted from those of WT animals:

mean WT - mean SERT-KO

mean WT - mean SERT-HT

mean WT - mean PLPOVR

Following creation of DTI parameter subtraction maps from FSL coregistered images, these difference images were colour-coded in ImageJ.

The whole registration process, and the creation of the FA subtraction map, is summarised using the example of WT and SERT-KO mice in Fig. 2-1.

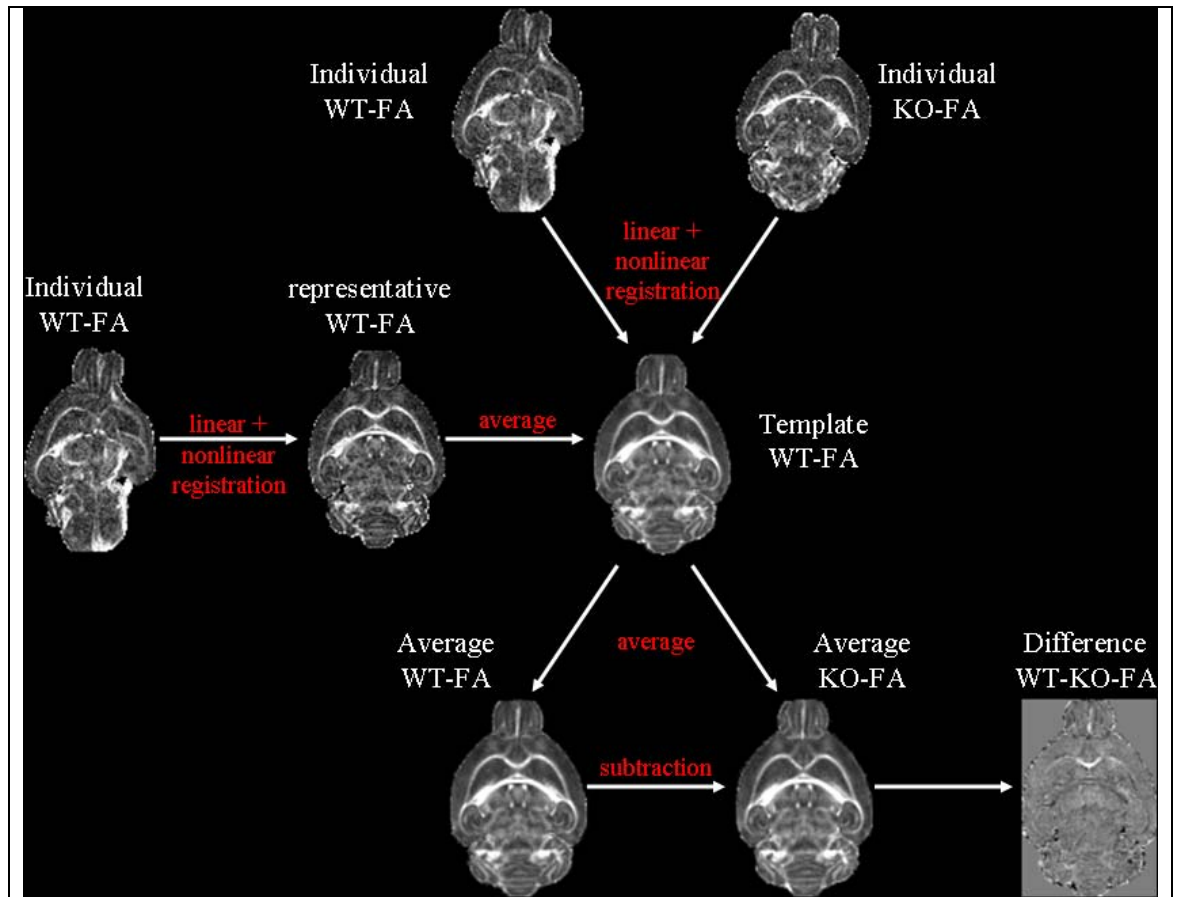


**Fig. 2-1. Illustration of the WT FA template creation, coregistration of individual FA maps, generation of group averages and subtraction maps.**

A representative WT FA map was chosen, all other individual WT FA images were then coregistered to that and were subsequently averaged to create the WT FA template. Following creation of the WT FA template, WT and SERT-KO were coregistered to that template before group averaging was performed. Lastly, the average SERT-KO FA map was subtracted from the average WT FA map in order to create the difference image.

### **TBSS analyses on DTI parameter maps (FSL).**

Individual FSL coregistered DTI parameter maps were fed into the TBSS package designed for DTI data analysis (Smith et al., 2006). Statistical comparisons were made between WT and SERT-KO, WT versus SERT-HT, both in chapter 3 (page 129), and between WT and PLPOVR in chapter 4 (page 169). The explanation provided here is for the WT vs. SERT-KO comparison but the same method was used to compare WT and SERT-HT, and WT versus PLPOVR groups. After coregistering the FA data for each animal, the FA maps from all WT and SERT-KO mice were averaged to produce a single dataset representing the average FA value in each voxel. From this image, the TBSS software derived a single line skeleton for the centres of each tract that were common to both WT and SERT-KO groups. Then, the coregistered FA map for each individual mouse

was projected onto this skeleton. The TBSS software attempts to compensate for errors in coregistration of the individual maps by searching in voxels immediately perpendicular to the skeleton for values that are higher than those covered by the skeleton (Fig. 2-2). If higher, the values in perpendicular voxels are substituted for the original lower value covered by the skeleton. Then the t-statistic for the comparison of the two groups was generated for each voxel within the skeleton. A threshold was then set such that all voxels with a t-value of greater than 1 were identified and this generated a statistical image which shows the spatial distribution of clusters in which the difference between WT and SERT-KO groups was significant at  $p < 0.05$ . The skeleton derived from the mean FA map was then used in the same way for the other DTI parameter maps, i.e.  $\lambda_1$ ,  $\lambda_2$ ,  $\lambda_3$ , MD and RD.

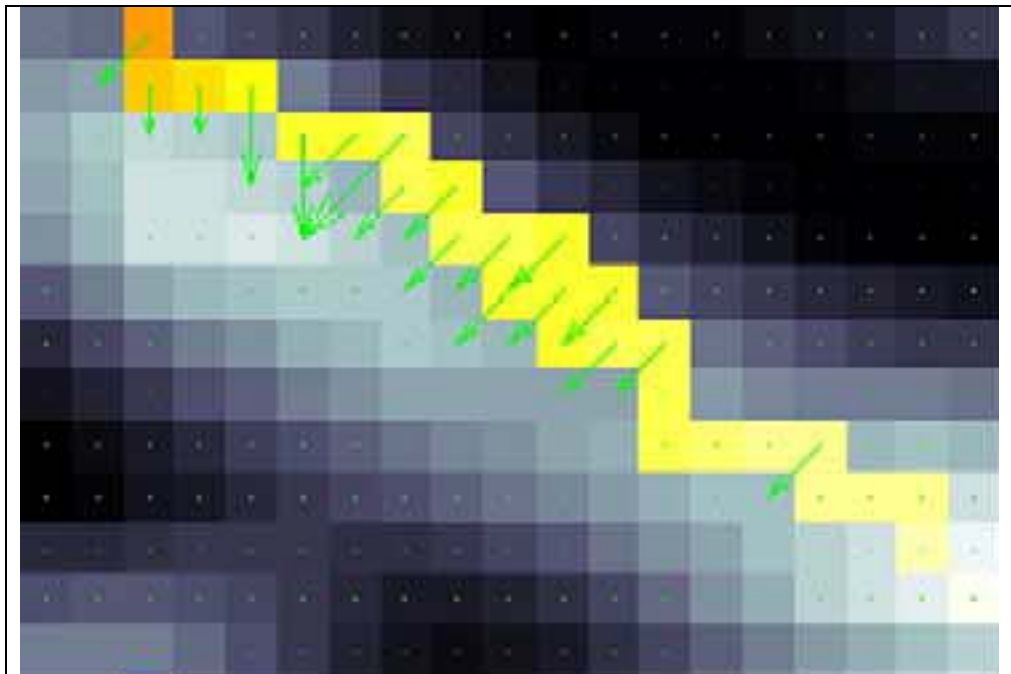


**Fig. 2-2. TBSS-generated skeleton is used to compensate for mis-registration.**

Individual FA maps are projected onto the skeleton (yellow). Green arrows point to voxels perpendicular to the tract that have higher FA values compared to those currently covered by the skeleton. These higher FA values will subsequently be copied onto the nearest skeleton voxel.

Taken from Smith *et al.* (Smith *et al.*, 2006).

## **2.2 Histology on mice with white matter pathology.**

This section describes how the mouse brain tissue processed for DTI imaging (see material and methods in chapter 2, page 40) in chapter 4 (page 159) has been further processed and analysed for immunohistochemistry after DTI data were acquired. In addition, on a separate set of animals within the study described in chapter 4 (page 190), electron microscopy data was acquired as outlined below (page 50).

### **Animals – tissue for immunohistochemistry.**

Note that the cutting and collection of these sections was done by Joan Stewart, Division of Clinical Neuroscience, Wellcome Surgical Institute, Glasgow University. Further tissue processing (see below) was done by our collaborators, i.e. Jennifer Barrie, Applied Neurobiology Group, Glasgow University.

For immunohistochemistry, DTI scanned heads were used (WT and PLPOVR, n = 5 each group, all female, see page 161), and their brains removed from the skull. The brains were placed into plastic cassettes and processed using a tissue processor for paraffin embedding (Shandon Citadel 1000 automatic processor, Miles Scientific, Rugby) (appendices, page A). Following this, the brains were embedded in paraffin blocks, and mounted onto chucks for cutting. The brains were then cut on a microtome (Leica RM 2135) into 6 µm sections for immunohistochemistry and mounted, 2 sections each slide, onto poly-L-lysine slides (appendices, page B). After collection of the sections, slides were washed in xylene to remove the wax and sections were then hydrated through a series of alcohols in decreasing concentrations down to water only. In order to unmask tissue antigens, sections were heated in a microwave in 0.01 M trisodium citrate buffer at pH 6.0 for 10 min. Subsequent incubation in 3 % H<sub>2</sub>O<sub>2</sub> for 30 min blocked endogenous peroxidase activity. To reduce nonspecific binding, sections were immersed in 10 % heat inactivated normal goat serum. This was followed by an overnight incubation at 4 °C in primary antibody made in 10 % normal goat serum. On the following day, sections were washed several times in PBS, followed by incubation with biotinylated link antibodies (Vector Labs) at a concentration of 1:100 for 1 h at room temperature. Sections were again washed several times in PBS before the avidin-biotin complex (ABC, Vector Labs) was applied for 30 min, which was again washed off several times in PBS. Preparation of 3,3'-diaminobenzidine (DAB) was done using Sigma Fast tablets. After the development of the chromogen, the sections were counterstained with haemalum, and subsequently dehydrated in several increasing

concentration steps of alcohol. Finally the sections were cleared in xylene and mounted onto slides using DPX (mounting medium) for analysis.

The primary antibodies used and their final concentrations were as follows:

Anti-MBP (Chemicon) 1:500

Anti-GFAP (Dako) 1:1000

Anti-APP (anti-amyloid  $\beta$ -precursor protein; Chemicon) 1:100

### Image analysis of immunohistochemistry data.

Overview images of representative MBP, APP, and GFAP images were captured by the author using a MCID basic system (7.0 Rev 1.0, build 207; Imaging Research Inc.). The following was done by Jennifer Barrie, Applied Neurobiology Group, Glasgow University.

Ten-fold magnified images were acquired using an Olympus IX70 microscope equipped with a QICAM Fast Digital Camera (QIMAGING). Image Pro-Plus 6.0 software (Media Cybernetics) was used to threshold and overlay a region-of-interest (ROI) onto the MBP and GFAP images bilaterally. The number of pixels within an ROI was counted automatically and was subsequently converted into area occupied by the pixels in  $\mu\text{m}^2$  per  $\mu\text{m}^2$  of area analysed [ $\mu\text{m}^2/\mu\text{m}^2$ ]. Haematoxylin-stained nuclei were counted automatically with the system set to detect elements per  $\mu\text{m}^2$  [ $1/\mu\text{m}^2$ ] within the ROI. APP-positive foci were counted manually using the same ROI. The ROI sizes were as follows:

<b>Bregma level [mm]</b>	<b>Structure</b>	<b>ROI size [mm<sup>2</sup>]</b>
1.10	Anterior Commissure	0.072376
1.10	Corpus Callosum	0.058308
0.14	Anterior Commissure	0.108564
0.14	Corpus Callosum	0.058308
-1.46	Corpus Callosum	0.058308
-1.46	Hippocampal Fimbria	0.112692

Rater (Jennifer Barrie) was unaware of the animal's identity during the analysis. Due to the subjectivity of thresholding the GFAP and MBP data, data were read by two raters (Jennifer Barrie and Fredrik Gruenenfelder, both Applied Neurobiology Group, Glasgow

University) independently, and the means of these two readings were taken for further use. All graphs were generated by the writer of this thesis.

### **Animals – tissue for electron microscopy.**

Tissue collection, processing and data analysis for electron microscopy (EM), except from graph generation, was performed by Jennifer Barrie, Applied Neurobiology Group, Glasgow University.

For the EM study, another set of animals was generated that was only processed for ultrastructural assessment. PLPOVR animals were generated as previously described by Readhead *et al.* (#72 strain) (Readhead *et al.*, 1994), and maintained at the animal unit at Garscube Estate, University of Glasgow. The mice were housed at a light/dark cycle of 12/12 h. Food and water was accessible *ad libitum*, and all experiments were carried out according to the guidelines laid out in the Animals Scientific Procedures Act under a project license from the UK Home Office and approved by the local ethical review panel. At P120, animals PLPOVR (n = 4, female) and control animals from the same in-bred colony (n = 3, female) were sacrificed by an overdose of CO<sub>2</sub> followed by transcardiac perfusion with saline until the effluent became clear, followed by 50 - 100 ml of Karnovsky fixative (appendices, page B). Subsequently the animals were immersed in Karnovsky fixative after perfusion for up to 3 h. Then the brain was removed and blocks of required regions were dissected out and stored in Karnovsky fixative until resin tissue processing for EM (generally several days).

Karnovsky fixed tissue blocks were processed in a Lynx tissue processor for resin embedding (appendices, page A). After processing, the tissue samples were oriented in resin-filled silicone moulds and then placed in an oven for 24 h at 60 °C to facilitate polymerisation.

In order to identify an appropriate area for EM in the resin embedded tissue, 1 µm thick sections were cut on an Ultracut-E ultratome (Reichert-Jung) using a glass knife, and subsequently stained with methylene blue/azur II for examination on a light microscope. Once identified, 70 nm thick sections were yielded using a diamond knife. The sections were then mounted onto 300-mesh 3.05 mm-diameter copper grids for staining. Following mounting, the grids were stained. Briefly, the EM grids were incubated in uranyl acetate for 10 min before they were washed twice in 50 % alcohol (appendices, page C). Subsequently, the grids were washed in 1 % distilled H<sub>2</sub>O followed by drying in air. As

next step, the dried grids were placed in Reynolds lead citrate in 1 M NaOH in a moistened chamber (appendices, page C), and then washed twice in 1 M NaOH followed by a wash in distilled H<sub>2</sub>O. Finally the grids were dried and used for EM acquisition. At a magnification of 8000x, 10 micrographs from each area of the stained grids were captured onto Kodak EM film using a JEOL CX100 EM. The negative films were then scanned and stored as digital images using an Epson perfection 3200 PHOTO scanner for further analysis.

**Image analysis of electron microscopy data.**

Assessment of axon density (axons/ $\mu\text{m}^2$ ) was achieved by superimposing a rectangle with a known area onto each individual EM micrograph image (see formula below). All axons contained within and intersecting with the south and west boundaries of that ROI were counted and the axon density was then calculated according to the formula given below. The axons intersecting with the north and east edges were not included in the axon count (Fig. 2-3).

$$\text{Axonal density} = \frac{\text{total number of axons}}{\text{ROI area (468.2 } \mu\text{m}^2)}$$

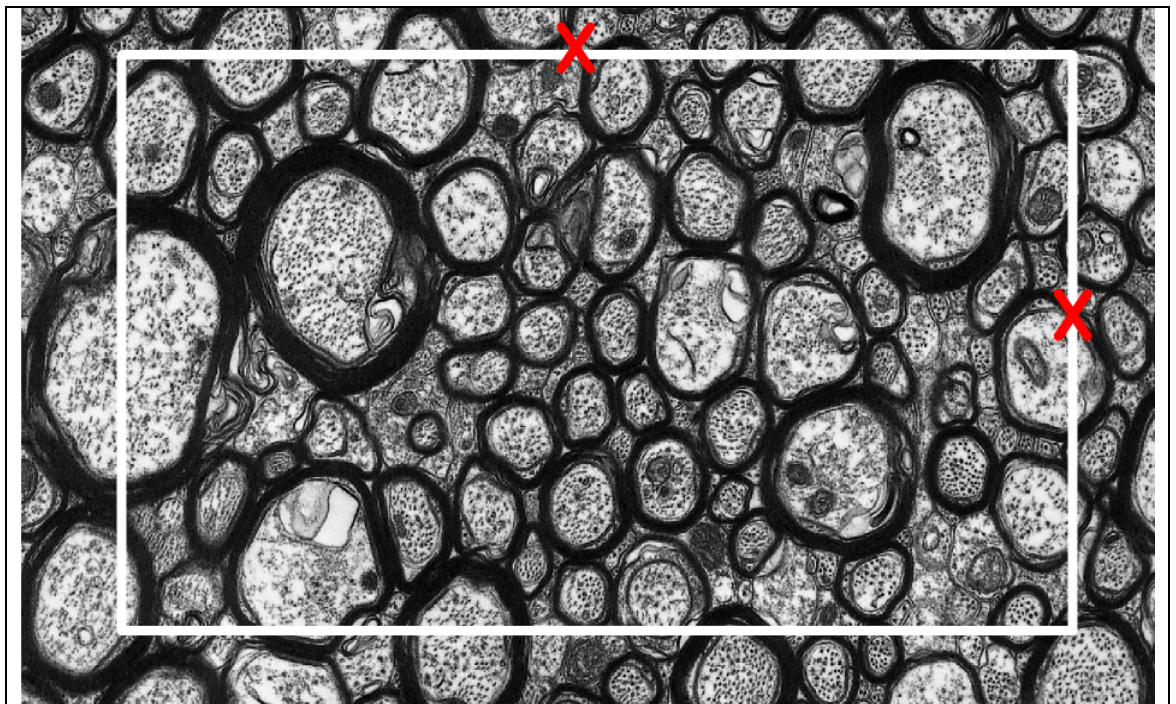


**Fig. 2-3. Determination of axon density on EM images.**

Axons within and intersecting with white rectangle (ROI) were counted except those intersecting with the north and east edges (red crosses).

Acquisition of EM image, and assessment of axonal density was performed by Jennifer Barrie, Applied Neurobiology Group, Glasgow University.

## Chapter 2 - Material and methods.

In order to determine the percentage of myelinated fibres, a line graph was superimposed onto each individual EM image, and myelinated and unmyelinated axons were counted that intersect with the superimposed lines (Fig. 2-4). The percentage of myelinated axons was then calculated according to the formula:

$$\% \text{ myelinated fibres} = \frac{\text{myelinated fibres}}{(\text{myelinated fibres}) + (\text{unmyelinated fibres})} * 100 .$$

For all EM data, only the corpus callosum at Bregma level 1.10 mm, and the hippocampal fimbria at Bregma level -1.46 mm were examined.

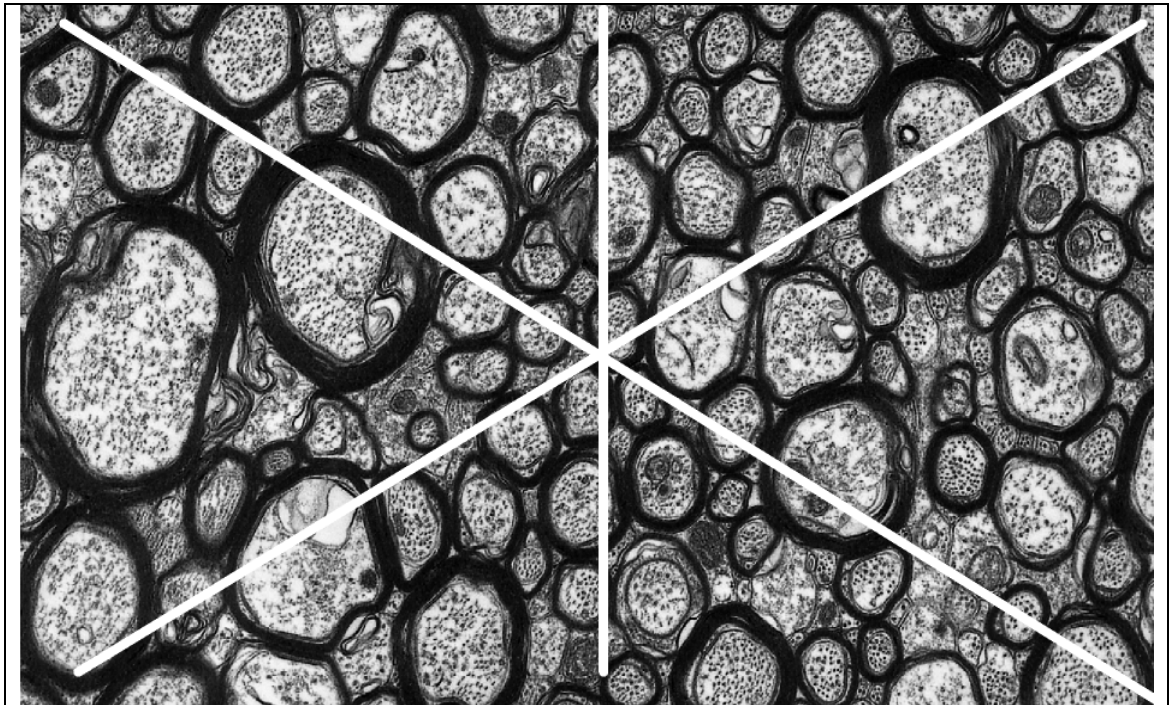


**Fig. 2-4. Determination of percentage of myelinated axons on EM images.**

Total number of axons intersecting with any line of the superimposed grid were compared to the number of axons being myelinated.

Acquisition of EM image, and assessment of number of myelinated fibres was performed by Jennifer Barrie, Applied Neurobiology Group, Glasgow University.

### 2.3 Pilot study to establish a rat model of SERT depletion using MDMA.

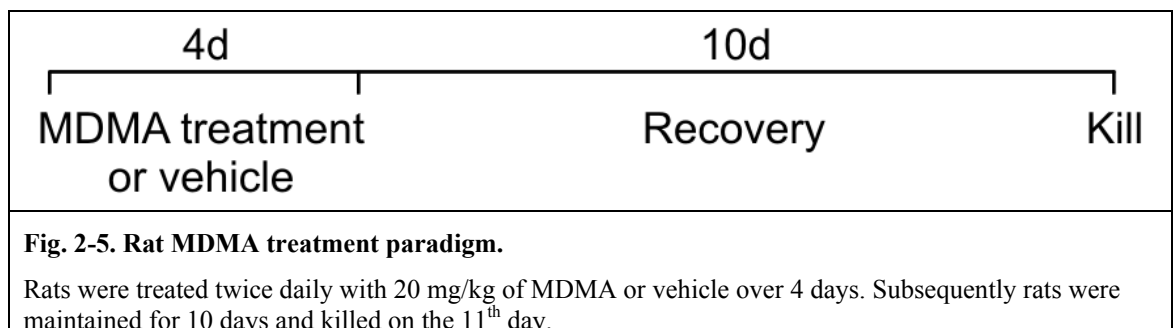
The study described here in this section established the rat model of SERT depletion using MDMA, whose effects were assessed using *in vitro* autoradiography. The formal study is shown in chapter 6 (page 242), where the effects of MDMA depletion on SERT were assessed using *in vivo* [<sup>125</sup>I]βCIT and [<sup>125</sup>I]ADAM SPECT, followed by validation using *ex vivo* and *in vitro* autoradiography.

#### Animals.

Sprague-Dawley rats (n = 8, male) weighing 146.6 ± 6.0 g (mean ± SD) on the day of arrival, were obtained from Harlan, UK. The rats were housed in groups of 4 at the animal unit at Garscube Estate, University of Glasgow, at a light/dark cycle of 12/12 h. Food and water was accessible *ad libitum*, and all experiments were carried out according to the guidelines laid out in the Animals Scientific Procedures Act under a project license from the UK Home Office and approved by the local ethical review panel. The experiment was started after an adaptation period of 11 days following arrival of the rats at the animal facility.

#### MDMA treatment regimen.

MDMA was purchased from Sigma-Aldrich, UK. MDMA was administered subcutaneously to a group of rats (20 mg/kg, twice daily, 12 h apart, in 1 ml/kg 0.9 % saline), for 4 consecutive days (Fig. 2-5). Control animals received injections of vehicle. The animals were weighed once in the morning, and the 2 daily MDMA, or vehicle injections were calculated according to this weight.



#### Tissue collection and processing.

Ten days after the final injection, the animals were deeply anaesthetised with 30 % O<sub>2</sub>, 70 % N<sub>2</sub>O, and 5 % isoflurane and the animals killed by dislocation of the neck, followed by decapitation. The brains were quickly removed, and split into 2 hemispheres along the

sagittal midline. The right hemisphere was reserved for autoradiography and was rapidly frozen in isopentane at  $\sim -42$  °C on dry ice for 10 min, wrapped in parafilm, and stored at  $-80$  °C until further use. The hemi-brains were subsequently mounted onto chucks using cryomatrix (Shandon, Runcorn), covered with M1 (Pittsburgh, USA) embedding matrix, and cut on a cryostat at  $-20$  °C. Coronal sections ( $20$   $\mu$ m) were cut according to the following scheme using the definitions of Paxinos *et al.* (Paxinos and Watson, 1998).

<b>Bregma level [mm]</b>	<b>Structures</b>
3.2	Prefrontal Cortex
1.0	Caudate-Putamen, Anterior Cingulate Cortex, Nucleus Accumbens, Septal Area
-2.3	Anterior Retrosplenial Cortex, Basolateral Amygdala, Central Amygdaloid Nucleus, Ventral Hypothalamus
-3.6	Hippocampus, Dorsal Thalamus, Perirhinal/Entorhinal Cortex, Piriform Cortex
-5.8	Superior Colliculus, Medial Geniculate Nucleus, Substantia Nigra
-8.3	Entorhinal Cortex, Inferior Colliculus, Dorsal Raphe
-10.04	Cerebellum

Sections were collected on gelatine/chrome alum subbed slides (appendices, page B), with 2 sections per slide for total binding, and one section for nonspecific binding. Subsequently, sections were dried overnight, followed by storage at  $-80$  °C until further use. Adjacent sections at each of these levels were processed for autoradiography as described below.

#### **Synthesis of [ $^{125}$ I] $\beta$ CIT.**

[ $^{125}$ I] $\beta$ CIT was synthesized as described elsewhere (Baldwin *et al.*, 1993). Briefly, the tributylstannyl precursor underwent electrophilic iododestannylation to yield [ $^{125}$ I] $\beta$ CIT. [ $^{125}$ I] $\beta$ CIT was formulated in 5 ml batches in isotonic citrate acetate buffer containing  $< 4$  % ethanol. [ $^{125}$ I] $\beta$ CIT had a radiochemical purity of  $> 99$  %. [ $^{125}$ I] $\beta$ CIT (specific activity 5.62 Ci/ $\mu$ mol) was synthesised by Dr. Sally Pimlott at the West of Scotland Radionuclide Dispensary.

#### ***In vitro* autoradiography using [ $^{125}$ I] $\beta$ CIT, [ $^3$ H]citalopram and [ $^3$ H]WIN 35, 428.**

Detailed autoradiographic procedures are given in Table 2-2. Briefly, slides were pre-incubated in buffer, then incubated in buffer in the presence of radiolabelled compound to define total binding. Nonspecific binding was defined with radiolabelled compound in the presence of respective displacers in buffer. Slides were washed, dried and then apposed to

Kodak Biomax MR film for varying periods of time in the presence of pre-calibrated [<sup>3</sup>H], or [<sup>125</sup>I]micro-scales, both purchased from Amersham.

Radioligand and reference	[ <sup>125</sup> I]βCIT McGregor <i>et al.</i> (McGregor <i>et al.</i> , 2003)	[ <sup>3</sup> H]citalopram Hébert <i>et al.</i> (Hebert <i>et al.</i> , 2001)	[ <sup>3</sup> H]WIN 35, 428 Andersen <i>et al.</i> (Andersen <i>et al.</i> , 2005)
Specific activity	1.48 - 5.62 Ci/μmol	83 Ci/mmol	83.6 - 85.9 Ci/mmol
Radioligand source	West of Scotland radionuclide dispensary	Amersham	PerkinElmer
Buffer	Tris-buffer: 50 mM Tris-HCl 120 mM NaCl 5 mM KCl pH 7.4	Tris-buffer: 50 mM Tris-HCl 120 mM NaCl 5 mM KCl pH 7.4	phosphate buffer: 25 mM Na <sub>2</sub> HPO <sub>4</sub> 25 mM NaH <sub>2</sub> PO <sub>4</sub> 50 mM NaCl pH 7.7
Pre-incubation	30 min in buffer at RT	15 min in buffer at RT	20 min in buffer at RT
Incubation	60 min incubation in buffer at RT:  Total SERT: 50 pM [ <sup>125</sup> I]βCIT 1 μM mazindol  Total DAT: 50 pM [ <sup>125</sup> I]βCIT 50 nM fluoxetine  NS: 50 pM [ <sup>125</sup> I]βCIT 1 μM mazindol 10 μM fluoxetine	120 min incubation in buffer at RT  Total SERT: 2 nM [ <sup>3</sup> H]citalopram  NS: 2 nM [ <sup>3</sup> H]citalopram 20 μM fluoxetine	120 min incubation at 4 °C in buffer:  Total DAT: 10 nM [ <sup>3</sup> H]WIN 35, 428  NS: 10 nM [ <sup>3</sup> H]WIN 35, 428 30 μM nomifensine
Displacer source	Tocris	Tocris	Sigma-Aldrich
Wash	All at 4 °C:  1 x 1 min, then 2 x 20 min  dip in distilled H <sub>2</sub> O	All at 4 °C:  4 x 2 min in buffer  dip in distilled H <sub>2</sub> O	All at 4 °C:  3 x 30 s in buffer  dip in distilled H <sub>2</sub> O
Dry	Gentle stream of air overnight	Gentle stream of air overnight	Gentle stream of air overnight
Film exposure	3 h - 6 days	5 weeks	11 weeks

**Table 2-2. *In vitro* autoradiography protocols for [<sup>125</sup>I]βCIT, [<sup>3</sup>H]citalopram and [<sup>3</sup>H]WIN 35, 428.**

Appropriate information about ligand concentrations, incubation buffers, wash steps, and references for the radioligands used for *in vitro* autoradiography. NS: nonspecific binding. RT: room temperature.

Some modifications to the original autoradiographic protocols were carried out as follows.

For *in vitro* [<sup>125</sup>I]βCIT autoradiography:

Note that the definition of nonspecific binding differed from that described by McGregor *et al.* (McGregor *et al.*, 2003). The authors used separate sets of sections, i.e. to define nonspecific binding to SERT, 10 μM GBR12909 was used with 50 pM [<sup>125</sup>I]βCIT, while DAT was defined using 10 μM fluoxetine. In this study, only 1 set for the definition of nonspecific binding was used, as outlined above. In addition, the original protocol used a phosphate buffer, while here a Tris-buffer, as described by Hébert *et al.* (Hebert *et al.*, 2001), was used instead.

For *in vitro* [<sup>3</sup>H]WIN 35, 428 (2β-carbomethoxy-3β-(4-fluorophenyl)tropane) autoradiography to label DAT:

The original protocol described by Andersen *et al.* used 30 μM cocaine to define nonspecific binding (Andersen *et al.*, 2005). Here however, 30 μM nomifensine (1,2,3,4-tetrahydro-2-methyl-4-phenyl-8-isoquinolinamine) was used instead.

### **Image analysis for autoradiography data.**

Autoradiographic films were digitised and analysed using a MCID basic system (7.0 Rev 1.0, build 207; Imaging Research Inc.). The optical density was measured and converted to the tissue equivalent in fmol/mg using a standard curve that was calculated with a range of pre-calibrated [<sup>3</sup>H]micro-scales (for [<sup>3</sup>H]citalopram and [<sup>3</sup>H]WIN 35, 428) or [<sup>125</sup>I]micro-scales (for [<sup>125</sup>I]βCIT), respectively. Activity of [<sup>125</sup>I]βCIT and the [<sup>125</sup>I]micro-scales were decay corrected, however because of the long half-life (> 12 years) of [<sup>3</sup>H], radioactive decay for tritiated ligands has not been taken into account.

## **Results.**

### **Effects of MDMA treatment on animal body weight.**

The animals' weight gain was closely monitored during the whole experiment. From animal arrival to the first day of treatment no visually obvious differences were observed between vehicle- and MDMA-treated groups (Fig. 2-6). However on the second day of treatment, the MDMA-treated animals lost weight which lasted until the end of the treatment period. Over the subsequent 10 days animals regained weight apparently at a steeper rate than the vehicle group and the two groups had almost the same weights on the final day of the experiment.

The original treatment plan was to use MDMA administration of 20 mg/kg, twice daily over 4 days. However, the first injection on day 1 consisted of 25 mg/kg due to a calculation error. The following injections were performed as planned using 20 mg/kg of MDMA.

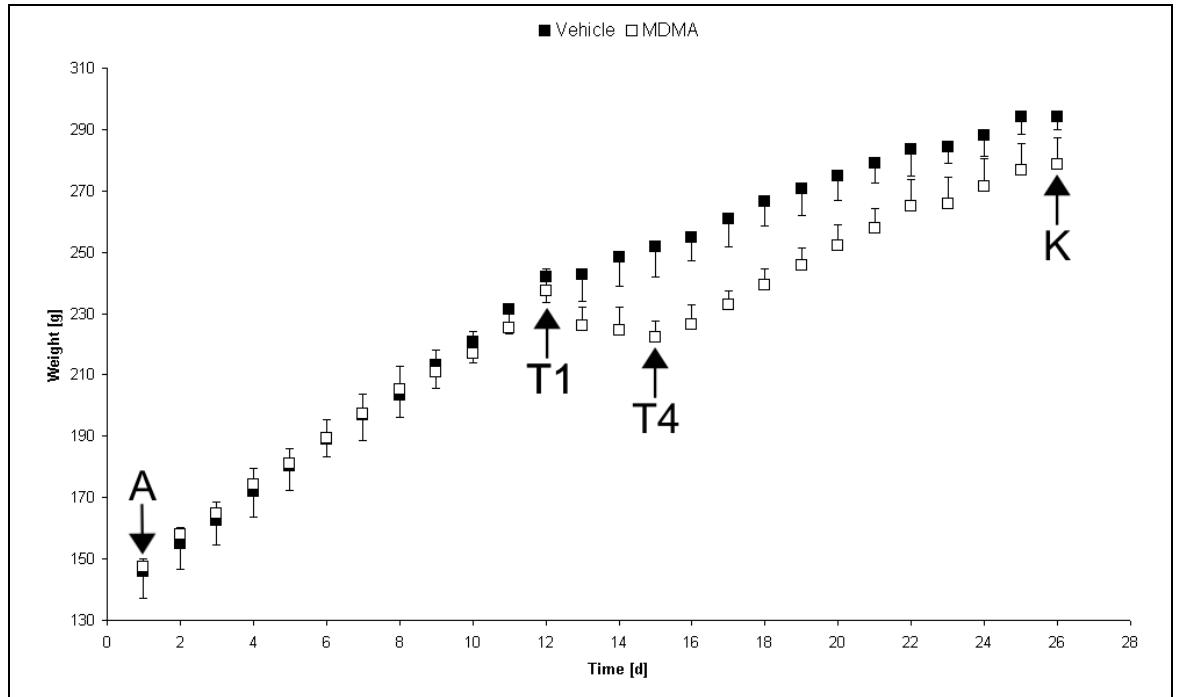


**Fig. 2-6. MDMA treatment reduces body weight of treated rats.**

No differences were observed in body weight gain between vehicle- and MDMA-treated animals until T1. From T2 - T4 MDMA-treated animals lost weight, and started to gain again the day after the end of the MDMA treatment period.

A: arrival; T1: first day of treatment; T4: fourth and last day of MDMA or vehicle treatment; K: kill.

### ***In vitro* autoradiography.**

Because of the consistency of [<sup>3</sup>H]citalopram, [<sup>3</sup>H]WIN 35, 428, and [<sup>125</sup>I]βCIT radioligand binding between the pilot and the formal study, representative images from the pilot study are only presented for inspection of total versus nonspecific binding. The formal study is presented in full (Chapter 6, page 272), and the reader is referred to those presented representative figures, i.e. for [<sup>3</sup>H]citalopram (Fig. 6-15, page 274), and [<sup>3</sup>H]WIN 35, 428 (Fig. 6-17, page 281). Representative sections showing [<sup>125</sup>I]βCIT-labelling of SERT, DAT and [<sup>125</sup>I]βCIT in absence of any displacers are shown in Fig. 6-19 (page 285), Fig. 6-22 (page 291), and Fig. 6-24 (page 296), respectively.

*[<sup>3</sup>H]citalopram autoradiography to label SERT.*

Levels of nonspecific [<sup>3</sup>H]citalopram binding defined in the presence of fluoxetine.

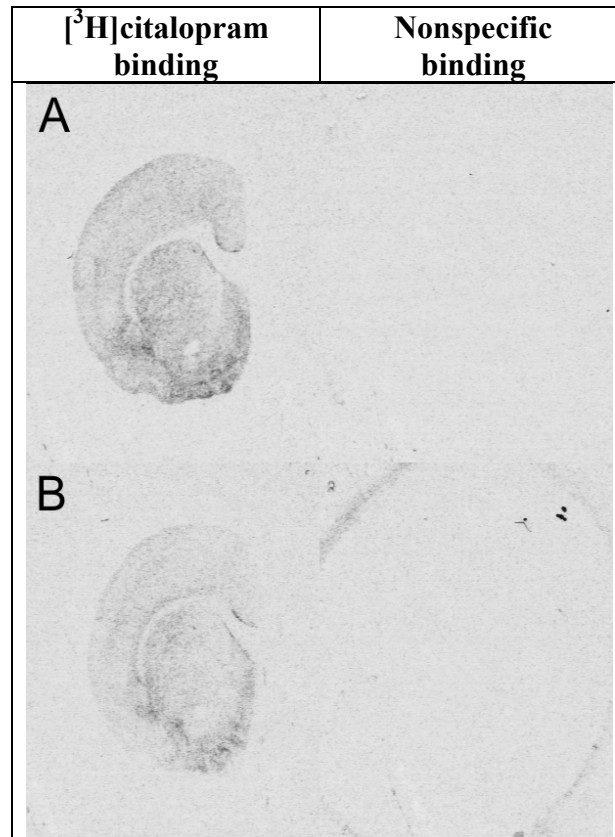


**Fig. 2-7. Nonspecific *in vitro* [<sup>3</sup>H]citalopram binding is low.**

Nonspecific binding was assessed using fluoxetine to displace [<sup>3</sup>H]citalopram.

Left: representative section showing total binding to SERT.

Right: representative section showing nonspecific binding defined in the presence of fluoxetine.

A: vehicle-treated representative animal.

B: MDMA-treated representative animal.

Nonspecific binding of [<sup>3</sup>H]citalopram was low, and comparable between treatment groups.

Levels of nonspecific binding of [<sup>3</sup>H]citalopram binding in the presence of fluoxetine were visually inspected. Representative sections collected at the level of the caudate-putamen are shown in Fig. 2-7. While MDMA treatment reduced the level of total [<sup>3</sup>H]citalopram binding compared to vehicle administration (Fig. 2-7, A, left vs. B, left, respectively), levels of nonspecific binding defined using fluoxetine were very low in both treatment groups (Fig. 2-7, A, right vs. right B, right, respectively). Visual examination could not detect any differences between groups in nonspecific binding.

**Analysis of [<sup>3</sup>H]citalopram binding in vehicle- and MDMA-treated animals.**

Administration of MDMA over a treatment period of 4 days resulted in widespread loss of [<sup>3</sup>H]citalopram binding. The data indicate that MDMA had successfully depleted SERT in a number of different brain regions. The reductions were notable in various cortical regions, i.e. the prefrontal, retrosplenial, and piriform cortices, and thalamic structures such as the dorsal thalamus and the medial geniculate nucleus where [<sup>3</sup>H]citalopram binding was significantly lower in animals treated with MDMA treatment compared to vehicle-treated control rats (Table 2-3).

Structure	Treatment		Rel. Diff. [%] <sup>a</sup>
	Vehicle	MDMA	
Prefrontal Cortex	41.74 ± 4.31	19.50 ± 2.46 *	-53.27
Anterior Cingulate Cortex	25.98 ± 7.68	7.73 ± 2.22 *	-70.26
Caudate-Putamen	32.17 ± 2.62	21.15 ± 5.19 *	-34.26
Septal Area	43.82 ± 6.39	29.42 ± 1.18 *	-32.87
Nucleus Accumbens	46.98 ± 5.16	15.66 ± 6.20 *	-66.67
Retrosplenial Cortex	21.55 ± 9.79	8.53 ± 1.92 *	-60.43
Basolateral Amygdala	135.78 ± 40.27	82.00 ± 15.08	-39.60
Central Amygdaloid Nucleus	42.47 ± 9.98	15.20 ± 1.61	-64.22
Ventral Hypothalamus	36.61 ± 7.01	23.72 ± 5.03	-35.20
Dorsal Thalamus	76.31 ± 2.54	18.59 ± 6.17 *	-75.64
Habenula	36.33 ± 9.86	10.08 ± 5.49 *	-72.26
Hippocampus	33.73 ± 2.25	16.56 ± 2.11 *	-50.89
Perirhinal / Entorhinal Cortex	51.57 ± 4.83	11.92 ± 2.86 *	-76.89
Piriform Cortex	28.79 ± 6.68	5.93 ± 1.43 *	-79.41
Substantia Nigra	77.92 ± 11.77	80.19 ± 17.55	+2.91
Medial Geniculate Nucleus	34.02 ± 6.25	12.09 ± 2.37 *	-64.46
Superior Colliculus	90.95 ± 14.98	23.06 ± 7.82 *	-74.65
Inferior Colliculus	22.35 ± 5.24	5.61 ± 1.97	-74.87
Dorsal Raphe	91.21 ± 15.15	74.19 ± 14.93	-18.66
Entorhinal Cortex	37.99 ± 6.36	14.37 ± 1.87	-62.17
Cerebellum	2.05 ± 1.87	1.05 ± 1.23	-48.86

**Table 2-3. MDMA treatment causes widespread reductions in *in vitro* [<sup>3</sup>H]citalopram binding to SERT.**

Thirteen out of 21 structures are significantly different between vehicle- and MDMA-treated animals. Data are mean ± SD for n = 3 - 4 vehicle-, and n = 3 - 4 for MDMA-treated rats.

Units of measurement are fmol/mg.

Two-tailed Mann-Whitney U, \*p < 0.05 relative to vehicle group.

Relative difference (Rel. Diff.) = <sup>a</sup> (MDMA - vehicle)/(vehicle)\*100 %.

A maximal significant difference of -79 % in MDMA-treated animals relative to vehicle controls was observed in the piriform cortex. In total 12 out of 21 structures examined in the rat brains were significantly affected by the MDMA treatment. Large percentage differences between groups did not always produce statistical significance, as observed for example for the inferior colliculus. This structure experienced a reduction of 75 % [<sup>3</sup>H]citalopram binding in MDMA-treated rats relative to controls even though SDs were small. This is probably due to the small group size (n = 3).

*[<sup>3</sup>H]WIN 35, 428 autoradiography to label DAT.*

Levels of nonspecific [<sup>3</sup>H]WIN 35, 428 binding defined in the presence of nomifensine.

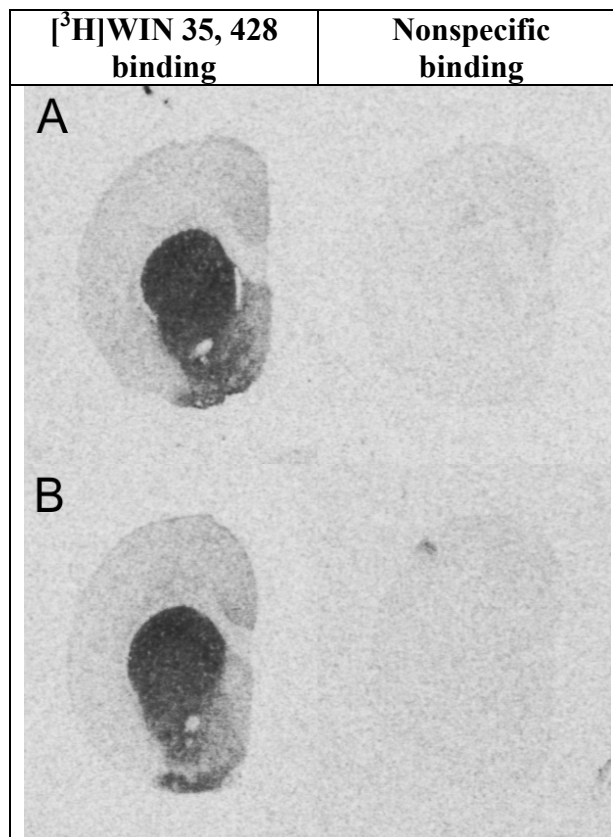


**Fig. 2-8. Nonspecific *in vitro* [<sup>3</sup>H]WIN 35, 428 binding is low.**

Nonspecific binding was assessed using nomifensine to displace [<sup>3</sup>H]WIN 35, 428.

Left: representative sections showing total binding to DAT.

Right: representative sections showing nonspecific binding defined in the presence of nomifensine.

A: vehicle-treated representative animal.

B: MDMA-treated representative animal.

Nonspecific binding of [<sup>3</sup>H]WIN 35, 428 was approximately at the level of the cortex, and was comparable between treatment groups.

Levels of nonspecific binding of [<sup>3</sup>H]WIN 35, 428 binding in the presence of nomifensine were visually inspected. Representative sections at the level of the caudate-putamen are shown in Fig. 2-8. MDMA treatment did not affect the level of nonspecific [<sup>3</sup>H]WIN 35, 428 binding compared to vehicle administration as the levels being very low

in both treatment groups. The density of nonspecific binding sites was comparable to that of total binding in the cerebral cortex in the absence of any displacers. Visual examination could not detect any differences between groups in nonspecific binding.

**Analysis of [<sup>3</sup>H]WIN 35, 428 binding in vehicle- and MDMA-treated animals.**

Significant differences between vehicle- and MDMA-treated animals were detected only in the nucleus accumbens and the retrosplenial cortex (Table 2-4). Even though some structures show large percentage differences between the groups, the variability of the [<sup>3</sup>H]WIN 35, 428 binding in regions with low DAT density meant that these were not significant. For example, the thalamus in MDMA-treated animals displayed a DAT reduction of 79 % compared to control animals, however the SD of the mean is just as large as the mean itself.

Structure	Treatment		Rel. Diff. [%] <sup>a</sup>
	Vehicle	MDMA	
Prefrontal Cortex	8.21 ± 1.77	6.67 ± 2.48	-18.73
Anterior Cingulate Cortex	10.42 ± 4.18	10.36 ± 3.15	-0.60
Caudate-Putamen	80.69 ± 9.15	79.77 ± 9.58	-1.14
Septal Area	16.52 ± 3.40	9.82 ± 2.64	-40.57
Nucleus Accumbens	58.19 ± 3.09	44.22 ± 5.61 *	-24.01
Retrosplenial Cortex	5.95 ± 1.12	3.67 ± 0.39 *	-38.35
Lateral Hypothalamus	19.82 ± 4.99	12.48 ± 2.60	-37.01
Ventral Hypothalamus	9.15 ± 3.25	4.66 ± 2.06	-49.12
Dorsal Thalamus	2.18 ± 2.97	0.67 ± 0.63	-69.15
Thalamus	2.15 ± 2.75	0.45 ± 0.40	-79.01
Hippocampus	1.60 ± 2.61	0.80 ± 0.48	-49.81
Piriform Cortex	1.64 ± 2.84	0.75 ± 1.05	-54.04
Substantia Nigra	12.39 ± 6.83	16.40 ± 2.58	+32.34
Medial Geniculate Nucleus	5.58 ± 2.89	5.24 ± 1.59	-5.99
Superior Colliculus	9.67 ± 5.46	4.75 ± 1.34	-50.90
Ventral Tegmental Area	25.57 ± 12.30	26.93 ± 7.40	+5.29
Inferior Colliculus	3.27 ± 0.78	0.93 ± 1.51	-71.46
Dorsal Raphe	21.07 ± 10.08	15.66 ± 4.31	-25.68
Entorhinal Cortex	5.60 ± 1.23	2.44 ± 1.86	-56.48
Locus Coeruleus	20.30 ± 2.71	16.98 ± 6.95	-16.36
Cerebellum	2.72 ± 1.78	2.55 ± 1.38	-6.10

**Table 2-4. Overall *in vitro* [<sup>3</sup>H]WIN 35, 428 binding to DAT is unaffected by MDMA treatment.**

Two out of 21 structures are significantly different between vehicle- and MDMA-treated animals.

Data are mean ± SD for n = 3 - 4 vehicle-, and n = 4 for MDMA-treated rats.

Units of measurement are fmol/mg.

Two-tailed Mann-Whitney U, \*p < 0.05 relative to vehicle group.

Relative difference (Rel. Diff.) = <sup>a</sup> (MDMA - vehicle)/(vehicle)\*100 %.

### ***[<sup>125</sup>I]βCIT autoradiography - SERT labelling defined in the presence of mazindol.***

As described by McGregor *et al.* (McGregor *et al.*, 2003), even though [<sup>125</sup>I]βCIT binds to both SERT and DAT, it is possible to break down the autoradiographic [<sup>125</sup>I]βCIT signal into SERT and DAT components by pharmacologically blocking one of the transporters in the incubation mix by inclusion of respective displacers. By including mazindol to block DAT in the incubate, the SERT component of the [<sup>125</sup>I]βCIT signal is revealed.

**Levels of nonspecific [ $^{125}$ I] $\beta$ CIT binding defined in the presence of mazindol and fluoxetine.**

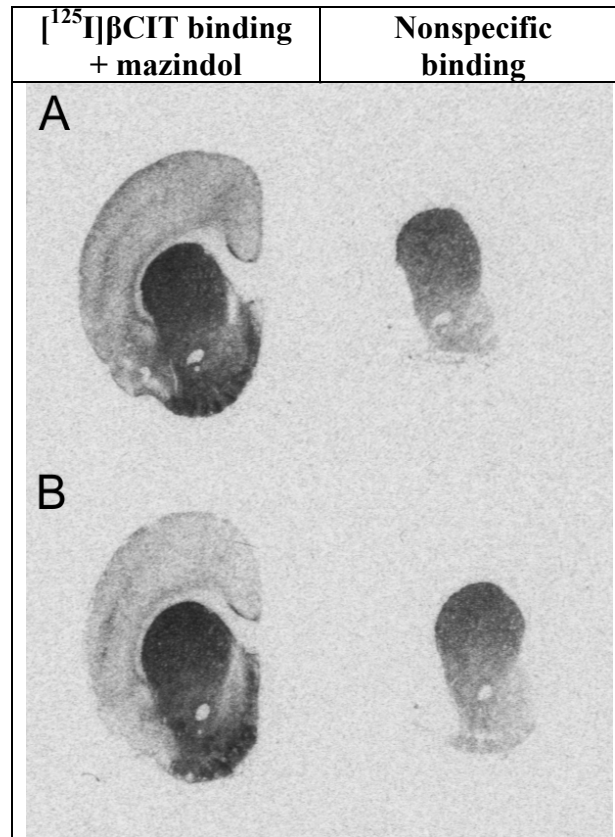


**Fig. 2-9. Nonspecific *in vitro* [ $^{125}$ I] $\beta$ CIT binding is low in SERT-rich, but high in DAT-rich regions.**

Nonspecific binding was addressed using mazindol and fluoxetine to displace [ $^{125}$ I] $\beta$ CIT from DAT and SERT, respectively.

Left: total binding to SERT using mazindol to block DAT.

Right: nonspecific binding defined by pharmacological blockage of DAT with mazindol, and SERT with fluoxetine.

A: vehicle-treated representative animal.

B: MDMA-treated representative animal.

Nonspecific binding was high in DAT-rich structures, i.e. caudate-putamen, nucleus accumbens, and tubercle area. SERT-rich regions, i.e. cortex and septal area appear to have low nonspecific binding.

Nonspecific binding of [ $^{125}$ I] $\beta$ CIT was defined in the presence of mazindol and fluoxetine, while total binding of [ $^{125}$ I] $\beta$ CIT to SERT was achieved by blocking the DAT component of the signal with the inclusion of mazindol (Fig. 2-9). MDMA treatment caused loss of [ $^{125}$ I] $\beta$ CIT total signal primarily in the cerebral cortex when compared to vehicle-treated control animals (Fig. 2-9, A, left vs. B, left). However no differences in nonspecific binding due to the treatment were observed as assessed by visual inspection (Fig. 2-9, A, right vs. B, right). Structures known to have a high density of DAT showed high nonspecific binding, such as the caudate-putamen, nucleus accumbens, and the tubercle area. On the other hand, regions low in DAT and high in SERT displayed low nonspecific binding, e.g. in the cortex and the septal area.

**Analysis of SERT-specific [<sup>125</sup>I]βCIT binding defined in the presence of mazindol in vehicle- and MDMA-treated animals.**

Visually detected changes were confirmed by quantitative autoradiographic analysis (Table 2-5). Twenty one structures were examined, and 12 showed significant effects due to MDMA treatment compared to vehicle-treated controls, including cortical structures such as the prefrontal, anterior cingulate, retrosplenial, and piriform cortices. Thalamic regions, important because of being those of the few structures identifiable in [<sup>125</sup>I]βCIT *in vivo* SPECT data showed significant reductions in SERT availability in animals that underwent MDMA treatment compared to vehicle controls.

Structure	Treatment		Rel. Diff. [%] <sup>a</sup>
	Vehicle	MDMA	
Prefrontal Cortex	1.22 ± 0.27	0.62 ± 0.05 *	-48.87
Anterior Cingulate Cortex	0.85 ± 0.18	0.25 ± 0.06 *	-70.00
Caudate-Putamen	1.73 ± 0.16	1.47 ± 0.46	-15.15
Septal Area	2.40 ± 0.37	1.73 ± 0.13 *	-28.06
Nucleus Accumbens	1.75 ± 0.08	1.22 ± 0.12 *	-30.04
Retrosplenial Cortex	0.59 ± 0.27	0.18 ± 0.06 *	-68.82
Basolateral Amygdala	3.33 ± 0.37	1.90 ± 0.05 *	-42.82
Central Amygdaloid Nucleus	1.23 ± 0.53	0.64 ± 0.19	-47.70
Ventral Hypothalamus	1.23 ± 0.22	0.71 ± 0.14 *	-42.48
Dorsal Thalamus	1.46 ± 0.19	0.35 ± 0.14 *	-76.14
Habenula	0.76 ± 0.33	0.24 ± 0.12 *	-68.26
Hippocampus	0.52 ± 0.08	0.24 ± 0.10 *	-54.59
Perirhinal / Entorhinal Cortex	0.81 ± 0.09	0.28 ± 0.05	-65.67
Piriform Cortex	0.62 ± 0.09	0.18 ± 0.06 *	-71.10
Substantia Nigra	2.96 ± 1.35	2.63 ± 0.34	-11.23
Medial Geniculate Nucleus	0.93 ± 0.06	0.30 ± 0.05 *	-67.28
Superior Colliculus	2.26 ± 0.45	0.56 ± 0.12	-75.04
Inferior Colliculus	1.06 ± 0.20	0.27 ± 0.04	-74.72
Dorsal Raphe	6.22 ± 1.84	4.80 ± 1.27	-22.85
Entorhinal Cortex	1.72 ± 0.14	0.61 ± 0.08	-64.48
Cerebellum	0.13 ± 0.04	0.07 ± 0.01	-42.13

**Table 2-5. MDMA treatment causes widespread reductions in *in vitro* SERT-specific [<sup>125</sup>I]βCIT binding.**

*In vitro* [<sup>125</sup>I]βCIT SERT-specific binding was defined in the presence of mazindol. Twelve out of 21 structures are significantly different between vehicle- and MDMA-treated animals. Data are mean ± SD for n = 3 - 4 vehicle-, and n = 3 - 4 for MDMA-treated rats. Units of measurement are fmol/mg. Two-tailed Mann-Whitney U, \*p < 0.05 relative to vehicle group. Relative difference (Rel. Diff.) = <sup>a</sup> (MDMA - vehicle)/(vehicle)\*100 %.

*[<sup>125</sup>I]βCIT autoradiography - DAT labelling defined in the presence of fluoxetine.*

**Levels of nonspecific [<sup>125</sup>I]βCIT binding defined in the presence of mazindol and fluoxetine.**

Note that the sections for the determination of nonspecific binding in DAT-specific [<sup>125</sup>I]βCIT binding are identical to those used in the determination of nonspecific binding in SERT-specific [<sup>125</sup>I]βCIT binding (Fig. 2-10, right).

Nonspecific binding of [<sup>125</sup>I]βCIT was defined in the presence of mazindol and fluoxetine, while specific binding of [<sup>125</sup>I]βCIT to DAT was achieved by blocking the SERT component of the signal with the inclusion of fluoxetine (Fig. 2-10). MDMA treatment caused only a subtle loss of [<sup>125</sup>I]βCIT total signal in the cerebral cortex when compared to vehicle-treated control animals (Fig. 2-10, A, left vs. B, left). However no differences in nonspecific binding due to the treatment were observed as assessed by visual inspection (Fig. 2-10 A, right vs. B, right). Structures known to have a high density of DAT showed high nonspecific binding, such as the caudate-putamen, nucleus accumbens, and the tubercle area. On the other hand, regions low in DAT and high in SERT displayed low nonspecific binding, e.g. in the cortex and in the septal area.

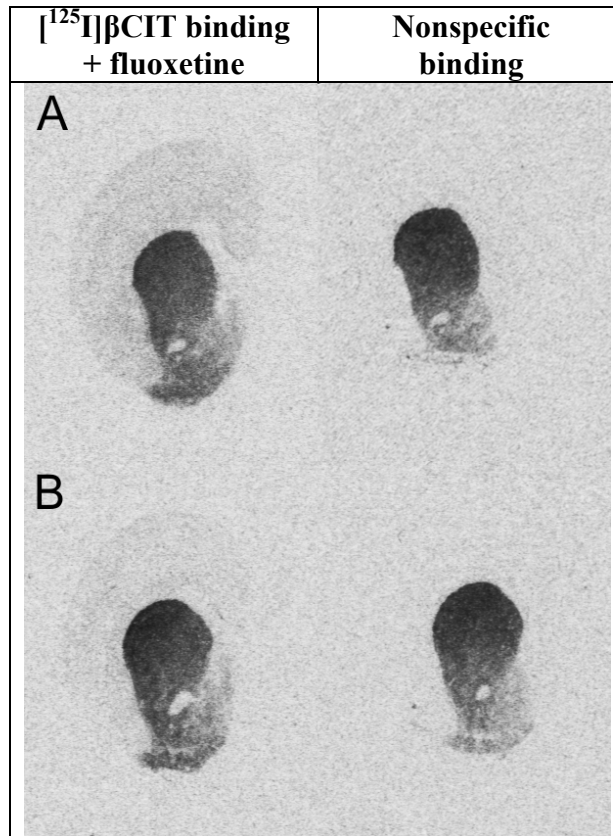


**Fig. 2-10. Nonspecific *in vitro*  $[^{125}\text{I}]\beta\text{CIT}$  binding is low in SERT-rich, but high in DAT-rich regions.**

Nonspecific binding was addressed using mazindol and fluoxetine to displace  $[^{125}\text{I}]\beta\text{CIT}$  from DAT and SERT, respectively.

Left: total binding to DAT using fluoxetine to block SERT.

Right: nonspecific binding defined by pharmacological blockage of DAT with mazindol, and SERT with fluoxetine.

A: vehicle-treated representative animal.

B: MDMA-treated representative animal.

Nonspecific binding was high in DAT-rich structures, i.e. caudate-putamen, nucleus accumbens, and tubercle area. SERT-rich regions, i.e. cortex and septal area appear to have low nonspecific binding.

### **Analysis of DAT-specific $[^{125}\text{I}]\beta\text{CIT}$ binding defined in the presence of fluoxetine in vehicle- and MDMA-treated animals.**

In accordance with the ambiguity between  $[^{125}\text{I}]\beta\text{CIT}$  labelling of DAT and  $[^3\text{H}]\text{WIN 35, 428}$  in terms of specificity, more structures show significant differences in the former when comparing vehicle- to MDMA-treated animals (Table 2-6). Twenty one structures were examined, and 8 showed significant effects of MDMA treatment compared to vehicle-treated controls, including cortical structures such as the prefrontal and piriform cortex. In contrast, in the  $[^3\text{H}]\text{WIN 35, 428}$  autoradiography described above (Table 2-4, page 62), only the retrosplenial cortex, and the nucleus accumbens showed significantly different DAT densities. Thalamic regions, important because of being those of the few structures identifiable in  $[^{125}\text{I}]\beta\text{CIT}$  *in vivo* SPECT data showed significant reductions in

DAT availability in animals that underwent MDMA treatment compared to vehicle controls.

Structure	Vehicle	MDMA	Rel. Diff. [%] <sup>a</sup>
Prefrontal Cortex	1.09 ± 0.20	0.43 ± 0.06 *	-60.12
Anterior Cingulate Cortex	0.76 ± 0.27	0.41 ± 0.14	-45.64
Caudate-Putamen	5.17 ± 0.76	5.58 ± 0.43	+8.07
Septal Area	1.42 ± 0.27	1.17 ± 0.36	-17.85
Nucleus Accumbens	3.81 ± 0.54	3.59 ± 0.77	-5.87
Retrosplenial Cortex	0.54 ± 0.30	0.24 ± 0.12	-56.58
Basolateral Amygdala	3.82 ± 0.88	1.86 ± 0.11	-51.15
Central Amygdaloid Nucleus	1.97 ± 1.22	1.07 ± 0.64	-45.56
Ventral Hypothalamus	1.02 ± 0.20	0.57 ± 0.17 *	-43.90
Dorsal Thalamus	1.18 ± 0.10	0.29 ± 0.07 *	-75.86
Habenula	0.77 ± 0.08	0.33 ± 0.12 *	-56.95
Hippocampus	0.47 ± 0.03	0.22 ± 0.01 *	-52.41
Perirhinal / Entorhinal Cortex	0.79 ± 0.08	0.30 ± 0.07 *	-61.83
Piriform Cortex	0.52 ± 0.03	0.24 ± 0.07 *	-53.55
Substantia Nigra	2.51 ± 1.13	2.39 ± 0.15	-4.64
Medial Geniculate Nucleus	0.83 ± 0.02	0.28 ± 0.02 *	-66.08
Superior Colliculus	1.82 ± 0.28	0.46 ± 0.14	-74.91
Inferior Colliculus	1.16 ± 0.20	0.39 ± 0.06	-66.80
Dorsal Raphe	4.10 ± 0.70	3.70 ± 0.69	-9.63
Entorhinal Cortex	1.45 ± 0.08	0.75 ± 0.09	-48.39
Cerebellum	0.18 ± 0.03	0.12 ± 0.02	-33.87

**Table 2-6. MDMA treatment causes widespread reductions in *in vitro* DAT-specific [<sup>125</sup>I]βCIT binding.**

*In vitro* [<sup>125</sup>I]βCIT DAT-specific binding was defined in the presence of fluoxetine. Eight out of 21 structures are significantly different between vehicle- and MDMA-treated animals. Data are mean ± SD for n = 3 - 4 vehicle- and n = 3 - 4 for MDMA-treated rats. Units of measurement are fmol/mg. Two-tailed Mann-Whitney U, \*p < 0.05 relative to vehicle group. Relative difference (Rel. Diff.) = <sup>a</sup> (MDMA - vehicle)/(vehicle)\*100 %.

***[<sup>125</sup>I]βCIT autoradiography defined in the absence of any displacers.***

Since *in vivo* SPECT imaging with [<sup>125</sup>I]βCIT (chapter 6, page 242) was carried out in the absence of pharmacological blockers, the last experiment in the pilot study was carried out to more closely mimic the conditions applicable to *in vivo* [<sup>125</sup>I]βCIT SPECT, and the subsequent analysis of the scanned brains excised and processed for *ex vivo* autoradiography. This experiment used [<sup>125</sup>I]βCIT in the absence of any displacers for assessing SERT and DAT density.

**Analysis of [<sup>125</sup>I]βCIT binding defined in the absence of any displacers in vehicle- and MDMA-treated animals.**

MDMA treatment reduced SERT density in the cortex and thalamus as assessed by [<sup>3</sup>H]citalopram and SERT-specific [<sup>125</sup>I]βCIT autoradiography. Using [<sup>125</sup>I]βCIT in the absence of any displacers, there were significant reductions of binding in MDMA-treated animals compared to vehicle controls in 9 out of 21 structures measured. These included regions of the cortex (prefrontal, anterior cingulate, and piriform), and thalamic structures, such as the dorsal thalamus, and the medial geniculate nucleus (Table 2-7). In addition, there was a significant difference between MDMA- and vehicle-treated rats in the cerebellum. This is of importance because this region is commonly used as a reference region in *in vivo* SPECT imaging. This significant difference was observed only using [<sup>125</sup>I]βCIT in the absence of any displacers.

Taking all these findings from the pilot study together, a widespread loss of SERT binding detected by [<sup>3</sup>H]citalopram and [<sup>125</sup>I]βCIT in regions such as the cortex and thalamus assured us that the model of MDMA-induced SERT depletion was established. Hence a level of confidence was reached to conduct the *in vivo* SPECT study described below (chapter 6, page 242).

Structure	Treatment		Rel. Diff. [%] <sup>a</sup>
	Vehicle	MDMA	
Prefrontal Cortex	8.48 ± 0.71	5.20 ± 0.27 *	-38.65
Anterior Cingulate Cortex	5.69 ± 0.95	2.50 ± 0.19 *	-56.12
Caudate-Putamen	8.87 ± 0.89	9.04 ± 0.77	+1.84
Septal Area	14.03 ± 1.95	11.34 ± 0.67	-19.16
Nucleus Accumbens	8.50 ± 0.57	6.75 ± 1.03	-20.58
Retrosplenial Cortex	4.64 ± 0.89	2.33 ± 0.09 *	-49.74
Basolateral Amygdala	16.26 ± 1.98	13.03 ± 1.37	-19.85
Central Amygdaloid Nucleus	5.08 ± 1.87	3.85 ± 1.38	-24.29
Ventral Hypothalamus	8.28 ± 1.51	5.10 ± 1.05	-38.35
Dorsal Thalamus	8.62 ± 0.25	1.89 ± 0.76 *	-78.03
Habenula	5.87 ± 1.20	2.32 ± 0.58 *	-60.52
Hippocampus	3.76 ± 0.37	1.42 ± 0.50 *	-62.13
Perirhinal / Entorhinal Cortex	7.05 ± 0.36	1.97 ± 0.35	-72.07
Piriform Cortex	5.07 ± 0.37	1.15 ± 0.56 *	-77.35
Substantia Nigra	13.90 ± 6.65	12.66 ± 2.98	-8.91
Medial Geniculate Nucleus	4.58 ± 0.59	1.03 ± 0.42 *	-77.41
Superior Colliculus	11.90 ± 2.58	3.58 ± 1.64	-69.92
Inferior Colliculus	6.73 ± 1.76	2.08 ± 0.44	-69.03
Dorsal Raphe	29.80 ± 3.64	27.11 ± 4.50	-9.03
Entorhinal Cortex	10.84 ± 1.59	5.47 ± 0.46	-49.58
Cerebellum	1.22 ± 0.09	0.36 ± 0.05 *	-70.80

**Table 2-7. MDMA treatment causes widespread reductions in *in vitro* [<sup>125</sup>I]βCIT binding.**

[<sup>125</sup>I]βCIT binding was defined in the absence of any displacers.

Nine out of 21 structures show significant reductions [<sup>125</sup>I]βCIT binding.

Data are mean ± SD for n = 3 - 4 in vehicle-, and n = 3 - 4 in MDMA-treated group.

Units of measurement are fmol/mg.

Two-tailed Mann-Whitney U, \*p < 0.05 relative to vehicle group.

Relative difference (Rel. Diff.) = <sup>a</sup> (MDMA - vehicle)/(vehicle)\*100 %.

## **2.4 Pilot study to develop protocol for *in vitro* [<sup>125</sup>I]ADAM autoradiography.**

In the following pilot study, the aim was set to develop an *in vitro* protocol for [<sup>125</sup>I]ADAM autoradiography to be used to assess the relative abilities of this ligand compared to [<sup>125</sup>I]βCIT in the detection of changes in SERT densities induced by MDMA treatment. As in the formal *in vivo* SPECT study using [<sup>125</sup>I]ADAM, there were problems associated with this ligand *in vitro* (chapter 6, pages 91, 257 and 268).

### **Animals - sample tissue.**

As common practice at the Wellcome Surgical Institute, brains are collected from research studies that do not need brain tissue and these are used for practising section cutting and autoradiography procedures. These brains were used for the [<sup>125</sup>I]ADAM autoradiographic assays and so no details, only where specifically noted, about age, strain, and treatment of the rats were known. Whole brain tissue was cut and sectioned, then mounted on slides with 2 sections for total and 2 for nonspecific binding as described above (page 53).

### ***In vitro* autoradiography using [<sup>125</sup>I]ADAM.**

As no protocol for *in vitro* [<sup>125</sup>I]ADAM autoradiography was available in the published literature, several experiments, in which the experimental conditions in the autoradiographic procedure were varied, were carried out as summarised in Table 2-8. The general procedure, as described for *in vitro* autoradiography above, was followed (page 54), and described in more detail in the results section (page 72).

Experiments	1	2	3
Reference date / batch	31.01.08 / 2	01.04.08 / 4	01.04.08 / 4
Sections used	Spare sections		Vehicle / MDMA
Specific activity	2.162 Ci/ $\mu$ mol		
Source	MAP, Finland		
Buffer	Tris-buffer: 50 mM Tris-HCl, 120 mM NaCl, 5 mM KCl, pH 7.4		
Pre-incubation	15 min in buffer at RT	30 min in buffer at RT	
Incubation	60 min incubation in buffer at RT:		
	Total SERT: 150 pM $[^{125}\text{I}]\text{ADAM}$  NS: 150 pM $[^{125}\text{I}]\text{ADAM}$ 1 $\mu$ M paroxetine	Total SERT: 150 pM $[^{125}\text{I}]\text{ADAM}$  NS: 150 pM $[^{125}\text{I}]\text{ADAM}$ 1 $\mu$ M fluoxetine	Total SERT: 150 pM $[^{125}\text{I}]\text{ADAM}$ 0.1 % BSA  NS: 150 pM $[^{125}\text{I}]\text{ADAM}$ 1 $\mu$ M paroxetine 0.1 % BSA
Source of displacer	Sigma-Aldrich	Tocris	Sigma-Aldrich
Wash temperature	All at 4 °C:		
Wash experiment 1:	1 x 1 min, then 2 x 20 min	None	4 x 2 min in buffer
Wash experiment 2:		3 x 30 s in buffer	
Wash experiment 3:		4 x 2 min in buffer	
Wash experiment 4:		2 x 10 min	
Wash experiment 5:		1 x 1 min, then 2 x 20 min	
Post wash	dip in distilled H <sub>2</sub> O		
Dry	Gentle stream of air overnight		
Film exposure	12 h	29 h	24 h
<p><b>Table 2-8. Experimental conditions to develop protocol for <math>[^{125}\text{I}]\text{ADAM}</math> autoradiography.</b></p> <p>Three experiments were carried out, in which various conditions were altered.            Experiment 1: based on McGregor et al. for <math>[^{125}\text{I}]\beta\text{CIT}</math>.            Experiment 2: several experimental washing steps were probed (wash experiment 1 - 5).            Experiment 3: BSA was added in incubation mix in an attempt to reduce nonspecific binding.            BSA: bovine serum albumin.            RT: room temperature.</p>			

## Results.

### Experiment 1: using a previously published protocol for [<sup>125</sup>I]βCIT.

An initial protocol for [<sup>125</sup>I]ADAM autoradiography was derived from the protocol for [<sup>125</sup>I]βCIT autoradiography described by McGregor *et al.* (McGregor *et al.*, 2003). A concentration of [<sup>125</sup>I]ADAM was selected based on the dissociation constant ( $K_D = 150$  pM) determined by Choi *et al.* (Choi *et al.*, 2000) and the displacer for assessment of nonspecific binding was 1 μM paroxetine as this was previously used in an autoradiographic study that characterised a similar ligand to [<sup>125</sup>I]ADAM, [<sup>3</sup>H]MADAM (Chalon *et al.*, 2003). Qualitative comparison of representative sections incubated with [<sup>125</sup>I]ADAM (batch 2) in the absence or presence of paroxetine (total vs. nonspecific binding) shows more binding in total binding sections compared to nonspecific sections indicating the presence of specific [<sup>125</sup>I]ADAM binding (Fig. 2-11). SERT-rich regions, like the caudate-putamen (Bregma 1.10 mm), dorsal thalamus (Bregma -2.30 mm), the superior colliculus (Bregma -8.3 mm) and the brainstem (Bregma -10.04 mm) appeared to have high binding of [<sup>125</sup>I]ADAM, while white matter regions (e.g. corpus callosum, anterior commissure, internal and external capsule), the central amygdaloid nucleus and the cerebellum show less intense binding in total binding sections. However an inhomogeneous binding pattern was observed at the edges of the images, i.e. in the cortex at Bregma 1.10 mm and in the cerebellum. This was also evident in the same regions in nonspecific binding sections. In addition, central parts of nonspecific binding sections appear lighter than more lateral parts.

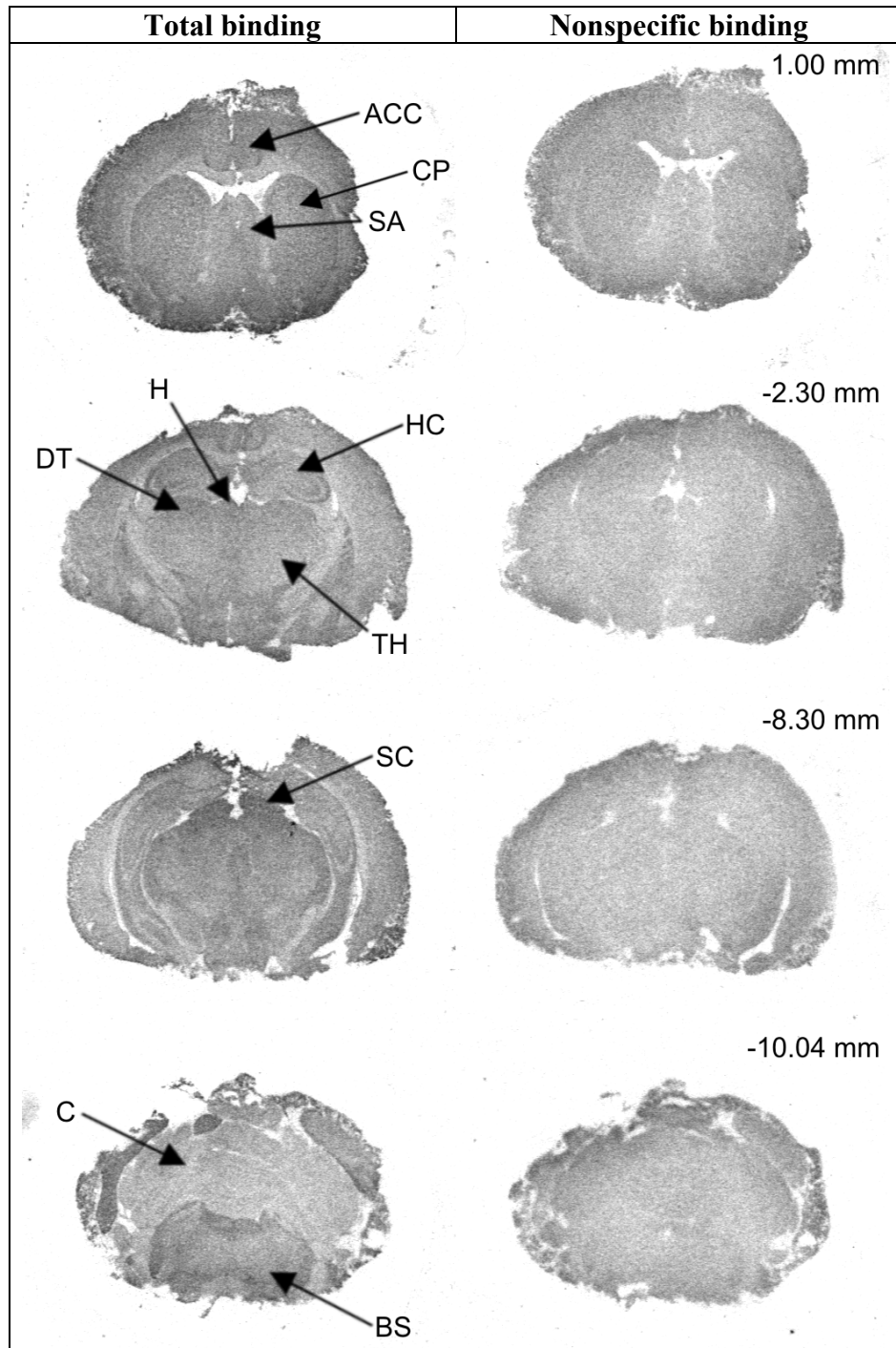


**Fig. 2-11. Initial results for *in vitro* [<sup>125</sup>I]ADAM pilot autoradiography do suggest specific binding to SERT-rich regions.**

Representative sections showing total binding of 150 pM [<sup>125</sup>I]ADAM (left), and nonspecific binding of 150 pM [<sup>125</sup>I]ADAM in the presence of 1 μM paroxetine. ACC: anterior cingulate cortex; SA: septal area; CP: caudate-putamen; H: habenula; HC: hippocampus; DT: dorsal thalamus; TH: thalamus; SC: superior colliculus; C: cerebellum; BS: brainstem. Batch 2, experiment was conducted on the 30.01.2008. Bregma level is indicated in top right corner.

Generally, nonspecific binding is high (Table 2-9). As expected, lowest binding is in the cerebellum with 9 % specific binding. The highest percentage of specific binding was

observed in the superior colliculus with 46 %. The binding ratio, defined as region / cerebellum, was highest in the superior colliculus. Overall, the binding ratios were low.

Structure	<sup>125</sup> I]ADAM Binding			% SB	R/C
	TB	NS	SB		
Anterior Cingulate Cortex	4.78	3.71	1.07	22.40	1.30
Caudate-Putamen	4.57	3.90	0.68	14.83	1.25
Septal Area	4.03	3.00	1.03	25.50	1.10
Dorsal Thalamus	5.08	3.05	2.04	40.10	1.39
Thalamus	4.25	2.95	1.29	30.45	1.16
Habenula	4.94	3.28	1.67	33.73	1.35
Hippocampus	4.79	3.27	1.52	31.81	1.31
Superior Colliculus	6.46	3.47	3.00	46.38	1.76
Brainstem	5.36	3.19	2.16	40.38	1.46
Cerebellum	3.67	3.36	0.31	8.45	1.00

**Table 2-9. Initial results for *in vitro* [<sup>125</sup>I]ADAM pilot autoradiography do suggest specific binding to SERT-rich regions.**

TB: total binding; NS: nonspecific binding; SB: specific binding (SB = TB - NS); % SB: percentage specific binding (% SB = 100 - (100 / TB \* NS)); R / C: ratio region / cerebellum. One animal only. Units of measurement are fmol/mg for TB, NS, and SB. R / C is dimensionless.

**Experiment 2: using a variety of section wash times.**

The protocol was modified in an attempt to increase the levels of specific binding. It was possible that in the previous experiment (experiment 1, page 72), nonspecifically bound [<sup>125</sup>I]ADAM was either not washed off enough, or that the washing step was too long and so specifically-bound ligand was washed off. Therefore, several experiments were carried out to assess the influence of increasing or reducing the washing time on the [<sup>125</sup>I]ADAM signal, as outlined in Table 2-8 (page 71). A different batch (4) of [<sup>125</sup>I]ADAM from the one used above (batch 2) was used to carry out these experiments. Visual inspection of the autoradiographic images revealed that nonspecific sections were generally lower in intensity compared to total binding (Fig. 2-12 to Fig. 2-16). This indicated that some specific [<sup>125</sup>I]ADAM binding was present at all wash times examined. As the total wash time increased, sections appeared less intense, consistent with the assumption that longer washing periods would wash off more ligand. However, there was little indication that the darkness of the images corresponded to the known distribution of SERT-rich structures, as shown in previous sections using either [<sup>125</sup>I]βCIT (page 63) or [<sup>3</sup>H]citalopram (page 58). This was observed through all washing experiments in this section. Moreover, the patterns of total and nonspecific binding obtained in experiment 1 (page 72) using batch 2 of [<sup>125</sup>I]ADAM were not observed in any experiment. The batch referred to in this section (4) was first used to conduct all the SPECT imaging, so only a few μl were kept aside for the

autoradiography while the batch (2) used in experiment 1 (page 72) was fresh and not used before. At this stage it is believed that mainly free [<sup>125</sup>I] was in the remaining liquid as this is possibly very sticky and an exchange between the fluid and the vial walls is the most reasonable explanation.

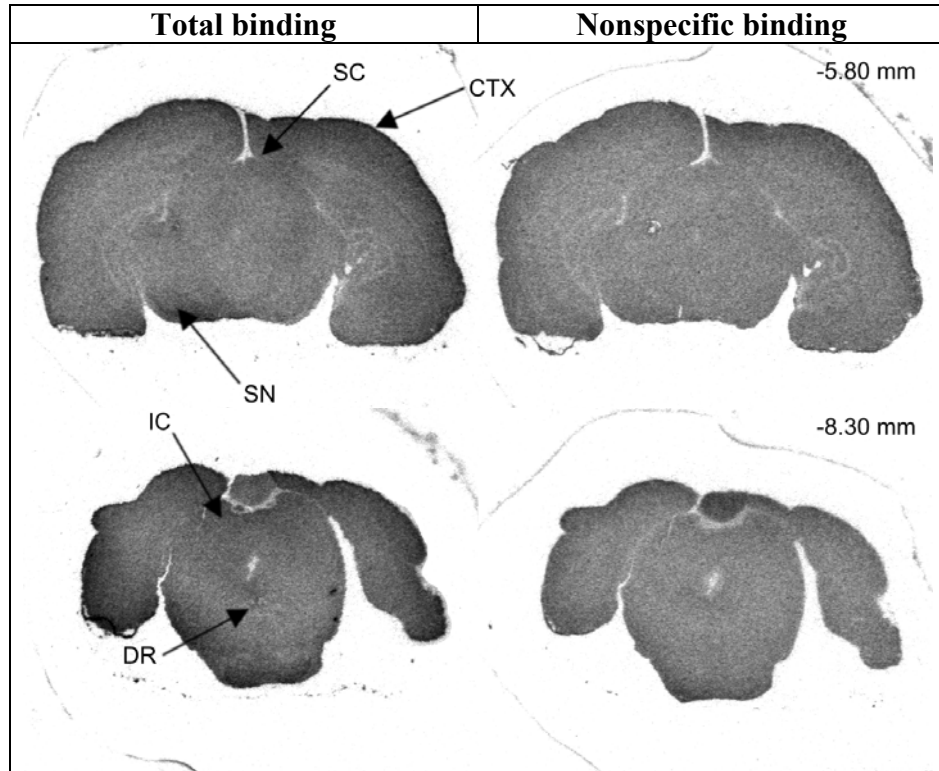


**Fig. 2-12. Varying washing times for *in vitro* [<sup>125</sup>I]ADAM pilot autoradiography do not show specific binding to SERT-rich regions (1 dip in dH<sub>2</sub>O).**

Representative sections show total binding of 150 pM [<sup>125</sup>I]ADAM (left), and nonspecific binding of 150 pM [<sup>125</sup>I]ADAM in the presence of 1 μM fluoxetine. Slides were washed in dH<sub>2</sub>O only (1 dip).

SC: superior colliculus; CTX: cortex; SN: substantia nigra; IC: inferior colliculus; DR: dorsal raphe.

Batch 4, experiment was conducted on the 23.04.2008. Bregma level is indicated in top right corner.

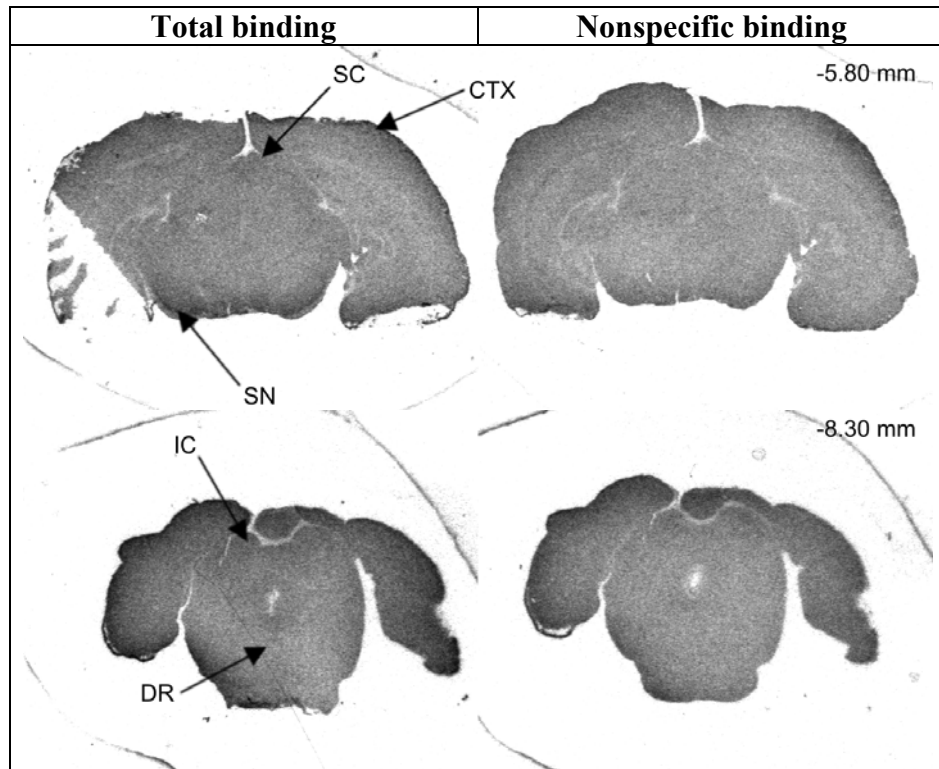


**Fig. 2-13. Varying washing times for *in vitro* [<sup>125</sup>I]ADAM pilot autoradiography do not show specific binding to SERT-rich regions (3 x 30 s in buffer).**

Representative sections show total binding of 150 pM [<sup>125</sup>I]ADAM (left), and nonspecific binding of 150 pM [<sup>125</sup>I]ADAM in the presence of 1 μM fluoxetine. Slides were washed in buffer for 3 x 30 s.

SC: superior colliculus; CTX: cortex; SN: substantia nigra; IC: inferior colliculus; DR: dorsal raphe.

Batch 4, experiment was conducted on the 23.04.2008. Bregma level is indicated in top right corner.

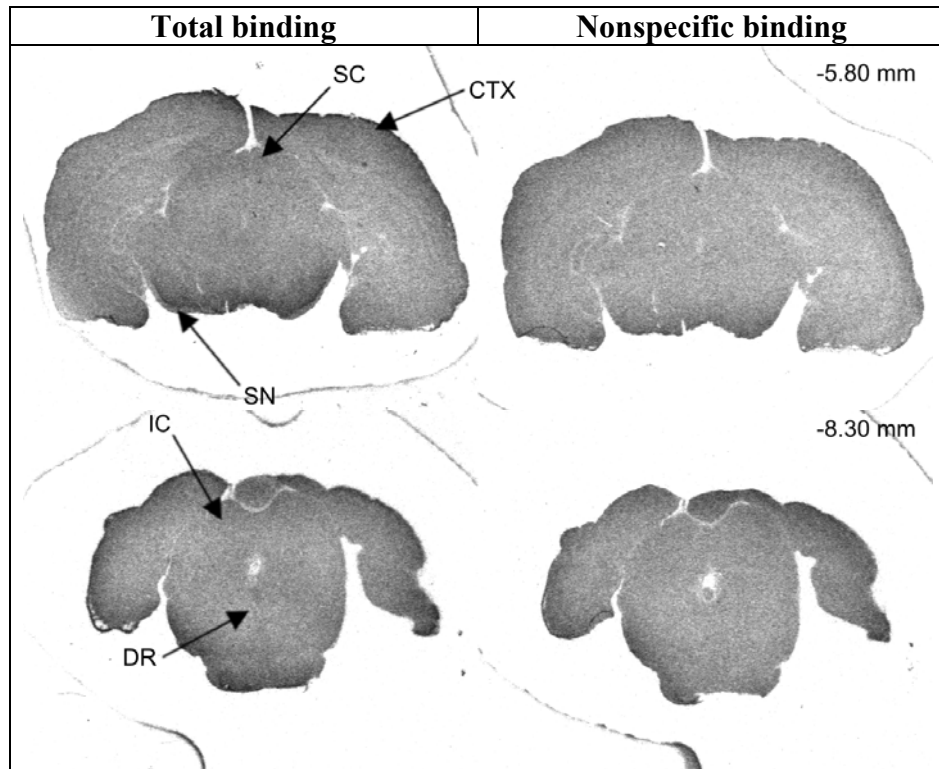


**Fig. 2-14. Varying washing times for *in vitro* [<sup>125</sup>I]ADAM pilot autoradiography do not show specific binding to SERT-rich regions (4 x 2 min in buffer).**

Representative sections show total binding of 150 pM [<sup>125</sup>I]ADAM (left), and nonspecific binding of 150 pM [<sup>125</sup>I]ADAM in the presence of 1 μM fluoxetine. Slides were washed in buffer for 4 x 2 min.

SC: superior colliculus; CTX: cortex; SN: substantia nigra; IC: inferior colliculus; DR: dorsal raphe.

Batch 4, experiment was conducted on the 23.04.2008. Bregma level is indicated in top right corner.

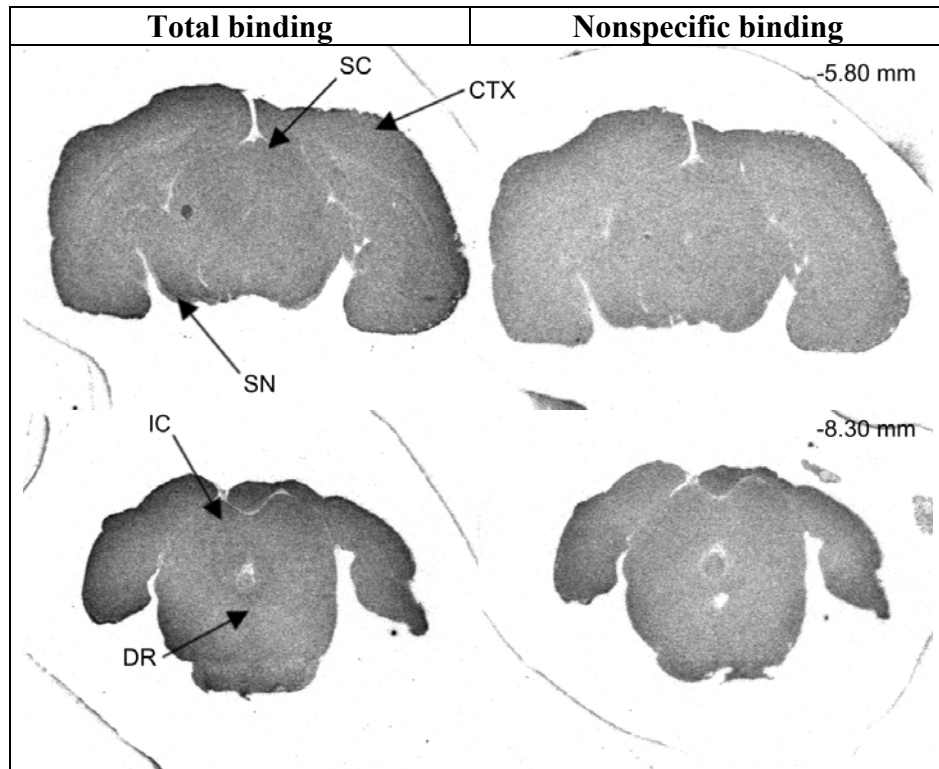
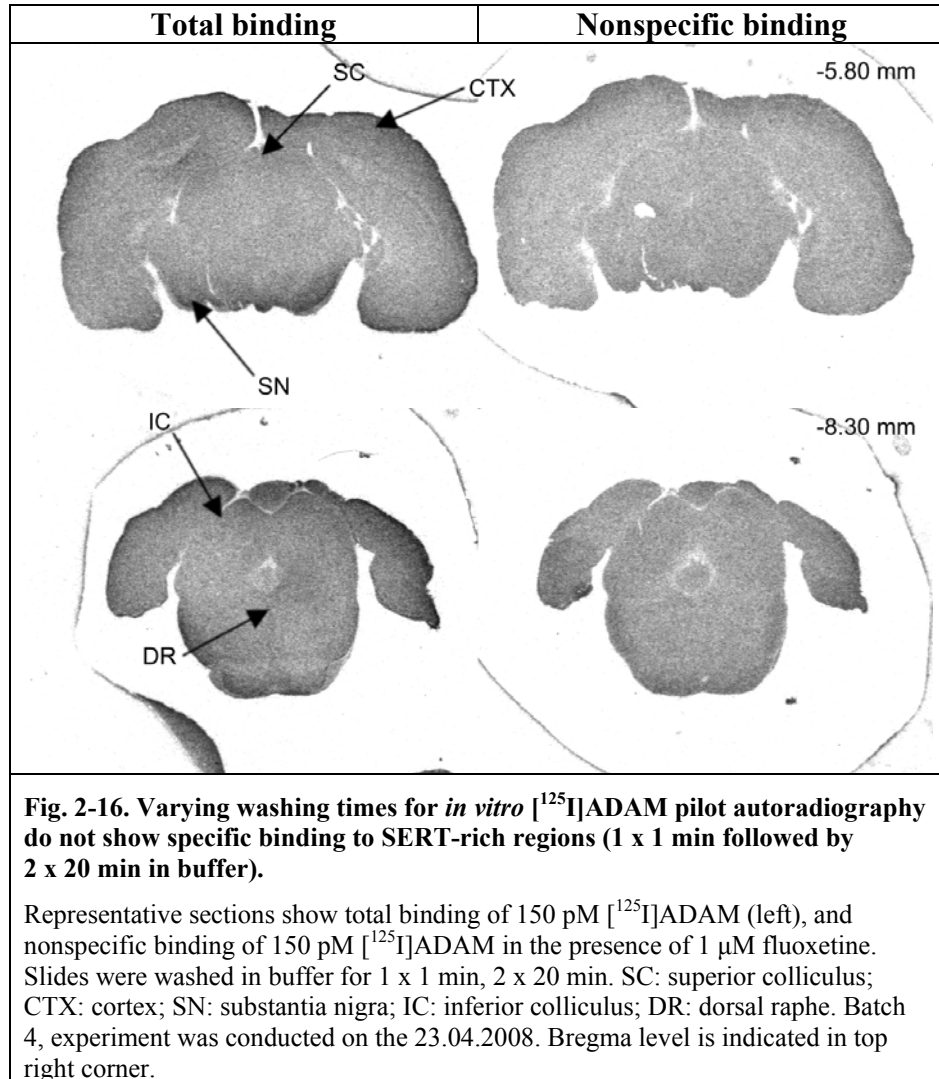


**Fig. 2-15. Varying washing times for *in vitro* [<sup>125</sup>I]ADAM pilot autoradiography do not show specific binding to SERT-rich regions (2 x 10 min in buffer).**

Representative sections show total binding of 150 pM [<sup>125</sup>I]ADAM (left), and nonspecific binding of 150 pM [<sup>125</sup>I]ADAM in the presence of 1 μM fluoxetine. Slides were washed in buffer for 2 x 10 min.

SC: superior colliculus; CTX: cortex; SN: substantia nigra; IC: inferior colliculus; DR: dorsal raphe.

Batch 4, experiment was conducted on the 23.04.2008. Bregma level is indicated in top right corner.



### Experiment 3: using sections derived from vehicle- and MDMA-treated animals.

In experiment 3, another approach was taken trying to assess whether sections obtained from MDMA-treated animals had less binding of [<sup>125</sup>I]ADAM compared to vehicle-treated control animals. Some unprocessed slides containing sectioned MDMA-treated and vehicle control brains obtained from the formal study shown in chapter 6 were used in this experiment (page 246). The autoradiographic protocol was slightly modified to include 0.1 % bovine serum albumin in the incubation buffer in order to test whether nonspecific binding, particularly in the form of free [<sup>125</sup>I], could be reduced. In general, comparison to the analogous experiment described in experiment 2 (page 74), where sections were washed 4 x 2 min (Fig. 2-14), reveals that the images (Fig. 2-17 and Fig. 2-18) are much fainter - even though the film exposure time was comparable (29 h in experiment 2 (page 74), vs. 24 h used here). This could possibly be attributed to the addition of 0.1 % bovine serum albumin in the incubation buffer. Visual comparison of total binding to nonspecific binding sections showed minimal differences and this was the case for both sections

derived from vehicle- and MDMA-treated animals. This is in contrast to the previous experiments, where nonspecific binding section images were less intense compared to total binding images.

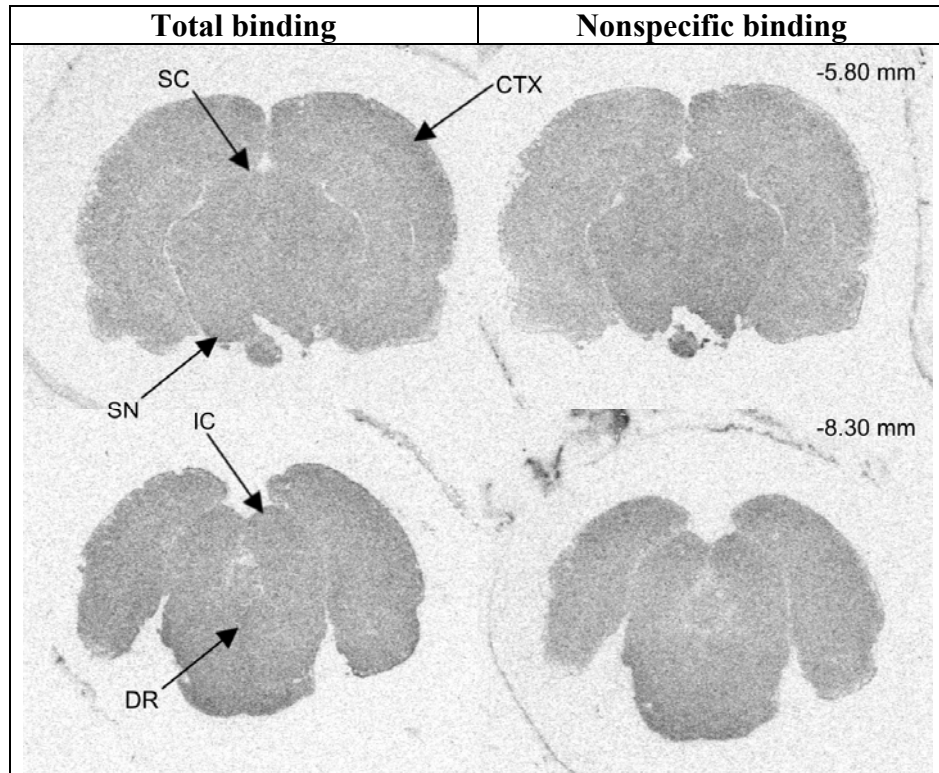
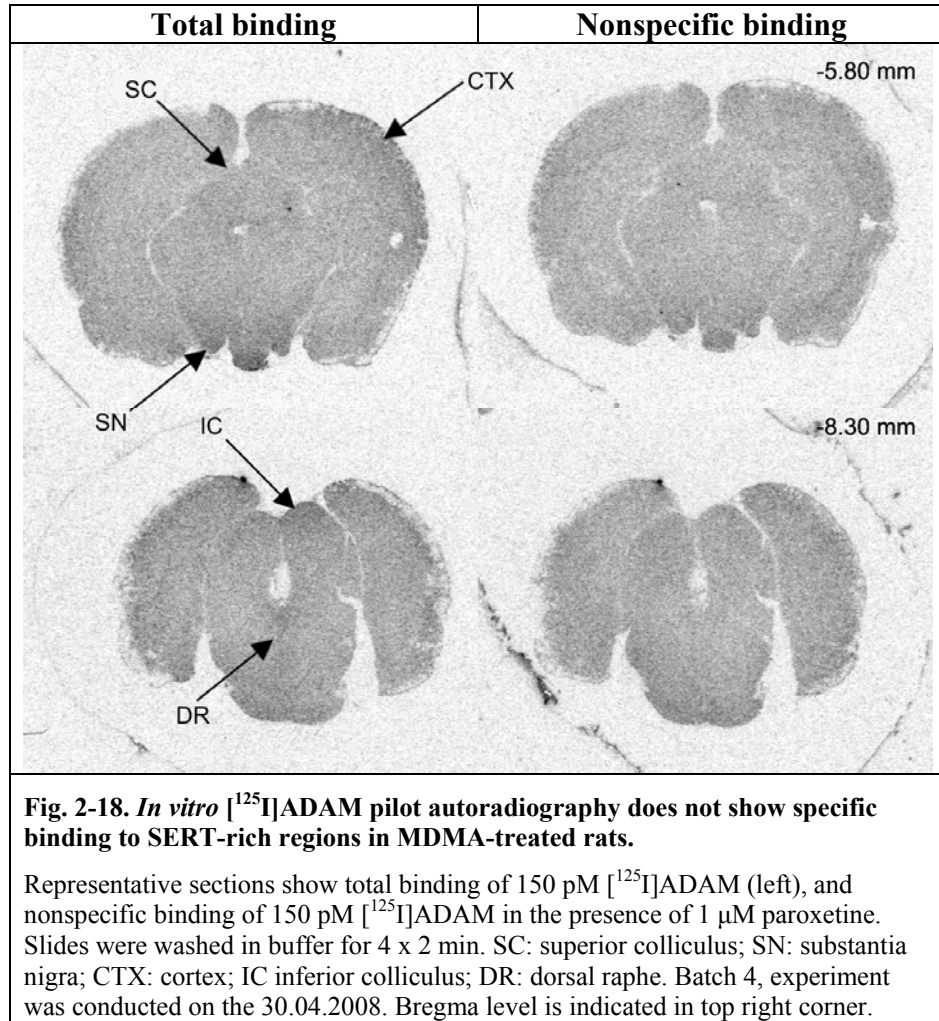
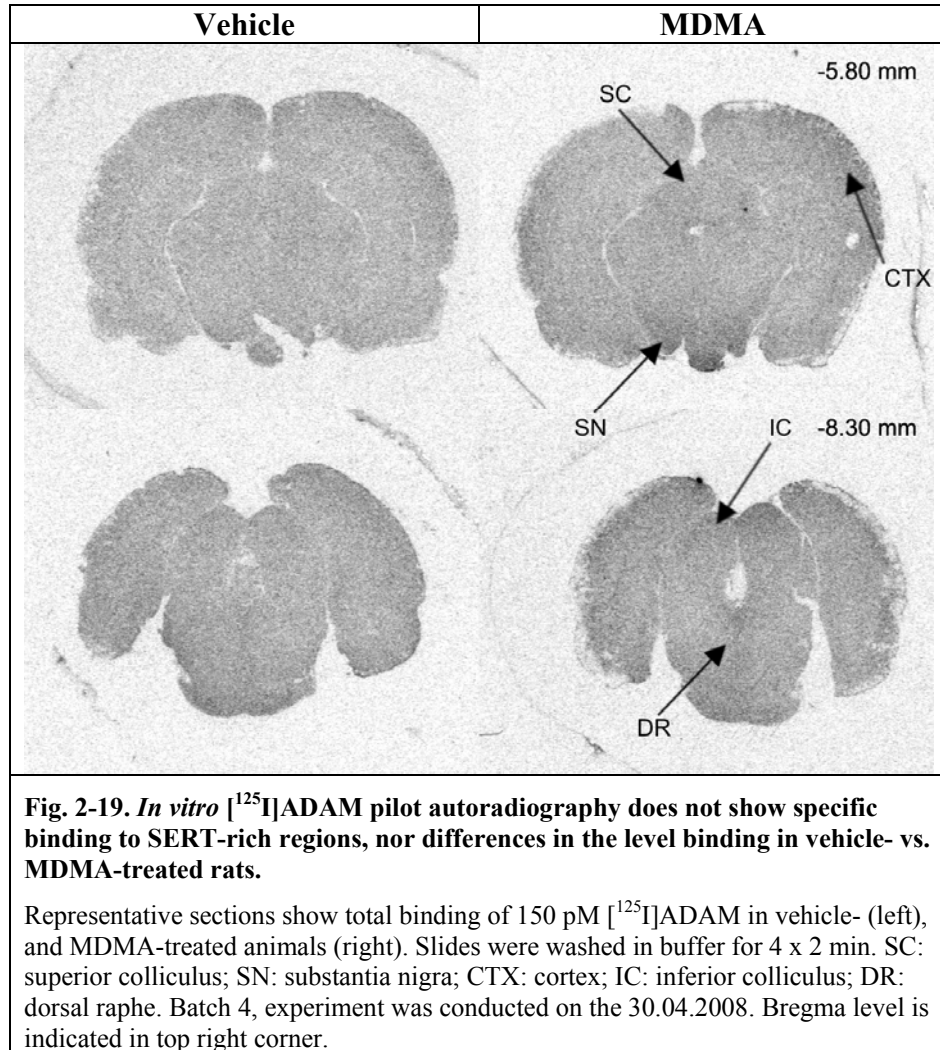


**Fig. 2-17. *In vitro* [<sup>125</sup>I]ADAM pilot autoradiography does not show specific binding to SERT-rich regions in vehicle-treated rats.**

Representative sections show total binding of 150 pM [<sup>125</sup>I]ADAM (left), and nonspecific binding of 150 pM [<sup>125</sup>I]ADAM in the presence of 1 μM paroxetine. Slides were washed in buffer for 4 x 2 min. SC: superior colliculus; SN: substantia nigra; CTX: cortex; IC: inferior colliculus; DR: dorsal raphe. Batch 4, experiment was conducted on the 30.04.2008. Bregma level is indicated in top right corner.



In Fig. 2-19 total binding sections derived from vehicle- and MDMA-treated animals are shown side by side. The region around the substantia nigra in MDMA-treated animals appears to display more intense binding of [<sup>125</sup>I]ADAM compared to vehicle-treated animals. However this appears to be due to inhomogeneities in nonspecific binding which are present at the edges of the sections. The area of the inferior colliculus, for example, also appeared to have higher intensities in MDMA-treated animals while the cortex looked patchy, in both sections derived from vehicle- and MDMA-treated animals. Faint binding of [<sup>125</sup>I]ADAM in the dorsal raphe was present in both groups.



In summary for the pilot study where it was tried to establish a [<sup>125</sup>I]ADAM *in vitro* autoradiography protocol it needs to be concluded that all attempts to do so failed. The best results were obtained in experiment 1 (page 72), with a fresh, unused batch (2) of [<sup>125</sup>I]ADAM. The nonspecific binding was very high though. In the experiments described in experiment 2 (page 74), and experiment 3 (page 79), a batch (4) was used that was previously applied in [<sup>125</sup>I]ADAM SPECT imaging, and only a few  $\mu$ l were kept aside for the autoradiography experiments. No abnormalities were observed in the *ex vivo* autoradiography conducted with the 10 day maintenance [<sup>125</sup>I]ADAM SPECT scanned animals (Fig. 6-8, page 260). Adjusting wash times (experiment 2, page 74) showed higher binding in the total binding compared to section treated for nonspecific binding indicating some specific binding. However this specific binding seemed not to match *a priori* known SERT-rich regions and was very low if present at all. A final attempt was made to use a positive control (experiment 3, page 79), where SERT depletion has taken place using prior treatment of rats with MDMA. In addition 0.1 % bovine serum albumin was added

## Chapter 2 - Material and methods.

into the incubation mix to possibly block free [ $^{125}\text{I}$ ]. Visual comparison of vehicle- vs. MDMA-treated animals showed no differences. Also visual comparison of total vs. nonspecific sections, regardless of which group, showed only minimal reductions in [ $^{125}\text{I}$ ]ADAM binding in nonspecific sections. The sections looked much fainter compared to the analogous experiment (wash time 4 x 2 min, experiment 2, page 74) indicating some effect of the 0.1 % bovine serum albumin that was included.

This all indicated that there was not enough radiolabelled [ $^{125}\text{I}$ ]ADAM in the incubation mix used in experiment 2 (page 74) and experiment 3 (page 79). Activities used in this experiment were assured by measurement in a scintillation counter. Therefore the activity measured is thought to represent mainly free [ $^{125}\text{I}$ ].

## **2.5 *In vivo* micro-SPECT imaging and *ex vivo* autoradiography of SERT-depleted rats using the radioligands [<sup>125</sup>I]βCIT and [<sup>125</sup>I]ADAM.**

This section describes the micro-SPECT scanner, animal treatment with MDMA or vehicle, rat preparation for SPECT scanning, and gives details on the scanning procedure, and image analysis of [<sup>125</sup>I]βCIT or [<sup>125</sup>I]ADAM data, all of which forms part of the study presented in chapter 6 (page 242). Information is also given regarding *ex vivo* and *in vitro* autoradiography. The latter highlights deviations from the respective pilot studies described above (pages 53 - 56).

### **Micro-SPECT.**

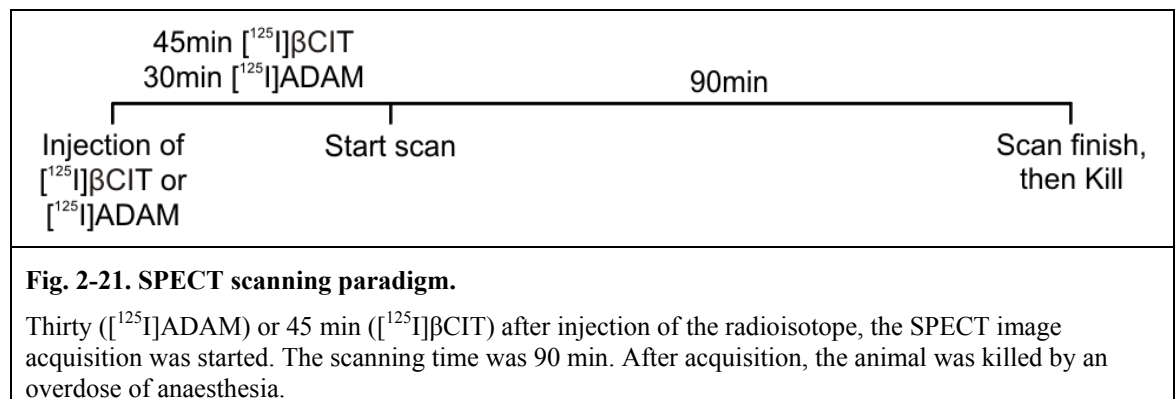
The small animal micro-SPECT scanner MollyQ 50<sup>TM</sup> (Neurophysics Corp., Shirley, MA, USA) possesses eight detector heads, each consisting of a 10,042-hole point focus long-bore collimator coupled to a 54 x 81 mm X- and gamma-ray sensitive crystal array. The detected counts are passed onto six 19 mm photomultiplier tubes per detector head. Each detector head scans tangentially across the field-of-view and makes 38 radial steps in order to obtain full x- and y- sampling within each axial section. The field-of-view is 50 mm yielding a resolution of 0.8 mm (full width at half maximum) (0.512 mm<sup>3</sup>). The image acquisition covered a rostro-caudal distance of 30 mm, yielded 75 coronal slices and took a total of 90 min to complete. Two samples were acquired per 0.8 mm in order to avoid spatial aliasing, i.e. every 0.347 mm in-plane, and 0.4 mm in z-direction through bed increments.

### ***In vivo* SPECT imaging.**

After treatment with either MDMA or vehicle (see pilot study for treatment details, page 53), animals were allocated for SPECT imaging with either [<sup>125</sup>I]βCIT or [<sup>125</sup>I]ADAM. In the [<sup>125</sup>I]βCIT scanning group with a 10 day maintenance period, 7 animals received vehicle, while there were 4 animals that underwent MDMA treatment (page 248). In the [<sup>125</sup>I]ADAM 10 day maintenance group, there were n = 3 vehicle-treated rats, and 4 animals that received MDMA.(page 257), while in the 30 day maintenance group 4 animals were subjected to vehicle injections, and n = 6 underwent the MDMA paradigm. A 30 day maintenance group was generated because of technical problems that prevented us from adhering to the initially planned 10 day maintenance period (page 263). The treatment schedule is summarised in Fig. 2-20.



different (Hwang et al., 2007). Fig. 2-21 summarises the scanning protocol for both, [<sup>125</sup>I]βCIT and [<sup>125</sup>I]ADAM.



After image acquisition, the animals were killed by an overdose of anaesthesia, and brains were processed as described in the pilot *in vitro* autoradiography study (page 53).

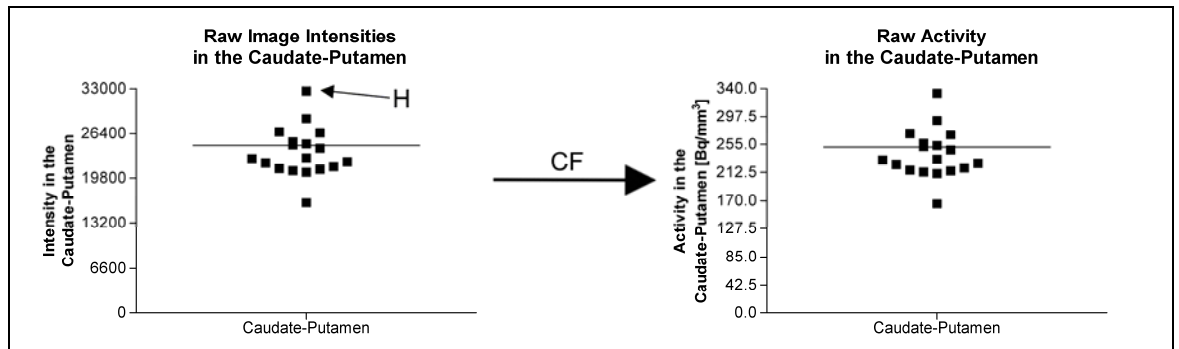
**Image reconstruction.**

After image acquisition, the raw data were reconstructed using the Neurophysics reconstruction software, which resulted in an image with a matrix size of 144 x 144 x 75 and a voxel size of 0.347 mm x 0.347 mm in-plane, and 0.4 mm in the z-direction. Images were stored in ANALYZE format for image processing. Note that only raw signal intensities were extracted, and not calibrated values, since the calibration factor would cancel out in the later analysis, where the intensities are normalised to the cerebellum. Conversion from raw intensities (as measured below, page 88) into Bq/mm<sup>3</sup> is defined by the following formula:

$$\frac{\text{Bq}}{\text{mm}^3} = \frac{\text{Signal Intensity} * \text{Calibration Factor}}{1.4}$$

A calibration factor is necessary since the data are inherently of float type (32 bit), which cannot be stored in a 16 bit image, where only integer voxel values of up to 32767 are allowed. During reconstruction of the raw SPECT data into a 16 bit image, the largest reconstructed value is set equal to an intensity value of 32767 to maintain the highest possible dynamic range. Then the calibration factor is calculated which provides the link between the signal intensity in the image, and the activity detected. The scanner detects in units of emissions per second, hence the conversion 1 disintegration/second = 1Bq = 1.4 emissions/second. The process described above is

summarised in Fig. 2-22 using the caudate-putamen of a [ $^{125}\text{I}$ ] $\beta\text{CIT}$  SPECT scan as example.

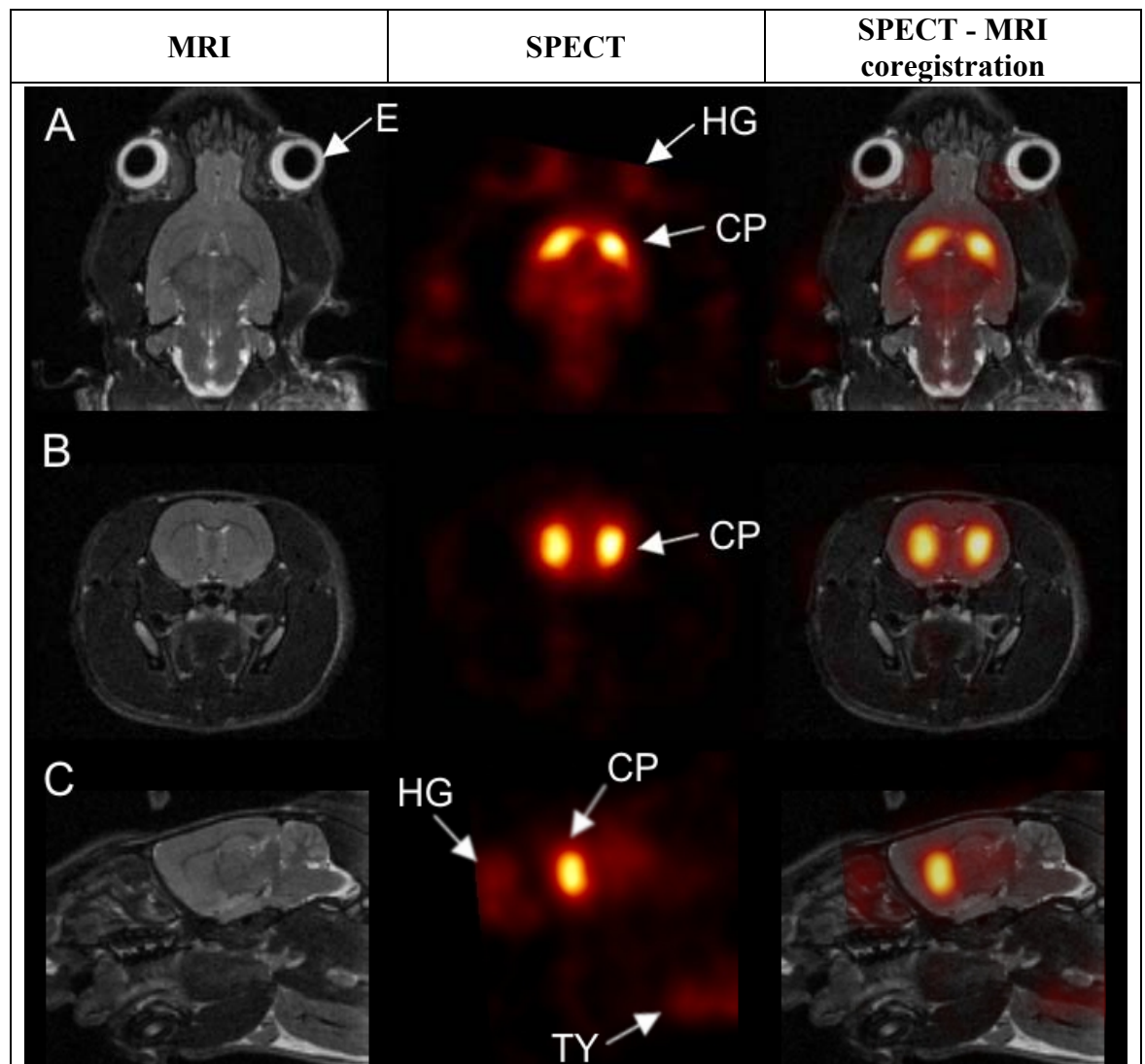


**Fig. 2-22. Illustration of voxel intensity and calibration to obtain the activity detected.**

The left graph shows simulated data points derived from the caudate-putamen. The highest reconstructed value is assigned to an intensity of 32767 (H) in a 16 bit image by the reconstructor to maintain the highest possible dynamic range. The caudate-putamen has therefore a reproducible intensity of  $\sim 25000$ , because it has the highest level of [ $^{125}\text{I}$ ] $\beta\text{CIT}$  binding. Multiplication with a calibration factor (CF) links the image intensity back to the activity detected by the scanner (right graph).

Bars in scatter plots represent mean. The data points represent voxels within the caudate-putamen. Note that this figure is for illustration purposes only. Therefore the number of voxels in the caudate-putamen ( $n = 20$ ) does not correspond to the actual number defined on the MRI.

## SPECT image analysis.

Image processing of [ $^{125}\text{I}$ ] $\beta\text{CIT}$  scans.

**Fig. 2-23. Alignment of [ $^{125}\text{I}$ ] $\beta\text{CIT}$  SPECT image to an MRI scan.**

The SPECT image was manually aligned to a T2-weighted MRI obtained from an age-matched rat of the same strain. The caudate-putamen provided an easy identifiable structure in both modalities for initial alignment. Following this, the Harderian glands were used to align the [ $^{125}\text{I}$ ] $\beta\text{CIT}$  SPECT scan anteriorly. Fine adjustments were then performed using rotations about the x-, y-, and z-axis.

A: transverse view.

B: coronal view.

C: sagittal view.

CP: caudate-putamen; E: eye; HG: Harderian glands; TY: thyroid.

The average weight of all animals on the day of the [ $^{125}\text{I}$ ] $\beta\text{CIT}$  SPECT scan was calculated ( $278 \pm 14$  g) and a T2-weighted MRI scan was selected for a rat of similar weight (263 g) from the database of scans held in the MRI unit. This served as a template for ROI analysis. Since this strain of rats (Sprague-Dawley) is highly inbred and no structural abnormalities are known to occur in these animals, there was no reason to object the use of another rat of that same strain that was of similar age/weight. SPECT scans were coded so

analyses could be performed blind to the treatment received by the animal. All coded [<sup>125</sup>I]βCIT SPECT scans plus the T2-weighted MRI were loaded into AMIDE, an image coregistration tool (Loening and Gambhir, 2003). The SPECT scan was aligned with the MRI scan by placing the caudate-putamen, clearly identified in the SPECT scan as having the highest level of [<sup>125</sup>I]βCIT binding, over the caudate-putamen visible in the T2-weighted MRI scan. The Harderian glands were also used as a landmark to refine the anterior positioning of the SPECT scan. Fine adjustment of the alignment was performed using rotations about the x-, y-, and z-axis (Fig. 2-23).

ROIs of the caudate-putamen, thalamus, area of the central canal, and the cerebellum were then defined bilaterally on the T2-weighted MRI image as follows. On 3 consecutive coronal slices on the MRI, the caudate-putamen and thalamus were delineated. For the area of the central canal and the cerebellum, ellipsoid sampling areas were placed on 3 consecutive MRI slices. One ellipsoid cylinder for each cerebellar hemisphere was placed in such a way that the vermis of the cerebellum was avoided since this area is reported to have significant SERT density (Meyer, 2007).

As the coregistration of SPECT and MRI images is prone to errors, the ROIs were then adjusted manually to match more closely the respective regions in each individual [<sup>125</sup>I]βCIT scan. Fig. 2-24 illustrates the definition of the ROIs on the T2-weighted MRI, and the subsequent intensity value extraction from the coregistered [<sup>125</sup>I]βCIT SPECT image. The measurement of the raw signal intensities as an average within the ROIs was then obtained and the binding ratio was calculated as follows, using the method of de Win *et al.* (de Win *et al.*, 2004).

$$\text{Binding Ratio} = \frac{\text{Region}}{\text{Cerebellum}}.$$

Thus three regions were analysed: the caudate-putamen, thalamus and the area of the central canal. The cerebellum was used as a reference region. The definition of the ROIs on the MRI, as well as the coregistration of the [<sup>125</sup>I]βCIT scans to that MRI were performed 3 times in order to evaluate the intra-rater variability. These 3 measurements were then averaged to yield a single value.

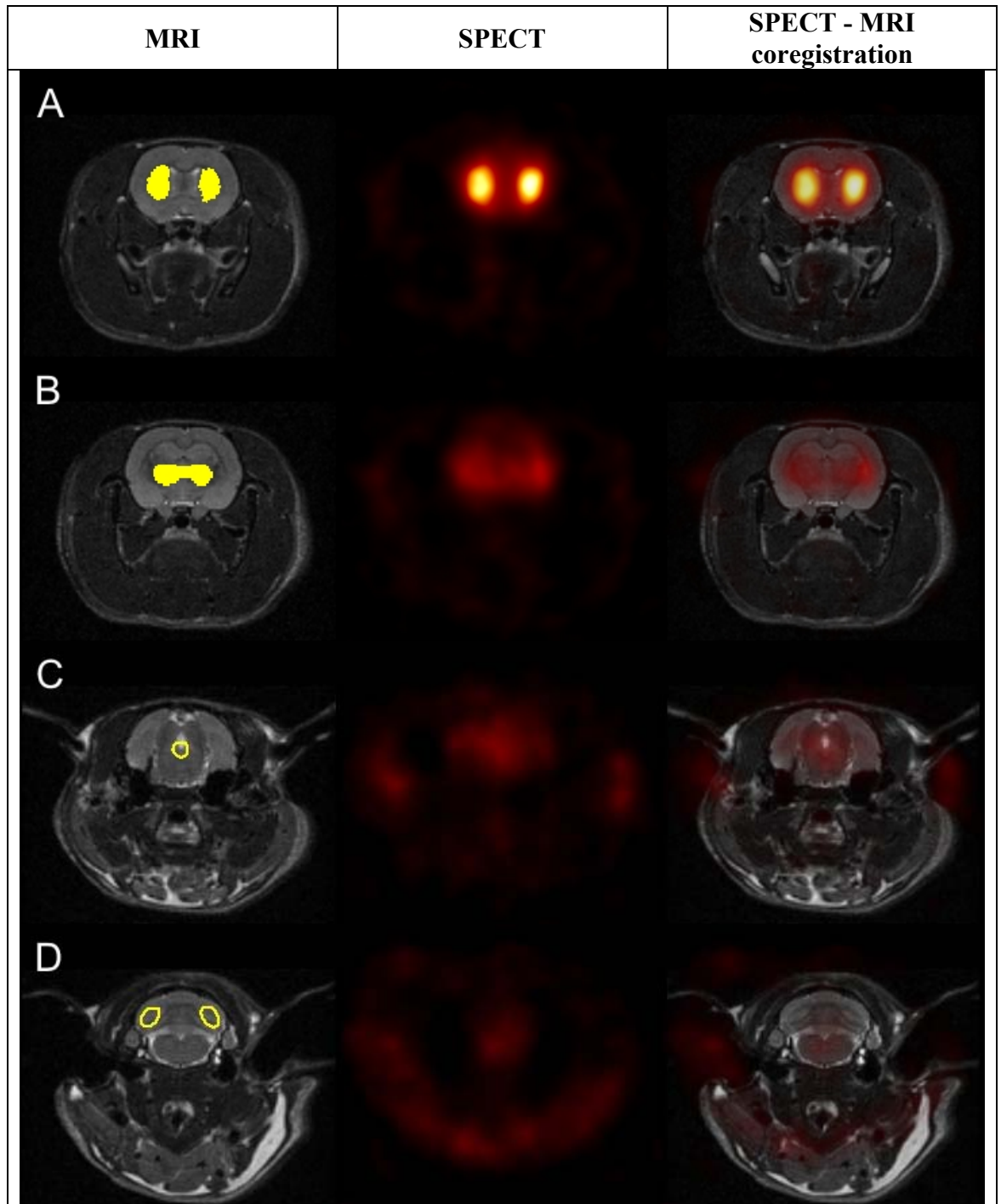


**Fig. 2-24. Definition of ROIs on coronal T2-weighted rat MRI and extraction of data from [<sup>125</sup>I]βCIT SPECT scan.**

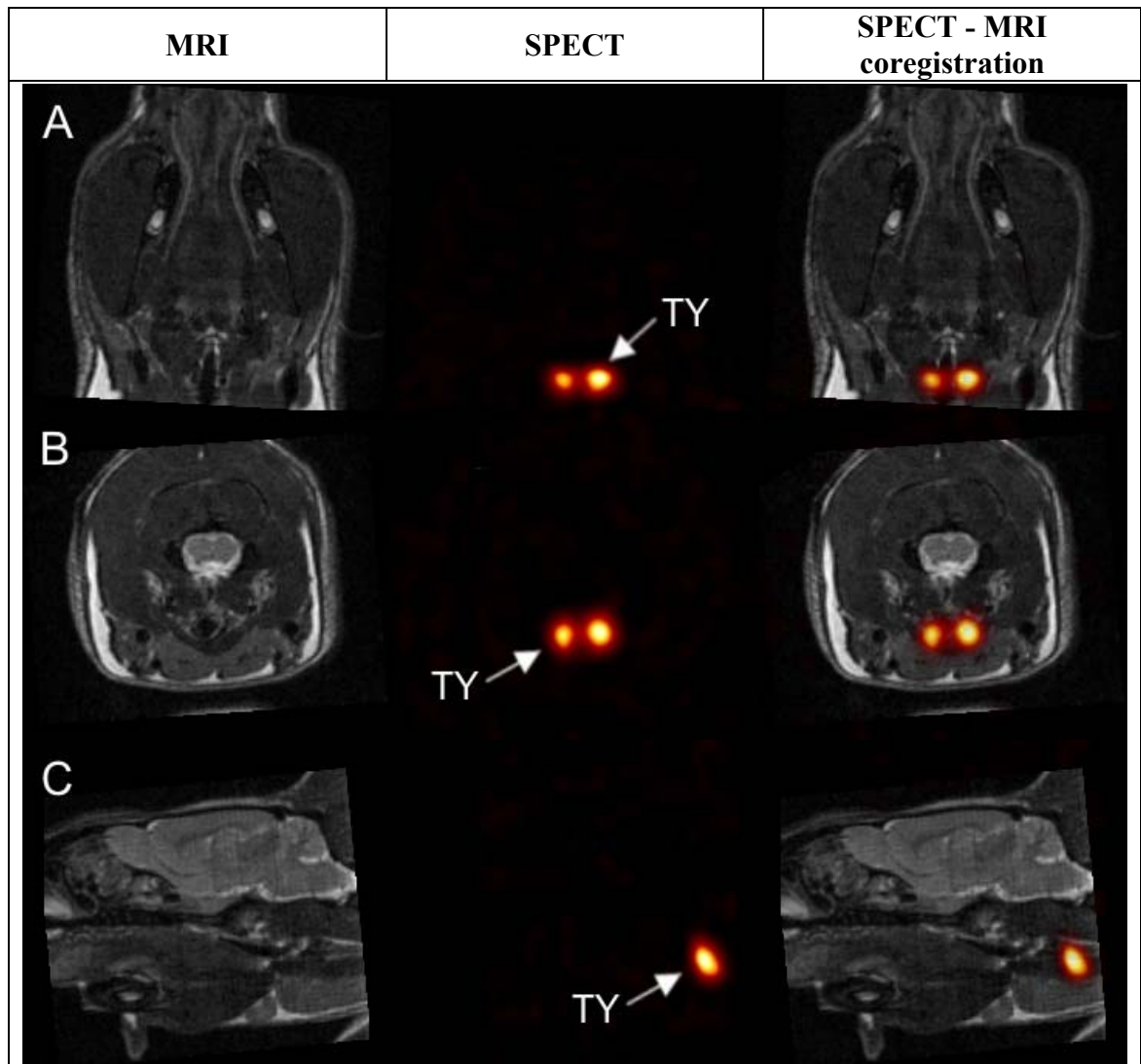
ROIs for the caudate-putamen, thalamus, area of the central canal, and cerebellum were defined on an age-matched T2-weighted rat MRI on 3 consecutive slices and subsequently superimposed on coregistered [<sup>125</sup>I]βCIT SPECT images for measurements.

A: caudate-putamen at Bregma level 1.10 mm.

B: thalamus at Bregma level -3.60 mm.

C: area of the central canal at Bregma level -8.3 mm.

D: cerebellum at Bregma level -10.04 mm.

Image processing of [ $^{125}$ I]ADAM scans.

**Fig. 2-25. Initial [ $^{125}$ I]ADAM SPECT scan coregistration to T2-weighted rat MRI image.**

Initial reconstructed [ $^{125}$ I]ADAM SPECT images showed much higher uptake in the thyroid compared to the brain. Therefore during reconstruction, maximal values of 32767, which is the maximum value allowed in a 16 bit image, were assigned to the thyroid by the image reconstruction software leaving the rest of the brain invisible. However rough positional and orientational adjustments were performed to align the thyroid with an age-matched rat MRI obtained from the scan database.

A: transverse view.

B: coronal view.

C: sagittal view.

TY: thyroid.

After reconstruction of the [ $^{125}$ I]ADAM data sets, only the thyroid was visible. This is due to the limits described above regarding storage of float data into a 16 bit image (Fig. 2-22, page 87), i.e. there was higher uptake in the thyroid than binding in the brain which resulted in inappropriate scaling of the data because the highest reconstructed value (which was likely in the thyroid) was assigned the highest voxel intensity (compared to the caudate-putamen in the [ $^{125}$ I] $\beta$ CIT scans). This initial image was used to roughly align the thyroid with the T2-weighted rat MRI in the x-, y-, and z-plane by means of rotational fine

adjustments using the AMIDE software package for multimodal coregistration (Fig. 2-25), as described for [<sup>125</sup>I]βCIT. However, because it was not possible to reconstruct images, which showed activity in the brain, unreconstructed raw SPECT files were sent to Dr. Dale Martin at Neurophysics Corp., the manufacturer of the micro-SPECT, for modification. As mentioned above, during reconstruction of the data, the largest reconstructed value is assigned a value of 32767 in a 16 bit image together with a single scalar calibration factor to refer back to the original reconstructed values, expressed as (emissions/seconds)/mm<sup>3</sup>. Dr. Martin reconstructed the images using a multiplication factor of 20x, or 10x where appropriate, in order to manually maintain full dynamic range within the ROIs. The process described above is summarised in Fig. 2-26.

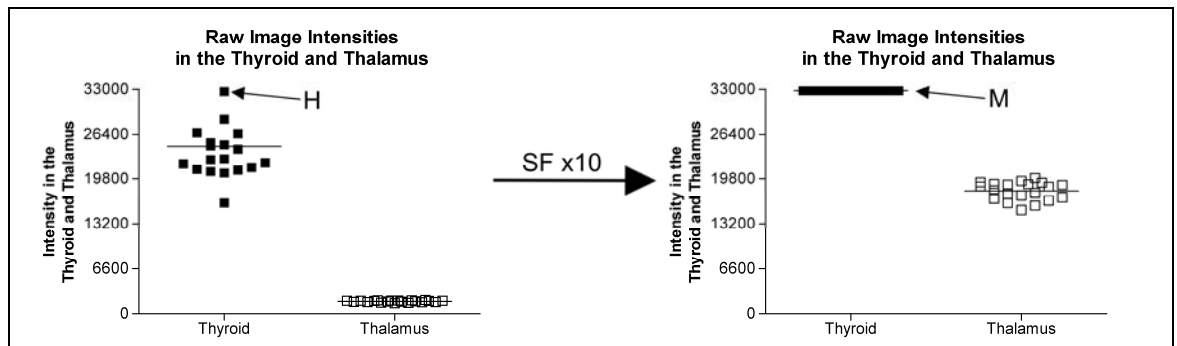


**Fig. 2-26. Illustration of reconstruction problem using [<sup>125</sup>I]ADAM.**

Left graph shows simulated data points derived from the thyroid. The highest reconstructed value is assigned to an intensity of 32767 (H) in a 16 bit image by the reconstructor to maintain the highest possible dynamic range. The thalamus, because of its low [<sup>125</sup>I]ADAM binding relative to thyroid uptake of free [<sup>125</sup>I], is not detectable. Multiplication with a scaling factor (SF, x10) amplifies all voxel intensities in the SPECT image by a factor of 10x (right graph) with the aim to detect thalamic uptake, which however results in a saturated thyroid in the image as the maximum voxel intensity (M) that can be stored in a 16 bit image is 32727.

Bar in scatter plots represents mean. The data points represent voxels within a given structure under investigation, i.e. the thyroid or the thalamus, respectively. Note that this figure is for illustration purposes only, so at no point the thyroid was assessed. Also the number of voxels in the thalamus (n = 20) does not correspond to the actual number defined on the MRI.

The rescaled images obtained from Neurophysics were loaded into the AMIDE coregistration software and the translations and rotations performed on the original images were applied to the rescaled images to roughly bring them into the MRI space. The Harderian glands were visible in the rescaled images so z-position was kept fixed and only the x-, y-axis and rotations were adjusted in order to align them with the MRI. ROIs for the thalamus, midbrain, and cerebellum were defined bilaterally on an age-matched T2-weighted rat MRI obtained from the database of the preclinical MRI facility at Glasgow University. The thalamus was delineated on 3 consecutive coronal slices on the rat MRI. For the cerebellum, ellipsoid sampling ROIs were placed on 3 consecutive MRI slices in each hemisphere such that the vermis of the cerebellum was avoided (the vermis of the

## Chapter 2 - Material and methods.

cerebellum is reported to have significant SERT density (Meyer, 2007). The midbrain was defined by placing a sphere-like ROI beneath the central canal at Bregma -5.8 mm. Fig. 2-28 illustrates the ROIs on the T2-weighted MRI, and the subsequent coregistration with the [<sup>125</sup>I]ADAM SPECT image. Rather than moving the ROIs as done with the relatively easily identifiable structures on [<sup>125</sup>I]βCIT SPECT scans, the whole [<sup>125</sup>I]ADAM SPECT scan was shifted in such a way along the x- and y-axis so that it appeared centred on the MRI in order to compensate for small scale mis-registrations.

Because of the poor image quality and the lack of identifiable regions on the [<sup>125</sup>I]ADAM scans, definition of the ROIs on the MRI, coregistration of the [<sup>125</sup>I]ADAM SPECT scan to the age-matched T2-weighted MRI, and subsequent measurements were performed only once. The rater was unaware of the identity of the respective SPECT scan until all measurements were concluded. The binding ratio was then calculated as follows:

$$\text{Binding Ratio} = \frac{\text{Region}}{\text{Cerebellum}},$$

where the regions were either the average signal intensity within the ROI for thalamus, or the midbrain. The cerebellum was used as reference region.

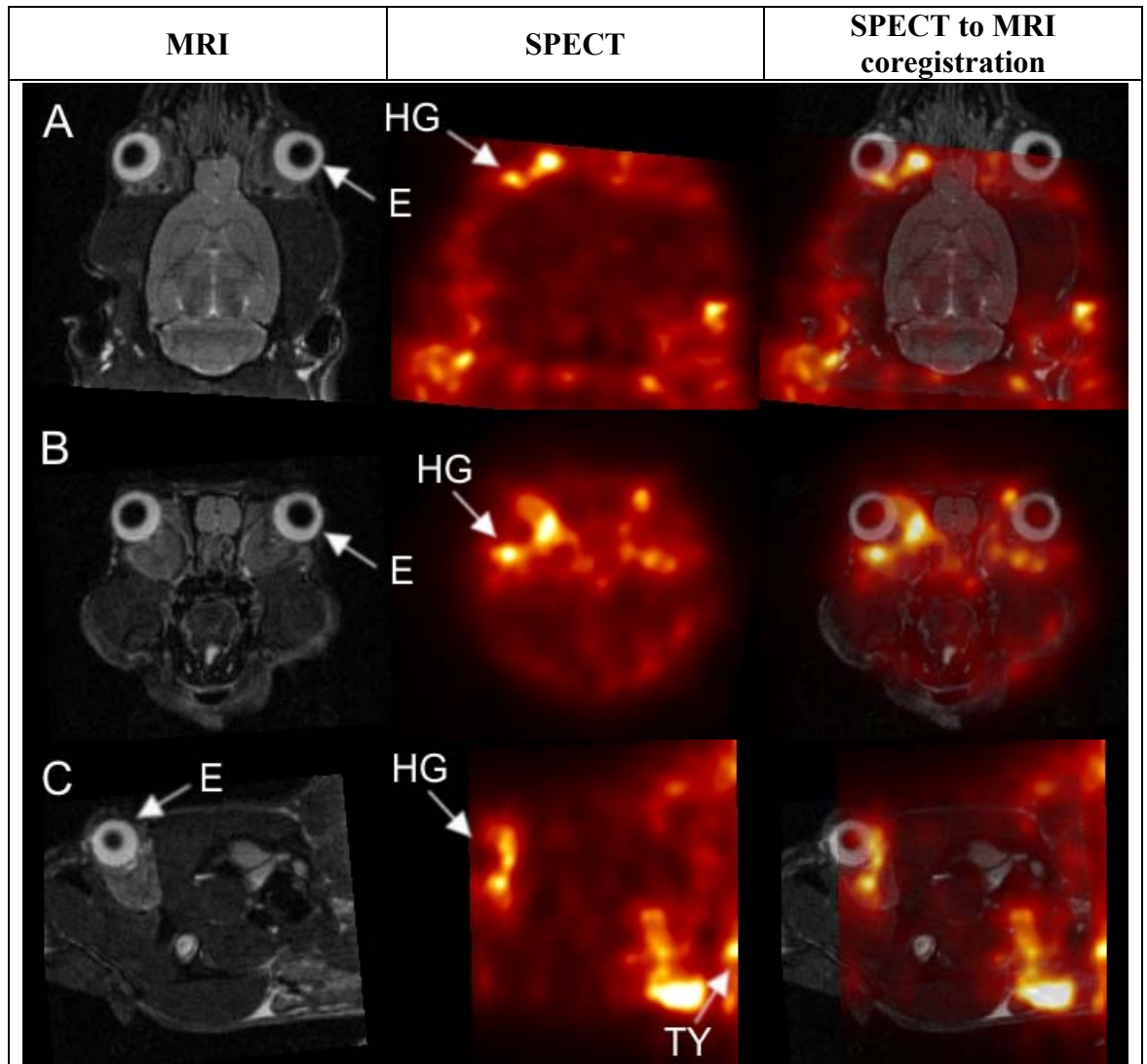


**Fig. 2-27. Final [ $^{125}\text{I}$ ]ADAM SPECT to T2-weighted MRI coregistration.**

After reconstruction using a multiplication factor to rescale signal intensities (done by Neurophysics Corp., Shirley, MA, USA), the translations and rotations obtained from the thyroid alignment (Fig. 2-25) were applied to the rescaled [ $^{125}\text{I}$ ]ADAM SPECT images, and subsequently alignment was more finely adjusted using the Harderian gland which became visible after image rescaling. The z-position was kept fixed to hold positioning achieved in the previous step.

A: transverse view.

B: coronal view.

C: sagittal view.

E: eye; HG: Harderian glands; TY: thyroid.

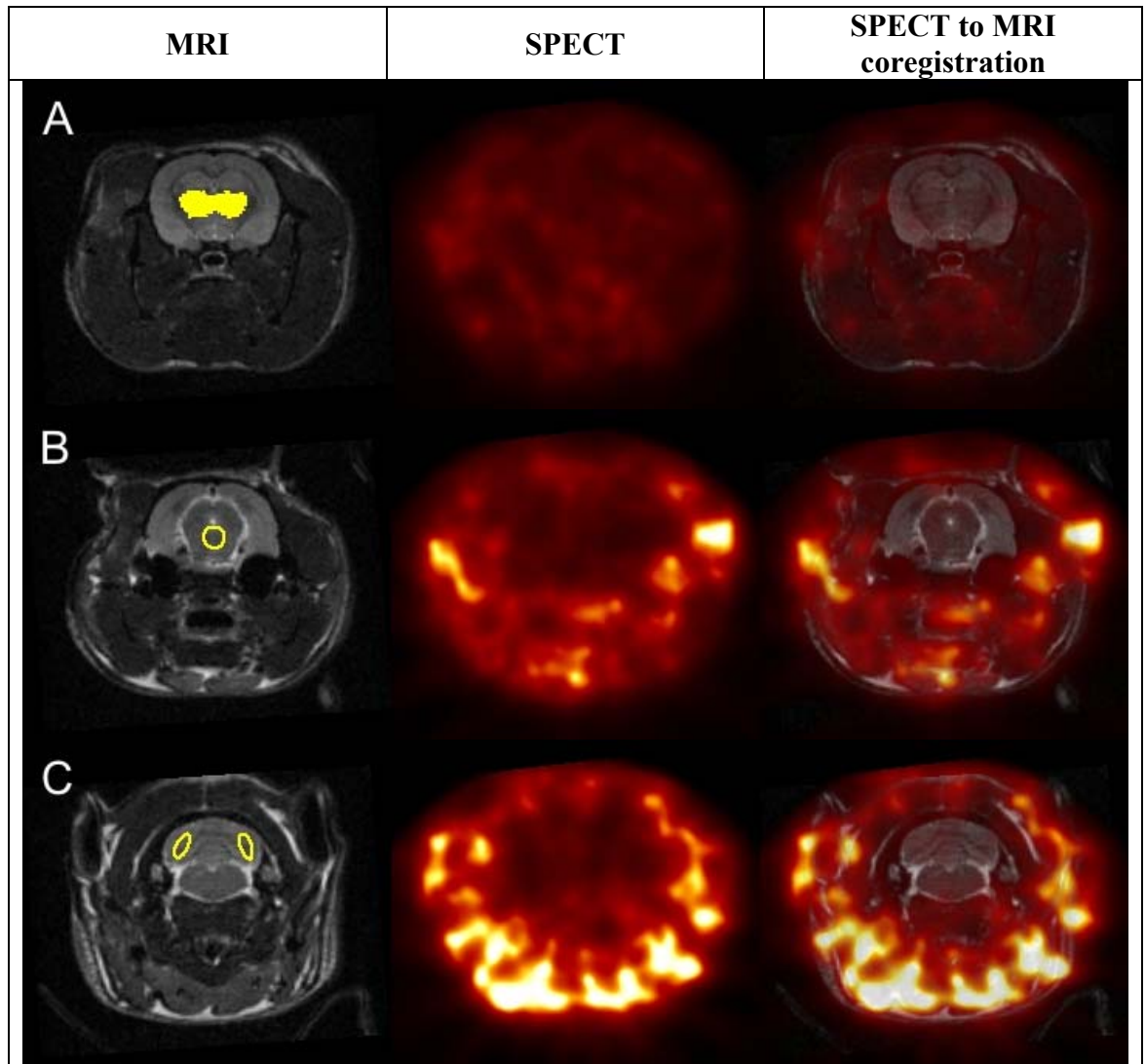


**Fig. 2-28. Definition of ROIs on coronal T2-weighted rat MRI and extraction of data from [<sup>125</sup>I]ADAM SPECT scan.**

ROIs for the thalamus, midbrain, and cerebellum were defined on an age-matched rat MRI. The thalamus and the cerebellum were defined on 3 consecutive slices, and a sphere-like ROI was placed on the midbrain and subsequently superimposed on coregistered [<sup>125</sup>I]ADAM SPECT images for measurements.

A: thalamus at Bregma level -3.60 mm.

B: midbrain at Bregma level -5.8 mm.

C: cerebellum at Bregma level -10.04 mm.

### ***In vitro* and *ex vivo* autoradiography.**

Tissue processing, *in vitro* autoradiography ([<sup>3</sup>H]citalopram, [<sup>3</sup>H]WIN 35, 428, and [<sup>125</sup>I]βCIT) and bilateral analysis of the autoradiography data for this study was performed as outlined in detail in the respective pilot study (pages 53 - 56). Two sections per level for total, and 2 sections for nonspecific binding were analysed. A few more structures were sampled compared to the pilot study, which included the tubercle area (Bregma 1.00 mm), globus pallidus (Bregma -0.92 mm), lateral hypothalamus (Bregma -2.30 mm), the whole thalamus (Bregma -3.60 mm), and the locus coeruleus (Bregma -10.04 mm). Removed was the perirhinal/entorhinal cortex area (Bregma -3.60 mm).

## Chapter 2 - Material and methods.

The tissue processing procedure of *ex vivo* brains of animals that were previously [<sup>125</sup>I]βCIT and [<sup>125</sup>I]ADAM SPECT scanned was similar to the *in vitro* autoradiography (pages 53 - 56), except that no radiolabelled ligand other than that used for SPECT imaging was applied. Two sections per level were collected and analysed. The film exposure time for [<sup>125</sup>I]βCIT scanned animals ranged between 3.5 h and 24 h, and was 14 days for [<sup>125</sup>I]ADAM scanned animals. *Ex vivo* autoradiographic films were then digitized and analyzed using a MCID basic system (7.0 Rev 1.0, build 207; Imaging Research Inc.). The optical density of the structures was measured bilaterally and data was then normalised to the optical density of the cerebellum to obtain the binding ratio:

$$\text{Binding Ratio} = \frac{\text{Region}}{\text{Cerebellum}}.$$

## 2.6 Statistics.

All data within this thesis are expressed as mean  $\pm$  SD. All statistical comparisons between WT, SERT-KO and SERT-HT mice in chapter 3 (page 98) were performed using a one-way analysis of variance (ANOVA) Kruskal-Wallis test, followed by a 2-tailed Mann-Whitney U test in case of significance to determine group differences. Statistical comparisons between WT versus PLPOVR mice in chapter 4 (page 158) and 5 (page 224), and vehicle- versus MDMA-treated rats in chapter 6 (page 242) were performed using a 2-tailed Mann-Whitney U test. The level of significance for both tests (ANOVA Kruskal-Wallis, and Mann-Whitney U, respectively) was set to  $p < 0.05$ . Where appropriate, a Spearman rank order correlation coefficient was calculated. TBSS on DTI parameter maps (WT vs. SERT-KO; WT vs. SERT-HT) (WT vs. PLPOVR) was performed using a nonparametric test that determines significant clusters (cluster-based thresholding), where the significance threshold was set to  $p < 0.05$  (see details on TBSS on page 46). Corrections for multiple comparisons were performed only where TBSS was used. A 2-tailed statistical image was computed from the 1-tailed statistical images provided by the nonparametric statistical test algorithm included in FSL, called randomise (Nichols and Holmes, 2002), using a script provided by Ged Ridgway, University College London, UK, according to details given on the statistical nonparametric mapping (SnPM) website (<http://www.sph.umich.edu/ni-stat/SnPM/man.html>), a nonparametric statistics toolbox written by Nichols *et al.* (Nichols and Holmes, 2002) for the analysis software statistical parametric mapping (SPM) (Ashburner and Friston, 2000).

**Chapter 3 - DTI of the brain in mice deficient in SERT.**

## Chapter 3 - DTI of the brain in mice deficient in SERT.

### 3.1 Introduction.

The serotonin system plays a key role in major mood disorders, in particular depression. Serotonin is a neurotransmitter that is one of the earliest to be present in the developing animal, and may therefore serve as a growth factor. In development, the earliest appearing serotonin receptor, 5-HT<sub>1A</sub>, acts in the raphe nuclei, the main source of serotonergic fibres in the brain, as an inhibitory autoreceptor to the outgrowth of the serotonergic system. Thus the initial overshoot of serotonin-containing fibres resulting in a more than necessary innervation of target tissue can be regulated via a negative feedback loop. During a critical phase in brain development, serotonin levels are therefore tightly regulated, and interference with synaptic serotonin levels can cause severe malfunctions (for review see Whitaker-Azmitia *et al.* (Whitaker-Azmitia, 2005)). The SERT regulates these levels by shunting released serotonin back into the presynaptic terminal where it can either be recycled, or broken down by the enzyme MAO. The SERT is thought to be a key player in depression, and is the main target for certain classes of antidepressants, which functionally impair the transport of serotonin into the presynaptic terminal, thereby enhancing neurotransmission onto the postsynaptic neuron (Kandel *et al.*, 2000).

The advent of genetic tools to modify genes to either become non-functional, or to be overexpressed in the living animal, has greatly enhanced our knowledge of diseases in general, and specifically here in the context of depression. Lira *et al.* showed that SERT gene deletion in mice causes behavioural deficits associated with depression (Lira *et al.*, 2003). The same behavioural deficits could be replicated by treating mice postnatally with the SSRI fluoxetine, which is used to treat depression (Ansorge *et al.*, 2004). That antidepressant treatment during pregnancy will interfere with normal brain development was shown previously by Cabrera-Vera *et al.*, who demonstrated that SERT densities were altered in prepubescent rat progeny (Cabrera-Vera and Battaglia, 1998). Apart from behavioural deficits, deleting the SERT gene also causes structural alterations in the developing brain. In SERT-KO mice there was a 50 % reduction in dorsal raphe neurons (Lira *et al.*, 2003), one of the sites providing most of the serotonin fibres in the brain (Beck *et al.*, 2004). In addition, Persico *et al.* showed that the barrel field in the somatosensory cortex of rodents, which is a direct representation of the whiskers, is absent in SERT-KO mice (Persico *et al.*, 2001). Esaki *et al.* investigated the functional consequences in these mice within the whisker-to-barrel cortex pathway, and found that whisker stimulation

### Chapter 3 - DTI of the brain in mice deficient in SERT.

evoked a metabolic response in SERT-KO mice, however, this response was much lower than in WT mice. Reducing serotonin in SERT-KO mice during development restored metabolism, indicating excessive serotonin due to the genetic deletion of SERT to be responsible for the effect (Esaki et al., 2005). To further investigate the contribution of serotonin to the structural development of the brain, another study by Persico *et al.* on SERT-KO mice showed that apoptosis is decreased in these mice in several brain regions (Persico et al., 2003). Another model of enhanced serotonin neurotransmission is the MAO-KO mouse, in which the gene for MAO is knocked out. MAO-KO mice show abnormal development of retinal projections to the dorsal lateral geniculate nucleus. During normal development in mammals, retinal projections innervate the dorsal lateral geniculate nucleus bilaterally, and segregation of these fibres occurs later, so that the ipsilateral eye innervates the contralateral dorsal lateral geniculate nucleus. In MAO-KO mice, this segregation does not take place appropriately, and the elevated serotonin levels caused by MAO-KO were held responsible for this structural abnormality (Upton et al., 1999).

The various studies described indicate that manipulation of normal levels of serotonin during brain development results in behavioural, functional and structural abnormalities. MRI has been successfully applied to detect structural brain abnormalities in a range of human diseases. For instance, Sheline *et al.* showed that the hippocampus in depressed patients was shrunken compared to normal controls (Sheline et al., 1999, Sheline et al., 1996).

In small animals, MRI has been employed in models of human neurological diseases. *In vivo* MRI of a transgenic rat model of Huntington's disease showed an enlargement in lateral ventricles, indicative of brain atrophy (von Horsten et al., 2003). Thus MRI makes longitudinal studies in a rat model of Huntington's disease feasible with the opportunity to evaluate different treatment regimens. Further advances in MRI imaging were made by scanning brain tissue *ex vivo*, hence allowing data acquisition over long periods of time, resulting in improved spatial resolution. For example, microscopic MRI was performed in the DAT knockout mouse, where subtle changes in striatal volume were identified (Cyr et al., 2005).

While conventional MRI is capable to deliver high quality images of subcortical structures on the basis of their different MRI relaxation properties, DTI, another MRI technique,

### **Chapter 3 - DTI of the brain in mice deficient in SERT.**

takes advantage of the restricted diffusion of water in the sample of interest. Due to the special arrangement of fibres that constitute white matter, i.e. long directional tracts ensheathed with myelin, reminiscent of an insulated wire that does hinder the passage of a current, water diffusion is favoured along the axon rather than across it. This is in contrast to grey matter, where water diffusion is less restricted and diffusion is therefore less favoured in a particular direction. There is growing evidence of the usefulness of this method in order to evaluate the structure of white matter in healthy and diseased brains. In humans, clinical DTI studies of depression show consistently reductions in FA, one of the measures that can be extracted from DTI providing an assessment of fibre integrity, in frontal cortical areas (Bae et al., 2006, Li et al., 2007b, Ma et al., 2007, Yang et al., 2007a). In high resolution *ex vivo* animal DTI studies, models of multiple sclerosis (Song et al., 2005), and dysmyelination in general (Tyszka et al., 2006), showed that DTI provides valuable information on white matter integrity using FA as a measure of fibre integrity, but also the RD providing a measure of water diffusion across the tract.

Since serotonin is involved in the development of the brain, it was of interest to apply high resolution *ex vivo* DTI to a mouse model of depression. Given the evidence for altered white matter integrity detectable using DTI in depressed humans, we hypothesised that SERT-KO mice would display differences in white matter structure that could be identified with DTI.

#### **3.2 Aims of the study.**

- I. Establish methodology for *ex vivo* DTI analysis of DTI parameters obtained from fixed mouse brains. The methodology is described in detail in the material and methods chapter (Chapter 2, page 39).
  
- II. Investigate whether the deletion of the gene encoding for the SERT has any influence on measures derived from DTI.

### 3.3 Material and methods.

#### Animals.

SERT-KO mice, mice heterozygous for the SERT deletion (SERT-HT), and WT mice were generated and maintained, and subsequently the heads shipped to Glasgow by our collaborators, Drs. Mark Ansorge and Jay Gingrich at Columbia University, New York, USA. For details on the generation of the animals, see Lira *et al.* (Lira et al., 2003). At Columbia, an initial batch of SERT-KO ( $n = 5$ ;  $31.4 \pm 6.4$  g), SERT-HT ( $n = 5$ ;  $31.1 \pm 4.1$  g), and control WT animals ( $n = 5$ ;  $30.5 \pm 6.0$  g), was prepared and sent to Glasgow that was followed up with a second batch providing total animals of SERT-KO  $n = 7$  ( $30.8 \pm 5.4$  g), SERT-HT  $n = 5$  ( $31.1 \pm 4.1$  g) and control WT animals  $n = 8$  ( $28.9 \pm 5.1$  g) with the same genetic background (129S6 / SvEv, all male) in order to validate results obtained from the initial batch. At Columbia, mice were killed and processed as described in detail in the material and methods in chapter 2 (section 2.1, page 40). Note that the DTI from one SERT-HT mouse was excluded from the analysis, as the respective S0 image appeared patchy, i.e. alternating high and low signal was present, possibly through freezing during transport (Fig. 3-40, page 148).

Subsequent to the scanning of the 20 brains described above, another batch of mouse heads was received from Dr. Ansorge's laboratory. This consisted of SERT-KO ( $n = 5$ ;  $27.2 \pm 2.3$  g), and WT ( $n = 5$ ;  $25.9 \pm 5$  g) animals with the same genetic background (129S6 / SvEv, all male). These additional animals were requested to confirm whether the finding of shorter callosal length is a strain, or SERT dosage issue (see below).

For this batch of animals, the heads were stored with constant agitation for  $11.8 \pm 0.4$  days at  $4^\circ\text{C}$  in a solution of 200 ml PBS with 0.01 % sodium azide and 0.5 % multihance. Prior to MRI scanning, the heads were allowed to equilibrate to room temperature for  $9.8 \pm 3.5$  h in the same solution prior to skull removal. Brains were placed in a container filled with fomblin prior to scanning. However due to unexpected MRI scanner downtime, the period which the brains from this batch of mice spent in fomblin prior to scanning was substantially different than those in the first two batches ( $41.2 \pm 41$  h). Further storage of the brains in multihance would have resulted in more diffusion of this T1 reducing compound into the brains, while storing the brains in PBS would have resulted in its leaking out. Since fomblin is a lubricant that does not mix with aqueous solutions, it was considered to be the best storage solution. Another difference, discovered after the brains

## Chapter 3 - DTI of the brain in mice deficient in SERT.

had been scanned, was that some of the animals in this second batch were perfused with PFA made up in water instead of PBS. Therefore these additional brains were only used for measuring the corpus callosal length (see Fig. 3-7, page 110).

Times Spent In / For:	Genotype					
	WT		SERT-KO		Rel. Diff. [%] <sup>a</sup>	
PBS [d]	17.00	± 2.14	17.29	± 1.80	+1.68	
Contrast [d]	11.97	± 0.59	12.18	± 0.37	+1.73	
RT acclimatisation [h]	8.40	± 3.46	12.71	± 5.31	+51.43	
Fomblin [h]	3.66	± 3.00	6.41	± 10.77	+75.18	

Times Spent In / For:	Genotype					
	WT		SERT-HT		Rel. Diff. [%] <sup>b</sup>	
PBS [d]	17.00	± 2.14	17.80	± 2.39	+4.71	
Contrast [d]	11.97	± 0.59	12.46	± 0.20	+4.11	
RT acclimatisation [h]	8.40	± 3.46	14.70	± 5.85	*	+75.03
Fomblin [h]	3.66	± 3.00	1.54	± 0.35	-57.84	

**Table 3-1. Group comparison of experimental conditions suggests only significant differences between WT and SERT-HT for the period of brain equilibration to RT.**

Data are mean ± SD for n = 8 for WT, n = 7 for SERT-KO, and n = 4 for SERT-HT.

Units of measurements are days [d] for PBS and contrast, and hours [h] for RT (room temperature) acclimatisation and fomblin. Relative difference (Rel. Diff.) = <sup>a</sup> (SERT-KO - WT)/(WT)\*100 %.

Relative difference (Rel. Diff.) = <sup>b</sup> (SERT-HT - WT)/(WT)\*100 %.

After overnight fixation, the heads were stored in PBS and subsequently shipped from New York to Glasgow at 4 °C. After a period of 17.3 ± 2 (all genotypes) days, heads were transferred into a solution of PBS and multihance (contrast) for 12.2 ± 0.5 h (all genotypes) and stored at 4 °C. Prior to DTI acquisition, heads were allowed to equilibrate to RT for 11.5 ± 5.3 h (all genotypes), and subsequent to extraction of the brain transferred to fomblin for 4.1 ± 6.6 h (all genotypes).

As significant differences were detected between WT and SERT-HT in some DTI measures, periods of time spent in conditions stated were separated for the genotypes in order to assess possible differences in tissue treatment. Significant differences were detected between WT and SERT-HT in the period of time the heads spent to acclimatise to RT.

One-way ANOVA Kruskal-Wallis followed by a 2-tailed Mann-Whitney U, \*p < 0.05 relative to WT group in case significant differences were detected.

DTI image acquisition (section 2.1, page 41), and image analyses (section 2.1, page 42) are described in detail in the material and methods chapter.

### 3.4 Results.

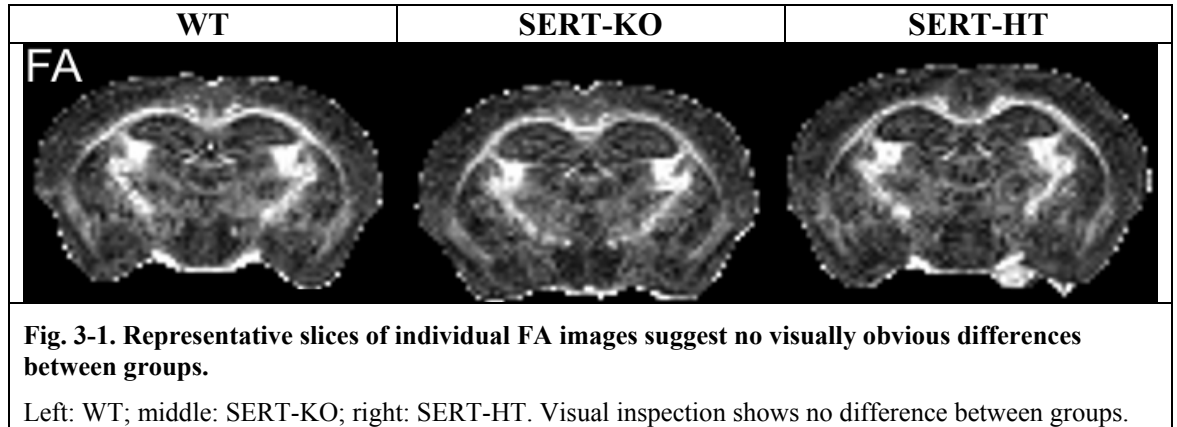
#### 3.4.1 DTI.

##### Individual parameter maps (FA, and $\lambda_i$ ).

After DTI acquisition, DWI images were fed into the dtifit routine, which is part of FSL, in order to calculate the metrics of the diffusion tensor (FA,  $\lambda_1$ ,  $\lambda_2$ ,  $\lambda_3$ ). For each animal the

### Chapter 3 - DTI of the brain in mice deficient in SERT.

FA maps were visually inspected (Fig. 3-1). On FA images, the white matter represented by high directionality and therefore high FA values could easily be discerned from grey matter that displayed only low FA. However no major differences between groups were visually obvious at this stage of the analysis.



The 3 eigenvalues describe the diffusion of water within a tract, with  $\lambda_1$  being the diffusion coefficient in the least restricted direction of water diffusion (generally along the white matter tract), and  $\lambda_2$  and  $\lambda_3$ , respectively, are the diffusion coefficients perpendicular to  $\lambda_1$  and to each other. Image intensities decrease in the order  $\lambda_1 > \lambda_2 > \lambda_3$ , as expected by definition (Fig. 3-2). No obvious difference in eigenvalue maps could be observed visually between WT, SERT-KO and SERT-HT.

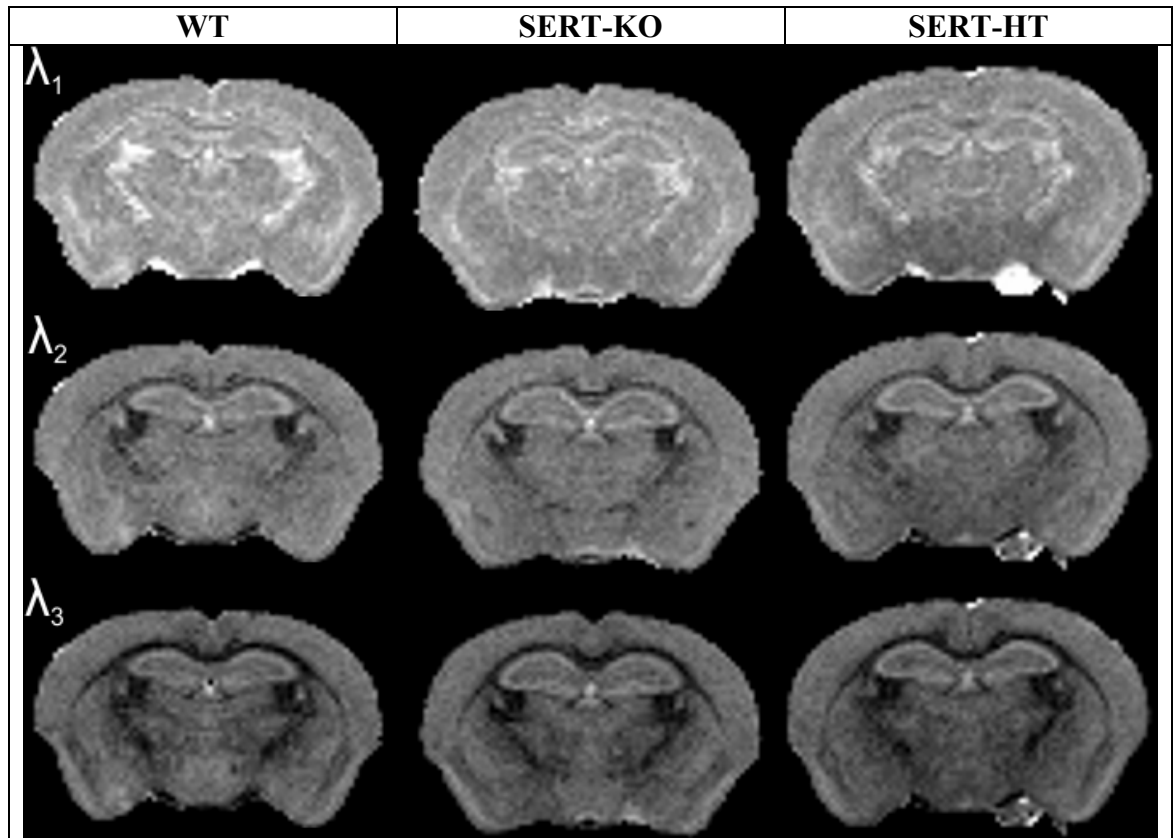


**Fig. 3-2. Representative slices of individual eigenvalue images suggest no visually obvious differences between groups.**

Left: WT; middle: SERT-KO; right: SERT-HT. Visual inspection showed no difference between groups in  $\lambda_1$ ,  $\lambda_2$ , and  $\lambda_3$ .

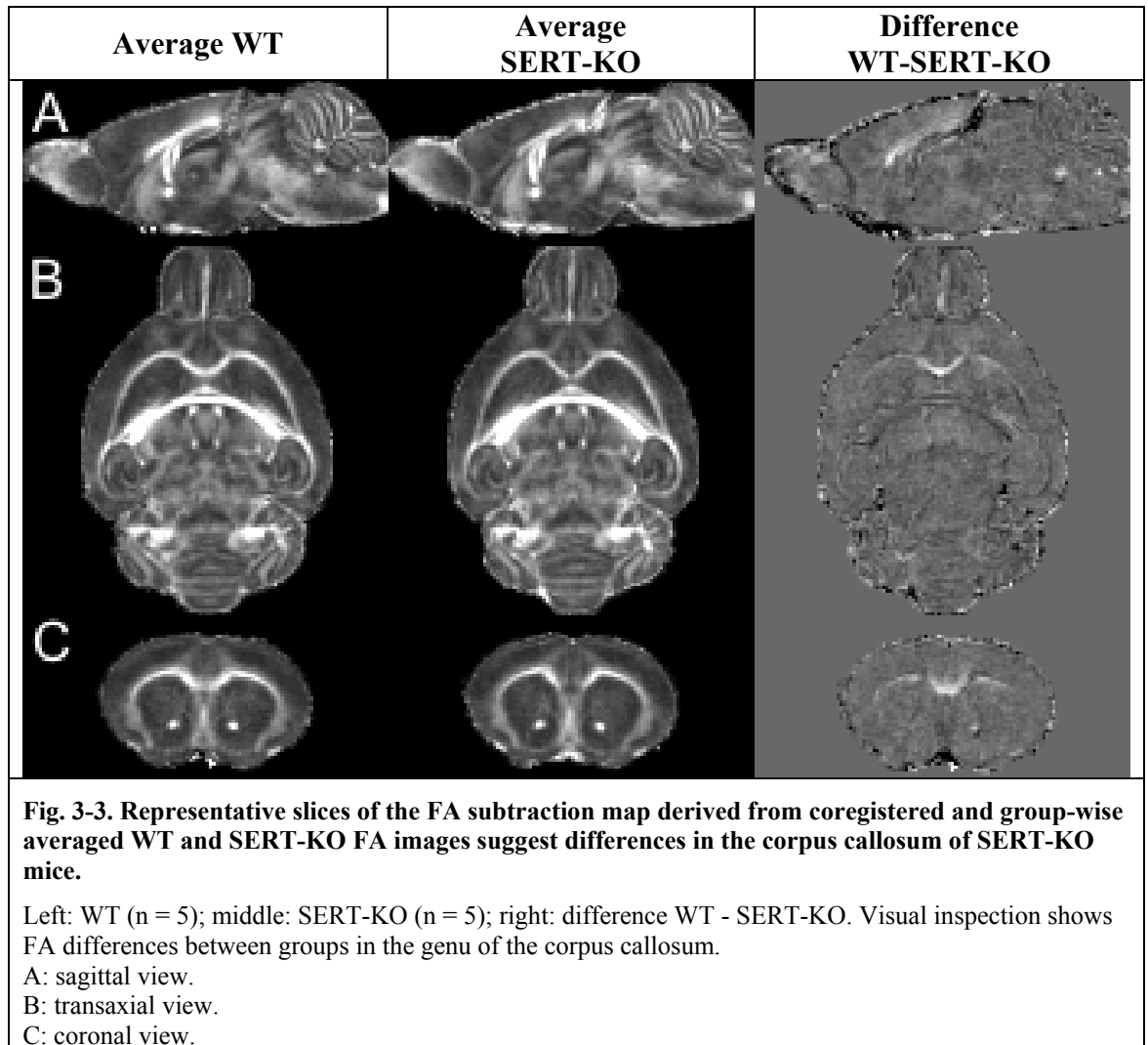
$\lambda_1$ , axial diffusion.

$\lambda_2$ , perpendicular diffusion.

$\lambda_3$ , perpendicular diffusion.

### Initial mean FA subtraction map analyses (AIR).

Individual FA maps of SERT-KO (n = 5) and WT (n = 5) animals from the initial batch of brains received from Dr. Ansorge's laboratory were coregistered using AIR to a FA template generated from WT data. Once coregistered, group averages were calculated, followed by subtraction of average SERT-KO from average WT in order to identify obvious group differences in FA intensity (Fig. 3-3). Intensities in the difference image of WT - SERT-KO FA were roughly around background for most of the brain. However the genu of the corpus callosum showed substantial differences in the SERT-KO mice as indicated by positive FA values in the difference map. This reflected lower FA values in SERT-KO mice due to either an inherently lower degree of integrity within the corpus callosum, or that morphological differences were present, i.e. missing structure.



### Abnormalities in SERT-KO mice.

The initial subtraction map analysis indicated that the genu of the corpus callosum was a region possibly affected due to deletion of the SERT gene. Subsequent to this, the individual coregistered FA images from all animals in the SERT-KO group were visually inspected to identify whether only a subset or the whole SERT-KO group showed differences in FA in the corpus callosum (Fig. 3-4). Two of the five SERT-KO mice appeared to have a distinct phenotype compared to WT animals, and will therefore be referred to “aberrant”. The corpus callosum obviously did not connect the two hemispheres at the same level in the SERT-KO compared to the WT as observed in the coronal views. In addition, the anterior two thirds of the corpus callosum encompassing the genu and the body, were absent in the aberrant SERT-KO mice at the midline level as confirmed by inspection of the sagittal slices (Fig. 3-4).

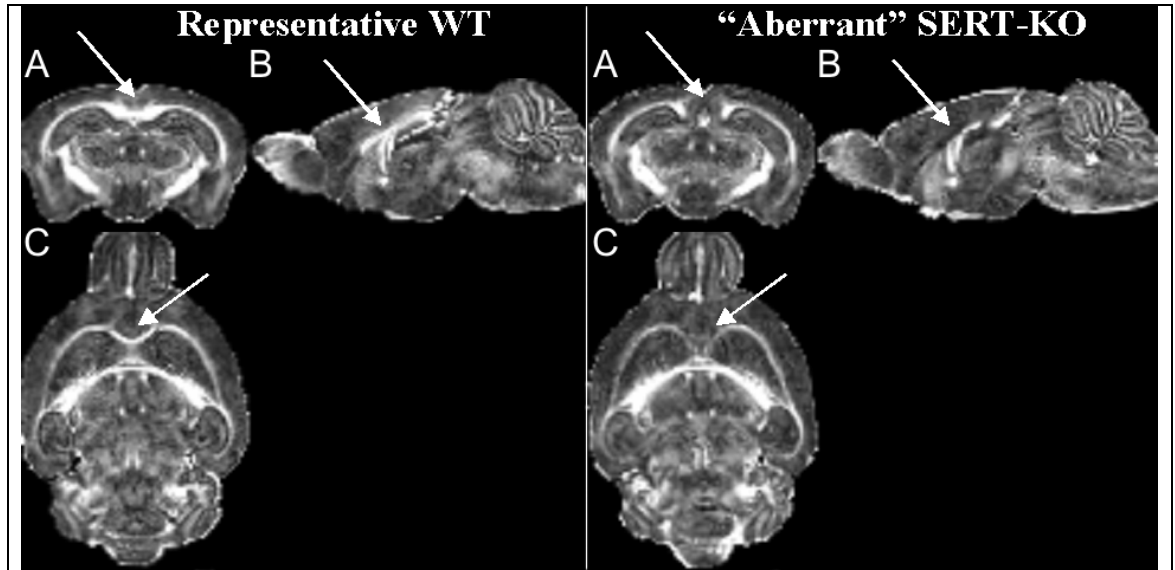


**Fig. 3-4. Representative slices of individual coregistered WT vs. "aberrant" SERT-KO FA maps show structural abnormalities in the corpus callosum of some SERT-KO mice.**

Left: WT; right: "aberrant" SERT-KO. Arrows indicate major differences. Visual inspection shows FA differences between groups in the genu, and the body of the corpus callosum. The splenium of the corpus callosum appears normal.

A: coronal view.

B: sagittal view.

C: transaxial view.

#### **Line intensity profiles on FA images (AIR).**

Visual inspection of the FA images indicated that there might be differences between WT and SERT-KO mice in the corpus callosum. In order to provide a quantitative assessment of the corpus callosum abnormality observed in the images, an identically-sized, rectangular ROI was placed onto individual, coregistered transaxial FA maps at the level of the genu of the corpus callosum and external capsule at the same position (Fig. 3-5, inset). This was done for all animals in WT, SERT-KO, and SERT-HT groups of the initial batch. A spatial intensity line profile was then extracted with FA values within the ROI plotted against the distance in x-direction (Fig. 3-5). The spatial intensity profiles indicated that FA values in the external capsule were visually comparable between the WT, SERT-HT, and SERT-KO mice. However, FA values in the genu of the corpus callosum were reduced in SERT-HT and SERT-KO compared to WT animals. This reduction was observed in the order WT > SERT-HT > SERT-KO.

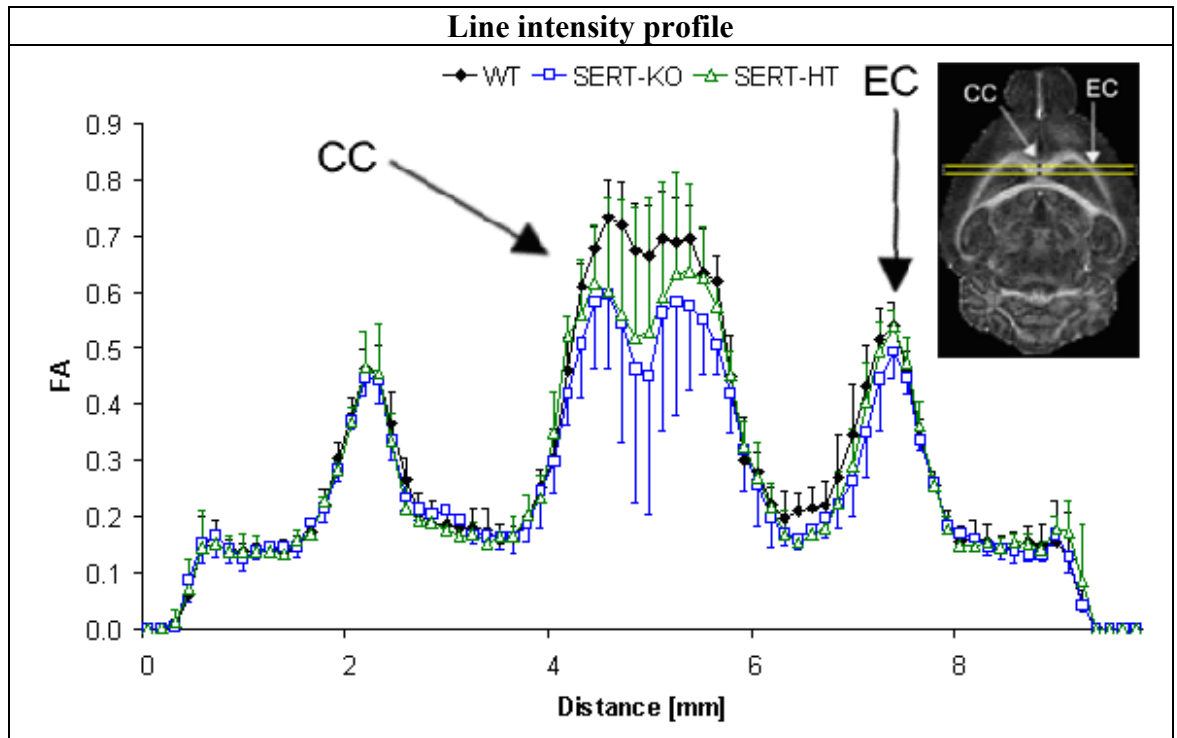


**Fig. 3-5. Line intensity profile through the corpus callosum (CC) and external capsule (EC) shows differences in FA between WT, SERT-HT and SERT-KO in the CC.**

Data are mean  $\pm$  SD. For WT and SERT-KO n = 5, respectively, and n = 4 for SERT-HT.

Units of measurement are dimensionless for FA, and mm for in-plane distance.

Black line: WT; blue line: SERT-KO; green line: SERT-HT.

A rectangular ROI identical in size and position was superimposed onto each individual FA image previously coregistered to the WT FA template (inset). For the external capsule no differences were visually detected. However callosal FA values are reduced in SERT-KO and SERT-HT mice relative to those measured in WT animals in the following order: WT > SERT-HT > SERT-KO.

### Measuring anterioposterior extent of the corpus callosum.

The anterior-posterior length of the corpus callosum was measured on individual, unregistered S0 images to avoid potential errors due to deformation that took place when registering the FA maps. In MRIcro (Rorden and Brett, 2000), the most anterior slice, in which the corpus callosum first appeared to connect the two hemispheres, and the most posterior slice where the corpus callosum still connected the 2 hemispheres, were used to define the anterior and posterior extents. The number of slices encompassed within these 2 slices (which were included) was then multiplied by the voxel dimension along the z-axis, (0.13 mm), to calculate the length of the corpus callosum along the anterioposterior axis. The FA images were viewed in coronal orientation to confirm the measurements and adjustments made if necessary (Fig. 3-6).

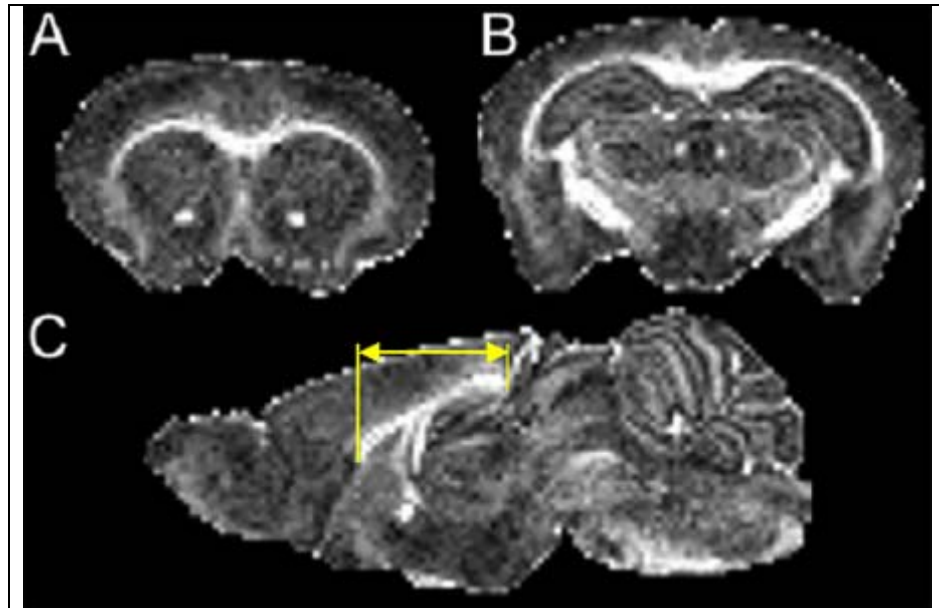


**Fig. 3-6. Measuring the anteroposterior extent of the corpus callosum on individual, unregistered FA images.**

Only slices comprising interhemispheric connection of the corpus callosum were included in the measurement.

A: first coronal slice, where the corpus callosum connects the two hemispheres.

B: last coronal slice, where the corpus callosum interconnects both hemispheres.

C: sagittal view on the anteroposterior extent of the corpus callosum.

As only 2 SERT-KO brains appeared to have an abnormally shortened corpus callosum and the initial animal numbers (initial batch) were too low (for WT and SERT-KO  $n = 5$ , respectively, SERT-HT  $n = 4$ ) to draw any conclusions from, it was decided to increase animal numbers for WT ( $n = 8$ ) and SERT-KO ( $n = 7$ ), and subsequently measure the anterior to posterior extent of the corpus callosum on coronal slices on unregistered individual S0 and FA images (data not shown, see below Fig. 3-7). The callosal length considered to be abnormal was set to be less than 1 mm. Statistical analysis showed there to be no significant differences between WT, SERT-KO, and SERT-HT mice. However within the SERT-KO group, there were still two out of seven animals, which had markedly shorter callosal lengths than other animals in the group. Thus the additional SERT-KO mice that were included to increase the animal numbers in this group (second batch) did not have a shortened corpus callosum. The promising results obtained from measuring the callosal length were compared to previously reported findings in the literature in order to examine the novelty of the observation that some SERT-KO mice had shortened callosal length. Wahlsten *et al.* published several observations in which a missing corpus callosum in mice was associated with their genetic background. A high incidence of a shortened corpus callosum appeared to be inbred into 129 strain mice (Wahlsten *et al.*, 2001, Wahlsten *et al.*, 2003). A sub-strain of this background was used in the current study. As

### Chapter 3 - DTI of the brain in mice deficient in SERT.

shortened callosal length was only detected in SERT-KO mice in the first batch of animals, the number of animals in the WT and SERT-KO groups was increased again. The final number of animals in which callosal length was measured was therefore  $n = 13$  in the WT,  $n = 12$  in SERT-KO, and  $n = 4$  in the SERT-HT group. Note that these additional animals were only used to examine the corpus callosal length, as these brains were processed differently than the previous batch (see page 102 for details). Amongst these, 1 animal in the WT group displayed a shortened corpus callosum, while  $n = 3$  were observed in the SERT-KO mice, and none in the group that was heterozygous for the SERT gene deletion (Fig. 3-7).

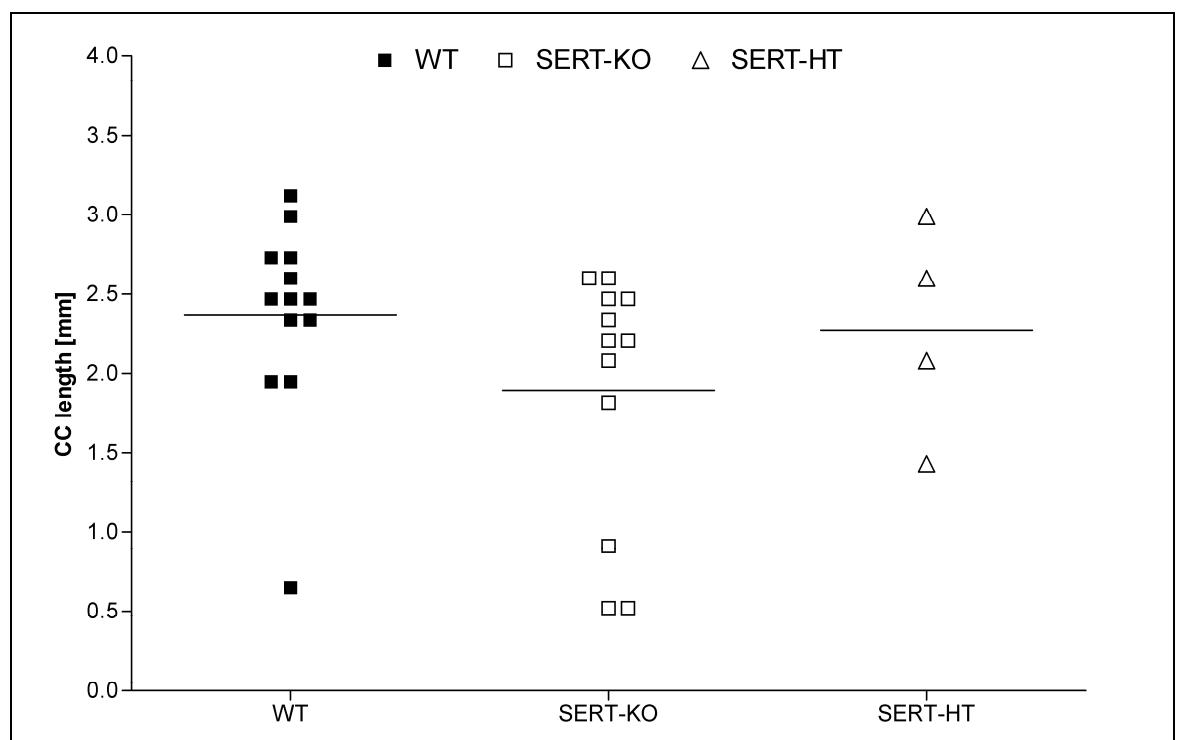


**Fig. 3-7. The anterioposterior extent of the corpus callosum is abnormally short (< 1 mm) in 1 WT, and 3 SERT-KO mice as measured on individual, unregistered FA images.**

Data are presented in mm. For WT  $n = 13$ , SERT-KO  $n = 12$ , and SERT-HT  $n = 4$ .

In the WT group 1 mouse, and in the SERT-KO group 3 mice with shortened corpus callosum were present. In SERT-HT group, no mice with shortened corpus callosum were present. One-way ANOVA Kruskal-Wallis ( $p < 0.05$ ). No significant differences were detected.

#### Measuring anterioposterior length of the brain.

The anterioposterior length of the brain, excluding the olfactory bulbs, was defined on individual  $S_0$  images. All slices between the most anterior slice where the cortex appeared, and the last, where the cerebellum was still visible, were included (including the 2 outer most slices). The voxel dimension in the z-direction (0.13 mm) was multiplied by the number of slices determined in the previous step to generate the brain length (Fig. 3-8). No significant differences were observed between groups (Fig. 3-9).

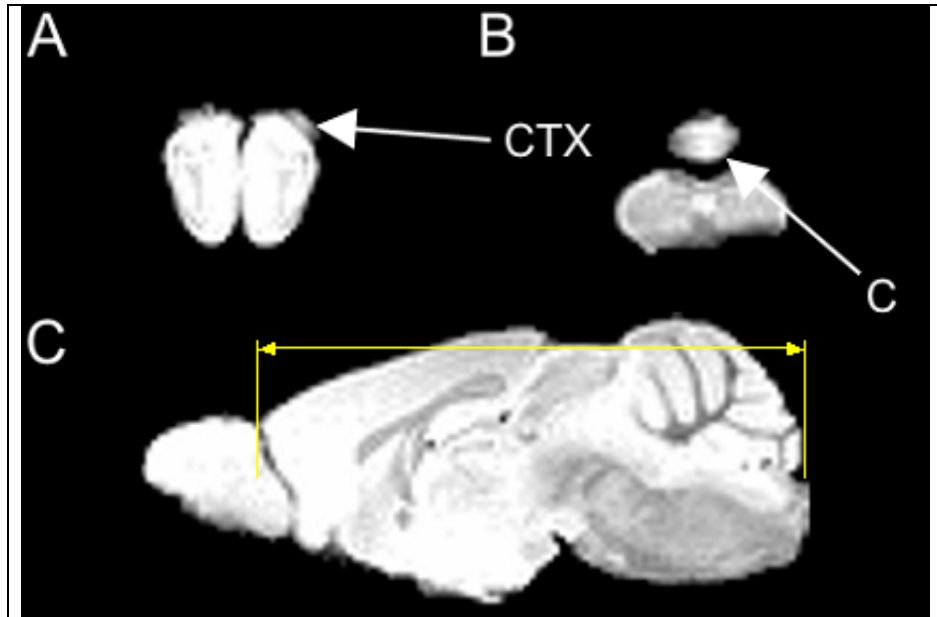


**Fig. 3-8. Measuring the brain length on individual, unregistered S0 images.**

Only slices comprising the cortex rostrally and the cerebellum caudally were included in the measurement.

A: first coronal slice, where the cortex (CTX) appears.

B: last coronal slice, where the cerebellum (C) disappears.

C: sagittal view showing the rostral to caudal extent of the brain.

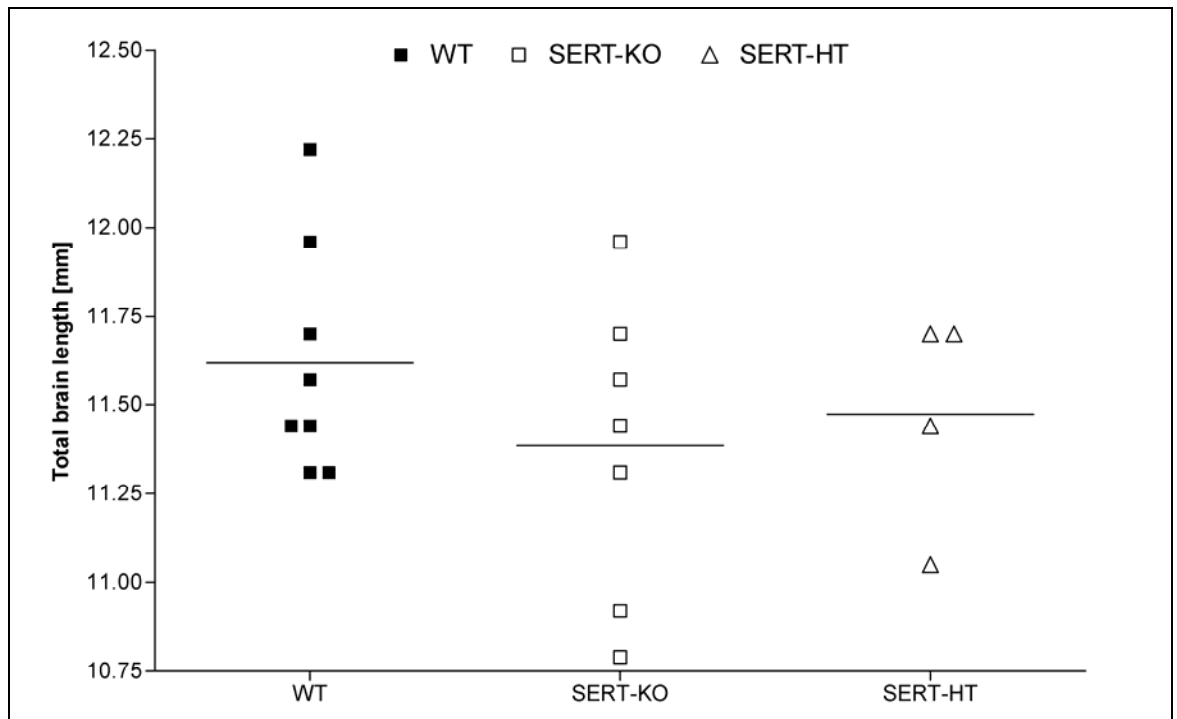


**Fig. 3-9. Brain length is not different between groups as measured on individual, unregistered S0 images.**

Units of measurements are mm. Bars represent mean. For WT n = 8, SERT-KO n = 7, and SERT-HT n = 4. One-way ANOVA Kruskal-Wallis ( $p < 0.05$ ). No significant differences were detected.

### Chapter 3 - DTI of the brain in mice deficient in SERT.

The relationship between callosal length and total brain length was examined by computing the ratio callosal length / brain length (Fig. 3-10). No significant differences were detected between WT, SERT-KO, and SERT-HT. The ratio is clustered around a ratio of 0.2, except for the 2 SERT-KO mice, which have a shortened corpus callosum. A ratio of around 0.04 and 0.08 was observed for these, respectively.

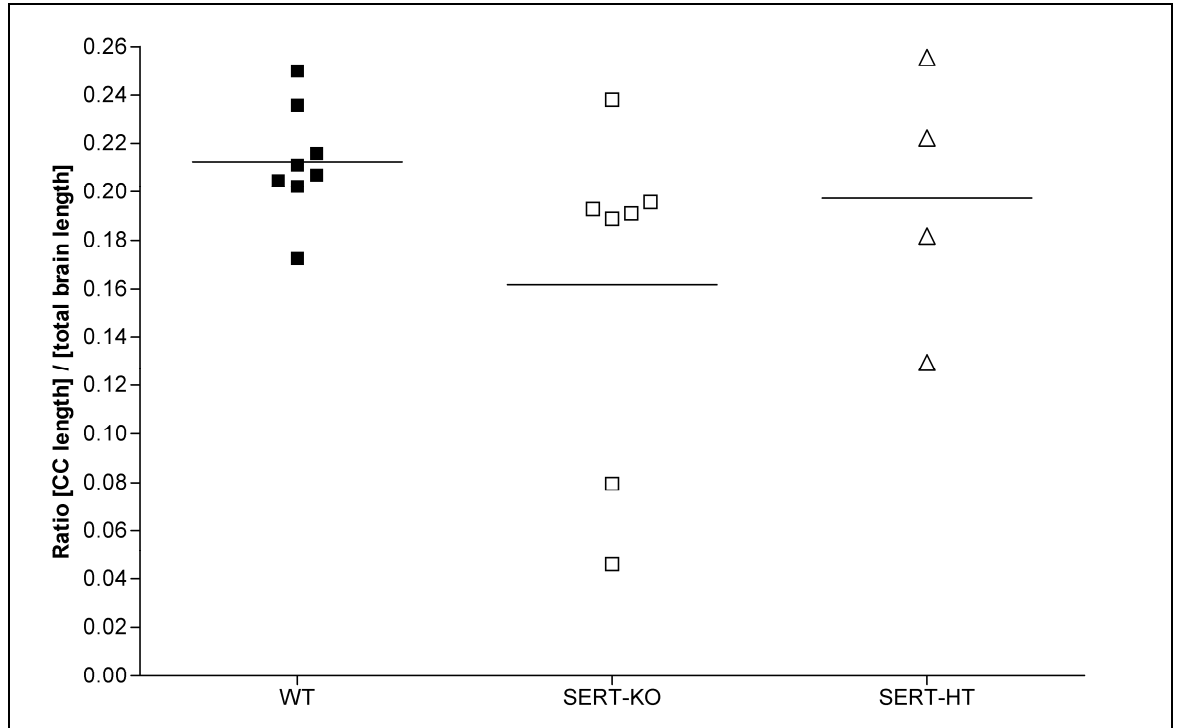


**Fig. 3-10. Ratio of corpus callosal length to brain length shows low ratios for 2 SERT-KO mice.**

Units of measurement are dimensionless for the ratio (corpus callosum / brain length). Bars represent mean. For WT n = 8, SERT-KO n = 7, and SERT-HT n = 4. One-way ANOVA Kruskal-Wallis ( $p < 0.05$ ). No significant differences were detected. The 2 animals that displayed a shortened corpus callosum in the SERT-KO group show low ratios here.

#### Subtraction map analyses (FSL).

Subsequent to the initial analyses described above, the image analysis group at Oxford University made available a software package within FSL in order to analyse DTI data. The routine, TBSS (Smith et al., 2006), automatically coregisters FA maps, and allows the other DTI parameter maps (FA,  $\lambda_1$ ,  $\lambda_2$ ,  $\lambda_3$ , MD, RD) to be brought into coregistered FA space. Group averages and subtraction maps can then be easily computed. Therefore a more thorough subtraction analysis, involving the other DTI parameter maps, was conducted and the DTI parameter maps derived from WT, SERT-KO, and SERT-HT were analysed statistically.

#### **Mean FA subtraction map analyses.**

In order to assess abnormalities in anisotropy, FA images were first coregistered, averaged and images then underwent a group-wise subtraction, i.e. WT minus SERT-KO, and WT minus SERT-HT to identify gross differences between groups (Fig. 3-11). The WT minus SERT-KO, as well as the WT minus SERT-HT subtraction map identified the corpus callosum with higher FA in WT compared to SERT-KO and SERT-HT, respectively, as shown by the red colour. Also the anterior commissure appeared to have higher anisotropy in WT than in SERT-KO and SERT-HT, respectively. On the other hand, the hippocampal commissure displayed higher FA in SERT-KO compared to WT mice as identified by the blue colour-coding.

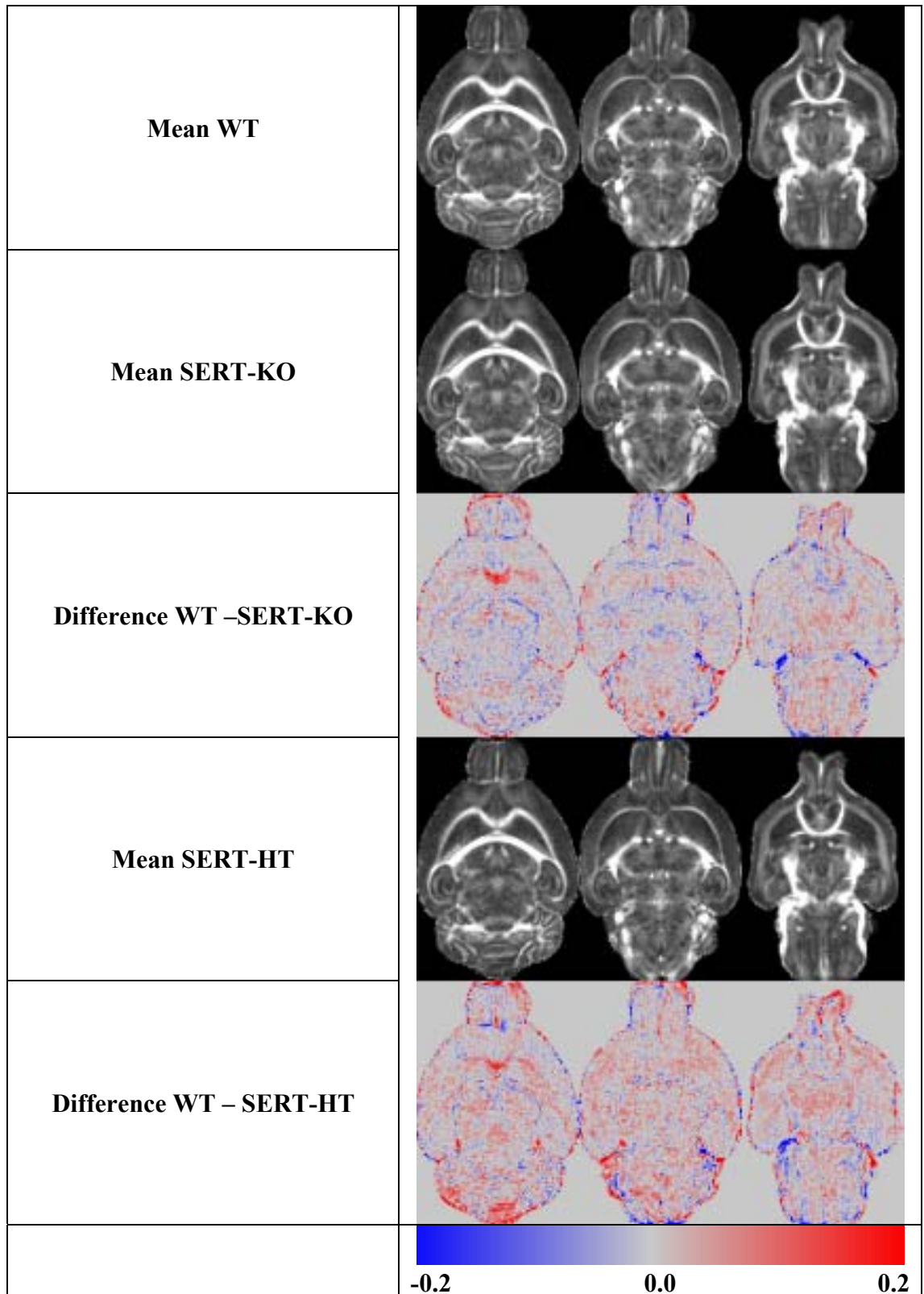


**Fig. 3-11. Representative slices of the subtraction map derived from coregistered and group-wise averaged FA images suggest no major group differences.**

Units of measurement are dimensionless for FA.

Scale bar: blue indicates where SERT-KO or SERT-HT > WT; red indicates where WT > SERT-KO or SERT-HT (n = 7 for WT, n = 7 for SERT-KO, n = 4 for SERT-HT). Anisotropy appeared to be higher in the corpus callosum, and anterior commissure in WT, when compared to SERT-KO and SERT-HT mice, respectively. The SERT-KO hippocampal commissure had higher FA in SERT-KO compared to WT animals.

#### Mean eigenvalue subtraction map analyses.

Following mean FA subtraction map analysis, the average eigenvalue maps of WT were compared to those of SERT-KO (Fig. 3-12), and SERT-HT (Fig. 3-13), respectively, in order to identify group differences in diffusivity of white matter tracts. The corpus callosum appears to have higher  $\lambda_1$  and  $\lambda_3$  diffusivities in SERT-KO compared to WT, whereas there seemed to be a trend in the anterior commissure towards higher  $\lambda_2$  and  $\lambda_3$  in SERT-KO when compared to WT mice. All eigenvalues tended to have higher values in WT compared to SERT-KO animals. However, overall the difference maps appeared to be at background level indicating comparable diffusivities in WT and SERT-KO.

This was in contrast to the eigenvalue difference maps obtained from subtracting the mean SERT-HT maps from those of WT. WT animals appeared to have widespread higher diffusivities, as indicated by the red colour, when compared to SERT-HT mice. White matter specific decreases in  $\lambda_1$  were observed in the hippocampal and anterior commissure in SERT-HT mice. Trends towards increasing  $\lambda_2$ , and  $\lambda_3$  were obvious in the corpus callosum, and trends to increase in the anterior commissure of SERT-HT mice compared to WT animals. However, overall the difference maps appeared to be at background level in white matter tracts indicating comparable diffusivities in WT and SERT-HT.

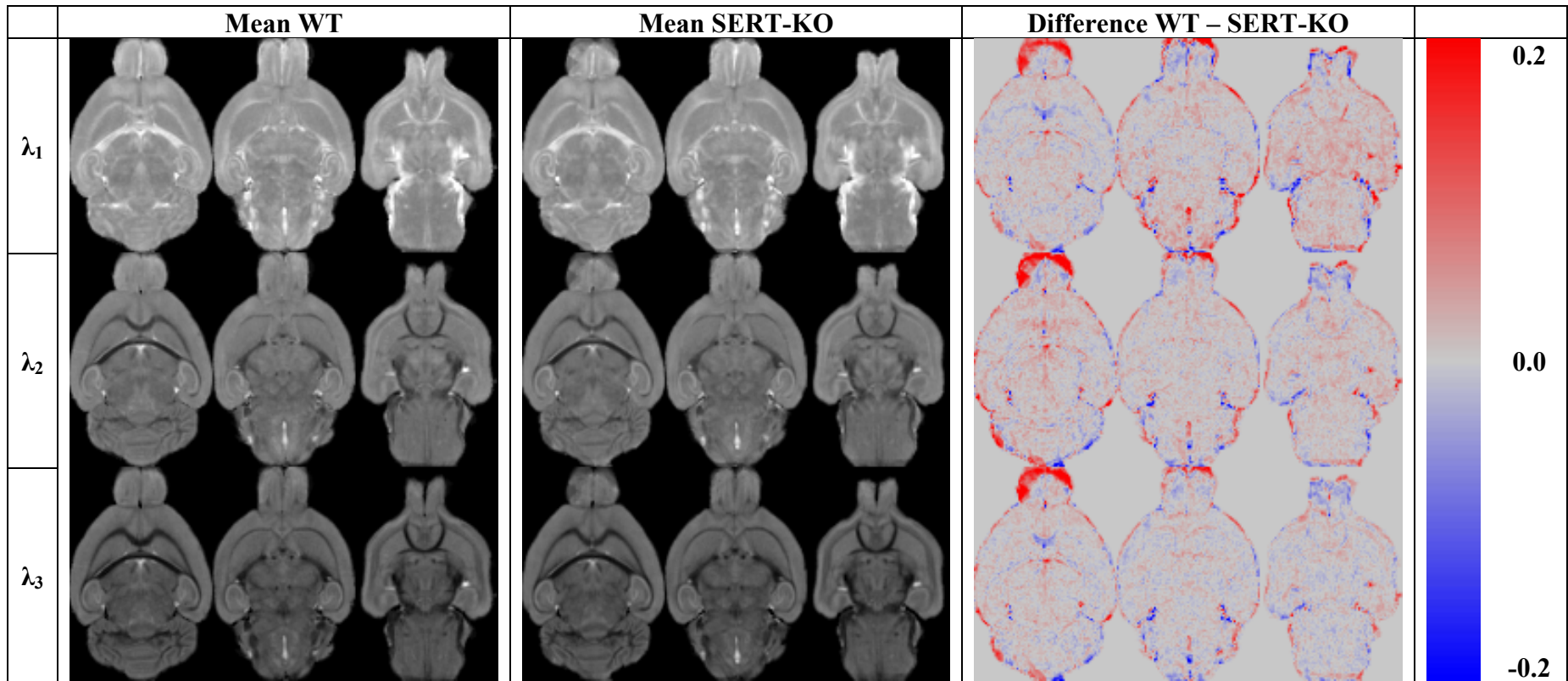


**Fig. 3-12. Representative slices of the subtraction map derived from coregistered and group-wise averaged eigenvalue images suggest no major differences between WT and SERT-KO.**

Units of measurement are  $\mu\text{m}^2/\text{ms}$  for diffusion measures ( $\lambda_1$ ,  $\lambda_2$ ,  $\lambda_3$ ).

Scale bar: blue indicates where SERT-KO > WT; red indicates where WT > SERT-KO (n = 7 for WT, n = 7 for SERT-KO).

WT showed widespread higher water diffusion properties compared to SERT-KO mice in all three eigenvalues. White matter specific reductions in  $\lambda_1$  in SERT-KO compared to WT mice were observed in the anterior commissure, whereas an increase in  $\lambda_1$  was detected in the corpus callosum. In contrast, increased  $\lambda_2$  and  $\lambda_3$  diffusivities in SERT-KO compared to WT were detected in the anterior commissure. Higher perpendicular diffusivity as measured with  $\lambda_3$  was seen in the corpus callosum in SERT-KO mice relative to their WT counterparts. However, overall diffusivities appeared to be comparable between WT and SERT-KO mice.

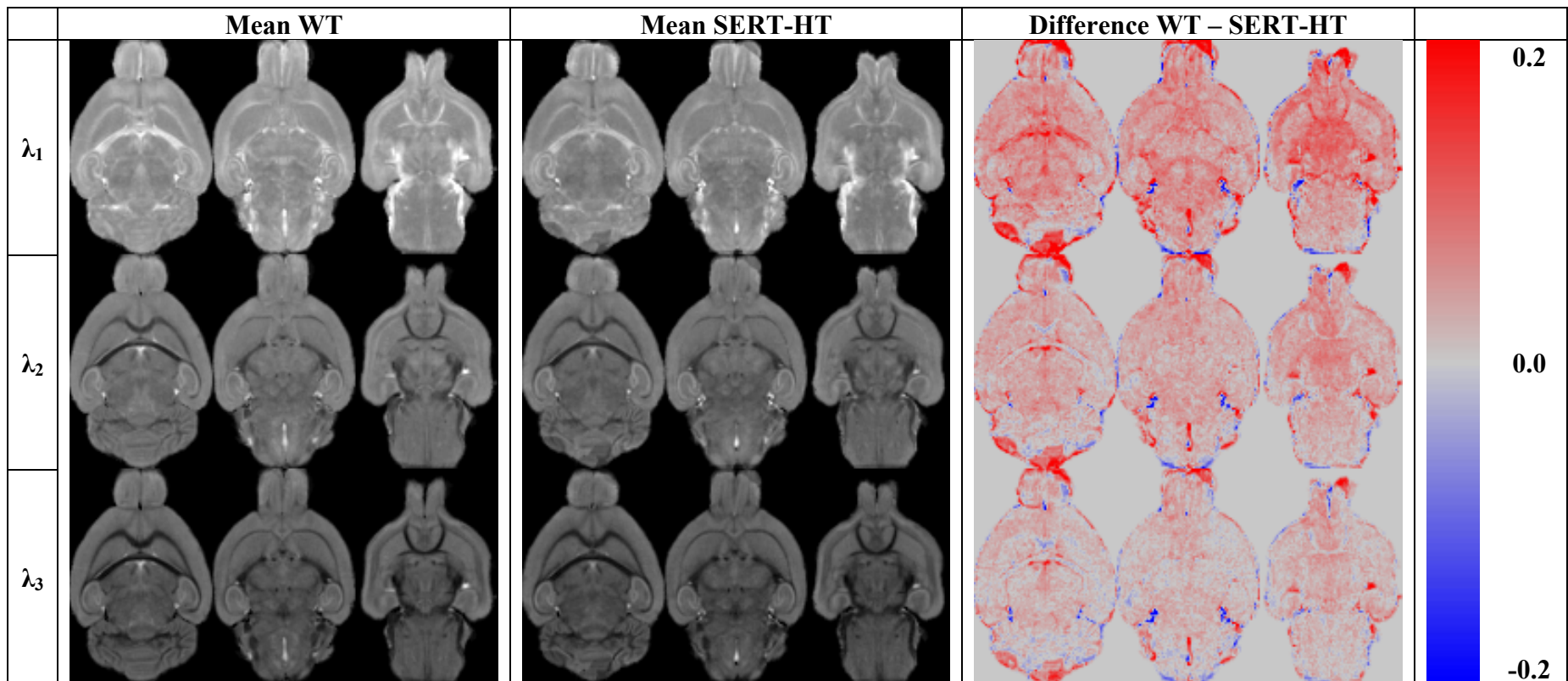


**Fig. 3-13. Representative slices of the subtraction map derived from coregistered and group-wise averaged eigenvalue images suggest no major differences between WT and SERT-HT.**

Units of measurement are  $\mu\text{m}^2/\text{ms}$  for diffusion measures ( $\lambda_1$ ,  $\lambda_2$ ,  $\lambda_3$ ).

Scale bar: blue indicates where SERT-HT > WT; red indicates where WT > SERT-HT (n = 7 for WT, n = 4 for SERT-HT).

WT showed widespread higher water diffusion properties compared to SERT-HT mice in all three eigenvalues. White matter specific reductions in  $\lambda_1$  in SERT-HT compared to WT mice were observed in the hippocampal and anterior commissures. In contrast, equal to increased  $\lambda_2$  and  $\lambda_3$  diffusivities in SERT-HT compared to WT were detected in the corpus callosum, and anterior commissure. However, overall diffusivities in white matter tracts appeared to be comparable between WT and SERT-HT mice.

#### **Mean MD and RD subtraction map analyses.**

The MD is the average of all three eigenvalues and summarises diffusion properties within the structure under examination. In general the difference map between WT and SERT-KO MD showed only background signal (Fig. 3-14). Only in the corpus callosum there was a trend towards more positive MD in the SERT-KO compared to the WT animals. The same pattern was observed in the WT minus SERT-HT subtraction map, suggesting only a trend towards more positive diffusion properties in the corpus callosum of SERT-HT animals. The overall grey matter MD however is lower in SERT-HT mice implying a widespread decrease.

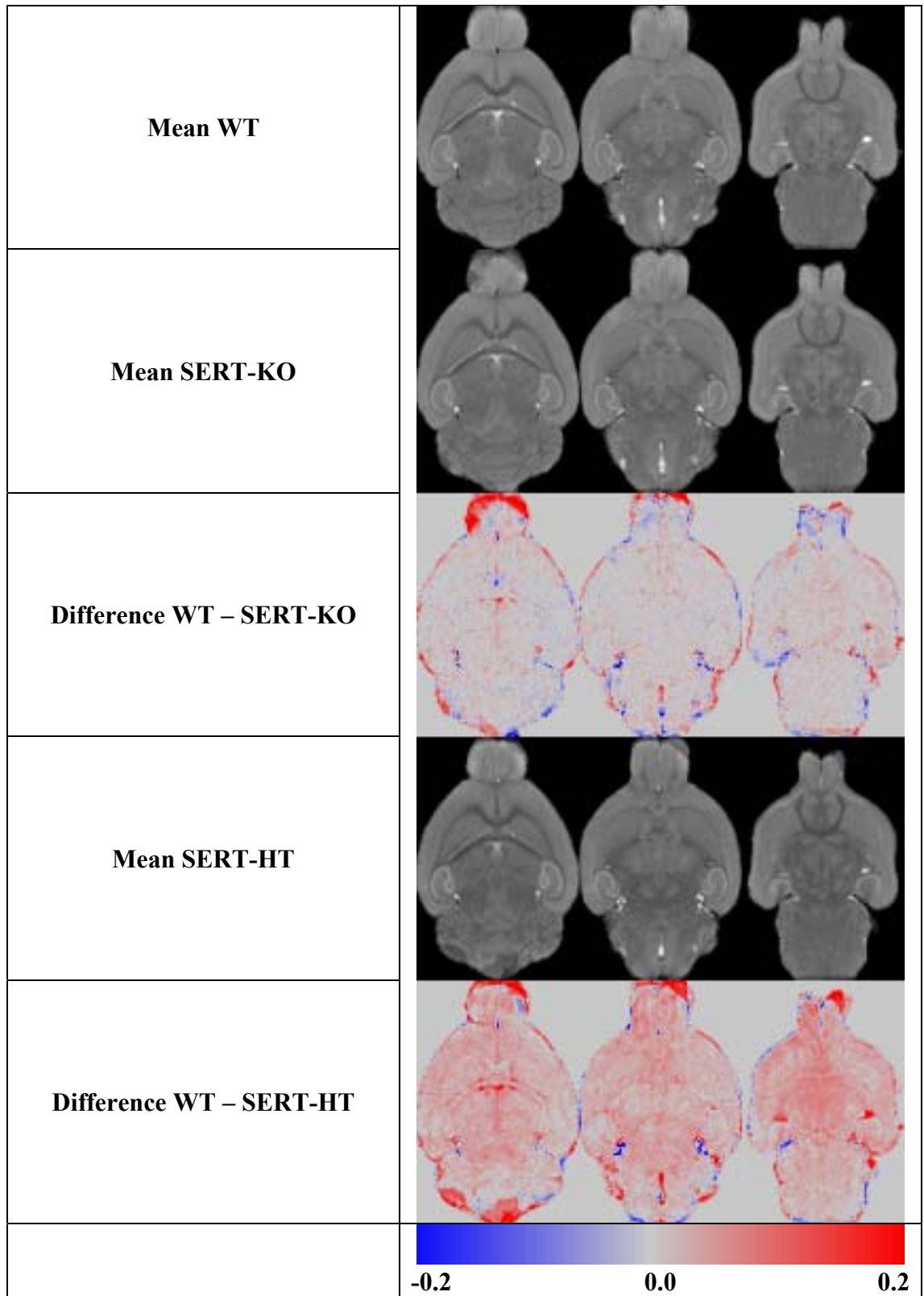


**Fig. 3-14. Representative slices of the subtraction map derived from coregistered and group-wise averaged MD images suggest no major differences.**

Units of measurement are  $\mu\text{m}^2/\text{ms}$ .

Scale bar: blue indicates where SERT-KO or SERT-HT > WT; red indicates where WT > SERT-KO or SERT-HT (n = 7 for WT, n = 7 for SERT-KO, n = 4 for SERT-HT). Comparing WT minus SERT-KO to WT minus SERT-HT subtraction maps, widespread reductions in MD could be observed in SERT-HT mice. Increases in MD were only observed in the corpus callosum of both, SERT-KO and SERT-HT, respectively, when compared visually to their WT counterparts.

### **Chapter 3 - DTI of the brain in mice deficient in SERT.**

The RD is the average of the second and third eigenvalue, and therefore could give valuable information about the diffusion that is directed perpendicular to the white matter tract. Differences between mean WT and mean SERT-KO RD were observed in the corpus callosum with increased RD in SERT-KO mice (Fig. 3-15). In addition SERT-KO mice display trends towards higher RD in the anterior commissure. The WT minus SERT-HT subtraction map also indicated that the corpus callosum had higher RD in SERT-HT mice. Widespread decreases in RD were observed in SERT-HT mice, i.e. in the cortex and thalamus, with specific white matter RD values being equal with trends to higher RD in the anterior commissure.

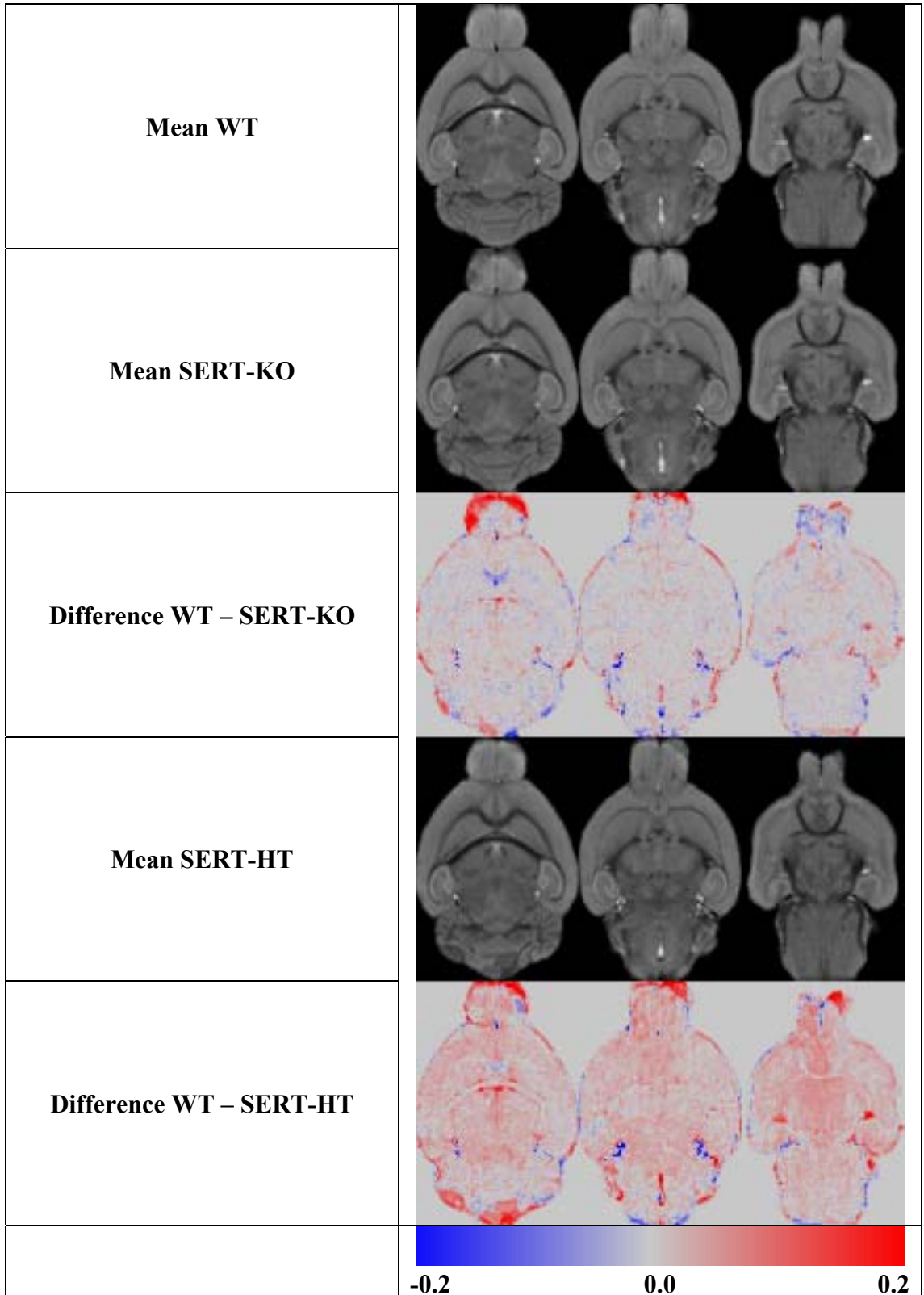


**Fig. 3-15. Representative slices of the subtraction map derived from coregistered and group-wise averaged RD images suggest no major differences.**

Units of measurement are  $\mu\text{m}^2/\text{ms}$ .

Scale bar: blue indicates where SERT-KO or SERT-HT > WT; red indicates where WT > SERT-KO or SERT-HT (n = 7 for WT, n = 7 for SERT-KO, n = 4 for SERT-HT). Comparing WT minus SERT-KO to WT minus SERT-HT subtraction maps, clear, widespread reduced RD could be observed in SERT-HT mice. The corpus callosum, and the anterior commissure showed increases in RD when comparing SERT-KO and SERT-HT, respectively, to their WT counterparts.

**ROI analysis of DTI parameter maps (FA,  $\lambda_1$ , MD, and RD) (AIR).**

The corpus callosum was defined on unregistered S0 image slices, where an interhemispheric connection was present, and ROIs included the cingulum for simplicity (Fig. 3-16). The callosal masks were superimposed onto the DTI parameter maps and the respective mean intensities for  $\lambda_1 - \lambda_3$ , as well as for FA were calculated.

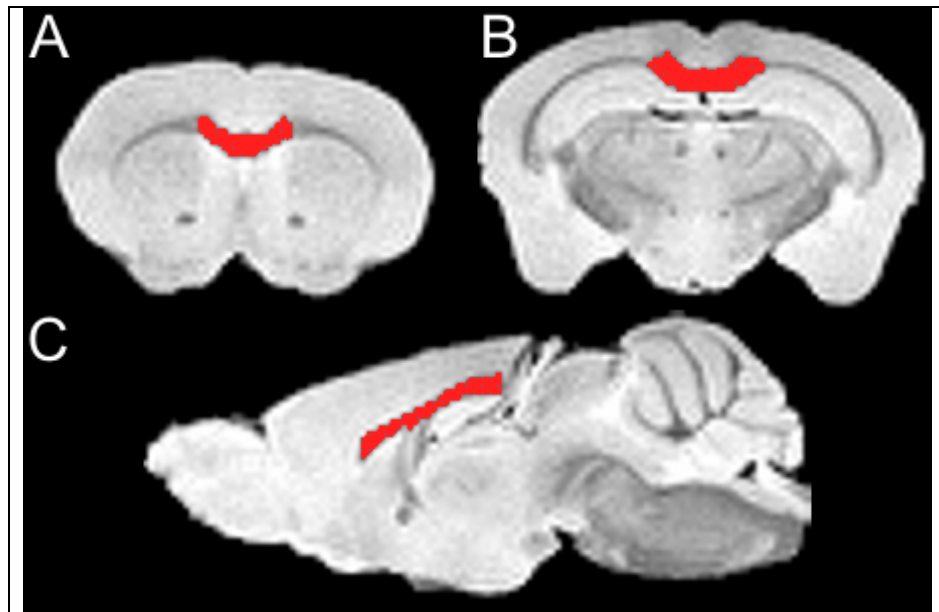


**Fig. 3-16. Segmentation of corpus callosum on unregistered S0 images.**

Only slices comprising interhemispheric connection of the corpus callosum were included in the measurement. The corpus callosum was defined on coronal slices until the lateral boundaries of the anterior cingulate cortex, i.e. including the cingulum. Derived ROIs were then superimposed onto DTI parameter maps (FA,  $\lambda_1$ ,  $\lambda_2$ ,  $\lambda_3$ ) to extract respective values.

A: first coronal slice, where the corpus callosum starts to connect the two hemispheres.

B: last coronal slice, where the corpus callosum still interconnects both hemispheres.

C: sagittal view on the anteroposterior extent of the corpus callosum.

The hippocampal and the anterior commissures were defined on coregistered, transaxial S0 images, and the internal capsule was defined on coronal slices using MRICro (Fig. 3-17). The derived masks were superimposed onto the DTI parameter maps and the respective mean intensities for  $\lambda_1 - \lambda_3$  as well as for the FA were extracted. Please note that the segmentation, data generation and collection for the hippocampal and anterior commissures were done by Sheonagh Law as part of her BMedSci project.

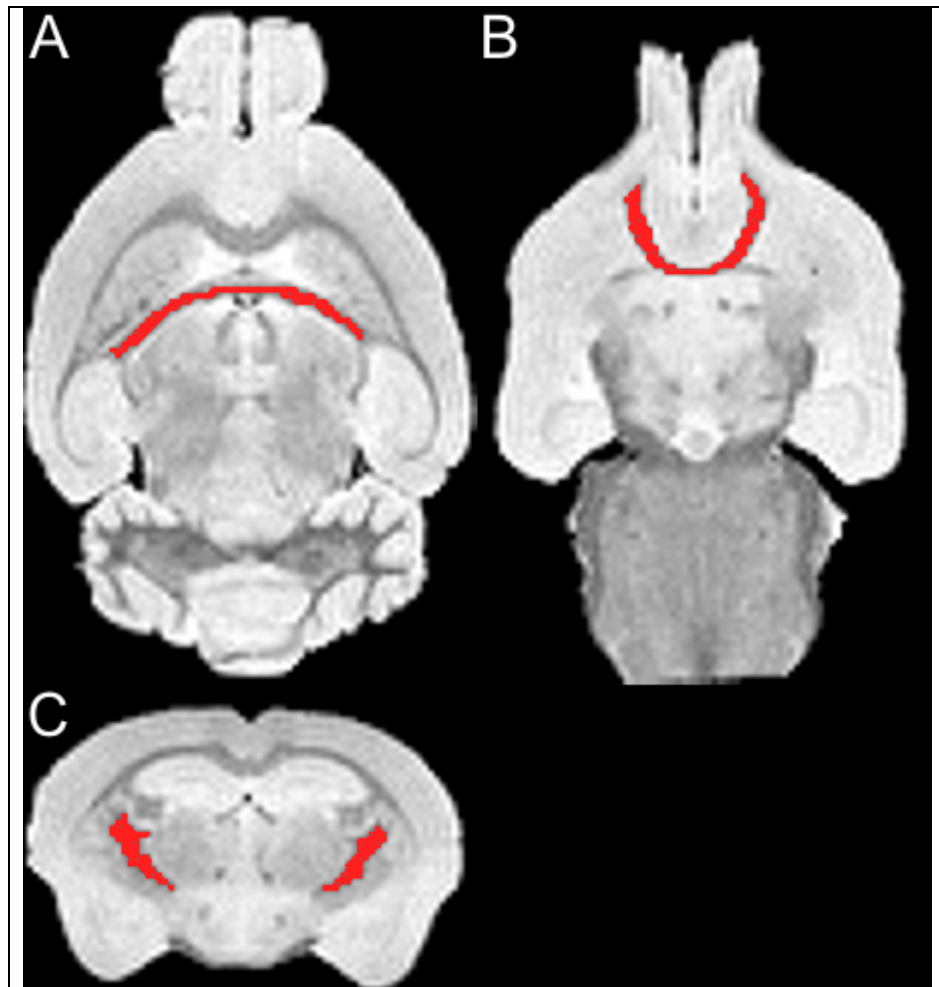
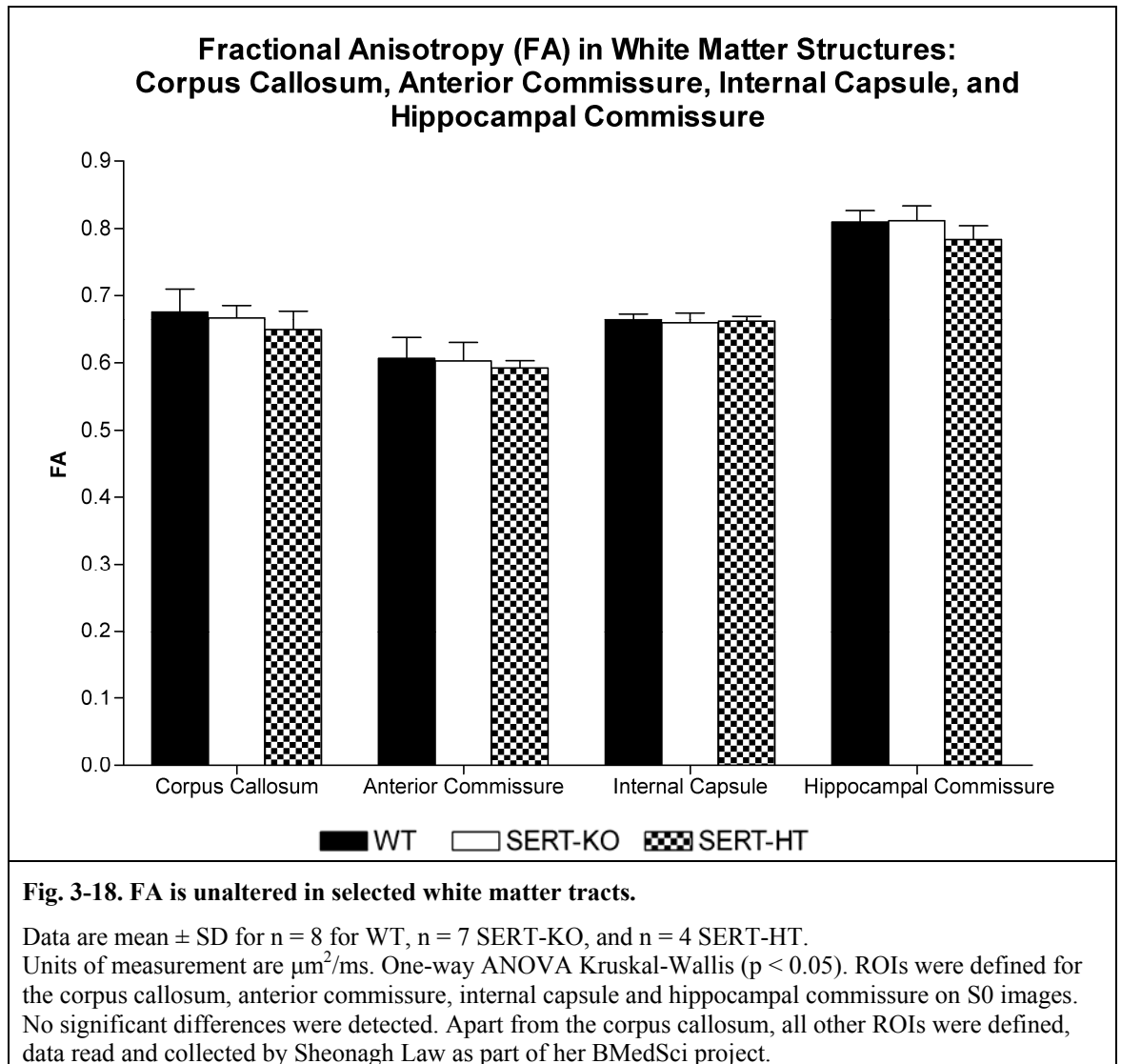


**Fig. 3-17. Segmentation of hippocampal and anterior commissures, and internal capsule on coregistered S0 images.**

The ROIs for the hippocampal (A) and anterior commissures (B) were derived from selected consecutive transaxial slices, for the internal capsule (C) from coronal slices of individual, coregistered S0 images. Subsequently those derived ROIs were superimposed onto DTI parameter maps (FA,  $\lambda_1$ ,  $\lambda_2$ ,  $\lambda_3$ ) to extract respective values. The segmentation and data generation was done by Sheonagh Law as part of her BMedSci project.

FA values between tracts appeared to be comparable, apart from the hippocampal commissure, which showed substantially higher anisotropy compared to the anterior commissure, corpus callosum and internal capsule (Fig. 3-18). No significant differences between WT, SERT-KO and SERT-HT were observed for any white matter structures.



As a next step, the first eigenvalues were compared between WT, SERT-KO, and SERT-HT in the corpus callosum, internal capsule, and anterior and hippocampal commissures, respectively (Fig. 3-19). Within the hippocampal commissure the highest axonal diffusivity ( $\lambda_1$ ) was observed while the values for the anterior commissure and internal capsule appeared to be comparable as determined visually. The corpus callosum displayed the lowest  $\lambda_1$ . No significant differences between genotypes could be detected in any of the white matter structures investigated. However a non-significant reduction in SERT-HT  $\lambda_1$  compared to WT and SERT-KO was observed in all structures, i.e. in the corpus callosum, internal capsule, and anterior and hippocampal commissures.

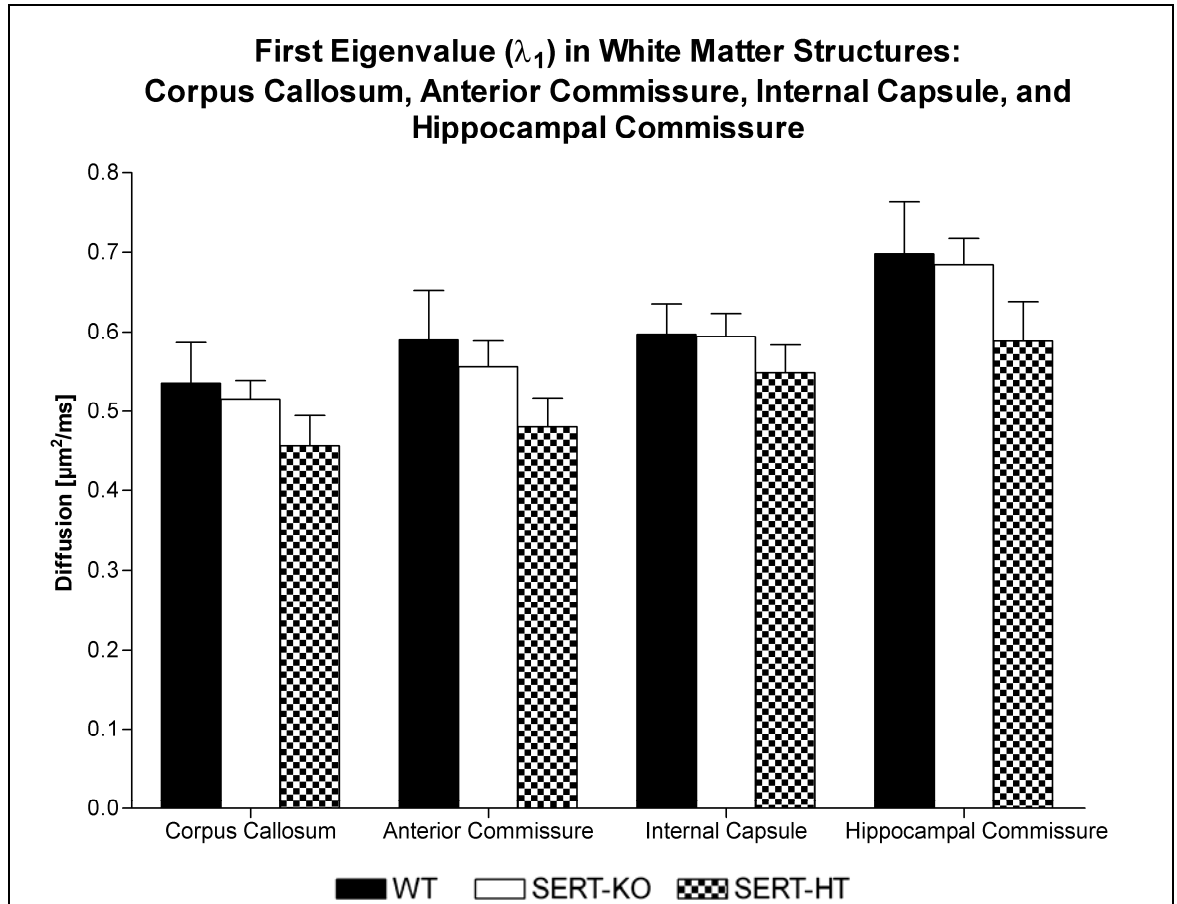


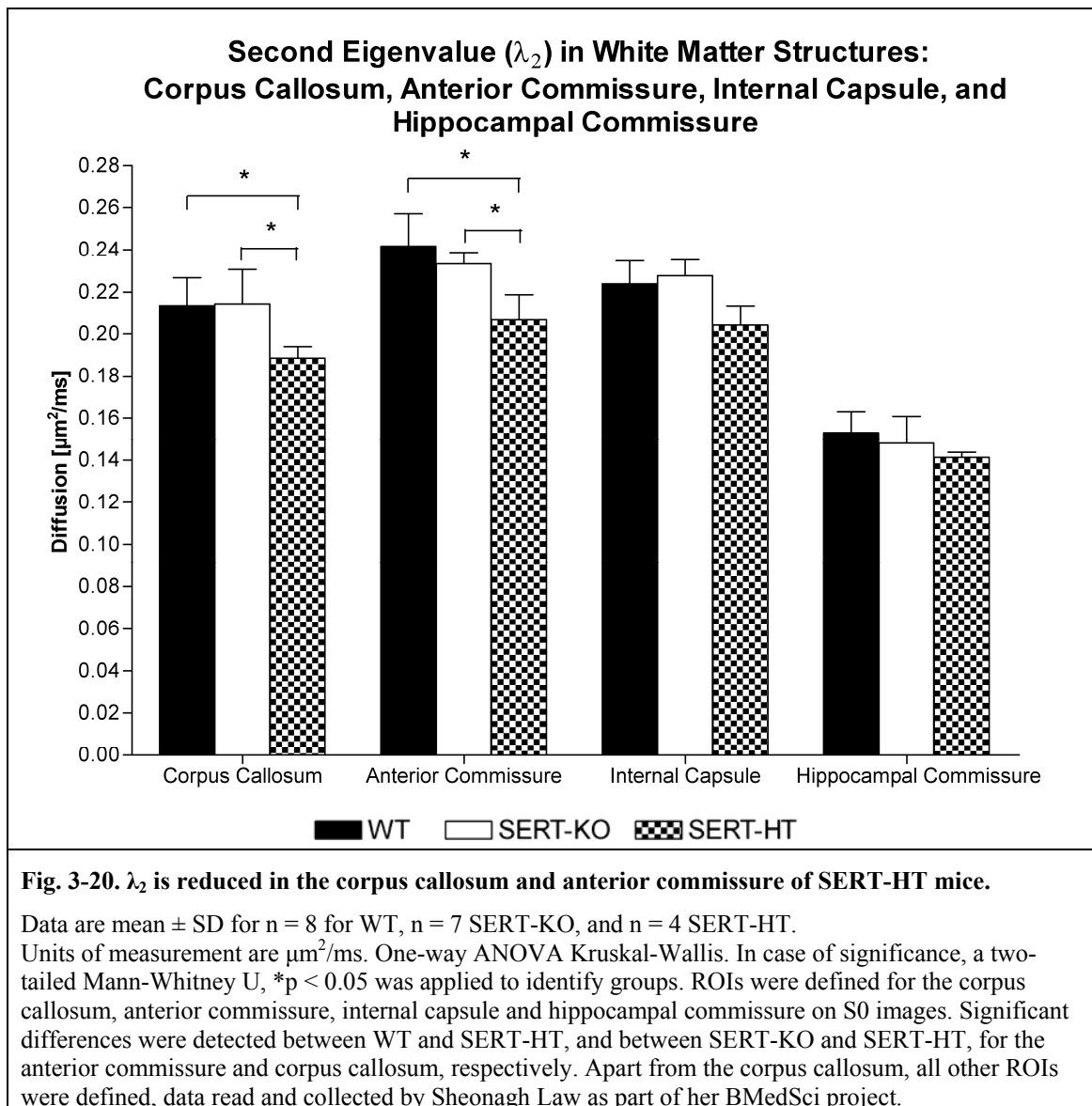
**Fig. 3-19.  $\lambda_1$  is unaltered in selected white matter tracts.**

Data are mean  $\pm$  SD for n = 8 for WT, n = 7 SERT-KO, and n = 4 SERT-HT.

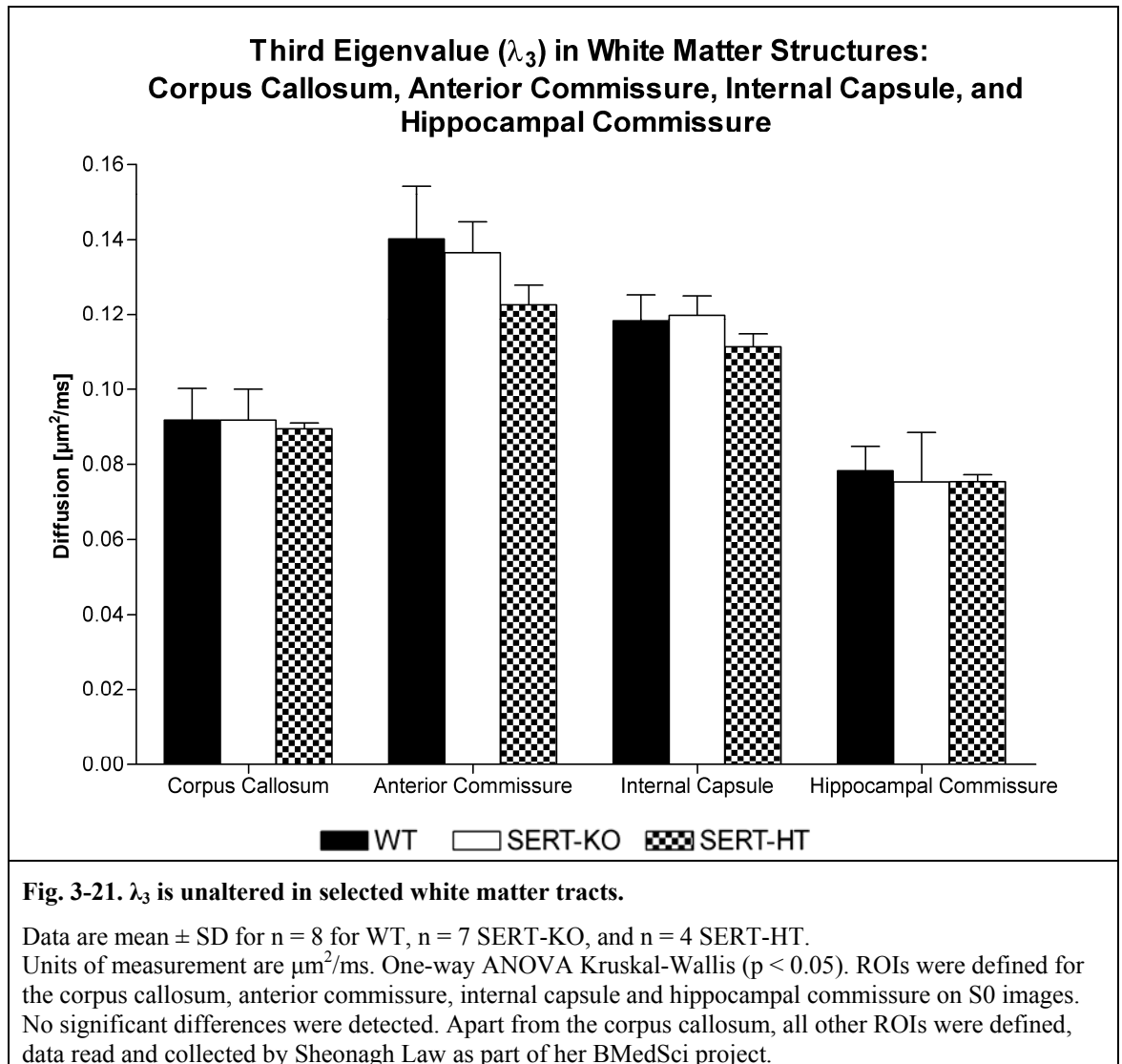
Units of measurement are  $\mu\text{m}^2/\text{ms}$ . One-way ANOVA Kruskal-Wallis ( $p < 0.05$ ). ROIs were defined for the corpus callosum, anterior commissure, internal capsule and hippocampal commissure on S0 images.

No significant differences were detected. Apart from the corpus callosum, all other ROIs were defined, data read and collected by Sheonagh Law as part of her BMedSci project.

Second eigenvalues were highest in the anterior commissure, followed by the internal capsule, and corpus callosum (Fig. 3-20). The hippocampal commissure showed lowest perpendicular diffusivity as measured by  $\lambda_2$ . Generally, the second eigenvalue is lower in any given white matter tract in SERT-HT mice compared to WT and SERT-KO. These reductions became significant in the anterior commissure and corpus callosum, in both cases, i.e. where SERT-HT mice were compared to WT or SERT-KO, respectively.



Resembling the second eigenvalue in terms of rank order in white matter tracts, the relationship of  $\lambda_3$  between tracts can be summarised as anterior commissure > internal capsule > corpus callosum > hippocampal commissure. However, this order was much more pronounced in the third compared to the second eigenvalue. Large, though non-significant reductions in  $\lambda_3$  were observed in SERT-HT compared to WT or SERT-KO, respectively, in the anterior commissure and internal capsule.



The MD is generally the value preferred by clinicians to summarise the water diffusion properties in brain tissue, and was calculated as the average of all eigenvalues. It was observed that calculating the average of the three eigenvalues could cancel out possible effects otherwise observed when comparing the eigenvalues separately, or summarised into only in  $\lambda_1$  and RD (Fig. 3-22). There was no difference in MD between the hippocampal commissure and the internal capsule. Also the anterior commissure shows similar MD values to those observed in the hippocampal commissure and internal capsule. The corpus callosum showed the lowest MD values between tracts. SERT-HT stood out again because of lower MD in all white matter tracts examined compared to WT and SERT-KO, respectively. These reductions were significant between SERT-HT and WT, or SERT-KO, respectively in the anterior commissure only.

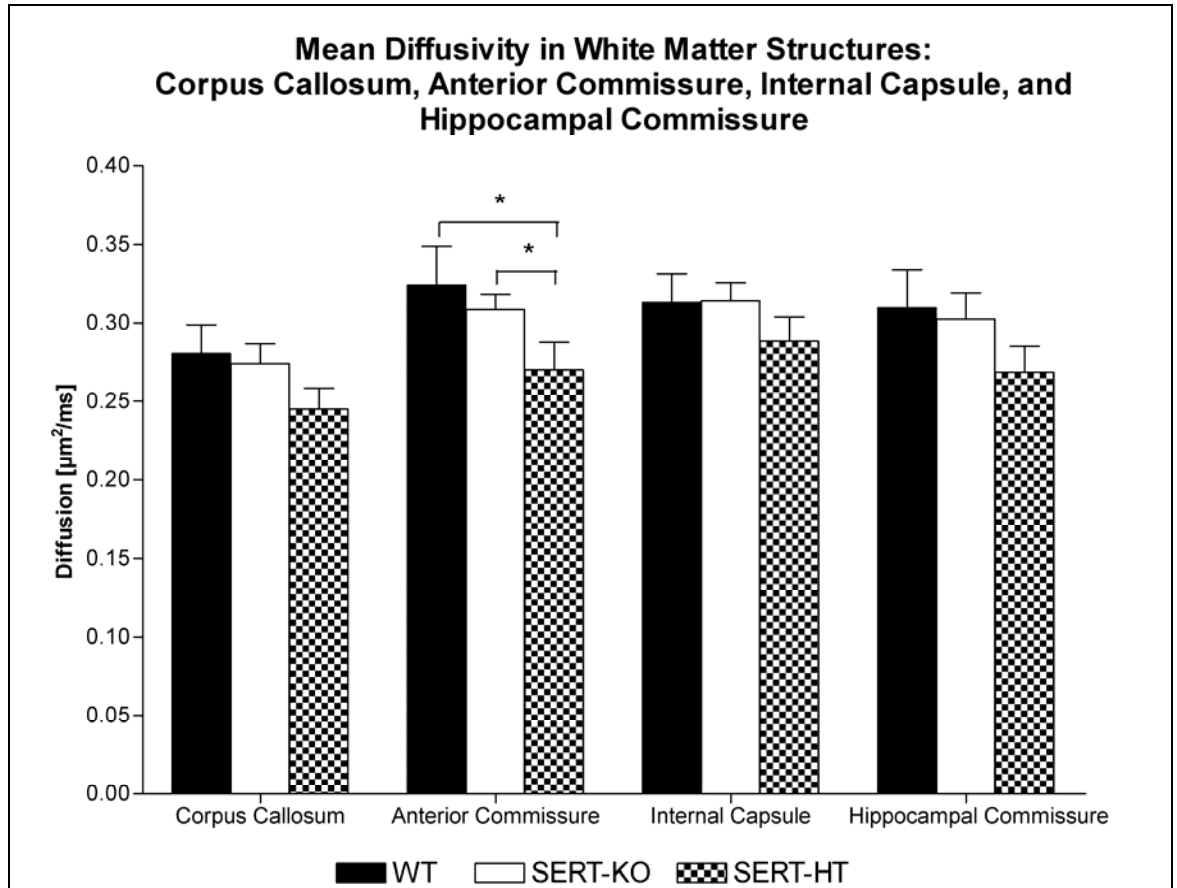


**Fig. 3-22. MD is reduced in the corpus callosum of SERT-HT mice.**

Data are mean  $\pm$  SD for n = 8 for WT, n = 7 SERT-KO, and n = 4 SERT-HT. Units of measurement are  $\mu\text{m}^2/\text{ms}$ . One-way ANOVA Kruskal-Wallis. In case of significance, a two-tailed Mann-Whitney U, \*p < 0.05 was applied to identify groups. ROIs were defined for the corpus callosum, anterior commissure, internal capsule and hippocampal commissure on S0 images. Significant differences were detected between WT and SERT-HT, and between SERT-KO and SERT-HT, for the anterior commissure. Apart from the corpus callosum, all other ROIs were defined, data read and collected by Sheonagh Law as part of her BMedSci project.

RD as defined by the mean of  $\lambda_2$  and  $\lambda_3$  showed a more pronounced difference between tracts as compared to MD, indicating a loss of information in the latter due to averaging. The order of decreasing RD can be summarised by the relationship anterior commissure > internal capsule > corpus callosum > hippocampal commissure. Significantly reduced RD values were detected in the anterior commissure and corpus callosum, respectively, of SERT-HT mice when compared to WT, or SERT-KO animals, respectively.

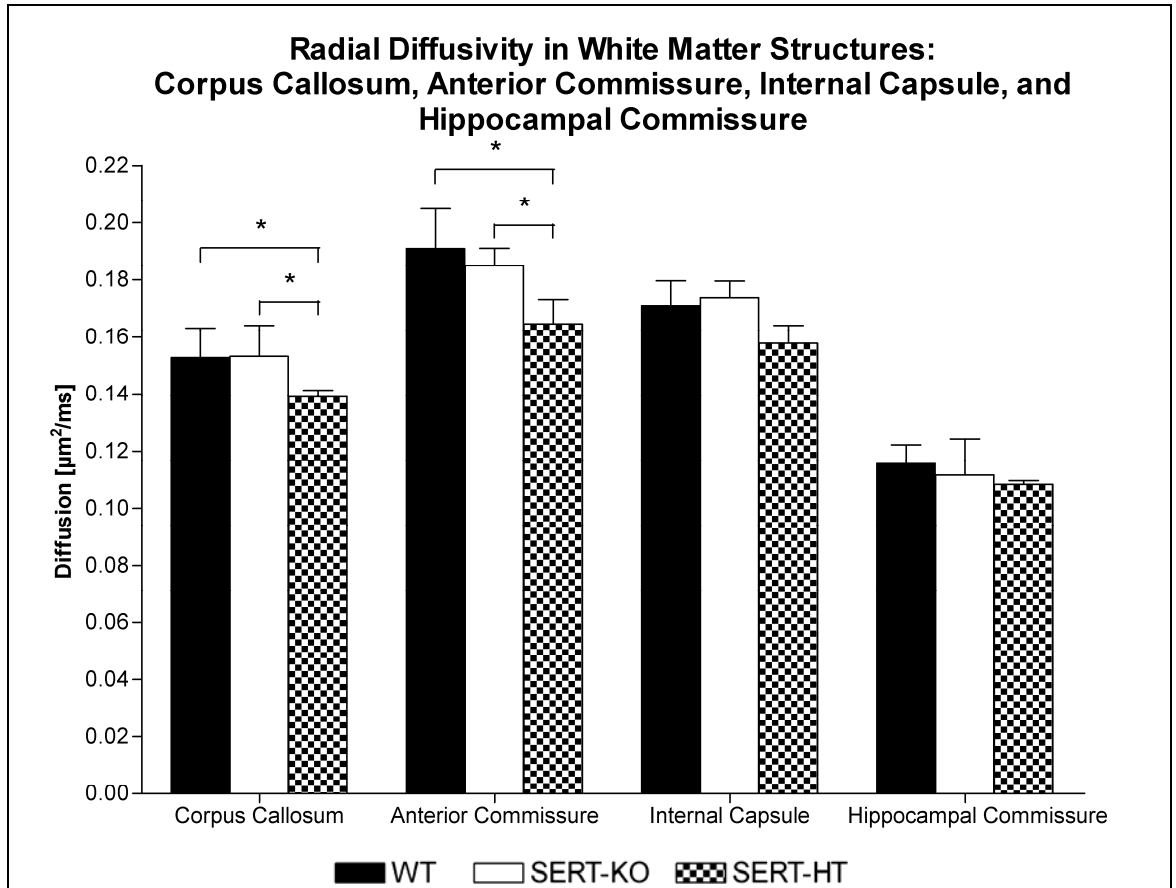


**Fig. 3-23. RD is reduced in the corpus callosum and anterior commissure of SERT-HT mice.**

Data are mean  $\pm$  SD for n = 8 for WT, n = 7 SERT-KO, and n = 4 SERT-HT. Units of measurement are  $\mu\text{m}^2/\text{ms}$ . One-way ANOVA Kruskal-Wallis. In case of significance, a two-tailed Mann-Whitney U, \*p < 0.05 was applied to identify groups. ROIs were defined for the corpus callosum, anterior commissure, internal capsule and hippocampal commissure on S0 images. Significant differences were detected between WT and SERT-HT, and between SERT-KO and SERT-HT, for the anterior commissure and corpus callosum, respectively. Apart from the corpus callosum, all other ROIs were defined, data read and collected by Sheonagh Law as part of her BMedSci project.

### Statistical analyses of DTI parameter maps (FSL).

#### WT versus SERT-KO.

TBSS was employed in order to obtain a general overview of differences of WT versus SERT-KO, and WT versus SERT-HT, which might reveal abnormalities in tracts other than those manually delineated (see above). Comparisons between WT and SERT-KO for all DTI parameters showed no significant differences (Fig. 3-24 - Fig. 3-29).

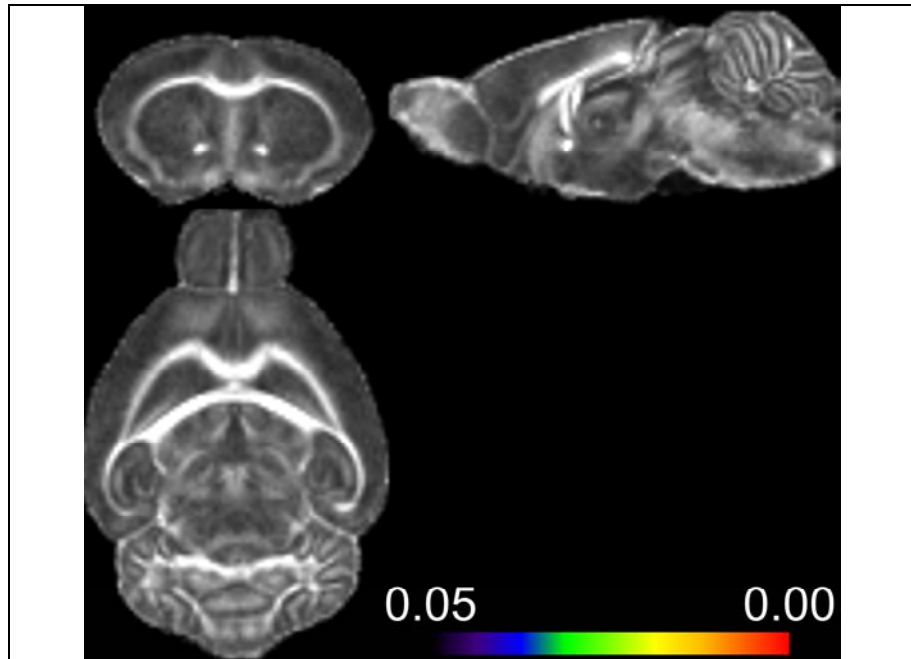


**Fig. 3-24. TBSS statistical analysis shows no significant differences in FA (WT vs. SERT-KO).**

TBSS-derived significant clusters ( $n = 7$  for WT, and  $n = 7$  for SERT-KO) were overlaid onto average WT FA map. Clusters were formed as follows: t-values were calculated by comparing WT to SERT-KO, and were then thresholded at 1. No significant differences were detected between WT and SERT-KO FA. Colour bar represents p-values ranging from 0.05 to 0.00.

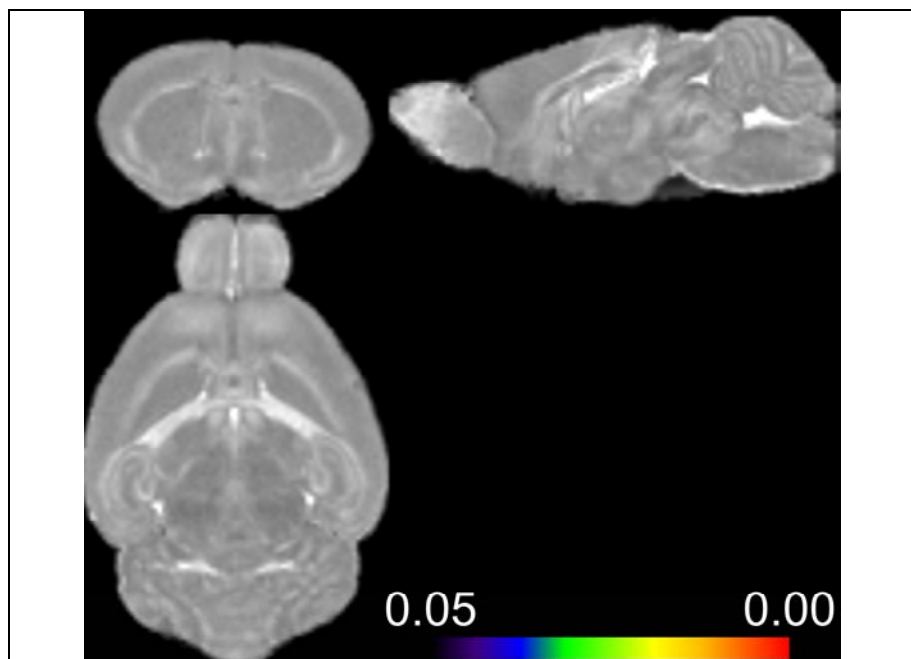


**Fig. 3-25. TBSS statistical analysis shows no significant differences in  $\lambda_1$  (WT vs. SERT-KO).**

TBSS-derived significant clusters ( $n = 7$  for WT, and  $n = 7$  for SERT-KO) were overlaid onto average WT  $\lambda_1$  map. Clusters were formed as follows: t-values were calculated by comparing WT to SERT-KO, and were then thresholded at 1. No significant differences were detected between WT and SERT-KO  $\lambda_1$ . Colour bar represents p-values ranging from 0.05 to 0.00.

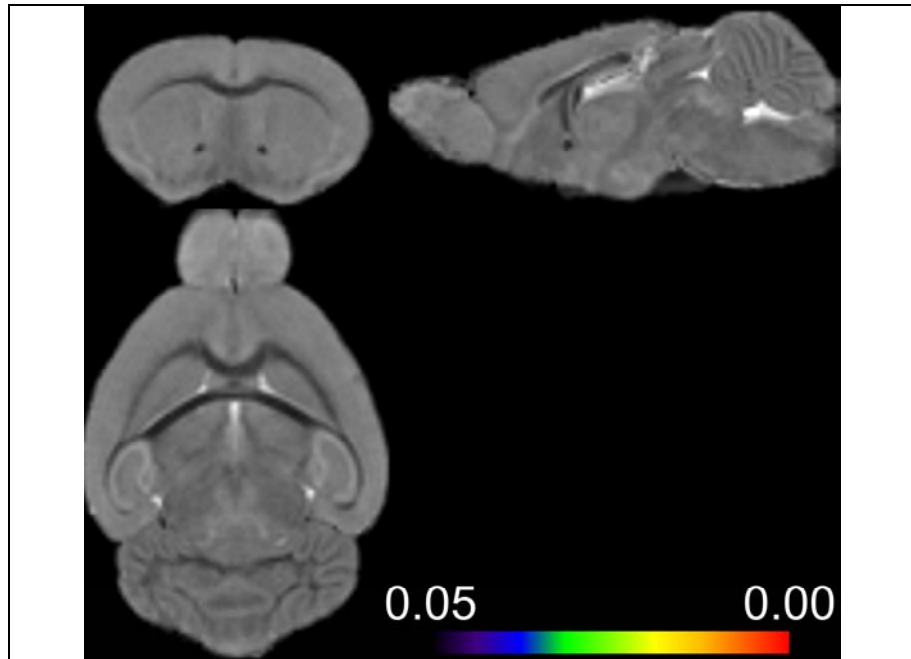


**Fig. 3-26. TBSS statistical analysis shows no significant differences in  $\lambda_2$  (WT vs. SERT-KO).**

TBSS-derived significant clusters ( $n = 7$  for WT, and  $n = 7$  for SERT-KO) were overlaid onto average WT  $\lambda_2$  map. Clusters were formed as follows: t-values were calculated by comparing WT to SERT-KO, and were then thresholded at 1. No significant differences were detected between WT and SERT-KO  $\lambda_2$ . Colour bar represents p-values ranging from 0.05 to 0.00.

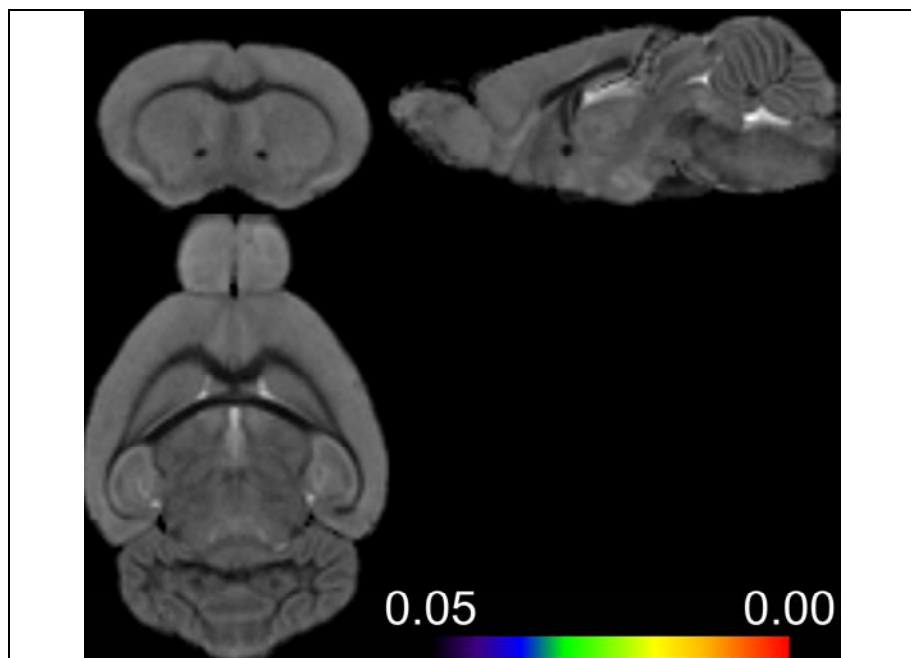


**Fig. 3-27. TBSS statistical analysis shows no significant differences in  $\lambda_3$  (WT vs. SERT-KO).**

TBSS-derived significant clusters ( $n = 7$  for WT, and  $n = 7$  for SERT-KO) were overlaid onto average WT  $\lambda_3$  map. Clusters were formed as follows: t-values were calculated by comparing WT to SERT-KO, and were then thresholded at 1. No significant differences were detected between WT and SERT-KO  $\lambda_3$ . Colour bar represents p-values ranging from 0.05 to 0.00.

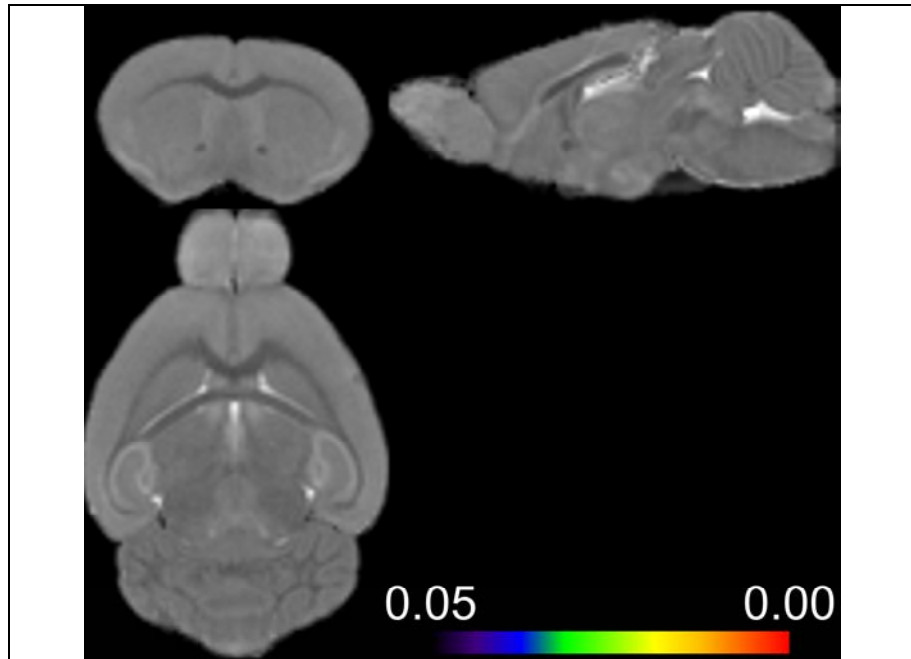


**Fig. 3-28. TBSS statistical analysis shows no significant differences in MD (WT vs. SERT-KO).**

TBSS-derived significant clusters (n = 7 for WT, and n = 7 for SERT-KO) were overlaid onto average WT MD map. Clusters were formed as follows: t-values were calculated by comparing WT to SERT-KO, and were then thresholded at 1. No significant differences were detected between WT and SERT-KO MD. Colour bar represents p-values ranging from 0.05 to 0.00.

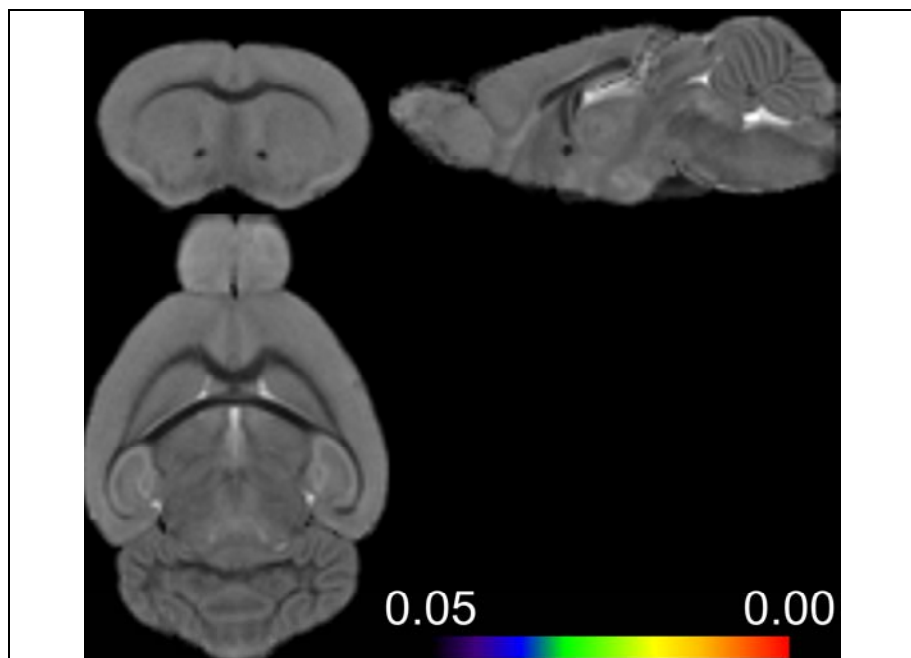


**Fig. 3-29. TBSS statistical analysis shows no significant differences in RD (WT vs. SERT-KO).**

TBSS-derived significant clusters (n = 7 for WT, and n = 7 for SERT-KO) were overlaid onto average WT RD map. Clusters were formed as follows: t-values were calculated by comparing WT to SERT-KO, and were then thresholded at 1. No significant differences were detected between WT and SERT-KO RD. Colour bar represents p-values ranging from 0.05 to 0.00.

**WT versus SERT-HT.**

No significance was reached for FA,  $\lambda_3$ , and RD when comparing WT and SERT-HT using the TBSS software package (Fig. 3-30, Fig. 3-33, Fig. 3-35, respectively). However SERT-HT mice significantly differed from WT animals in  $\lambda_1$ ,  $\lambda_2$ , and MD (Fig. 3-31, Fig. 3-32, and Fig. 3-34, respectively). Significance was reached in white matter tracts such as the corpus callosum, external capsule, and hippocampal commissure in these measures. In addition to these white matter structures, significance was also reached in grey matter regions such as at the lateral boundary of the anterior cingulate cortex, but also in the region of the dorsal raphe nucleus when comparing  $\lambda_1$ ,  $\lambda_2$ , and MD between WT and SERT-HT mice.

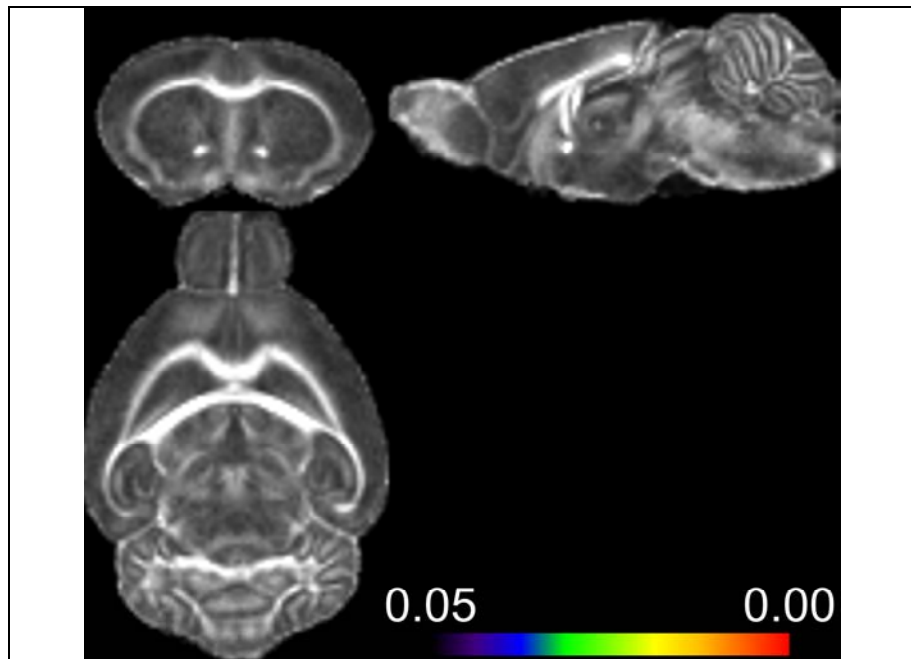


**Fig. 3-30. TBSS statistical analysis shows no significant differences in FA (WT vs. SERT-HT).**

TBSS-derived significant clusters ( $n = 7$  for WT, and  $n = 4$  for SERT-HT) were overlaid onto average WT FA map. Clusters were formed as follows: t-values were calculated by comparing WT to SERT-HT, and were then thresholded at 1. No significant differences were detected between WT and SERT-HT FA. Colour bar represents p-values ranging from 0.05 to 0.00.

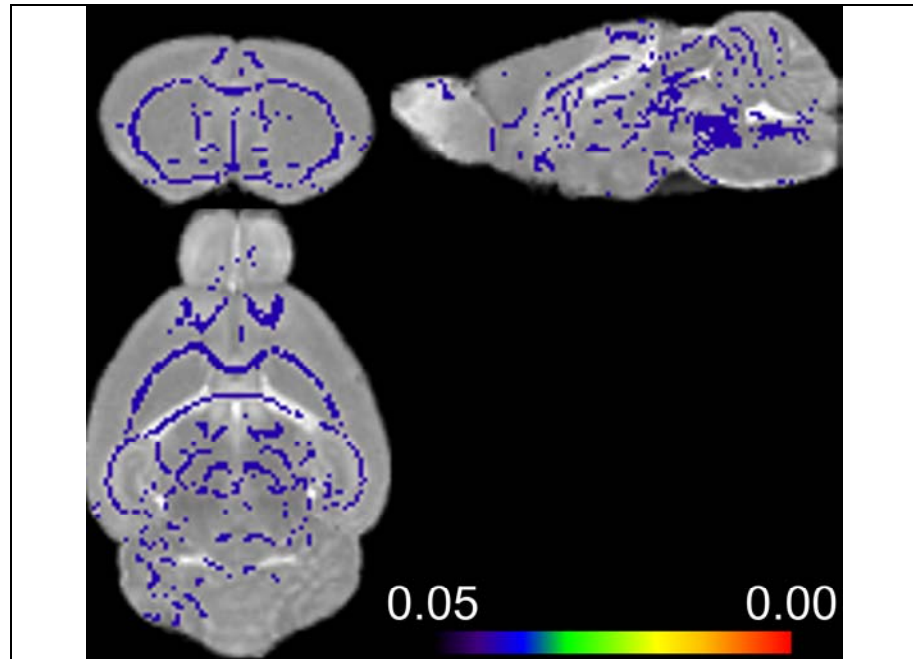


**Fig. 3-31. TBSS statistical analysis shows significant differences in  $\lambda_1$  (blue clusters; WT vs. SERT-HT).**

TBSS-derived significant clusters ( $n = 7$  for WT, and  $n = 4$  for SERT-HT) were overlaid onto average WT  $\lambda_1$  map. Clusters were formed as follows: t-values were calculated by comparing WT to SERT-HT, and were then thresholded at 1. Colour bar represents p-values ranging from 0.05 to 0.00. The white matter of the corpus callosum, external capsule, anterior and hippocampal commissures showed significant differences between WT and SERT-HT mice. Grey matter structures such as the boundary of the anterior cingulate cortex, and dorsal raphe appeared significantly different in  $\lambda_1$  between WT and SERT-HT mice.

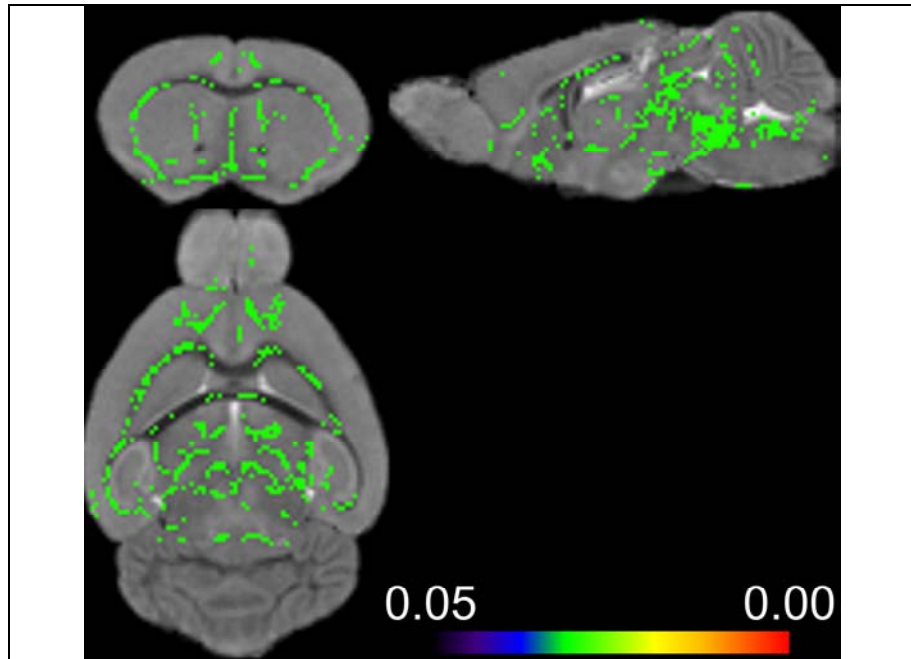


**Fig. 3-32. TBSS statistical analysis shows significant differences in  $\lambda_2$  (green clusters; WT vs. SERT-HT).**

TBSS-derived significant clusters ( $n = 7$  for WT, and  $n = 4$  for SERT-HT) were overlaid onto average WT  $\lambda_2$  map. Clusters were formed as follows: t-values were calculated by comparing WT to SERT-HT, and were then thresholded at 1. Colour bar represents p-values ranging from 0.05 to 0.00. White matter tracts, external capsule and hippocampal commissure, showed significant differences between WT and SERT-HT mice. Grey matter structures such as the boundary of the anterior cingulate cortex, and dorsal raphe appeared significantly different in  $\lambda_2$  between WT and SERT-HT mice.

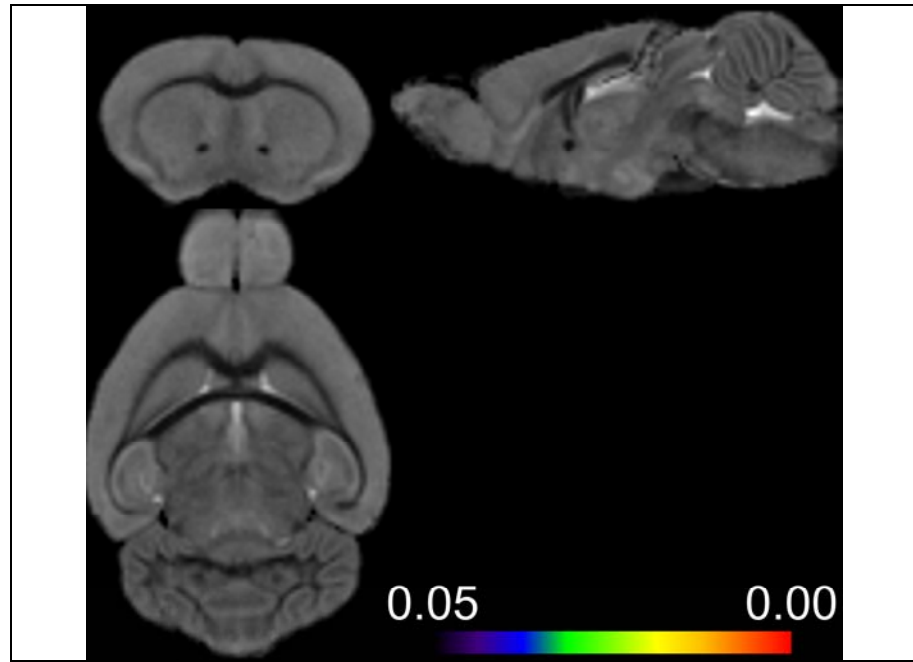


**Fig. 3-33. TBSS statistical analysis shows no significant differences in  $\lambda_3$  (WT vs. SERT-HT).**

TBSS-derived significant clusters ( $n = 7$  for WT, and  $n = 4$  for SERT-HT) were overlaid onto average WT  $\lambda_3$  map. Clusters were formed as follows: t-values were calculated by comparing WT to SERT-HT, and were then thresholded at 1. No significant differences were detected between WT and SERT-HT  $\lambda_3$ . Colour bar represents p-values ranging from 0.05 to 0.00.

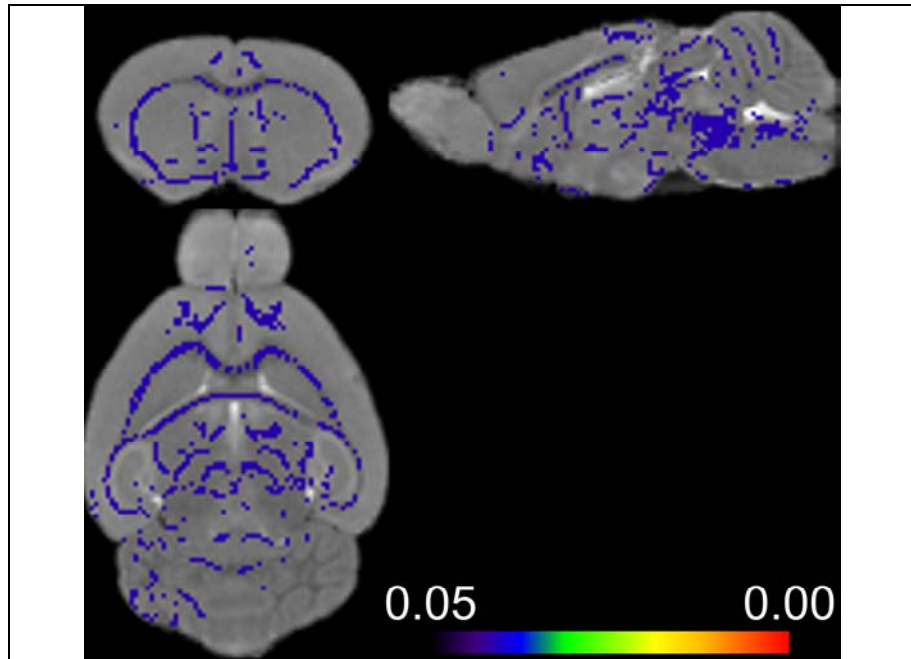
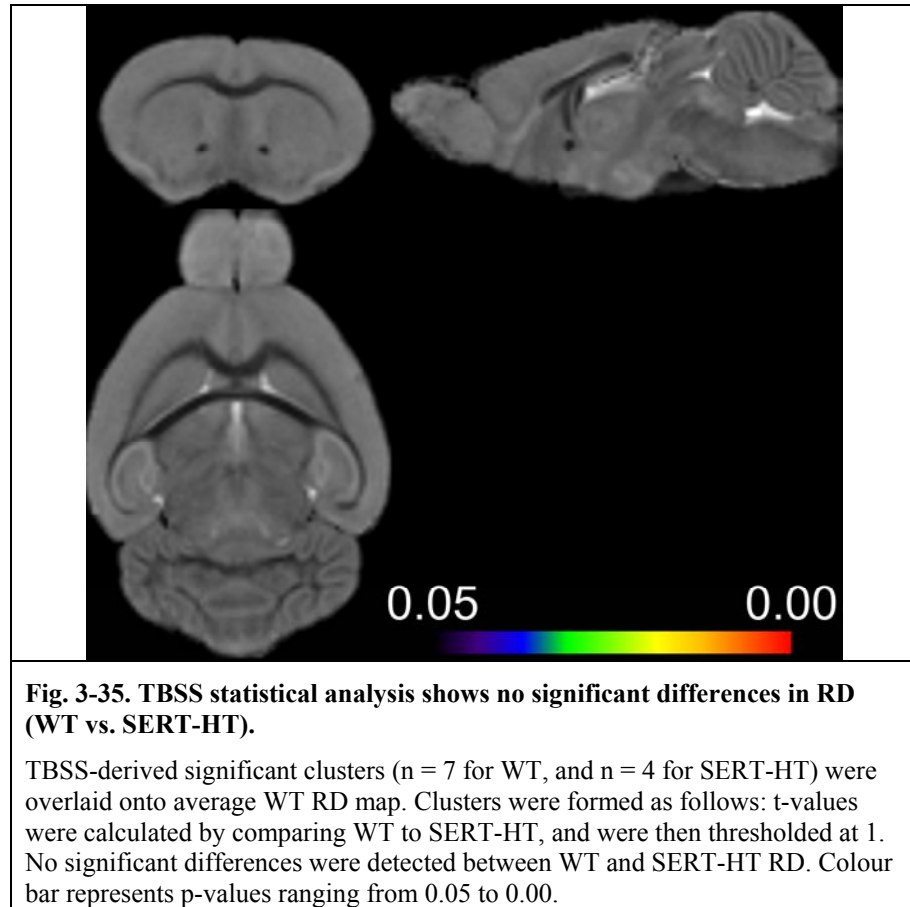


**Fig. 3-34. TBSS statistical analysis shows significant differences in MD (blue clusters; WT vs. SERT-HT).**

TBSS-derived significant cluster ( $n = 7$  for WT, and  $n = 4$  for SERT-HT) were overlaid onto average WT MD map. Clusters were formed as follows: t-values were calculated by comparing WT to SERT-HT, and were then thresholded at 1. Colour bar represents p-values ranging from 0.05 to 0.00. The white matter of the corpus callosum, external capsule, anterior and hippocampal commissures showed significant differences between WT and SERT-HT mice. Grey matter structures such as the boundary of the anterior cingulate cortex, and dorsal raphe appeared significantly different in MD between WT and SERT-HT mice.



Results obtained from ROI and TBSS analyses of WT vs. SERT-HT mice were qualitatively compared in order to identify consistencies between the 2 methods (Table 3-2). For WT to SERT-KO comparisons, the 2 methods fully comply with each other as both detected no significant differences in any tract, and any DTI parameter examined. Consistency between ROI and TBSS analyses was observed also in FA and  $\lambda_3$  in any tract, of SERT-HT compared to WT mice where no differences were present. Both statistics identified the MD to be significantly altered in the anterior commissure, while both did not detect any differences in RD in the internal capsule and hippocampal commissure. Disparity was seen in the axial diffusivity, where TBSS identified significant differences in all tracts examined, while the ROI-based approach did not. This was also the case in MD in the corpus callosum, internal capsule, and hippocampal commissure, i.e. TBSS detected differences, while ROI measurements did not. RD was unaltered in the TBSS approach, for all tracts investigated, while manual delineations detected significant differences in the corpus callosum and anterior commissure. In  $\lambda_2$ , a measure of perpendicular diffusion, ROI-based analyses revealed differences in the corpus callosum and anterior commissure, while some ambiguity was present in the corpus callosum, internal capsule and hippocampal commissure using TBSS. This was because only some small clusters

### Chapter 3 - DTI of the brain in mice deficient in SERT.

appeared significant in these tracts which involved subjective judgement as to whether the tract was altered or not (Fig. 3-32, page 135).

DTI Measurement	Corpus Callosum		Anterior Commissure		Internal Capsule		Hippocampal Commissure	
	ROI	TBSS	ROI	TBSS	ROI	TBSS	ROI	TBSS
FA	no	no	no	no	no	no	no	no
$\lambda_1$	no	yes	no	yes	no	yes	no	yes
$\lambda_2$	yes	partly	yes	no	no	partly	no	partly
$\lambda_3$	no	no	no	no	no	no	no	no
MD	no	yes	yes	yes	no	yes	no	yes
RD	yes	no	yes	no	no	no	no	no

**Table 3-2. Agreement between ROI-based approach and TBSS data derived from the statistical analyses between WT vs. SERT-HT.**

Table summarises outcome of ROI and TBSS-based analyses, respectively ( $p < 0.05$ ).

No: respective method (ROI or TBSS) did not detect significant differences between WT and SERT-HT.

Yes: respective method (ROI or TBSS) did detect significant differences between WT and SERT-HT. Partly: TBSS only. As TBSS uses clusters comprising individual voxels for comparison, while the ROI-based approach uses the whole structure of interest comprised of multiple voxels,  $\lambda_2$  cannot be easily decided as individual voxels in the TBSS analysis lie scattered on the corpus callosum, internal capsule, and hippocampal commissure.

There is agreement in the results of FA and  $\lambda_3$  of both measurements where no significant differences in any tract were detected. Significant differences in  $\lambda_1$  were detected only using TBSS analyses in all tracts examined. Significant differences in MD were detected using TBSS analyses in all tracts examined, while the ROI-based approach only detects differences in the anterior commissure.

Significance was reached in RD only in the corpus callosum and anterior commissure using the ROI-based approach.

#### 3.4.2 Structural analyses.

##### Volumetry of the whole brain.

In order to check whether the deletion of the SERT gene, which would result in no SERT expression, or only in 50 % availability of the gene product available in WT animals (in case of SERT-HT), would influence the total brain volume relative to WT, the brain masks which were created to restrict the reconstruction of the DTI metrics to the brain only were used to determine the brain volume (section 2.1, page 43). All voxels with values greater than zero were included in the analysis and this number of voxels was then multiplied by the voxel dimension ( $0.13 \times 0.13 \times 0.13 \text{ mm}^3$ ), to obtain the whole brain volume (Fig. 3-36). No significant differences were observed between WT ( $n = 8$ ; animal weight:  $28.9 \pm 5.1 \text{ g}$ ), SERT-KO ( $n = 7$ ; animal weight:  $30.8 \pm 5.4 \text{ g}$ ) and SERT-HT ( $n = 4$ ; animal weight:  $31 \pm 4.1 \text{ g}$ ). Mean brain volume appeared higher in SERT-HT mice, however this is likely because of the small number of animals used in this study. The range of the data, for example, is comparable to that of SERT-KO, or WT.

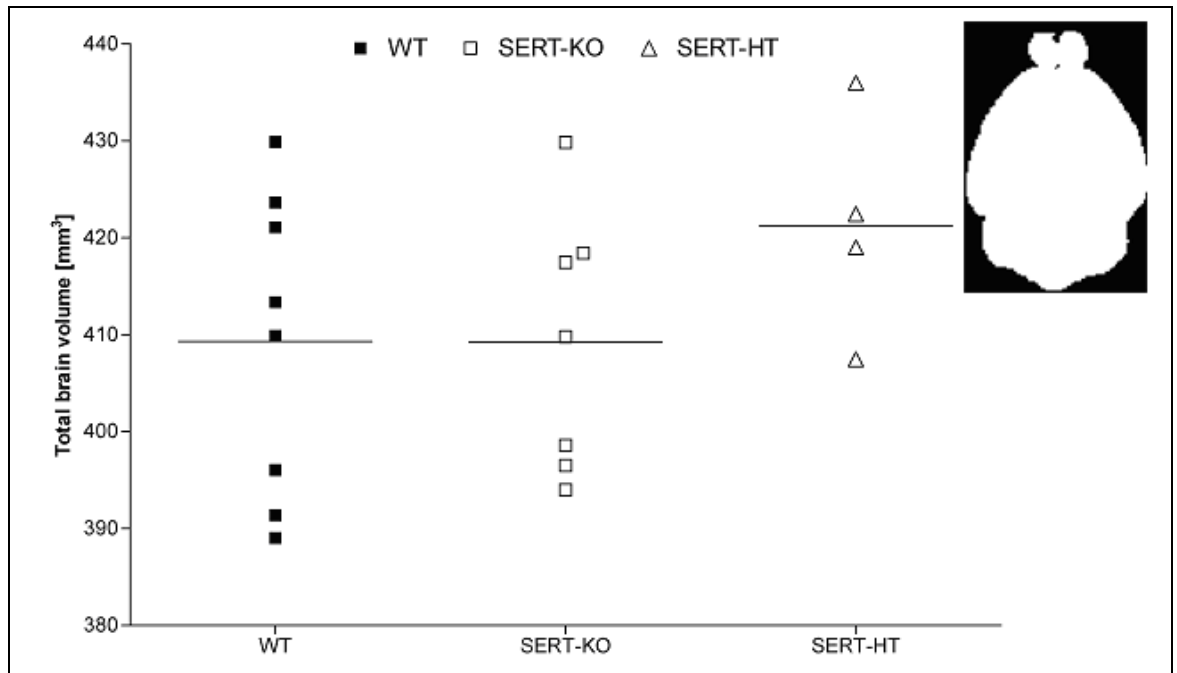


**Fig. 3-36. No group differences in whole brain volume were detected.**

Total brain volume was computed using binary masks of unregistered brains created for brain extraction (inset). Voxels with a value greater than 0 were counted and multiplied by the voxel dimensions. Units of measurement are mm<sup>3</sup>. Bar represents mean for WT n = 8 (animal weight: 28.9 ± 5.1 g), SERT-KO n = 7 (animal weight: 30.8 ± 5.4 g), and SERT-HT n = 4 (animal weight: 31 ± 4.1 g). One-way ANOVA Kruskal-Wallis ( $p < 0.05$ ). No significant differences were detected.

### Volumetry of the hippocampus and caudate-putamen.

The hippocampus was manually segmented on unregistered S0 images using anatomical guidance in form of the mouse atlas published by Paxinos *et al.* (Paxinos and Franklin, 2001). The hippocampus was defined as CA1, CA2, CA3, the dentate gyrus, subiculum and parts of the presubiculum. Firstly using MRICro, an MRI image viewer, the hippocampus was outlined on coronal slices from rostral to caudal (Fig. 3-37, A). Subsequently, the rest of the more caudal parts were identified on sagittal slices (Fig. 3-37, B), and the whole structure was then tidied up, i.e. holes in the mask were filled to complete the structure. Then the number of voxels within that created mask was extracted and multiplied with the voxel dimensions, i.e. 0.13 x 0.13 x 0.13 mm<sup>3</sup>, to obtain the hippocampal volume.

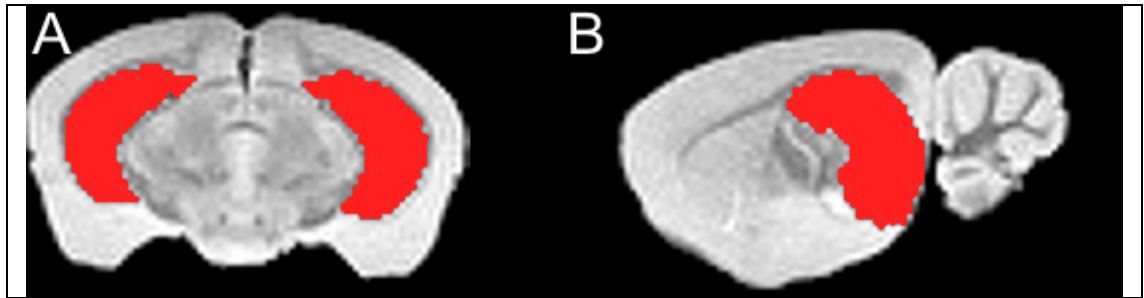


**Fig. 3-37. Volumetric assessment of the hippocampus on unregistered S0 images.**

A: initially the hippocampus was delineated on coronal slices from rostral to caudal levels.

B: following coronal segmentation, the hippocampus was "tidied" up on sagittal slices.

The number of voxels was then multiplied by the voxel dimensions to obtain the volume.

Using MRICro on unregistered, transaxial S0 images (Fig. 3-38, A), the caudate-putamen was defined using the definition given by Paxinos *et al.* (Paxinos and Franklin, 2001). Then in coronal orientation (Fig. 3-38, B), the inferior portion of the caudate-putamen was identified followed by a sagittal assessment of the structure with tidying up the structure (Fig. 3-38, C) in coronal view. The total number of voxels contained in this generated mask was extracted and multiplied with the voxel dimensions, (0.13 x 0.13 x 0.13 mm<sup>3</sup>), which yielded the caudate-putamen volume.

Reproducibility measurements were performed on caudate-putamen data from 3 WT animals. For these 3 animals, the caudate-putamen was delineated twice, and relative differences, as well as the kappa ( $\kappa$ ) indices were computed between the first and the second measurement. The kappa index was computed as follows:

$$\kappa(I_{ref}, I_{seg}) = \frac{2|I_{ref} \cap I_{seg}|}{|I_{ref}| + |I_{seg}|}$$

where  $I_{ref}$  is the caudate-putamen volume of the second segmentation (regarded as the reference), and  $I_{seg}$  the volume of the first segmentation. The more similar the segmentations are, the closer the  $\kappa$  index is to unity (Zaidi et al., 2006). Relative differences were calculated as  $(I_{seg} - I_{ref})/I_{ref} * 100 \%$ .

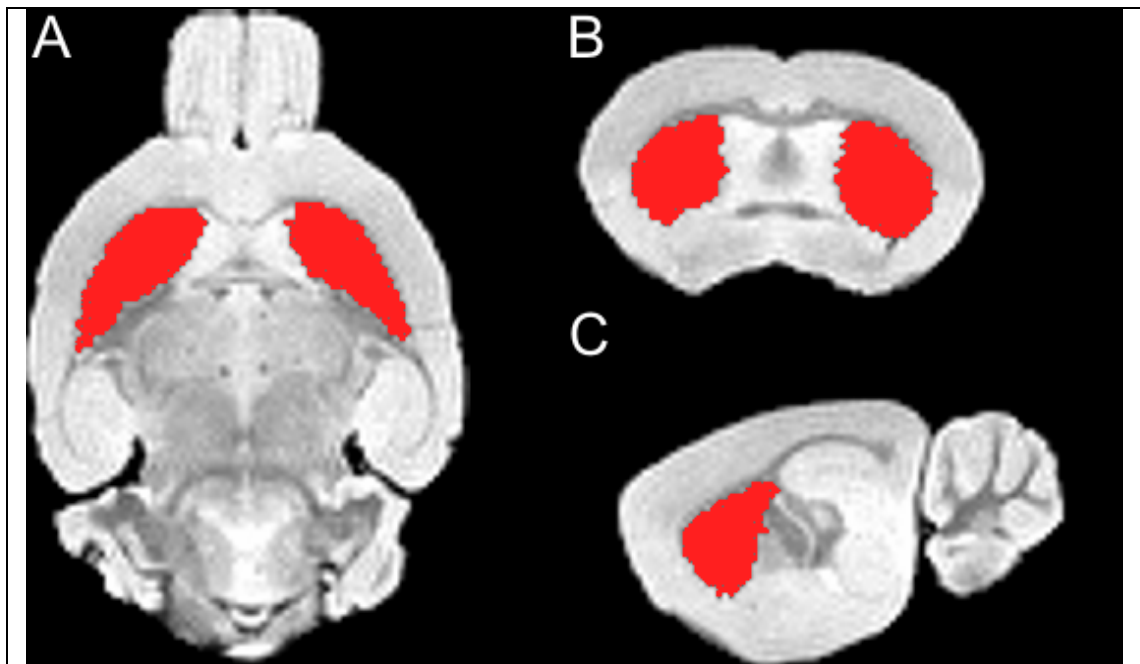


**Fig. 3-38. Volumetric assessment of the caudate-putamen on unregistered S0 images.**

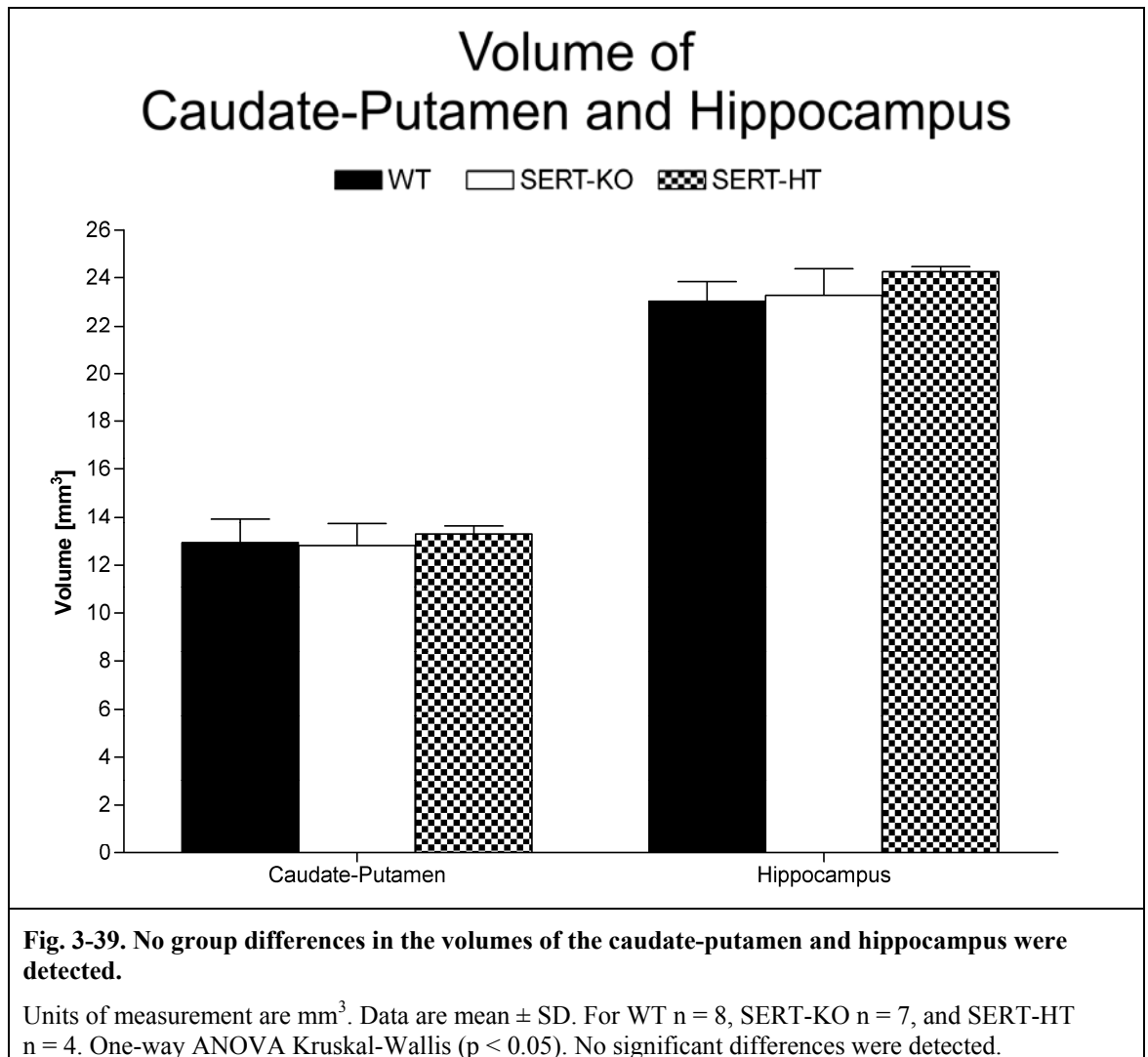
A: initially the caudate-putamen was delineated on transaxial slices.

B: following transaxial segmentation, the segmentation was refined on coronal slices for better inferior definition.

C: subsequently the caudate-putamen was delineated on sagittal slices to improve segmentation of the lateral portions.

Finally the structure was "tidied" up on coronal slices. The number of voxels was then multiplied by the voxel dimensions to obtain the volume.

The 2 reproducibility measurements of the caudate-putamen indicated good agreement, with absolute relative differences below 12 % (-4 %, -4 %, and 12 %) for the 3 WT animals. The  $\kappa$  indices were above 0.9 (0.91, 0.91, and 0.92). A  $\kappa$  index of  $> 0.7$  was reported to indicate excellent agreement (Archibald et al., 2003) For caudate-putamen volume measures, the second measurements of these 3 WT animals were used for further calculations. There was no significant difference between groups in either the hippocampus, or the caudate-putamen (Fig. 3-39).



### 3.5 Discussion.

To our knowledge, this was the first study that applied DTI to a mouse model of depression. DTI of fixed mouse brains was employed in order to investigate whether deletion of the SERT gene, and therefore enhanced serotonin neurotransmission, would result in structural white matter abnormalities, i.e. tract integrity and possibly altered tract trajectory. FA subtraction map analyses were carried out between WT and SERT-KO mice that identified the corpus callosum as a region with an abnormality. This was confirmed by line profile investigations of the corpus callosum. Callosal length was measured which identified 3 SERT-KO (total n = 12), and 1 WT (total n = 13) animal with abnormally shortened corpus callosum. Manual delineations of the corpus callosum, anterior and hippocampal commissures, and internal capsule and subsequent extraction of DTI parameters (FA,  $\lambda_i$ , MD, and RD) were performed on WT, SERT-KO and SERT-HT mice. These tracts were selected because of the abnormalities observed in the corpus callosum, and the relatively easy identification of the others that formed part of a BMedSci student project, which included also an assessment of histopathology of these tracts (data not

### Chapter 3 - DTI of the brain in mice deficient in SERT.

shown). No significant differences were detected between WT and SERT-KO mice, but significance was reached when comparing the former with SERT-HT mice. This included reductions in perpendicular diffusion as measured with  $\lambda_2$  and RD in the corpus callosum and anterior commissure, while significant reductions in MD were only found in the corpus callosum. More sophisticated statistical comparisons were carried out with the novel TBSS software package dedicated to DTI analyses to identify changes in tracts other than those mentioned. This form of analyses was consistent with the ROI-approach in case of WT to SERT-KO comparisons, i.e. no differences were found. TBSS and ROI-based analyses showed some degree of disparity when WT and SERT-HT mice were compared, which will be addressed. Furthermore, structures reported to be involved in depression, such as the caudate-putamen and the hippocampus, were checked for volume differences between groups. No differences were found. Below, technical issues concerning fixed vs. *in vivo* DTI acquisition, as well as TBSS vs. ROI analyses, but also the validity of SERT-KO mice as a model of depression are addressed. This is followed by a comparison of the here presented findings to the current literature, i.e. shortened callosal length, and differences in white matter tracts between WT and SERT-HT are discussed. This is believed to be of particular interest as SERT deletion is not strictly a genetic model of depression (Kalueff et al., 2006), with the SERT-HT being actually a closer model to depressed human short-allele carriers of the SERT gene (Murphy et al., 2003).

#### 3.5.1 Technical considerations.

##### DTI of fixed *ex vivo* tissue vs. *in vivo* data acquisition.

It has been shown by Sun *et al.* that *ex vivo* DTI is feasible and comparable to measurements performed *in vivo*. RA, and RD were virtually unchanged after tissue fixation, while a reduction of 50 - 75 % in the Tr that is analogue to the MD used in the current study, was observed. A 38 % reduction was expected by Sun due to temperature differences, i.e. 37 °C *in vivo* vs. 20 °C *ex vivo*, indicating that temperature does not completely account for the loss of Tr. However, since  $\lambda_1$  and RD (both normalised to the Tr, e.g.  $\lambda_1/\text{Tr}$ ) remain unchanged, the authors concluded that the eigenvalues reduce proportionally, therefore supporting the use of fixed brain tissue (Sun et al., 2003). The benefit of using fixed tissue for DTI scanning is obvious. Tissue can be scanned without monitoring life-sustaining parameters therefore minimizing labour. No motion artefacts are expected, and scans can be performed without time limit, thus increasing the spatial resolution of the already tiny structures in small animal brains. In addition, DTI sequences providing better image quality can be used, i.e. a spin-echo sequence as used in the current

### Chapter 3 - DTI of the brain in mice deficient in SERT.

study compared to a fast, but image distorting echo-planar imaging sequence. In our particular case, the use of fixed mouse brains made the collaboration with Drs. Jay Gingrich and Mark Ansorge from Columbia University, New York, USA, possible.

#### **TBSS vs. conventional ROI analysis.**

Using ROI-based analysis, a structure needs to be selected manually by the investigator. Furthermore, structure delineation is time consuming and prone to intra-, and even more to inter-investigator variability. ROI-based analysis gives information about how much the parameter has changed. In contrast, TBSS analysis can show where significant differences are, and provides statistical assessment of the whole data set that is unbiased, meaning that it does not require user input that could interfere with the objectivity of the analysis. On the other hand, automated analysis like TBSS are “black boxes”, in which sophisticated statistical processes take place that are not easily understood and require training so that the analysis gives meaningful results, while ROI-based analyses are fairly easy to understand. However the advantages of TBSS analyses are obvious and should find more application in clinical DTI data, and particularly in preclinical studies where this approach is rarely applied. Therefore an attempt was made to apply TBSS to our animal data, and a qualitative comparison to the results of the ROI-based method was made.

In this study, ROIs from DTI data of the corpus callosum, anterior and hippocampal commissures plus the internal capsule were selected to identify possible abnormalities within these tracts. Significant differences were only detected in perpendicular diffusion  $\lambda_2$  and RD parameter maps between WT and SERT-HT (but not SERT-KO) using conventional ROI-based analysis of the corpus callosum and anterior commissure. Cluster analysis (TBSS) using FSL was performed on the whole 3D brain DTI dataset (Smith et al., 2006). This technique fully confirmed the results of the ROI-based analyses for comparisons of WT to SERT-KO mice, i.e. no differences were present in any examined tract. In addition, consistency between ROI and TBSS analyses was found when WT were compared to SERT-HT mice in FA and  $\lambda_3$  for all tracts (no significant differences), while data from  $\lambda_2$ , MD and RD give partly opposing results.

The disparity between the 2 methods likely reflect the small animal numbers used particularly in the SERT-HT group (n = 4). Since there are no differences between WT (n = 7 - 8) and SERT-KO (n = 7) mice, which included almost twice as many animals as the SERT-HT mice, results should be regarded with caution and meaningfulness of the initial data concerning differences in SERT-HT mice need to be addressed in further

### Chapter 3 - DTI of the brain in mice deficient in SERT.

studies. The values of the encompassed structures tended to be lower in SERT-HT mice compared to WT in all diffusion sensitive measures ( $\lambda_i$ , MD and RD), which suggests that differences are borderline, meaning that significance could possibly be reached in the ROI-based approach by including more animals / reducing the variability of the ROI measurement. Thus this highlights one problem of the ROI-based approach that concerns the repeatability. Slight variations in tract definition between animals can have a big impact on the variability of the data. A one-to-one comparison of ROI to TBSS analyses is not useful either, because the ROI measurement provides only one mean value per tract (and DTI parameter) that is tested for significance, while clusters derived from the comparison of individual voxel values (that are covered by the TBSS-derived skeleton) are compared between groups. This is independent of a specific tract, i.e. the software does not “know” to which tract a particular voxel belongs as only individual voxels are compared. This may explain the different results obtained from ROI and TBSS analyses. Hence the methods should be tested in a model that shows more robust (as demonstrated in chapter 4, page 159), rather than such subtle, borderline differences that might not be of biological relevance.

Nevertheless, recently published DTI findings on human depression - to our knowledge no animal models of depression were previously used in DTI studies - will be brought in context with our observations in SERT-HT mice compared to WT (DTI data, see below). It is also worth mentioning that there are dangers in relating so-called animal models of a human disease to the actual disease. The SERT-KO mice used in this study are reported to show behavioural signs that are associated with depression, i.e. lack of explorative drive, and latency in feeding (Lira et al., 2003). However as Kalueff *et al.* pointed out, SERT deletion would not be a genetic model of depression (Kalueff et al., 2006). This is in agreement with Murphy *et al.* who suggest that SERT-HT mice are more likely to correspond to human short-allele carriers of SERT (Murphy et al., 2003). Especially in this light the differences between WT and SERT-HT are interesting and are worth discussing.

### 3.5.2 Callosal length.

From the subtraction analysis of FA images from the initial groups of WT (n = 5) and SERT-KO (n = 5) mice, the genu of the corpus callosum was identified as a structure with abnormally low anisotropy. Measuring the anteroposterior extent of the corpus callosum revealed that 2 animals in the SERT-KO group had a shortened corpus callosum. At this stage of the project it appeared as if the SERT-deficient mice might have exhibited a structural abnormality in a major white matter tract. In other studies of SERT KO mice differences in brain morphology were reported when compared to WT animals. Upton *et al.* examined the ipsilateral, and contralateral retinal projections to the dorsal lateral geniculate nucleus and superior colliculus, respectively. In WT mice, initial innervation of these 2 structures is intermingled, and segregation takes place later where neurons retract and start to target their final destination. However, this process was shown to be altered in SERT-KO mice such that contralateral fibres in the dorsal lateral geniculate nucleus fail to retract and innervate the tissue at sites where ipsilateral fibres make connections. However the number of the latter was not altered. An increase in ipsilateral fibres was observed in the superior colliculus (Upton *et al.*, 2002).

Persico *et al.* examined the barrel cortex of SERT-KO and SERT-HT mice where each whisker is connected to one barrel-like cortical region in the somatosensory cortex. In SERT-KO mice, the cortical barrel organisation is almost completely lost, while SERT-HT barrels are largely unaffected (Persico *et al.*, 2001). This resulted in functional impaired somatosensory cortex activation through whisker stimulation in SERT-KO mice (Esaki *et al.*, 2005). Furthermore, Altamura *et al.* measured cortical thickness and showed a consistent reduction of cortex layer 4 in SERT-KO mice compared to both WT and SERT-HT animals (Altamura *et al.*, 2007). Thus while there are reports of morphological abnormalities in SERT-KO mice there was no previous evidence for a shortened or absent corpus callosum related to altered serotonin function in mice. However, some evidence relating excessive serotonin levels to a shortened corpus callosum comes from the human condition of autism. Autistic children display high blood serotonin levels which may enter the brain and interfere with normal brain development (for review see Whitaker-Azmitia *et al.* (Whitaker-Azmitia, 2005)). It was shown in human patients suffering from autism that the area of the genu of the corpus callosum is reduced (Manes *et al.*, 1999, Vidal *et al.*, 2006). However, in the current study, only a few animals within the SERT-KO group exhibited a shortened corpus callosum. A more plausible explanation for this phenotype

### Chapter 3 - DTI of the brain in mice deficient in SERT.

was described by Wahlsten *et al.*. The authors point to problems with highly inbred mouse strains, such as the 129 strain used in the current study. In many 129 strains the phenotype of a shortened corpus callosum has a frequency of more than 30 % (Wahlsten *et al.*, 2001). Crossing experiments performed in the same laboratory identified the presence of 2 genetic loci in 129 strains which cause the deficit (Livy and Wahlsten, 1991). Wahlsten proposed a model that would explain that 129 mice being homozygous recessive at one of these loci produced an incomplete CC, while mice homozygous recessive at both locations had a completely absent corpus callosum. (Wahlsten *et al.*, 2003). In order to test the hypothesis that a shortened corpus callosum was independent of the SERT deficiency, more animals were scanned in the current DTI study. The results showed that in the WT group, 1 animal out of 13 had a shortened corpus callosum and 3 out of 12 in the SERT-KO also exhibited this feature. In the smaller SERT-HT group no animal exhibited a shortened corpus callosum. However it is worth mentioning that one animal in the SERT-HT group had to be excluded since its S0 image of the brain showed signs of abnormalities consisting of patches of high, alternating with low signal intensities, possibly due to sample freezing during transport (Fig. 3-40).

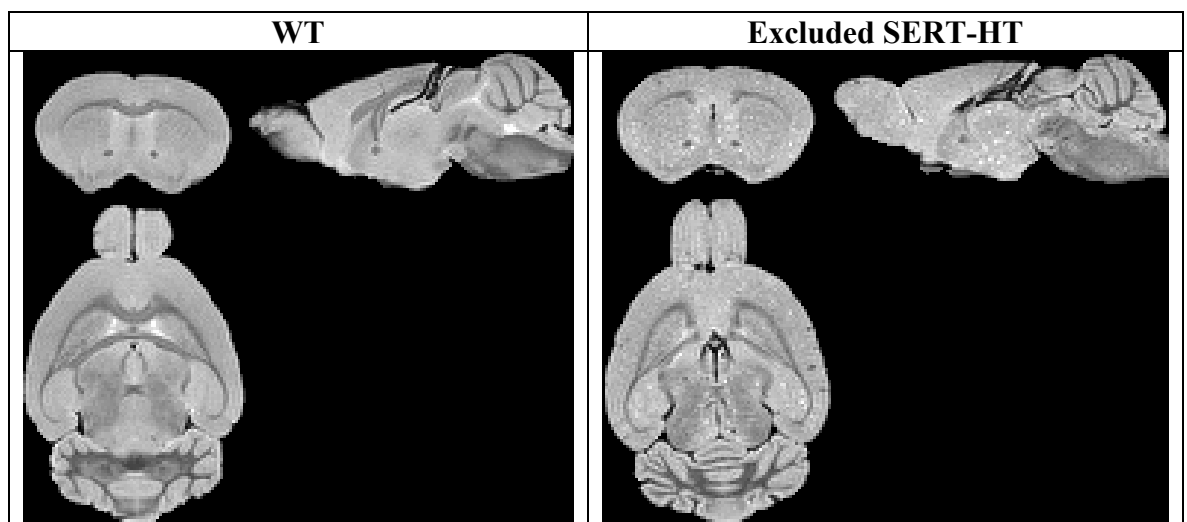


**Fig. 3-40. Exclusion of DTI data from 1 SERT-HT mouse because of signal abnormalities.**

S0 images show representative WT animal (left), and excluded SERT-HT mouse (right). Images are unregistered. Please note the patchy looking scan of the SERT-HT mouse, while that of the WT appears smooth. Also note the missing corpus callosum in coronal, sagittal, and transaxial view in the SERT-HT mouse.

In this animal, there was virtually no corpus callosum connecting the hemispheres. Because of the high frequency at which this phenotype occurs in SERT-KO mice compared to WT animals, it cannot completely be ruled out that there would not be an interaction between SERT deletion and the gene loci responsible for a shortened corpus

callosum. However the genetic presence of these loci, and the inconsistency of occurrence of the phenotype within the SERT-KO group is reason enough to not regard this effect as characteristic for the SERT deletion.

#### 3.5.3 DTI data.

Recent clinical DTI studies comparing healthy subjects to depressed patients consistently show reductions in FA in frontal cortical areas (Bae et al., 2006, Li et al., 2007b, Ma et al., 2007, Yang et al., 2007a). In addition, 2 studies were performed that tried to assess whether remission from depression is associated with higher FA values compared to patients who would not remit. Alexopoulos *et al.* found reduced FA in the anterior cingulate cortex, prefrontal cortex and the genu of the corpus callosum (Alexopoulos et al., 2008). This was in contrast to reports from Taylor and his colleagues where the authors found significant increases in FA of non-remitting patients in the prefrontal cortex and anterior cingulate cortex (Taylor et al., 2008). It is difficult to integrate the results presented in this study with current findings in this field, as no FA changes were observed in either SERT-KO or SERT-HT mice. In all these studies mentioned, only Taylor *et al.* and Bae *et al.* presented MD along with FA as parameters investigated. In both cases, MD remained unchanged (Bae et al., 2006, Taylor et al., 2008). The MD is not the most representative parameter as changes in  $\lambda_1$ ,  $\lambda_2$ , and  $\lambda_3$  may be balanced out by averaging, hence would indicate no change in MD. In the current study, ROIs for the anterior commissure, internal capsule and hippocampal fimbria comprised most of the structure, while the studies performed in humans were very localised by using small ROI sizes (Bae et al., 2006, Li et al., 2007b, Nobuhara et al., 2006, Taylor et al., 2008, Yang et al., 2007a). In order to gain a more global overview to check for differences, cluster-based thresholding was performed, that is more comparable to voxel-based morphometry studies performed by Alexopoulos *et al.*, Zou *et al.*, and Ma *et al.* (Alexopoulos et al., 2008, Ma et al., 2007, Zou et al., 2008), respectively. In voxel-based morphometry-based approaches, medical images of 2 groups, i.e. healthy versus diseased subjects, are compared voxel-by-voxel in order to identify differences in the local signal intensities (Ashburner and Friston, 2000), which may code for a variety of parameters including radiolabelled tracer uptake (SPECT), grey or white matter concentrations (MRI), or water diffusion (DTI).

Species differences in brain organisation also contribute to measurements being performed differently. For instance the human cortex is highly gyrified resulting in highly functionally organised areas where processing takes place. This cortical gyrification does

not take place in rodents. Using the cluster-based thresholding technique, structures that were not covered by the ROI analysis could be detected in SERT-HT mice to be significantly different from WT animals.

#### **DTI measures in the corpus callosum are significantly altered only in SERT-HT mice.**

Significance in the largest interhemispheric connection, the corpus callosum, was detected in SERT-HT compared to WT animals, in both the cluster-based thresholding technique for  $\lambda_1$ ,  $\lambda_2$  (partly), MD, and in the ROI-based approach in  $\lambda_2$ , and RD. The data from the cluster-based approach indicates an overall decrease in diffusivity, while the ROI technique was more sensitive to perpendicular diffusion. Published data on depression only show differences in FA and no other diffusion parameters were examined. FA appeared to be comparable between genotypes, and was only non-significantly reduced. In agreement with lower FA values is Alexopoulos *et al.*'s data using a voxel-based morphometry approach where remitters and non-remitters were compared (Alexopoulos *et al.*, 2008). However the majority of reports were not able to support this finding (Bae *et al.*, 2006, Ma *et al.*, 2007, Nobuhara *et al.*, 2006, Yang *et al.*, 2007a, Zou *et al.*, 2008). In this study, the corpus callosum also showed up consistently in the subtraction maps where diffusion parameter maps were subtracted from those of the WT. However this must not be overrated as there was a difference in range of roughly 1 mm in callosal length in WT, and even more, about 1.5 mm in SERT-HT mice. This is reflected by the difference in the subtraction maps. In agreement with this, Wahlsten *et al.* reported that there is a continuum of callosal length in mice (Wahlsten *et al.*, 2003). On the other hand, ROIs in the manual approach encompassed only the corpus callosum, and not tissue where it was expected to be. In addition, the cluster-based thresholding technique could detect significant differences, and the approach used in the TBSS routine incorporated in the FSL is designed to deal with mis-registrations (Smith *et al.*, 2006). A shortened structure could possibly be classified as a mis-registration, but the differences in callosal length may be too large. Evidence for altered diffusion properties in the corpus callosum comes rather from autism research. For instance, Alexander *et al.* reported that in a subgroup of subjects suffering from autism that was accompanied with lower IQs and a smaller corpus callosum (see for comparison also the corpus callosal length above), MD and RD was increased while FA was decreased (Alexander *et al.*, 2007). However in the study presented here the FA was not altered, and the RD (ROI-based approach) is significantly reduced, and not increased, in the corpus callosum of SERT-HT mice.

#### **DTI measures in the anterior commissure are significantly altered only in SERT-HT mice.**

Significant differences were also observed in DTI parameters of the anterior commissure of SERT-HT mice compared to WT animals. In the ROI-based approach,  $\lambda_2$ , MD, and RD appeared to be altered, while using the cluster-based thresholding technique,  $\lambda_1$  and MD appeared significantly different from WT animals. In summary, it could be concluded that overall diffusion was decreased, indicating a gain of structural composition in the sampled structure of SERT-HT versus WT mice. In order for this to be true, an increase in FA would have been expected (see Fig. 1-5, page 10). However, anisotropy was non-significantly decreased in SERT-HT mice. The anterior commissure, next to the corpus callosum, is known to provide a route to transfer information between hemispheres, specifically between the human temporal lobes. In addition, the size of the anterior commissure was shown to predict sexual orientation, and a dimorphism exists in humans (Allen and Gorski, 1992). This appeared also to be true for rats. As in humans, normal female rats have a larger anterior commissure compared to males. In a rat model of prenatal stress where the pregnant rat underwent an external stress regimen (heat, light, and restraint stressor), stressed females' offspring had an equal to normal male sized anterior commissure. Prenatally stressed males had a larger anterior commissure than their unstressed male counterparts (Jones et al., 1997). A recent DTI study in paediatric traumatic injury supported furthermore the vulnerability of this tract in animal and human brain development. Children having had severe head impact injury displayed an anterior commissure that was smaller in volume, and, in addition, a significant decrease in FA when compared to normal developing children (Wilde et al., 2006).

As SERT-HT mice are the offspring of animals heterozygous for the SERT deletion, the parents might have experienced stress comparable to that of the pregnant rats that were exposed to external stressors. A depression-like phenotype that might exist in SERT-HT mice could cause social stress with their littermates. Also depression itself, without the presence of an external factor, can represent a stress factor. Unfortunately, no other diffusion sensitive parameter was given in the study performed by Wilde *et al.* (Wilde et al., 2006). However a decrease in FA is usually associated with an increase in diffusion (Fig. 1-5, page 10), which is again just the contrary of what is reported in the current study. Another factor that was already mentioned with regard to the shortened corpus callosum is in fact of genetic origin. Livy *et al.* could show in mice with absent corpus callosum, including the 129 strains, that there was an increase of 17 % in unmyelinated fibres in

### **Chapter 3 - DTI of the brain in mice deficient in SERT.**

these mice in the anterior commissure compared to mice having an unaffected corpus callosum indicating possible compensation mechanisms. The area of the anterior commissure, as well as the number of myelinated axons, however, was unchanged in acallosal mice when compared to that of normal corpus callosum carriers (Livy et al., 1997). As the diameter stayed the same, and the number of myelinated fibres as well, the additional nonmyelinated fibres could have caused an increase in FA which in turn could have reduced diffusivity in acallosal mice, as nonmyelinated fibres contribute to FA as well (Jito et al., 2008). In addition, the higher density of parallel running fibres may increase anisotropy too. Apart from the FA, a reduction of diffusivity was actually observed in the current study in SERT-HT mice.

#### **DTI measures in the internal capsule are significantly altered only in SERT-HT mice.**

By conducting a voxel-based morphometry analysis, the anterior limb of the internal capsule was previously identified as possessing lower FA values in patients suffering from major depressive disorder compared to healthy volunteers (Zou et al., 2008). Other studies performing voxel-based morphometry in the depressed vs. normal subjects could not detect any differences between groups in this tract (Alexopoulos et al., 2008, Ma et al., 2007). In addition, Bae *et al.* placed ROIs at about the same position (Bae et al., 2006), at which Zou *et al.* detected differences in the internal capsule. No differences could be found (Zou et al., 2008). In the here presented study using the cluster-based thresholding approach, the internal capsule appeared to be significantly altered in SERT-HT mice compared to WT animals in  $\lambda_1$ , and MD. Inspection of the data derived from the manually delineated structure showed non-significant reductions in all DTI parameters except in FA (no reductions), which remained unaltered, in SERT-HT mice. This indicates an overall decrease in diffusion, which appears to be mainly driven by a reduction in axial diffusivity. Under this condition, it would have been assumed that the anisotropy increases (Fig. 1-5, page 10), however it remained unaltered in SERT-HT mice. With a limited number of SERT-HT mice included in this study, this result would need to be confirmed with a larger sample size.

#### **DTI measures in the hippocampal commissure are significantly altered only in SERT-HT mice.**

The hippocampal commissure is a well defined tract in rodents providing interhemispheric connections to hippocampal substructures (Voneida et al., 1981). This tract underwent evolutionary reductions in humans, so that it was long believed to be absent or non-

### Chapter 3 - DTI of the brain in mice deficient in SERT.

functional (Wilson et al., 1990, Wilson et al., 1991). However there is evidence that it actually is functional and that it is involved in discharge propagation during a temporal lobe epilepsy episode (Gloor et al., 1993, Spencer et al., 1987). Probably due to the ambiguity of this tract in humans, no reports bringing this structure into the context of depression are available. However since the hippocampus appears to be one of the most important structures in depression treatment, i.e. in terms of atrophy, neurogenesis, and its serotonergic input, it is conceivable that the hippocampal commissure could contribute to the pathology observed in depression. The hippocampus itself in terms of its volume appeared to be unaffected. It is worth mentioning that this tract displayed, shown by the ROI-based approach to derive DTI measurements, the highest degree of anisotropy, the highest axonal diffusivity ( $\lambda_1$ ), and therefore the lowest perpendicular diffusion as measured by  $\lambda_2$ ,  $\lambda_3$ , and RD when compared to the other white matter tracts under investigation, i.e. the anterior commissure, corpus callosum, and internal capsule. This is indicative of the hippocampal commissure exhibiting the highest degree of axonal packaging or myelination, with the lowest perpendicular diffusion. These differences between tracts, however, are balanced out in the MD. Significant differences in the hippocampal commissure were only detected between WT and SERT-HT mice using the cluster-based thresholding technique, where  $\lambda_1$  and MD were significantly altered. Large, but non-significant reductions in these measures were observed when delineating the whole structure. Reductions in hippocampal commissure size were also reported in this kind of mouse strains (129) where the corpus callosum was completely absent. For instance, Wahlsten *et al.* reported that 1 out of 20 129S1 / SvImJ mice investigated displayed an abnormally small hippocampal commissure (Wahlsten et al., 2003). In the study presented here, no small hippocampal commissures were observed in any genotype group under investigation.

#### **DTI measures in the external capsule are significantly altered only in SERT-HT mice.**

The external capsule in rodents is a prominent tract flanking the corpus callosum bilaterally in coronal slices. In humans, it carries mainly corticostriatal fibres that descend from the primary and supplementary motor areas. It consists also of some association fibres (Berke, 1960). Therefore it is not surprising that lower FA values in the external capsule in very low birth weight children correlated with impaired motor function, such as impaired fine motor control and visual motor integration compared to children who had normal weight at term birth. In addition, subjects in the low birth weight group had lower IQ, but also social skill deficits as assessed by autism spectrum screening that was

### Chapter 3 - DTI of the brain in mice deficient in SERT.

associated with lower FA in the external capsule compared to term children (Skranes et al., 2007). In another DTI study of depression, patients who did not remit to antidepressant treatment displayed FA reductions not only in the splenium of the corpus callosum, but also in the external capsule (Li et al., 2007). However a big criticism of the latter study is that the latter finding is only described in the discussion, but not in the results section, possibly indicating some confusion during write-up. To the author's knowledge, no other previous reports, apart from that of Li and colleagues, have linked differences in DTI parameters in the external capsule to major depression. Therefore the significance of these differences observed in the here presented study using the cluster-based thresholding technique, i.e. in  $\lambda_2$  (partly) and MD, remain elusive. It is worth mentioning that it was not attempted to delineate the external capsule as it is a very thin appearing tract in coronal view, not more than 1 voxel wide at some locations.

#### **DTI measures in the anterior cingulate cortex are significantly altered only in SERT-HT mice.**

Using the cluster-based thresholding approach, the anterior cingulate cortex was found to have significantly altered. Visual inspection of the mean images on  $\lambda_1$ ,  $\lambda_2$ , and MD was performed in order to elucidate the direction of change (data not shown). This confirmed higher diffusivities in WT compared to SERT-HT animals in this area. This signifies overall loss of diffusivity and would usually go side-by-side with an increase in FA as the structure investigated (SERT-HT) would be more organised than the reference material (WT) (Fig. 1-5). However, visual inspection of the FA images showed that SERT-HT animals had comparable FA values in the anterior cingulate cortex compared to WT (data not shown). Tyszka *et al.* reported that FA is a less sensitive measure of white matter pathology compared to measures of diffusion like  $\lambda_1$ ,  $\lambda_2$ ,  $\lambda_3$ , and the Tr (Tyszka et al., 2006). A reduction in FA is in line with findings reported by Alexopoulos *et al.*, where depressed patients not responding to antidepressants show lower FA in the anterior cingulate cortex compared to those who do remit (Alexopoulos et al., 2008). However no statement can be made about the decreased diffusivity observed in SERT-HT mice, as no other parameters were reported in other studies showing reduced FA in this area. Murphy *et al.* mentioned that SERT-HT mice would display the highest degree of similarity to depressed patients carrying the short SERT allele (Murphy et al., 2003). In support of this, Ruhe and colleagues showed that antidepressant treatment in carriers of the short allele has a non-beneficial outcome (Ruhe et al., 2008).

### 3.5.4 Structural analyses.

#### **Whole brain volume is not altered.**

The total brain volume measured in SERT-KO and SERT-HT mice appeared to be unchanged relative to WT animals. This is consistent with clinical observations made in depressed patients compared to healthy subjects where no change in total brain size was detected (Sheline et al., 1999).

#### **Hippocampal volume is not altered.**

The advent of *in vivo* structural brain MRI made it feasible to examine the effects of major mood disorders on the volumes of various brain structures. The limbic-cortical-striatal-pallidal-thalamic loop received particular attention, as the limbic system is concerned with mood processing (Yang et al., 2007). The data presented here on the hippocampal volume, which is part of this loop, suggest that this structure is not affected by SERT dosage. This is in contrast to studies performed in humans, where hippocampal volume was shown to be reduced in patients suffering from major depression (Sheline et al., 1996, Videbech and Ravnkilde, 2004, Campbell et al., 2004, Sheline et al., 1999). In addition, Czeh *et al.* showed that in tree shrews subjected to psychosocial stress, hippocampal volume was reduced compared to control animals. In a subset of animals, however, that was treated with antidepressants, the hippocampal volume reversed again (Czeh et al., 2001). Given these findings that include meta-analyses of previous findings (Campbell et al., 2004, Videbech and Ravnkilde, 2004), whether hippocampal volume shrinks with depression is however still under debate, as some studies failed to show a relationship. Posener *et al.*, for instance, could not detect any changes in size, concluded though that the shape of the hippocampus was different in depression (Posener et al., 2003). In line with this contradiction, no significant change in hippocampal volume was observed compared to control subjects by Rusch *et al.*, however the volume of the right hippocampus appeared to be significantly larger in the depressed compared to the left in the same subject (Rusch et al., 2001).

In the current study, the hippocampus was defined so that it includes CA1, CA2, CA3, dentate gyrus, subiculum, and parts of the presubiculum. Comprising all these substructures, loss of volume in one substructure might have been compensated by gain of size in another. In addition, the hippocampus was delineated bilaterally, neglecting possible lateralisation that was not anticipated in rodents. This assumption was also made

by Czeh *et al.*, who also pooled the volumes of individual tree shrew hippocampi (Czeh *et al.*, 2001).

#### **Caudate-putamen volume is not altered.**

The second structure whose volume was assessed in the current study that is also part of the limbic-cortical-striatal-pallidal-thalamic loop was the caudate-putamen (Drevets *et al.*, 1992). No significant differences between WT, SERT-KO and SERT-HT, respectively were observed for this structure. The caudate nucleus in humans was shown previously to be reduced in the depressed compared to healthy subjects using MRI (Kim *et al.*, 2008, Krishnan *et al.*, 1992, Parashos *et al.*, 1998). In addition, caudate nucleus volume was directly linked to the 5-HTTLPR polymorphism (Hickie *et al.*, 2007). In this variation, the promoter region of the SERT gene exists in 2 alleles, a long and a short version, where the latter is associated with traits of depression (for review see Murphy *et al.* and Lesch *et al.* (Lesch and Gutknecht, 2005, Murphy *et al.*, 2004)). The shorter promoter region in s-carriers causes a lower expression of SERT, and has been shown to influence antidepressant outcome negatively in depressed patients (Ruhe *et al.*, 2008). In fact, Murphy *et al.* noted that SERT-HT mouse phenotypes would match up the closest with those observed in human SERT polymorphism (Murphy *et al.*, 2003). However no reduction in caudate-putamen could be observed in these mice either. Since the caudate and putamen are in fact merged in only one structure in rodents, compensatory mechanisms could have taken place so that no volume differences were detected in either SERT-KO or SERT-HT mice.

#### **3.6 Final conclusions.**

In this study, WT, SERT-KO and SERT-HT mice were compared for white matter differences using DTI. No significant differences were obtained when comparing WT to SERT-KO mice using DTI. Interestingly in SERT-HT mice the overall diffusivity as measured with the MD was generally decreased without affecting the anisotropy. In addition, SERT-HT mice are assumed to correspond more likely to human short-allele carriers of SERT (Murphy *et al.*, 2003). It appears illogical that SERT-HT would display altered water diffusion properties, while a more severe elevation of serotonin interfering with normal brain development in SERT-KO does not, however compensatory mechanisms may only be recruited in the full absence of SERT. DTI subtraction map analyses seemed not to give meaningful information either, as specific changes in tracts appeared to be very subtle. ROI analysis gave better insights because mean DTI parameter values were used while subtraction maps give only a visual impression of the difference

### Chapter 3 - DTI of the brain in mice deficient in SERT.

between groups within that slice investigated. More research would need to be conducted in order to support a role of the findings here presented in depression in terms of insufficient SERT expression, as it occurs in SERT-HT mice. Firstly, even though the volumes of the caudate-putamen and the hippocampus were not altered, their shapes might have been altered due to SERT dosage. Ongoing research from our collaborators at Columbia University is currently addressing these issues, see for instance Xu *et al.* (Xu *et al.*, 2007). A second consideration is that DTI measures the average water diffusion in one voxel ( $0.13 \times 0.13 \times 0.13 \text{ mm}^3$ ). This could mean that the resolution used here in the study might not be high enough to detect subtle changes in the SERT-KO group relative to WT animals. However the fact that DTI was able to detect differences between WT and SERT-HT opposes these raised issues of DTI sensitivity. Thirdly, the strain of mice used here are obviously not the best to assess white matter pathology with all the inherent problems these mice carry.

It is also worth mentioning, that the anterior and hippocampal commissures, as well as the internal capsule were selected from the DTI data set to perform ROI analyses on them as part of Sheonagh Law's BMedSci work. In her BMedSci project, she used a marker for phosphorylated neurofilament, SMI-31, to assess integrity of the axonal cytoskeleton in a subset of WT and SERT-KO mice that were used here for DTI analyses. Consistently, SMI-31 immunoreactivity was elevated in all tracts examined in SERT-KO mice, in case of the anterior commissure and internal capsule even significantly (data not shown). More disparity was observed in MBP immunoreactivity, a marker of compact myelin, where elevations were present in the anterior and hippocampal commissures, the former, which was significant (data not shown). This was our first attempt to characterise tissue integrity using immunohistochemistry and correlate this with DTI measures. In the next chapter this approach to characterising what changes in DTI parameters reflect at the level of the tissue has been developed by studying a model of demyelination using a combination of DTI and quantitative histopathology.

Chapter 4 - Investigating the structural correlates of DTI measures in the PMD mouse model of white matter pathology.

**Chapter 4 - Investigating the structural correlates of DTI measures in the PMD mouse model of white matter pathology.**

## **Chapter 4 - Investigating the structural correlates of DTI measures in the PMD mouse model of white matter pathology.**

### **Chapter 4 - Investigating the structural correlates of DTI measures in the PMD mouse model of white matter pathology.**

#### **4.1 Introduction.**

DTI can provide unique insights into a variety of neurological and psychiatric conditions through its capability of measuring water diffusion in the brain, in particular by measuring restricted diffusion as it occurs in white matter tracts. For example, Bester *et al.* showed that patients who presented an optic neuritis, which may be an early sign of multiple sclerosis, displayed reduced FA values in the splenium of the corpus callosum, and FA values reduced further only in those patients who went on to have their definitive diagnosis of multiple sclerosis (Bester *et al.*, 2008). DTI also proved to be capable of distinguishing between infiltrative glioblastoma multiforme and noninfiltrative brain metastases, thereby providing a more precise prognosis for patients with glioblastoma multiforme (Wang *et al.*, 2008). In the brains of low dose, short-term ecstasy users DTI was able to detect subtle white matter changes, as indicated by lower FA and increased MD values (de Win *et al.*, 2008). The usefulness and sensitivity of DTI to detect changes in white matter has also been explored in psychiatric conditions. Hoptman and colleagues were able to identify FA differences, i.e. a reduction in the anterior cingulate, in the brains of subjects with high genetic risk of developing schizophrenia, defined as having a first-degree and/or multiple second-degree relative diagnosed with schizophrenia, compared to healthy controls (Hoptman *et al.*, 2008). Application of DTI to age-related depression was demonstrated in a study performed by Alexopoulos *et al.*, where depressed patients that respond to antidepressants were compared to those who failed to do so. FA in frontal areas was significantly reduced in depressed non-responders compared to those that did respond to the SSRI escitalopram (Alexopoulos *et al.*, 2008).

Although DTI is being increasingly and successfully applied in clinical studies, of which some have been mentioned above, there is still minimal understanding of what changes in different DTI measures reflect at the tissue level. In the previous chapter (chapter 3, page 99), a DTI study was performed on the brains of mice deficient in SERT. It was hypothesized that a genetically engineered knockout of the SERT (SERT-KO), which induces behavioural signs of depression (Lira *et al.*, 2003), would be associated with abnormalities in the white matter. Possible abnormalities could have included aberrant trajectories and innervation patterns of axons, but also structural changes within white

## **Chapter 4 - Investigating the structural correlates of DTI measures in the PMD mouse model of white matter pathology.**

matter of the knockout mice. However, overall, we were not able to detect any differences in white matter as measured by DTI, which could be attributed to the SERT-KO, although it is possible that subtle changes in white matter structure may have been missed. While other groups have applied DTI to analyses of fixed mouse brain (Harms et al., 2006, Sun et al., 2003, Tyszkka et al., 2006, Verma et al., 2005), this was the first time the methodology had been examined using the 7T MRI scanner in Glasgow. As DTI of fixed brain was still a relatively novel technique, it was decided to apply it to a mouse model in which white matter structure was abnormal. By doing so we would be able to confirm that our methodology was able to detect white matter pathology.

In collaboration with Dr. Julia Edgar, we sought to apply our DTI methodology to a “positive control” mouse model in which there was some evidence that white matter structure is altered. In addition we also aimed to extract novel data about this mouse model using DTI. Dr. Edgar’s work is focused on the formation of myelin by oligodendrocytes and the dys- and demyelination that occur in response to mutations or alterations in genes encoding myelin proteins. Her research uses a murine model of PMD, which is an X-chromosome linked disease of central nervous system myelin that is due to mutations in the *Plp1* gene. Duplication of the *Plp1* gene region is the most common cause of PMD (Garbern, 2007). PMD is characterised by diffuse hypomyelination, has an early onset in life, and patients die prematurely (Johnson et al., 1991). Therefore, a valid animal model of PMD is a transgenic mouse strain overexpressing *Plp1* (line #72) (Readhead et al., 1994). It has been shown that this model of PMD has robust and reproducible demyelination in the optic nerve (Dr. J. M. Edgar, unpublished observation), however the nature and extent of myelin changes in the brain are unknown.

### **4.2 Aims of the study.**

- I. To test the ability of the DTI methodology applied in chapter 3 (page 98) to detect white matter changes in a mouse model of a myelin disorder in which brain white matter was predicted to be abnormal. The DTI methodology is described in detail in the material and methods chapter (chapter 2, page 39).
- II. To characterise the extent of DTI changes in the brains of PLPOVR mice in order to provide greater insight into the anatomical distribution of pathology in this model.

## **Chapter 4 - Investigating the structural correlates of DTI measures in the PMD mouse model of white matter pathology.**

- III. To examine the relationships between DTI measures and an extensive set of histological measures acquired from the PLPOVR mouse brains in Dr. Edgar's laboratory. Histological techniques are described in the material and methods chapter (chapter 2, page 48).

### **4.3 Material and methods.**

#### **Animals.**

PLPOVR animals were generated as previously described by Readhead *et al.* (#72 strain) (Readhead *et al.*, 1994), and bred at the animal facility at Glasgow University at a light/dark cycle of 12/12 h. Food and water was accessible *ad libitum*, and all experiments were carried out according to the guidelines laid out in the Animals Scientific Procedures Act under a project license from the UK Home Office and approved by the local ethical review panel. Tissue collection and preparation for DTI was performed using a protocol described by Tyszka *et al.* with slight modifications (Tyszka *et al.*, 2006). At P120, PLPOVR (n = 5, female) and control animals from the same in-bred colony (n = 5, female) were sacrificed by an overdose of CO<sub>2</sub>. Further tissue processing is described in the material and methods (section 2.1, page 40).

DTI image acquisition (section 2.1, page 41), and image analyses (section 2.1, page 42) are described in detail in the material and methods chapter. Histopathology was addressed in Dr. Edgar's laboratory, and a detailed protocol of the histology, immunohistochemistry, and EM methodology is given in the material and methods chapter (section 2.2, page 48).

### **4.4 Results.**

#### **4.4.1 DTI.**

##### **Individual parameter maps (FA, $\lambda_i$ , MD, and RD).**

Fig. 4-1 - Fig. 4-3 show representative coronal images at the level of the dorsal hippocampus from 1 individual WT and 1 PLPOVR mouse obtained after reconstruction of DTI datasets using the FSL software package. The FA images are shown for illustration of the images obtained from representative individual mice in both WT and PLPOVR groups.

**Chapter 4 - Investigating the structural correlates of DTI measures in the PMD mouse model of white matter pathology.**

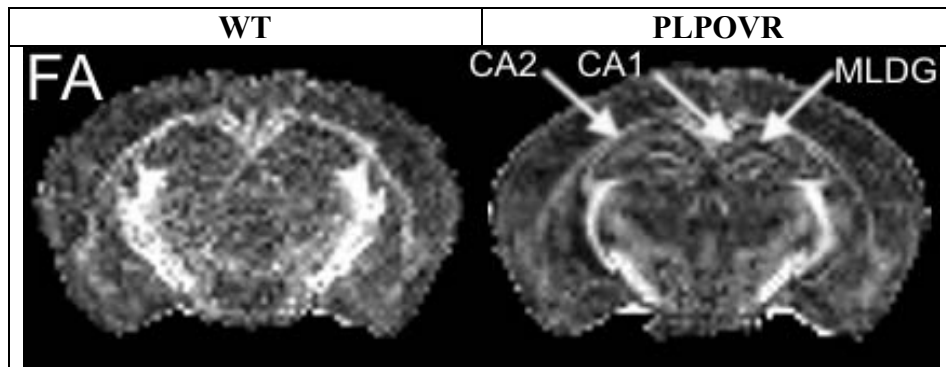


**Fig. 4-1. Representative slices of individual FA images suggest visual differences between groups.**

FA of the PLPOVR mouse shows higher intensities in hippocampal substructures (CA1, CA2) while lower FA appears to be present in the molecular layer of the dentate gyrus (MLDG) when compared to the WT mouse.

In the FA images, white matter tracts such as the corpus callosum and internal capsule appear bright in comparison to grey matter in the cerebral cortex both in WT and PLPOVR mice. Visual differences between WT and PLPOVR are not so obvious in the FA images (Fig. 4-1). The molecular layer of the dentate gyrus in PLPOVR mice displays lower anisotropy compared to WT, and hippocampal substructures (CA1, CA2) have gained higher anisotropy properties due to transgene expression. This is evident through lower, or higher intensities in these regions, respectively.

Maps of individual eigenvalue maps are shown in Fig. 4-2. In all eigenvalue images, PLPOVR show hyperintensities compared to WT in the corpus callosum, the cortex but also subcortical regions such as for instance the thalamus and hippocampal substructures (CA1, CA2, CA3). Thus this indicates widespread increase in water diffusion across the brain of PLPOVR mice.

**Chapter 4 - Investigating the structural correlates of DTI measures in the PMD mouse model of white matter pathology.**

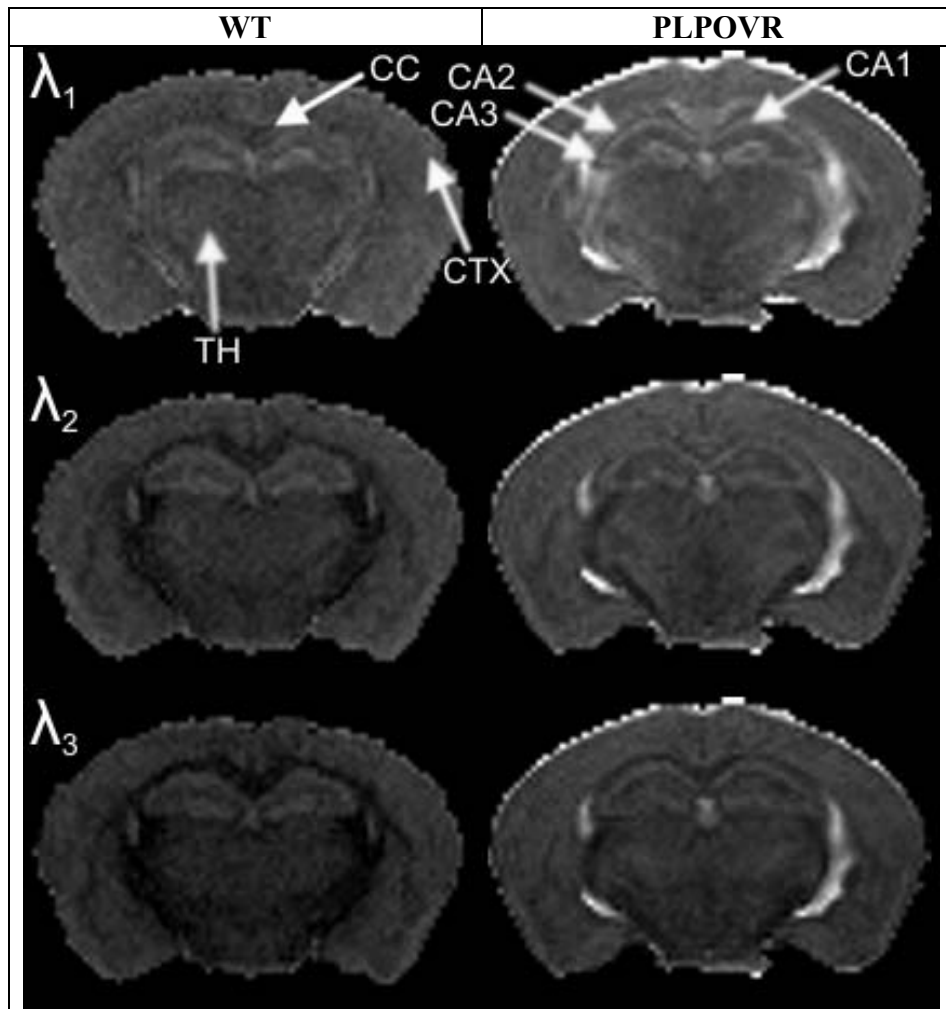


**Fig. 4-2. Representative slices of individual eigenvalue images suggest visual differences between groups.**

$\lambda_1$ , axial diffusivity.

$\lambda_2$ , perpendicular diffusion.

$\lambda_3$ , perpendicular diffusion.

As expected by definition, intensity decreases in the order  $\lambda_1 > \lambda_2 > \lambda_3$ . Compared to WT, PLPOVR mice display overall increased diffusion indicated by brighter eigenvalue images. In particular, the corpus callosum (CC), cortex (CTX), thalamus (TH), and substructures of the hippocampus (CA1, CA2, CA3), are affected as shown by arrows.

Maps of MD and RD derived from the eigenvalues are shown in Fig. 4-3. The images basically resemble those of the eigenvalue maps in such a way that PLPOVR generally show a signal hyperintensity in the corpus callosum, the cortex but also subcortical regions such as for instance the thalamus and hippocampal substructures (CA1, CA2, CA3) when compared to WT mice.

## Chapter 4 - Investigating the structural correlates of DTI measures in the PMD mouse model of white matter pathology.

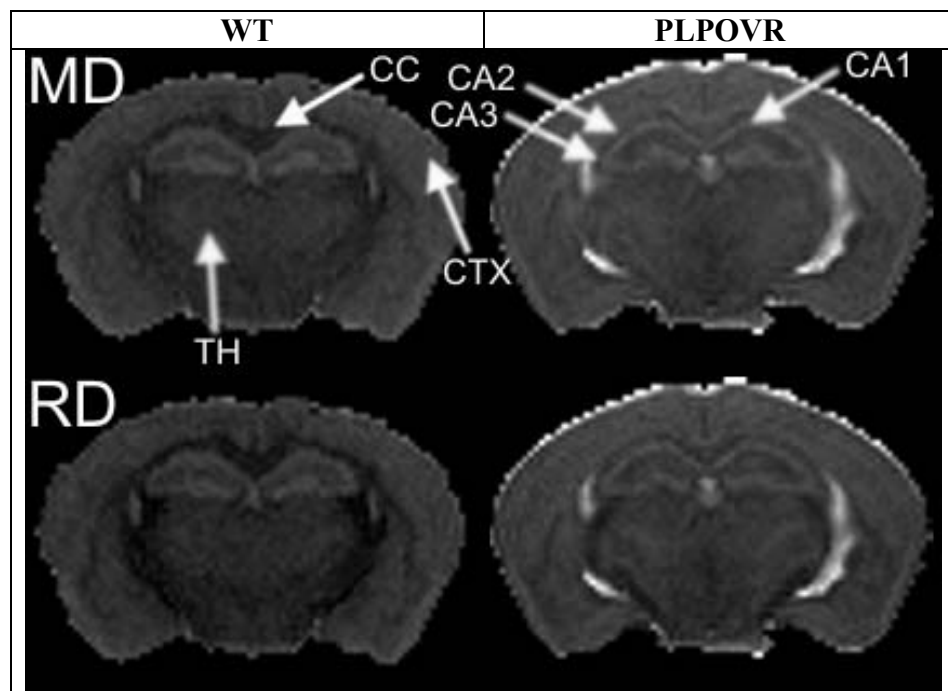


**Fig. 4-3. Representative slices of individual MD and RD images suggest visual differences between groups.**

Diffusion in RD is lower than MD. Compared to WT, PLPOVR mice display overall increased diffusion indicated by brighter parameter images. In particular, the corpus callosum (CC), cortex (CTX), thalamus (TH), and substructures of the hippocampus (CA1, CA2, CA3), are affected as shown by arrows.

### Subtraction map analyses.

Group averages of the WT, and the PLPOVR mice FA MD, RD and  $\lambda_i$  images were generated using the command line image calculator included in FSL. Subsequently subtraction images were calculated by subtracting the mean parameter maps (FA,  $\lambda_i$ , MD, and RD) of the PLPOVR animals from those of the WT. Colour-coding, and appropriate scale bars for the subtraction maps were generated using the ImageJ image processing and analysis software package. Fig. 4-4 - Fig. 4-7 illustrate the group average images and subtraction maps for different DTI parameters. In the colour-coded difference images, blue denotes the regions in which PLPOVR mice have higher values, and red where values are lower than those of WT. The FA difference image (Fig. 4-4) shows a loss of anisotropy, particularly in the corpus callosum, internal and external capsules, anterior commissure, as well as cerebellar white matter, in PLPOVR compared to WT mice. The reduction in FA in the PLPOVR mice implies structural impairments within these white matter tracts. There is also a diffuse, widespread reduction of FA in the grey matter of both genotypes compared to white matter, which reflects the disorganised arrangement of axons in grey matter. Over

#### **Chapter 4 - Investigating the structural correlates of DTI measures in the PMD mouse model of white matter pathology.**

and above, there is a further reduction in FA in the PLPOVR mice compared to WT, which probably reflects hypomyelination.

For all measures of water diffusion, i.e. the eigenvalues ( $\lambda_1$ ,  $\lambda_2$ , and  $\lambda_3$ , Fig. 4-5), MD (Fig. 4-6), and RD (Fig. 4-7), the white matter of PLPOVR animals show higher intensities, indicating greater water diffusion.

**Chapter 4 - Investigating the structural correlates of DTI measures in the PMD mouse model of white matter pathology.**

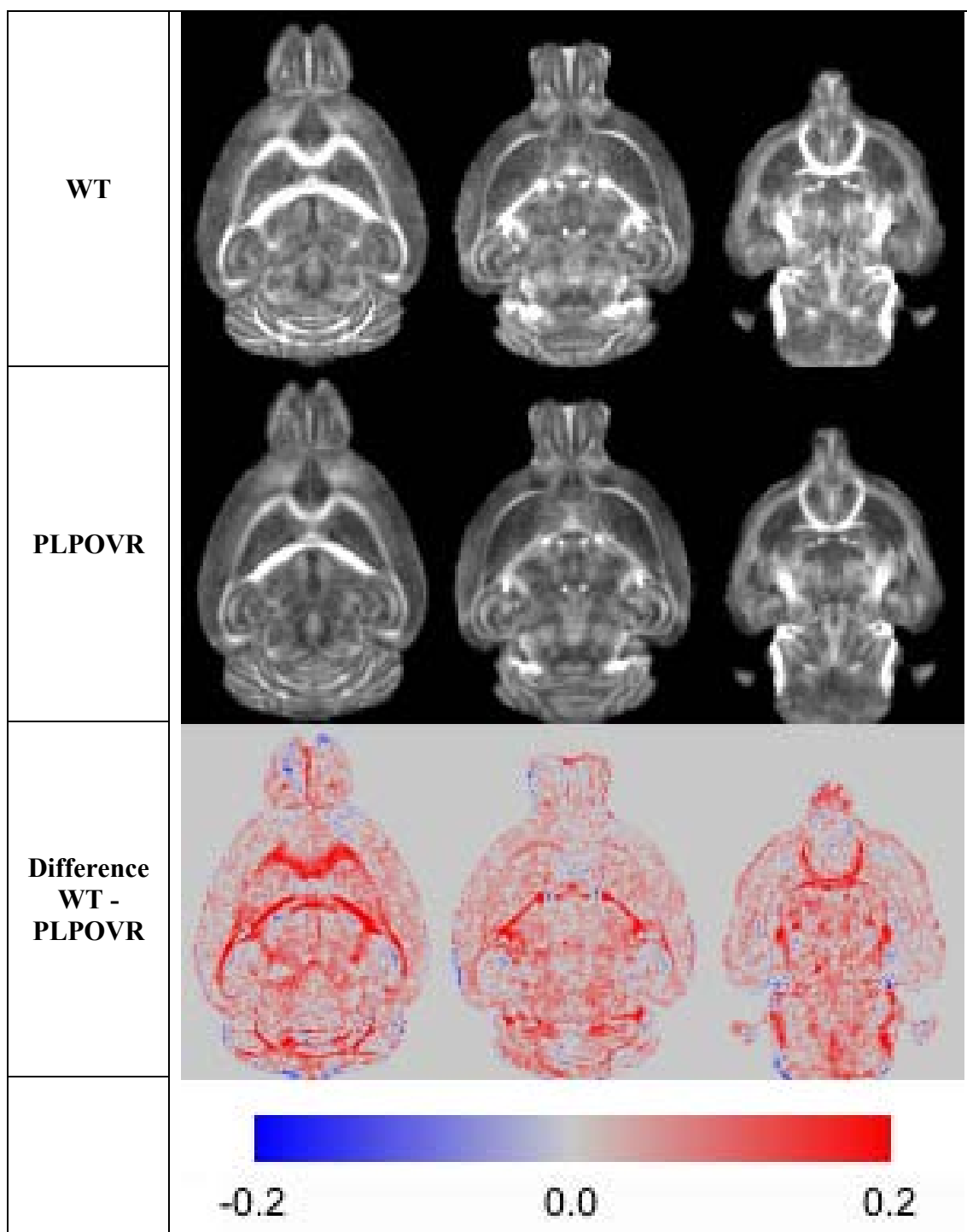


**Fig. 4-4. Representative slices of the subtraction map derived from coregistered and group-wise averaged FA images suggest large group differences between WT and PLPOVR mice.**

Units of measurement for FA are dimensionless. Scale bar: blue indicates where PLPOVR > WT; red indicates where WT > PLPOVR (n = 5 per group). FA values of PLPOVR animals are reduced in the corpus callosum, internal and external capsules, anterior commissure and in the cerebellum.

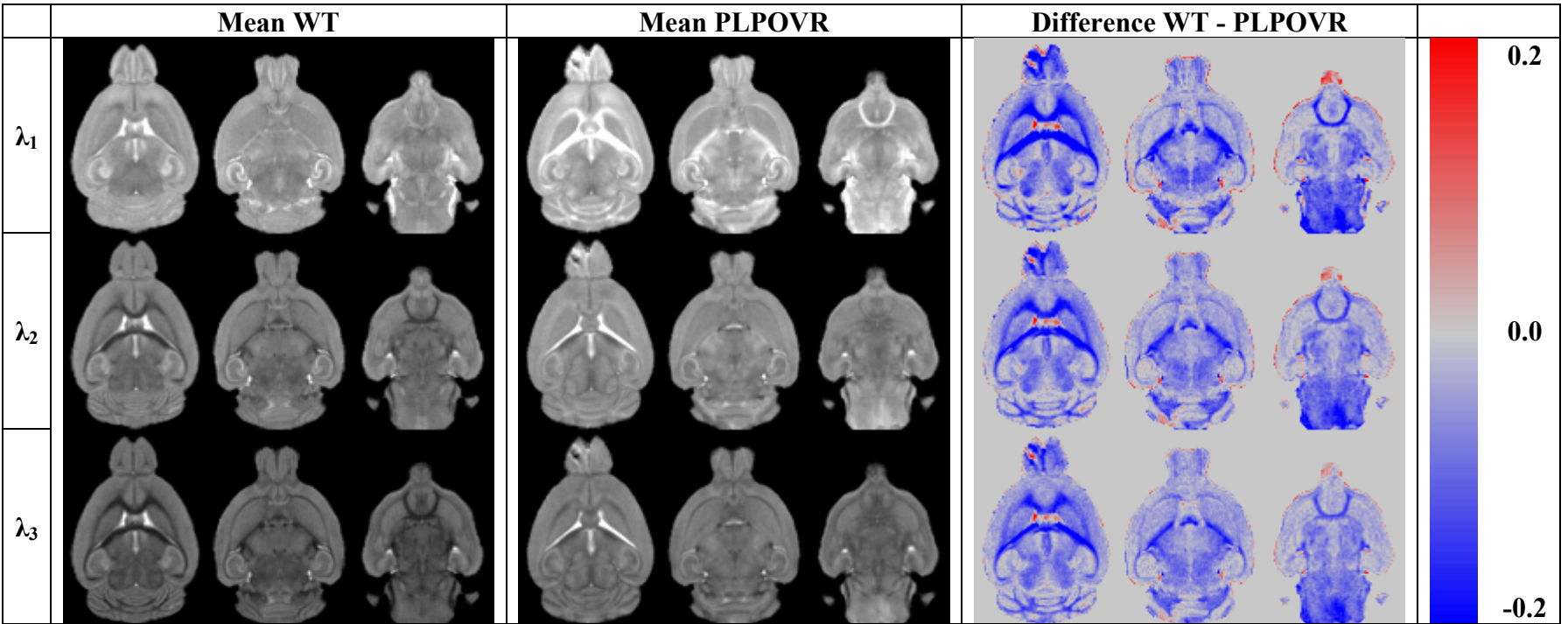


**Fig. 4-5. Representative slices of the subtraction map derived from coregistered and group-wise averaged eigenvalue images suggest large widespread differences between WT and PLPOVR mice.**

Units of measurement are  $\mu\text{m}^2/\text{ms}$ .

Scale bar: blue indicates where PLPOVR > WT; red indicates where WT > PLPOVR (n = 5 per group).

For all eigenvalue maps  $\lambda_1$ ,  $\lambda_2$ , and  $\lambda_3$ , PLPOVR animals show increased diffusivity in corpus callosum, internal and external capsules, anterior commissure as well as in the cerebellum.

**Chapter 4 - Investigating the structural correlates of DTI measures in the PMD mouse model of white matter pathology.**

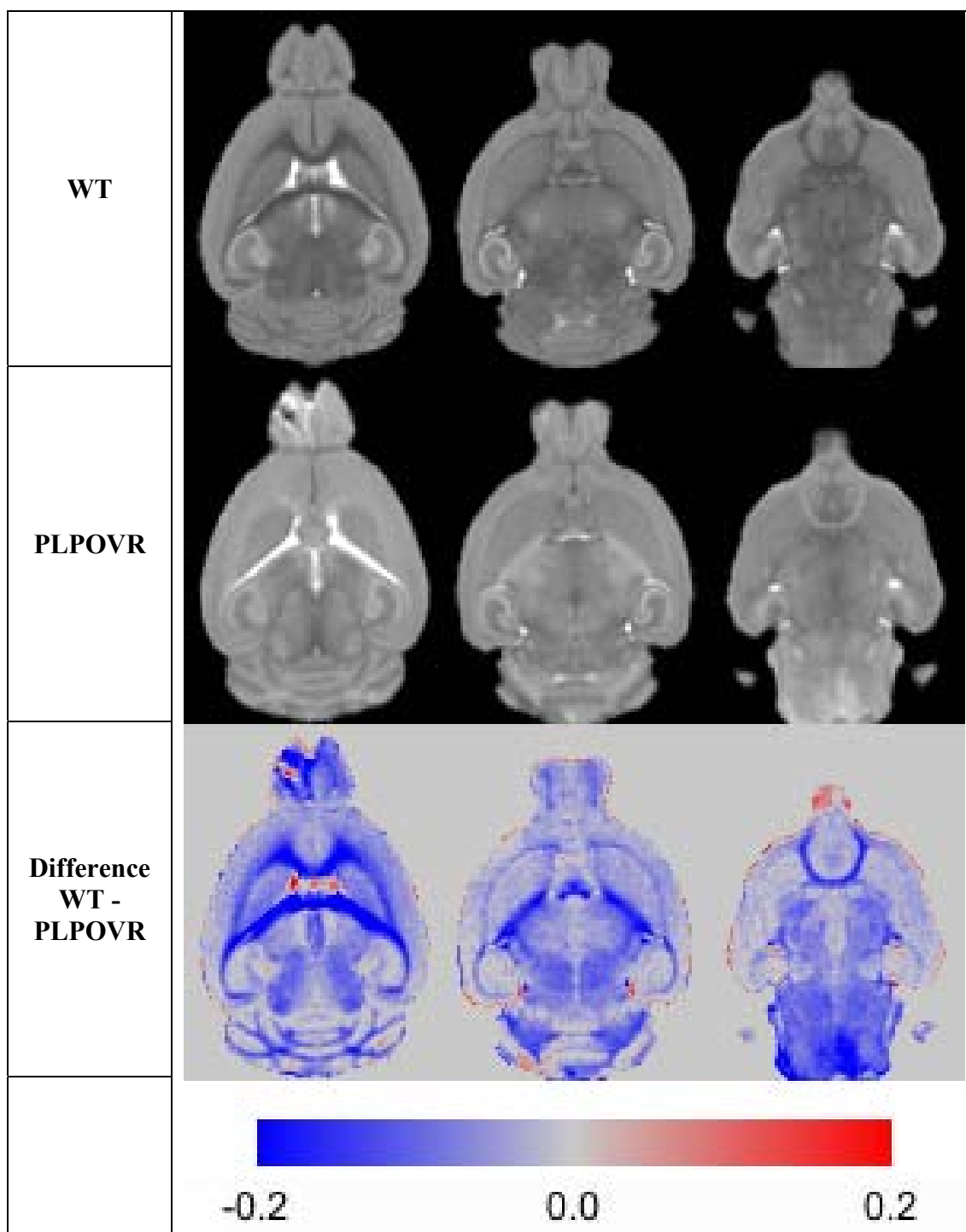


**Fig. 4-6. Representative slices of the subtraction map derived from coregistered and group-wise averaged MD images suggest large widespread differences between WT and PLPOVR mice.**

Units of measurement are  $\mu\text{m}^2/\text{ms}$ . Scale bar: blue indicates where PLPOVR > WT; red indicates where WT > PLPOVR (n = 5 per group). PLPOVR animals show increased MD in corpus callosum, internal and external capsules, anterior commissure as well as in the cerebellum.

**Chapter 4 - Investigating the structural correlates of DTI measures in the PMD mouse model of white matter pathology.**

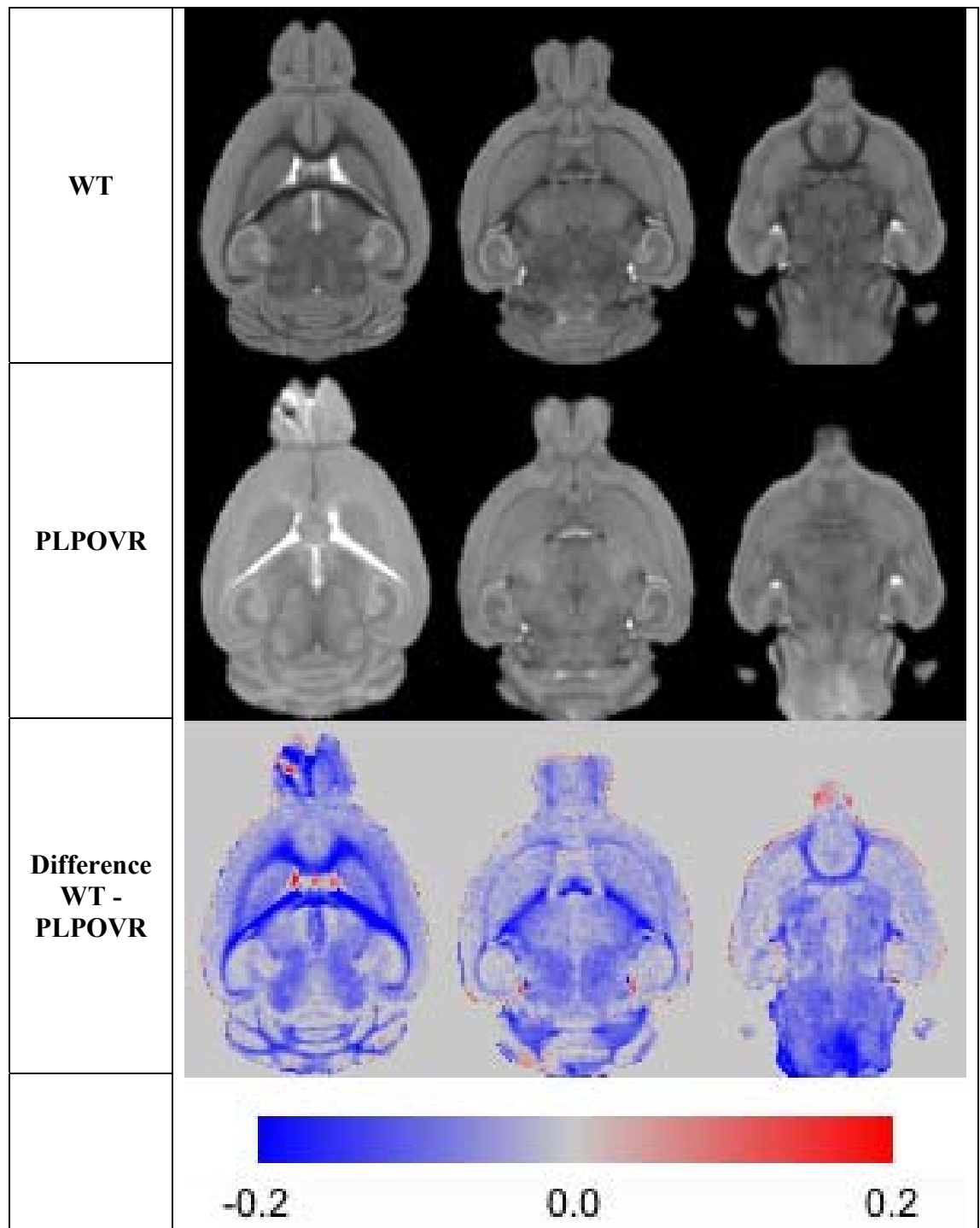


**Fig. 4-7. Representative slices of the subtraction map derived from coregistered and group-wise averaged RD images suggest large widespread differences between WT and PLPOVR mice.**

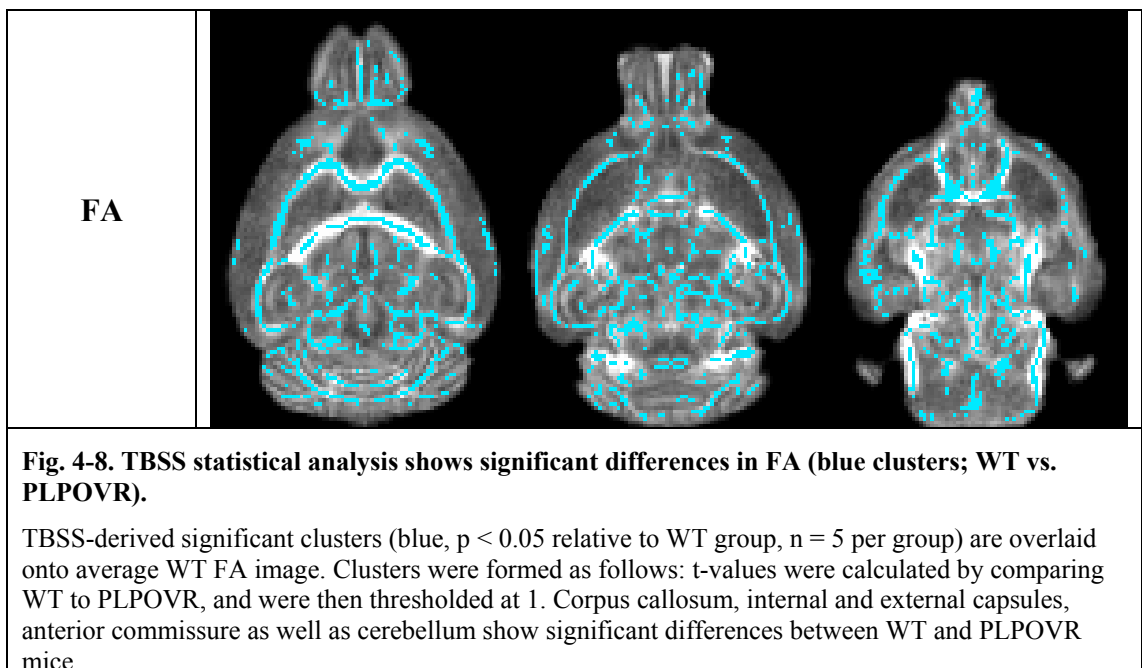
Units of measurement are  $\mu\text{m}^2/\text{ms}$ . Scale bar: blue indicates where PLPOVR > WT; red indicates where WT > PLPOVR (n = 5 per group). PLPOVR animals show increased diffusivity in corpus callosum, internal and external capsules, anterior commissure as well as in the cerebellum.

**Statistical analyses of DTI parameter maps.**

Visual inspection of the subtraction maps revealed clear differences between WT and PLPOVR mice. In order to identify the anatomical distribution of group differences a TBSS analysis was performed to obtain statistical significance. The cluster defined in blue

## Chapter 4 - Investigating the structural correlates of DTI measures in the PMD mouse model of white matter pathology.

showing the statistically significant differences between WT and PLPOVR (clusters were formed as follows: t-values were calculated by comparing WT to PLPOVR, and were then thresholded at 1) derived from the group-wise statistical analysis of the individual brains is superimposed onto mean WT DTI parameter maps shown in Fig. 4-8 - Fig. 4-10. The spatial distribution of the statistically significant clusters resembles the white matter regions identified in the difference maps (Fig. 4-4 - Fig. 4-7). There is also striking similarity in the regional distribution of statistically significant differences in the DTI parameters examined (FA,  $\lambda_i$ , MD, and RD). Statistically significant differences between WT and PLPOVR were detected in the corpus callosum, external capsule, hippocampal fimbria, internal capsule, anterior commissure, and cerebral peduncle / spinal trigeminal tract for all DTI parameters examined. Overall the data demonstrate that there is an anatomically widespread loss of anisotropy and an increase in water diffusion in the PLPOVR mice compared to WT.



**Chapter 4 - Investigating the structural correlates of DTI measures in the PMD mouse model of white matter pathology.**

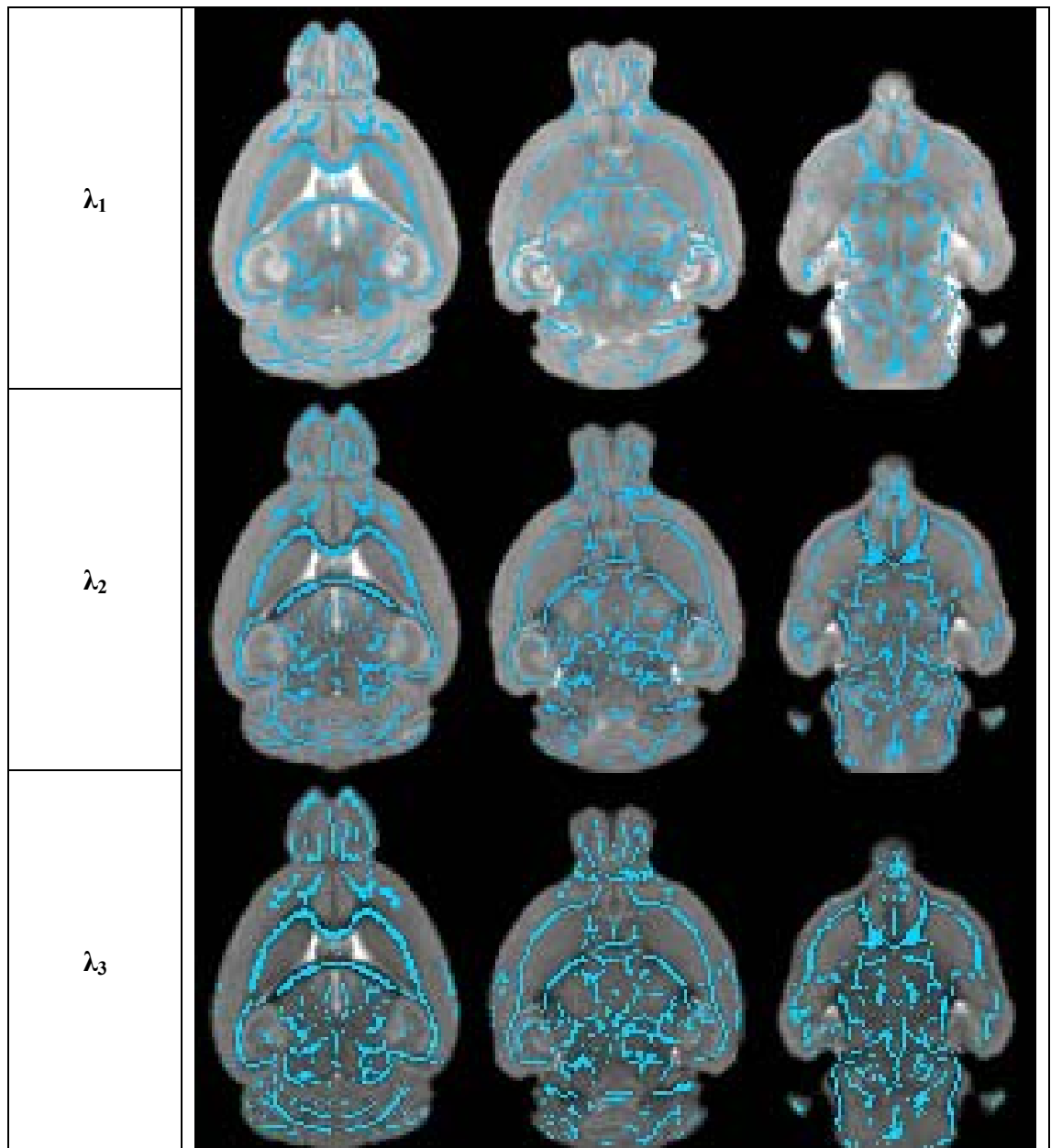
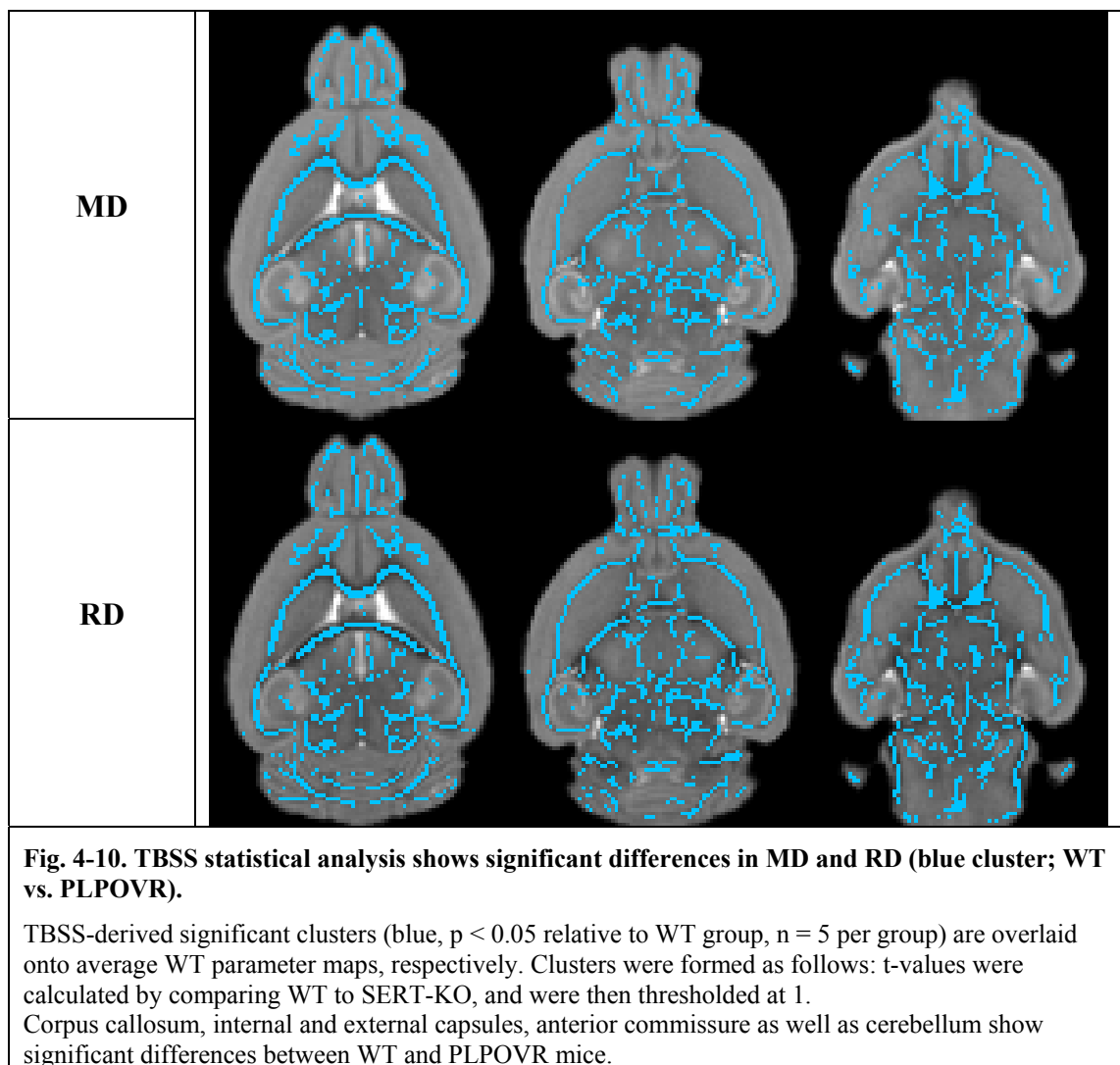


**Fig. 4-9. TBSS statistical analysis shows significant differences in all 3 eigenvalues (blue clusters; WT vs. PLPOVR).**

TBSS-derived significant cluster (blue,  $p < 0.05$  relative to WT group,  $n = 5$  per group) are overlaid onto average WT parameter maps, respectively. Clusters were formed as follows: t-values were calculated by comparing WT to SERT-KO, and were then thresholded at 1.

Corpus callosum, internal and external capsules, anterior commissure as well as cerebellum show significant differences between WT and PLPOVR mice.

## Chapter 4 - Investigating the structural correlates of DTI measures in the PMD mouse model of white matter pathology.



### ROI analysis of DTI parameter maps (FA, $\lambda_i$ , MD, and RD).

Further to the TBSS analysis, a ROI-approach was employed in order to assess the magnitude of change, and subsequently correlate the DTI parameters to histology data. Selected white matter tracts, i.e. the anterior commissure, the corpus callosum, and the hippocampal fimbria, were isolated bilaterally on 3 levels that could subsequently easily be analyzed on EM images as the fibres run perpendicular to the cutting plane. The Bregma levels 1.10 mm, 0.14 mm and -1.46 mm were identified on the individual coregistered FA images (Fig. 4-11). All references to Bregma coordinates in this chapter refer to those defined by Paxinos *et al.* (Paxinos and Franklin, 2001).

## Chapter 4 - Investigating the structural correlates of DTI measures in the PMD mouse model of white matter pathology.

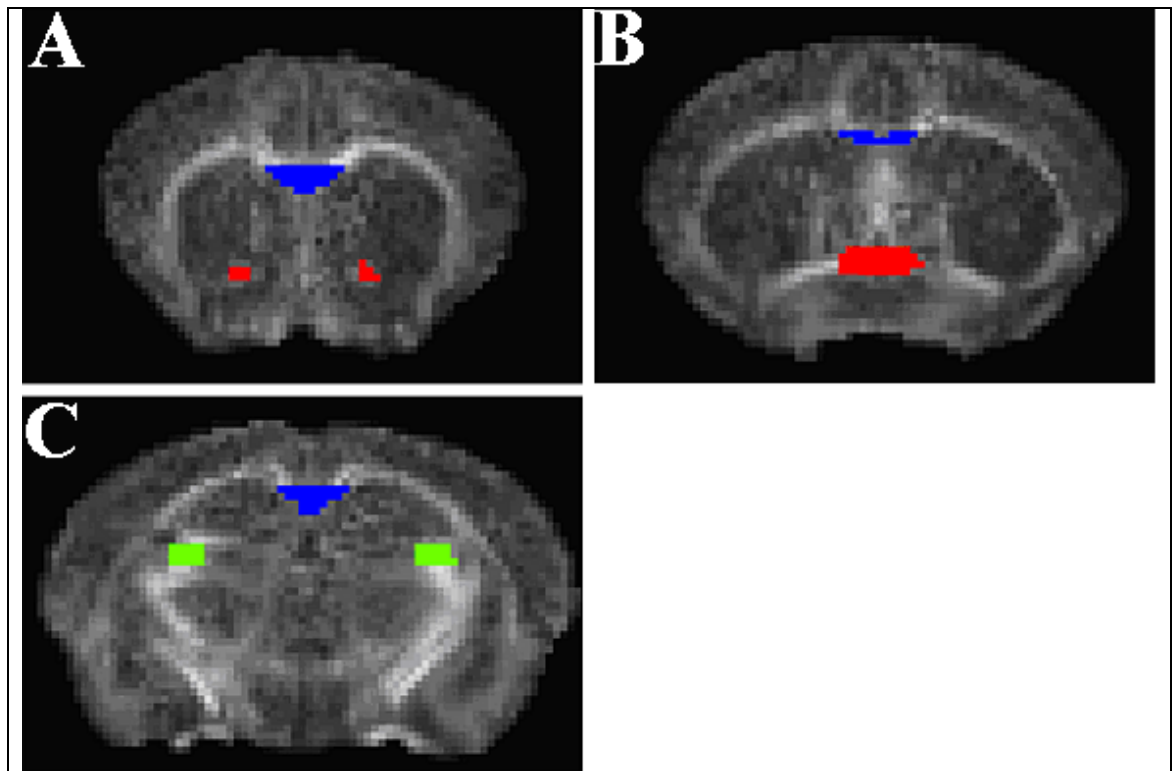


**Fig. 4-11. Defining ROIs on individual coregistered FA images.**

ROIs were defined on three different slices of individual coregistered FA images, and subsequently overlaid onto the other DTI parameter maps ( $\lambda_i$ , MD, and RD) for extraction of the respective values. Measurements were repeated 3 times on different days and the measures for each parameter were then averaged.

A: Bregma 1.10 mm.

B: Bregma 0.14 mm.

C: Bregma -1.46 mm.

ROIs:

Blue: corpus callosum.

Red: anterior commissure.

Green: hippocampal fimbria.

Slices A, B, C were defined using the mouse atlas of Paxinos *et al.* (Paxinos and Franklin, 2001).

The rater, i.e. the author of this thesis, was unaware of the identity of the animals until ROI data were extracted. The ROI masks derived from the FA images were subsequently superimposed onto the other parameter maps ( $\lambda_i$ , MD, and RD) to extract the respective mean values. To assess repeatability of the delineations, the ROIs were defined on the FA images on three individual occasions, respectively and the mean of these individual measures was taken for each of the DTI parameters extracted for statistical analysis.

FA values in all ROIs examined were significantly lower in PLPOVR animals compared to controls indicating a loss of anisotropy in the mutant mice. The least affected region was the hippocampal fimbria (Bregma -1.46 mm) where FA was 13 % lower in PLPOVR compared to WT (Fig. 4-12) while the corpus callosum (Bregma 0.14 mm) was the most

#### **Chapter 4 - Investigating the structural correlates of DTI measures in the PMD mouse model of white matter pathology.**

affected region, FA being 26 % lower in the mutant mice (Fig. 4-12). Thus, the loss of white matter anisotropy associated with overexpression of *Plp1* appeared to be greatest in the corpus callosum.

In all of the ROIs examined, as expected by definition, the eigenvalues decrease in the order  $\lambda_1 > \lambda_2 > \lambda_3$ . In PLPOVR, all three eigenvalues are significantly higher than in the WT mice in all of the ROIs examined. The minimum relative difference between groups for  $\lambda_1$  is an increase of 31 % in the anterior commissure, and the maximum is an increase of 54 % in the corpus callosum (both at Bregma 1.10 mm, Fig. 4-13). For  $\lambda_2$  the minimum relative group differences are a 53 % increase in the anterior commissure and the maximal increase was 91 % in the corpus callosum, both at Bregma 0.14 mm (Fig. 4-14). For  $\lambda_3$  the minimum relative group difference was an increase of 82 % in the anterior commissure, and the maximal relative differences was 108 % in the corpus callosum both at Bregma 1.10 mm (Fig. 4-15). Therefore the greatest difference between WT and PLPOVR was apparent in  $\lambda_3$ .

As predicted, MD values are higher than RD values. The smallest relative group difference in MD was an increase of 46 % in the anterior commissure (Bregma 1.10 mm, Fig. 4-16), and the highest relative difference was in the corpus callosum at Bregma 0.14 mm (72 %, Fig. 4-16). Finally, the lowest relative difference in RD (66 %, Fig. 4-17) was in the anterior commissure at Bregma 1.10 mm, and the highest relative difference (90 %, Fig. 4-17) was in the corpus callosum at Bregma 0.14 mm. These data suggest that for the water diffusion sensitive measures ( $\lambda_1$ ,  $\lambda_2$ ,  $\lambda_3$ , MD, and RD) the anterior commissure is the least affected white matter tract, whereas the corpus callosum contains the most compromised fibres. The water diffusion sensitive measures seem to be more sensitive in detecting differences between WT and PLPOVR compared to the FA index.

**Chapter 4 - Investigating the structural correlates of DTI measures in the PMD mouse model of white matter pathology.**

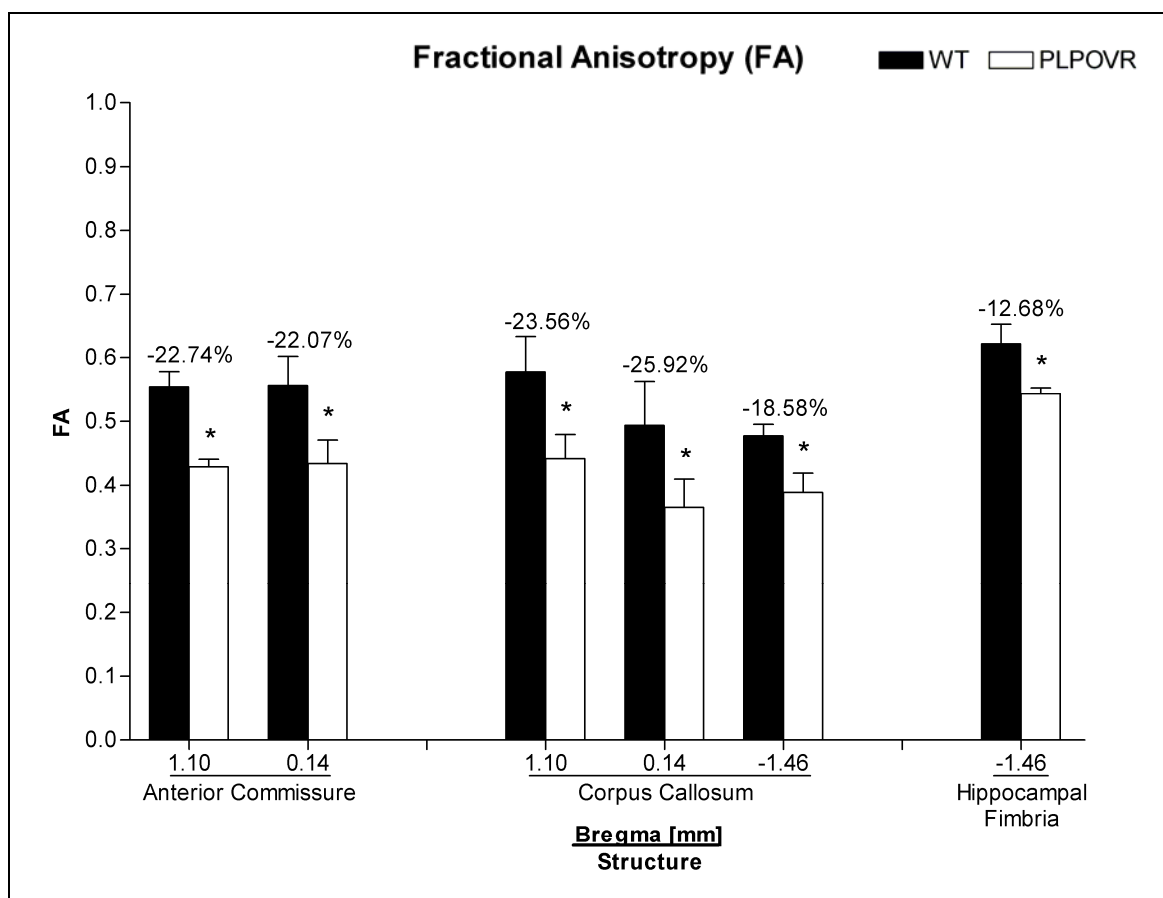


**Fig. 4-12. FA is reduced in all selected white matter tracts of PLPOVR mice.**

Each bar graph of an individual structure is organized from anterior to posterior. Data are mean  $\pm$  SD for n = 5 per group. Units of measurement are dimensionless. Two-tailed Mann-Whitney U, \*p < 0.05 relative to WT group. Relative differences are shown over bars, where  $(PLPOVR - WT)/(WT) \times 100\%$ .

All structures, at all levels examined show a significant reduction in FA in PLPOVR mice.

**Chapter 4 - Investigating the structural correlates of DTI measures in the PMD mouse model of white matter pathology.**

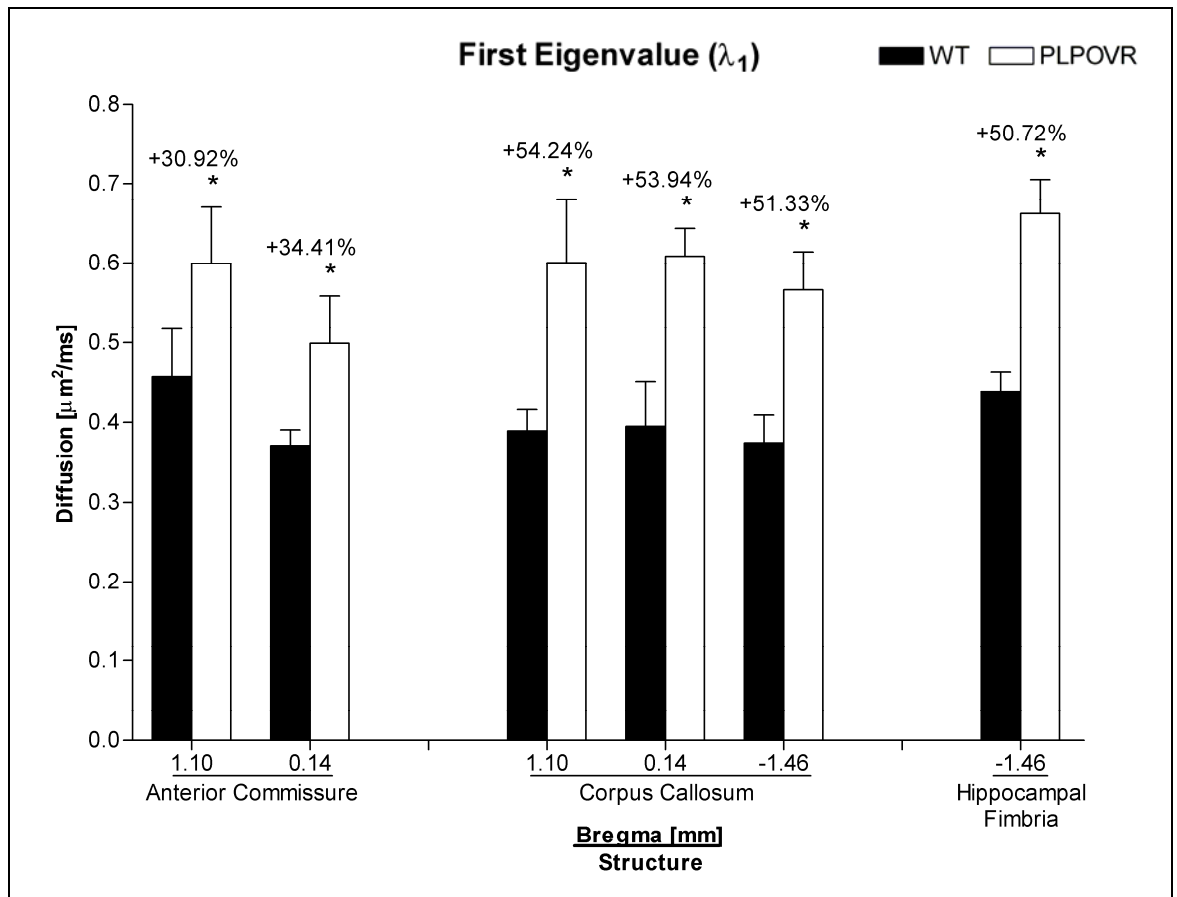


**Fig. 4-13.  $\lambda_1$  is increased in all selected white matter tracts of PLPOVR mice.**

Each bar graph of an individual structure is organized from anterior to posterior. Data are mean  $\pm$  SD for n = 5 per group. Units of measurement are  $\mu\text{m}^2/\text{ms}$ . Two-tailed Mann-Whitney U, \*p < 0.05 relative to WT group. Relative differences are shown over bars, where (PLPOVR - WT)/(WT)\*100 %.

All structures, at all levels examined show a significant increase in  $\lambda_1$  in PLPOVR mice.

**Chapter 4 - Investigating the structural correlates of DTI measures in the PMD mouse model of white matter pathology.**

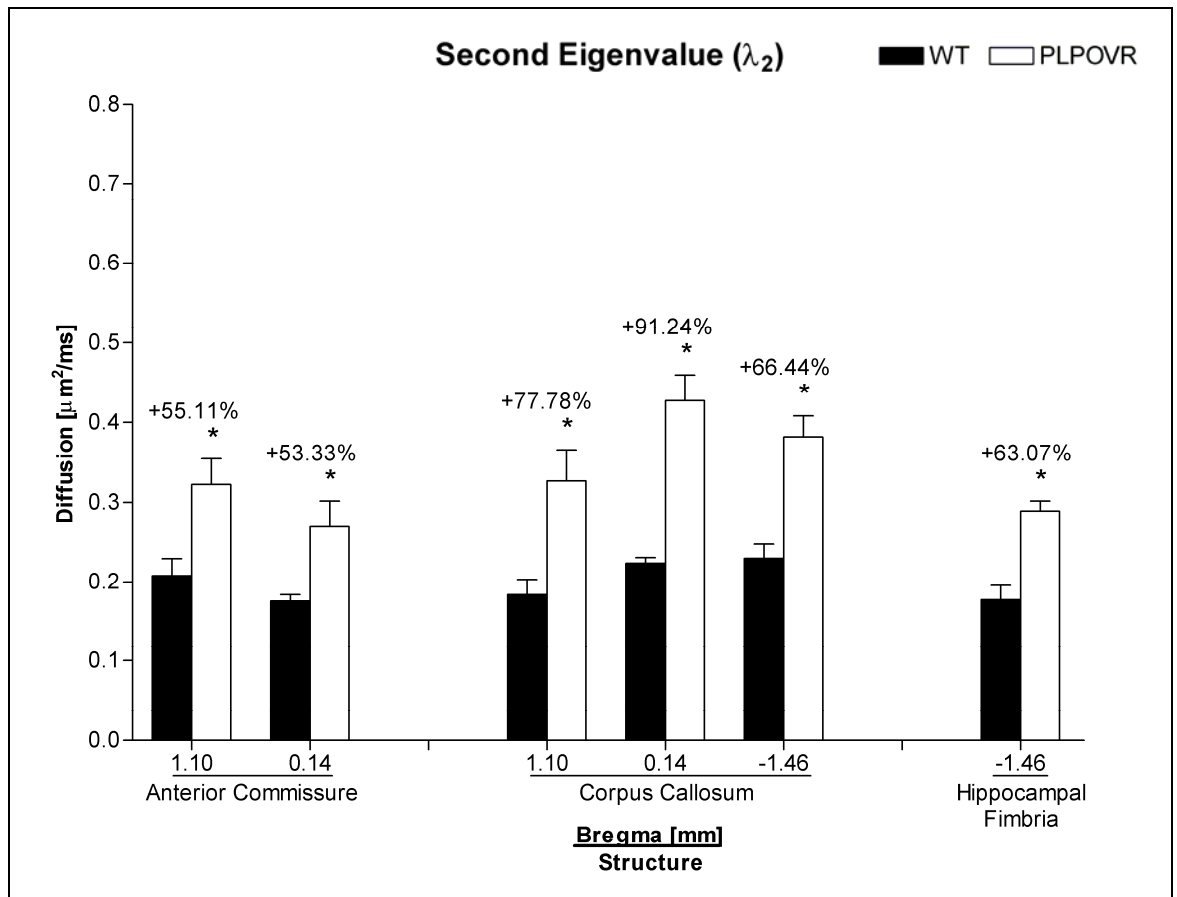


**Fig. 4-14.  $\lambda_2$  is increased in all selected white matter tracts of PLPOVR mice.**

Each bar graph of an individual structure is organized from anterior to posterior. Data are mean  $\pm$  SD for n = 5 per group. Units of measurement are  $\mu\text{m}^2/\text{ms}$ . Two-tailed Mann-Whitney U, \*p < 0.05 relative to WT group. Relative differences are shown over bars, where (PLPOVR - WT)/(WT)\*100 %.

All structures, at all levels examined show a significant increase in  $\lambda_2$  in PLPOVR mice.

**Chapter 4 - Investigating the structural correlates of DTI measures in the PMD mouse model of white matter pathology.**

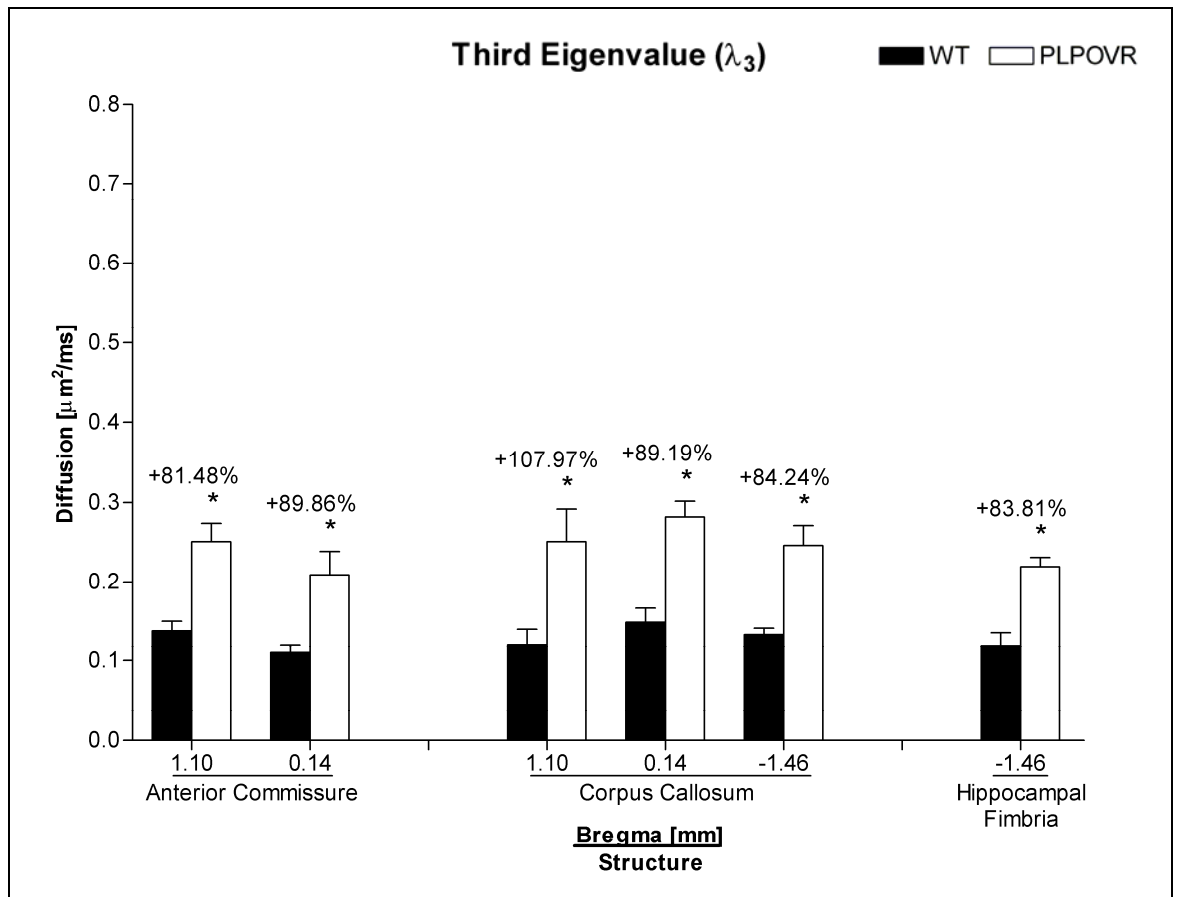


**Fig. 4-15.  $\lambda_3$  is increased in all selected white matter tracts of PLPOVR mice.**

Each bar graph of an individual structure is organized from anterior to posterior. Data are mean  $\pm$  SD for n = 5 per group. Units of measurement are  $\mu\text{m}^2/\text{ms}$ . Two-tailed Mann-Whitney U, \*p < 0.05 relative to WT group. Relative differences are shown over bars, where (PLPOVR - WT)/(WT)\*100 %.

All structures, at all levels examined show a significant increase in  $\lambda_3$  in PLPOVR mice.

**Chapter 4 - Investigating the structural correlates of DTI measures in the PMD mouse model of white matter pathology.**

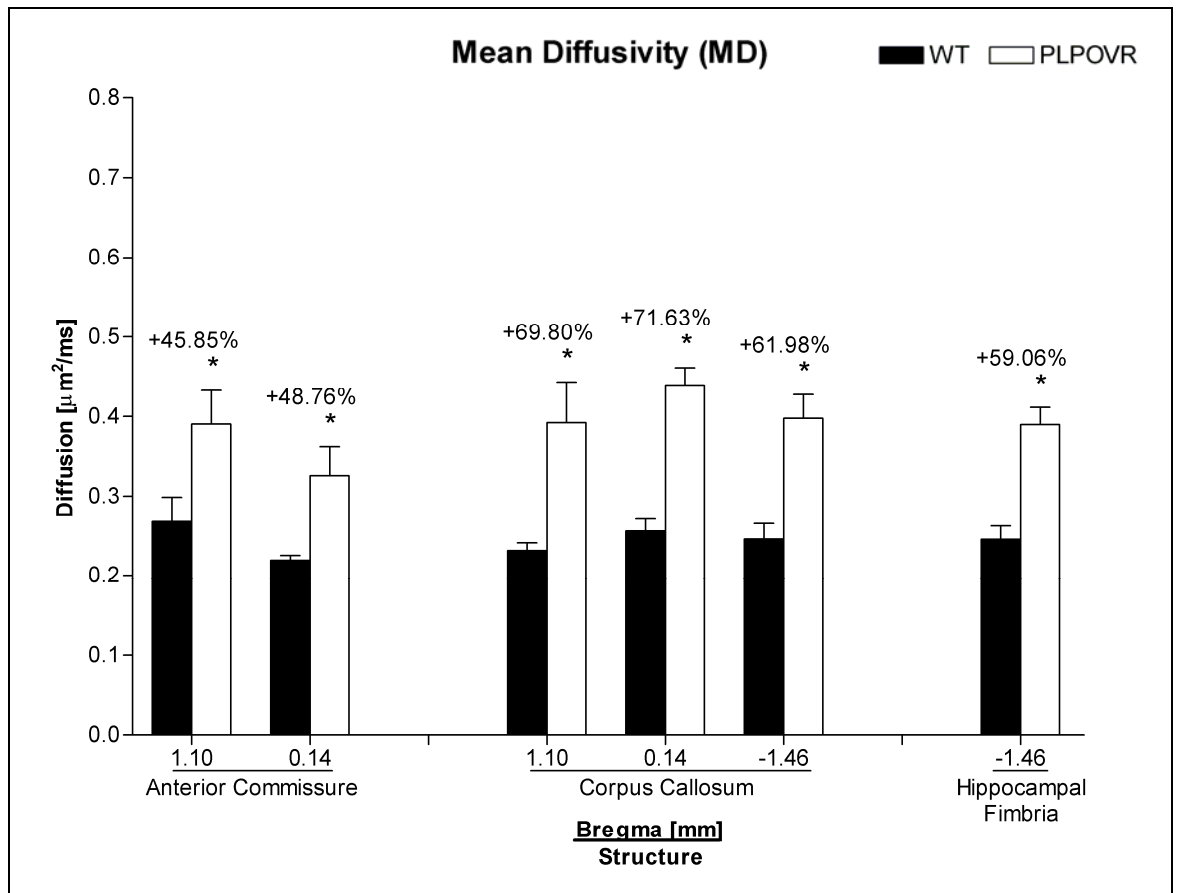


**Fig. 4-16. MD is increased in all selected white matter tracts of PLPOVR mice.**

Each bar graph of an individual structure is organized from anterior to posterior. Data are mean  $\pm$  SD for n = 5 per group. Units of measurement are  $\mu\text{m}^2/\text{ms}$ . Two-tailed Mann-Whitney U, \*p < 0.05 relative to WT group. Relative differences are shown over bars, where  $(\text{PLPOVR} - \text{WT})/(\text{WT}) * 100 \%$ .

All structures, at all levels examined show a significant increase in MD in PLPOVR mice.

**Chapter 4 - Investigating the structural correlates of DTI measures in the PMD mouse model of white matter pathology.**

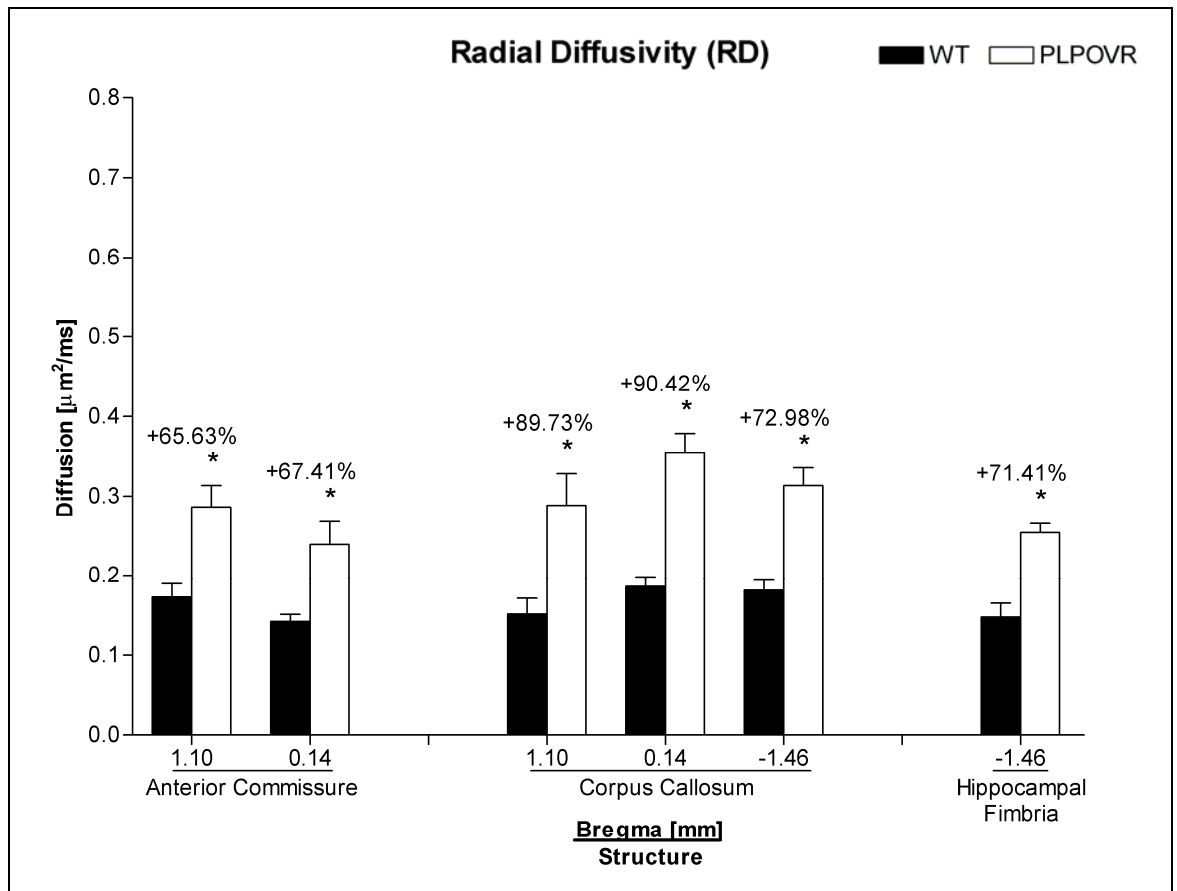


**Fig. 4-17. RD is increased in all selected white matter tracts of PLPOVR mice.**

Each bar graph of an individual structure is organized from anterior to posterior. Data are mean  $\pm$  SD for  $n = 5$  per group. Units of measurement are  $\mu\text{m}^2/\text{ms}$ . Two-tailed Mann-Whitney U, \* $p < 0.05$  relative to WT group. Relative differences are shown over bars, where  $(\text{PLPOVR} - \text{WT})/(\text{WT}) * 100\%$ .

All structures, at all levels examined show a significant increase in RD in PLPOVR mice.

#### 4.4.2 Structural analysis.

##### Volumetry of the whole brain.

For brain volume calculation, the mask generated in section 2.1 (page 43) was analyzed using the MRICro MRI image viewer software. The number of voxels comprising the brain was calculated and then multiplied with the voxel dimensions to obtain the brain volume, i.e.  $0.13 \text{ mm} \times 0.13 \text{ mm} \times 0.13 \text{ mm}$  ( $0.002197 \text{ mm}^3$ ). There was no significant difference in whole brain volumes between WT and PLPOVR animals. Fig. 4-18 depicts the volumes of the 2 groups and although no statistical difference was detected, there was a slight trend towards greater brain volume in PLPOVR mice ( $461.64 \pm 14.82 \text{ mm}^3$ ) compared to WT animals ( $440.27 \pm 16.2 \text{ mm}^3$ ).

## Chapter 4 - Investigating the structural correlates of DTI measures in the PMD mouse model of white matter pathology.

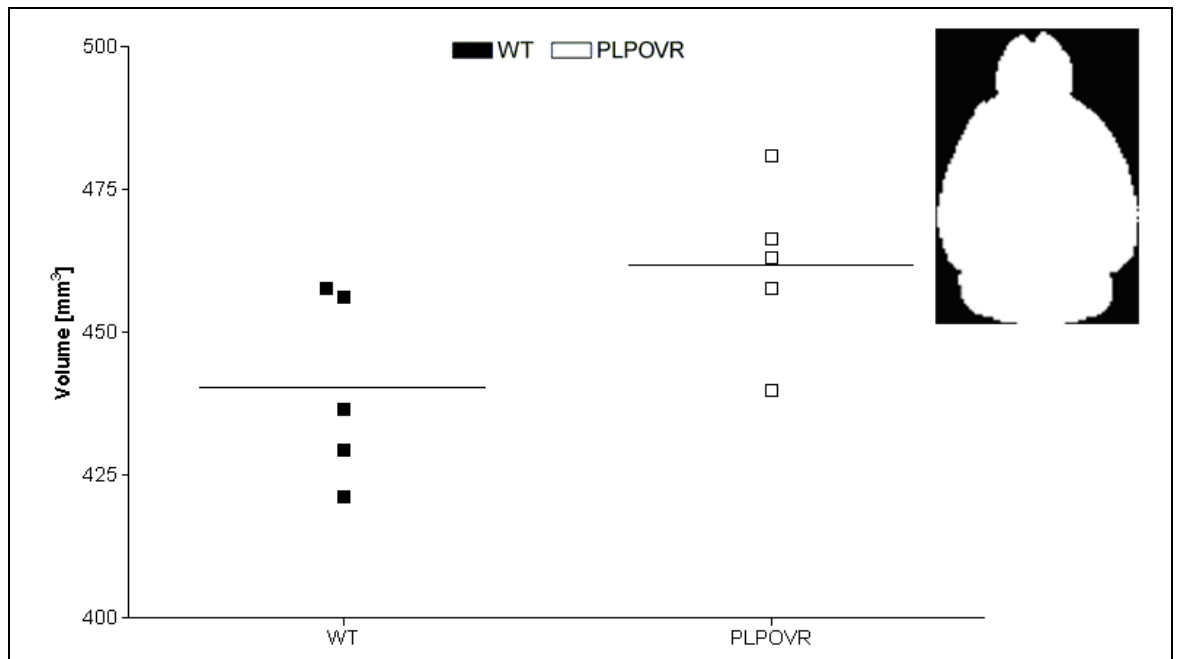


**Fig. 4-18. No group differences in whole brain volume were detected.**

Total brain volume was computed using binary masks of unregistered brains created for brain extraction (inset). Voxels with a value greater than 0 were counted and multiplied by the voxel dimensions. Units of measurement are mm<sup>3</sup>. Bar represents mean for n = 5 per group.

Two-tailed Mann-Whitney U ( $p < 0.05$ ) suggests a non-significant increase in brain volume in PLPOVR mice.

### 4.4.3 Analysis of brain tissue.

The DTI analyses demonstrated that in PLPOVR mice significant abnormalities were present in anatomically widespread areas including a number of major white matter tracts. In order to gain insight into what types of pathological features within the brain tissue were associated with the changes in DTI measures, the brains of the mice were examined by immunohistochemistry and histology. A range of markers for the major components of white matter: myelin; axons; astrocytes and cell nuclei were employed and based on the DTI results three ROIs within white matter tracts were selected for analysis. The tissue staining and quantitative analyses were performed by Jennifer Barrie, (and Fredrik Gruenenfelder for quantification of MBP and GFAP data) Applied Neurobiology Group, Glasgow University. In this results section a general description of the pathological changes is provided before the associations between DTI and pathological measures are presented. All the animals that underwent DTI scanning were processed for immunohistochemistry (n = 5 per group, see chapter 2, page 48 for processing details). For assessing tissue ultrastructure, a separate set of animals consisting of 3 WT and 4 PLPOVR mice were processed for EM (see chapter 2, page 50 for processing details).

## **Chapter 4 - Investigating the structural correlates of DTI measures in the PMD mouse model of white matter pathology.**

### **MBP immunohistochemistry – assessment of myelin damage.**

MBP is a major myelin protein and alterations in MBP immunoreactivity were predicted to reflect damage to the myelin sheath. Representative low power images of MBP immunostaining in WT and PLPOVR mice are shown in Fig. 4-19. The PLPOVR show widespread reductions in MBP immunoreactivity particularly evident in the cerebral cortex, corpus callosum, anterior commissure, septal area, and the area of the olfactory tubercle. In the higher power microscopic image of the corpus callosum a massive loss of MBP immunoreactivity is evident in PLPOVR compared to WT mice. Quantitative analysis of the area of MBP immunoreactivity within the defined ROIs demonstrates that this is significantly reduced in PLPOVR compared to WT mice in all regions examined (Fig. 4-20). Generally the anterior commissure is least affected by *Plp1* overexpression, with relative differences between the groups of approximately -47 %. Relative differences between PLPOVR and WT were greater in the corpus callosum (a loss of 53 - 70 % in PLPOVR) and maximal in the hippocampal fimbria (a loss of 87 % in PLPOVR). However this rank order in MBP immunoreactivity is based on rather marginal differences between corpus callosum and anterior commissure. For instance at Bregma 1.10 mm the relative difference for the anterior commissure is -47 %, whereas for the corpus callosum it is -53 %. Thus the reductions in MBP availability are comparable between these tracts. The most affected tract is the hippocampal fimbria, just over the corpus callosum as indicated above.

**Chapter 4 - Investigating the structural correlates of DTI measures in the PMD mouse model of white matter pathology.**

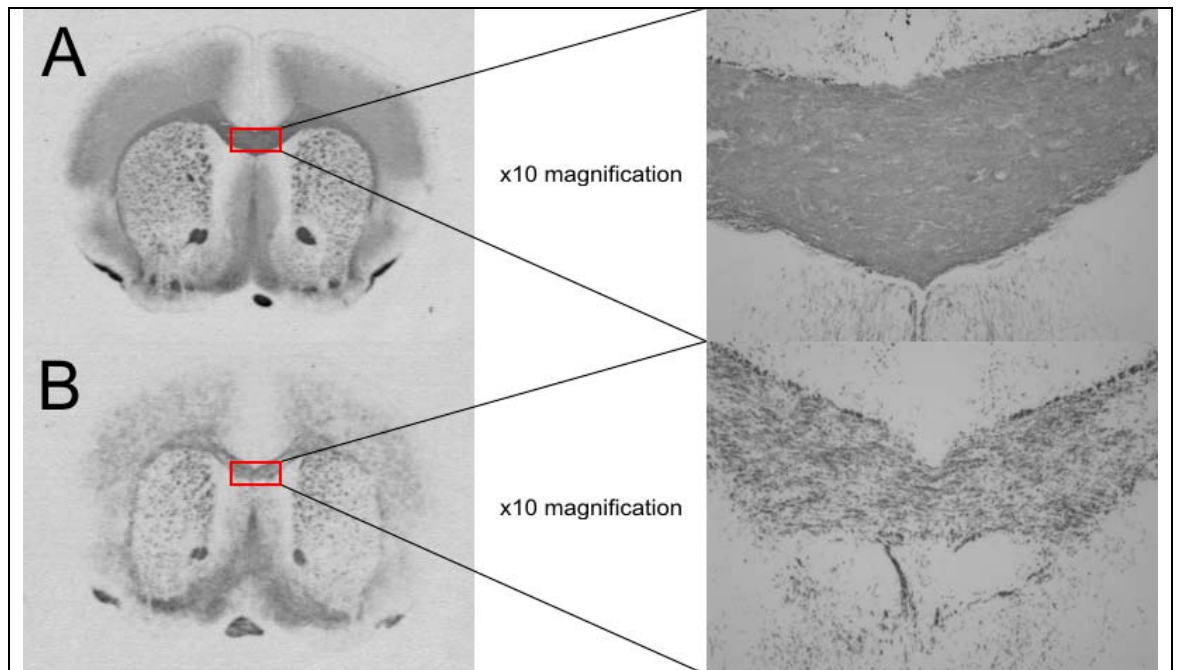


**Fig. 4-19. MBP immunoreactivity is reduced in the corpus callosum of PLPOVR mice.**

Left panels: representative images of sections at Bregma level 1.10 mm from one WT (A) and one PLPOVR (B) mouse stained with an antibody against MBP. There was widespread reduction in MBP immunostaining in the PLPOVR mice compared to WT.

Right panels: the red rectangle indicates the magnified area in the corpus callosum.

Immunostaining and quantification of MBP areas were performed by Jennifer Barrie and Fredrik Gruenfelder (quantification only), Applied Neurobiology Group, Glasgow University.

**Chapter 4 - Investigating the structural correlates of DTI measures in the PMD mouse model of white matter pathology.**

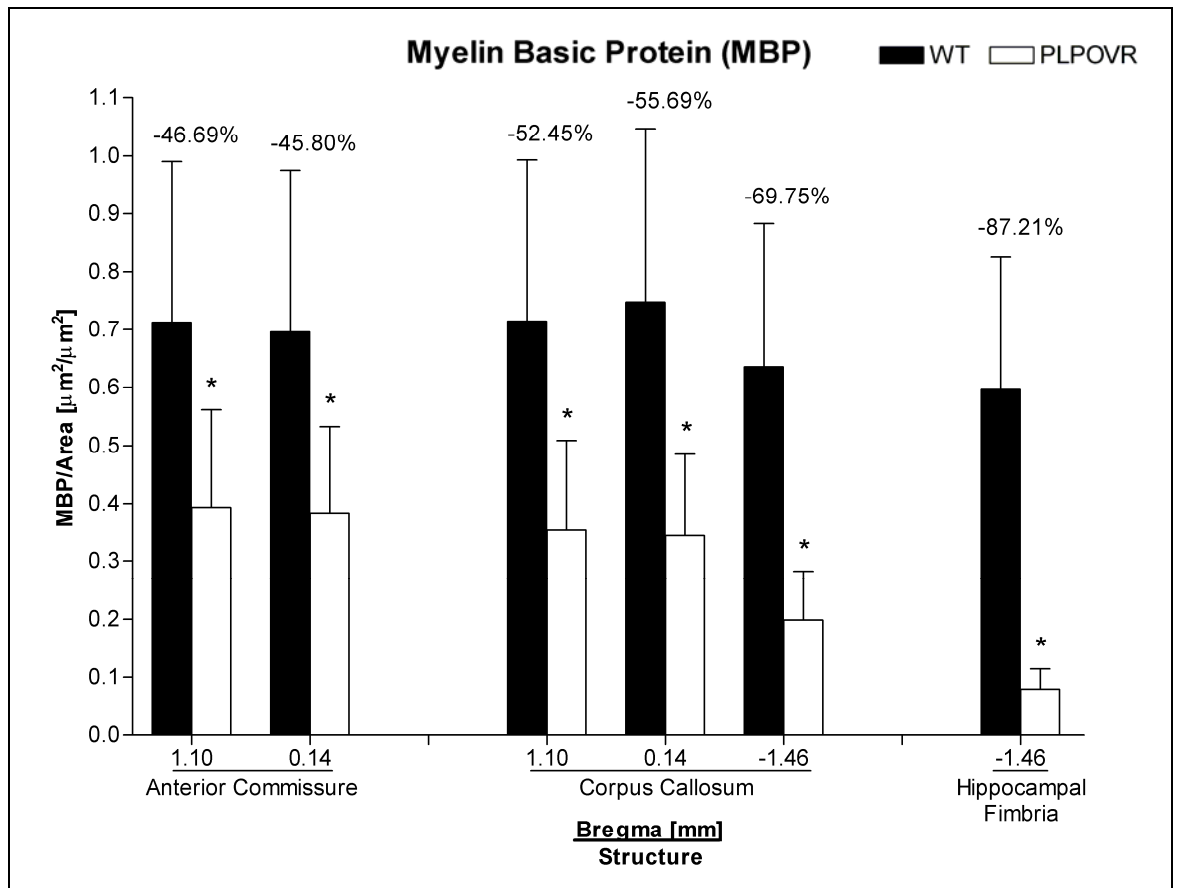


**Fig. 4-20. MBP immunoreactivity is reduced in all selected white matter tracts of PLPOVR mice.**

Each bar graph of an individual structure is organized from anterior to posterior. Data are mean  $\pm$  SD for  $n = 5$  per group. Units of measurement are: MBP/Area [ $\mu\text{m}^2/\mu\text{m}^2$ ]. Two-tailed Mann-Whitney U, \* $p < 0.05$  relative to WT group. Relative differences are shown over bars, where  $(\text{PLPOVR} - \text{WT})/(\text{WT}) * 100\%$ .

All structures, at all levels examined show a significant reduction in MBP immunostaining in PLPOVR overexpressing mice.

Immunostaining and quantification of MBP areas were performed by Jennifer Barrie and Fredrik Gruenfelder (quantification only), Applied Neurobiology Group, Glasgow University.

**APP immunohistochemistry – assessment of axonal damage.**

APP undergoes fast axonal transport and accumulation of APP-positive swellings in white matter is widely regarded as an indicator of axonal damage (Sherriff et al., 1994). Representative low power images of APP immunostaining in WT and PLPOVR mice are shown in Fig. 4-21. The PLPOVR shows a slightly higher intensity of background staining in the corpus callosum and anterior commissure compared to the WT counterpart. In the higher power microscopic images numerous APP-positive foci are visible in the PLPOVR mice but not in the WT. The density of APP-positive foci was significantly increased in PLPOVR compared to WT in all ROIs examined (Fig. 4-22). Using APP immunostaining to assess axonal pathology in the PLPOVR white matter, the anterior commissure appears

#### Chapter 4 - Investigating the structural correlates of DTI measures in the PMD mouse model of white matter pathology.

to be more severely affected than the corpus callosum. The relative difference between PLPOVR and WT is an increase of 5680 %, and 2713 % in the anterior commissure at Bregma 1.10 mm and 0.14 mm, respectively, whereas for the corpus callosum the increases are 2850 %, and 450 %, respectively. The least affected tract is the hippocampal fimbria, with a relative difference between PLPOVR and WT of +1929 % at Bregma - 1.46 mm. Thus the rank order of the ROIs in terms of severity of axonal pathology is not the same as with either MBP immunostaining or DTI measurements.

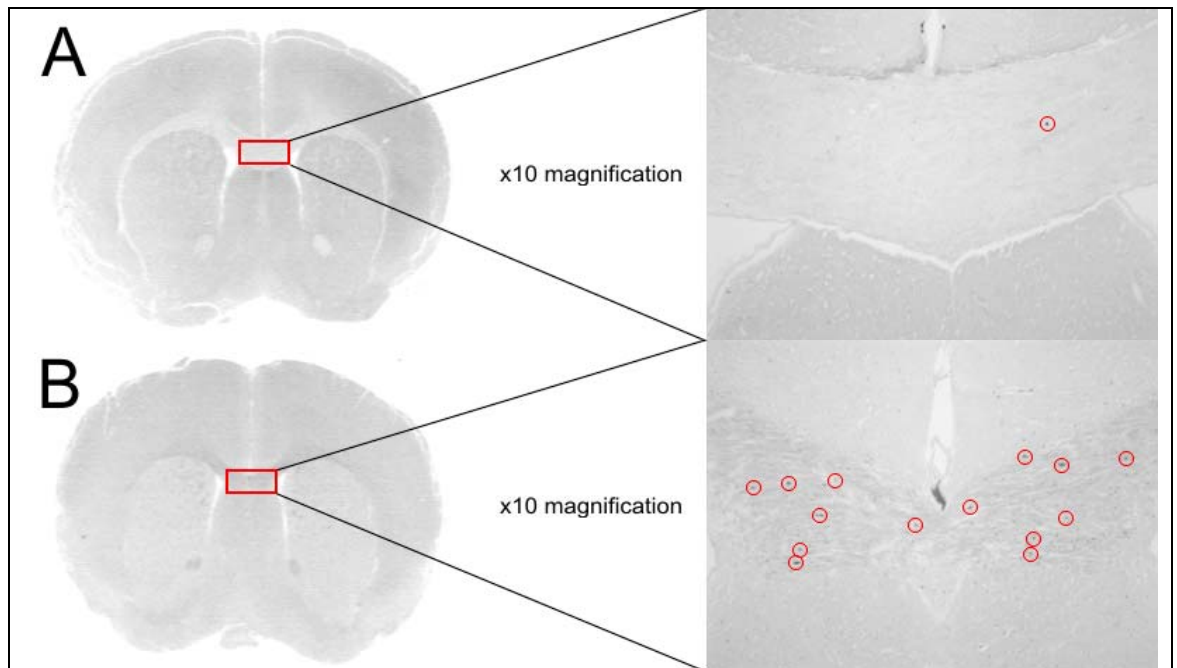


**Fig. 4-21. APP immunoreactivity is increased in the corpus callosum of PLPOVR mice.**

Left: representative overview images at Bregma level 1.10 mm with red rectangle indicating area of magnification (x10, right). Immunostaining of APP reveals elevated numbers of APP-positive foci indicated by red circles in PLPOVR (B) compared to WT (A). Note different background staining in white matter: WT white matter appears bright, PLPOVR white matter dark.

Immunostaining and quantification of APP-positive foci were performed by Jennifer Barrie, Applied Neurobiology Group, Glasgow University.

**Chapter 4 - Investigating the structural correlates of DTI measures in the PMD mouse model of white matter pathology.**

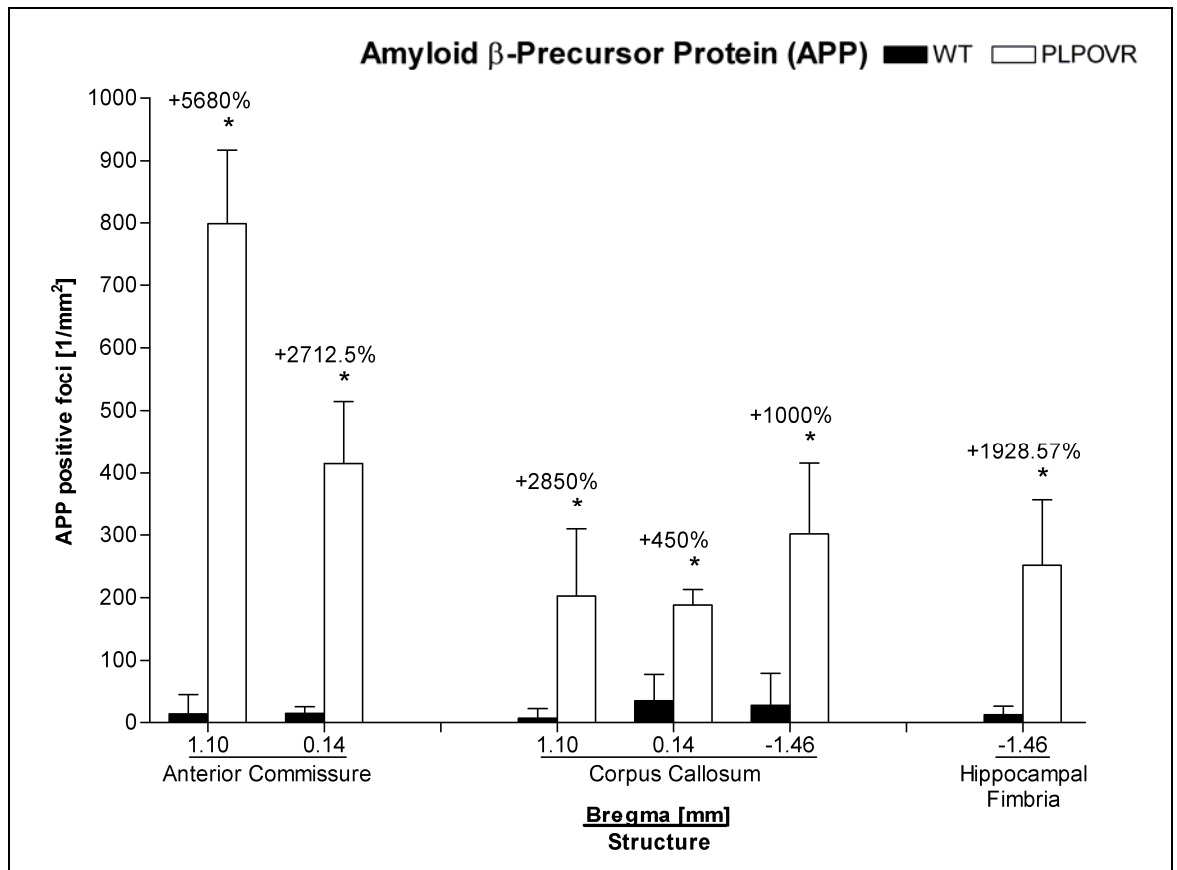


**Fig. 4-22. APP immunoreactivity is increased in all selected white matter tracts of PLPOVR mice.**

Each bar graph of an individual structure is organized from anterior to posterior. Data are mean  $\pm$  SD for n = 5 per group. Units of measurement are: APP/Area [1/mm<sup>2</sup>]. Two-tailed Mann-Whitney U, \*p < 0.05 relative to WT group. Relative differences are shown over bars, where (PLPOVR - WT)/(WT)\*100 %.

All structures, at all levels examined show a significant increase in APP-positive foci in PLPOVR mice.

Immunostaining and quantification of APP areas were performed by Jennifer Barrie, Applied Neurobiology Group, Glasgow University.

**GFAP immunohistochemistry – assessment of astrocytes.**

GFAP is present in astrocytes which hypertrophy in response to many different forms of injury and disease (Yong, 1998). Representative low power images of GFAP immunostaining in WT and PLPOVR mice are shown in Fig. 4-23. In the low power images a widespread increase in GFAP immunoreactivity is evident in PLPOVR mice compared to WT with higher densities of staining in the cerebral cortex, caudate-putamen, the area of the olfactory tubercle, the corpus callosum, and particularly the anterior commissure. In the higher power microscopic images of the corpus callosum the amount of GFAP immunostaining is substantially less pronounced in the WT than in the PLPOVR indicative of a marked astrocytosis in PLPOVR mice. Quantitative analysis of the area of GFAP immunoreactivity within the defined ROIs demonstrates that this is significantly

## Chapter 4 - Investigating the structural correlates of DTI measures in the PMD mouse model of white matter pathology.

increased in the PLPOVR in all regions examined (Fig. 4-24). The data suggest that the corpus callosum is the most affected area in the PLPOVR mice with a maximal increase in GFAP staining of 1426 % compared to WT in one of the three ROIs examined in this structure. However, the increases were less pronounced in other ROIs within the corpus callosum (Fig. 4-24). The increase in GFAP staining in the PLPOVR mice was of the order of 859 - 879 % in the anterior commissure while in the hippocampal fimbria the increase compared to WT was approximately 563 %.

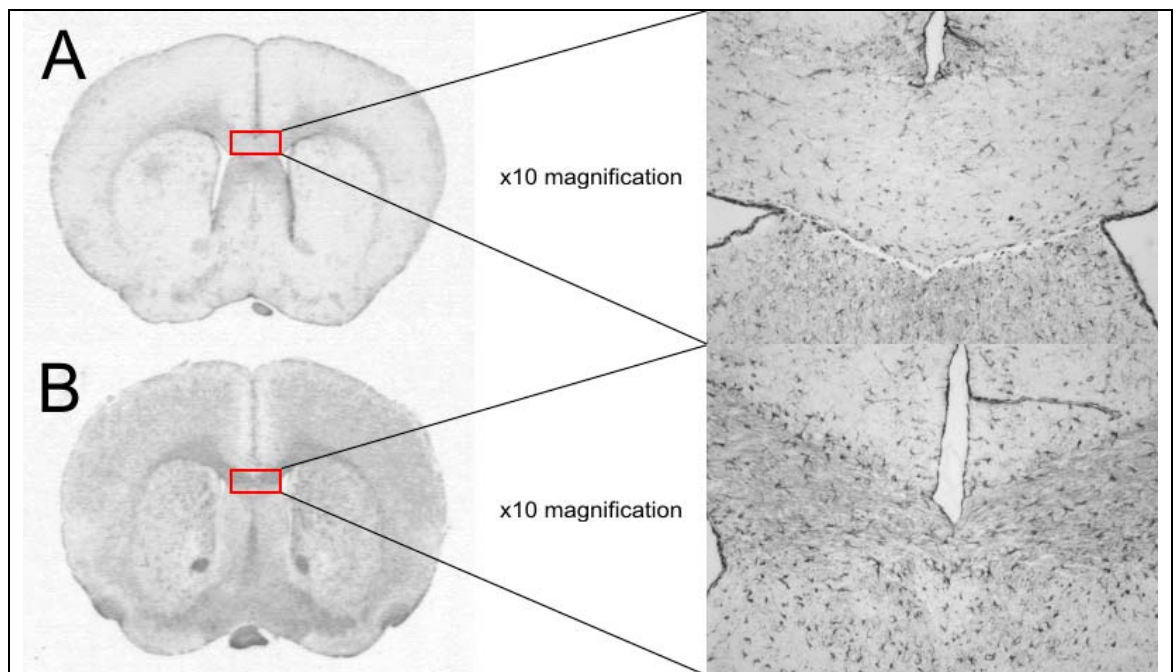


**Fig. 4-23. GFAP immunoreactivity is increased in the corpus callosum of PLPOVR mice.**

Left: representative overview images at Bregma level 1.10 mm with red rectangle indicating area of magnification (x10, right).

Immunohistochemistry against GFAP reveals widespread increases in PLPOVR (B) mice compared to WT (A).

Immunostaining and quantification of GFAP areas were performed by Jennifer Barrie, Applied Neurobiology Group, Glasgow University.

**Chapter 4 - Investigating the structural correlates of DTI measures in the PMD mouse model of white matter pathology.**

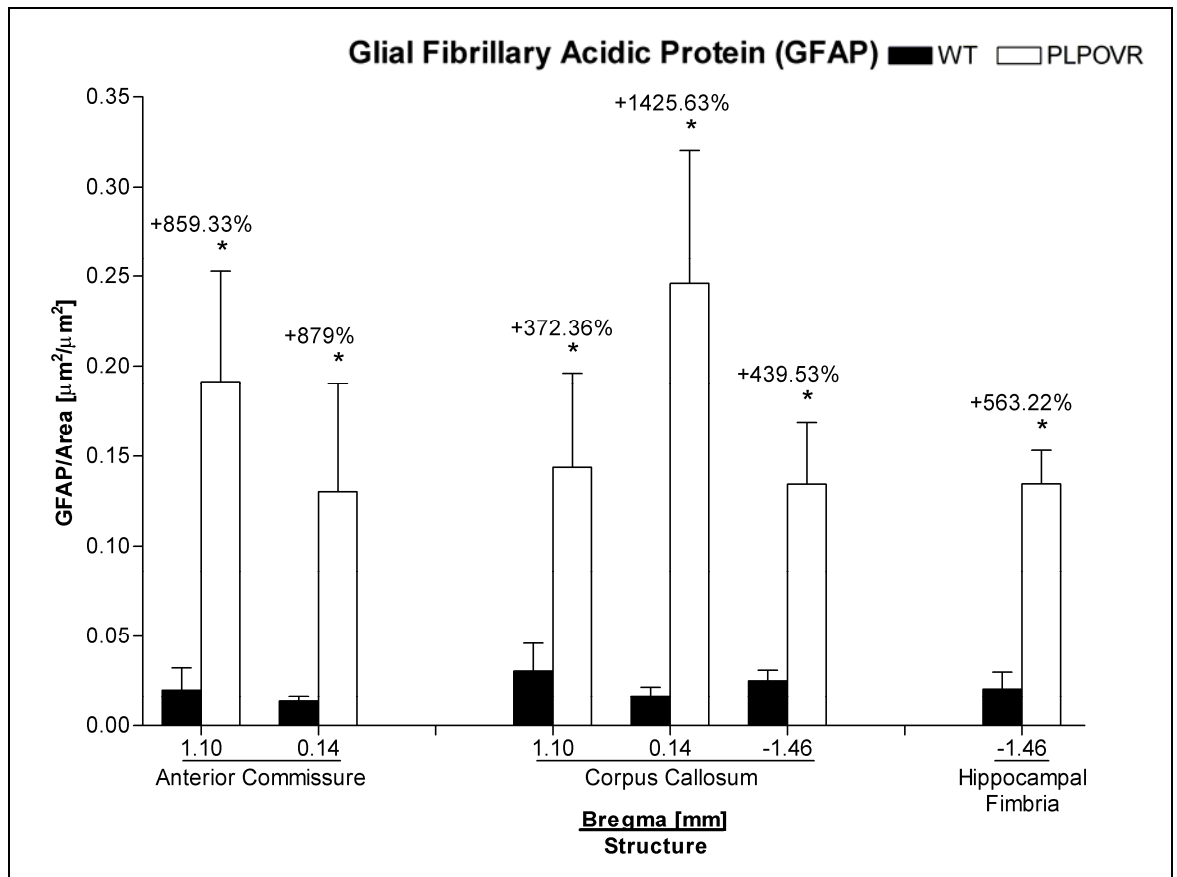


**Fig. 4-24. GFAP immunoreactivity is increased in all selected white matter tracts of PLPOVR mice.**

Each bar graph of an individual structure is organized from anterior to posterior. Data are mean  $\pm$  SD for  $n = 5$  per group. Units of measurement are: GFAP/Area [ $\mu\text{m}^2/\mu\text{m}^2$ ]. Two-tailed Mann-Whitney U,  $*p < 0.05$  relative to WT group. Relative differences are shown over bars, where  $(\text{PLPOVR} - \text{WT})/(\text{WT}) * 100 \%$

All structures, at all levels examined show a significant increase in GFAP immunoreactivity in PLPOVR overexpressing mice.

Immunostaining and quantification of GFAP areas were performed by Jennifer Barrie and Fredrik Gruenfelder (quantification only), Applied Neurobiology Group, Glasgow University.

**Haematoxylin staining – assessment of cell density.**

Haematoxylin is a basophilic stain that gives a blue colour to the nucleus of a cell, for example. Haematoxylin stains all cell nuclei and was used to determine total cell densities in the defined white matter ROIs. Representative microscopic images of staining in the corpus callosum of PLPOVR and WT mice are shown in Fig. 4-25, and the anterior commissure is shown in Fig. 4-26. Quantification of haematoxylin-stained cell nuclei revealed that cell densities in the corpus callosum and the hippocampal fimbria are not altered in PLPOVR compared to WT mice. However the density of cells in the anterior commissure was significantly higher in PLPOVR mice compared to WT (Fig. 4-27).

**Chapter 4 - Investigating the structural correlates of DTI measures in the PMD mouse model of white matter pathology.**

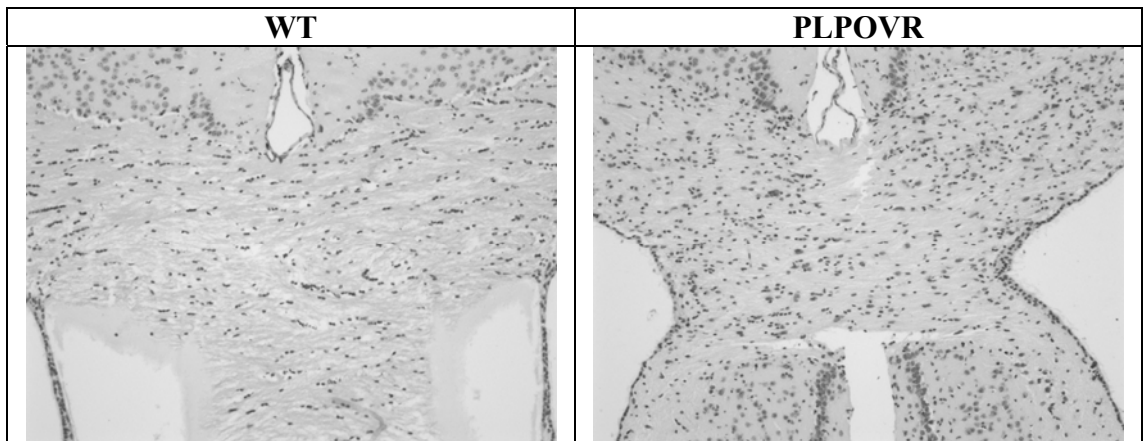


**Fig. 4-25. Haematoxylin-stained cell nuclei density is unaltered in the corpus callosum of PLPOVR mice.**

Images show the corpus callosum at x10 magnification at Bregma level 1.10 mm. Total cell density in the corpus callosum is not altered significantly in PLPOVR mice (right) compared to WT (left).

Staining and quantification of haematoxylin areas were performed by Jennifer Barrie, Applied Neurobiology Group, Glasgow University.

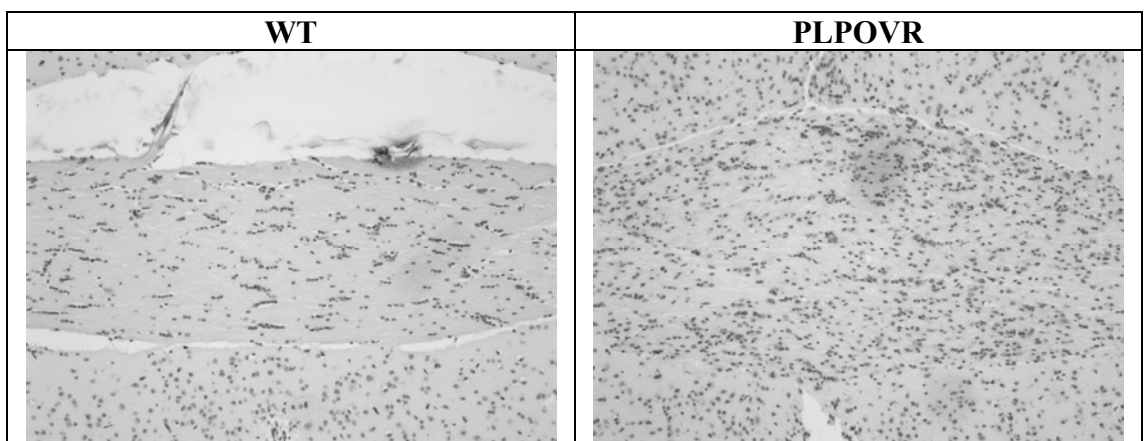


**Fig. 4-26. Haematoxylin-stained cell nuclei density is increased in the anterior commissure of PLPOVR mice.**

Images show the anterior commissure at x10 magnification at Bregma level 1.10 mm. Total cell density in the anterior commissure is significantly increased in PLPOVR (right) mice compared to WT (left).

Staining and quantification of haematoxylin areas were performed by Jennifer Barrie, Applied Neurobiology Group, Glasgow University.

## Chapter 4 - Investigating the structural correlates of DTI measures in the PMD mouse model of white matter pathology.

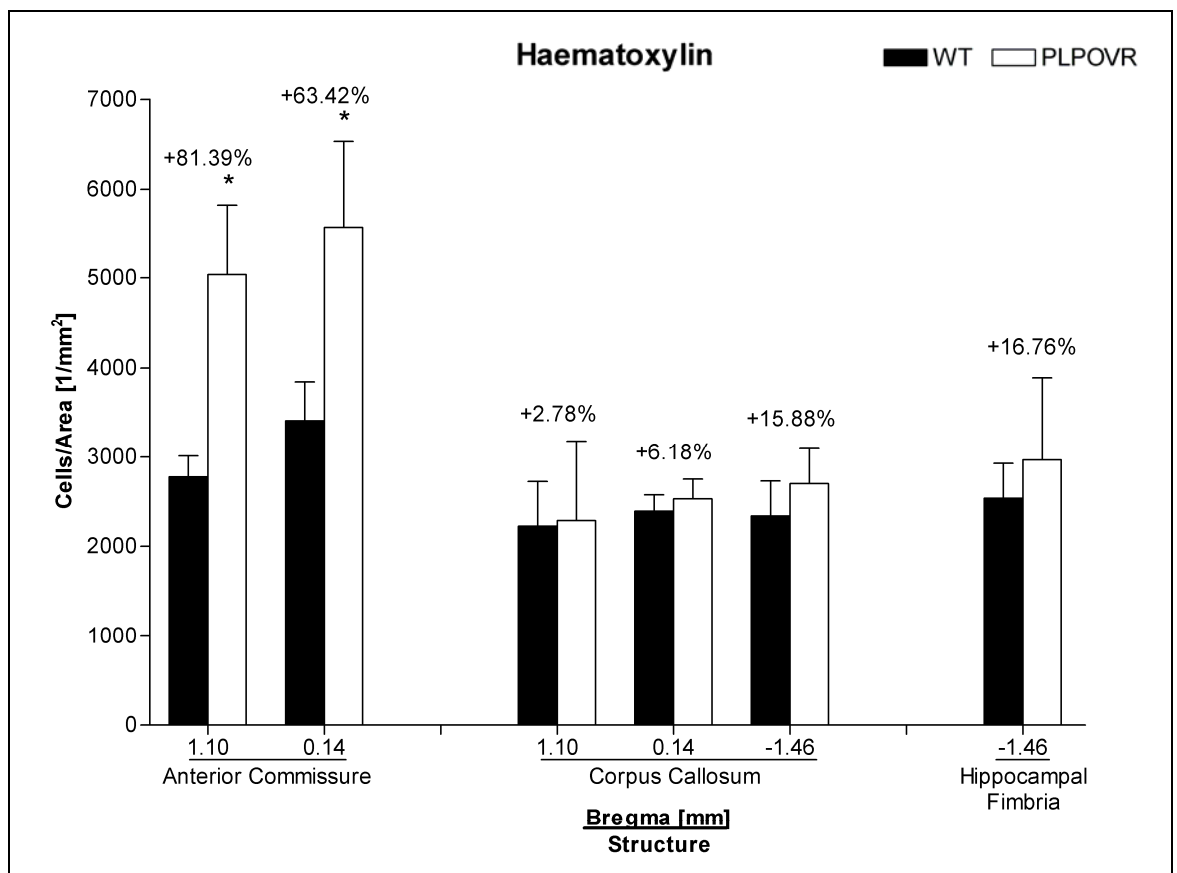


**Fig. 4-27. Haematoxylin-stained cell nuclei density is increased only in the anterior commissure of PLPOVR mice.**

Each bar graph of an individual structure is organized from anterior to posterior. Data are mean  $\pm$  SD for  $n = 5$  per group. Units of measurement are: Cells/Area [1/ $\mu\text{m}^2$ ]. Two-tailed Mann-Whitney U, \* $p < 0.05$  relative to WT group. Relative differences are shown over bars, where  $(\text{PLPOVR} - \text{WT})/(\text{WT}) * 100\%$ .

Significant differences were detected only in the anterior commissure at both Bregma levels examined.

Staining and quantification of haematoxylin areas were performed by Jennifer Barrie, Applied Neurobiology Group, Glasgow University.

### Light and electron microscopy.

As the quantity of available MBP is also affected by *Plp1* overexpression (Karim et al., 2007), ultrastructural EM was performed in order to assess the myelin content. Myelin is electron dense, and therefore appears as a black layer ensheathing the less electron dense axons in EM images. Light microscopy overview images were acquired at a 100x magnification (Fig. 4-28). Because of the lack of myelin, axons are less easy to discern in these light micrographs of PLPOVR mice compared to WT. In addition, large astrocyte processes were observed that support the demyelinated axons. Fig. 4-29 shows representative EM images taken from the corpus callosum at Bregma 1.10 mm at an 8000x magnification. The WT mice (left) show well-developed myelin sheaths surrounding the

#### **Chapter 4 - Investigating the structural correlates of DTI measures in the PMD mouse model of white matter pathology.**

axons. By contrast, the PLPOVR (right) at an age of P120 have virtually no myelin ensheathing the axons, however some astrocytes can be seen in the EM image. Axonal density measurements, as well as assessment of myelinated fibres (as a percentage of the total number of axons) were performed on the corpus callosum (Bregma 1.10 mm, Fig. 4-30, A, B, respectively), and on the hippocampal fimbria (Bregma -1.46 mm, Fig. 4-30, C, D, respectively). None of the measures on these tracts showed significant differences, however massive relative differences were observed. This is likely because of the low animal numbers used for EM. The axonal density in the corpus callosum was increased by 27 %, whereas the percentage of myelinated fibres was decreased by 94 % in PLPOVR compared to WT mice. The axonal density in the hippocampal fimbria was even more increased (94 %), and the number of myelinated fibres was decreased by 97 %. These results suggest that the increase in axon density is due to the denser packaging of axons as a result of myelin loss.

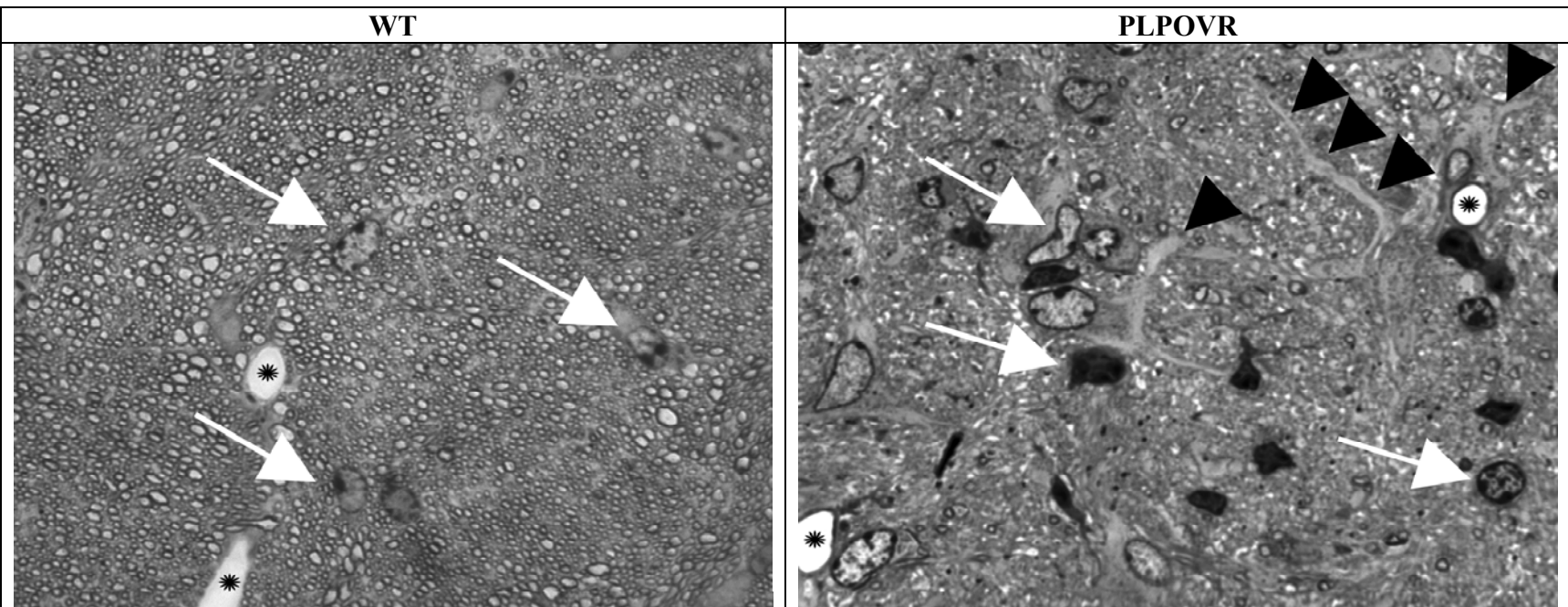


**Fig. 4-28. Light microscopy reveals astrocyte hypertrophy (black arrows) in the corpus callosum of PLPOVR mice.**

Black arrowheads show astrocyte processes. White arrows denote cells. Asterisks are drawn into blood vessels.

At Bregma level 1.10 mm with a magnification of 100x, astrocyte processes are not readily discerned in WT (left) animals, whereas hypertrophy of astrocytes is evident in PLPOVR (right) mice in form of enlarged processes indicating a supportive role to axons.

Images were provided by Dr. J Edgar.

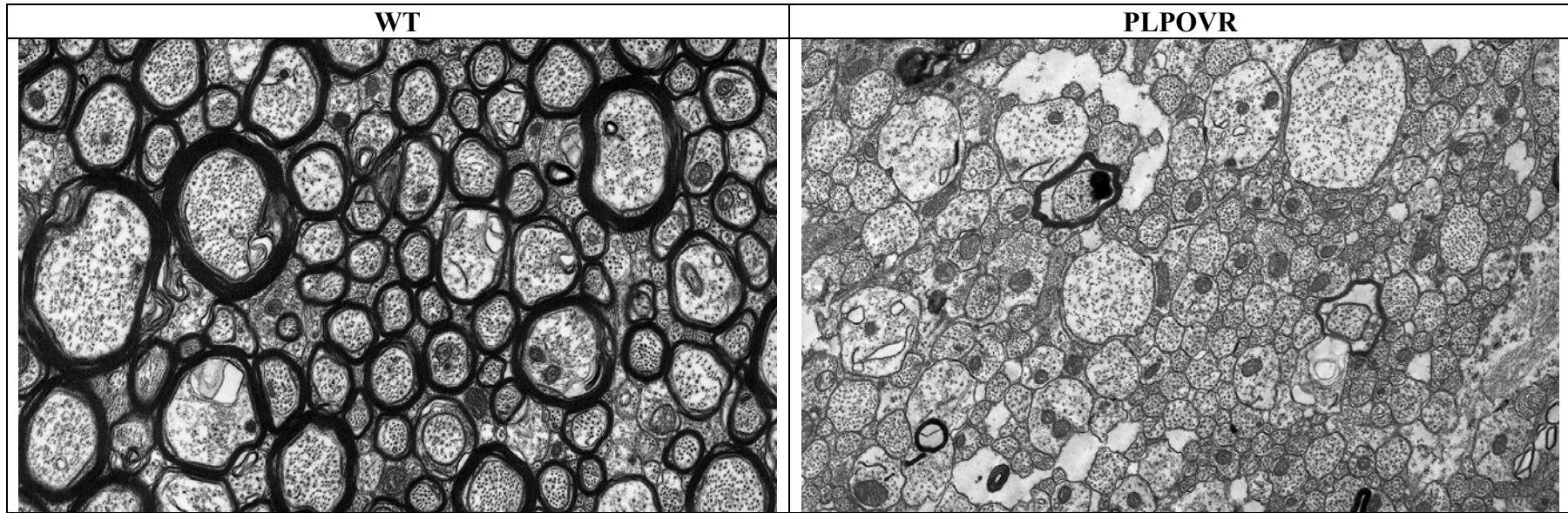


**Fig. 4-29. Electron microscopy shows almost completely demyelinated axons in the corpus callosum of PLPOVR mice.**

At P120, and a magnification of 8000x, almost all axons in PLPOVR (right) animals are demyelinated compared to WT (left). Staining and quantification of EM sections were performed by Jennifer Barrie, Applied Neurobiology Group, Glasgow University.

**Chapter 4 - Investigating the structural correlates of DTI measures in the PMD mouse model of white matter pathology.**

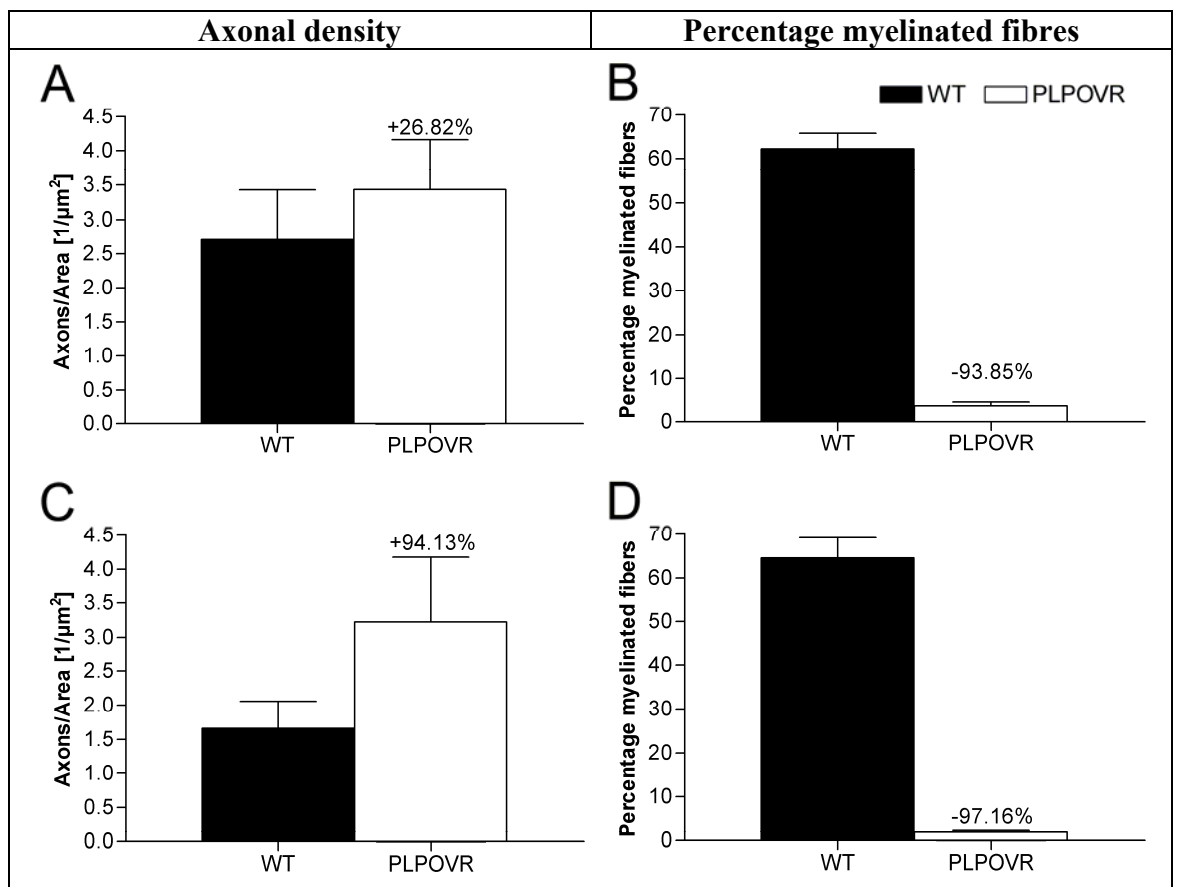


**Fig. 4-30. Axonal density is increased, while the percentage of myelinated fibers is reduced in PLPOVR mice.**

Data are mean  $\pm$  SD for n = 3 for WT, and n = 4 for PLPOVR. Units of measurement are: Axons/Area [ $1/\mu\text{m}^2$ ] for axonal density. Two-tailed Mann-Whitney U ( $p < 0.05$ ).

Relative differences are shown over bars, where  $(\text{PLPOVR} - \text{WT})/(\text{WT}) * 100 \%$ .

A, B: corpus callosum at Bregma level 1.10 mm.

C, D: hippocampal fimbria at Bregma level -1.46 mm.

Massive differences do not prove to be significant likely because of the low animal numbers used.

Staining and quantification of EM sections were performed by Jennifer Barrie, Applied Neurobiology Group, Glasgow University.

**4.4.4 Comparison of DTI measures to histopathology.**

The quantitative pathology data demonstrate that the PLPOVR mice have extensive alterations in white matter elements (myelin, axons, astrocytes, cell density) in the white matter tracts where changes in DTI measures were also observed. The two datasets were then compared to examine potential associations in an attempt to understand how different pathologies affect DTI measures.

**Comparisons with MBP staining of myelin.**

The relative % differences between PLPOVR and WT mice for FA and MBP are shown in Fig. 4-31. Loss of anisotropy is of similar magnitude in all white matter tracts examined, neither a particular tract is more severely affected over others, nor can a notable

#### **Chapter 4 - Investigating the structural correlates of DTI measures in the PMD mouse model of white matter pathology.**

anterioposterior gradient be observed. Likewise for the MBP immunohistochemistry data, the magnitude of loss of MBP immunoreactivity in the PLPOVR is of the same order for the majority of white matter tracts. However there is a possible trend towards an anteroposterior gradient, with the corpus callosum and hippocampal fimbria being more affected in caudal levels. For further comparison, the area of MBP staining was plotted against all of the DTI measures obtained for the least and most affected tract in the MBP measurements; the anterior commissure (Bregma 0.14 mm) and hippocampal fimbria, respectively (Fig. 4-32 and Fig. 4-33).

**Chapter 4 - Investigating the structural correlates of DTI measures in the PMD mouse model of white matter pathology.**

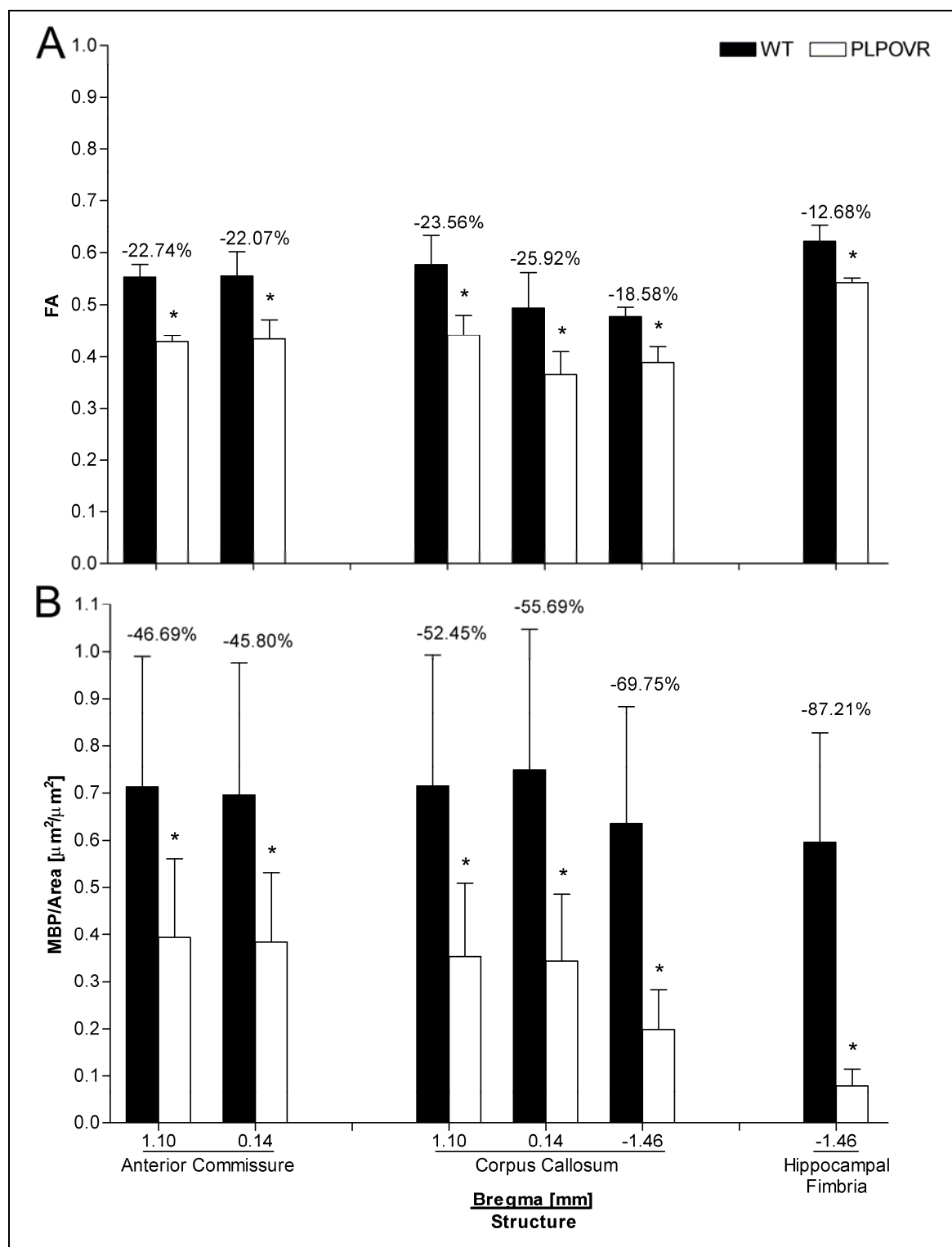


**Fig. 4-31. Comparison of FA index (A) to MBP immunoreactivity (B).**

Each bar graph of an individual structure is organized from anterior to posterior.

Data are mean  $\pm$  SD for n = 5 per group.

Units of measurement are: MBP: MBP/Area [ $\mu\text{m}^2/\mu\text{m}^2$ ]; FA is dimensionless.

Two-tailed Mann-Whitney U, \*p < 0.05 relative to WT group.

Relative differences are shown over bars, where  $(\text{PLPOVR} - \text{WT})/(\text{WT}) * 100 \%$ .

For B immunostaining and quantification of MBP areas were performed by Jennifer Barrie and Fredrik Gruenfelder (quantification only), Applied Neurobiology Group, Glasgow University.

**Chapter 4 - Investigating the structural correlates of DTI measures in the PMD mouse model of white matter pathology.**

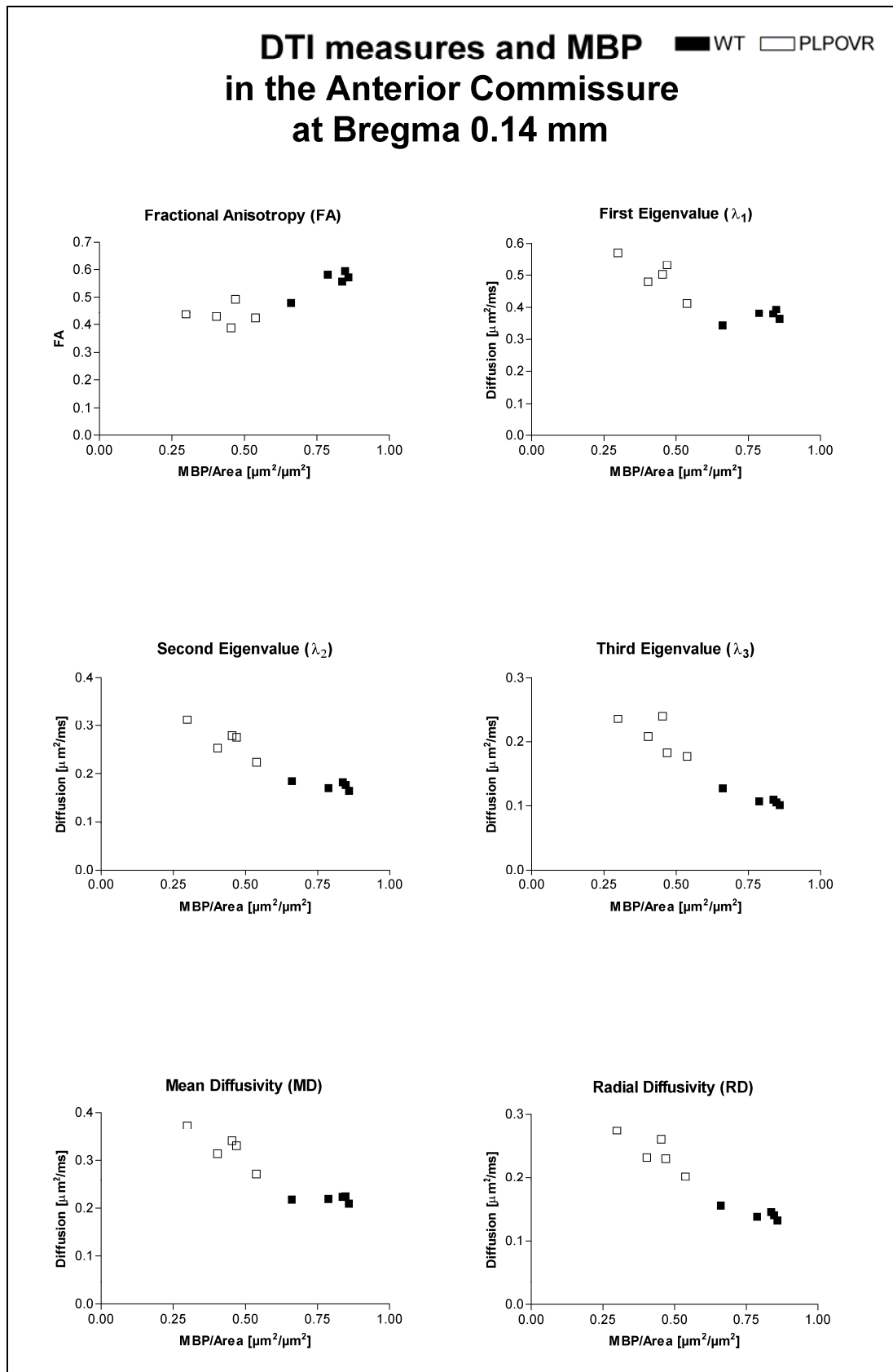


**Fig. 4-32. Scatter plot of diffusion parameter values (FA,  $\lambda_1$ ,  $\lambda_2$ ,  $\lambda_3$ , MD, RD) vs. MBP immunohistochemistry on individual animals at the level of the anterior commissure (Bregma 0.14 mm).**

**Chapter 4 - Investigating the structural correlates of DTI measures in the PMD mouse model of white matter pathology.**

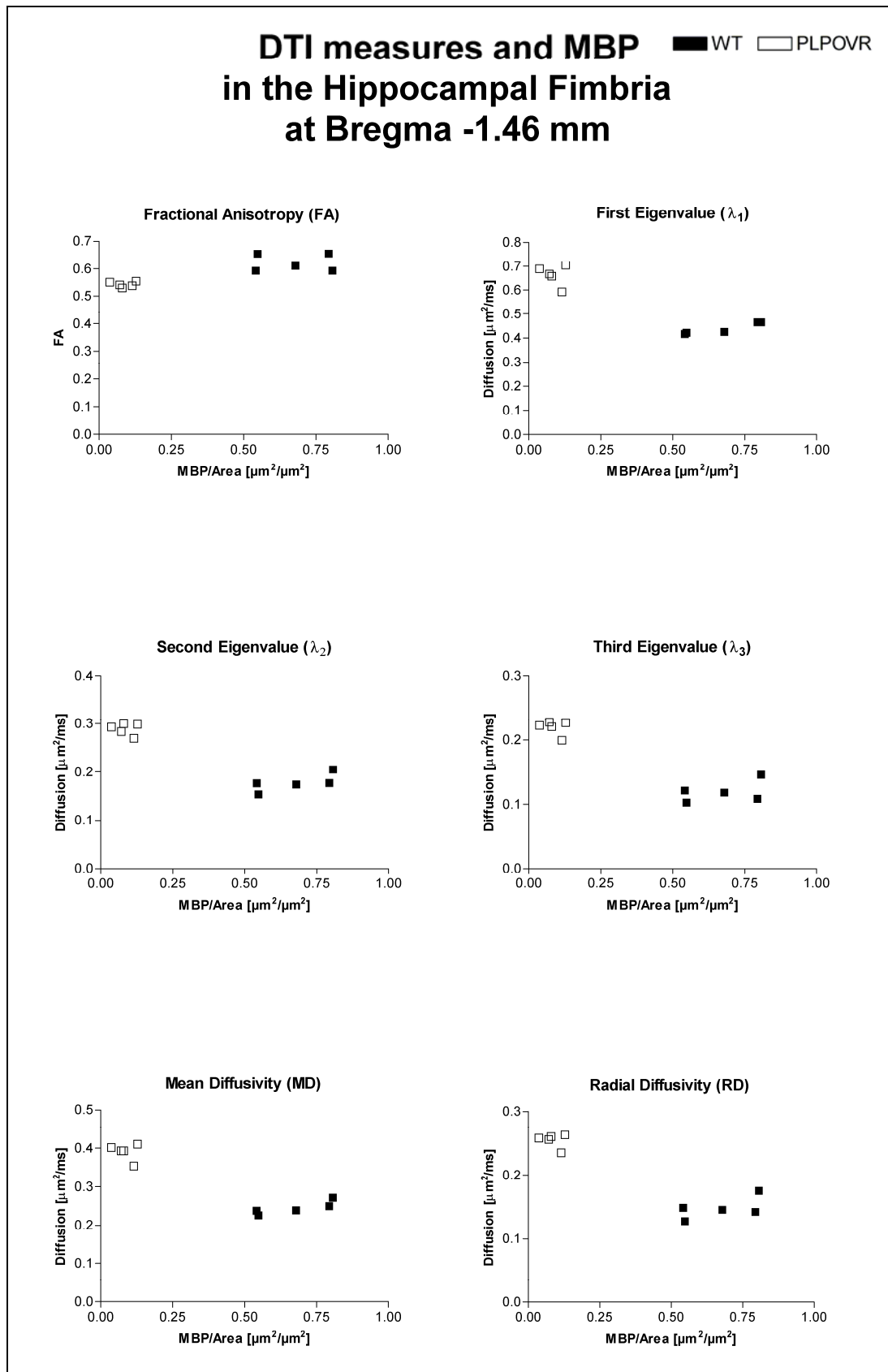


**Fig. 4-33. Scatter plot of diffusion parameter values (FA, λ<sub>1</sub>, λ<sub>2</sub>, λ<sub>3</sub>, MD, RD) vs. MBP immunohistochemistry on individual animals at the level of the hippocampal fimbria (Bregma -1.46 mm).**

**Chapter 4 - Investigating the structural correlates of DTI measures in the PMD mouse model of white matter pathology.**

Anterior Commissure 0.14 mm			Hippocampal Fimbria -1.46 mm		
MBP vs.	Genotype		MBP vs.	Genotype	
	WT	PLPOVR		WT	PLPOVR
	r	r		r	r
FA	0.50	-0.20	FA	-0.10	0.10
$\lambda_1$	0.30	-0.60	$\lambda_1$	0.90	0.00
$\lambda_2$	-0.70	-0.70	$\lambda_2$	0.70	0.10
$\lambda_3$	-0.90	-0.70	$\lambda_3$	0.30	-0.20
MD	0.00	-0.70	MD	0.90	0.00
RD	-0.70	-0.90	RD	0.30	0.30

**Table 4-1. Correlation after Spearman of MBP vs. DTI measures (FA,  $\lambda_i$ , MD, and RD) in the anterior commissure and hippocampal fimbria (sampled at Bregma levels given).**

r is the Spearman correlation coefficient.

In the anterior commissure, where MBP staining is least affected in PLPOVR, there is a clear separation between WT and PLPOVR groups when DTI measures are plotted against MBP area (Fig. 4-32). The plots show that in general the greater the density of MBP the higher the FA index. Conversely, for diffusion sensitive measures ( $\lambda_i$ , MD, and RD), the lower the MBP density, the higher the diffusion. For all DTI measures, it can be seen from the plots that the data for WT animals are tightly clustered while there is more spread within the PLPOVR group. In the anterior commissure of PLPOVR mice, varying amounts of demyelination are associated with variation in DTI measures. This suggestion is supported by the Spearman rank r-values when the WT and PLPOVR groups are examined separately (Table 4-1). Spearman rank correlations were undertaken to examine the relative strengths of associations rather than to determine the statistical significance of each individual correlation. The small group size and the issue of multiple correlations with one measure (MBP) mean, the statistical values are of limited value.

Within the anterior commissure in the PLPOVR group, diffusion sensitive measures ( $\lambda_1$ ,  $\lambda_2$ ,  $\lambda_3$  and RD) seem to be influenced by MBP density as indicated by the negative correlation coefficients. The strongest association is between MBP density and RD in PLPOVR animals. Spearman r-values are also relatively high for  $\lambda_2$ ,  $\lambda_3$  and RD in WT animals, indicating a relationship between those measures and MBP immunoreactivity in the anterior commissure (Table 4-1). In contrast to other measures, FA values in PLPOVR animals are similar across a fairly large range of MBP densities (Fig. 4-32), and this is

## **Chapter 4 - Investigating the structural correlates of DTI measures in the PMD mouse model of white matter pathology.**

reflected in a low correlation coefficient (Table 4-1). This could suggest that factors other than the density of myelin contribute to the FA index in PLPOVR.

The relationships between DTI measures and MBP in the most severely demyelinated tract, the hippocampal fimbria, were dissimilar to those in the least demyelinated tract, the anterior commissure. Separation of WT and PLPOVR groups due to loss of MBP immunoreactivity is much more obvious when plotted against DTI measures (Fig. 4-33). This could suggest an anteroposterior gradient in the severity of demyelination at P120 in PLPOVR mice. In the hippocampal fimbria, as for the anterior commissure, FA values in PLPOVR mice are lower, and diffusion sensitive measures ( $\lambda_i$ , MD, and RD) are higher compared to WT counterparts. However, the data points for all DTI measures vs. MBP in the hippocampal fimbria of PLPOVR mice are more densely clustered compared to the data derived from the anterior commissure. This is reflected in the low correlation coefficients observed between MBP density and DTI measures in the PLPOVR group alone (Table 4-1). These findings might indicate a temporal pattern of tract demyelination, with the anterior commissure being affected later as disease progresses compared to the hippocampal fimbria as indicated by much more severe loss of MBP. FA values are still high for the hippocampal fimbria (WT  $0.62 \pm 0.03$  and PLPOVR  $0.54 \pm 0.01$ , see also Fig. 4-31) and the anterior commissure (WT  $0.56 \pm 0.05$  and PLPOVR  $0.43 \pm 0.04$ , see also Fig. 4-31), suggesting that it is not the most sensitive parameter derived from the DTI dataset for measuring the extent of demyelination. On the other hand it might suggest that other effects could influence anisotropy, possibly a high degree of parallel running fibres as shown above in the EM data for the hippocampal fimbria, where an increase in axon density per area unit was detected in PLPOVR compared to WT (Fig. 4-30, page 194).

### **Comparisons with APP staining of axonal damage.**

DTI measures were plotted against the number of APP-positive foci in the anterior commissure at Bregma 0.14 mm and the hippocampal fimbria at Bregma -1.47 mm (Fig. 4-34 and Fig. 4-35). For the anterior commissure, the WT group forms a distinct tight cluster having almost no APP-positive foci, with higher FA and lower diffusion values compared to PLPOVR. Although there are varying severities of axonal damage within the PLPOVR group alone, there is little indication that this is strongly associated with any DTI-derived parameter (Table 4-2). In the hippocampal fimbria, as for the anterior commissure, the PLPOVR and WT groups are well separated when APP-positive foci are plotted against DTI measures (Fig. 4-35). However the correlation coefficient shows that

#### **Chapter 4 - Investigating the structural correlates of DTI measures in the PMD mouse model of white matter pathology.**

there is minimal evidence that FA is associated with APP-stained foci ( $r = 0.00$ ) in WT animals (Table 4-2). The r-value for FA versus APP immunoreactivity is moderately high with  $r = 0.70$  in PLPOVR mice, implying a relationship between these measurements.

**Chapter 4 - Investigating the structural correlates of DTI measures in the PMD mouse model of white matter pathology.**

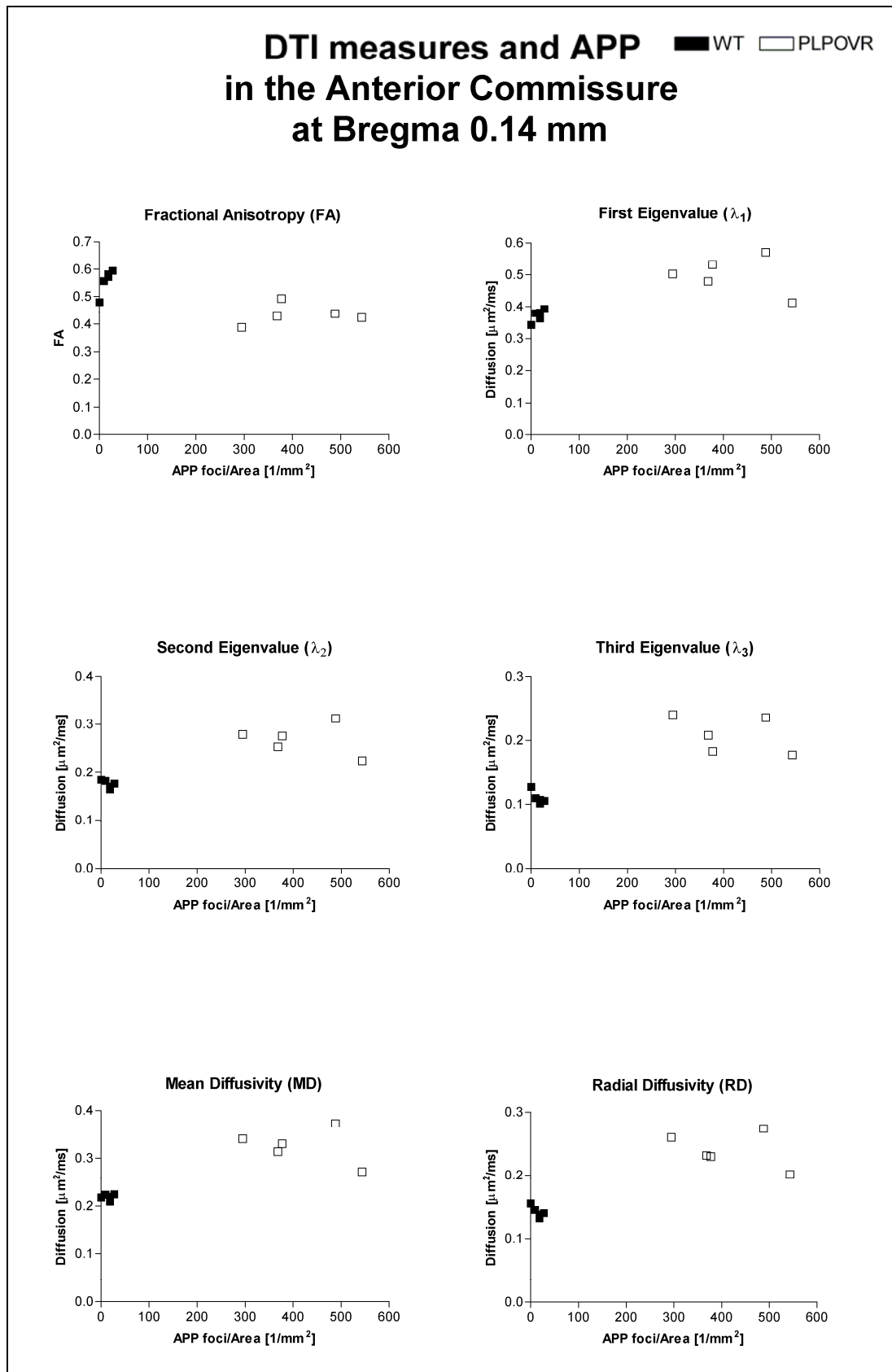


**Fig. 4-34. Scatter plot of diffusion parameter values (FA,  $\lambda_1$ ,  $\lambda_2$ ,  $\lambda_3$ , MD, RD) vs. APP immunohistochemistry on individual animals at the level of the anterior commissure (Bregma 0.14 mm).**

Chapter 4 - Investigating the structural correlates of DTI measures in the PMD mouse model of white matter pathology.

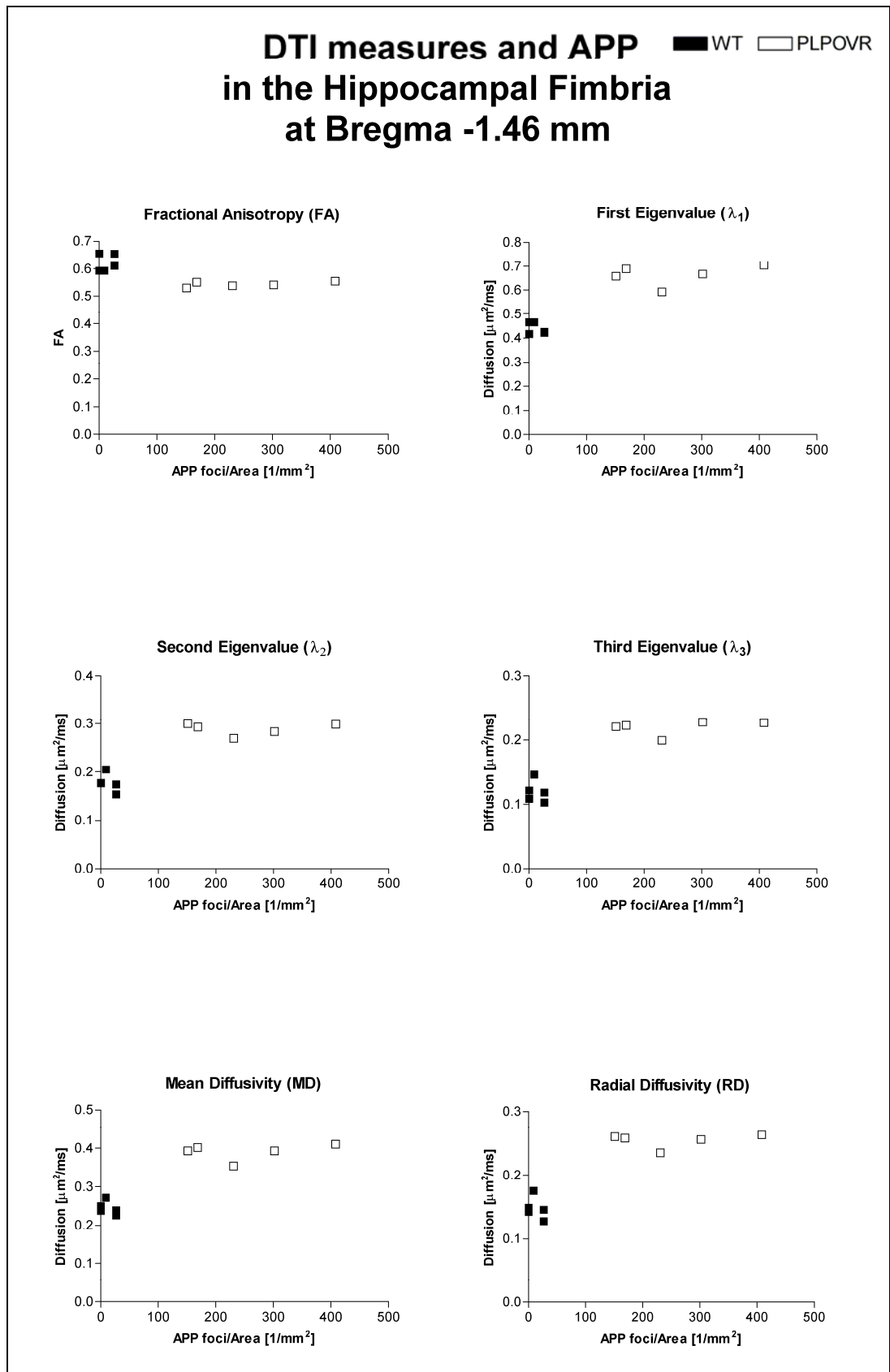


Fig. 4-35. Scatter plot of diffusion parameter values (FA,  $\lambda_1$ ,  $\lambda_2$ ,  $\lambda_3$ , MD, RD) vs. APP immunohistochemistry on individual animals at the level of the hippocampal fimbria (Bregma -1.46 mm).

**Chapter 4 - Investigating the structural correlates of DTI measures in the PMD mouse model of white matter pathology.**

Anterior Commissure 0.14 mm			Hippocampal Fimbria -1.46 mm		
APP vs.	Genotype		APP vs.	Genotype	
	WT	PLPOVR		WT	PLPOVR
	r	r		r	r
FA	0.97	0.30	FA	0.00	0.70
$\lambda_1$	0.82	-0.10	$\lambda_1$	-0.16	0.50
$\lambda_2$	-0.67	-0.30	$\lambda_2$	-0.63	-0.30
$\lambda_3$	-0.82	-0.70	$\lambda_3$	-0.32	0.60
MD	0.41	-0.30	MD	-0.32	0.50
RD	-0.67	-0.40	RD	-0.32	0.10

**Table 4-2. Correlation after Spearman of APP vs. DTI measures (FA,  $\lambda_i$ , MD, and RD) in the anterior commissure and hippocampal fimbria (sampled at Bregma levels given).**

r is the Spearman correlation coefficient.

**Comparisons with GFAP staining of astrocytes.**

DTI measures were plotted against the area of GFAP staining in the anterior commissure at Bregma 0.14 mm and the hippocampal fimbria at Bregma -1.47 mm (Fig. 4-36 and Fig. 4-37). For the anterior commissure the WT group forms a distinct tight cluster having little GFAP immunoreactivity with higher FA and lower diffusion values compared to PLPOVR. This is in contrast to the PLPOVR group where there is more spread and varying amounts of GFAP that are associated with variations particularly in diffusion sensitive measures ( $\lambda_i$ , MD, and RD), i.e. the higher the area occupied by GFAP, the higher the diffusion. This suggestion is supported by the Spearman rank r-values when the WT and PLPOVR groups are examined separately (Table 4-3). FA values in the anterior commissure in PLPOVR animals appear to associate with GFAP densities which is reflected in the correlation coefficient ( $r=0.7$ ). Thus these data suggest an effect of increasing GFAP immunoreactivity in PLPOVR on DTI-derived parameters in the anterior commissure.

Separation of WT and PLPOVR groups due to increased GFAP density in the hippocampal fimbria is much more obvious when plotted against DTI measures compared to the anterior commissure (Fig. 4-37). These findings might indicate a temporal pattern of tract demyelination, with the anterior commissure being affected later as disease progresses compared to the hippocampal fimbria. Moderate correlation coefficients were calculated for  $\lambda_1$ , and MD for the hippocampal fimbria in both, PLPOVR as well as for WT mice. However in both cases, these coefficients had opposing leading signs (Table 4-3).

**Chapter 4 - Investigating the structural correlates of DTI measures in the PMD mouse model of white matter pathology.**

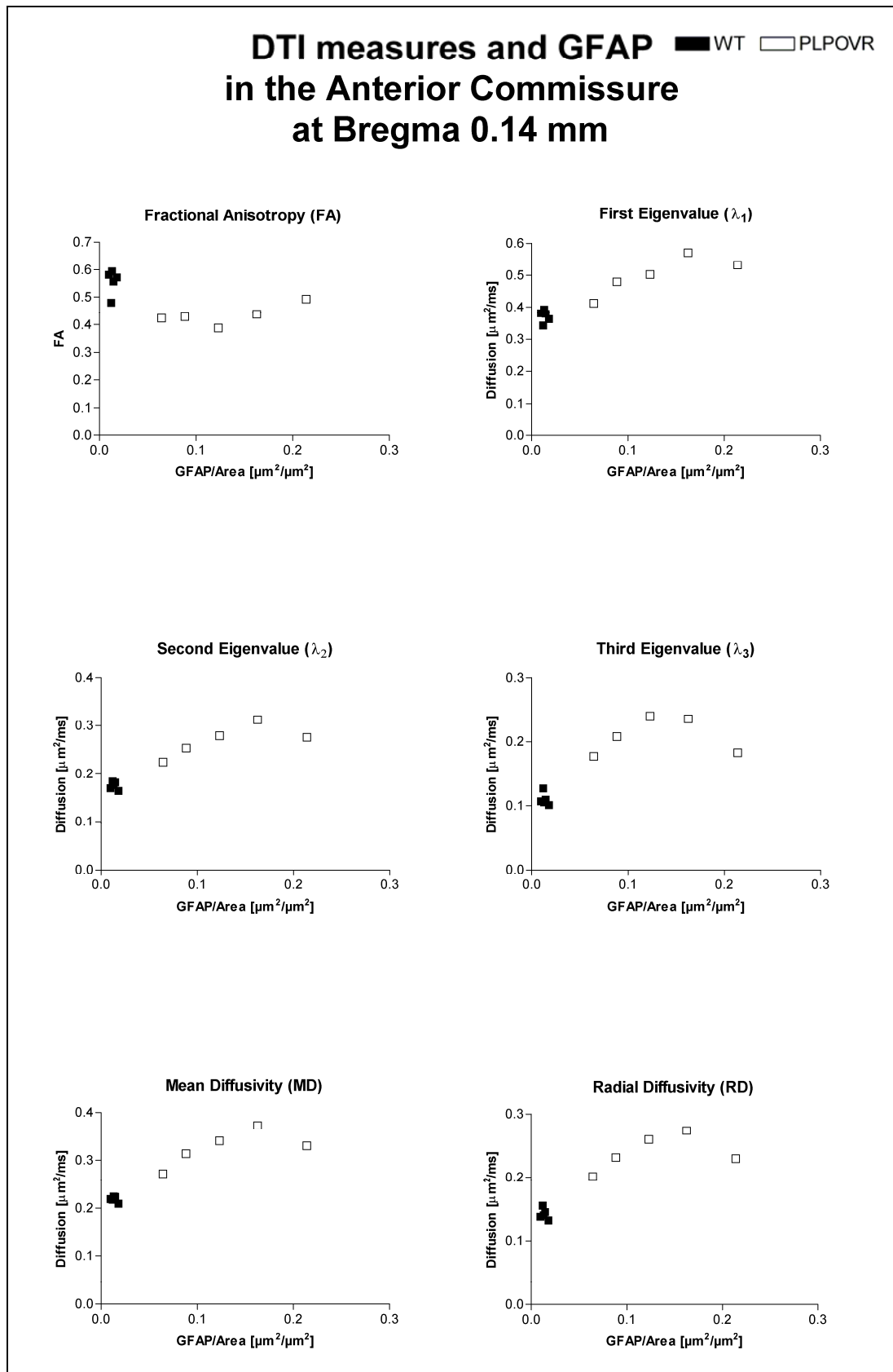


**Fig. 4-36. Scatter plot of diffusion parameter values (FA,  $\lambda_1$ ,  $\lambda_2$ ,  $\lambda_3$ , MD, RD) vs. GFAP immunohistochemistry on individual animals at the level of the anterior commissure (Bregma 0.14 mm).**

**Chapter 4 - Investigating the structural correlates of DTI measures in the PMD mouse model of white matter pathology.**

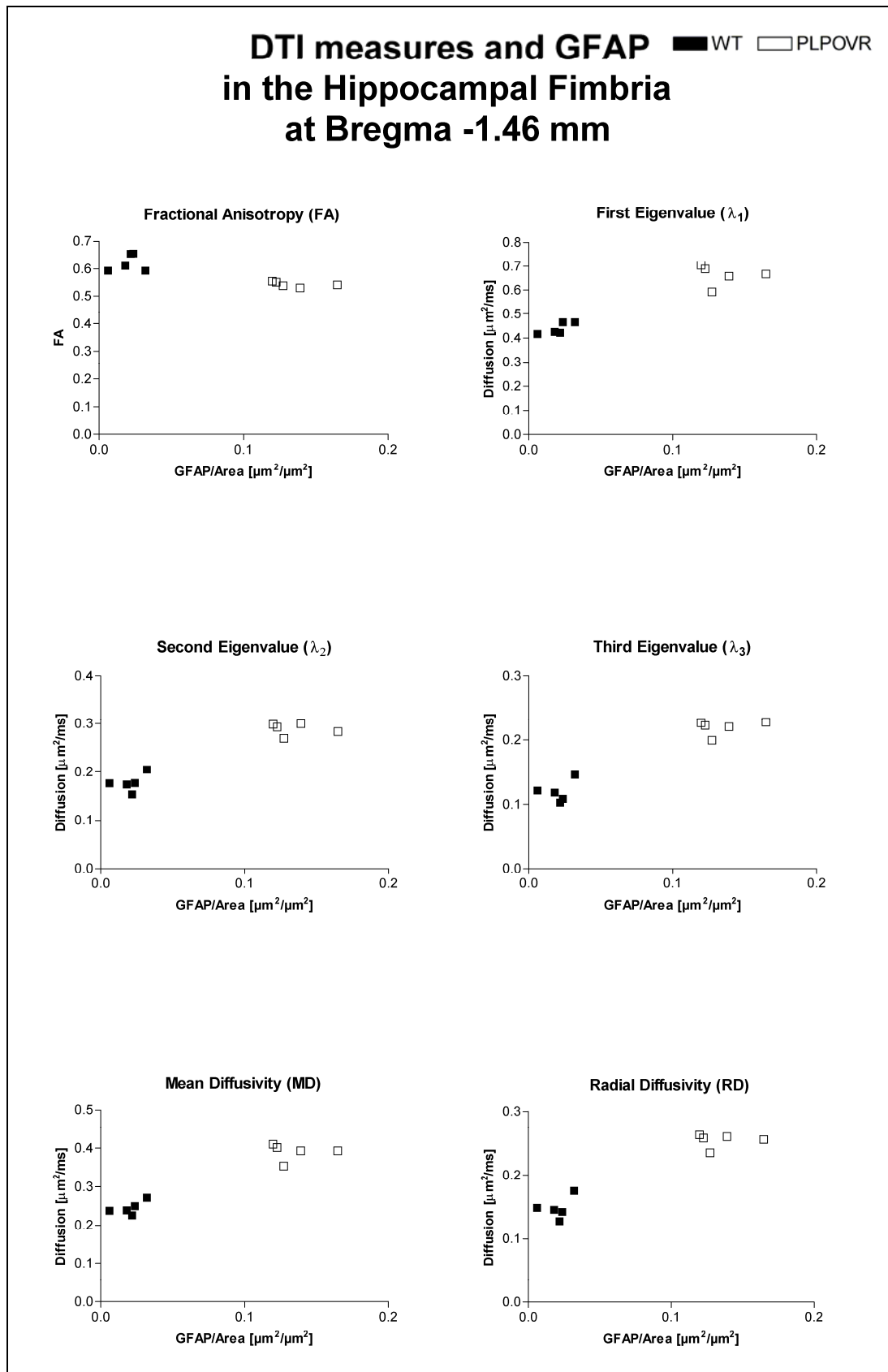


**Fig. 4-37. Scatter plot of diffusion parameter values (FA,  $\lambda_1$ ,  $\lambda_2$ ,  $\lambda_3$ , MD, RD) vs. GFAP immunohistochemistry on individual animals at the level of the hippocampal fimbria (Bregma -1.46 mm).**

**Chapter 4 - Investigating the structural correlates of DTI measures in the PMD mouse model of white matter pathology.**

Anterior Commissure 0.14 mm			Hippocampal Fimbria -1.46 mm		
GFAP vs.	Genotype		GFAP vs.	Genotype	
	WT	PLPOVR		WT	PLPOVR
	r	r		r	r
FA	-0.10	0.70	FA	0.00	-0.70
$\lambda_1$	-0.20	0.90	$\lambda_1$	0.80	-0.60
$\lambda_2$	-0.30	0.70	$\lambda_2$	0.60	-0.20
$\lambda_3$	-0.50	0.30	$\lambda_3$	0.10	0.10
MD	-0.20	0.70	MD	0.70	-0.60
RD	-0.30	0.40	RD	0.10	-0.50

**Table 4-3. Correlation after Spearman of GFAP vs. DTI measures (FA,  $\lambda_i$ , MD, and RD) in the anterior commissure and hippocampal fimbria (sampled at Bregma levels given).**

r is the Spearman correlation coefficient.

**Comparisons with haematoxylin staining of cell nuclei.**

Further to the immunohistochemistry shown above, haematoxylin-stained nuclear counts were plotted against all DTI measures extracted from the anterior commissure (Bregma 0.14 mm, Fig. 4-38) and hippocampal fimbria (Bregma -1.47 mm, Fig. 4-39).

In the anterior commissure, where MBP staining is least affected in PLPOVR, there is a clear separation between WT and PLPOVR groups when DTI measures are plotted against the number of haematoxylin-stained cell nuclei, with higher FA and lower diffusion values in WT compared to PLPOVR (Fig. 4-38). Although there are varying (and higher) numbers of haematoxylin-stained cell nuclei compared to WT in the PLPOVR group, there is little indication that this is strongly associated with FA in either group (Table 4-4). The plots show that in general the higher the cell density, the higher the diffusion sensitive measures ( $\lambda_i$ , MD, and RD) in PLPOVR animals. This is reflected by moderately high positive correlation coefficients for these measures in PLPOVR mice. In contrast, perpendicular diffusion measures ( $\lambda_2$ ,  $\lambda_3$ , and RD) are negatively associated with increasing cell numbers in WT animals, i.e. the higher the cell counts, the lower the perpendicular diffusion.

It is worth noting here that the anterior commissure was the only tract where significant increases in haematoxylin-stained cell nuclei were detected in PLPOVR compared to WT mice (Fig. 4-27). Therefore it is not surprising that in the hippocampal fimbria data points for haematoxylin-stained nuclei overlap for WT and PLPOVR (Fig. 4-39). As mentioned

#### **Chapter 4 - Investigating the structural correlates of DTI measures in the PMD mouse model of white matter pathology.**

above, the DTI measures are separated, i.e. there is greater anisotropy, and lower diffusivities ( $\lambda_i$ , MD, and RD) in WT compared to PLPOVR mice in the hippocampal fimbria. Inspection of the Spearman's rank order correlation coefficients shows no association between haematoxylin staining and DTI measures in WT, while moderate negative correlations, particularly in the perpendicular diffusivities ( $\lambda_2$  and RD), were evident in PLPOVR when compared to haematoxylin detected cell nuclei.

These findings suggest once more that there might be a temporal delay, i.e. the hippocampal fimbria is affected earlier than the anterior commissure in the short lifespan of PLPOVR mice.

**Chapter 4 - Investigating the structural correlates of DTI measures in the PMD mouse model of white matter pathology.**

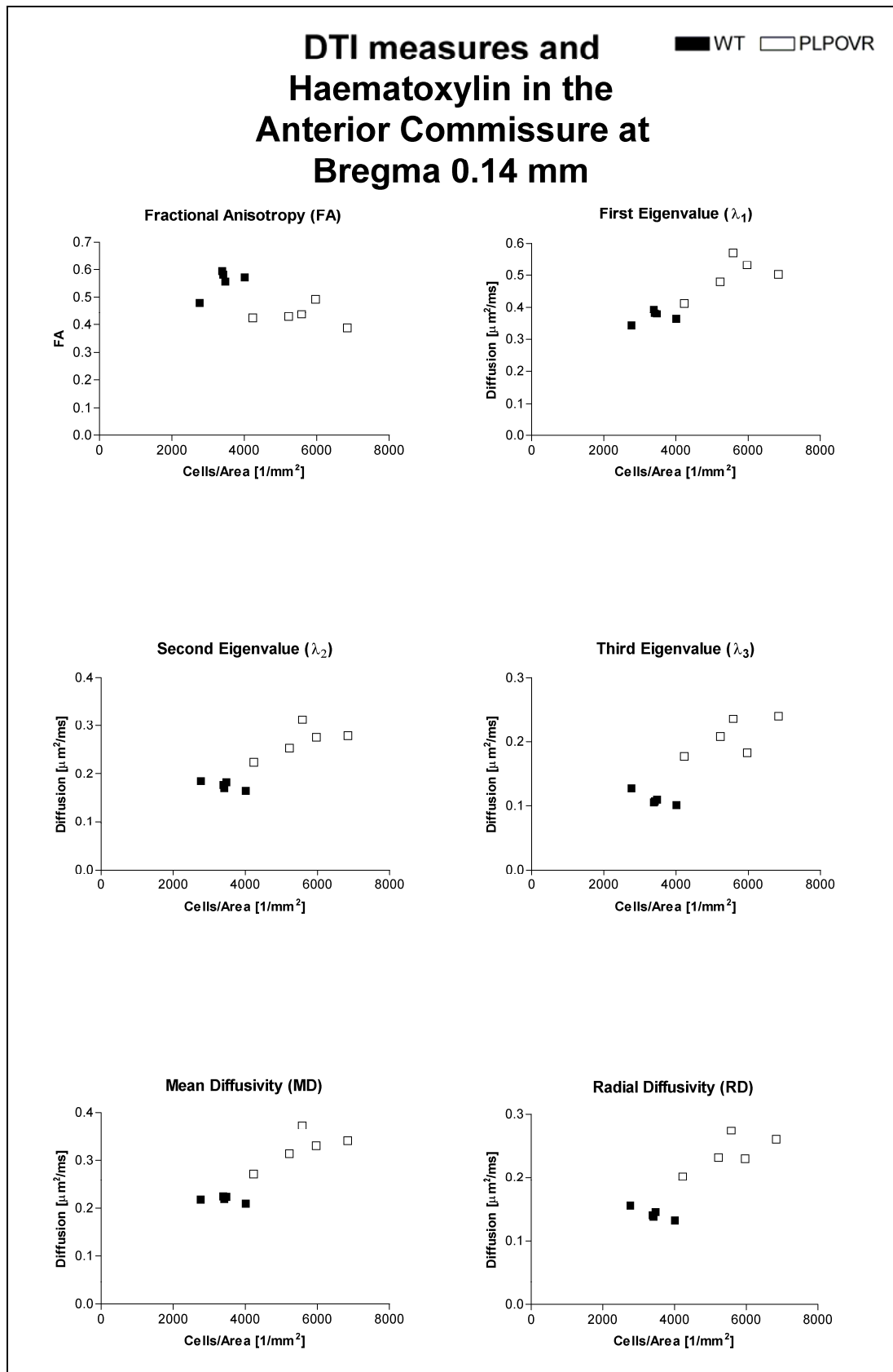


**Fig. 4-38. Scatter plot of diffusion parameter values (FA,  $\lambda_1$ ,  $\lambda_2$ ,  $\lambda_3$ , MD, RD) vs. haematoxylin histology on individual animals at the level of the anterior commissure (Bregma 0.14 mm).**

**Chapter 4 - Investigating the structural correlates of DTI measures in the PMD mouse model of white matter pathology.**

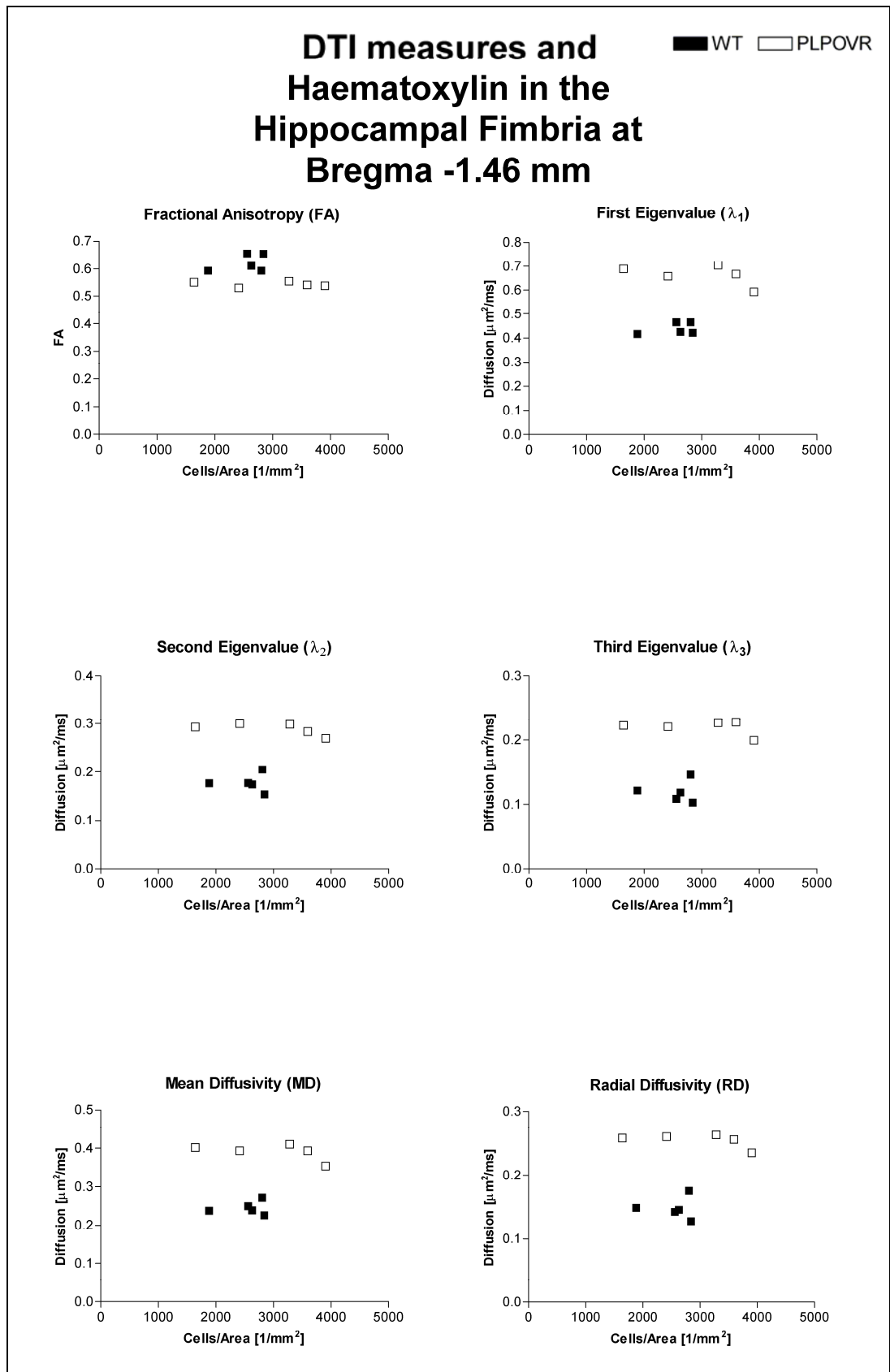


**Fig. 4-39. Scatter plot of diffusion parameter values (FA,  $\lambda_1$ ,  $\lambda_2$ ,  $\lambda_3$ , MD, RD) vs. haematoxylin histology on individual animals at the level of the hippocampal fimbria (Bregma -1.46 mm).**

**Chapter 4 - Investigating the structural correlates of DTI measures in the PMD mouse model of white matter pathology.**

Anterior Commissure 0.14 mm			Hippocampal Fimbria -1.46 mm		
	Genotype			Genotype	
	WT	PLPOVR		WT	PLPOVR
Haematoxylin vs.	r	r	Haematoxylin vs.	r	r
FA	0.00	0.10	FA	0.00	-0.20
$\lambda_1$	0.00	0.60	$\lambda_1$	0.10	-0.50
$\lambda_2$	-0.70	0.70	$\lambda_2$	-0.30	-0.70
$\lambda_3$	-0.60	0.70	$\lambda_3$	-0.30	-0.10
MD	-0.30	0.70	MD	-0.10	-0.50
RD	-0.70	0.50	RD	-0.30	-0.60

**Table 4-4. Correlation after Spearman of haematoxylin vs. DTI measures (FA,  $\lambda_i$ , MD, and RD) in the anterior commissure and hippocampal fimbria (sampled at Bregma levels given).**

r is the Spearman correlation coefficient.

**4.5 Discussion.**

To our knowledge, this was the first time that DTI was employed in a mouse model of *Plp1* overexpression, with extensive assessment of histopathology. In this study we demonstrated widespread differences in the white matter of PLPOVR using DTI that were associated with histopathology. FA decreased, and all diffusion sensitive measures ( $\lambda_i$ , MD, and RD) increased in several white matter tracts such as the anterior commissure, corpus callosum and hippocampal fimbria in PLPOVR mice as illustrated with subtraction map analyses. These findings were confirmed statistically using the DTI analysis software TBSS, and by conventional ROI-based analysis for the tracts mentioned. In the following, only FA,  $\lambda_1$ , MD, and RD will be discussed as there is limited information on  $\lambda_2$ , and  $\lambda_3$  in the literature. In the tracts mentioned above, myelin pathology in PLPOVR mice was detected as a reduction of MBP immunoreactivity and was confirmed in ultrastructural assessment of the white matter with EM. APP and GFAP immunoreactivity were increased in PLPOVR mice confirming axonal pathology, and astrocytic hypertrophy, respectively. DTI and histopathology measures were checked for associations in the anterior commissure (least affected in MBP immunohistochemistry data) and hippocampal fimbria (most affected in MBP immunohistochemistry data). No correlations were found between FA and MBP in any tract of PLPOVR mice. Negative correlations were observed for MBP and  $\lambda_1$ , MD and RD, respectively, in the anterior commissure of PLPOVR mice. Increased APP immunoreactivity was associated with increases in all DTI-derived parameters except RD in the hippocampal fimbria of PLPOVR mice. Similarly, all DTI parameters, except

## **Chapter 4 - Investigating the structural correlates of DTI measures in the PMD mouse model of white matter pathology.**

RD, were positively associated with increases in the GFAP-stained area as measured in the anterior commissure, while in the hippocampal fimbria, negative correlations with DTI-extracted parameters were observed in PLPOVR mice.

### **4.5.1 DTI data.**

#### **FA is significantly reduced in all white matter tracts examined in PLPOVR mice.**

Significant reductions of FA in PLPOVR mice compared to WT were detected in all white matter tracts examined. This was shown by all methods of analysis: subtraction maps (only visual inspection), ROI-based measurements, and the relatively novel technique of TBSS. This indicates that the white matter integrity within the tracts reported is compromised in PLPOVR compared to WT mice. This is consistent with previous DTI studies of white matter injury, such as demyelination in humans, as well as in animal models of diseases. As an example of the latter, Song *et al.* treated mice with cuprizone, for 3, 6 and 12 weeks. Cuprizone is a toxin that selectively leads to demyelination of the corpus callosum and this model is regarded as a model for investigating remyelination because when drug treatment is ceased, remyelination occurs. During the time course mentioned above, a reduction of 14, 22, and 31 %, respectively, was observed in RA in the corpus callosum of cuprizone-treated mice (Song et al., 2005). In the present study the reduction in FA was maximal in the corpus callosum (26 %) followed by around 22 % in the anterior commissure and 13 % in the hippocampal fimbria. Likewise, Harsan *et al.* showed in the *jimpy* mouse model of PMD that the FA was reduced by 35 % in the corpus callosum, and 33 % in the anterior commissure (Harsan et al., 2007). Our data is also in line with a report of DTI on PMD patients, where FA was significantly reduced compared to normal controls (Laukka et al., 2006). Thus our data on FA are comparable to other reports and suggest that FA is a good marker of myelin status.

It is clear from developmental DTI studies, both in humans and animals, that increases in FA are paralleled with brain maturation that involves myelination of fibre tracts (Huppi et al., 1998, Jito et al., 2008, Saksena et al., 2008). However it should be noted that there is considerable anisotropy before myelination takes place in human preterm babies, which Huppi *et al.* referred to as a pre-myelination step. The physical explanation for this may be the increase in fibre calibre, and membrane changes that make the axons permissive for the early wrapping of oligodendrocytes (Huppi et al., 1998).

## Chapter 4 - Investigating the structural correlates of DTI measures in the PMD mouse model of white matter pathology.

### $\lambda_1$ , MD, and RD are significantly increased in all white matter tracts examined in PLPOVR mice.

In contrast to FA, diffusion sensitive measures ( $\lambda_1$ , MD, and RD) were all significantly increased in PLPOVR mice using all of the image analysis techniques described above. There is good consistency between the literature and the results discussed here in terms of FA as a marker of fibre integrity and RD as a marker of myelin injury (Song et al., 2002). The former is usually decreased, while the RD is consistently increased in pathology involving white matter. We report here an increase in RD of 90 % in the corpus callosum, 71 % in the hippocampal fimbria, and in the anterior commissure of 66 %. The former is comparable to the *in vivo* report by Harsan and colleagues, where an increase in *jimpy* mice of 84 % in the corpus callosum, but only 38 % was observed in the anterior commissure (Harsan et al., 2007). Likewise, in the mouse cuprizone study that models remyelination observed in MS, an increase of 47 % in the corpus callosum in RD after 12 weeks of treatment was detected (Song et al., 2005). For comparison, it is worth looking at reports of other structures. For instance, Sun reports an increase in the optic nerve and tract in RD of 156 % and 86 %, respectively, or in the dorsal column of the spinal cord in an EAE model which caused an 81 % increase in DeBoy *et al.* (DeBoy et al., 2007, Sun et al., 2007). In addition in a recent human MS DTI study, RD was significantly elevated giving further support for this finding (Roosendaal et al., 2009). The origins of RD changes have been linked to the pathology of the myelin sheath, where remyelination of the corpus callosum after experimental demyelination with the drug cuprizone normalised RD (Song et al., 2005). In general during brain maturation, the overall diffusion decreases (MD), which parallels the time course of increasing presence of myelinated fibres (Jito et al., 2008).

However, MD, which is often reported in clinical studies to assess overall water displacement, shows some degree of disparity in the literature. This may reflect the fact that MD is the average of all 3 eigenvalues, and is therefore a rather crude marker for white matter pathology assessment: there may be clinical conditions that affect  $\lambda_1$  and the two perpendicular diffusion constants ( $\lambda_2$  and  $\lambda_3$ ), in an opposing manner, i.e. an increase in  $\lambda_1$  due to a pathological state could be balanced out by a decrease in  $\lambda_2$  and  $\lambda_3$ . For instance, Song *et al.* reported a significant increase in RD in the anterior commissure of *shiverer* mice compared to WT animals, while  $\lambda_1$  remained unchanged which may have resulted in an otherwise overlooked myelin deficiency if only the MD (in fact Tr) had been used, which was found to be reduced (Song et al., 2002). This finding is in contrast to Tyszka's

#### **Chapter 4 - Investigating the structural correlates of DTI measures in the PMD mouse model of white matter pathology.**

DTI study on *shiverer* mice, where a significant increase in the Tr was shown (Tyszka et al., 2006). The increase in MD that we have observed was of the magnitude of 72 %, 59 %, and 46 % in the corpus callosum, hippocampal fimbria, and anterior commissure, respectively, and an increase is consistent with the *jimpy* model of PMD, where a 34 % and a 21 % increase was observed in the corpus callosum, and anterior commissure, respectively (Harsan et al., 2007). An increase was also reported after 12 weeks of cuprizone treatment in the corpus callosum of treated mice (Song et al., 2005), and in a DTI study of human MS compared to healthy volunteers (Ceccarelli et al., 2009). However there is also inconsistency in the literature including a study in human PMD, where MD appears to be decreased to approximately 40 % of normal. Unfortunately this study has been reported only in poster form and not in a fully peer-reviewed publication (Laukka et al., 2006). Therefore it is suggested that reporting RD,  $\lambda_1$  and FA is preferable in order to preserve information that would be lost through the data averaging performed to calculate MD.

Apart from increased RD and MD, we found significant increases in  $\lambda_1$ , a marker of axonal integrity (Song et al., 2002), of 54, 51, and 31 % for the corpus callosum, hippocampal fimbria and anterior commissure, respectively, while Harsan reported a 13 % increase in the corpus callosum, and 10 % in the anterior commissure of *jimpy* mice (Harsan et al., 2007). The differences might reflect that these data were obtained *in vivo*, and / or that the *jimpy* mice have a more severe phenotype such that the male animals had to be scanned at P25 as *jimpy* mice die prematurely at around P30. However, a 38 % reduction in Tr is expected due to temperature differences *in vivo* and *ex vivo* (Sun et al., 2003). Therefore this effect can be ruled out, as we found a massive increase in  $\lambda_1$  despite the fact that the study was conducted *ex vivo*. Hence it is more likely that the mouse models differ substantially in terms of the severity of white matter pathology. Nevertheless the trend towards an increase in  $\lambda_1$  is consistent with our data, as well as findings in other demyelination models, like the *shiverer* mouse (Tyszka et al., 2006), and in a study of MS patients (Roosendaal et al., 2009). Despite this evidence, there is also some inconsistency in the literature regarding  $\lambda_1$ . For example, in spinal cords of rats with EAE (DeBoy et al., 2007), and both spinal cords (Budde et al., 2008, Kim et al., 2006), and brains of mice with EAE (Sun et al., 2007),  $\lambda_1$  was significantly reduced. Moreover, in the *shiverer* mouse, Song *et al.* found that  $\lambda_1$  was unaltered compared to control mice (Song et al., 2002), which is in contrast to Tyszka's work mentioned above (Tyszka et al., 2006). There is no

## **Chapter 4 - Investigating the structural correlates of DTI measures in the PMD mouse model of white matter pathology.**

evidence of pathological axonal changes in *shiverer* mice, i.e. no APP-positive foci or axonal swellings (Dr. J. M. Edgar, unpublished observation). Song *et al.* also reported a non-significant, but trend towards reduced  $\lambda_1$  in the corpus callosum of cuprizone-treated animals (Song *et al.*, 2005). The reason for this inconsistency in change of  $\lambda_1$  in models of myelin pathology, i.e. EAE (decrease) compared to cuprizone (no change), is unknown, but may reflect different pathology processes that could possibly be identified with  $\lambda_1$ . The EAE literature appears to be consistent in all reports to date (to the author's knowledge) that  $\lambda_1$  is reduced (Budde *et al.*, 2008, DeBoy *et al.*, 2007, Kim *et al.*, 2006, Sun *et al.*, 2007). Efforts have been made to link particular signal features of DWI and DTI to different characteristics of diseases. For example, Ono *et al.* suggested when applying standard DWI (not DTI) to mouse models of PMD (*jimpy* mouse), which is a dysmyelinating disorder, and Krabbe's disease (*twitcher* mouse), which is a demyelinating disease, that these 2 disorders could be told apart. The authors found that diffusion anisotropy is unaltered in *jimpy* mice compared to WT, while *twitcher* mice displayed decreased anisotropy relative to controls (Ono *et al.*, 1995). Similarly,  $\lambda_1$  might be used to distinguish different pathologies, however this parameter is not often reported.

In summary, our findings on FA and RD are consistent with literature on animal models and human pathological conditions that support the notion that FA decreases as a result of loss of fibre integrity and myelin injury. This is supported by observations made during mouse white matter development and recovery from demyelination (remyelination) which show that FA increases, and RD (as well as MD) decreases during myelination (Jito *et al.*, 2008, Song *et al.*, 2005). Thus this suggests that FA and RD are general markers of white matter integrity, while  $\lambda_1$  may potentially be used to differentiate pathologies: in all the reports where the EAE model was used, the  $\lambda_1$  was reduced compared to controls (Budde *et al.*, 2008, DeBoy *et al.*, 2007, Kim *et al.*, 2006, Sun *et al.*, 2007).

### **4.5.2 Histopathology.**

#### **MBP-stained area is significantly decreased in all white matter tracts examined in PLPOVR mice.**

In parallel to the DTI data presented above, our collaborators acquired an extensive set of pathological measures in the same set of animals that were used for DTI acquisition. In addition, another set of mice was generated to elucidate the ultra-structural differences between WT and PLPOVR mice using EM. Significant reductions were found for all tracts

## **Chapter 4 - Investigating the structural correlates of DTI measures in the PMD mouse model of white matter pathology.**

examined using MBP in order to explore the myelination status in PLPOVR compared to WT animals. MBP is a marker of compact myelin that accounts for 30 % of total myelin protein and is the second most abundant myelin protein just after PLP (50 %) in normal white matter (Karim et al., 2007). Our data showed that in PLPOVR mice the hippocampal fimbria contained the most compromised fibres in terms of loss of MBP-stained area (87 %), followed by the corpus callosum (53 - 70 %), with the anterior commissure having lost 47 % of MBP relative to WT animals. This rank order led us to select the hippocampal fimbria (the most affected tract), and the anterior commissure (the least affected tract) for correlation analyses between histopathology and DTI measures.

### **MBP-stained area does not correlate with FA, but correlates negatively with $\lambda_1$ , MD, and RD in the anterior commissure of PLPOVR mice.**

While FA does not correlate to the MBP-stained area, there is a consistent association in  $\lambda_1$ , MD, and RD in the anterior commissure of PLPOVR mice. This is in accordance with previously published data showing that loss of myelin is associated with an increase in RD indicating that myelin acts as a restriction barrier preventing water molecules to pass (Assaf et al., 2008, Budde et al., 2008, Harsan et al., 2007, Harsan et al., 2006, Song et al., 2002, Song et al., 2005, Sun et al., 2007). However a reduction in MBP-stained area in the hippocampal fimbria of 87 % in PLPOVR compared to WT mice does not translate into an association with any DTI-derived parameter. This might be indicative of the hippocampal fimbria being affected earlier in the disease progression compared to the anterior commissure. Unfortunately, only 1 time point, P120, was investigated, which might also be the reason why no association between FA and MBP was found. At P120, PLPOVR animals die prematurely because of seizures (Readhead et al., 1994), which might also mark a plateau phase in the hippocampal fimbria at which all myelin is already deteriorated and therefore would have no more influence on  $\lambda_1$ , MD, and RD. This is obviously in contrast to the anterior commissure (MBP reduced by 47 %), where MBP immunoreactivity suggests that there is still enough myelin present at P120 in PLPOVR mice. Another indication suggesting that the anterior commissure is affected later in PLPOVR lifespan is supported by the comparable amounts of MBP-stained area between anterior commissure, corpus callosum, and hippocampal fimbria in WT mice. The EM data clearly shows that the axon density in the hippocampal fimbria is increased by more than 90 %. Apart from myelin, other factors have been proposed to contribute to anisotropy, such as axon alignment and greater packaging, in addition to an increase in membrane barriers (Beaulieu, 2002). All these events could be postulated to occur in PLPOVR mice,

#### **Chapter 4 - Investigating the structural correlates of DTI measures in the PMD mouse model of white matter pathology.**

as our data suggest that the percentage of myelinated fibres is reduced by more than 90 % in the hippocampal fimbria and corpus callosum, which in turn resulted in higher packaging as shown by higher axonal densities. This implies an increase in membranes belonging to not only nonmyelinated axons, but also an increased number of astrocyte processes in apposition to these axons. This is certainly reflected in relatively small differences in FA ranging from -13 % to -26 % when WT were compared to PLPOVR mice.

Thus our data suggest that myelin availability is associated with altered directional diffusion of water only in the anterior commissure, while FA appears not to correlate with MBP density at this terminal stage of the disease in both tracts examined. These findings may imply that the hippocampal fimbria is affected earlier in disease progression than the anterior commissure.

In the current literature, methodologies vary in terms of MBP quantification. In this study, an arbitrary threshold level was selected visually to binarise the digitised image of a section stained for MBP. This set the MBP-stained area to a pixel intensity of 1, while the remainder was merged to a background level of 0. In contrast, in the *jimpy* model of PMD, Harsan *et al.* only visually inspected fluorescent MBP. A massive reduction in MBP was observed in *jimpy* mice compared to controls (Harsan *et al.*, 2007). This was also the case in an immunohistochemical assessment of MBP in the #66 mouse strain model of PMD, when visually compared to control mice (Readhead *et al.*, 1994). The #66 strain of mice were also used by Karim *et al.* to quantify myelin volume with EM, which appeared to be reduced by roughly 60 % in these mice compared to WT at P20 (Karim *et al.*, 2007). Our EM data is also in line with this, where myelinated, relative to total number of fibres, were reduced by more than 90 % at P120 in PLPOVR compared to WT.

#### **Number of APP-positive foci is significantly increased in all white matter tracts examined in PLPOVR mice.**

APP is a marker for impaired axonal transport, and is therefore often reported to be involved in axonal degeneration. In case of axonal injury, APP, which undergoes fast axonal transport, is accumulated at the site, to which the proximal end is still functional, however distal to the block the axon is undergoing degeneration (for review see Coleman *et al.* (Coleman, 2005)). We assessed the number of APP-positive foci in PLPOVR and WT by immunohistochemistry and found significant elevations in all tracts examined in

#### **Chapter 4 - Investigating the structural correlates of DTI measures in the PMD mouse model of white matter pathology.**

PLPOVR mice compared to WT, markedly in the anterior commissure (2713 - 5680 %), followed by the hippocampal fimbria (1929 %), and the corpus callosum (450 - 2850 %).

#### **Number of APP-positive foci correlates positively with DTI data in the hippocampal fimbria of PLPOVR mice.**

In spinal cord preparations of mice that underwent a procedure to induce EAE, Kim and colleagues reported an increase in APP (no numeric value was given) that would be associated with reduced  $\lambda_1$  (appeared to be in the order of ~25 %) (Kim et al., 2006). Indeed, an association, a positive however, between APP-positive foci and DTI parameters (FA,  $\lambda_1$ , MD) was found in our study in the hippocampal fimbria of PLPOVR mice, while only small associations were present in the anterior commissure. As Shigematsu and colleagues pointed out, microglia are capable of removing APP from injured neurons (Shigematsu et al., 1992). This could indicate that there may be differences in the temporal progression between the anterior commissure and the hippocampal fimbria: an augmentation of APP-positive foci in the anterior commissure may precede the activation of microglia (indicated by increased haematoxylin-stained nuclei). This could have just taken place at the time the PLPOVR animals were culled, with no effect yet on an association between DTI parameters and APP staining in this tract. This may be in contrast to the events that might have had taken place in the hippocampal fimbria, where it appears that this response has already passed, resulting in normal numbers of haematoxylin-stained cells (likely mainly microglia) compared to WT, which in turn is supported by the positive associations where increased APP immunoreactivity in PLPOVR was found to translate into greater values of DTI-derived parameters. Thus, the associations between APP and DTI measures may be a secondary response, driven by the reductions of microglia representing diffusion barriers.

In a setup where DTI and APP measurements were checked at various time points, Song *et al.* reported increased APP in the corpus callosum of cuprizone-treated mice compared to WT. However the time course of APP increase, which peaked at 3 weeks (the mean appeared to be around 400 %, ranging between 150 - 700 %) of continuous treatment and declined rapidly thereafter (no statistical significance compared to control animals after 12 weeks of treatment), did not match the one of RD, which was becoming significant only after 6 weeks. A non-significant reduction in  $\lambda_1$  from 0.28 to 0.25 (supposedly  $\mu\text{m}^2/\text{ms}$ , units were not given), which converts to ~10 %, over a 3 weeks time course was also observed (Song et al., 2005). The rapid APP response is in line with clinical studies of MS,

#### **Chapter 4 - Investigating the structural correlates of DTI measures in the PMD mouse model of white matter pathology.**

where in biopsied tissue it appeared that  $\sim 400$  APP-positive axons/mm<sup>2</sup> were found in acute MS lesions (disease duration < 1 year), while  $\sim 100$  APP-positive axons/mm<sup>2</sup> were counted in chronic patients with a disease duration of > 10 years (Kuhlmann et al., 2002). The notion that APP would cause a reduction in  $\lambda_1$ , as suggested by Kim *et al.*, cannot be confirmed as we see a huge increase in this parameter (see below for more). As APP and DTI measures were not measured at various time points, we cannot make a clear statement about an association of these measurements. In fact only one time point was selected in the Kim *et al.* study either (Kim et al., 2006). Thus it is more likely that these 2 measures are not directly related as shown in the study performed by Song and colleagues (Song et al., 2005).

Therefore, even though APP immunostaining appears to correlate with DTI measures in the hippocampal fimbria in this study, this could reflect normal variations and would need to be validated in a longitudinal study. It should be pointed out though that similarities between the aforementioned study performed by Song and colleagues and the current study exist in terms of lowered FA (RA in Song *et al.*), and increased MD and RD (Song et al., 2005).

#### **GFAP-stained area is significantly increased in all white matter tracts examined in PLPOVR mice.**

GFAP is an astrocytic protein that is upregulated when astrocytes become activated due to various pathological processes in the central nervous system and is therefore a marker for general injury in the brain (Yong, 1998). This marker is significantly increased in PLPOVR mice compared to WT, affecting the corpus callosum (372 - 1426 %) the most, the anterior commissure (859 - 879 %) second, with the hippocampal fimbria (563 %) being the tract where the least increase in GFAP was detected. GFAP-expressing astrocytes may assume a supportive role to injured axons. This view is supported by findings in the spinal cords of GFAP knockout mice in which EAE was induced. GFAP knockout mice showed more severe clinical signs compared to normal WT mice, both with induced EAE, which was accompanied with a more widespread lesion area in GFAP knockout mice, as opposed to WT. This led the authors to conclude that intimate astrocyte contact is necessary to stabilize the injured axon and restrict EAE lesion size and clinical symptoms (Liedtke et al., 1998). Interestingly, in spinal cords of rats that received a cervical lateral funiculotomy, astrocytes were reported to align perpendicular to the spinal cord white matter, which could be detected by DTI. This changed the orientation of the

#### **Chapter 4 - Investigating the structural correlates of DTI measures in the PMD mouse model of white matter pathology.**

principal eigenvector from along the white matter tract to perpendicular to it (Schwartz et al., 2005). However it has been reported by another group that astrocytes normally would wrap the injured axon longitudinally (parallel), i.e. along the long axon axis. Indeed, the same authors also showed that astrocytes respond to an extracellularly applied voltage gradient in such a way that they change their orientation slightly ( $\sim 10^\circ$ ), in the nearby unlesioned white matter of the rat spinal cord. The voltage gradient was applied arbitrarily (Moriarty and Borgens, 2001), so it could be possible that a condition existed that led to a change of astrocyte orientation perpendicular to the tract as reported by Schwartz *et al.* (Schwartz et al., 2005). But even though the orientation of the principal vector might have changed,  $\lambda_1$  would still have the highest value and could therefore not be confused with RD. There is some evidence that could lead to an increase in  $\lambda_1$ , since astrocytes, as shown by Oshio *et al.*, contain water channels, so called aquaporins. These are co-localised with GFAP in astrocytes of the mouse spinal cord (Oshio et al., 2004). The same laboratory showed that in the central nervous system grey matter of aquaporin knockout mice, the osmotic water permeability is reduced compared to WT (Solenov et al., 2002). More recently, Harsan *et al.* demonstrated in a DTI study of the *jimpy* mouse model of PMD an increase in  $\lambda_1$  (and RD), which the authors attributed to astrocyte hypertrophy. The authors measured aquaporin protein expression levels, and found a 16 % increase relative to control mice. This was in contrast to oligo-TTK mice in the same study that did not show such a severe astrocyte hypertrophy, however reduced  $\lambda_1$ . Thus the authors linked this astrogliosis to the observed increase in  $\lambda_1$  (Harsan et al., 2007). The oligo-TTK mouse is a transgenic model of demyelination, in which a truncated form of the herpes simplex virus 1 thymine kinase gene under the control of the *MBP* promoter is expressed by oligodendrocytes. Upon injection of ganciclovir, the transgene thymine kinase renders this substrate into a toxin for mitotic oligodendrocytes thereby leading to demyelination (Harsan et al., 2006).

#### **GFAP-stained area correlates positively with DTI data in the anterior commissure, and negatively in the hippocampal fimbria of PLPOVR mice.**

As pointed out above, GFAP-stained area was higher in the anterior commissure (second to the corpus callosum) compared to the hippocampal fimbria. Therefore this could provide more evidence supporting that the hippocampal fimbria is affected earlier in disease by demyelination than the anterior commissure. Activated astrocytes pursue a role in regeneration by removing debris, may neutralise toxins, and can release growth factors to stimulate differentiation of oligodendrocytes that form myelin (Yong, 1998). Interestingly

#### **Chapter 4 - Investigating the structural correlates of DTI measures in the PMD mouse model of white matter pathology.**

there is a consistent association of all DTI parameters with GFAP, however the direction of these associations is different between the 2 tracts examined. In the anterior commissure, a positive correlation was found between DTI parameters and GFAP-stained area. FA increases in this tract as GFAP augments, which may be indicative of astrocytes attempting to fix, supposedly successfully, white matter myelin lesions. At the same time, diffusion sensitive measures ( $\lambda_1$ , MD, and RD) increase that Harsan *et al.* have associated with the increase of activated astroglia, hence facilitating directional water diffusion (see Harsan *et al.* above (Harsan et al., 2007)). In contrast, in the hippocampal fimbria negative associations were found between DTI measures and GFAP-stained area. This might be due to the fact that astrocyte promoted recovery is failing as demyelination is constantly progressing. Myelin loss could not be compensated for any longer, and therefore an increasing GFAP immunoreactivity would result in a negative association between GFAP and diffusion sensitive measures ( $\lambda_1$ , MD, and RD) in PLPOVR mice. Glial scars may form that consist of various cell types, myelin debris, and collagen bundles (Yong, 1998). These scars likely hinder water diffusion, which might explain the negative trend in the associations.

However it is surprising that the mere increase of aquaporin, that is associated with astrocyte hypertrophy, would be the reason for increased diffusion, particularly along the axon ( $\lambda_1$ ). Unfortunately, the only 2 known studies where DTI and GFAP measurements were undertaken do not report any numerical value of how much change was observed in  $\lambda_1$  or GFAP (Ramu et al., 2008, Schwartz et al., 2005). Therefore the claim made by Harsan *et al.* that an increase in astrocyte hypertrophy is associated with an increase in  $\lambda_1$ , while dysmyelination with little activated astrocytes results in a reduced  $\lambda_1$  (Harsan et al., 2007), would need to be confirmed in further studies.

#### **Haematoxylin staining correlates positively with DTI data in the anterior commissure, and negatively in the hippocampal fimbria of PLPOVR mice.**

An increase in haematoxylin-stained cell nuclei was detected that was only significant in the anterior commissure. Similarly to GFAP data, positive associations between the number of nuclei and diffusion sensitive measures ( $\lambda_1$ , MD, and RD) were observed, but only for the anterior commissure, while negative associations between these measures were detected in case of the hippocampal fimbria. Haematoxylin is a nonspecific marker for cell nuclei. Thus specific cell types cannot be discerned using this method. The light microscopy images of the corpus callosum may suggest that there are astrocytes and

## **Chapter 4 - Investigating the structural correlates of DTI measures in the PMD mouse model of white matter pathology.**

microglia in PLPOVR mice that cannot be observed in WT mice at that level of magnification (Fig. 4-28). The latter are thought to act as the innate immune system of the central nervous system and upon activation may resume a phagocytotic role to remove debris (Garden and Moller, 2006). Therefore the positive association between increasing cell numbers and increasing diffusion sensitive measures in the anterior commissure could indicate axonal and myelin injury. Microglia may remove APP that possibly blocked the water diffusion within the axon. In contrast, in the hippocampal fimbria, this response may have already declined, because most of the myelin is deteriorated and debris is removed or is interwoven to form a glial scar. Hence the cell density as detected with haematoxylin staining has almost normalised, with barriers present in form of glial scars that may be reflected by a negative correlation between cell nuclei staining and DTI measures ( $\lambda_1$ , MD, and RD).

### **One developmental stage vs. various developmental stages.**

In the presented study, only one developmental time point, P120, which approximates the time point of premature death in PLPOVR mice, was selected. This is a big caveat as it compromises the results obtained by correlation. Since the progression of white matter demyelination is stereotypic and therefore reproducible, there is not much spread in histology data, and not in the DTI-derived measurements either. Thus, for example, expected correlations between MBP and FA were not detected. Further studies would need to be conducted in order to more thoroughly elucidate these relationships. The main aim of this study was to answer the question whether the DTI image processing methodology that was applied in the study described in chapter 3 (page 98) was appropriate. This is apparently the case.

### ***Plp1* overexpression as a model of PMD.**

Even though the most common cause of human PMD is the duplication of the *PLP1* gene, it must be recalled here that the mouse strain used in the current study (#72, (Readhead et al., 1994)) is bearing 6 copies of the *Plp1* transgene. In addition, the disease in humans is extremely heterogeneous, reflecting the complexity of the disease. The size of the duplicated segment varies, and can even translocate to different locations on the X-chromosome. These are only 2 aspects that might influence the severity of this disease (see Hudson *et al.* for review (Hudson, 2003)). This mouse model simplifies the analysis by the reduction of variation.

## **Chapter 4 - Investigating the structural correlates of DTI measures in the PMD mouse model of white matter pathology.**

### **4.6 Final conclusions.**

While we were able to successfully apply the DTI image processing technique developed in chapter 3 (page 98), some issues could not be resolved. It appears clear that FA and RD are associated with fibre integrity and myelin status, respectively, which are directly linked to the presence of myelin. However not much is known about  $\lambda_1$  that was claimed to be an indicator of axonal injury. Therefore the aim to shed more light onto the meaning of DTI-derived parameters, particularly  $\lambda_1$  in terms of finding the histological basis of changes in the latter, was not successfully addressed. This was particularly because only 1 fixed time point was chosen in our experiment, which was at which the animals would die prematurely (P120). Thus the time course of histopathology measures could not be associated directly with evolving changes in DTI-extracted parameters. The disease progression in PLPOVR mice is stereotypic and reproducible so that there is not sufficient spread in the data to provide enough evidence supporting or objecting to associations between DTI-derived measures and histopathology. Animal numbers in both groups were low as well which complicates the interpretation of correlation studies. In addition to these limitations, it appears that there is no standard way in reporting DTI data that would make comparisons easier. For example in most studies, only the FA and MD are reported. FA is not the most sensitive parameter of the DTI-derived data set, and MD has limitations as it contains pooled information from all 3 eigenvalues whose changes may cancel each other out as they may be directed in opposite directions.

In summary, this mouse model of PMD (#72 strain) was never before assessed for brain myelin and axonal pathology using *ex vivo* DTI. In addition, this is one of the most extensive studies that associated various markers for myelin and axon integrity to DTI-derived parameters. We also may have identified that there may be the anterior commissure affected later in disease progression compared to the hippocampal fimbria, which was not reported before.

Chapter 5 - Autoradiographic measurements of SERT and DAT densities in a mouse model of PMD.

**Chapter 5 - Autoradiographic measurements of SERT and DAT densities in a mouse model of PMD.**

## **Chapter 5 - Autoradiographic measurements of SERT and DAT densities in a mouse model of PMD.**

### **Chapter 5 - Autoradiographic measurements of SERT and DAT densities in a mouse model of PMD.**

#### **5.1 Introduction.**

The detection of a massive loss of white matter integrity using conventional immunohistochemistry, histology, and advanced MRI technologies like DTI lead us to hypothesise that this loss might have effects on serotonin and dopamine systems. Changes in white matter structure are implicated in a range of psychiatric conditions, including depression and schizophrenia. Given the link between psychiatric diseases and the function of monoaminergic systems, the question could therefore be asked: is widespread demyelination and axonal damage associated with abnormalities in monoaminergic transporters? One mechanism by which this could happen is indicated by a general concept in synaptic plasticity, which states "what fires together, wires together". A postsynaptic neuron receives multiple inputs from presynaptic neurons from all over the brain. It is important that activation of the postsynaptic neuron is done in temporal coincidence by all its presynaptic neurons to reach a certain threshold of depolarisation for activation. As the distance between presynaptic neurons and the postsynaptic neuron is different for most of the presynaptic neurons, myelin can act as a regulator to reduce or increase conduction velocity so that action potentials arrive at the postsynaptic neuron in temporal coincidence with other action potentials from other presynaptic neurons. Optimal conduction velocities are given by a g-ratio of  $\sim 0.65$ , and any deviation from that could potentially reduce conduction velocity. If demyelination occurs, activation of the postsynaptic neuron may not be possible anymore as action potentials are likely to arrive out of synchrony (for review see Fields *et al.* (Fields, 2008)). After the concept "what fires together, wires together", this would mean that connections would potentially be lost. Furthermore as shown in the previous chapter, PLPOVR mice, compared to WT showed high incidence of APP-positive foci indicating disruption of axonal transport. This could possibly lead to axonal degeneration, i.e. Wallerian degeneration whereby the portion of the axon distal to the transport impairment degenerates. Or it may be the consequence of distal degeneration, i.e. the degeneration starts from the terminals and progresses retrogradely. In either case the terminals could be lost (for review see Coleman *et al.* (Coleman, 2005)).

Qualitatively, altered diffusion properties in substructures of the hippocampus were observed in PLPOVR animals compared to WT using DTI. This indicated possible

## **Chapter 5 - Autoradiographic measurements of SERT and DAT densities in a mouse model of PMD.**

alterations in the hippocampal circuitry. The hippocampus is known to undergo atrophy in depression (Bremner et al., 2000), and stress-related atrophy of the hippocampus has been shown to reverse during antidepressant treatment (Czeh et al., 2001). PLPOVR animals also displayed seizures, which might have had their origin in the temporal lobes (Bonilha et al., 2009). Segal *et al.* showed that the hippocampus receives serotonergic input from the raphe nuclei (Segal, 1975), while Theodore *et al.* summarised evidence that emerged indicating a role of serotonin, e.g. in the hippocampus, in epilepsy (Theodore, 2003). In addition, it has been known for more than 30 years that there is an interaction between myelin components and serotonin. For example, Root-Bernstein *et al.* presented a model for a binding site for serotonin (Root-Bernstein, 1983), which was identified by Field *et al.* located in the tryptophan-containing region of MBP (Field et al., 1971). The essential serotonin binding sequence within MBP was determined to be Phe-Ser-Trp (Root-Bernstein and Westall, 1984). Interestingly, the peptide fragment of bovine MBP containing the amino acid (115 - 123) sequence Phe-Ser-Trp-Gly-Ala-Glu-Gly-Gln-Lys (note the essential serotonin binding sequence at the n-terminal), when injected into animals, is known to induce EAE, a demyelinating condition considered to be a model for multiple sclerosis (for review see Kies *et al.* (Kies, 1985)). Saakov *et al.* demonstrated that injection of serotonin intracisternally in dog spines resulted in demyelination (Saakov et al., 1977). Furthermore, Azmitia *et al.*, after having made the observation that the majority of unmyelinated serotonergic fibres of the medial forebrain bundle are in close contact with non-serotonergic myelinated fibres, concluded that sprouting serotonergic fibres would use myelinated fibres as cues to reach their target (Azmitia and Gannon, 1983). More recently, Hatzidimitriou *et al.* examined the brains of monkeys that had been treated with MDMA seven years previously. MDMA is known to be neurotoxic and destroys serotonergic terminals. In the MDMA-treated animals Hatzidimitriou *et al.* found that axons were more likely to re-grow if they were in close proximity to myelinated fibres (Hatzidimitriou et al., 1999), thus supporting the hypothesis suggested previously by Azmitia *et al.* (Azmitia and Gannon, 1983).

### **5.2 Aim of the study.**

- I. To test the hypothesis that demyelination could have an influence on the density of serotonergic and dopaminergic terminals using *in vitro* [<sup>3</sup>H]citalopram and [<sup>3</sup>H]WIN 35, 428 autoradiography.

## Chapter 5 - Autoradiographic measurements of SERT and DAT densities in a mouse model of PMD.

### 5.3 Material and methods.

#### Animals.

PLPOVR animals were generated as previously described by Readhead *et al.* (#72 strain) (Readhead *et al.*, 1994), and bred at the animal facility at Glasgow University at a light/dark cycle of 12/12 h. Food and water was accessible *ad libitum*, and all experiments were carried out according to the guidelines laid out in the Animals Scientific Procedures Act under a project license from the UK Home Office and approved by the local ethical review panel. At P120, PLPOVR (n = 5, female) and control mice collected over several months (no littermates) with the same genetic background (n = 4, female) were deeply anaesthetized by supplying gas consisting of 30 % O<sub>2</sub>, 70 % N<sub>2</sub>O, and 5 % isoflurane. The animals were then sacrificed by dislocation of the neck, followed by decapitation and processed as outlined in the material and methods (page 53).

The following levels and regions were then identified as defined by Paxinos *et al.* (Paxinos and Franklin, 2001). Subsequently 1 slide for total, and 1 for nonspecific binding, on which 2 brain sections each were mounted, were used for [<sup>3</sup>H]citalopram and [<sup>3</sup>H]WIN 35, 428 autoradiography. The autoradiography protocols and details on the analysis of autoradiographic data are provided in detail in the material and methods section (page 54).

Bregma level [mm]	Structures
1.98	Prefrontal Cortex
1.10	Anterior Cingulate Cortex, Striatum, Lateral Septum, Nucleus Accumbens
-0.46	Globus Pallidus
-1.46	Retrosplenial Cortex, Basolateral Amygdala, Central Amygdaloid Nucleus, Lateral and Ventral Hypothalamus
-1.82	Dorsal Thalamus, Thalamus, Medial Habenula, CA1, CA3, Dentate Gyrus, Molecular Layer of the Dentate Gyrus, Piriform Cortex
-3.52	Substantia Nigra, Ventral Tegmental Area, Medial Geniculate Nucleus, Superior Colliculus
-4.84	Entorhinal Cortex
-5.68	Cerebellum

## 5.4 Results.

### $[^3\text{H}]$ citalopram autoradiography to label SERT.

#### Levels of nonspecific $[^3\text{H}]$ citalopram binding defined in the presence of fluoxetine.

The levels of nonspecific  $[^3\text{H}]$ citalopram binding were very low and similar in WT and PLPOVR mice. Representative sections from a WT and a PLPOVR animal, respectively, comparing total and nonspecific binding, are shown in Fig. 5-1. Percentages of the total binding that represented specific binding were lowest in PLPOVR dentate gyrus, ( $87 \pm 12 \%$ , data not shown) compared to  $98 \pm 2 \%$  (data not shown) in WT animals. The percentage specific binding of total was highest in the septal area of both WT and PLPOVR (near 100 %, data not shown).

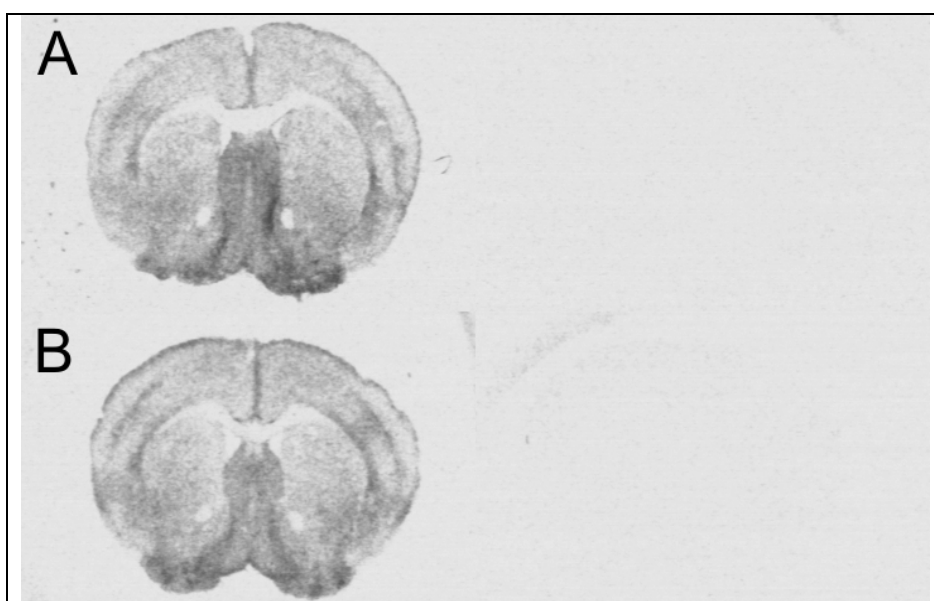


**Fig. 5-1. Nonspecific *in vitro*  $[^3\text{H}]$ citalopram binding is low.**

Nonspecific binding was assessed using fluoxetine to displace  $[^3\text{H}]$ citalopram from SERT.

Left: representative sections showing total binding to SERT.

Right: representative sections showing nonspecific binding defined by pharmacological blockade of SERT with fluoxetine.

A: WT.

B: PLPOVR.

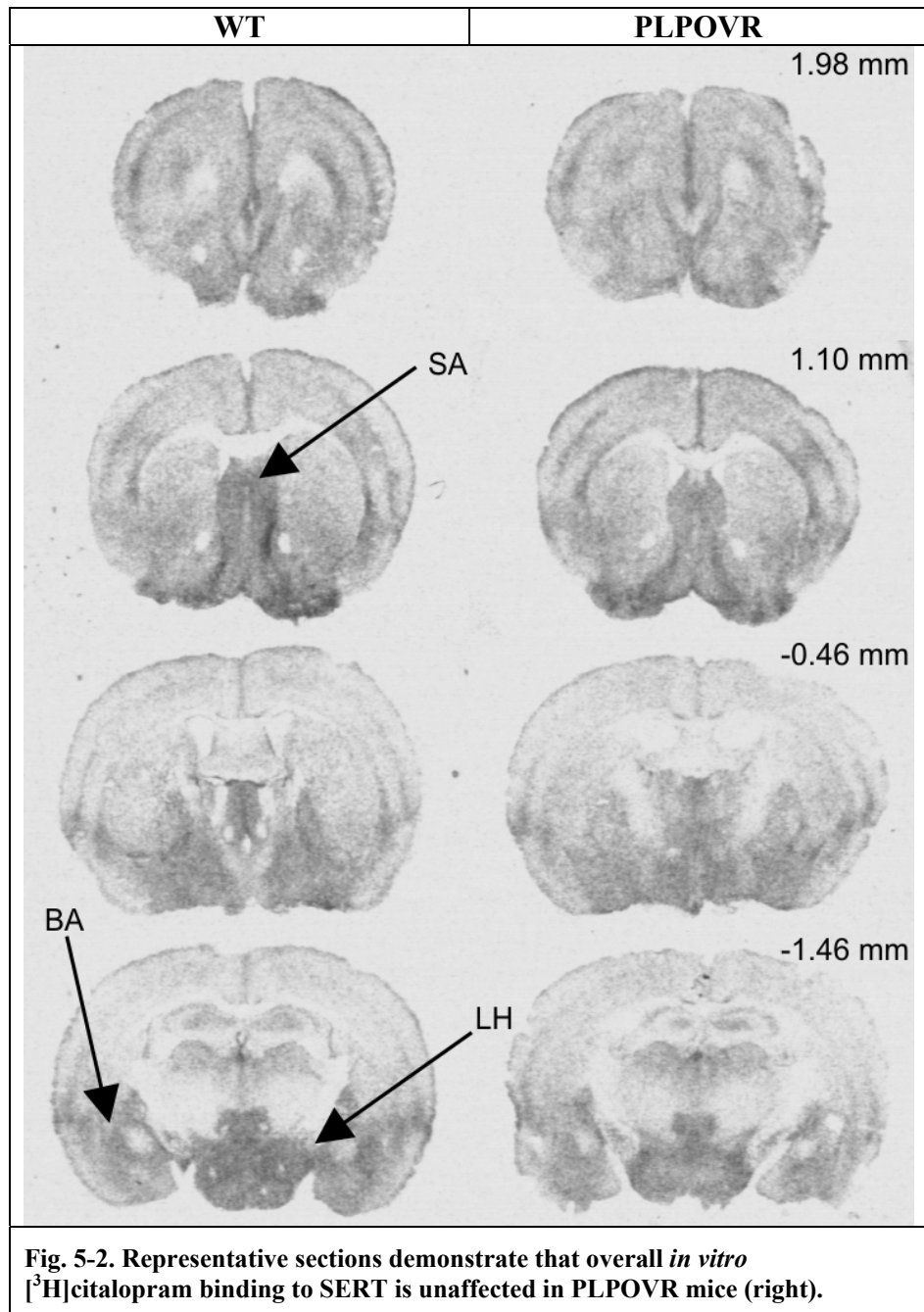
Nonspecific binding of  $[^3\text{H}]$ citalopram was low, and comparable between treatment groups.

#### Visual comparison of representative sections of $[^3\text{H}]$ citalopram binding in WT and PLPOVR animals.

Representative images of total  $[^3\text{H}]$ citalopram binding at all coronal levels analysed from WT and PLPOVR mice are shown in Fig. 5-2. Known SERT-rich structures, including the

**Chapter 5 - Autoradiographic measurements of SERT and DAT densities in a mouse model of PMD.**

septal area, dorsal thalamus, basolateral amygdala, lateral hypothalamus, superior colliculus and substantia nigra show intense [<sup>3</sup>H]citalopram binding in both WT and PLPOVR.



**Chapter 5 - Autoradiographic measurements of SERT and DAT densities in a mouse model of PMD.**

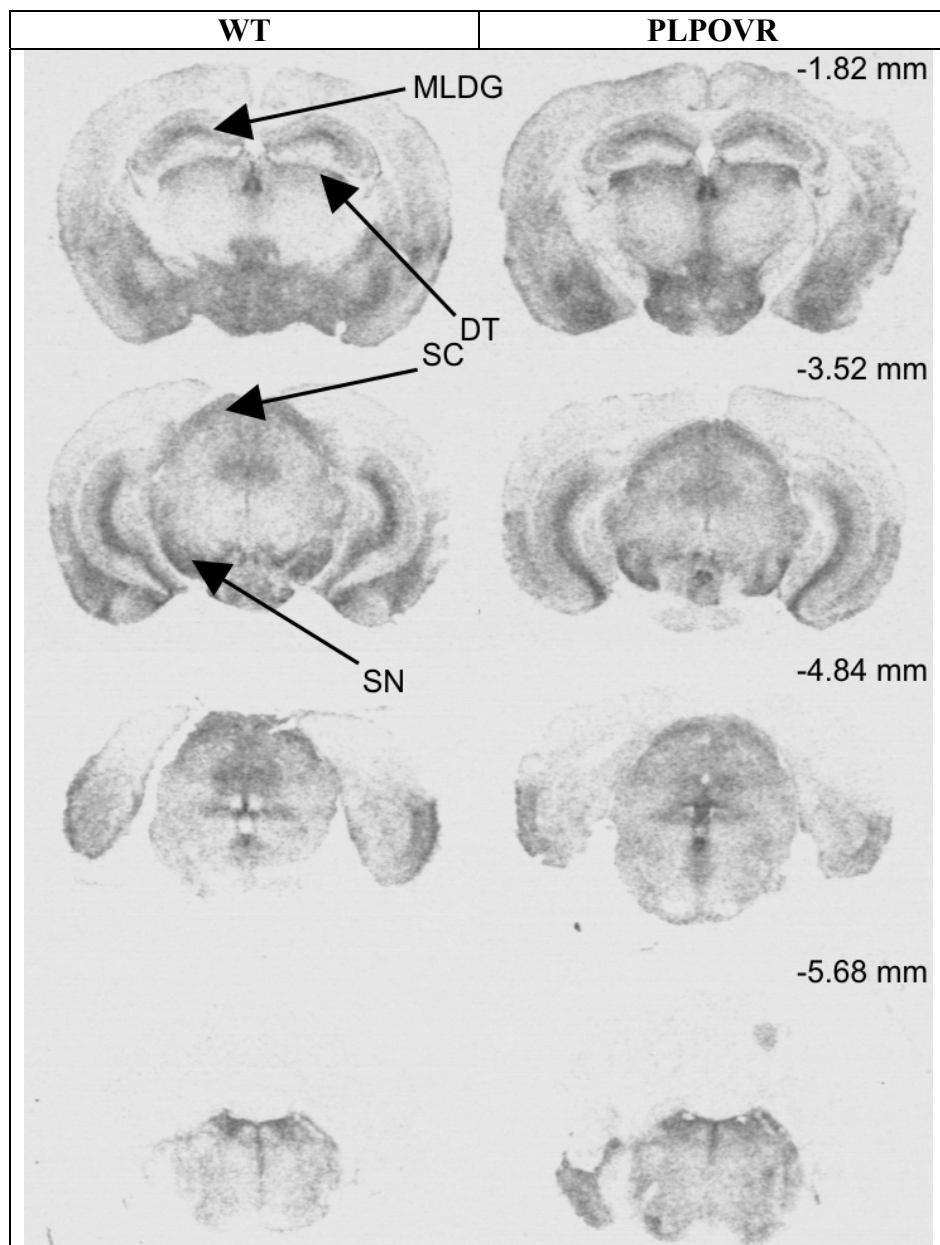


**Fig. 5-2. continued.**

Arrows show SERT-rich binding sites, SA: septal area; BA: basolateral amygdala; LH: lateral hypothalamus; MLDG: molecular layer of dentate gyrus; DT: dorsal thalamus; SC: superior colliculus; SN: substantia nigra. Bregma level is indicated in top left corner.

**Analysis of [<sup>3</sup>H]citalopram binding in WT and PLPOVR animals.**

In none of the structures investigated could a statistically significant difference in specific binding be detected between groups (Table 5-1).

**Chapter 5 - Autoradiographic measurements of SERT and DAT densities in a mouse model of PMD.**

Structure	Genotype		Rel. Diff. [%] <sup>a</sup>
	WT	PLPOVR	
Prefrontal Cortex	71.60 ± 7.00	70.22 ± 3.69	-1.92
Anterior Cingulate Cortex	40.38 ± 10.08	47.54 ± 17.55	+17.72
Caudate-Putamen	44.49 ± 14.25	50.88 ± 13.29	+14.36
Septal Area	119.83 ± 57.65	118.32 ± 35.19	-1.26
Nucleus Accumbens	69.95 ± 28.99	75.23 ± 24.77	+7.54
Globus Pallidus	98.76 ± 23.18	100.47 ± 14.14	+1.73
Retrosplenial Cortex	28.06 ± 5.59	28.62 ± 11.11	+2.01
Basolateral Amygdala	151.84 ± 11.51	130.57 ± 49.85	-14.01
Central Amygdaloid Nucleus	57.26 ± 11.74	42.07 ± 11.07	-26.51
Lateral Hypothalamus	152.37 ± 33.77	166.22 ± 20.70	+9.09
Ventral Hypothalamus	154.09 ± 17.25	96.03 ± 37.42	-37.68
Dorsal Thalamus	112.55 ± 9.37	125.18 ± 37.95	+11.22
Thalamus	74.74 ± 10.30	68.42 ± 29.68	-8.45
Habenula	84.54 ± 11.03	75.02 ± 40.05	-11.26
CA1	106.48 ± 8.64	70.52 ± 27.81	-33.78
CA3	50.41 ± 2.37	39.81 ± 19.25	-21.02
Dentate Gyrus	38.76 ± 4.79	33.18 ± 13.81	-14.40
Molecular Layer of the Dentate Gyrus	162.18 ± 6.87	138.09 ± 44.08	-14.85
Piriform Cortex	67.37 ± 11.92	57.67 ± 22.87	-14.41
Substantia Nigra	228.96 ± 24.94	222.10 ± 37.79	-3.00
Ventral Tegmental Area	224.49 ± 28.47	259.68 ± 25.88	+15.68
Medial Geniculate Nucleus	83.99 ± 13.83	101.78 ± 24.11	+21.18
Superior Colliculus	117.88 ± 24.85	125.54 ± 40.58	+6.49
Entorhinal Cortex	71.49 ± 18.33	47.45 ± 21.75	-33.63
Cerebellum	6.84 ± 1.45	10.17 ± 2.34	+48.77

**Table 5-1. Overall *in vitro* [<sup>3</sup>H]citalopram binding to SERT is unaffected in PLPOVR mice.**

Data are mean ± SD for n = 3 - 4 for WT, and n = 3 - 4 for PLPOVR animals.

Units of measurement are fmol/mg.

Two-tailed Mann-Whitney U, \*p < 0.05 relative to WT group.

<sup>a</sup> Relative difference (Rel. Diff.) = (PLPOVR - WT)/(WT)\*100 %.

No significant differences between WT and PLPOVR could be detected.

**[<sup>3</sup>H]WIN 35, 428 autoradiography to label DAT.**

**Levels of nonspecific [<sup>3</sup>H]WIN 35, 428 binding defined in the presence of nomifensine.**

Representative sections showing the level of nonspecific binding for [<sup>3</sup>H]WIN 35, 428 in the presence of nomifensine are shown in Fig. 5-3. Percentages specific binding of total binding were lowest in PLPOVR entorhinal cortex 16 ± 14 % (data not shown), (in WT it

## Chapter 5 - Autoradiographic measurements of SERT and DAT densities in a mouse model of PMD.

was  $31 \pm 11$  %, data not shown), while the maximum was observed in the caudate-putamen  $93 \pm 1$  % (data not shown) in WT (in PLPOVR it was  $80 \pm 24$  %, data not shown).

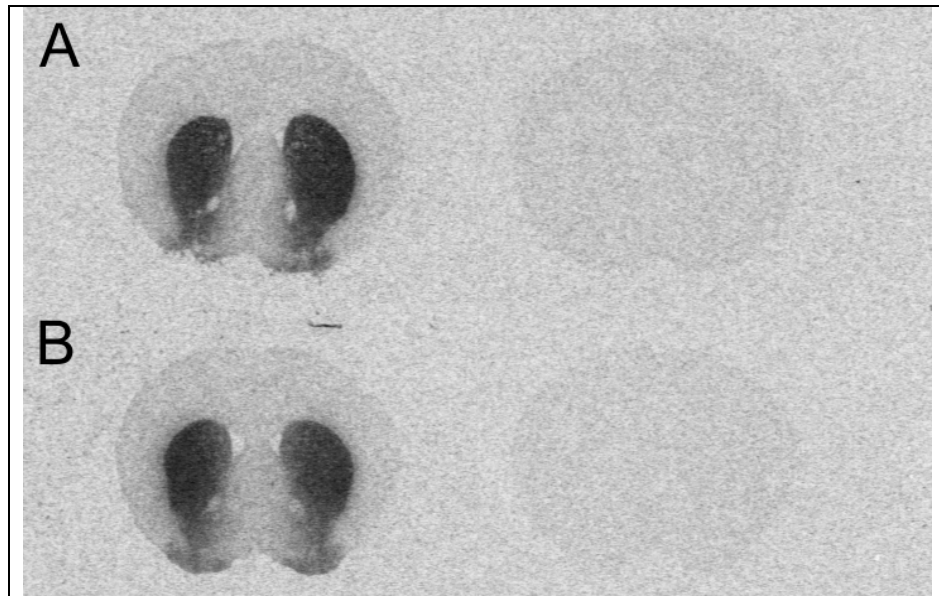


**Fig. 5-3. Nonspecific *in vitro* [<sup>3</sup>H]WIN 35, 428 binding is low.**

Nonspecific binding was assessed using nomifensine to displace [<sup>3</sup>H]WIN 35, 428 from DAT.

Left: representative sections showing total binding to DAT.

Right: representative sections showing nonspecific binding defined by pharmacological blockade of DAT with nomifensine.

A: WT.

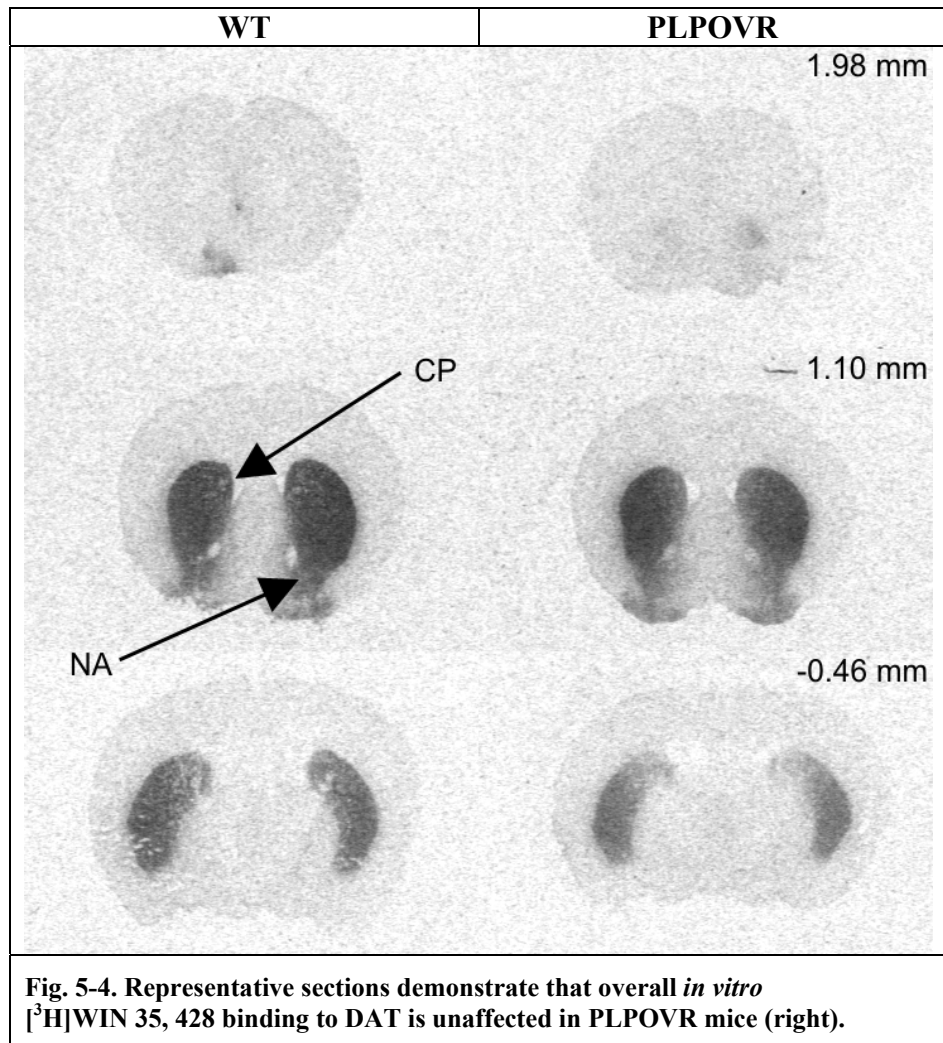
B: PLPOVR.

Nonspecific binding of [<sup>3</sup>H]WIN 35, 428 was approximately at the level of the cortex, and was comparable between treatment groups.

### Visual comparison of representative sections of [<sup>3</sup>H]WIN 35, 428 binding in WT and PLPOVR animals.

Representative images of total [<sup>3</sup>H]WIN 35, 428 binding at all levels examined are depicted for WT and for PLPOVR mice (Fig. 5-4). DAT-rich structures are indicated with arrows. The caudate-putamen and the nucleus accumbens, as well as the ventral tegmental area and substantia nigra show intense [<sup>3</sup>H]WIN 35, 428 binding in both WT and PLPOVR.

**Chapter 5 - Autoradiographic measurements of SERT and DAT densities in a mouse model of PMD.**



**Chapter 5 - Autoradiographic measurements of SERT and DAT densities in a mouse model of PMD.**

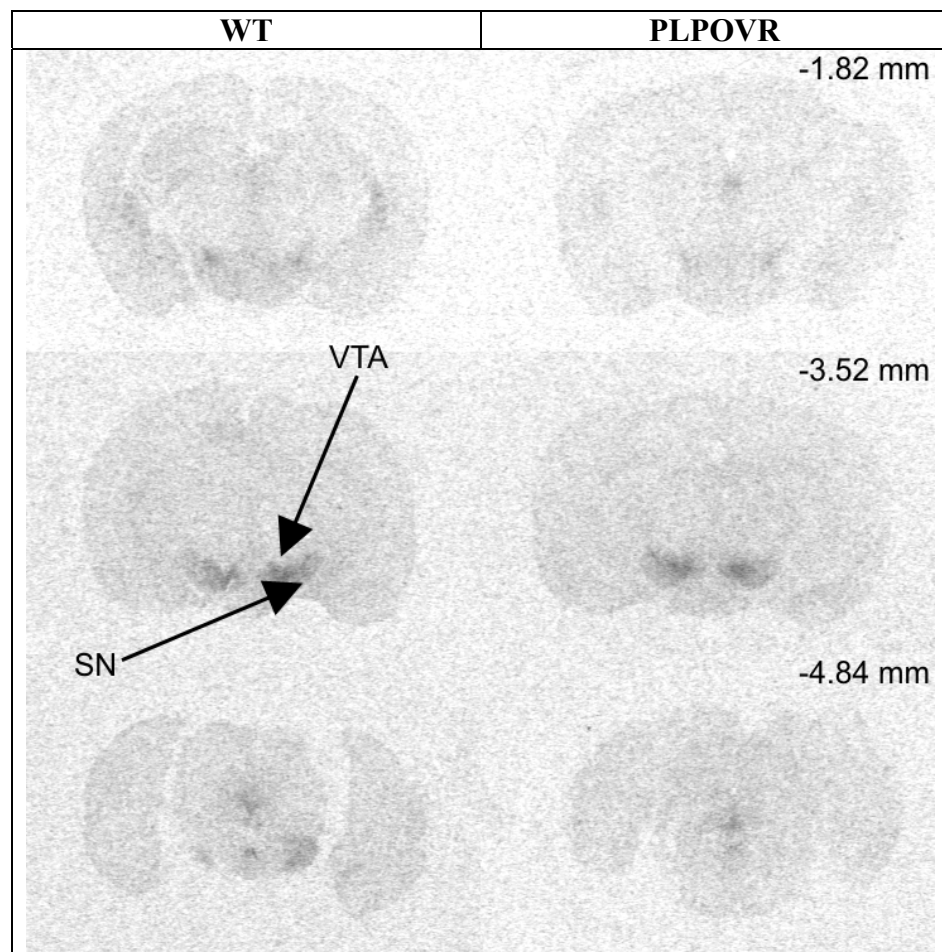


**Fig. 5-4. continued.**

Arrows show DAT-rich binding sites, CP: caudate-putamen; NA: nucleus accumbens; VTA: ventral tegmental area; SN: substantia nigra. Bregma level is indicated in top left corner.

**Analysis of [<sup>3</sup>H]WIN 35, 428 binding in WT and PLPOVR animals.**

In none of the structures investigated could a statistically significant difference in specific binding be detected between groups. Relative differences in specific [<sup>3</sup>H]WIN 35, 428 binding between WT and PLPOVR mice in the caudate-putamen were -29 %, for the nucleus accumbens -35 %, and for the substantia nigra, -34 % and -15 % for the ventral tegmental area. However, despite these relative differences between WT and PLPOVR groups none were statistically significant.

**Chapter 5 - Autoradiographic measurements of SERT and DAT densities in a mouse model of PMD.**

Structure	Genotype		Rel. Diff. [%] <sup>a</sup>
	WT	PLPOVR	
Prefrontal Cortex	6.60 ± 2.21	6.40 ± 1.96	-3.12
Caudate-Putamen	137.86 ± 22.79	97.40 ± 78.61	-29.35
Septal Area	14.37 ± 3.16	10.91 ± 6.33	-24.10
Nucleus Accumbens	61.29 ± 6.74	39.77 ± 34.69	-35.11
Globus Pallidus	16.15 ± 3.30	13.28 ± 3.98	-17.78
Thalamus	4.72 ± 1.95	3.79 ± 1.75	-19.69
Hippocampus	3.77 ± 1.28	2.66 ± 0.46	-29.49
Substantia Nigra	25.14 ± 4.79	16.65 ± 9.64	-33.80
Ventral Tegmental Area	61.67 ± 10.17	52.75 ± 19.27	-14.46
Superior Colliculus	7.40 ± 2.23	5.69 ± 2.90	-23.11
Entorhinal Cortex	5.36 ± 2.28	2.40 ± 1.94	-55.25

**Table 5-2. Overall *in vitro* [<sup>3</sup>H]WIN 35, 428 binding to DAT is unaffected in PLPOVR mice.**  
 Data are mean ± SD for n = 4 for WT, and n = 3 - 4 for PLPOVR animals.  
 Units of measurement are fmol/mg.  
 Two-tailed Mann-Whitney U, \*p < 0.05 relative to WT group.  
<sup>a</sup> Relative difference (Rel. Diff.) = (PLPOVR - WT)/(WT)\*100 %.  
 No significant differences between WT and PLPOVR could be detected.

**Abnormalities in individual mice.**

Irregularities in brain morphology and radioligand binding were observed in both WT and PLPOVR.

**Abnormalities in brain morphology detected with haematoxylin.**

A noticeable morphological abnormality was observed in haematoxylin-stained sections in one of the original group of 5 PLPOVR mice. Compared to the other PLPOVR mice in the group, one mouse showed severe malformation of the brain (Fig. 5-5). The brain appeared swollen, the shape of the hippocampus was irregular and the majority of brain structures were not identifiable. There was no report of abnormal behaviour for any of the mice in this cohort. However, it was decided that this animal be excluded from the autoradiographic study because the severity of abnormalities made the analysis impossible.

## Chapter 5 - Autoradiographic measurements of SERT and DAT densities in a mouse model of PMD.

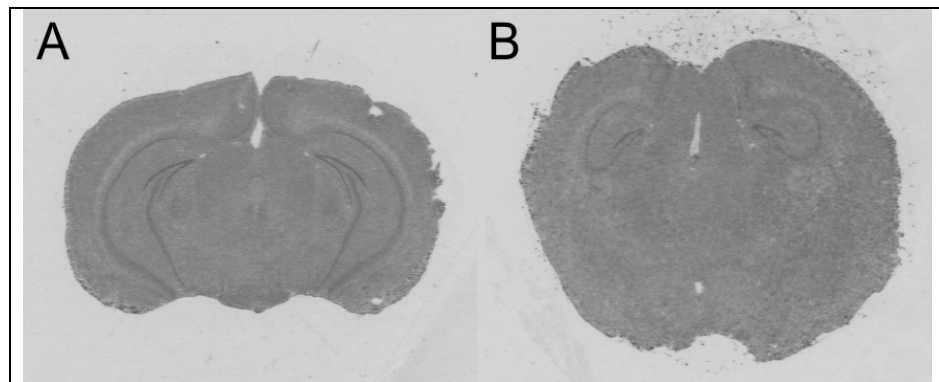


**Fig. 5-5. Haematoxylin staining shows abnormalities in a PLPOVR animal at Bregma -2.80 mm.**

A) depicts a PLPOVR animal with normal morphology, whereas B) shows a PLPOVR mouse with severe abnormalities. The brain is enlarged, the hippocampus is smaller than normal, and other structures are not readily visualised. This animal was excluded from the autoradiographic analyses.

Fig. 5-6 shows an example of mild abnormalities observed in one WT animal, compared to normal WT animals. The ventral hippocampus is not fully developed compared to the normal WT at Bregma -2.80 mm. The abnormality was considered mild, as other signs of malformation were not observed, nor were any behavioural changes reported. Therefore we included that animal in the study.

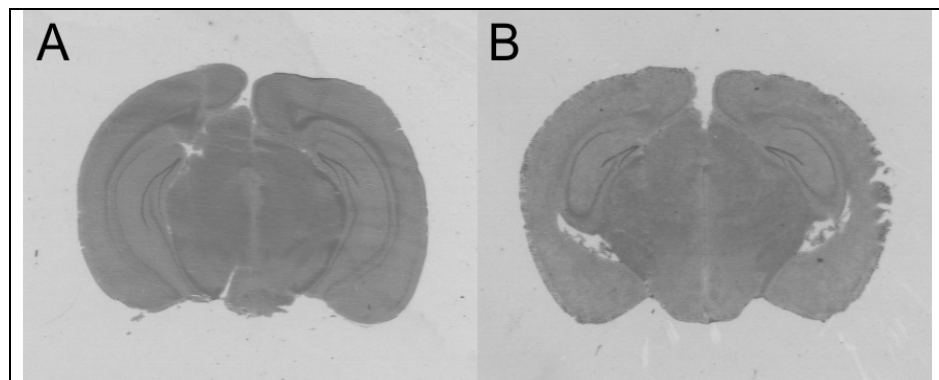


**Fig. 5-6. Haematoxylin staining shows abnormalities in a WT animal at Bregma -2.80 mm.**

A) depicts a normal WT animal, whereas B) shows a WT animal with mild abnormalities. The hippocampus is not fully extended ventrally. Animal was included.

### **Abnormalities in brain monoamine transporter densities detected with [<sup>3</sup>H]citalopram and [<sup>3</sup>H]WIN 35, 428 binding.**

Another animal within the original cohort of PLPOVR mice showed abnormally low levels of monoamine transporter binding compared to both WT and other PLPOVR mice. [<sup>3</sup>H]WIN 35, 428 binding is almost absent in structures known to be dense in DAT, such as

## Chapter 5 - Autoradiographic measurements of SERT and DAT densities in a mouse model of PMD.

the caudate-putamen (Fig. 5-7). Very low levels of [<sup>3</sup>H]citalopram binding were also observed in this animal (Fig. 5-8). A technical failure could be excluded, because this particular animal showed loss of binding at all levels investigated, independent of the ligand used and there was no other reason to exclude the animal from the data analyses. The inclusion of this animal in the dataset may explain the large SDs obtained (Table 5-1 and Table 5-2).

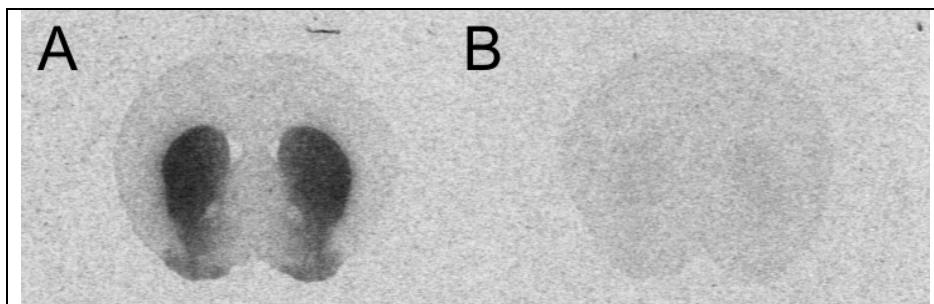


**Fig. 5-7.** [<sup>3</sup>H]WIN 35, 428 autoradiography shows abnormalities in a PLPOVR animal at Bregma 1.10 mm.

A) depicts a normal PLPOVR animal, whereas B) shows a PLPOVR mouse with severe reductions in [<sup>3</sup>H]WIN 35, 428 binding. This particular animal (B) shows loss of binding at all levels examined, using [<sup>3</sup>H]WIN 35, 428 as well as [<sup>3</sup>H]citalopram.

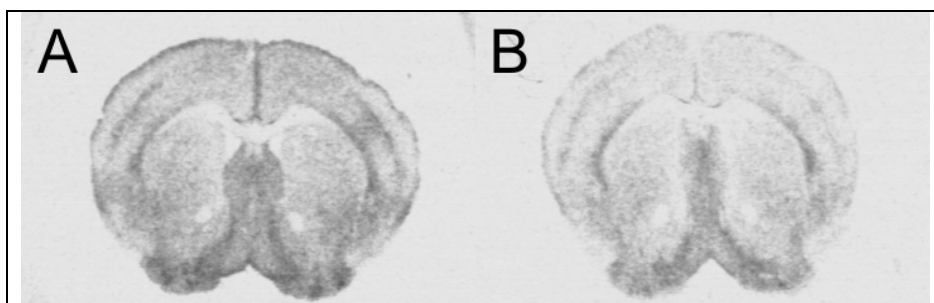


**Fig. 5-8.** [<sup>3</sup>H]citalopram autoradiography shows abnormalities in a PLPOVR animal at Bregma 1.10 mm.

A) depicts a normal PLPOVR animal, whereas B) shows a PLPOVR mouse with severe reductions in [<sup>3</sup>H]citalopram binding. This particular animal (B) shows loss of binding at all levels examined, using [<sup>3</sup>H]citalopram as well as [<sup>3</sup>H]WIN 35, 428.

### 5.5 Discussion.

To our knowledge, this was the first *in vitro* autoradiography study performed on the PLPOVR model of diffuse hypomyelination to assess whether there is a relationship between myelin abnormalities and changes in monoamine transporter densities, i.e. SERT and DAT. However, none of the structures examined showed significantly altered DAT or SERT densities in PLPOVR compared to WT animals. Thus, the widespread demyelination and axonal pathology in this mouse model, as detected by both MRI and histopathology in the previous study (page 159), did not appear to be accompanied by

## **Chapter 5 - Autoradiographic measurements of SERT and DAT densities in a mouse model of PMD.**

major deficits in monoaminergic transporters. Some of the structures showed mean differences between the groups that were reasonably high with comparable SDs, e.g., in the caudate-putamen where an increase of [<sup>3</sup>H]citalopram binding of 14 % was observed in PLPOVR relative to WT animals. Also the ventral tegmental area shows an increase in SERT binding of 16 %. On the other hand, [<sup>3</sup>H]WIN 35, 428 DAT binding is reduced by 29 %, and 15 % in these regions, respectively. However, these differences could be due to the inclusion of 1 animal in the PLPOVR group that showed very abnormal levels of SERT and DAT accounting for the large SDs observed. If higher SERT densities were present in PLPOVR mice, this may indicate lower synaptic serotonin concentrations as re-uptake of the transmitter is facilitated. An inhibitory role of serotonin on dopamine release in the caudate-putamen has been proposed previously (Ennis et al., 1981). Therefore less serotonin tone could disinhibit dopaminergic neurotransmission, and a long-term increase in DAT would be expected as an adaptation to increased synaptic dopamine. However this is not the case as DAT densities were not significantly altered. A general observation of PLPOVR mice compared to WT was made concerning their gait in that they were reported to have slight ataxia (Dr. T. J. Anderson, personal communication), however given the widespread demyelination in the brains of PLPOVR mice, and the ambiguous results from autoradiography, it is more likely that the observed ataxia is rather the result of white matter pathology, which is one of the features of PMD for which *Plp1* overexpression is a model for. However the mechanisms of how ataxia develops in the PLPOVR model are unknown. Although it has been shown that particularly small axon diameter fibres, like the optic nerve, corticospinal tract, as well as the fasciculus gracilis, are affected in PLPOVR mice (Anderson et al., 1998). The ataxia therefore could be attributed to the degeneration of axons within the fasciculus gracilis of the spinal cord that carries sensory information, particularly from proprioceptors, of the lower body up to the brain.

One reason why we did not detect loss of SERT or DAT may relate to the morphology of monoaminergic axons. Neither serotonergic, nor catecholaminergic neurons including dopamine- and noradrenaline-containing fibres are myelinated in rodents (for serotonin see Azmitia *et al.* (Azmitia and Gannon, 1983); for catecholamines see Hokfelt *et al.* (Hokfelt and Ungerstedt, 1973)). Thus these fibres are not likely to be affected directly by demyelination.

## **Chapter 5 - Autoradiographic measurements of SERT and DAT densities in a mouse model of PMD.**

However, we measured non-significant reductions in SERT in hippocampal substructures, with a maximum of 34 % relative to WT in the CA1. The loss of hippocampal SERT may relate to the presence of seizures in the PLPOVR mice. Serotonin neurons in the raphe nuclei, which project to the hippocampus, receive input not only from nonmyelinated catecholaminergic fibres projecting from the locus coeruleus and substantia nigra (Sakai et al., 1977), but also from glutamatergic (from structures like the hypothalamus and prefrontal cortex) (Lee et al., 2003), and GABAergic neurons. GABAergic neurons in the raphe were shown to be able to control theta oscillations within the hippocampus (Li et al., 2005). Therefore seizures in PLPOVR mice could indicate abnormalities in excitatory vs. inhibitory activity in the hippocampus. How could serotonin function influence this? It was proposed that serotonergic inhibition of hippocampal oscillations by the medial raphe could be attenuated by inhibition of the raphe due to release of GABA (Li et al., 2005). Glutamate, in turn, was shown to keep the medial raphe neurons activated, hence inhibiting theta oscillations (Varga et al., 1998). Although it is not clear if the axons of these glutamatergic or GABAergic projections are myelinated or not, an explanation for the observed seizures in PLPOVR mice could be a failure of GABAergic inhibition in the medial raphe nuclei if the function of these fibres is impaired due to the overexpression of *Plp1* (resulting in demyelination). This would likely result in an increase in serotonin tone, which may be accompanied by upregulations in SERT. Interestingly, adjunctive treatment of epileptic patients with the SSRI fluoxetine improved their seizures incidence (Favale et al., 1995). Antidepressant treatment with a SSRI would result in an increase in synaptic serotonin levels, and therefore may increase seizure incidence. Worsening of epileptic symptoms was actually observed in another study, hence opposing findings from Favale *et al.* (Gigli et al., 1994, Favale et al., 1995). As SERT availability may only be an indirect marker of synaptic serotonin levels, its contributions (with reductions described here in the hippocampus) to seizures remain unclear.

An alternative and simpler explanation is that the seizures in PLPOVR mice are due to the severe demyelination that would cause excitation of adjacent tissue along the axons as the action potentials are not constrained to the axons anymore.

### **5.6 Final conclusions.**

The hypothesis that myelin and the serotonergic system interact could not be confirmed in this model of severe hypomyelination, however not rejected either. Some structures show large alterations in SERT and DAT binding of the specific ligands [<sup>3</sup>H]citalopram and

## **Chapter 5 - Autoradiographic measurements of SERT and DAT densities in a mouse model of PMD.**

[<sup>3</sup>H]WIN 35, 428, respectively, when PLPOVR were compared to WT mice. The biggest limitation of this study was the lack of a sufficient number of animals. This resulted in large variations of the data. Therefore more animals would need to be included in further studies.

Chapter 6 - Autoradiographic and micro-SPECT imaging of SERT depletion in rats using the radioligands [<sup>125</sup>I]βCIT and [<sup>125</sup>I]ADAM.

**Chapter 6 - Autoradiographic and micro-SPECT  
imaging of SERT depletion in rats using the  
radioligands [<sup>125</sup>I]βCIT and [<sup>125</sup>I]ADAM.**

## **Chapter 6 - Autoradiographic and micro-SPECT imaging of SERT depletion in rats using the radioligands [<sup>125</sup>I]βCIT and [<sup>125</sup>I]ADAM.**

## **Chapter 6 - Autoradiographic and micro-SPECT imaging of SERT depletion in rats using the radioligands [<sup>125</sup>I]βCIT and [<sup>125</sup>I]ADAM.**

### **6.1 Introduction.**

#### **SPECT imaging of SERT in humans.**

##### **[<sup>123</sup>I]βCIT SPECT.**

[<sup>123</sup>I]βCIT, a cocaine derivative, is one of the best characterised SPECT ligands used to image SERT in human studies. It has been successfully applied to imaging SERT in depression, but also to studies assessing the neurotoxicity of MDMA (ecstasy). For instance, de Win *et al.* carried out a study in short-term ecstasy users to identify possible changes in SERT using [<sup>123</sup>I]βCIT (de Win *et al.*, 2008). Surprisingly, the authors were not able to detect any changes between before and after drug abuse. In contrast, the same group performed a similar study in long-term users of MDMA and were able to detect reduced [<sup>123</sup>I]βCIT binding in the thalamus (de Win *et al.*, 2008) suggesting that only long-term abuse of MDMA caused a reduction in brain SERT. By imaging SERT in depression using [<sup>123</sup>I]βCIT and SPECT, valuable information has been obtained about the effects of antidepressant treatment. For example, Malison *et al.* showed that [<sup>123</sup>I]βCIT binding was reduced in the brainstem of drug-free depressed patients compared to healthy volunteers (Malison *et al.*, 1998c). In addition, in a 6 month follow-up study Laasonen-Balk *et al.* were able to show that recovery from depression in patients that received treatment (benzodiazepines and antidepressants) was associated with increased [<sup>123</sup>I]βCIT binding in the midbrain. This was in contrast to patients who did not respond to medication (Laasonen-Balk *et al.*, 2004). More recently a [<sup>123</sup>I]βCIT SPECT study was performed in Glasgow in which the authors recruited patients taking antidepressant medication at the time of the SPECT scan in order to investigate the levels of unblocked SERT in responders and non-responders. Surprisingly, there was no difference in the levels of residual, unblocked SERT, as detected by [<sup>123</sup>I]βCIT, between patients who showed clinical response to their antidepressant treatment and those who did not (Cavanagh *et al.*, 2006). Such studies using [<sup>123</sup>I]βCIT have increased our knowledge about the status of SERT in depression and during antidepressant treatment. However, [<sup>123</sup>I]βCIT has a significant limitation in that it is not selective for SERT and binds also to DAT (Farde *et al.*, 1994).

## **Chapter 6 - Autoradiographic and micro-SPECT imaging of SERT depletion in rats using the radioligands [<sup>125</sup>I]βCIT and [<sup>125</sup>I]ADAM.**

### **[<sup>123</sup>I]ADAM SPECT.**

In contrast to the extensive use of [<sup>123</sup>I]βCIT for SPECT imaging of SERT, many fewer studies have been done to date using the more recently available selective, high affinity SPECT ligand for SERT, [<sup>123</sup>I]ADAM. The limited number of studies performed using [<sup>123</sup>I]ADAM have to some extent confirmed results previously obtained using [<sup>123</sup>I]βCIT SPECT imaging. For instance, Newman *et al.* conducted a preliminary study of [<sup>123</sup>I]ADAM binding to the midbrain comparing healthy controls and drug-free depressed patients. They reported a significant reduction in SERT density in depressed subjects relative to controls (Newberg *et al.*, 2005). In contrast, Herold *et al.* performed a similar study using [<sup>123</sup>I]ADAM but found no significant differences between controls and depressed subjects. A subset of the depressed patients in this study then received antidepressant treatment and [<sup>123</sup>I]ADAM SPECT imaging was used to assess SERT occupancy in the midbrain after 7 days of citalopram treatment. The reduction in [<sup>123</sup>I]ADAM binding due to citalopram treatment was of the order of 60 % (Herold *et al.*, 2006). Similarly, Klein *et al.* aimed to use [<sup>123</sup>I]ADAM SPECT to determine the dose of citalopram and escitalopram necessary to yield an 80 % blockade of SERT as this level of blocking has been suggested to reflect a clinically efficacious dose. Healthy volunteers were administered escitalopram or citalopram at various doses and SERT occupancy was calculated using a before and after drug treatment imaging paradigm. The results showed that [<sup>123</sup>I]ADAM was able to detect dose-dependent increases in SERT blockade by escitalopram ranging from 60 % (5 mg) to 75 % (20 mg) and by citalopram, ranging from 65 % (10 mg) to 70 % (20 mg) (Klein *et al.*, 2006). Therefore in human SPECT imaging studies, [<sup>123</sup>I]βCIT and [<sup>123</sup>I]ADAM have been used to assess SERT density in disease or by blockade of SERT by pharmacological agents.

### **SPECT imaging of SERT in experimental animals.**

#### **[<sup>123/125</sup>I]βCIT SPECT.**

[<sup>123/125</sup>I]βCIT SPECT imaging has been widely used in different animal species, with different scanners and in a variety of experimental paradigms. For the purpose of this chapter I have focused on two studies of direct relevance to the experiments conducted in this thesis. The first one validates [<sup>125</sup>I]βCIT SPECT imaging of SERT by means of pharmacological displacement in rat brain using the MollyQ 50<sup>TM</sup> micro-SPECT in our

## **Chapter 6 - Autoradiographic and micro-SPECT imaging of SERT depletion in rats using the radioligands [<sup>125</sup>I]βCIT and [<sup>125</sup>I]ADAM.**

laboratory. In the other study, rats were imaged using [<sup>123</sup>I]βCIT after SERT had been depleted.

Cain *et al.* validated the use of [<sup>125</sup>I]βCIT to image SERT with the newly installed MollyQ 50<sup>TM</sup> small animal micro-SPECT in Glasgow by means of an acute pharmacological displacement study. Rats received pre-treatment with either 10 mg/kg fluoxetine, or 5 mg/kg GBR12909 15 min before administration of intravenous [<sup>125</sup>I]βCIT (20 MBq), with another dose administered 30 min after ligand injection. Rats received 2 consecutive SPECT scans, each taking 140 min. During the first scan, fluoxetine significantly reduced [<sup>125</sup>I]βCIT binding to the thalamus relative to control animals, while leaving the caudate-putamen unchanged. In contrast, GBR12909 significantly reduced [<sup>125</sup>I]βCIT binding in the caudate-putamen but had minimal effect in other brain regions. These findings indicated that in the first scan, a major part of the [<sup>125</sup>I]βCIT signal in the thalamus reflected SERT while in the caudate-putamen it reflected DAT. This was in contrast to the observations made in the second scan, where fluoxetine did not significantly reduce the [<sup>125</sup>I]βCIT signal in the thalamus (interestingly, a significant increase in the caudate-putamen was observed), relative to control animals, while GBR12909 significantly reduced the signal in the caudate-putamen and in the thalamus. This suggests that the [<sup>125</sup>I]βCIT signal in the second scan predominantly reflects binding to DAT (Cain *et al.*, 2009). Therefore it was demonstrated that the MollyQ 50<sup>TM</sup> scanner and [<sup>125</sup>I]βCIT were capable of imaging both SERT and DAT in the same rat under conditions of acute pharmacological blockade.

Using a different type of small animal SPECT scanner, de Win *et al.* examined the effects of SERT depletion in rats treated with MDMA, a drug selectively neurotoxic to serotonergic fibres. Using a before and after treatment study paradigm, de Win and colleagues were able to detect significant reductions in [<sup>123</sup>I]βCIT binding to the thalamus in MDMA-treated rats compared to controls (de Win *et al.*, 2004).

### **[<sup>123</sup>I]ADAM SPECT.**

While several studies have been performed using small animal *in vivo* [<sup>123</sup>I]/[<sup>125</sup>I]βCIT SPECT imaging, only 2 studies have been published to date that used [<sup>123</sup>I]ADAM in *in vivo* SPECT imaging. In rabbits, Ye *et al.* investigated [<sup>123</sup>I]ADAM binding with fluoxetine blockade of SERT. In addition, serotonergic terminals were destroyed using

## **Chapter 6 - Autoradiographic and micro-SPECT imaging of SERT depletion in rats using the radioligands [<sup>125</sup>I]βCIT and [<sup>125</sup>I]ADAM.**

para-chloroamphetamine in another set of animals in order to validate the use of [<sup>123</sup>I]ADAM. In both experimental situations the specific binding ratio of [<sup>123</sup>I]ADAM appeared to be reduced to baseline corresponding to a specific binding ratio of about 0.5, while control animals displayed a peak specific binding ratio of 1.7 ((midbrain - cerebellum)/cerebellum) (Ye et al., 2004). A second study provided the methodological basis for the scanning schedule performed in the [<sup>125</sup>I]ADAM experiments described in this thesis. The study aimed to determine the level of SERT occupancy in rats reached by acute citalopram pre-treatment before injection of [<sup>123</sup>I]ADAM. A baseline scan was performed 1 week before the scan with citalopram pre-treatment. Using this paradigm, a SERT occupancy of 95.5 % was achieved demonstrating the feasibility of *in vivo* [<sup>123</sup>I]ADAM imaging using their combined SPECT/computed tomography tomograph. The authors also reported the specific binding ratio, which was 0.91 for the baseline scan, and 0.04 for the [<sup>123</sup>I]ADAM scan where the rats were pre-treated with citalopram (Hwang et al., 2007).

Taking the information from clinical and preclinical studies together, it appears that [<sup>123</sup>I]/[<sup>125</sup>I]βCIT SPECT imaging can be used to measure both the density of SERT and the availability of the transporters under conditions of pharmacological blockade. Although [<sup>123</sup>I]/[<sup>125</sup>I]βCIT SPECT imaging of the SERT was successfully applied preclinically and in clinical settings, its lack of selectivity for SERT often raises criticism. While this property has the advantage that both transporters can be measured in the same animal or patient, if the primary aim is to specifically measure SERT then [<sup>123</sup>I]ADAM is the more appropriate radioligand. However, [<sup>123</sup>I]ADAM has been much less widely used, particularly in experimental animals, and the SPECT imaging group in Glasgow had no previous experience with it either in humans or animals.

### **6.2 Aims of the study.**

- I. Conduct a pilot study to establish *in vitro* autoradiography procedures in order to examine the serotonin-depleting effect of MDMA administration. A regimen commonly used in the literature (20 mg/kg twice daily administered over 4 days (Lew et al., 1996)) yielded a 90 % reduction of total number of SERT in membrane preparations detected by [<sup>3</sup>H]paroxetine binding (Kelly et al., 2002). The pilot study forms part of the material and methods chapter (section 2.3, page 53).

## Chapter 6 - Autoradiographic and micro-SPECT imaging of SERT depletion in rats using the radioligands [<sup>125</sup>I]βCIT and [<sup>125</sup>I]ADAM.

- II. Conduct a pilot study to establish an *in vitro* autoradiography protocol for [<sup>125</sup>I]ADAM. This pilot study is included in the material and methods chapter (section 2.4, page 70).
- III. Assess [<sup>125</sup>I]ADAM SPECT imaging *in vivo* in rats using the MollyQ scanner and to compare it with [<sup>125</sup>I]βCIT in the ability to detect SERT depletion induced by MDMA administration.

### 6.3 Material and methods.

#### Animals.

Sprague-Dawley rats (Harlan, UK; n = 38, male) weighing  $233.0 \pm 21.9$  g on first treatment day (see pilot study for treatment details, page 53), were used. Eighteen rats were vehicle-treated, while 20 received a serotonin depleting MDMA regimen. After 10 days of maintenance 6 MDMA-treated animals, and 4 vehicle controls were used for *in vitro* autoradiography (see pilot study for details on the tissue processing and autoradiographic procedure, page 53). The rest of the animals (14 vehicle- and MDMA-treated animals, respectively) underwent SPECT scanning. In the [<sup>125</sup>I]βCIT scanning group, 4 rats underwent the SERT-depleting MDMA regimen, while 7 received vehicle only. 2 groups of rats with different maintenance periods were treated for [<sup>125</sup>I]ADAM SPECT: in the 10 day maintenance group, 4 received MDMA, and 3 were vehicle-treated. In the 30 day maintenance group, 6 underwent MDMA treatment, while 4 served as vehicle controls. For details on the SPECT scanning procedure the reader is referred to the material and methods chapter (section 2.5, page 84).

### 6.4 Results.

The pilot study confirmed that MDMA treatment caused depletion of SERT as detected by *in vitro* autoradiographic analyses with [<sup>3</sup>H]citalopram or [<sup>125</sup>I]βCIT (see pilot study, page 53). The development of a protocol for *in vitro* [<sup>125</sup>I]ADAM autoradiography was not successful, possibly because of technical issues with [<sup>125</sup>I]ADAM stability (see pilot study, page 70). In this study the relative abilities of [<sup>125</sup>I]βCIT and [<sup>125</sup>I]ADAM to detect MDMA-induced SERT depletion were explored using *in vivo* SPECT imaging and *ex vivo* autoradiography of SPECT scanned animals, followed by *in vitro* autoradiography for validation.

**Chapter 6 - Autoradiographic and micro-SPECT imaging of SERT depletion in rats using the radioligands [<sup>125</sup>I]βCIT and [<sup>125</sup>I]ADAM.**

**Effects of MDMA treatment on animal body weight.**

Animal body weight was monitored for 15 days, including the 4 days of treatment either with vehicle (n = 18) or MDMA (n = 20), and for 10 days following treatment. On the first day of treatment (T1), animals had a weight of 233 ± 21.9 g. Rats that received MDMA treatment lost weight over the 4 days of treatment, and regained weight post-treatment. Animals undergoing vehicle treatment showed an increase in body weight during the whole course of the experiment.

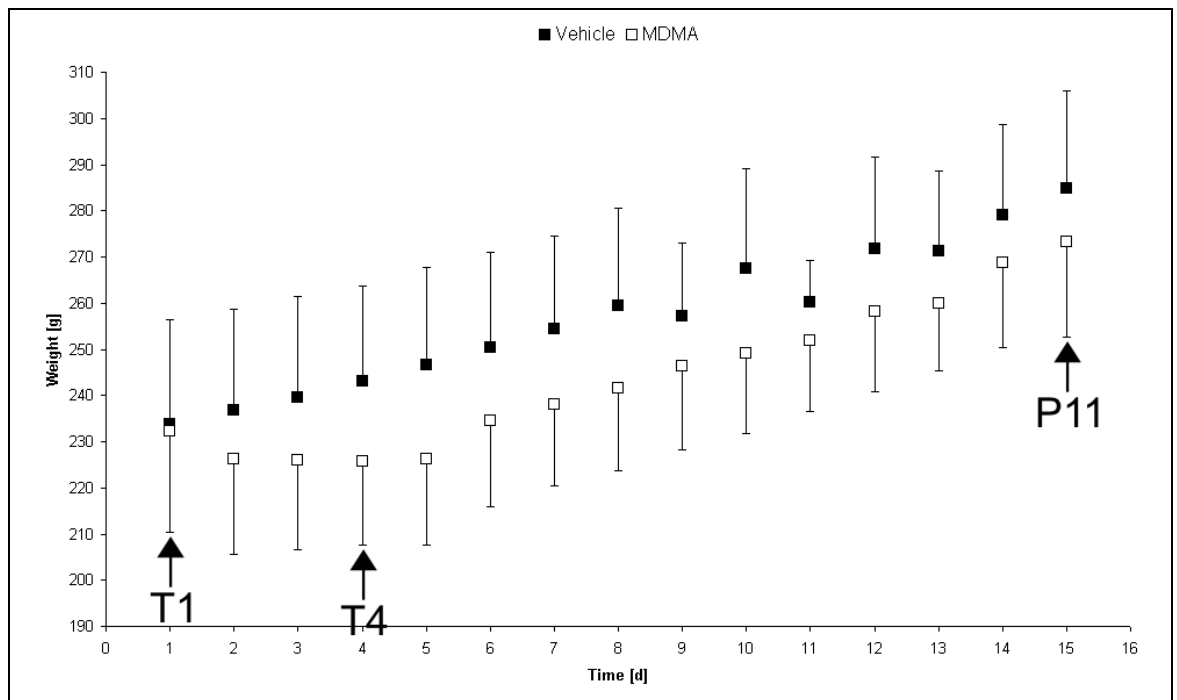


**Fig. 6-1. MDMA treatment reduces body weight of treated rats.**

Visual inspection showed no obvious differences in body weight between vehicle- and MDMA-treated animals on T1. From T2 - T4 MDMA-treated animals lost weight, and started to regain weight again the day after T4. The body weight of vehicle control animals increased constantly.

Data are mean ± SD for n = 18 vehicle-, and n = 20 for MDMA-treated rats.

T1: first day of treatment; T4: fourth and last day of treatment; P11: post-treatment day 11.

## Chapter 6 - Autoradiographic and micro-SPECT imaging of SERT depletion in rats using the radioligands [<sup>125</sup>I]βCIT and [<sup>125</sup>I]ADAM.

### 6.4.1 *In vivo* [<sup>125</sup>I]βCIT SPECT imaging and *ex vivo* autoradiography.

#### *In vivo* [<sup>125</sup>I]βCIT SPECT imaging.

*In vitro* autoradiographic analysis in the pilot study demonstrated that the MDMA treatment regimen used caused a widespread reduction in the density of SERT (material and methods, page 53). However, visual inspection of [<sup>125</sup>I]βCIT SPECT images from vehicle- and MDMA-treated animals revealed no striking differences between the two groups (Fig. 6-2).

Mean raw voxel intensities were then calculated from the ROIs, and the binding ratio between these structures, normalised to the cerebellum, were calculated. Measurements were repeated 3 times. The three separate measurements were averaged to obtain one value for each structure and animal (Fig. 6-3, left). The binding ratios indicate high specific binding relative to the cerebellum, the highest being in the caudate-putamen ( $21 \pm 8$  in vehicle-treated, and  $24 \pm 8$  in MDMA-treated animals) with the thalamus ( $8 \pm 2$  in vehicle-,  $6 \pm 2$  in MDMA-treated animals) and the area of the central canal ( $10 \pm 3$  in vehicle-,  $9 \pm 2$  in MDMA-treated rats) being more than half the caudate-putamen ratios.

No significant differences between vehicle- and MDMA-treated rats were detected for any of the structures examined. A trend towards higher binding ratios was observed in the caudate-putamen, and a trend towards reduced binding ratios was seen in the thalamus when comparing vehicle- to MDMA-treated animals. The area of the central canal appeared unchanged after MDMA treatment relative to vehicle control animals. To check for outliers and assess reproducibility of the measurements in the *in vivo* dataset the [<sup>125</sup>I]βCIT SPECT binding ratio data were examined by plotting the same measurements made on three individual days in a bar graph (Fig. 6-3, right). Measurements between days appeared to be comparable, with the trends maintained as described above.

Chapter 6 - Autoradiographic and micro-SPECT imaging of SERT depletion in rats using the radioligands [ $^{125}$ I] $\beta$ CIT and [ $^{125}$ I]ADAM.

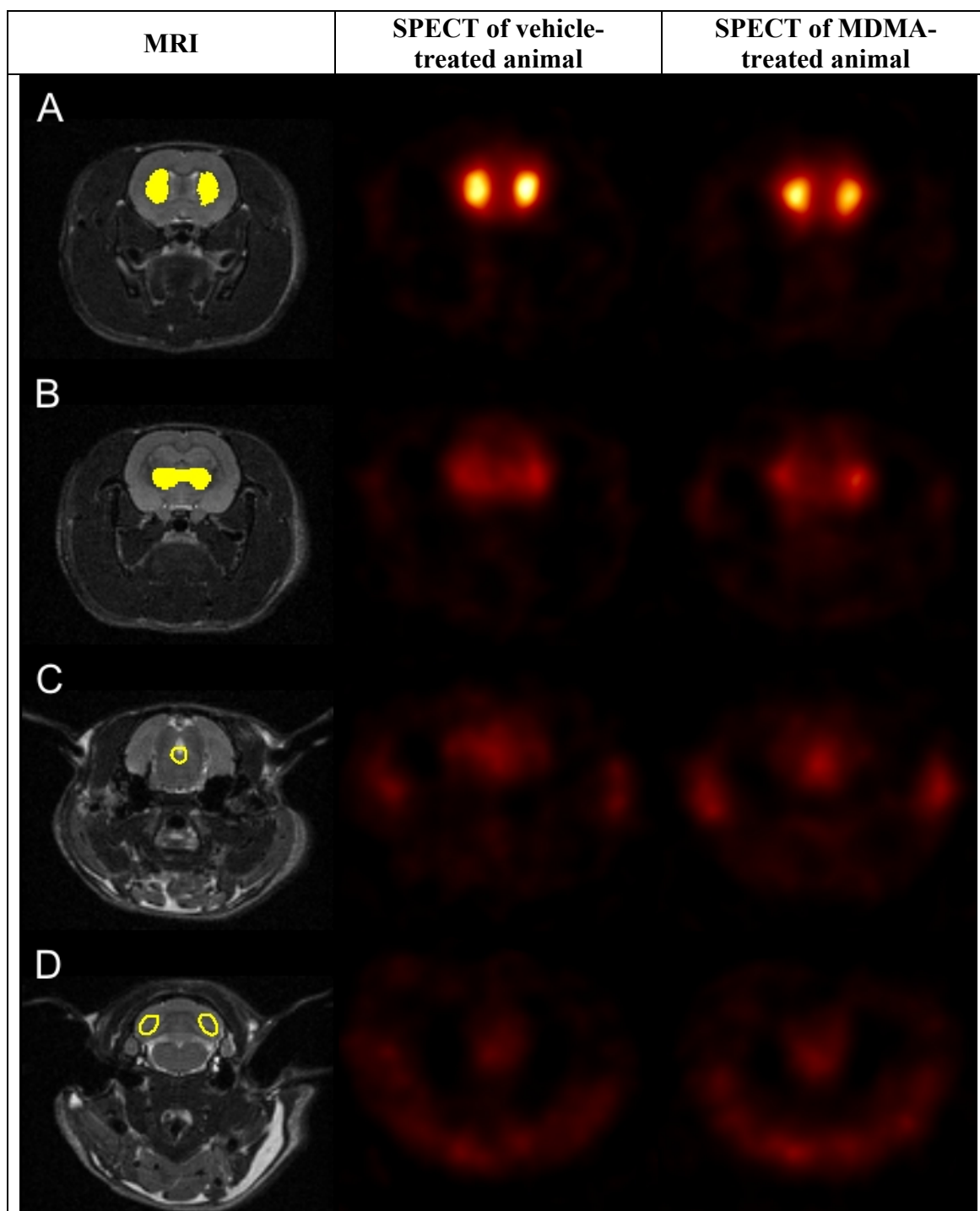


**Fig. 6-2. Representative *in vivo* [ $^{125}$ I] $\beta$ CIT SPECT images of vehicle- (middle) and MDMA-treated animals (right) do not appear different.**

ROIs (yellow) for the caudate-putamen, thalamus, area of the central canal, and cerebellum were defined using a T2-weighted MRI scan of an age-matched rat on 3 consecutive slices. These were subsequently superimposed on coregistered [ $^{125}$ I] $\beta$ CIT SPECT images for measurements. No visual differences were observed between vehicle- and MDMA-treated animals.

- A: caudate-putamen at Bregma level 1.10 mm.
- B: thalamus at Bregma level -3.60 mm.
- C: area of the central canal at Bregma level -8.3 mm.
- D: cerebellum at Bregma level -10.04 mm.

Chapter 6 - Autoradiographic and micro-SPECT imaging of SERT depletion in rats using the radioligands [ $^{125}$ I] $\beta$ CIT and [ $^{125}$ I]ADAM.

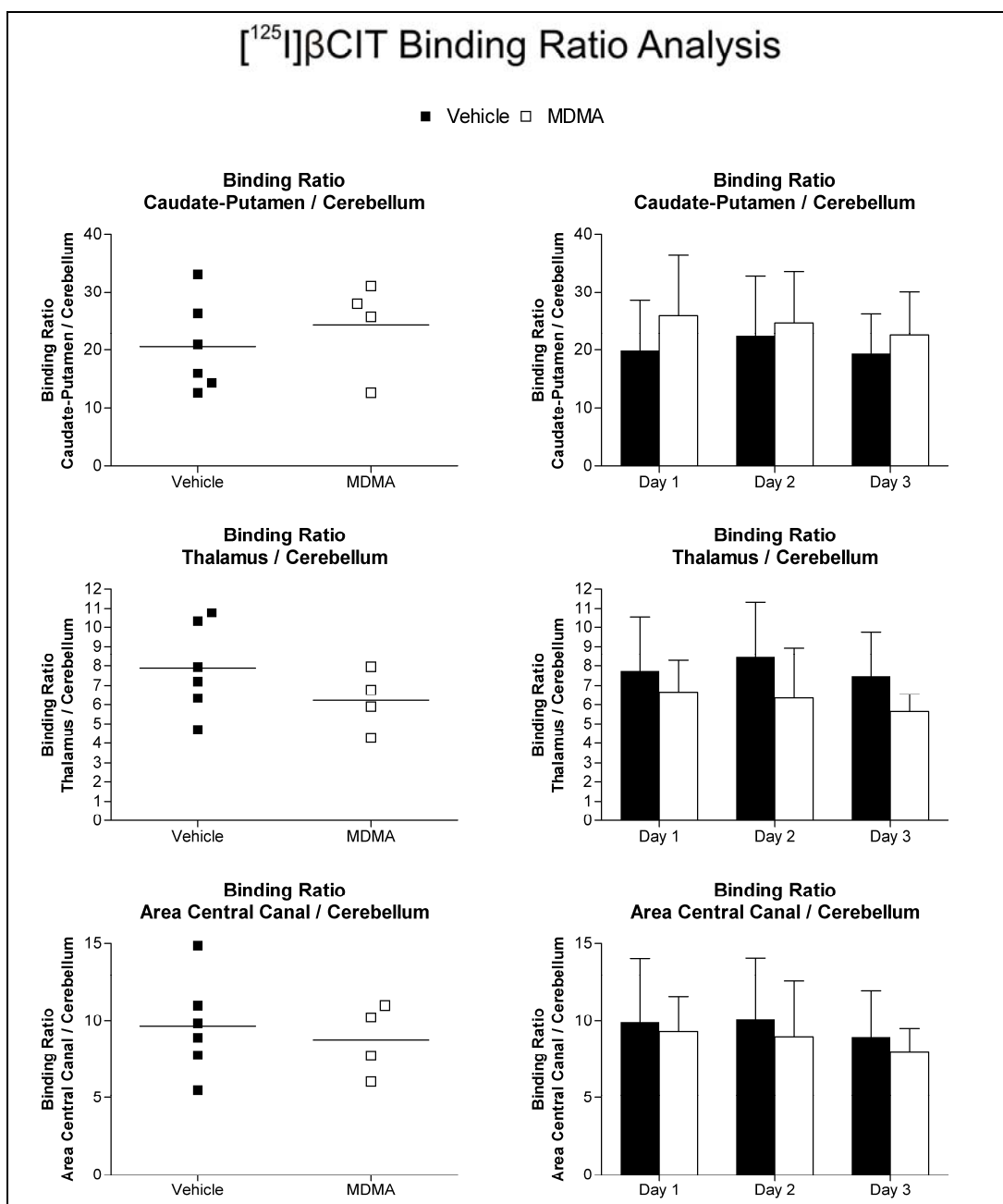


**Fig. 6-3. MDMA treatment does not affect *in vivo* [ $^{125}$ I] $\beta$ CIT SPECT-derived binding ratios.**

Binding ratios for each animal were calculated by normalizing mean image intensities within the ROIs (caudate-putamen, thalamus, and the area of the central canal) to the cerebellum. The left column of graphs shows the average of 3 separate readings taken from the same animal on different days for each structure. Bar graphs displayed in the right column show the results of the individual measurements performed on 3 consecutive days, before averaging to obtain graphs on the left. A slight increase in the binding ratio is observed in the caudate-putamen in MDMA-treated animals compared to vehicle controls while there is a slight reduction in the thalamus of MDMA-treated animals vs. vehicle-treated animals (left). However, neither difference was statistically significant. The reproducibility of the measurements made on different days is good. Visual inspection showed no obvious differences between days. Bar in scatter plot (left) represents mean. Data are mean  $\pm$  SD (right) for n = 6 in vehicle-, and n = 4 in MDMA-treated group. Two-tailed Mann-Whitney U ( $p < 0.05$ ).

**Chapter 6 - Autoradiographic and micro-SPECT imaging of SERT depletion in rats using the radioligands [<sup>125</sup>I]βCIT and [<sup>125</sup>I]ADAM.**

***Ex vivo* [<sup>125</sup>I]βCIT autoradiography.**

**Visual comparison of representative sections of [<sup>125</sup>I]βCIT binding in vehicle- and MDMA-treated animals.**

In Fig. 6-4, the distribution of [<sup>125</sup>I]βCIT in *ex vivo* sections from scanned animals is shown using representative animals from vehicle- and MDMA-treated groups. Visual comparison revealed thalamic structures, and the superior colliculus in MDMA-treated animals as having less [<sup>125</sup>I]βCIT binding compared to controls. However, overall MDMA-treated animals appear to normal [<sup>125</sup>I]βCIT binding compared to vehicle.

**Chapter 6 - Autoradiographic and micro-SPECT imaging of SERT depletion in rats using the radioligands [<sup>125</sup>I]βCIT and [<sup>125</sup>I]ADAM.**

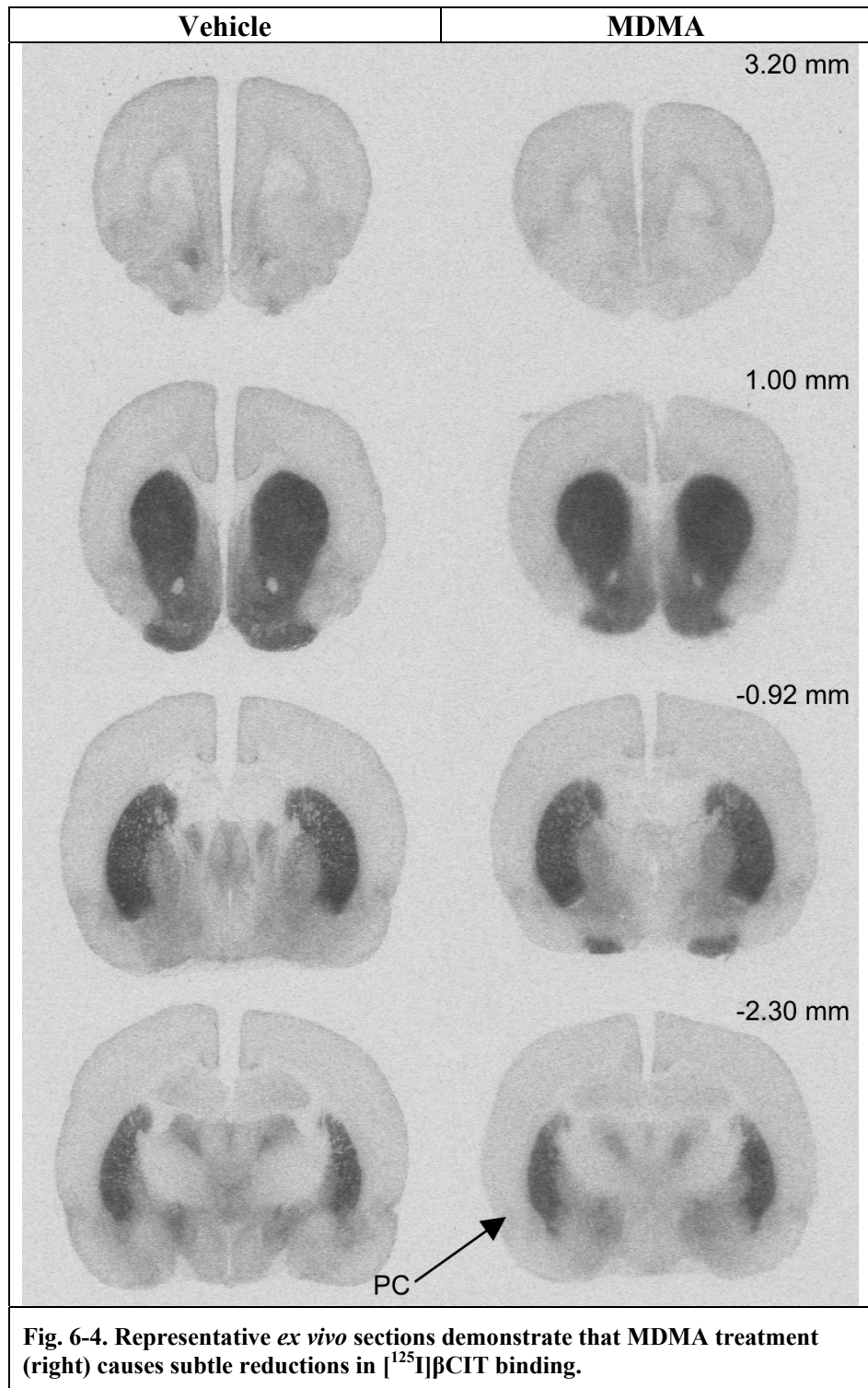


**Fig. 6-4. Representative *ex vivo* sections demonstrate that MDMA treatment (right) causes subtle reductions in [<sup>125</sup>I]βCIT binding.**

**Chapter 6 - Autoradiographic and micro-SPECT imaging of SERT depletion in rats using the radioligands [<sup>125</sup>I]βCIT and [<sup>125</sup>I]ADAM.**

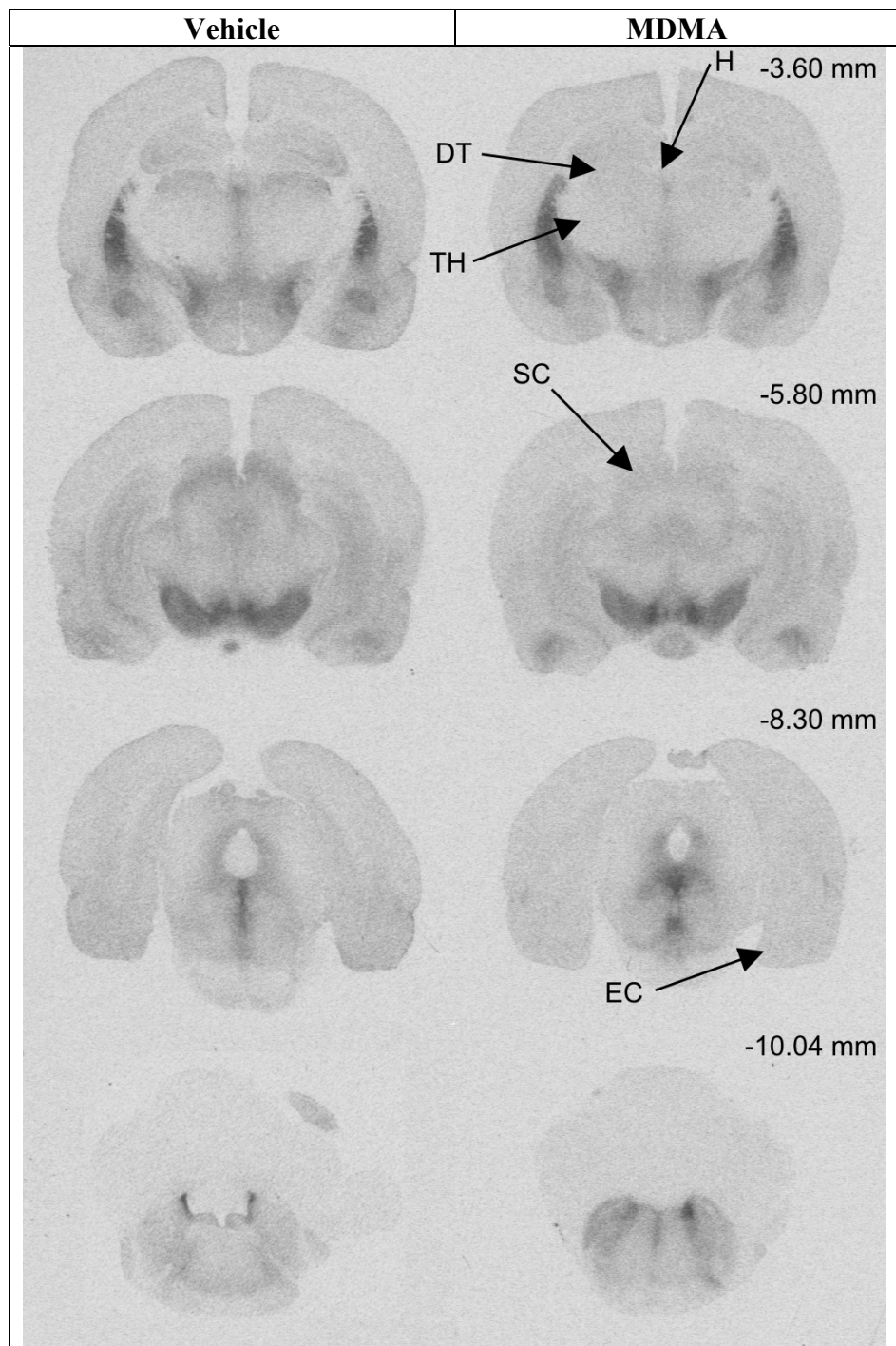


**Fig. 6-4. continued.**

Left: vehicle-, right: MDMA-treated animals both at the end of the experiment using ~20 MBq [<sup>125</sup>I]βCIT i. v.. Arrows indicate significant differences. MDMA-treated animals show less [<sup>125</sup>I]βCIT binding in the cortical regions (PC, EC); habenula (H); thalamic structures (DT, TH); superior colliculus (SC). DT: dorsal thalamus; TH: thalamus; EC: entorhinal cortex; PC: perirhinal cortex. Bregma level is indicated in top right corner.

## **Chapter 6 - Autoradiographic and micro-SPECT imaging of SERT depletion in rats using the radioligands [<sup>125</sup>I]βCIT and [<sup>125</sup>I]ADAM.**

### **Analysis of [<sup>125</sup>I]βCIT binding in vehicle- and MDMA-treated animals.**

Statistical analysis (Table 6-1) of data normalised to the cerebellum revealed that 6 out of 25 structures measured were significantly different in MDMA-treated animals when compared to their vehicle controls. These detected structures, i.e. the dorsal thalamus, thalamus, habenula, piriform cortex, superior colliculus, and the entorhinal cortex, were in agreement with the data derived from [<sup>125</sup>I]βCIT *in vitro* autoradiography where the [<sup>125</sup>I]micro-scales were used as external reference.

**Chapter 6 - Autoradiographic and micro-SPECT imaging of SERT depletion in rats using the radioligands [<sup>125</sup>I]βCIT and [<sup>125</sup>I]ADAM.**

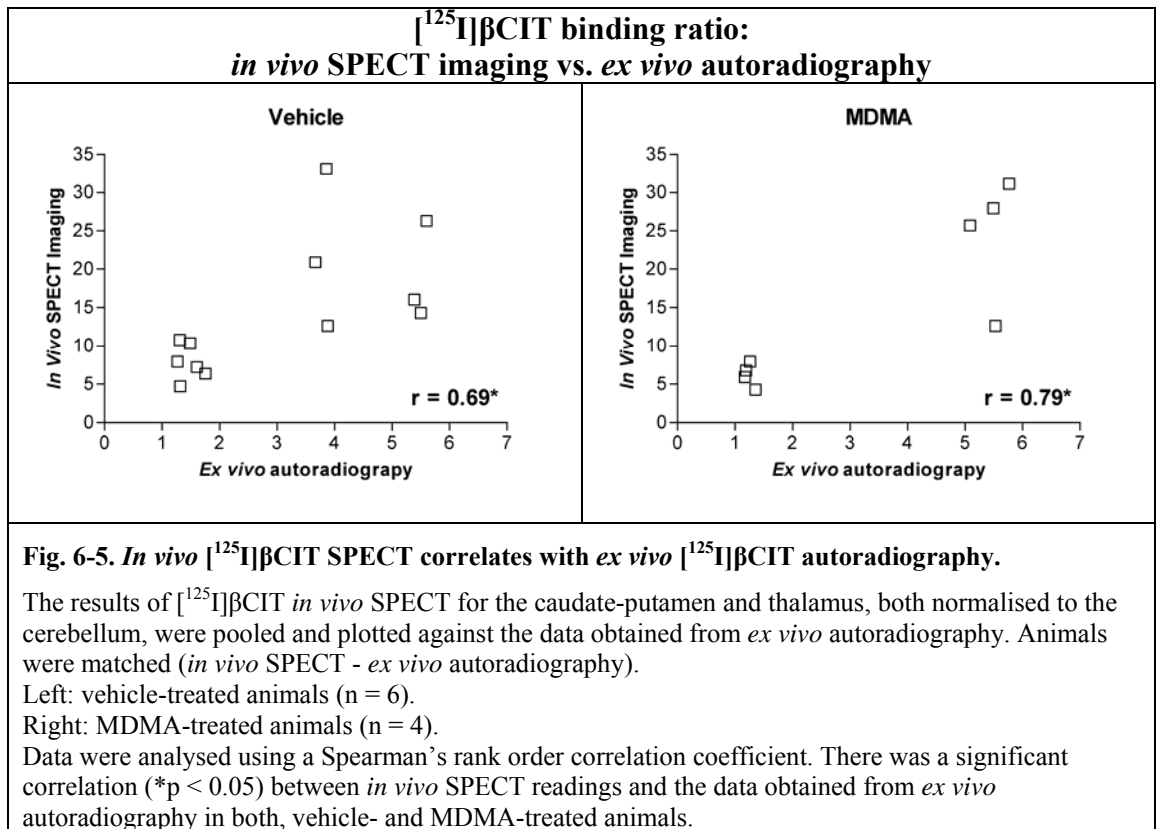
Structure	Treatment		Rel. Diff. [%] <sup>a</sup>
	Vehicle	MDMA	
Prefrontal Cortex	1.54 ± 0.23	1.40 ± 0.08	-9.10
Anterior Cingulate Cortex	1.54 ± 0.21	1.44 ± 0.13	-6.85
Caudate-Putamen	4.70 ± 0.86	5.47 ± 0.28	+16.31
Septal Area	2.04 ± 0.44	2.04 ± 0.16	+0.05
Nucleus Accumbens	3.73 ± 0.77	4.06 ± 0.41	+8.94
Tubercle Area	3.76 ± 0.82	3.85 ± 0.26	+2.32
Globus Pallidus	2.43 ± 0.59	2.44 ± 0.29	+0.50
Retrosplenial Cortex	1.36 ± 0.14	1.27 ± 0.06	-6.20
Basolateral Amygdala	2.46 ± 0.53	2.27 ± 0.26	-7.42
Central Amygdaloid Nucleus	1.67 ± 0.28	1.59 ± 0.13	-5.11
Lateral Hypothalamus	2.73 ± 0.64	2.94 ± 0.39	+7.59
Ventral Hypothalamus	1.57 ± 0.26	1.34 ± 0.13	-14.45
Dorsal Thalamus	1.72 ± 0.32	1.26 ± 0.10 *	-26.74
Thalamus	1.46 ± 0.18	1.25 ± 0.08 *	-14.64
Habenula	1.70 ± 0.27	1.32 ± 0.08 *	-22.43
Hippocampus	1.40 ± 0.15	1.25 ± 0.08	-10.49
Piriform Cortex	1.49 ± 0.17	1.23 ± 0.05 *	-17.48
Substantia Nigra	2.74 ± 0.74	2.78 ± 0.32	+1.61
Medial Geniculate Nucleus	1.49 ± 0.22	1.23 ± 0.13	-17.92
Superior Colliculus	2.19 ± 0.50	1.36 ± 0.20 *	-38.08
Ventral Tegmental Area	3.53 ± 0.90	3.96 ± 0.57	+12.16
Inferior Colliculus	1.21 ± 0.09	1.10 ± 0.04	-9.39
Dorsal Raphe	3.20 ± 0.64	3.59 ± 0.58	+12.04
Entorhinal Cortex	1.59 ± 0.30	1.18 ± 0.07 *	-26.21
Locus Coeruleus	4.31 ± 0.79	4.23 ± 0.58	-1.90

**Table 6-1. MDMA treatment causes widespread reductions in *ex vivo* [<sup>125</sup>I]βCIT autoradiography. Expressed as ratio region/cerebellum.**

Significant differences were detected in 6 out of 25 structures, i.e. in the dorsal thalamus, thalamus, habenula, piriform cortex, superior colliculus. and in the entorhinal cortex.  
 Data are mean ± SD for n = 7 vehicle-, and n = 4 for MDMA-treated rats.  
 Two-tailed Mann-Whitney U, \*p < 0.05 relative to vehicle group  
 Relative difference (Rel. Diff.) = <sup>a</sup> (MDMA - vehicle)/(vehicle)\*100 %

In order to examine the relationship between data obtained from *in vivo* [<sup>125</sup>I]βCIT SPECT imaging and the *ex vivo* autoradiography, the corresponding structures were plotted for each animal (Fig. 6-5). When plotted together the caudate-putamen to cerebellum and thalamus to cerebellum ratios in both groups were significantly correlated, with r = 0.7 for vehicle-treated animals and r = 0.8 in MDMA-treated animals.

**Chapter 6 - Autoradiographic and micro-SPECT imaging of SERT depletion in rats using the radioligands [<sup>125</sup>I]βCIT and [<sup>125</sup>I]ADAM.**



Chapter 6 - Autoradiographic and micro-SPECT imaging of SERT depletion in rats using the radioligands [<sup>125</sup>I]βCIT and [<sup>125</sup>I]ADAM.

6.4.2 *In vivo* [<sup>125</sup>I]ADAM SPECT imaging and *ex vivo* autoradiography.

*In vivo* [<sup>125</sup>I]ADAM SPECT of 10 day maintenance animals.

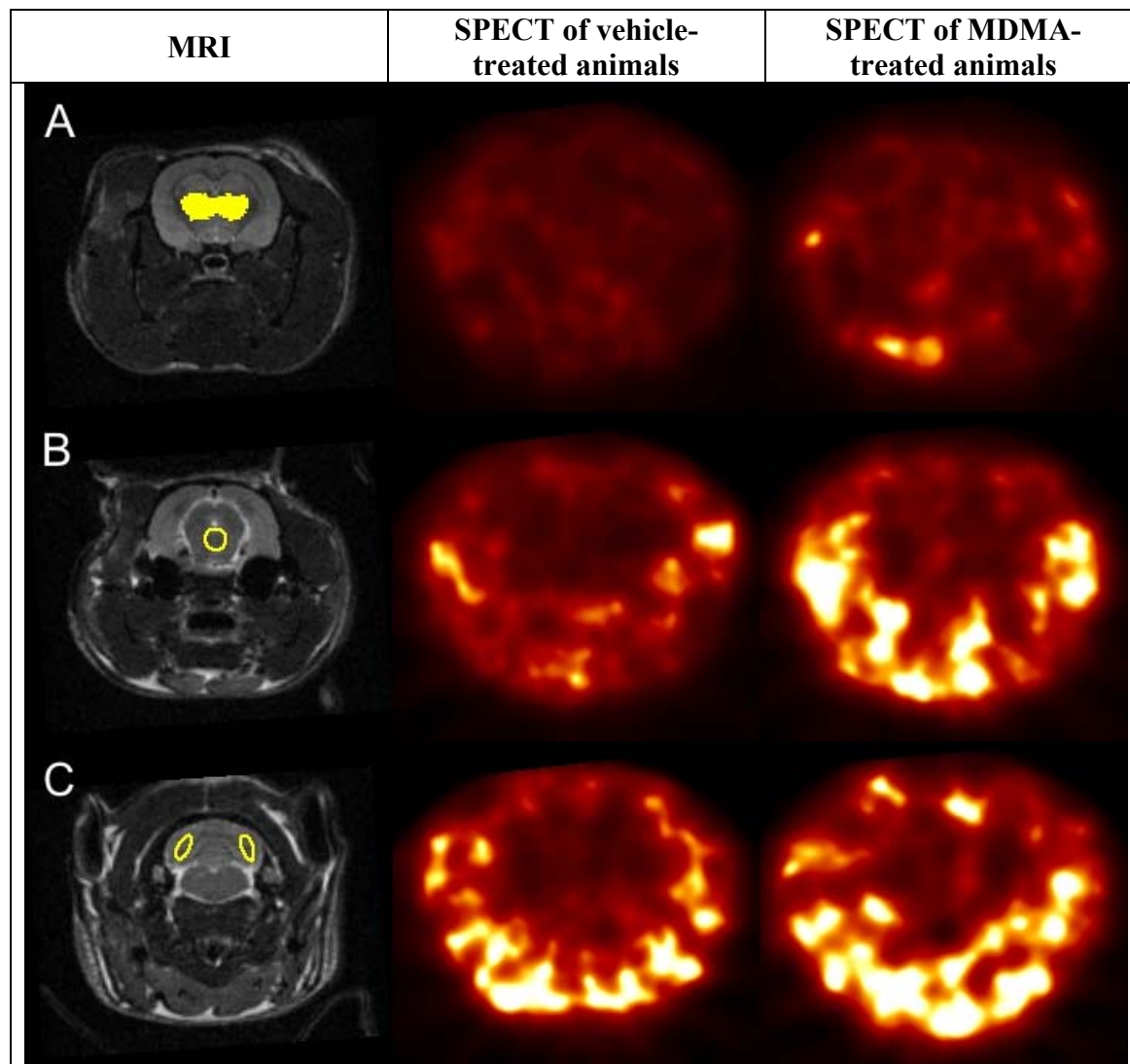


**Fig. 6-6. Representative *in vivo* [<sup>125</sup>I]ADAM SPECT images of vehicle- (middle) and MDMA-treated animals (right) after 10 days of maintenance do not appear different, and are of poor quality.**

ROIs (yellow) for the thalamus, midbrain, and cerebellum were defined on an age-matched rat T2-weighted MRI scan on 3 consecutive slices and subsequently superimposed on coregistered [<sup>125</sup>I]ADAM SPECT images for measurements. No differences were observed between vehicle- and MDMA-treated animals as no brain structure could be examined visually.

A: thalamus at Bregma level -3.60 mm.

B: midbrain at Bregma level -5.80 mm.

C: cerebellum at Bregma level -10.04 mm.

Animals received a [<sup>125</sup>I]ADAM *in vivo* SPECT scan following MDMA (n = 4) or vehicle treatment (n = 3) at the same time point after treatment as animals used for [<sup>125</sup>I]βCIT SPECT, see above. The SPECT scans were then aligned with an age-matched T2-weighted rat MRI, and ROIs for the thalamus, midbrain, and cerebellum were delineated on the MRI. The average weight of the animals was 312.5 ± 12.6 g. The corresponding rat, where

## Chapter 6 - Autoradiographic and micro-SPECT imaging of SERT depletion in rats using the radioligands [<sup>125</sup>I]βCIT and [<sup>125</sup>I]ADAM.

the T2-weighted MRI was taken from, was weighing 316 g on the day of acquisition. The ROIs were superimposed on the respective coregistered [<sup>125</sup>I]ADAM SPECT scan. Visual inspection of vehicle- and MDMA-treated animals showed no obvious differences between treatment groups (Fig. 6-6). No obvious structures could be identified visually in the [<sup>125</sup>I]ADAM images from either vehicle- or MDMA-treated groups. By comparison with the MRI images, the space which would be assumed to be occupied by the brain appears pale indicating low binding in the brain but high activity in tissues surrounding the brain.

After extraction of the values of the respective structures masked by the ROIs, i.e. the thalamus, midbrain and cerebellum, the binding ratio was calculated by dividing the raw voxel intensities of the thalamus and midbrain by the cerebellum (Fig. 6-7). No significant differences between vehicle- and MDMA-treated groups could be detected in neither the thalamus/cerebellum nor the midbrain/cerebellum ratios. A non-significant increase in the midbrain-to-cerebellum ratio of MDMA-treated rats relative to control counterparts was observed.

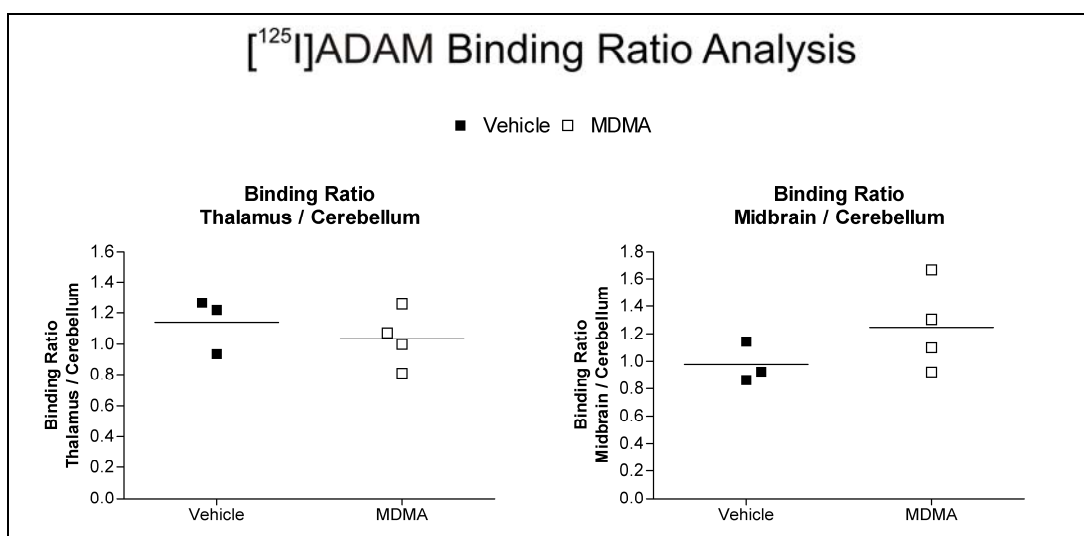


**Fig. 6-7. MDMA treatment does not affect *in vivo* [<sup>125</sup>I]ADAM SPECT-derived binding ratios after a 10 day maintenance period.**

Bars represent mean for n = 3 in vehicle- and n = 4 in MDMA-treated group.

Binding ratios for each animal were calculated by normalizing mean image intensities within the ROIs (thalamus and midbrain) to the cerebellum (regions/cerebellum). Left graph shows the binding ratio of the thalamus/cerebellum, whereas the right graph displays the ratio of the midbrain to the cerebellum. No significant differences were detected. However a non-significant increase in the binding ratio was observed in the midbrain in MDMA-treated animals compared to vehicle controls. Two-tailed Mann-Whitney U ( $p < 0.05$ ).

The normalisation to the cerebellum serves the purpose of accounting for different amounts of radioactivity administered to individual animals hence making SPECT scans

## **Chapter 6 - Autoradiographic and micro-SPECT imaging of SERT depletion in rats using the radioligands [<sup>125</sup>I]βCIT and [<sup>125</sup>I]ADAM.**

comparable to each other. Other criteria for choosing the cerebellum as a reference region is the fact that is low in SERT, and that it has low nonspecific binding. Therefore the normalisation of any structure to the cerebellum should yield a ratio with values  $\geq 1$ . As can be seen above, there are actually data points (representing binding ratios) that are lower than 1, indicating that the cerebellum had higher values than the structure under investigation (Fig. 6-7). This contradicts the use of the cerebellum as reference region in [<sup>125</sup>I]ADAM autoradiography. Even though non-significant differences could be detected in the midbrain-to-cerebellum ratio of MDMA-treated rats compared to vehicle controls, the ratios were actually too low to indicate any specific binding. For example values of approximately 1 were obtained in both the midbrain and thalamus. This contrasts with the much higher ratios obtained for [<sup>125</sup>I]βCIT (Table 6-1).

### ***Ex vivo* [<sup>125</sup>I]ADAM autoradiography of 10 day maintenance animals.**

#### **Visual comparison of representative sections of [<sup>125</sup>I]ADAM binding in vehicle- and MDMA-treated animals.**

*Ex vivo* autoradiograms generated after injection of [<sup>125</sup>I]ADAM and the following SPECT acquisition (120 min p. i.) are shown in Fig. 6-8. Visual inspection of *ex vivo* autoradiograms confirmed [<sup>125</sup>I]ADAM binding to structures known to be rich in SERT. The olfactory tubercle, lateral septum, globus pallidus, basolateral amygdala, lateral hypothalamus, dorsal thalamus, superior colliculus, substantia nigra, ventral tegmental area, and dorsal raphe are clearly identifiable in vehicle-treated animals. However there was a visible reduction in [<sup>125</sup>I]ADAM binding in MDMA-treated animals located in a number of structures including the basolateral amygdala, the dorsal thalamus, and the superior colliculus.

**Chapter 6 - Autoradiographic and micro-SPECT imaging of SERT depletion in rats using the radioligands [<sup>125</sup>I]βCIT and [<sup>125</sup>I]ADAM.**

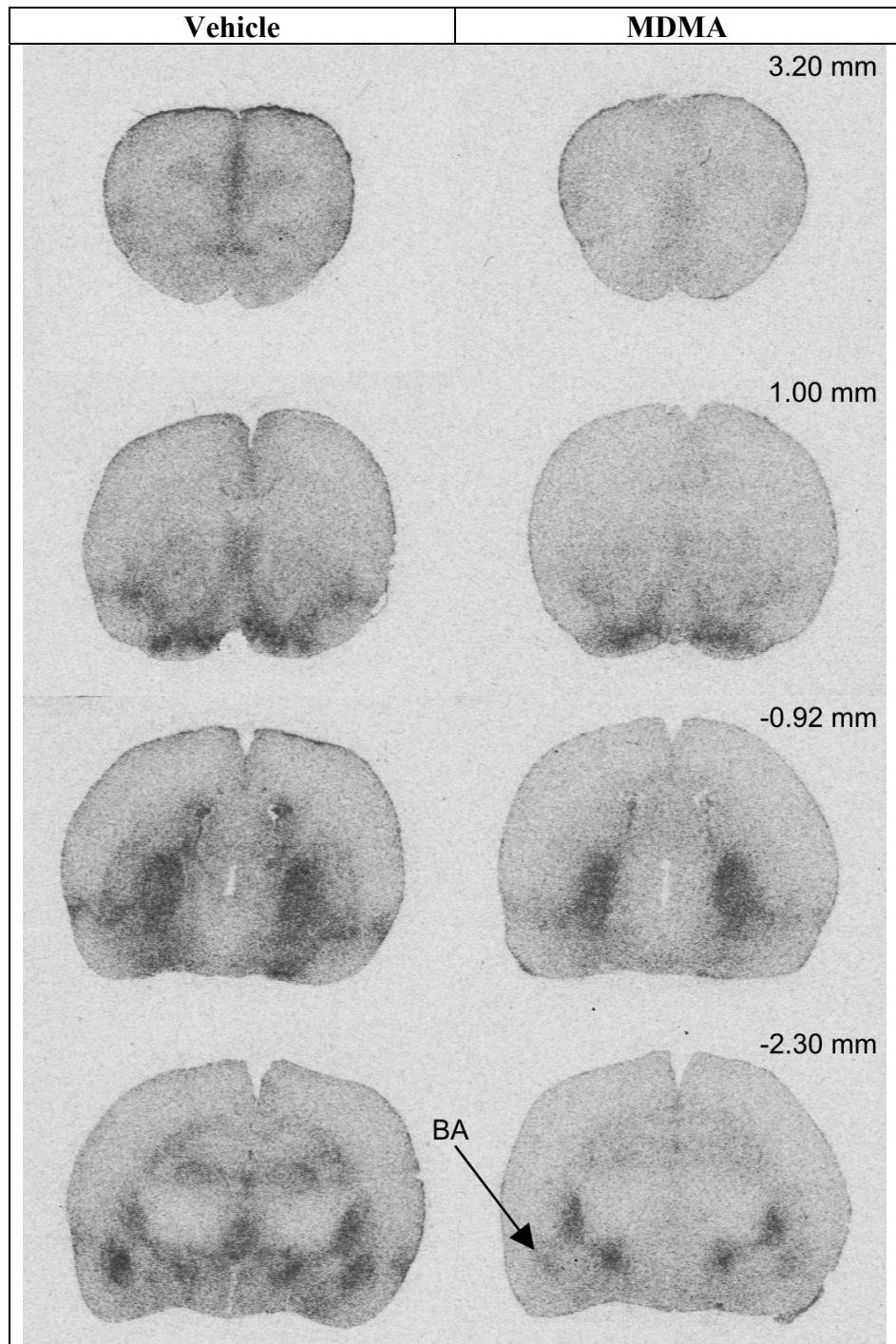


**Fig. 6-8. Representative *ex vivo* sections demonstrate that overall [<sup>125</sup>I]ADAM binding is unaffected by MDMA treatment (right) in animals of 10 day maintenance.**

**Chapter 6 - Autoradiographic and micro-SPECT imaging of SERT depletion in rats using the radioligands [<sup>125</sup>I]βCIT and [<sup>125</sup>I]ADAM.**

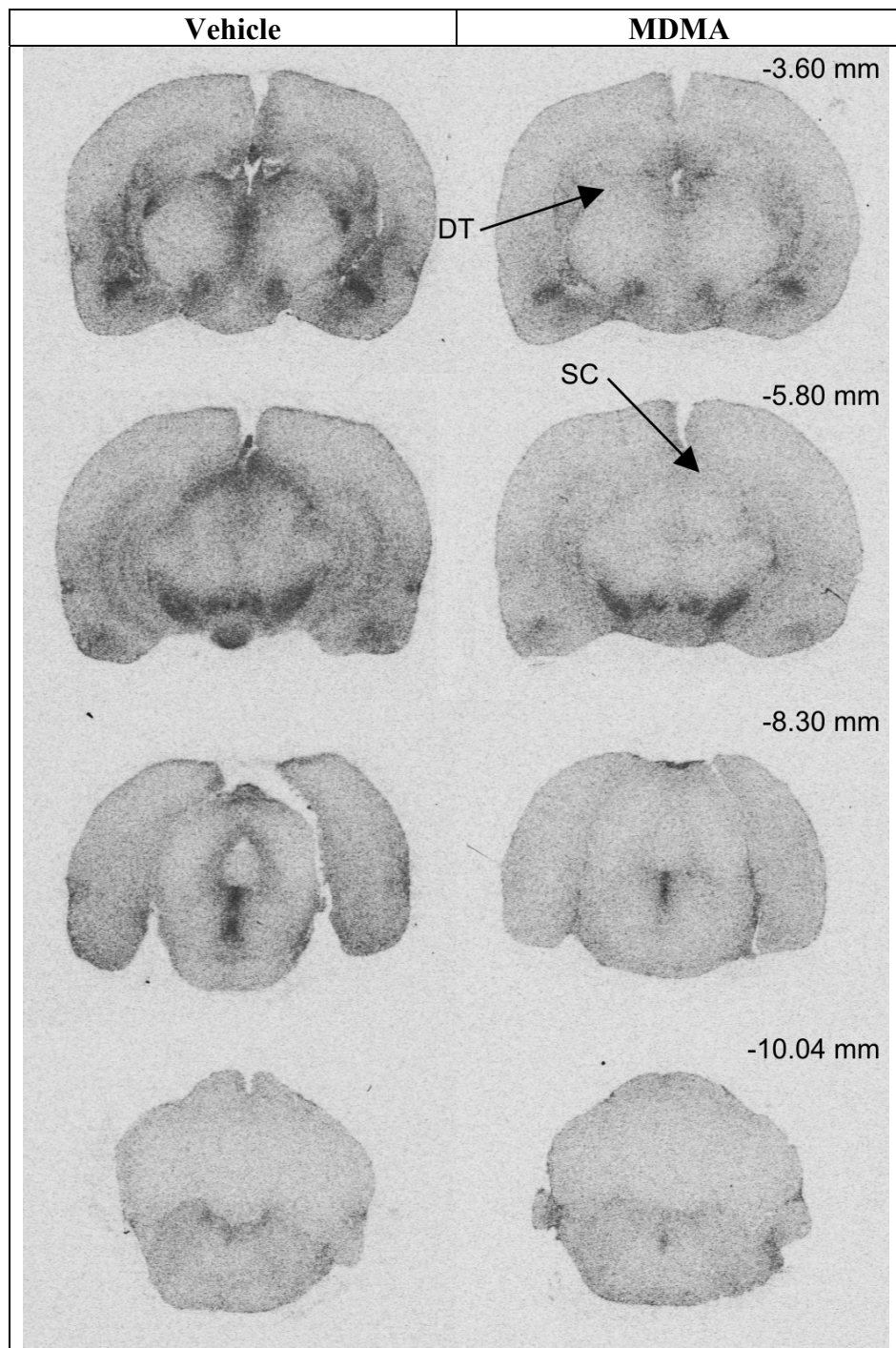


**Fig. 6-8. continued.**

Left: vehicle-, right: MDMA-treated animals both at the end of the experiment using ~16 MBq [<sup>125</sup>I]ADAM i. v.. No significant differences were detected in any of the 24 structures examined. Visually different appearing structures between MDMA- and vehicle-treated animals are indicated by an arrow. BA: basolateral amygdala; DT: dorsal thalamus; SC: superior colliculus. Note the higher background binding in vehicle- vs. MDMA-treated, i.e. in the cortex, while the cerebellum appears similar in intensity. Bregma level is indicated in top right corner.

**Chapter 6 - Autoradiographic and micro-SPECT imaging of SERT depletion in rats using the radioligands [<sup>125</sup>I]βCIT and [<sup>125</sup>I]ADAM.**

**Analysis of [<sup>125</sup>I]ADAM binding in vehicle- and MDMA-treated animals.**

Structure	Treatment		Rel. Diff. [%] <sup>a</sup>
	Vehicle	MDMA	
Prefrontal Cortex	1.39 ± 0.15	1.22 ± 0.07	-12.52
Anterior Cingulate Cortex	1.34 ± 0.05	1.38 ± 0.23	+3.23
Caudate-Putamen	1.18 ± 0.07	1.09 ± 0.05	-7.07
Septal Area	1.47 ± 0.12	1.36 ± 0.09	-8.00
Tubercle Area	1.73 ± 0.21	1.62 ± 0.22	-6.40
Globus Pallidus	1.70 ± 0.28	1.58 ± 0.21	-6.71
Retrosplenial Cortex	1.23 ± 0.06	1.14 ± 0.03	-7.40
Basolateral Amygdala	1.72 ± 0.38	1.49 ± 0.15	-13.13
Central Amygdaloid Nucleus	1.29 ± 0.11	1.21 ± 0.09	-5.90
Lateral Hypothalamus	1.67 ± 0.29	1.67 ± 0.24	+0.06
Ventral Hypothalamus	1.38 ± 0.11	1.26 ± 0.08	-8.62
Dorsal Thalamus	1.43 ± 0.18	1.19 ± 0.03	-16.22
Thalamus	1.23 ± 0.15	1.11 ± 0.02	-10.15
Habenula	1.49 ± 0.23	1.52 ± 0.06	+1.54
Hippocampus	1.18 ± 0.12	1.11 ± 0.02	-6.12
Piriform Cortex	1.27 ± 0.08	1.16 ± 0.04	-9.36
Substantia Nigra	1.95 ± 0.30	1.72 ± 0.30	-11.75
Medial Geniculate Nucleus	1.24 ± 0.08	1.15 ± 0.00	-6.76
Superior Colliculus	1.64 ± 0.25	1.22 ± 0.07	-25.82
Ventral Tegmental Area	2.04 ± 0.26	1.91 ± 0.10	-6.61
Inferior Colliculus	1.11 ± 0.03	1.07 ± 0.03	-3.83
Dorsal Raphe	2.14 ± 0.28	2.06 ± 0.36	-3.88
Entorhinal Cortex	1.47 ± 0.14	1.30 ± 0.05	-12.07
Locus Coeruleus	1.50 ± 0.17	1.33 ± 0.09	-11.39

**Table 6-2. Overall *ex vivo* [<sup>125</sup>I]ADAM autoradiography is unaffected by MDMA treatment in animals of 10 day maintenance. Expressed as ratio region/cerebellum.**

No significant differences were detected in any of the 24 structures examined.

Data are mean ± SD for n = 3 vehicle-, and n = 4 for MDMA-treated rats.

Two-tailed Mann-Whitney U (p < 0.05).

Relative difference (Rel. Diff.) = <sup>a</sup> (MDMA - vehicle)/(vehicle)\*100 %.

Analysis of the autoradiograms, expressing the ROI activity as a ratio of activity in the cerebellum indicated that these visual differences did not reach statistical significance (Table 6-2). Visual differences described above, i.e. in the basolateral amygdala, dorsal thalamus, and the superior colliculus, showed a 13 %, 16 %, and 26 % decrease in MDMA- relative to vehicle-treated animals, respectively. Note the high nonspecific binding in the cerebellum, which was not homogeneously distributed. The binding ratios obtained from *ex vivo* autoradiography are comparable to those extracted from the SPECT

## **Chapter 6 - Autoradiographic and micro-SPECT imaging of SERT depletion in rats using the radioligands [<sup>125</sup>I]βCIT and [<sup>125</sup>I]ADAM.**

dataset for the thalamus (1.23 in *ex vivo* autoradiography, vs. ~1.17 obtained from SPECT, both extracted from vehicle-treated animals). The highest binding ratio observed *ex vivo* was in the dorsal raphe for both, vehicle- and MDMA-treated animals (2.14 vs. 2.06, respectively). Hence there were higher binding ratios observed in *ex vivo* autoradiography vs. *in vivo* SPECT imaging, possibly indicating sensitivity issues with the latter technique.

While it appeared reasonable to check for associations between the measurements obtained from *in vivo* [<sup>125</sup>I]βCIT SPECT and *ex vivo* autoradiography, no scatter plots were generated for [<sup>125</sup>I]ADAM SPECT (for both 10 and 30 day maintenance) and *ex vivo* autoradiography. In [<sup>125</sup>I]βCIT SPECT images as well as in *ex vivo* autoradiography, the caudate-putamen and thalamus were reliably identifiable. However the poor image quality in [<sup>125</sup>I]ADAM SPECT images did not allow reliable measurements.

### ***In vivo* [<sup>125</sup>I]ADAM SPECT of 30 day maintenance animals.**

Technical problems with the scanner computer prevented the first set of animals that were generated from being scanned 10 days following the end of treatment. However, it was decided to maintain these animals for a longer period after the end of treatment as it has been shown previously that even 3 months after MDMA treatment changes in SERT function could be observed (McGregor et al., 2003). This also gave an additional opportunity to build up experience with the handling of [<sup>125</sup>I]ADAM and gain further information about the characteristics of this relatively new SERT SPECT ligand. The animal weight for the 30 day maintenance period on the day of SPECT image acquisition was  $310.2 \pm 24.7$  g for n = 4 vehicle- and n = 6 MDMA-treated animals. The same T2-weighted rat (316 g) MRI was used for coregistration as the one for the 10 day maintenance animals.

**Chapter 6 - Autoradiographic and micro-SPECT imaging of SERT depletion in rats using the radioligands [<sup>125</sup>I]βCIT and [<sup>125</sup>I]ADAM.**

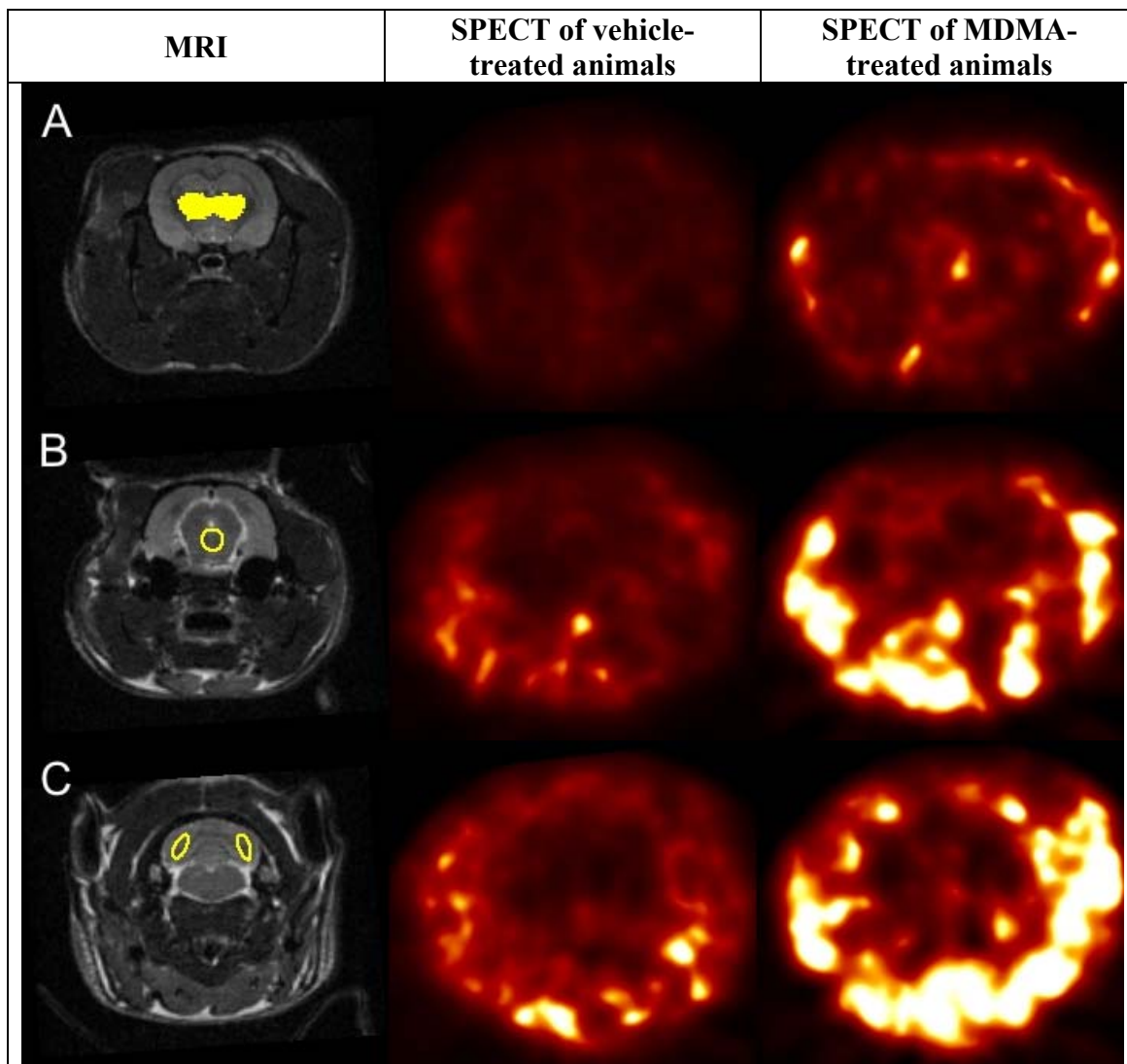


**Fig. 6-9. Representative *in vivo* [<sup>125</sup>I]ADAM SPECT images of vehicle- (middle) and MDMA-treated animals (right) after 30 days of maintenance do not appear different, and are of poor quality.**

ROIs (yellow) for the thalamus, midbrain, and cerebellum were defined on an age-matched rat T2-weighted MRI scan on 3 consecutive slices and subsequently superimposed on coregistered [<sup>125</sup>I]ADAM SPECT images for measurements. No differences were observed between vehicle- and MDMA-treated animals as no brain structure could be examined visually.

A: thalamus at Bregma level -3.60 mm.

B: midbrain at Bregma level -5.80 mm.

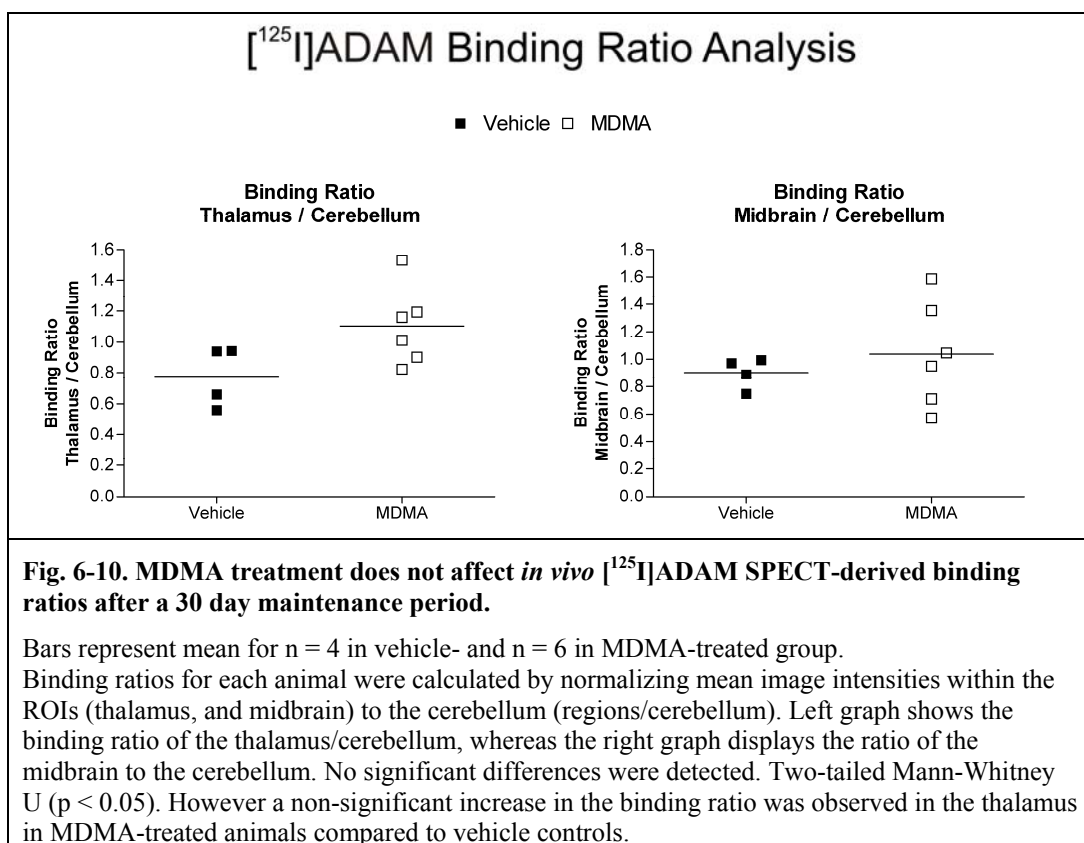
C: cerebellum at Bregma level -10.04 mm.

Representative slices of [<sup>125</sup>I]ADAM *in vivo* SPECT scans of rats 30 days after the end of treatment resemble to those scanned 10 days after treatment (Fig. 6-9). There was a similar lack of visible pattern within the scans and no obvious structures could be discerned. The space within the images which would supposedly contain the brain, based on comparison with the MRI images, appears pale indicating low [<sup>125</sup>I]ADAM binding in the brain. However high activity is detected in tissues surrounding the brain and in the thyroid (see

## Chapter 6 - Autoradiographic and micro-SPECT imaging of SERT depletion in rats using the radioligands [<sup>125</sup>I]βCIT and [<sup>125</sup>I]ADAM.

also Fig. 2-26 for explanation). It was not clear whether the high thyroidal uptake compared to [<sup>125</sup>I]βCIT SPECT scans is because of free [<sup>125</sup>I].

The binding ratios of the thalamus-to-cerebellum, and midbrain-to-cerebellum are shown in Fig. 6-10 and no difference between treatment groups was observed. This is consistent with data from the 10 day experiment. However, a non-significant increase in the thalamus/cerebellum in rats that underwent the SERT-depleting MDMA regimen was observed relative to control animals ( $1.1 \pm 0.3$  vs.  $0.8 \pm 0.2$ , respectively). This is in contrast to the 10 day data, where a non-significant increase in the midbrain/cerebellum ratio was detected in SERT-depleted animals relative to controls. The data from both sets of animals (10 and 30 days) should be treated with caution however, as discussed previously, since the ratios observed are close to 1 indicating that there is little or no specific [<sup>125</sup>I]ADAM binding in either vehicle- or MDMA-treated rats.



### ***Ex vivo* [<sup>125</sup>I]ADAM autoradiography of 30 day maintenance animals.**

#### **Visual comparison of representative sections of [<sup>125</sup>I]ADAM binding in vehicle- and MDMA-treated animals.**

The *ex vivo* distribution of [<sup>125</sup>I]ADAM in the 30 day animals resembled that seen in the 10 day animals (see Fig. 6-8, for 10 day, vs. Fig. 6-11 for 30 day animals). Identifiable

**Chapter 6 - Autoradiographic and micro-SPECT imaging of SERT depletion in rats using the radioligands [<sup>125</sup>I]βCIT and [<sup>125</sup>I]ADAM.**

structures in vehicle-treated animals were the olfactory tubercle (measured as tubercle area), lateral septum (measured as septal area), globus pallidus, basolateral amygdala, lateral hypothalamus, dorsal thalamus, superior colliculus, substantia nigra, ventral tegmental area, and dorsal raphe.

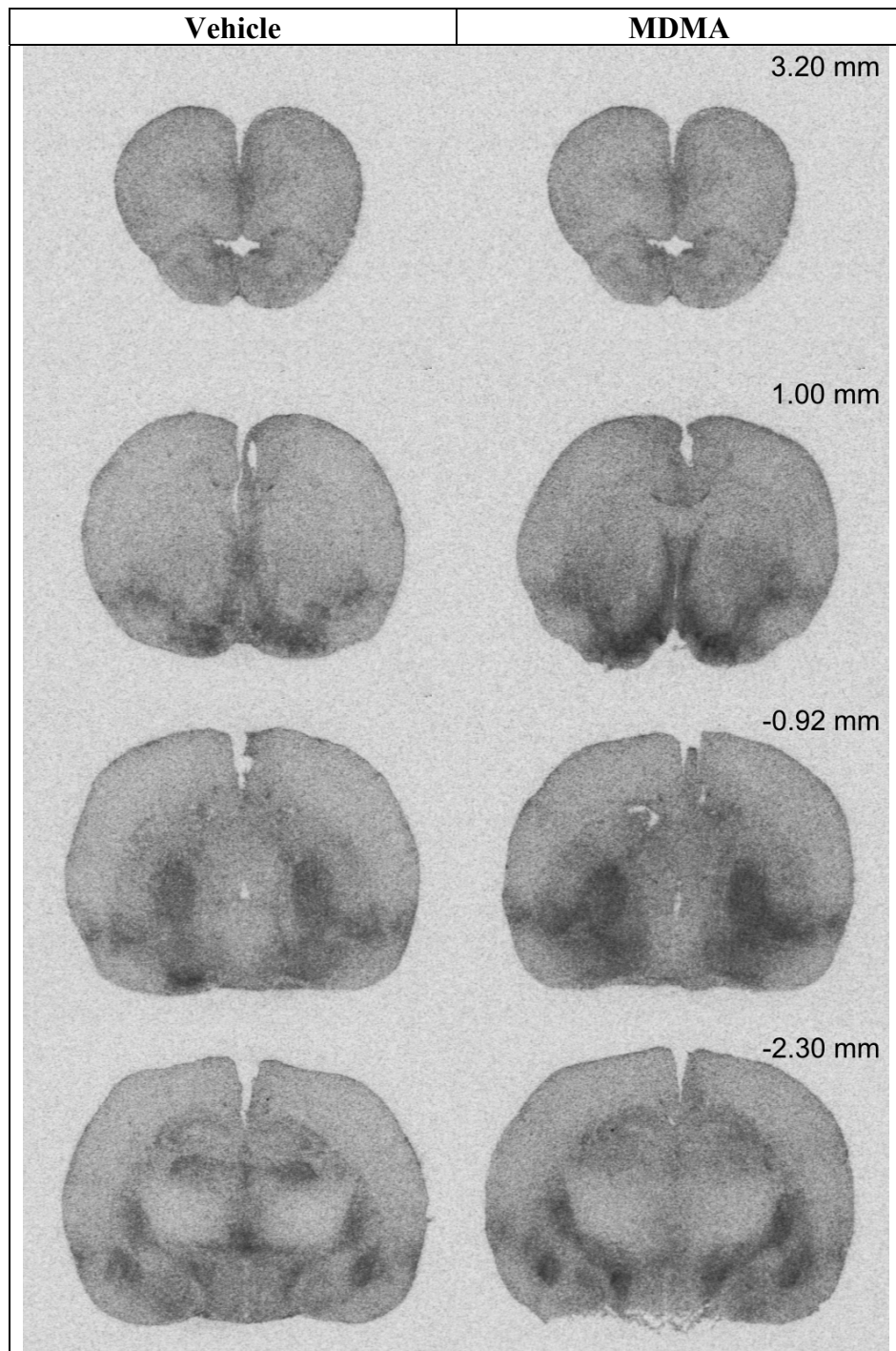


**Fig. 6-11. Representative *ex vivo* sections demonstrate that overall [<sup>125</sup>I]ADAM binding is unaffected by MDMA treatment (right) in animals of 30 day maintenance.**

**Chapter 6 - Autoradiographic and micro-SPECT imaging of SERT depletion in rats using the radioligands [<sup>125</sup>I]βCIT and [<sup>125</sup>I]ADAM.**

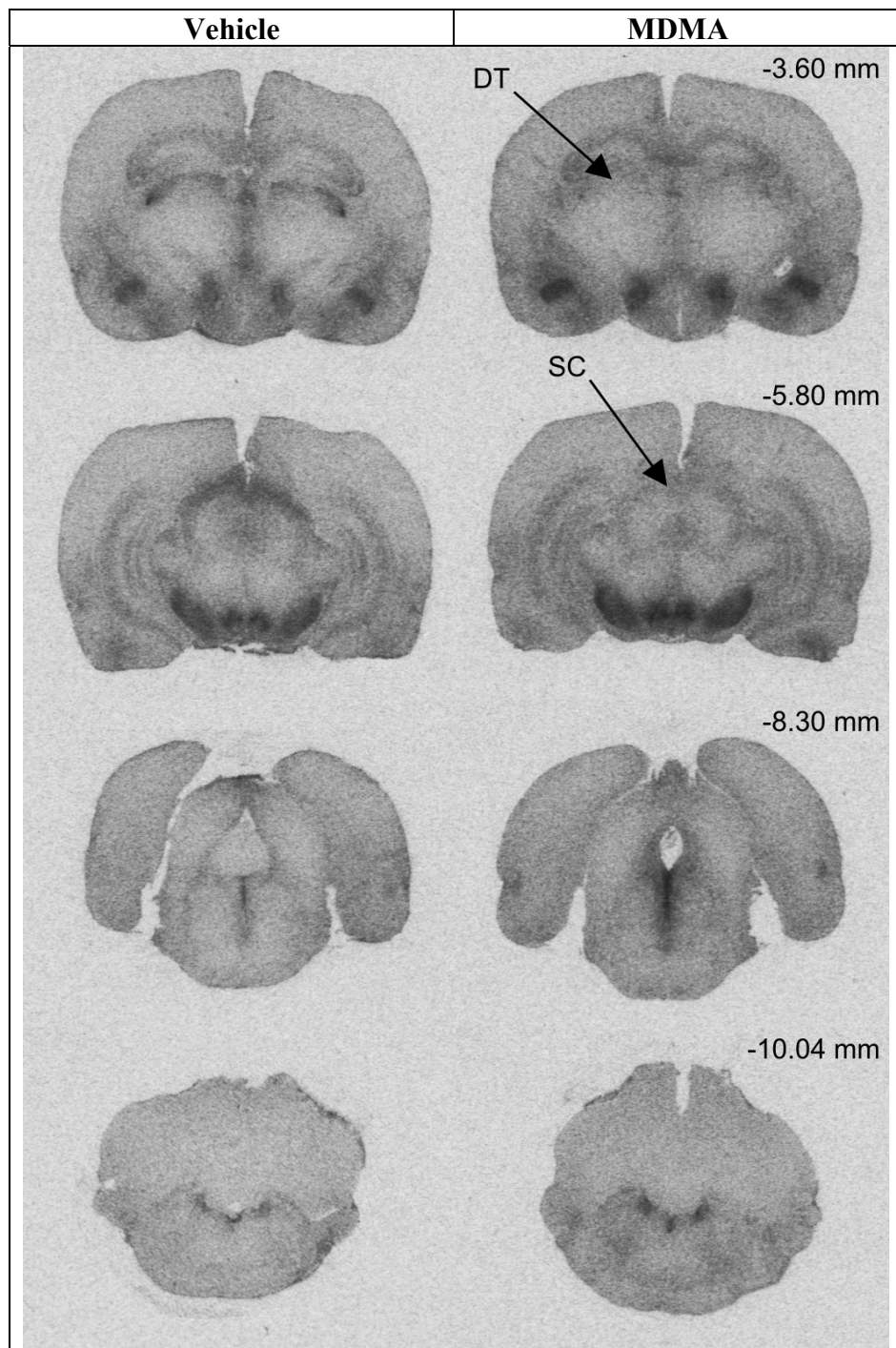


**Fig. 6-11. continued.**

Left: vehicle-, right: MDMA-treated animals both at the end of the experiment using ~16 MBq [<sup>125</sup>I]ADAM i. v.. No significant differences were detected in any of the 24 structures examined. Visually different appearing structures between MDMA- and vehicle-treated animals are indicated by an arrow. DT: dorsal thalamus; SC: superior colliculus. Bregma level is indicated in top right corner.

**Chapter 6 - Autoradiographic and micro-SPECT imaging of SERT depletion in rats using the radioligands [<sup>125</sup>I]βCIT and [<sup>125</sup>I]ADAM.**

**Analysis of [<sup>125</sup>I]ADAM binding in vehicle- and MDMA-treated animals.**

Structure	Treatment		Rel. Diff. [%] <sup>a</sup>
	Vehicle	MDMA	
Prefrontal Cortex	1.31 ± 0.23	1.24 ± 0.22	-5.45
Anterior Cingulate Cortex	1.14 ± 0.11	1.15 ± 0.10	+1.39
Caudate-Putamen	1.04 ± 0.05	1.05 ± 0.07	+0.86
Septal Area	1.27 ± 0.25	1.31 ± 0.27	+2.84
Tubercle Area	1.51 ± 0.39	1.50 ± 0.46	-0.49
Globus Pallidus	1.37 ± 0.33	1.36 ± 0.38	-0.14
Retrosplenial Cortex	1.15 ± 0.08	1.11 ± 0.07	-3.72
Basolateral Amygdala	1.47 ± 0.40	1.41 ± 0.41	-4.30
Central Amygdaloid Nucleus	1.12 ± 0.14	1.12 ± 0.14	+0.20
Lateral Hypothalamus	1.41 ± 0.34	1.29 ± 0.35	-8.83
Ventral Hypothalamus	1.26 ± 0.20	1.20 ± 0.09	-4.71
Dorsal Thalamus	1.25 ± 0.19	1.15 ± 0.11	-7.86
Thalamus	1.09 ± 0.11	1.05 ± 0.05	-3.96
Habenula	1.30 ± 0.09	1.29 ± 0.09	-1.31
Hippocampus	1.09 ± 0.10	1.08 ± 0.09	-0.67
Piriform Cortex	1.14 ± 0.13	1.08 ± 0.10	-5.04
Substantia Nigra	1.55 ± 0.52	1.63 ± 0.57	+5.17
Medial Geniculate Nucleus	1.17 ± 0.09	1.09 ± 0.05	-6.81
Superior Colliculus	1.49 ± 0.34	1.26 ± 0.13	-14.92
Ventral Tegmental Area	1.71 ± 0.61	1.71 ± 0.61	+0.20
Inferior Colliculus	1.05 ± 0.03	1.06 ± 0.02	+0.17
Dorsal Raphe	1.60 ± 0.42	1.91 ± 0.68	+19.71
Entorhinal Cortex	1.27 ± 0.18	1.21 ± 0.07	-5.00
Locus Coeruleus	1.32 ± 0.26	1.35 ± 0.33	+2.35

**Table 6-3. Overall *ex vivo* [<sup>125</sup>I]ADAM autoradiography is unaffected by MDMA treatment in animals of 30 day maintenance. Expressed as ratio region/cerebellum.**

No significant differences were detected in any of the 24 structures examined.

Data are mean ± SD for n = 4 vehicle-, and n = 6 for MDMA-treated rats.

Two-tailed Mann-Whitney U (p < 0.05).

Relative difference (Rel. Diff.) = <sup>a</sup> (MDMA - vehicle)/(vehicle)\*100 %.

As for the 10 day maintenance data, no significant differences were detected between groups using [<sup>125</sup>I]ADAM as shown in Table 6-3. However visual differences in [<sup>125</sup>I]ADAM binding in the dorsal thalamus, as well as in the superior colliculus were observed between vehicle- and MDMA-treated animals (Fig. 6-11). Those differences corresponded to an 8 % and 15 % reduction, respectively, in SERT availability (Table 6-3).

## Chapter 6 - Autoradiographic and micro-SPECT imaging of SERT depletion in rats using the radioligands [<sup>125</sup>I]βCIT and [<sup>125</sup>I]ADAM.

### Comparing different batches of [<sup>125</sup>I]ADAM.

The issues of the stability of [<sup>125</sup>I]ADAM were considered in the light of the lack of success in establishing a reliable protocol for [<sup>125</sup>I]ADAM *in vitro* autoradiography. In total, 4 batches of [<sup>125</sup>I]ADAM were used, reference dates 04.01.2008 (1), 31.01.2008 (2), 11.02.2008 (3) and 01.04.2008 (4). An enquiry was made about the stability to the manufacturer (MAP Finland) who provided assurance that there was still a high purity of [<sup>125</sup>I]ADAM up to 30 days after synthesis and information that batch (1) and (2) were from the same synthesis.

In the autoradiography experiments, batches (2) and (4) were used. While experiment 1 using batch (2) (page 72) appeared to be promising, almost identical experimental conditions did not reproduce these results using batch (4) (experiment 2, page 74). Only a single batch (4) of [<sup>125</sup>I]ADAM was used for *in vivo* SPECT imaging of 10 day maintenance rats, and visual inspection of the resulting *ex vivo* autoradiograms derived from those animals showed good animal-to-animal reproducibility of [<sup>125</sup>I]ADAM binding (Fig. 6-8). All the animals were scanned within a week to minimize variability. The autoradiography experiments described in experiment 2 (page 74) and experiment 3 (page 79) were performed roughly 2 weeks after all [<sup>125</sup>I]ADAM SPECT images were acquired. However it should be noted that only ~100 µl were left in the vial as most was used for *in vivo* [<sup>125</sup>I]ADAM SPECT imaging, and free [<sup>125</sup>I] is presumably very sticky, sticking to the walls of the vial. Therefore it is possible that the remaining [<sup>125</sup>I]ADAM in the vial was mainly constituted of re-suspended free [<sup>125</sup>I].

In order to address potential stability issues of [<sup>125</sup>I]ADAM, the *ex vivo* autoradiograms of animals that received injections from this batch (2) were scrutinised. Batch (2) was the batch that was used with the longest period between synthesis and use (approximately one month). Representative *ex vivo* sections of 2 vehicle-treated animals that were SPECT scanned shortly after [<sup>125</sup>I]ADAM arrival are presented in Fig. 6-12. Note that the film exposure duration, and the film onto which the sections were apposed to, were identical (Fig. 6-12). The injected doses of [<sup>125</sup>I]ADAM were 14.1 MBq and 20.5 MBq, respectively. In both animals, the superior colliculus, substantia nigra, ventral tegmental area, and the dorsal raphe showed binding of [<sup>125</sup>I]ADAM. In addition, the animal receiving 20.5 MBq displayed a stronger signal in the structures mentioned compared to the animal having received the lower dose. These 2 vehicle-treated animals were not

## Chapter 6 - Autoradiographic and micro-SPECT imaging of SERT depletion in rats using the radioligands [<sup>125</sup>I]βCIT and [<sup>125</sup>I]ADAM.

included in the SPECT study described above as the animals were killed 90 min after injection of [<sup>125</sup>I]ADAM, and not 120 min as for the other animals. However it is believed that these animals still give valuable information about [<sup>125</sup>I]ADAM as it is not expected that with an additional 30 min after injection, the ligand would have been completely washed out of the brain (see Fig. 6-8 for instance).

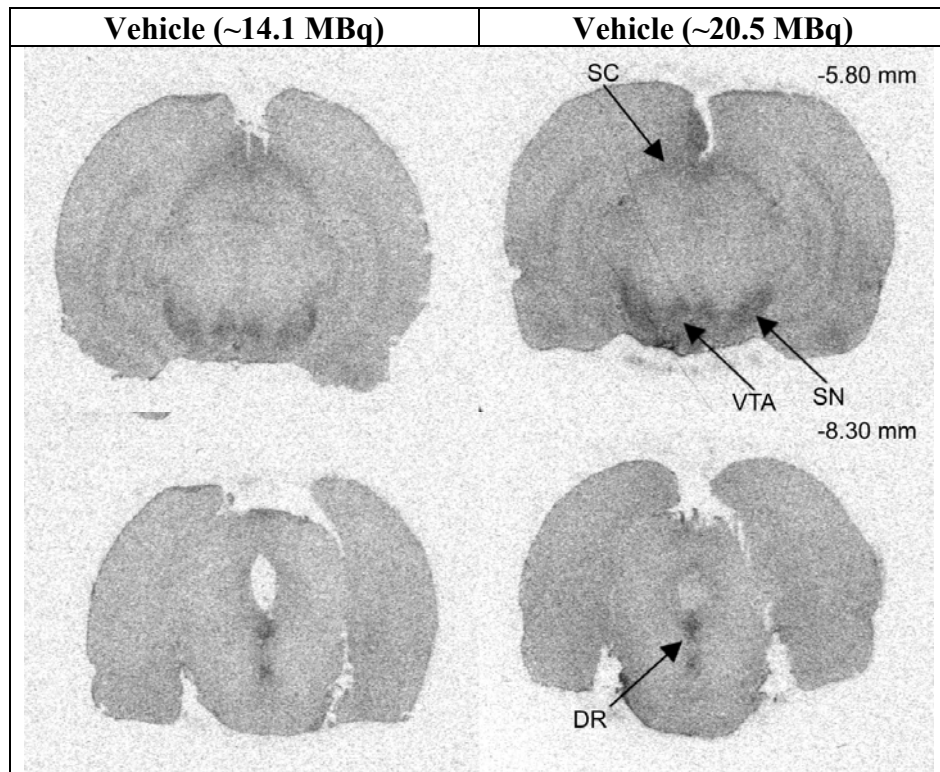


**Fig. 6-12. [<sup>125</sup>I]ADAM batch (2) in vehicle-treated animals demonstrates reasonable binding to SERT-rich regions.**

Representative sections show vehicle-treated animals. Left: animal received ~14.1 MBq of [<sup>125</sup>I]ADAM i. v.. Right: animal received ~20.5 MBq of [<sup>125</sup>I]ADAM i. v. Please note that these animals were not included in the study because they represented test animals to optimise the SPECT scanning routine and were killed 90 min after injection of [<sup>125</sup>I]ADAM. SC: superior colliculus; SN: substantia nigra; VTA: ventral tegmental area; DR: dorsal raphe. Batch 2, experiment was conducted on the 29.01.2008. Correspondence with MAP, Finland clarified that this batch was identical to the one calibrated to 04.01.2008. Note that film exposure duration was identical to sections presented in Fig. 6-13, however sections were apposed onto different films. Sections shown here in this figure were on the same film. Bregma level is indicated in top right corner.

Unfortunately, there were no vehicle-treated animals that received [<sup>125</sup>I]ADAM at a later time point after radioligand synthesis of batch 2, however 2 MDMA-treated animals in the 30 day experiment did (Fig. 6-13). Note that the film exposure duration was identical for the sections presented in Fig. 6-12 and Fig. 6-13. However both sections in Fig. 6-13 were apposed onto separate sheets of films. There was only weak binding of [<sup>125</sup>I]ADAM in the substantia nigra and ventral tegmental area, respectively, and those 2 structures could not

## Chapter 6 - Autoradiographic and micro-SPECT imaging of SERT depletion in rats using the radioligands [<sup>125</sup>I]βCIT and [<sup>125</sup>I]ADAM.

be discerned according to shapes, only including knowledge of spatial anatomy. The superior colliculus appeared weak in [<sup>125</sup>I]ADAM binding, but also the dorsal raphe was faint. The two scans were acquired only few days apart. The supposedly nonspecific binding was much higher in the animal having received the higher dose, which also finished off this batch. Even though a reduction of [<sup>125</sup>I]ADAM binding was expected in MDMA-treated animals due to the SERT-depleting regimen of MDMA, the ventral tegmental area, as well as the substantia nigra appeared comparable in representative sections shown for the 10 and 30 day maintenance experiments (Fig. 6-8 and Fig. 6-11, respectively).

After this scrutiny of the *ex vivo* autoradiograms, it was judged that no animals should be excluded because of concerns about radioligand stability since there was evidence that there was anatomically-localised [<sup>125</sup>I]ADAM binding, even if it was low.

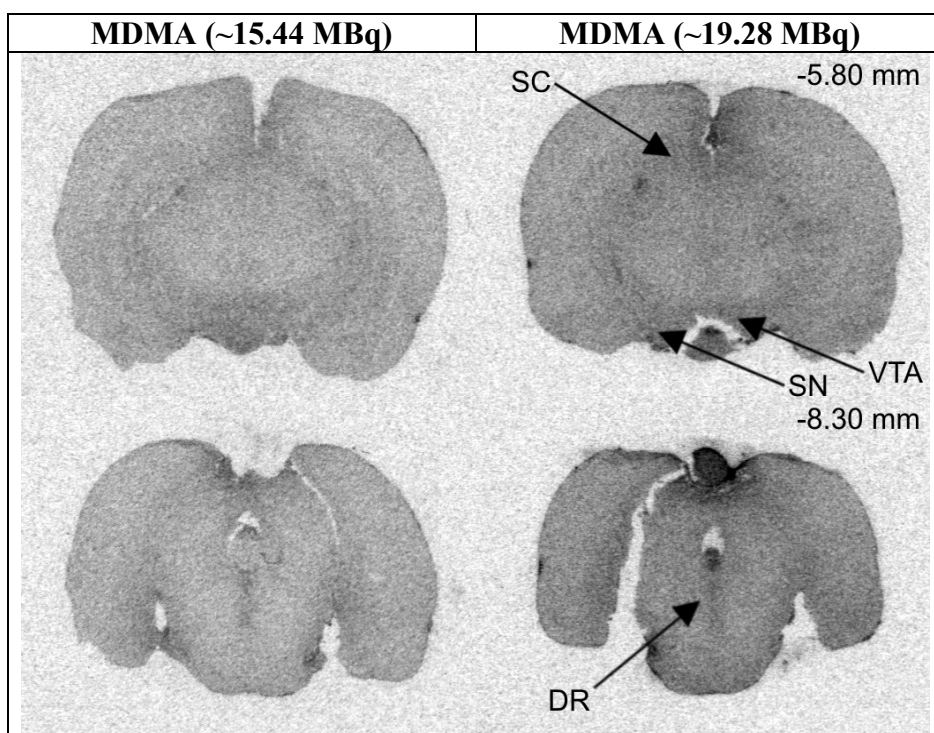


**Fig. 6-13. [<sup>125</sup>I]ADAM batch (2) in MDMA-treated animals demonstrates weak binding to SERT-rich regions.**

Representative sections show MDMA-treated animals. Left: animal received ~15.44 MBq of [<sup>125</sup>I]ADAM (batch 2) i. v. Right: animal received ~19.28 MBq of [<sup>125</sup>I]ADAM i. v. (batch 2). Experiment was conducted on the 26.02.2008 (left) and 28.02.2008 (right). Animals were killed ~2 h p. i.. Note that film exposure duration was identical to sections presented in Fig. 6-12, however sections were apposed onto different films. Sections shown here in this figure were on separate sheets of film. Bregma level is indicated in top right corner.

**Chapter 6 - Autoradiographic and micro-SPECT imaging of SERT depletion in rats using the radioligands [<sup>125</sup>I]βCIT and [<sup>125</sup>I]ADAM.**

**6.4.3 *In vitro* autoradiography.**

The following sections provide the validation of widespread depletion of SERT in animals treated with MDMA. The animals were treated at the same time as the animals for the SPECT study. It is worth mentioning that the results are very similar as those obtained in the pilot study using separate animals (section 2.3, page 53).

**[<sup>3</sup>H]citalopram autoradiography to label SERT.**

**Levels of nonspecific [<sup>3</sup>H]citalopram binding defined in the presence of fluoxetine.**

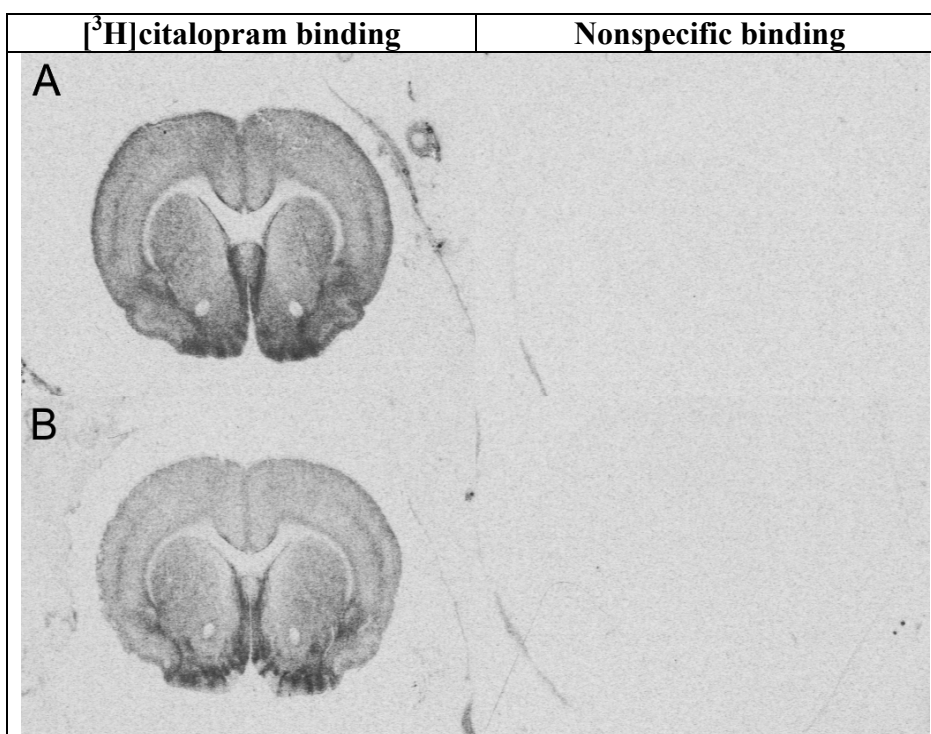


**Fig. 6-14. Nonspecific *in vitro* [<sup>3</sup>H]citalopram binding is low.**

Nonspecific binding was addressed using fluoxetine to displace [<sup>3</sup>H]citalopram from SERT.

Left: representative sections showing total binding to SERT.

Right: representative sections showing nonspecific binding defined by pharmacological blockage of SERT with fluoxetine.

A: vehicle-treated representative animal

B: MDMA-treated representative animal

Nonspecific binding of [<sup>3</sup>H]citalopram was low, and comparable between treatment groups.

Levels of nonspecific binding of [<sup>3</sup>H]citalopram binding in the presence of fluoxetine were visually inspected. Representative sections collected at the level of the caudate-putamen are shown in Fig. 6-14. While MDMA treatment reduced the level of total [<sup>3</sup>H]citalopram binding compared to vehicle administration (Fig. 6-14, A, left vs. B, left, respectively), levels of nonspecific binding defined using fluoxetine were very low in both treatment

## **Chapter 6 - Autoradiographic and micro-SPECT imaging of SERT depletion in rats using the radioligands [<sup>125</sup>I]βCIT and [<sup>125</sup>I]ADAM.**

groups (Fig. 6-14, A, right vs. right B, right, respectively). Visual examination could not detect any differences between groups in nonspecific binding.

### **Visual comparison of representative sections of [<sup>3</sup>H]citalopram binding in vehicle- and MDMA-treated animals.**

Fig. 6-15 shows the results of [<sup>3</sup>H]citalopram autoradiography, with representative vehicle-treated animals in the left column, and the MDMA-treated on the right. All cortical regions, i.e. prefrontal, anterior cingulate, retrosplenial, piriform, and entorhinal cortices show massive reductions in SERT availability after MDMA treatment as imaged with the selective SERT ligand [<sup>3</sup>H]citalopram. Also thalamic regions, such as the dorsal part, and the medial geniculate nucleus, are reduced in SERT, but also the hippocampus, the superior and inferior colliculi and the cerebellum. The latter, even though low in SERT density, is important, as it is commonly used as reference region for normalisation. The normalisation is thought to account for different amounts of radiolabelled ligand that might be injected, or delivered to the brain in an *in vivo* setting.

**Chapter 6 - Autoradiographic and micro-SPECT imaging of SERT depletion in rats using the radioligands [<sup>125</sup>I]βCIT and [<sup>125</sup>I]ADAM.**

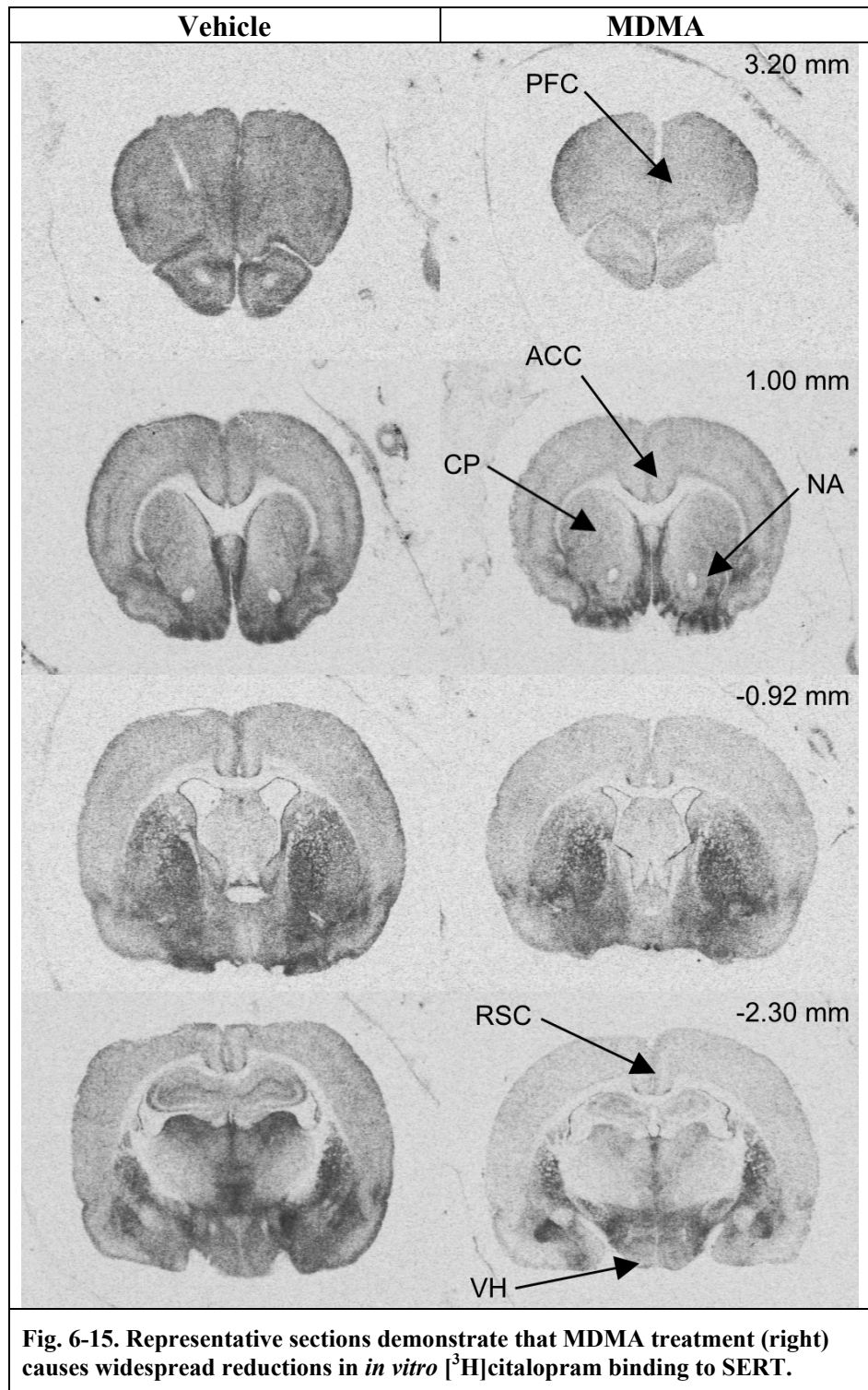


**Fig. 6-15. Representative sections demonstrate that MDMA treatment (right) causes widespread reductions in *in vitro* [<sup>3</sup>H]citalopram binding to SERT.**

**Chapter 6 - Autoradiographic and micro-SPECT imaging of SERT depletion in rats using the radioligands [<sup>125</sup>I]βCIT and [<sup>125</sup>I]ADAM.**

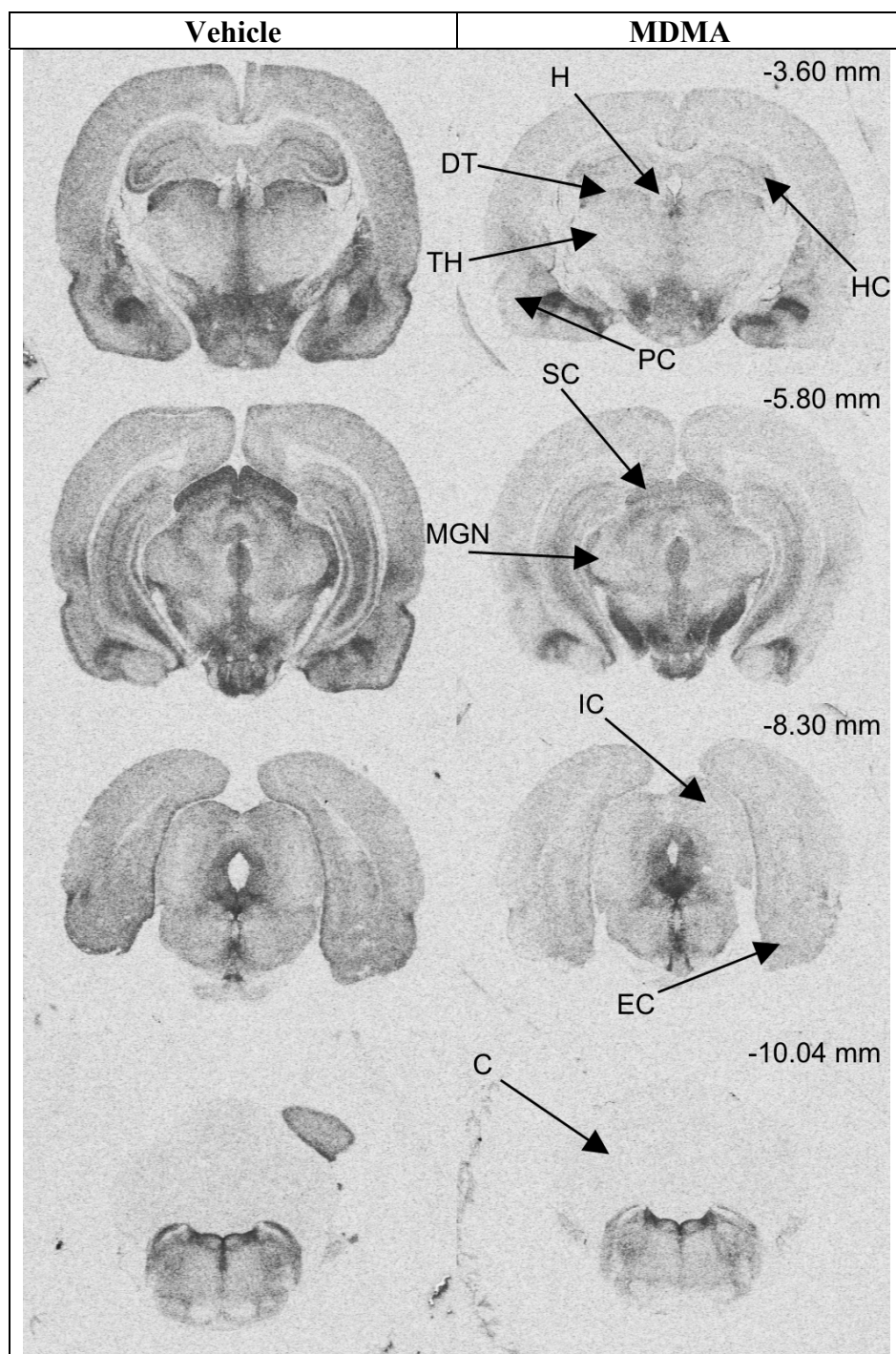


**Fig. 6-15. *continued.***

Left: vehicle-, right: MDMA-treated animals. Arrows indicate significant differences. MDMA-treated animals show less [<sup>3</sup>H]citalopram binding in cortical structures (PFC, ACC, RSC, PC, EC); caudate-putamen (CP); nucleus accumbens (NA); thalamic structures (DT, TH and MGN); ventral hypothalamus (VH); habenula (H); hippocampus (HC); superior and inferior colliculi (SC and IC); but also in the cerebellum (C). PFC: prefrontal cortex; ACC: anterior cingulate cortex; RSC: retrosplenial cortex; PC: piriform cortex; EC: entorhinal cortex; TH: thalamus; DT: dorsal thalamus; MGN: medial geniculate nucleus. Bregma level is indicated in top right corner.

## Chapter 6 - Autoradiographic and micro-SPECT imaging of SERT depletion in rats using the radioligands [<sup>125</sup>I]βCIT and [<sup>125</sup>I]ADAM.

### Analysis of [<sup>3</sup>H]citalopram binding in vehicle- and MDMA-treated animals.

Administration of MDMA over a treatment period of 4 days resulted in widespread loss of [<sup>3</sup>H]citalopram binding. The data indicate that MDMA had successfully depleted SERT in a number of different brain regions. The reductions were notable in various cortical regions, i.e. the prefrontal, retrosplenial, and piriform cortices, and thalamic structures such as the dorsal thalamus and the medial geniculate nucleus where [<sup>3</sup>H]citalopram binding was significantly lower in animals treated with MDMA compared to vehicle-treated control rats (Table 6-4).

In total 16 out of 26 structures examined in the rat brains were significantly affected by the MDMA treatment which included for instance the cerebellum, and the superior colliculus. The latter structure is one of the few structures identifiable in *ex vivo* [<sup>125</sup>I]ADAM autoradiography, and showed a reduced SERT availability of 64 %. Interestingly, all the structures that synthesise monoamines, such as the dorsal raphe, the locus coeruleus, the substantia nigra and ventral tegmental area, showed only low non-significant differences between MDMA- and vehicle-treated animals. In addition to the expression of the data relative to [<sup>3</sup>H]micro-scales, ratios were also calculated that normalise the data to the cerebellum in the same way as needed to be done for *in vivo* SPECT imaging (Table 6-5). In contrast to the data discussed above, only 10 out of the 25 sampled structures were significantly affected by MDMA treatment when compared to vehicle-treated animals. This indicates a disparity that is inherently present in the normalisation-to-the-cerebellum method. In addition, several structures that were detected to be significantly altered do not match those detected using the absolute quantification method. In particular, structures that display high SERT density and remained unaltered using the latter method, i.e. the septal area, tubercle area, lateral hypothalamus, dorsal raphe, and the locus coeruleus, were significantly altered using the ratio method indicating that these structures are highly influenced by altered SERT availability in the cerebellum.

**Chapter 6 - Autoradiographic and micro-SPECT imaging of SERT depletion in rats using the radioligands [<sup>125</sup>I]βCIT and [<sup>125</sup>I]ADAM.**

Structure	Treatment		Rel. Diff. [%] <sup>a</sup>
	Vehicle	MDMA	
Prefrontal Cortex	79.58 ± 12.01	58.33 ± 9.85 *	-26.71
Anterior Cingulate Cortex	59.25 ± 8.26	28.53 ± 3.93 *	-51.84
Caudate-Putamen	63.74 ± 8.20	46.88 ± 10.07 *	-26.45
Septal Area	115.13 ± 5.89	98.52 ± 14.49	-14.43
Nucleus Accumbens	84.12 ± 11.56	51.64 ± 15.44 *	-38.61
Tubercle Area	199.68 ± 16.14	169.88 ± 43.31	-14.92
Globus Pallidus	150.73 ± 23.16	133.46 ± 16.53	-11.46
Retrosplenial Cortex	32.25 ± 4.89	17.71 ± 3.62 *	-45.09
Basolateral Amygdala	158.35 ± 21.50	139.12 ± 26.27	-12.14
Central Amygdaloid Nucleus	44.01 ± 9.58	27.98 ± 12.97	-36.43
Lateral Hypothalamus	185.28 ± 27.86	172.45 ± 20.76	-6.92
Ventral Hypothalamus	86.39 ± 13.44	50.54 ± 8.24 *	-41.50
Dorsal Thalamus	117.79 ± 6.04	42.36 ± 19.27 *	-64.04
Thalamus	74.35 ± 12.08	31.28 ± 15.13 *	-57.93
Habenula	46.28 ± 5.58	22.36 ± 10.31 *	-51.68
Hippocampus	55.39 ± 4.30	25.82 ± 8.72 *	-53.39
Piriform Cortex	57.23 ± 10.35	17.10 ± 7.87 *	-70.13
Substantia Nigra	180.55 ± 11.55	177.59 ± 60.22	-1.64
Medial Geniculate Nucleus	53.42 ± 3.75	22.78 ± 7.55 *	-57.35
Superior Colliculus	160.11 ± 22.74	57.58 ± 20.47 *	-64.04
Ventral Tegmental Area	223.94 ± 26.50	210.79 ± 58.55	-5.87
Inferior Colliculus	41.91 ± 7.03	19.58 ± 5.14 *	-53.28
Dorsal Raphe	339.76 ± 49.17	344.30 ± 39.77	+1.34
Entorhinal Cortex	87.42 ± 10.22	48.13 ± 8.04 *	-44.94
Locus Coeruleus	233.15 ± 36.40	215.08 ± 19.09	-7.75
Cerebellum	12.67 ± 1.72	8.08 ± 1.64 *	-36.25

**Table 6-4. MDMA treatment causes widespread reductions in *in vitro* [<sup>3</sup>H]citalopram binding to SERT.**

Sixteen out of 26 structures are significantly different between vehicle- and MDMA-treated animals. Data are mean ± SD for n = 3 - 4 vehicle-, and n = 5 - 6 for MDMA-treated rats.

Units of measurement are fmol/mg.

Two-tailed Mann-Whitney U, \*p < 0.05 relative to vehicle group.

Relative difference (Rel. Diff.) = <sup>a</sup> (MDMA - vehicle)/(vehicle)\*100 %.

**Chapter 6 - Autoradiographic and micro-SPECT imaging of SERT depletion in rats using the radioligands [<sup>125</sup>I]βCIT and [<sup>125</sup>I]ADAM.**

Structure	Treatment		Rel. Diff. [%] <sup>a</sup>
	Vehicle	MDMA	
Prefrontal Cortex	6.31 ± 0.82	7.49 ± 2.06	+18.64
Anterior Cingulate Cortex	4.70 ± 0.51	3.63 ± 0.67 *	-22.78
Caudate-Putamen	5.04 ± 0.30	5.88 ± 0.89	+16.50
Septal Area	9.22 ± 1.39	12.44 ± 1.76 *	+34.96
Nucleus Accumbens	6.68 ± 0.86	6.32 ± 0.99	-5.36
Tubercle Area	15.87 ± 1.23	21.04 ± 3.03 *	+32.60
Globus Pallidus	12.33 ± 1.06	17.02 ± 3.43	+38.12
Retrosplenial Cortex	2.57 ± 0.43	2.24 ± 0.45	-12.79
Basolateral Amygdala	12.72 ± 2.72	17.77 ± 4.33	+39.73
Central Amygdaloid Nucleus	3.55 ± 1.01	3.43 ± 1.20	-3.37
Lateral Hypothalamus	14.83 ± 3.01	22.41 ± 6.99 *	+51.18
Ventral Hypothalamus	17.15 ± 3.94	27.29 ± 13.38	+59.12
Dorsal Thalamus	9.48 ± 1.87	5.23 ± 1.85 *	-44.81
Thalamus	5.90 ± 0.82	3.92 ± 1.62	-33.48
Habenula	3.71 ± 0.72	2.74 ± 0.96	-26.30
Hippocampus	4.47 ± 1.02	3.26 ± 0.96	-27.25
Piriform Cortex	4.59 ± 1.09	2.11 ± 0.75 *	-53.95
Substantia Nigra	14.38 ± 1.36	23.31 ± 10.44	+62.11
Medial Geniculate Nucleus	4.27 ± 0.63	2.87 ± 0.85 *	-32.76
Superior Colliculus	12.94 ± 3.47	7.19 ± 2.03 *	-44.45
Ventral Tegmental Area	18.03 ± 4.21	28.21 ± 13.90	+56.42
Inferior Colliculus	3.40 ± 1.02	2.42 ± 0.30	-28.97
Dorsal Raphe	27.13 ± 5.14	39.91 ± 6.97 *	+47.11
Entorhinal Cortex	7.04 ± 1.53	6.16 ± 1.55	-12.45
Locus Coeruleus	18.42 ± 1.95	28.24 ± 10.15 *	53.30

**Table 6-5. MDMA treatment causes widespread reductions in *in vitro* [<sup>3</sup>H]citalopram binding to SERT. Expressed as ratio region/cerebellum.**

Ten out of 25 structures are significantly different between vehicle- and MDMA-treated animals. Data are mean ± SD for n = 3 - 4 vehicle-, and n = 5 - 6 for MDMA-treated rats. Two-tailed Mann-Whitney U, \*p < 0.05 relative to vehicle group. Relative difference (Rel. Diff.) = <sup>a</sup> (MDMA - vehicle)/(vehicle)\*100 %.

**Chapter 6 - Autoradiographic and micro-SPECT imaging of SERT depletion in rats using the radioligands [<sup>125</sup>I]βCIT and [<sup>125</sup>I]ADAM.**

**[<sup>3</sup>H]WIN 35, 428 autoradiography to label DAT.**

**Levels of nonspecific [<sup>3</sup>H]WIN 35, 428 binding defined in the presence of nomifensine.**

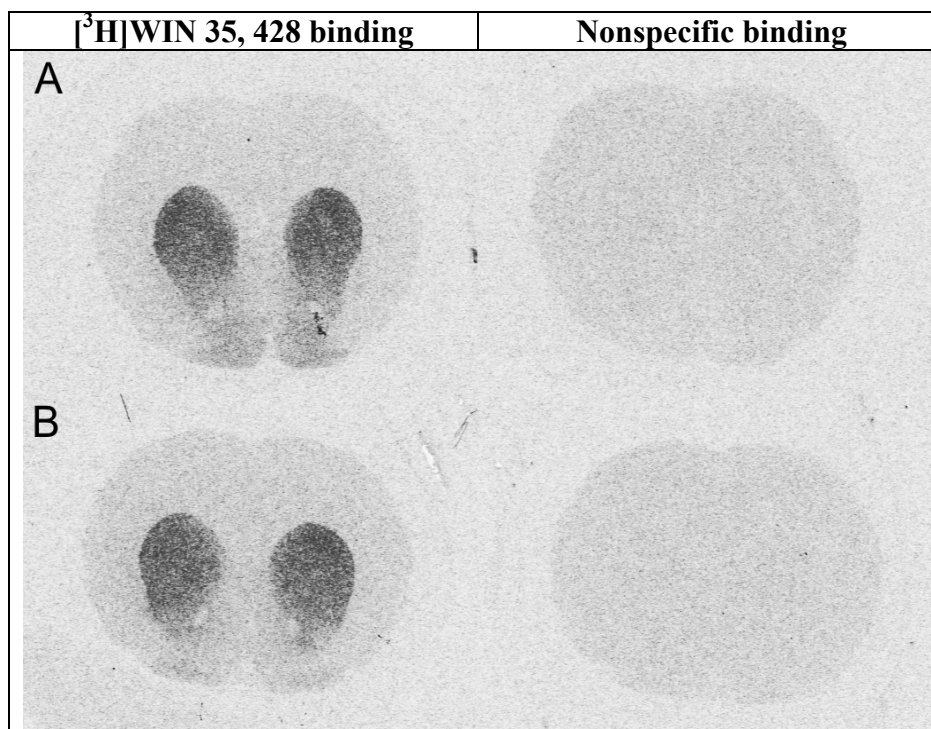


**Fig. 6-16. Nonspecific *in vitro* [<sup>3</sup>H]WIN 35, 428 binding is low.**

Nonspecific binding was addressed using nomifensine to displace [<sup>3</sup>H]WIN 35, 428 from DAT.

Left: representative sections showing total binding to DAT.

Right: representative sections showing nonspecific binding defined by pharmacological blockage of DAT with nomifensine.

A: vehicle-treated representative animal.

B: MDMA-treated representative animal.

Nonspecific binding of [<sup>3</sup>H]WIN 35, 428 was approximately at the level of the cortex, and was comparable between treatment groups.

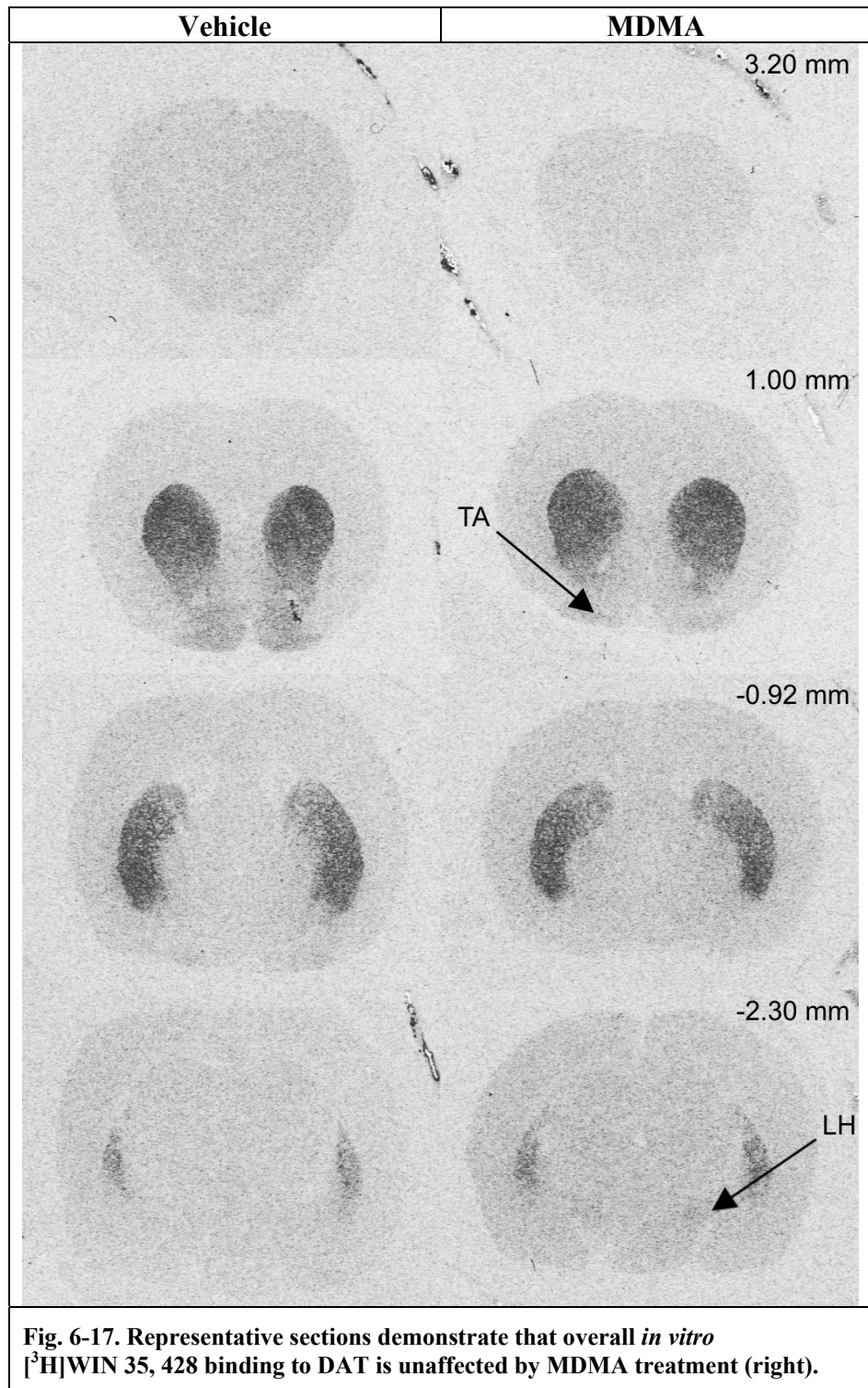
Levels of nonspecific binding of [<sup>3</sup>H]WIN 35, 428 binding in the presence of nomifensine were visually inspected. Representative sections at the level of the caudate-putamen are shown in Fig. 6-16. MDMA treatment did not affect the level of nonspecific [<sup>3</sup>H]WIN 35, 428 binding compared to vehicle administration as the levels being very low in both treatment groups. The density of nonspecific binding sites was comparable to that of total binding in the cerebral cortex in the absence of any displacers. Visual examination could not detect any differences between groups in nonspecific binding.

**Chapter 6 - Autoradiographic and micro-SPECT imaging of SERT depletion in rats using the radioligands [<sup>125</sup>I]βCIT and [<sup>125</sup>I]ADAM.**

**Visual comparison of representative sections of [<sup>3</sup>H]WIN 35, 428 binding in vehicle- and MDMA-treated animals.**

Visual comparison of [<sup>3</sup>H]WIN 35, 428 autoradiograms from vehicle- and MDMA-treated animals revealed generally low DAT densities in the rat brain, with the exception of the caudate-putamen, nucleus accumbens, substantia nigra, ventral tegmental area and the dorsal raphe (Fig. 6-17). Some structures shown in Fig. 6-17, i.e. the tubercle area, substantia nigra, and the locus coeruleus, showed different DAT availability when comparing MDMA- to vehicle-treated animals. This reflects the high variability from animal to animal as shown in Table 6-6.

**Chapter 6 - Autoradiographic and micro-SPECT imaging of SERT depletion in rats using the radioligands [<sup>125</sup>I]βCIT and [<sup>125</sup>I]ADAM.**



**Chapter 6 - Autoradiographic and micro-SPECT imaging of SERT depletion in rats using the radioligands [<sup>125</sup>I]βCIT and [<sup>125</sup>I]ADAM.**

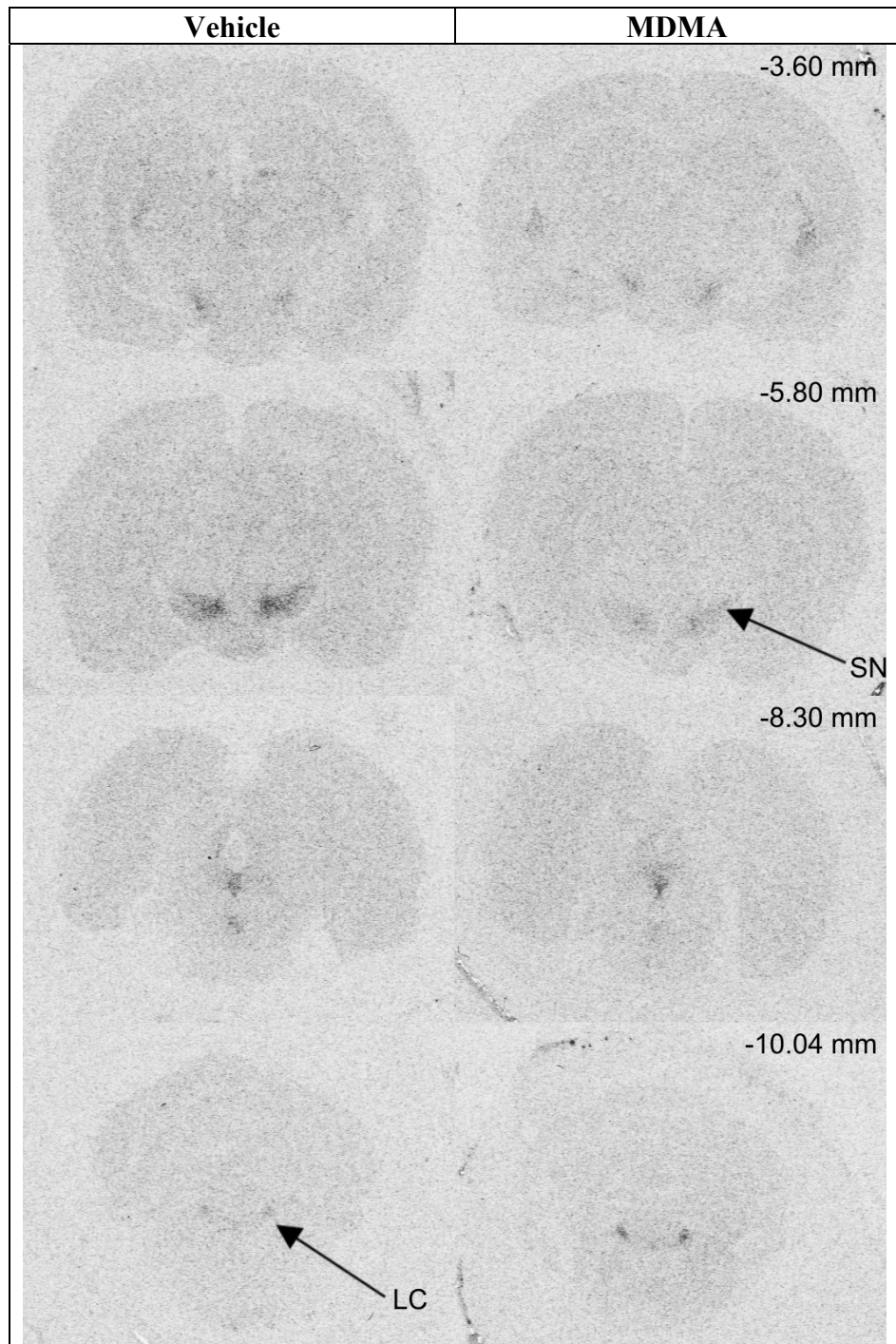


**Fig. 6-17. continued.**

Left: vehicle-, right: MDMA-treated animals. The only region which showed significant differences between vehicle- and MDMA-treated animals is the tubercle area (TA). Arrows highlight differences between groups. LH: lateral hypothalamus; SN: substantia nigra; LC: locus coeruleus. Bregma level is indicated in top right corner.

**Chapter 6 - Autoradiographic and micro-SPECT imaging of SERT depletion in rats using the radioligands [<sup>125</sup>I]βCIT and [<sup>125</sup>I]ADAM.**

**Analysis of [<sup>3</sup>H]WIN 35, 428 binding in vehicle- and MDMA-treated animals.**

Significant differences between vehicle- and MDMA-treated animals were detected only in the tubercle area (Table 6-6). Even though some structures show large percentage differences between the groups, the variability of the [<sup>3</sup>H]WIN 35, 428 binding in regions with low DAT density meant that these were not significant. For example, the thalamus in MDMA-treated animals displayed a DAT reduction of 51 % compared to control animals, however the SD of the mean is just as large as the mean itself.

Structure	Treatment		Rel. Diff. [%] <sup>a</sup>
	Vehicle	MDMA	
Prefrontal Cortex	3.10 ± 1.41	1.86 ± 2.56	-39.97
Anterior Cingulate Cortex	1.83 ± 2.47	2.68 ± 1.51	+46.56
Caudate-Putamen	66.79 ± 15.04	65.08 ± 8.61	-2.56
Septal Area	7.74 ± 6.01	7.40 ± 1.97	-4.37
Nucleus Accumbens	27.07 ± 7.21	26.85 ± 6.59	-0.83
Tubercle Area	22.77 ± 9.17	12.85 ± 2.98 *	-43.58
Globus Pallidus	11.24 ± 2.53	9.30 ± 2.33	-17.28
Retrosplenial Cortex	0.03 ± 0.06	0.05 ± 0.12	+58.76
Lateral Hypothalamus	8.64 ± 4.05	7.30 ± 2.54	-15.51
Ventral Hypothalamus	1.68 ± 1.19	0.84 ± 1.06	-49.90
Dorsal Thalamus	2.84 ± 2.00	3.18 ± 2.58	+12.16
Thalamus	3.70 ± 2.32	1.83 ± 1.71	-50.67
Hippocampus	2.12 ± 1.83	2.91 ± 2.13	+37.24
Piriform Cortex	0.65 ± 0.66	0.84 ± 0.86	+29.93
Substantia Nigra	11.46 ± 2.93	10.68 ± 4.02	-6.83
Medial Geniculate Nucleus	3.13 ± 1.45	3.17 ± 1.61	+1.05
Superior Colliculus	5.45 ± 2.12	2.99 ± 1.07	-45.18
Ventral Tegmental Area	27.40 ± 11.54	25.79 ± 5.71	-5.87
Inferior Colliculus	2.84 ± 2.57	1.53 ± 1.47	-46.28
Dorsal Raphe	26.65 ± 8.73	25.56 ± 5.50	-4.11
Entorhinal Cortex	3.54 ± 2.72	2.02 ± 2.05	-42.98
Locus Coeruleus	16.13 ± 6.98	18.88 ± 7.89	+17.01
Cerebellum	1.27 ± 1.69	0.60 ± 0.48	-52.97

**Table 6-6. Overall *in vitro* [<sup>3</sup>H]WIN 35, 428 binding to DAT is unaffected by MDMA treatment.**

One out of 23 structures is significantly different between vehicle- and MDMA-treated animals.

Data are mean ± SD for n = 4 vehicle-, and n = 4 - 6 for MDMA-treated rats.

Units of measurement are fmol/mg.

Two-tailed Mann-Whitney U, \*p < 0.05 relative to vehicle group.

Relative difference (Rel. Diff.) = <sup>a</sup> (MDMA - vehicle)/(vehicle)\*100 %.

**Chapter 6 - Autoradiographic and micro-SPECT imaging of SERT depletion in rats using the radioligands [<sup>125</sup>I]βCIT and [<sup>125</sup>I]ADAM.**

**[<sup>125</sup>I]βCIT autoradiography - SERT labelling defined in the presence of mazindol.**

**Levels of nonspecific [<sup>125</sup>I]βCIT binding defined in the presence of mazindol and fluoxetine.**

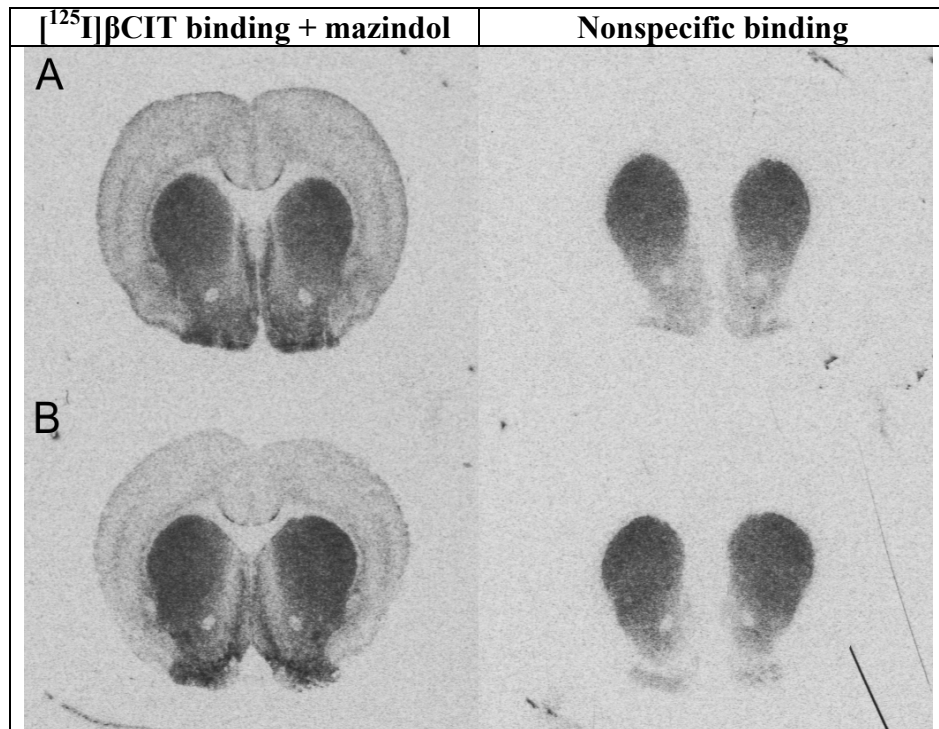


**Fig. 6-18. Nonspecific *in vitro* [<sup>125</sup>I]βCIT binding is low in SERT-rich, but high in DAT-rich regions.**

Nonspecific binding was addressed using mazindol and fluoxetine to displace [<sup>125</sup>I]βCIT from DAT and SERT, respectively.

Left: Total binding to SERT using mazindol to block DAT.

Right: Nonspecific binding defined by pharmacological blockage of DAT with mazindol, and SERT with fluoxetine.

A: vehicle-treated representative animal.

B: MDMA-treated representative animal.

Nonspecific binding was high in DAT-rich structures, i.e. caudate-putamen, nucleus accumbens, and tubercle area. SERT-rich regions, i.e. cortex and septal area appear to have low nonspecific binding.

Nonspecific binding of [<sup>125</sup>I]βCIT was defined in the presence of mazindol and fluoxetine, while specific binding of [<sup>125</sup>I]βCIT to SERT was achieved by blocking the DAT component of the signal with the inclusion of mazindol (Fig. 6-18). MDMA treatment caused loss of [<sup>125</sup>I]βCIT total signal primarily in the cerebral cortex when compared to vehicle-treated control animals (Fig. 6-18, A, left vs. B, left). However no differences in nonspecific binding due to the treatment were observed as assessed by visual inspection (Fig. 6-18, A, right vs. B, right). Structures known to have a high density of DAT showed high nonspecific binding, such as the caudate-putamen, nucleus accumbens, and the

**Chapter 6 - Autoradiographic and micro-SPECT imaging of SERT depletion in rats using the radioligands [<sup>125</sup>I]βCIT and [<sup>125</sup>I]ADAM.**

tubercle area. On the other hand, regions low in DAT and high in SERT displayed low nonspecific binding, e.g. in the cortex and the septal area.

**Visual comparison of representative sections of SERT-specific [<sup>125</sup>I]βCIT binding defined in the presence of mazindol in vehicle- and MDMA-treated animals.**

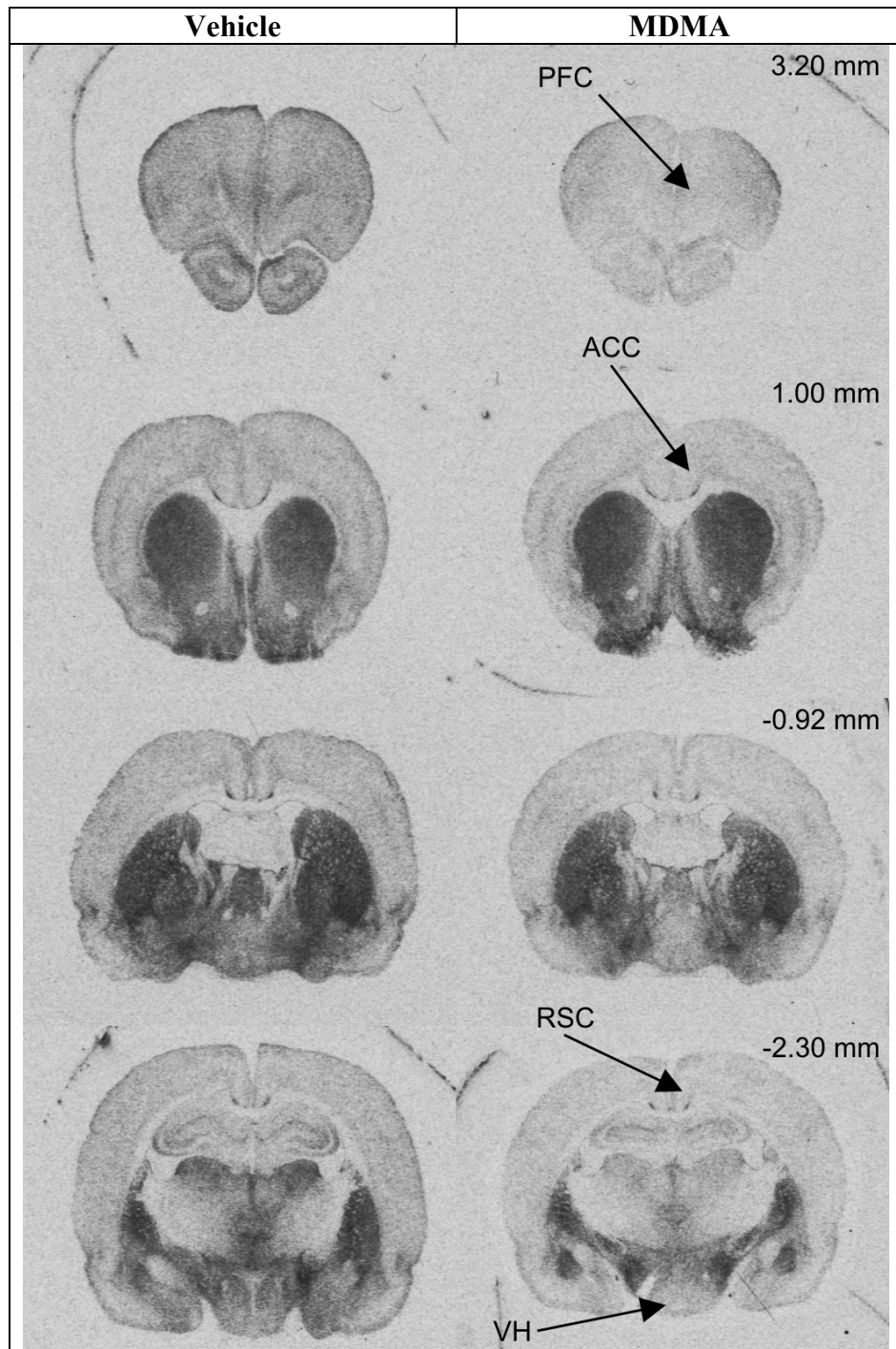


**Fig. 6-19. Representative sections demonstrate that MDMA treatment (right) causes widespread reductions in *in vitro* SERT-specific [<sup>125</sup>I]βCIT binding (in the presence of mazindol).**

**Chapter 6 - Autoradiographic and micro-SPECT imaging of SERT depletion in rats using the radioligands [<sup>125</sup>I]βCIT and [<sup>125</sup>I]ADAM.**

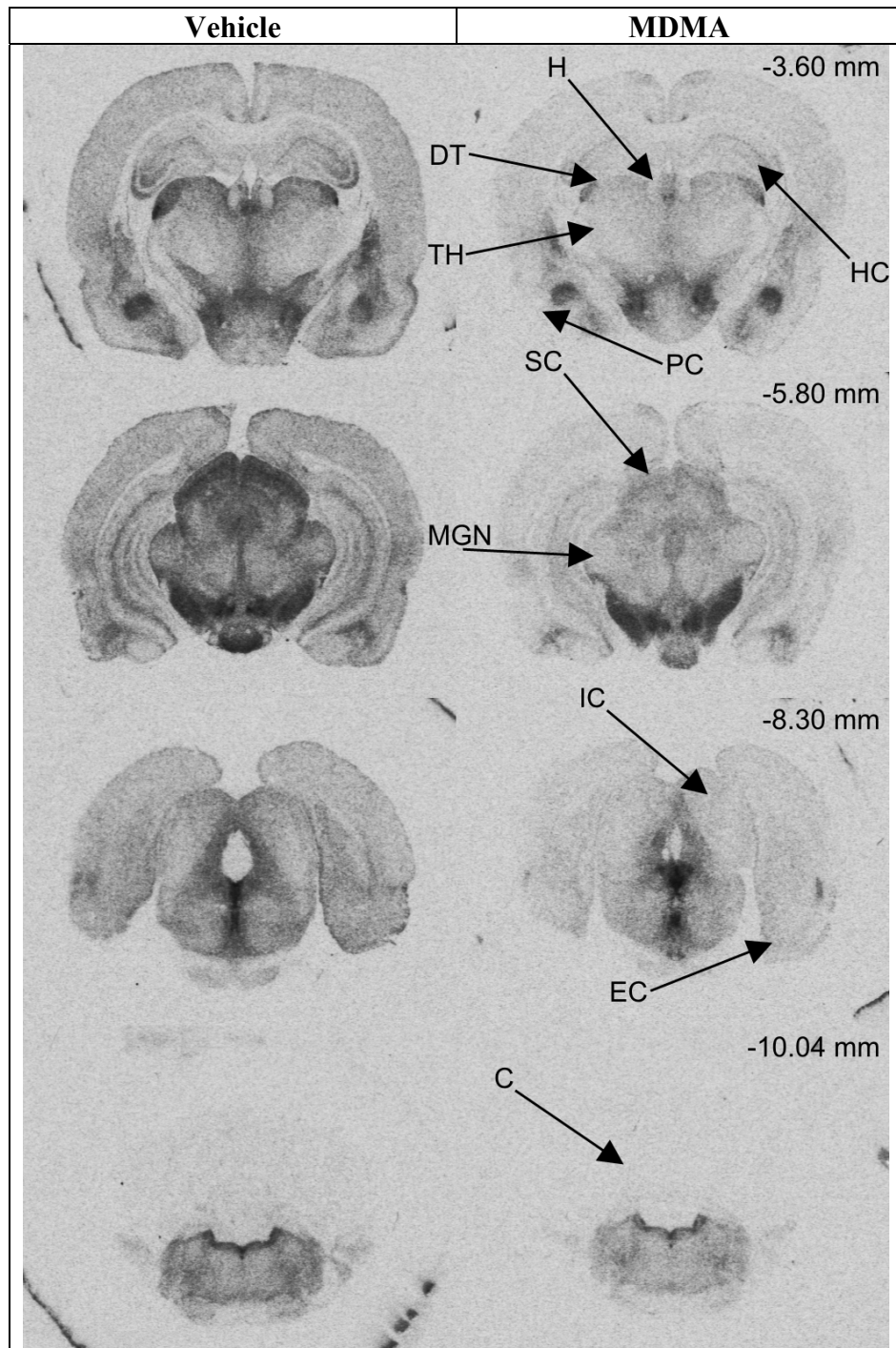


**Fig. 6-19. continued.**

Left: vehicle-, right: MDMA-treated animals. Arrows indicate significant differences. MDMA-treated animals show less [<sup>125</sup>I]βCIT binding in the presence of mazindol in cortical structures (PFC, ACC, RSC, PC, EC); thalamic structures (DT, TH and MGN); ventral hypothalamus (VH); habenula (H); hippocampus (HC); superior and inferior colliculi (SC and IC); but also in the cerebellum (C). PFC: prefrontal cortex; ACC: anterior cingulate cortex; RSC: retrosplenial cortex; PC: piriform cortex; EC: entorhinal cortex; TH: thalamus; DT: dorsal thalamus; MGN: medial geniculate nucleus. Bregma level is indicated in top right corner.

## **Chapter 6 - Autoradiographic and micro-SPECT imaging of SERT depletion in rats using the radioligands [<sup>125</sup>I]βCIT and [<sup>125</sup>I]ADAM.**

[<sup>125</sup>I]βCIT labelling in the presence of mazindol showed strong signal in structures known to be rich in SERT. This was observed in both, vehicle- and MDMA-treated animals, however with clearly decreased signal intensity in the latter group (Fig. 6-19). Cortical regions, including the prefrontal, anterior cingulate, retrosplenial, piriform and entorhinal cortices were reduced due to the SERT-depleting regimen of MDMA treatment. Also the inferior and superior colliculus, and thalamic regions including the dorsal portion and the medial geniculate nucleus displayed MDMA-induced depletion of SERT, as detected by a reduction in [<sup>125</sup>I]βCIT binding, compared to control animals. The cerebellum in vehicle-treated animals showed some degree of [<sup>125</sup>I]βCIT total binding, while in MDMA-treated rats SERT densities are comparable to that of the film background.

### **Analysis of SERT-specific [<sup>125</sup>I]βCIT binding defined in the presence of mazindol in vehicle- and MDMA-treated animals.**

Visually detected changes were confirmed by quantitative autoradiographic analysis (Table 6-7). Twenty six structures were examined, and 14 showed significant effects of MDMA treatment compared to vehicle-treated controls, including cortical structures such as the prefrontal, anterior cingulate, retrosplenial, piriform, and the entorhinal cortex as visually identified in the previous section. The reductions in cortical [<sup>125</sup>I]βCIT binding were in the range of 50 - 70 % in MDMA- relative to vehicle-treated animals.

Thalamic regions showed significant reductions in SERT availability in the range of 50 - 70 % in animals that underwent MDMA treatment compared to vehicle controls. The cerebellum experienced a reduction of 60 %, and the highest degree of SERT depletion was observed in the superior colliculus with more than 70 % loss of [<sup>125</sup>I]βCIT binding in the presence of mazindol. In agreement with [<sup>3</sup>H]citalopram detected number of binding sites (see above) is the finding that the structures, that synthesise monoamines, were mostly unaffected. Only the dorsal raphe showed a non-significant increase of 35 % in SERT availability in SERT-depleted rats compared to vehicle controls.

**Chapter 6 - Autoradiographic and micro-SPECT imaging of SERT depletion in rats using the radioligands [<sup>125</sup>I]βCIT and [<sup>125</sup>I]ADAM.**

Structure	Treatment		Rel. Diff. [%] <sup>a</sup>
	Vehicle	MDMA	
Prefrontal Cortex	0.42 ± 0.12	0.20 ± 0.03 *	-51.49
Anterior Cingulate Cortex	0.28 ± 0.05	0.12 ± 0.03 *	-57.51
Caudate-Putamen	0.29 ± 0.21	0.36 ± 0.06	+23.57
Septal Area	0.47 ± 0.16	0.37 ± 0.13	-22.84
Nucleus Accumbens	0.48 ± 0.06	0.39 ± 0.08	-18.85
Tubercle Area	1.12 ± 0.27	0.83 ± 0.22	-26.37
Globus Pallidus	1.34 ± 0.04	1.03 ± 0.12	-23.22
Retrosplenial Cortex	0.24 ± 0.04	0.10 ± 0.02 *	-58.75
Basolateral Amygdala	1.18 ± 0.11	0.89 ± 0.21	-24.35
Central Amygdaloid Nucleus	0.31 ± 0.12	0.19 ± 0.05	-39.81
Lateral Hypothalamus	1.57 ± 0.20	1.47 ± 0.16	-6.37
Ventral Hypothalamus	0.48 ± 0.09	0.25 ± 0.05 *	-48.61
Dorsal Thalamus	0.86 ± 0.04	0.29 ± 0.09 *	-66.82
Thalamus	0.54 ± 0.05	0.25 ± 0.05 *	-53.62
Habenula	0.40 ± 0.04	0.19 ± 0.07 *	-53.24
Hippocampus	0.29 ± 0.03	0.13 ± 0.04 *	-55.90
Piriform Cortex	0.27 ± 0.01	0.08 ± 0.03 *	-70.65
Substantia Nigra	1.94 ± 0.25	1.78 ± 0.18	-8.63
Medial Geniculate Nucleus	0.54 ± 0.07	0.20 ± 0.06 *	-62.55
Superior Colliculus	1.23 ± 0.06	0.34 ± 0.13 *	-72.73
Ventral Tegmental Area	2.40 ± 0.09	2.19 ± 0.31	-8.84
Inferior Colliculus	0.44 ± 0.12	0.13 ± 0.04 *	-69.52
Dorsal Raphe	2.64 ± 0.72	3.56 ± 0.62	+35.12
Entorhinal Cortex	0.46 ± 0.07	0.19 ± 0.05 *	-58.69
Locus Coeruleus	1.22 ± 0.29	1.19 ± 0.07	-2.20
Cerebellum	0.05 ± 0.01	0.02 ± 0.00 *	-61.42

**Table 6-7. MDMA treatment causes widespread reductions in *in vitro* SERT-specific [<sup>125</sup>I]βCIT binding.**

SERT-specific [<sup>125</sup>I]βCIT binding was defined in the presence of mazindol. Fourteen out of 26 structures are significantly different between vehicle- and MDMA-treated animals. Data are mean ± SD for n = 4 vehicle-, and n = 6 for MDMA-treated rats. Units of measurement are fmol/mg. Two-tailed Mann-Whitney U, \*p < 0.05 relative to vehicle group. Relative difference (Rel. Diff.) = <sup>a</sup> (MDMA - vehicle)/(vehicle)\*100 %.

Scatter plots of [<sup>3</sup>H]citalopram and [<sup>125</sup>I]βCIT binding (defined in the presence of mazindol to suppress the DAT signal) are shown in Fig. 6-20. The plots illustrate the association between the two methods for imaging SERT in animals with normal, and abnormal SERT densities. Calculation of the Spearman's rank order correlation coefficient for vehicle- and MDMA-treated animals showed high correlation between these two ligands.

**Chapter 6 - Autoradiographic and micro-SPECT imaging of SERT depletion in rats using the radioligands [<sup>125</sup>I]βCIT and [<sup>125</sup>I]ADAM.**

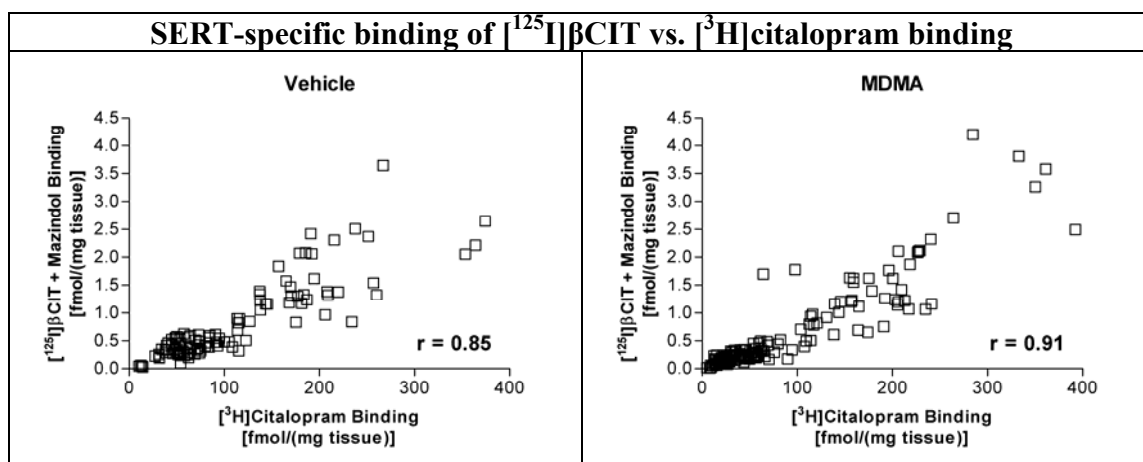


**Fig. 6-20. *In vitro* SERT-specific [<sup>125</sup>I]βCIT binding correlates with [<sup>3</sup>H]citalopram binding.**

[<sup>125</sup>I]βCIT binding to SERT was defined in the presence of mazindol. Each structure for each individual animal measured by [<sup>125</sup>I]βCIT was plotted against the equivalent data obtained from [<sup>3</sup>H]citalopram autoradiography. Units of measurement are fmol/mg. Spearman's rank order correlation coefficient (r) is given in the right bottom corner of the graphs. Left graph shows the data for the vehicle-, and right graph shows that of the MDMA-treated group. In both groups there is a high degree of correlation between specific [<sup>125</sup>I]βCIT binding to SERT and [<sup>3</sup>H]citalopram binding sites.

**[<sup>125</sup>I]βCIT autoradiography - DAT labelling defined in the presence of fluoxetine.**

**Levels of nonspecific [<sup>125</sup>I]βCIT binding defined in the presence of mazindol and fluoxetine.**

Note that the sections for the determination of nonspecific binding in DAT-specific [<sup>125</sup>I]βCIT binding are identical to those used in the determination of nonspecific binding in SERT-specific [<sup>125</sup>I]βCIT binding.

Nonspecific binding of [<sup>125</sup>I]βCIT was defined in the presence of mazindol and fluoxetine, while specific binding of [<sup>125</sup>I]βCIT to DAT was achieved by blocking the SERT component of the signal with the inclusion of fluoxetine (Fig. 6-21). MDMA treatment caused only a subtle loss of [<sup>125</sup>I]βCIT total signal in the cerebral cortex when compared to vehicle-treated control animals (Fig. 6-21, A, left vs. B, left). However no differences in nonspecific binding due to the treatment were observed as assessed by visual inspection (Fig. 6-21, A, right vs. B, right). Structures known to have a high density of DAT showed high nonspecific binding, such as the caudate-putamen, nucleus accumbens, and the tubercle area. On the other hand, regions low in DAT and high in SERT displayed low nonspecific binding, e.g. in the cortex and in the septal area.

**Chapter 6 - Autoradiographic and micro-SPECT imaging of SERT depletion in rats using the radioligands [<sup>125</sup>I]βCIT and [<sup>125</sup>I]ADAM.**

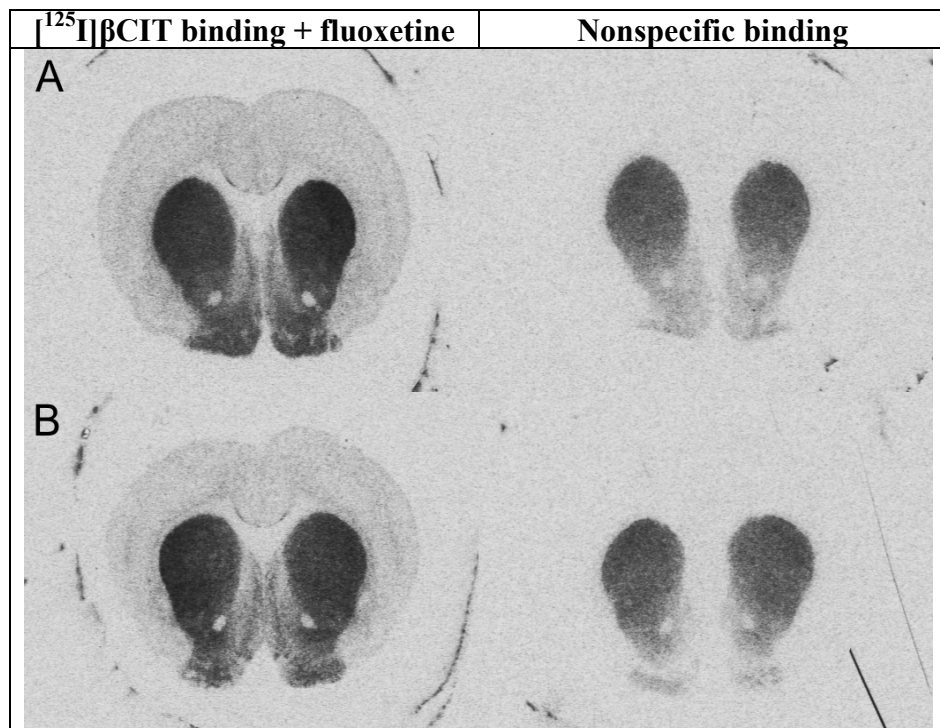


**Fig. 6-21. Nonspecific *in vitro* [<sup>125</sup>I]βCIT binding is low in SERT-rich, but high in DAT-rich regions.**

Nonspecific binding was addressed using mazindol and fluoxetine to displace [<sup>125</sup>I]βCIT from DAT and SERT, respectively.

Left: Total binding to DAT using fluoxetine to block SERT.

Right: Nonspecific binding defined by pharmacological blockage of DAT with mazindol, and SERT with fluoxetine.

A: vehicle-treated representative animal.

B: MDMA-treated representative animal.

Nonspecific binding was high in DAT-rich structures, i.e. caudate-putamen, nucleus accumbens, and tubercle area. SERT-rich regions, i.e. cortex and septal area appear to have low nonspecific binding.

**Visual comparison of representative sections of DAT-specific [<sup>125</sup>I]βCIT binding defined in the presence of fluoxetine in vehicle- and MDMA-treated animals.**

Visual inspection showed [<sup>125</sup>I]βCIT binding in the presence of fluoxetine to be high in regions known to have high densities of DAT, including the caudate-putamen, nucleus accumbens, tubercle area, substantia nigra and the ventral tegmental area in both, vehicle- (left) and MDMA-treated (right) animals (Fig. 6-22). Structures such as the globus pallidus, lateral hypothalamus, and the dorsal thalamus appear to be moderately rich in DAT as detected by [<sup>125</sup>I]βCIT. In addition, the basolateral amygdala, superior colliculus, dorsal raphe, and the locus coeruleus display a high DAT density. Visually it can be seen that MDMA-treated animals have lower binding of [<sup>125</sup>I]βCIT in cortical regions, thalamic substructures, hippocampus, and the inferior and superior colliculi.

**Chapter 6 - Autoradiographic and micro-SPECT imaging of SERT depletion in rats using the radioligands [<sup>125</sup>I]βCIT and [<sup>125</sup>I]ADAM.**

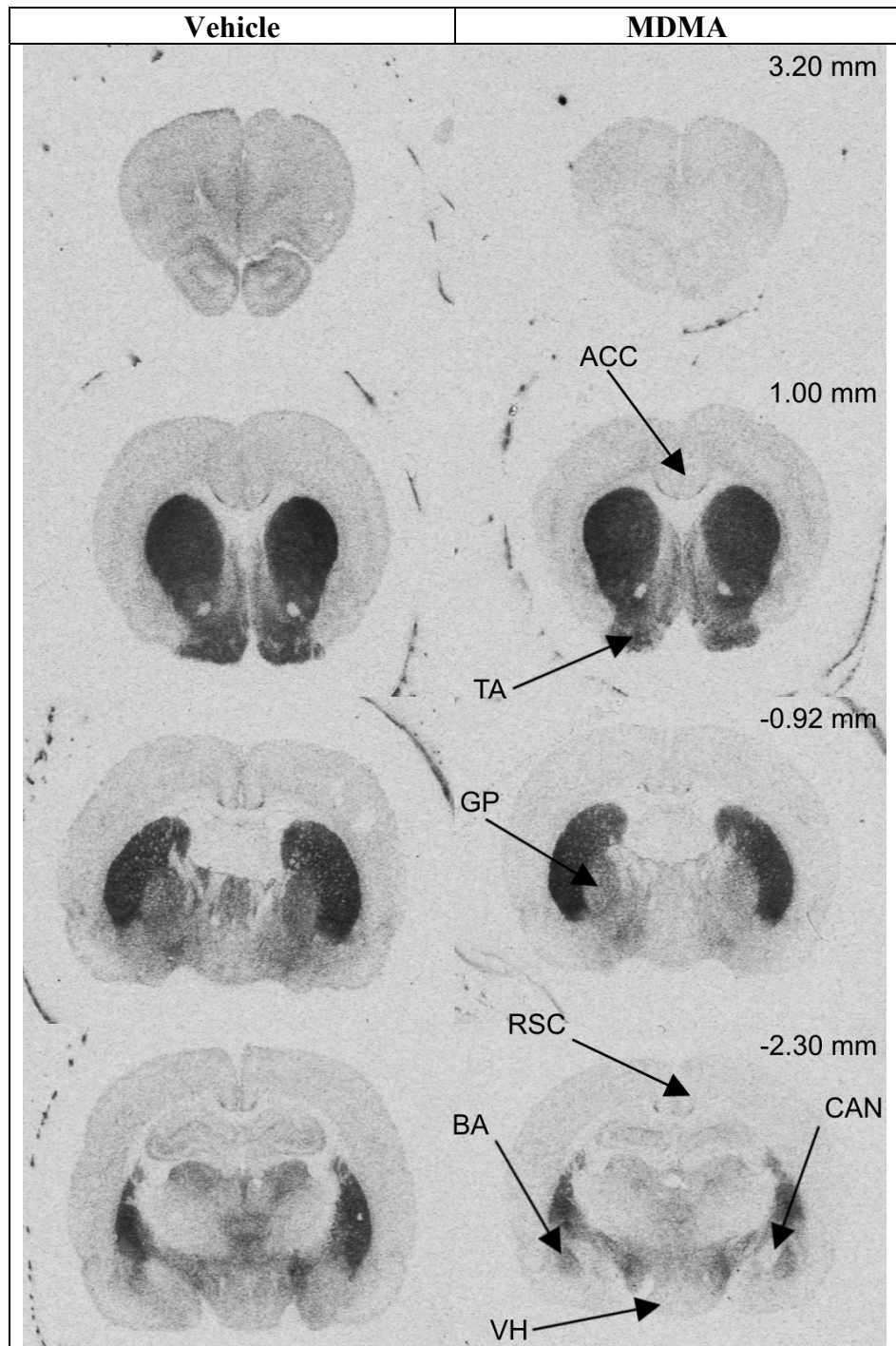


**Fig. 6-22. Representative sections demonstrate that MDMA treatment (right) causes widespread reductions in *in vitro* DAT-specific [<sup>125</sup>I]βCIT binding (in the presence of fluoxetine).**

**Chapter 6 - Autoradiographic and micro-SPECT imaging of SERT depletion in rats using the radioligands [<sup>125</sup>I]βCIT and [<sup>125</sup>I]ADAM.**

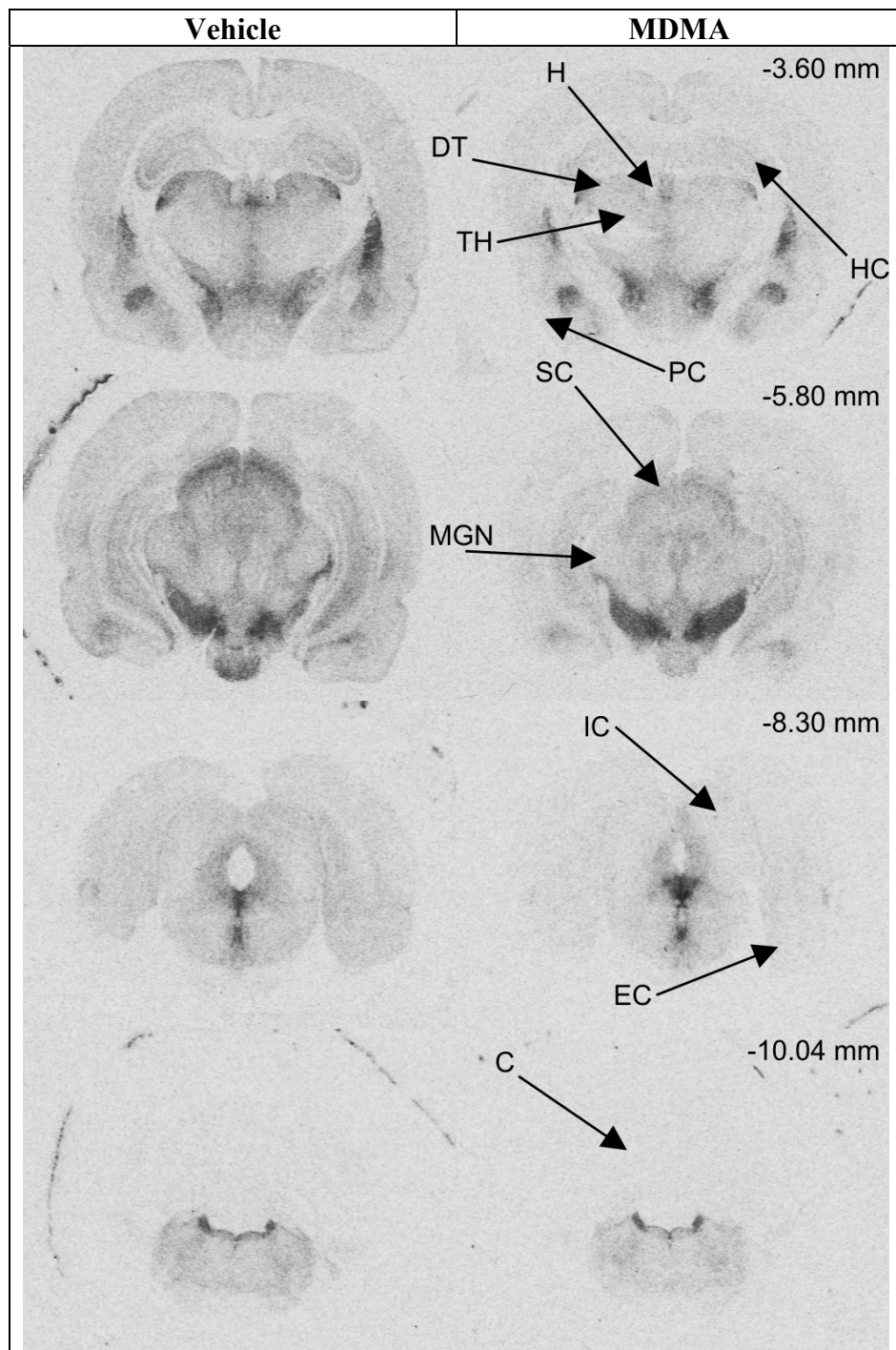


**Fig. 6-22. continued.**

Left: vehicle-, right: MDMA-treated animals. Arrows indicate significant differences between MDMA- and vehicle-treated groups. MDMA-treated animals show less [<sup>125</sup>I]βCIT binding in the presence of fluoxetine in cortical structures (ACC, RSC, PC, EC); tubercle area (TA); globus pallidus (GP); amygdala substructures (BA, CAN); thalamic structures (DT, TH and MGN); ventral hypothalamus (VH); habenula (H); hippocampus (HC); superior and inferior colliculi (SC and IC); but also in the cerebellum (C). ACC: anterior cingulate cortex; RSC: retrosplenial cortex; PC: piriform cortex; EC: entorhinal cortex; TH: thalamus; DT: dorsal thalamus; MGN: medial geniculate nucleus; BA: basolateral amygdala; CAN: central amygdaloid nucleus. Bregma level is indicated in top right corner.

## **Chapter 6 - Autoradiographic and micro-SPECT imaging of SERT depletion in rats using the radioligands [<sup>125</sup>I]βCIT and [<sup>125</sup>I]ADAM.**

### **Analysis of DAT-specific [<sup>125</sup>I]βCIT binding defined in the presence of fluoxetine in vehicle- and MDMA-treated animals.**

Out of the 26 structures measured, 17 were significantly reduced in MDMA-treated animals compared to controls using [<sup>125</sup>I]βCIT (in the presence of fluoxetine, Table 6-8). Cortical regions were reduced by 42 % for the retrosplenial cortex and 68 % for the entorhinal cortex in MDMA-treated animals. Additionally, MDMA treatment caused a reduction of 63 % and 71 % in the superior and inferior colliculus, respectively. Thalamic structures, including the dorsal and medial geniculate nucleus, as well as the whole thalamus, were reduced by between 48 % - 61 %. The results show that there was substantial impairment of dopamine reuptake in MDMA-treated rats as measured by [<sup>125</sup>I]βCIT binding in the presence of fluoxetine. Interestingly as with the detection of SERT by [<sup>125</sup>I]βCIT binding in the presence of mazindol a significant reduction in binding was detected in the cerebellum. In comparison to the more specific radioligand for DAT, [<sup>3</sup>H]WIN 35, 428 (53 %), a reduction of the same magnitude was observed in the cerebellum (57 %) which supports the use of [<sup>125</sup>I]βCIT binding in the presence of fluoxetine to label DAT.

**Chapter 6 - Autoradiographic and micro-SPECT imaging of SERT depletion in rats using the radioligands [<sup>125</sup>I]βCIT and [<sup>125</sup>I]ADAM.**

Structure	Treatment		Rel. Diff. [%] <sup>a</sup>
	Vehicle	MDMA	
Prefrontal Cortex	0.67 ± 0.27	0.46 ± 0.08	-30.93
Anterior Cingulate Cortex	0.56 ± 0.12	0.34 ± 0.06 *	-38.82
Caudate-Putamen	3.59 ± 0.39	3.73 ± 0.40	+3.89
Septal Area	0.94 ± 0.34	0.91 ± 0.24	-3.64
Nucleus Accumbens	2.05 ± 0.31	1.96 ± 0.15	-4.15
Tubercle Area	2.45 ± 0.24	2.02 ± 0.28 *	-17.36
Globus Pallidus	1.78 ± 0.17	1.50 ± 0.16 *	-15.89
Retrosplenial Cortex	0.30 ± 0.01	0.18 ± 0.05 *	-41.64
Basolateral Amygdala	1.21 ± 0.11	0.94 ± 0.22 *	-22.40
Central Amygdaloid Nucleus	0.44 ± 0.08	0.32 ± 0.06 *	-26.80
Lateral Hypothalamus	1.87 ± 0.21	1.82 ± 0.48	-2.96
Ventral Hypothalamus	0.45 ± 0.04	0.28 ± 0.09 *	-39.09
Dorsal Thalamus	0.98 ± 0.18	0.38 ± 0.12 *	-61.30
Thalamus	0.66 ± 0.11	0.34 ± 0.08 *	-48.21
Habenula	0.54 ± 0.05	0.29 ± 0.08 *	-46.08
Hippocampus	0.37 ± 0.06	0.21 ± 0.06 *	-43.62
Piriform Cortex	0.27 ± 0.01	0.14 ± 0.03 *	-48.56
Substantia Nigra	2.20 ± 0.23	2.06 ± 0.30	-6.46
Medial Geniculate Nucleus	0.65 ± 0.10	0.31 ± 0.09 *	-52.56
Superior Colliculus	1.24 ± 0.09	0.46 ± 0.17 *	-62.60
Ventral Tegmental Area	3.50 ± 0.31	3.47 ± 0.65	-0.79
Inferior Colliculus	0.42 ± 0.09	0.12 ± 0.08 *	-71.32
Dorsal Raphe	3.14 ± 0.59	3.47 ± 1.17	+10.68
Entorhinal Cortex	0.41 ± 0.10	0.13 ± 0.09 *	-67.52
Locus Coeruleus	2.15 ± 0.31	1.82 ± 0.30	-15.41
Cerebellum	0.06 ± 0.01	0.03 ± 0.02 *	-56.62

**Table 6-8. MDMA treatment causes widespread reductions in *in vitro* DAT-specific [<sup>125</sup>I]βCIT binding.**

DAT-specific [<sup>125</sup>I]βCIT binding was defined in the presence of fluoxetine.

Seventeen out of 26 structures are significantly different between vehicle- and MDMA-treated animals.

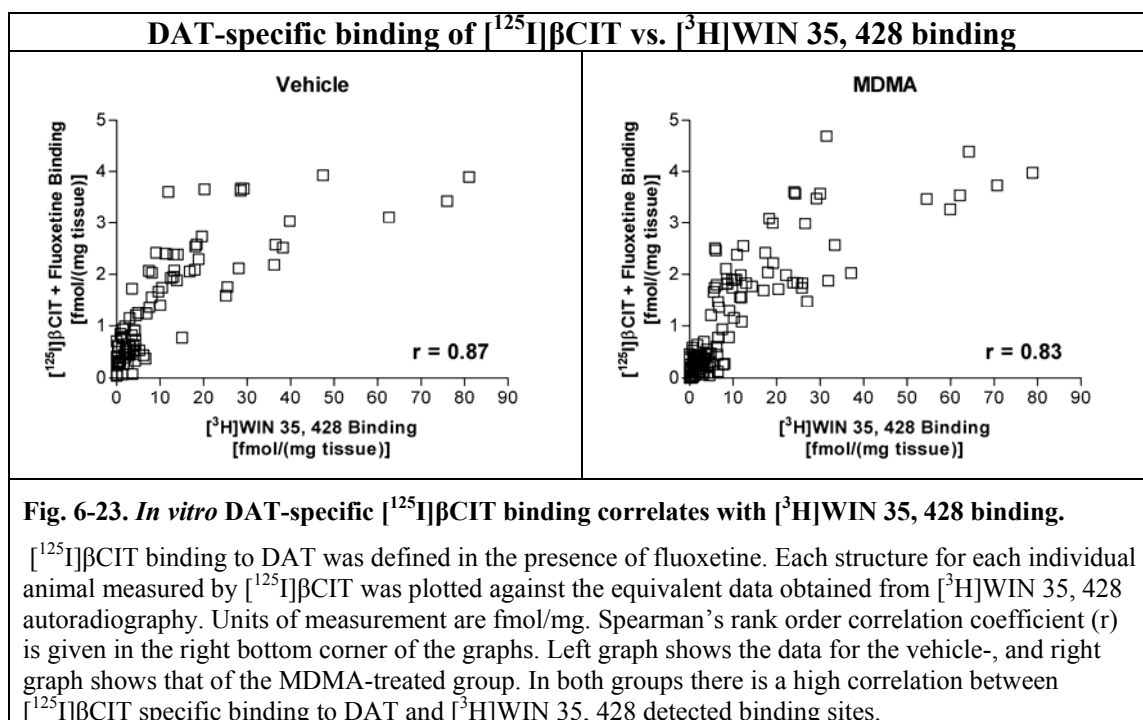
Data are mean ± SD for n = 4 vehicle-, and n = 6 for MDMA-treated rats.

Units of measurement are fmol/mg.

Two-tailed Mann-Whitney U, \*p < 0.05 relative to vehicle group.

Relative difference (Rel. Diff.) = <sup>a</sup> (MDMA - vehicle)/(vehicle)\*100 %.

**Chapter 6 - Autoradiographic and micro-SPECT imaging of SERT depletion in rats using the radioligands [<sup>125</sup>I]βCIT and [<sup>125</sup>I]ADAM.**



Scatter plots of [<sup>3</sup>H]WIN 35, 428 versus [<sup>125</sup>I]βCIT (in the presence of fluoxetine) show the association between the two autoradiographic measures of DAT density in both control and MDMA-treated rats (Fig. 6-23). Calculation of the Spearman's rank order correlation coefficient for vehicle- and MDMA-treated animals showed high degree of correlation between the two ligands.

**[<sup>125</sup>I]βCIT autoradiography defined in the absence of any displacers.**

**Visual comparison of representative sections [<sup>125</sup>I]βCIT binding defined in the absence of any displacers in vehicle- and MDMA-treated animals.**

In order to compare *in vitro* binding of [<sup>125</sup>I]βCIT to *ex vivo* autoradiograms obtained from animals that underwent SPECT, slides were incubated with [<sup>125</sup>I]βCIT in the absence of any displacers. Representative sections of vehicle- and MDMA-treated animals obtained from *in vitro* autoradiography are shown in Fig. 6-24. Arrows indicate significant differences between vehicle- and MDMA-treated animals (see also Table 6-9). By visual assessment of the images it can be seen that the cortex, the thalamus, superior and inferior colliculi, and the cerebellum show loss of [<sup>125</sup>I]βCIT binding in MDMA-treated animals.

Chapter 6 - Autoradiographic and micro-SPECT imaging of SERT depletion in rats using the radioligands [ $^{125}$ I] $\beta$ CIT and [ $^{125}$ I]ADAM.

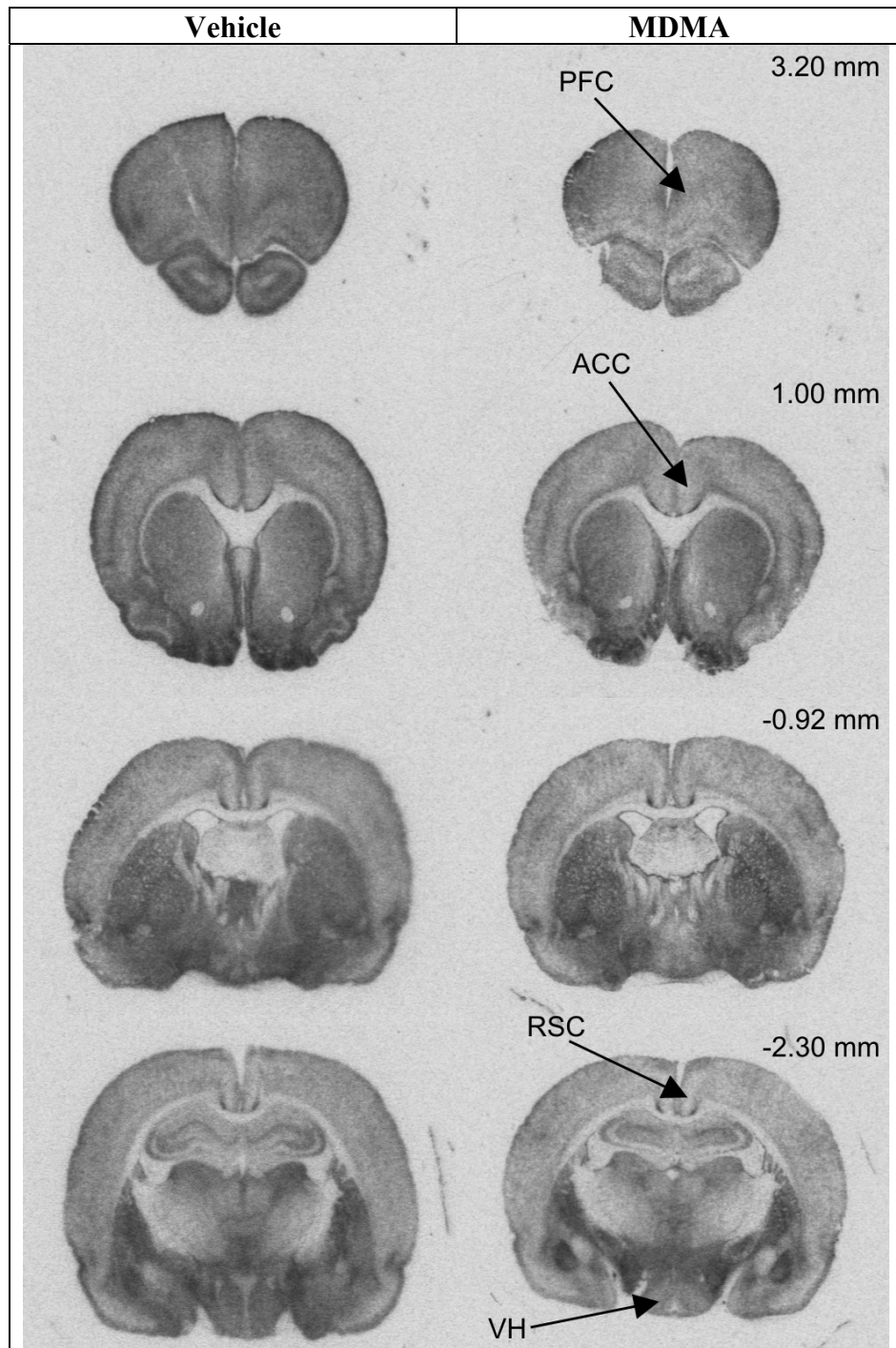
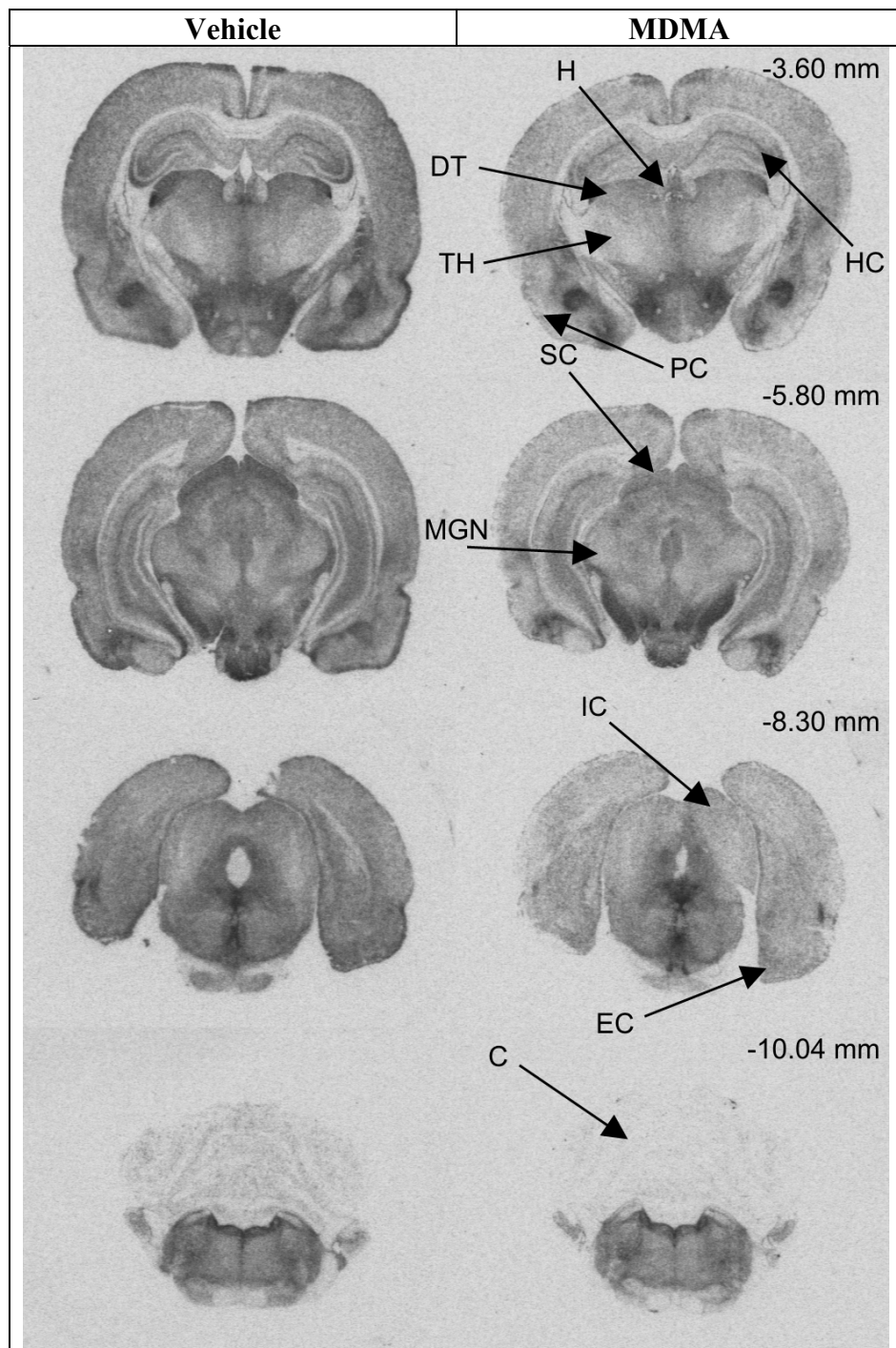


Fig. 6-24. Representative sections demonstrate that MDMA treatment (right) causes widespread reductions in *in vitro* [ $^{125}$ I] $\beta$ CIT binding (in the absence of any displacers).

**Chapter 6 - Autoradiographic and micro-SPECT imaging of SERT depletion in rats using the radioligands [<sup>125</sup>I]βCIT and [<sup>125</sup>I]ADAM.**



**Fig. 6-24. continued.**

Left: vehicle-, right: MDMA-treated animals. Arrows indicate significant differences. MDMA-treated animals show less [<sup>125</sup>I]βCIT binding in cortical structures (PFC, ACC, RSC, PC, EC), thalamic structures (DT, TH and MGN); ventral hypothalamus (VH); habenula (H); hippocampus (HC); superior and inferior colliculi (SC and IC), but also in the cerebellum (C). PFC: prefrontal cortex; ACC: anterior cingulate cortex; RSC: retrosplenial cortex; PC: piriform cortex; EC: entorhinal cortex; TH: thalamus; DT: dorsal thalamus; MGN: medial geniculate nucleus. Bregma level is indicated in top right corner.

## **Chapter 6 - Autoradiographic and micro-SPECT imaging of SERT depletion in rats using the radioligands [<sup>125</sup>I]βCIT and [<sup>125</sup>I]ADAM.**

### **Analysis of [<sup>125</sup>I]βCIT binding defined in the absence of any displacers in vehicle- and MDMA-treated animals.**

All cortical structures investigated show significant reductions in [<sup>125</sup>I]βCIT binding in MDMA-treated animals, with the prefrontal cortex being the least affected (33 %), and the piriform cortex the most vulnerable cortical region (65 %). In addition, the superior and inferior colliculi are significantly reduced by 58 % and 62 %, respectively, when comparing vehicle control rats to rats which underwent a SERT-depleting regimen of MDMA. Of particular interest are the caudate-putamen, thalamus, and the cerebellum as these structures can be detected in *in vivo* SPECT imaging in rats using [<sup>125</sup>I]βCIT as ligand. The binding of [<sup>125</sup>I]βCIT in the thalamus is significantly reduced by 41 %, whereas binding in the caudate-putamen is not affected by MDMA treatment. Note also the substantial decrease in [<sup>125</sup>I]βCIT binding in the cerebellum of MDMA-treated animals, which shows a difference relative to the vehicle group of 58 %.

Unlike quantitative autoradiography, the data obtained from SPECT images is not calculated relative to a range of standards with known amounts of radioactivity. No standards were available for the *in vivo* SPECT experiment. Therefore in many studies a reference region is selected to account for differences between animals in the amount of radioligand administered and differences in delivery to the brain, which is potentially affected by the treatment being studied. In studies of SERT the cerebellum is often selected as the reference region because it contains low densities of SERT. Activity in ROIs is then presented as a ratio of that in the cerebellum of the same animal. In Table 6-10, the data from Table 6-9 was expressed as a ratio of the ROI to the cerebellum in order to assess the effect of normalisation to the cerebellum, and to compare these data more directly to the *in vivo* SPECT and *ex vivo* autoradiography data.

**Chapter 6 - Autoradiographic and micro-SPECT imaging of SERT depletion in rats using the radioligands [<sup>125</sup>I]βCIT and [<sup>125</sup>I]ADAM.**

Structure	Treatment		Rel. Diff. [%] <sup>a</sup>
	Vehicle	MDMA	
Prefrontal Cortex	4.13 ± 0.36	2.75 ± 0.33 *	-33.39
Anterior Cingulate Cortex	3.23 ± 0.60	1.64 ± 0.27 *	-49.08
Caudate-Putamen	5.13 ± 0.42	5.26 ± 0.25	+2.62
Septal Area	4.46 ± 0.80	4.77 ± 0.74	+7.03
Nucleus Accumbens	4.59 ± 0.45	4.15 ± 0.41	-9.59
Tubercle Area	12.67 ± 0.97	11.27 ± 0.90	-11.06
Globus Pallidus	7.26 ± 0.64	6.96 ± 0.42	-4.10
Retrosplenial Cortex	2.46 ± 0.42	1.37 ± 0.22 *	-44.48
Basolateral Amygdala	9.74 ± 0.88	9.31 ± 1.54	-4.41
Central Amygdaloid Nucleus	1.80 ± 0.40	1.94 ± 0.63	+7.70
Lateral Hypothalamus	10.98 ± 0.68	11.33 ± 0.58	+3.20
Ventral Hypothalamus	5.33 ± 0.55	3.50 ± 0.83 *	-34.28
Dorsal Thalamus	5.66 ± 0.25	2.75 ± 0.73 *	-51.33
Thalamus	3.54 ± 0.43	2.10 ± 0.38 *	-40.62
Habenula	2.49 ± 0.41	1.77 ± 0.47 *	-28.67
Hippocampus	2.74 ± 0.11	1.57 ± 0.40 *	-42.56
Piriform Cortex	3.56 ± 0.51	1.26 ± 0.32 *	-64.64
Substantia Nigra	10.25 ± 1.28	10.97 ± 0.64	+7.04
Medial Geniculate Nucleus	3.10 ± 0.34	1.61 ± 0.45 *	-47.99
Superior Colliculus	7.60 ± 0.22	3.20 ± 0.97 *	-57.89
Ventral Tegmental Area	11.41 ± 0.59	10.99 ± 0.69	-3.67
Inferior Colliculus	3.41 ± 0.74	1.31 ± 0.32 *	-61.55
Dorsal Raphe	14.10 ± 1.28	14.37 ± 1.21	+1.92
Entorhinal Cortex	4.75 ± 0.56	1.85 ± 0.48 *	-61.06
Locus Coeruleus	11.54 ± 0.98	10.26 ± 1.69	-11.03
Cerebellum	0.67 ± 0.02	0.29 ± 0.06 *	-57.68

**Table 6-9. MDMA treatment causes widespread reductions in *in vitro* [<sup>125</sup>I]βCIT binding.**

[<sup>125</sup>I]βCIT binding was defined in the absence of any displacers.

Fourteen out of 26 structures show significant reductions [<sup>125</sup>I]βCIT binding.

Data are mean ± SD for n = 4 in vehicle-, and n = 6 in MDMA-treated group.

Units of measurement are fmol/mg.

Two-tailed Mann-Whitney U, \*p < 0.05 relative to vehicle group.

Relative difference (Rel. Diff.) = <sup>a</sup> (MDMA - vehicle)/(vehicle)\*100 %.

Interestingly, all the high uptake sites, i.e. regions that synthesise monoamines such as the substantia nigra, the ventral tegmental area, the dorsal raphe and the locus coeruleus are significantly different in MDMA-treated animals compared to controls when data was normalised to the cerebellum. In addition, the caudate-putamen, which shows no difference between vehicle- and MDMA-treated groups when SERT is measured using [<sup>3</sup>H]citalopram, shows a significant group difference in [<sup>125</sup>I]βCIT binding. The normalised

**Chapter 6 - Autoradiographic and micro-SPECT imaging of SERT depletion in rats using the radioligands [<sup>125</sup>I]βCIT and [<sup>125</sup>I]ADAM.**

data in these regions therefore provide different results compared to the data when they were expressed relative to [<sup>125</sup>I]micro-scales.

Structure	Treatment		Rel. Diff. [%] <sup>a</sup>
	Vehicle	MDMA	
Prefrontal Cortex	6.14 ± 0.67	9.98 ± 2.29 *	+62.54
Anterior Cingulate Cortex	4.80 ± 1.01	5.85 ± 0.89	+21.77
Caudate-Putamen	7.62 ± 0.78	19.15 ± 4.07 *	+151.25
Septal Area	6.62 ± 1.17	17.14 ± 3.63 *	+159.00
Nucleus Accumbens	6.81 ± 0.75	14.99 ± 2.93 *	+120.05
Tubercle Area	18.80 ± 1.57	40.60 ± 6.67 *	+115.93
Globus Pallidus	10.76 ± 0.82	25.42 ± 6.12 *	+136.31
Retrosplenial Cortex	3.66 ± 0.71	4.94 ± 1.20 *	+34.93
Basolateral Amygdala	14.31 ± 1.24	33.40 ± 6.10 *	+133.30
Central Amygdaloid Nucleus	2.94 ± 0.33	7.13 ± 3.24 *	+142.24
Lateral Hypothalamus	16.29 ± 1.03	41.18 ± 8.50 *	+152.75
Ventral Hypothalamus	7.90 ± 0.71	12.73 ± 4.13 *	+61.02
Dorsal Thalamus	8.40 ± 0.37	9.70 ± 1.72	+15.55
Thalamus	5.24 ± 0.58	7.51 ± 1.39 *	+43.38
Habenula	3.69 ± 0.64	6.54 ± 2.62	+77.16
Hippocampus	4.06 ± 0.18	5.53 ± 0.86 *	+36.33
Piriform Cortex	5.29 ± 0.80	4.45 ± 0.80	-15.85
Substantia Nigra	15.21 ± 1.90	39.83 ± 8.13 *	+161.95
Medial Geniculate Nucleus	4.61 ± 0.60	5.67 ± 1.01	+22.86
Superior Colliculus	11.27 ± 0.48	11.18 ± 2.33	-0.88
Ventral Tegmental Area	16.93 ± 0.83	40.20 ± 9.64 *	+137.51
Inferior Colliculus	5.07 ± 1.10	4.62 ± 0.63	-8.80
Dorsal Raphe	20.92 ± 1.85	52.39 ± 12.61 *	+150.46
Entorhinal Cortex	7.06 ± 0.95	6.61 ± 1.89	-6.38
Locus Coeruleus	17.12 ± 1.52	38.03 ± 12.83 *	+122.18

**Table 6-10. MDMA treatment causes widespread reductions in *in vitro* [<sup>125</sup>I]βCIT binding. Expressed as ratio region/cerebellum.**

[<sup>125</sup>I]βCIT binding was defined in the absence of any displacers.  
 Seventeen out of 25 structures are significantly different in MDMA-treated animals.  
 Data are mean ± SD for n = 4 in vehicle-, and n = 6 in MDMA-treated group.  
 Two-tailed Mann-Whitney U, \*p < 0.05 relative to vehicle group.  
 Relative difference (Rel. Diff.) = <sup>a</sup> (MDMA - vehicle)/(vehicle)\*100 %.

Taken that the data computed relative to the [<sup>125</sup>I]micro-scales is the most robust measure of binding density, comparing these to the data obtained from the normalisation-to-the-cerebellum method yields only a match of 4 structures, the prefrontal cortex, the ventral hypothalamus, the thalamus, and the hippocampus. The other 13 structures that were

## Chapter 6 - Autoradiographic and micro-SPECT imaging of SERT depletion in rats using the radioligands [<sup>125</sup>I]βCIT and [<sup>125</sup>I]ADAM.

identified as significantly different between MDMA- and vehicle-treated animals with the latter method could therefore be regarded as “false positives” (Table 6-9). In fact by using the cerebellum-normalisation method, it appears that the structures being significantly different are virtually the opposite of those determined using the [<sup>125</sup>I]micro-scales. Since the main focus of this study was the comparison of 2 different SPECT ligands to image the SERT *in vivo*, i.e. [<sup>125</sup>I]βCIT and [<sup>125</sup>I]ADAM, under normal and pathological condition, scatter plots were constructed of data derived from [<sup>3</sup>H]citalopram and [<sup>125</sup>I]βCIT binding in the absence of any displacers (Fig. 6-25). This was done in order to assess the degree to which the binding of the less specific radioligand, to be used *in vivo*, reflected a highly specific measure of SERT in normal (vehicle-treated group) and reduced (MDMA-treated group) SERT density conditions. Calculation of the Spearman’s rank order correlation coefficient for vehicle- and MDMA-treated animals showed high correlation between these two ligands. A high degree of correlation was found when comparing [<sup>3</sup>H]citalopram to [<sup>125</sup>I]βCIT binding in the absence of any displacers. The scatter plots give an excellent impression of this relationship. Data points are well lined up along a straight line.

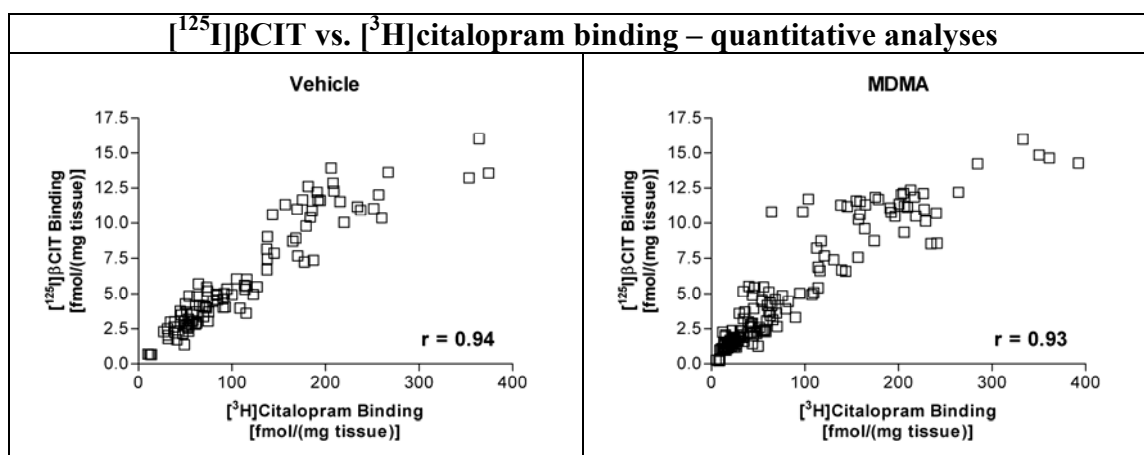


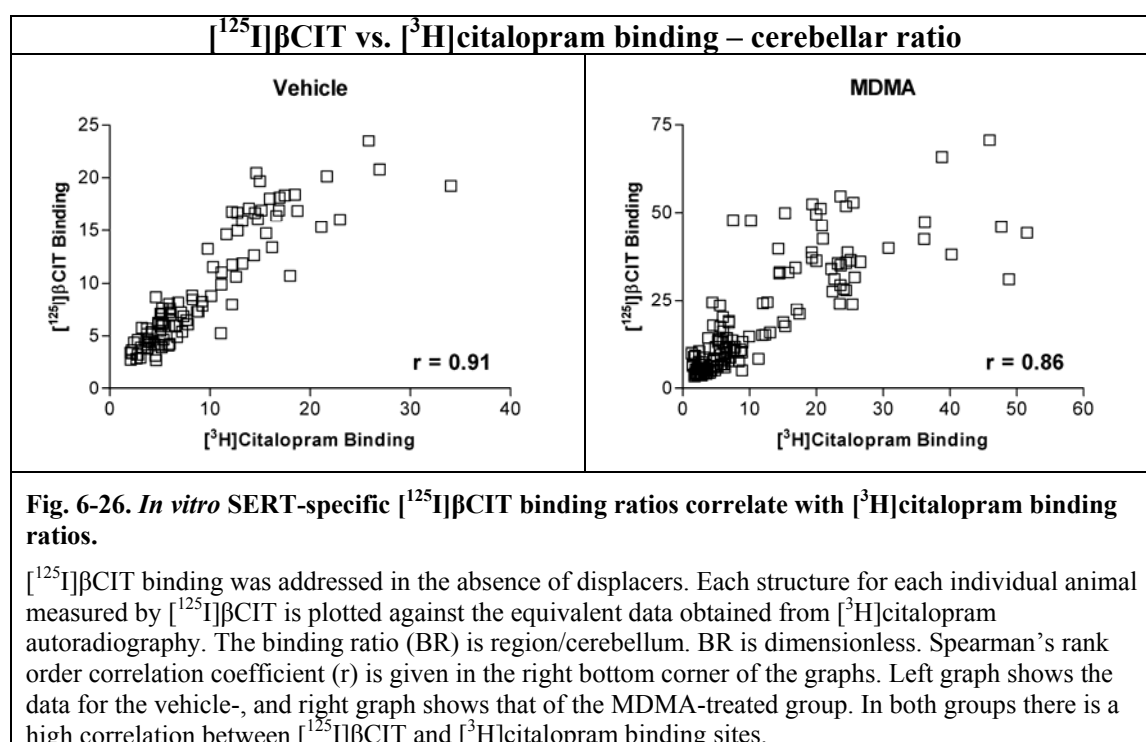
**Fig. 6-25. *In vitro* [<sup>125</sup>I]βCIT binding correlates with [<sup>3</sup>H]citalopram binding.**

[<sup>125</sup>I]βCIT binding was addressed in the absence of any displacers. Each structure for each individual animal measured with [<sup>125</sup>I]βCIT is plotted against [<sup>3</sup>H]citalopram binding. Units of measurement are fmol/mg. Spearman’s rank order correlation coefficient (r) is given in the right bottom corner of the graphs. Left graph shows the data for the vehicle-, and right graph shows that of the MDMA-treated group. In both groups there is a high degree of correlation between the densities of [<sup>125</sup>I]βCIT and [<sup>3</sup>H]citalopram binding sites.

Data obtained from *in vivo* SPECT imaging are often expressed as a ratio to a reference region and the cerebellum has been used in this study. The relationship between [<sup>125</sup>I]βCIT and [<sup>3</sup>H]citalopram binding ratios expressed in this way was therefore examined and the Spearman rank order correlation coefficient computed to determine the strength of the association between the two measures (Fig. 6-26). In both vehicle- and MDMA-treated

## Chapter 6 - Autoradiographic and micro-SPECT imaging of SERT depletion in rats using the radioligands [<sup>125</sup>I]βCIT and [<sup>125</sup>I]ADAM.

rats, a high r-value was obtained. However, visual inspection of the graphs shows that in MDMA-treated animals the data points look more dispersed than in the vehicle-treated animals. This suggests that when expressing the data in the ROIs as a ratio of the cerebellum, there is greater variability in the SERT-depleted animals between the 2 methods. It was shown above that the cerebellum is by no means free of SERT, and therefore interfering with SERT density in this region by treatment with MDMA could change the outcome of the analysis. This has been demonstrated in Table 6-5 for [<sup>3</sup>H]citalopram binding ratio and Table 6-10 for [<sup>125</sup>I]βCIT binding ratio data. Normalisation to the cerebellum clearly yields different results.



### 6.5 Discussion.

For the first time, the rat model of SERT-depletion using MDMA was examined using the novel SERT SPECT tracer [<sup>125</sup>I]ADAM with the micro-SPECT installed in Glasgow. In this study, a SERT-depleting MDMA regimen was successfully administered to rats, and the neurotoxic effects were confirmed using *in vitro* [<sup>3</sup>H]citalopram, [<sup>3</sup>H]WIN 35, 428, and [<sup>125</sup>I]βCIT autoradiography. Since the major aim of this thesis chapter was to compare the relative merits of [<sup>125</sup>I]βCIT and [<sup>125</sup>I]ADAM as *in vivo* SPECT tracers of SERT depletion attempts were made to establish an *in vitro* autoradiography protocol for [<sup>125</sup>I]ADAM, however this was not successful (material and methods, page 70). *In vivo* SPECT imaging using either [<sup>125</sup>I]βCIT and [<sup>125</sup>I]ADAM was unable to detect the reduction in SERT

## **Chapter 6 - Autoradiographic and micro-SPECT imaging of SERT depletion in rats using the radioligands [<sup>125</sup>I]βCIT and [<sup>125</sup>I]ADAM.**

density induced by MDMA administration, while *ex vivo* [<sup>125</sup>I]βCIT autoradiography did. While *ex vivo* [<sup>125</sup>I]ADAM autoradiography was quantifiable, *in vivo* [<sup>125</sup>I]ADAM SPECT images were of such low quality that analysis could not be carried out satisfactorily.

### **6.5.1 *In vitro* autoradiography.**

#### **MDMA treatment causes widespread SERT depletion.**

The SERT-depleting regimen of MDMA administration used in the current study, i.e. twice daily 20 mg/kg of MDMA over 4 days, was shown previously to produce a widespread loss of serotonin, and SERT binding in the rat brain (Battaglia et al., 1987, Commins et al., 1987, Kelly et al., 2002, Lew et al., 1996, O'Hearn et al., 1988, Reneman et al., 2002b, Sabol et al., 1996). These studies showed long-lasting (up to 52 weeks), and widespread decreases in serotonin concentrations and SERT density in rats that underwent the described MDMA-depleting regimen compared to vehicle-treated animals (Lew et al., 1996, Sabol et al., 1996). The maintenance phase of 10 days used in the present study was taken from Kelly *et al.* who showed a 90 % reduction in total number of SERT in frontal cortex membrane preparations using [<sup>3</sup>H]paroxetine as the SERT ligand (Kelly et al., 2002), while in the present study monoaminergic transporter densities were assessed by *in vitro* autoradiography using [<sup>125</sup>I]βCIT, [<sup>3</sup>H]citalopram, and [<sup>3</sup>H]WIN 35, 428. Both, the pilot and formal studies showed comparable levels of binding to SERT and DAT using these ligands in MDMA- and vehicle-treated animals. Thus the experimental procedure to achieve of SERT depletion is reproducible, and only the results of the formal study will be discussed further. Consistent with the present data for [<sup>125</sup>I]βCIT labelling specifically of SERT is the report from Lew *et al.* who did not detect any changes after a 2 weeks maintenance phase following MDMA administration in regions that synthesise monoamines, i.e. the dorsal raphe, substantia nigra and ventral tegmental area, but also structures that are rich in SERT like the lateral hypothalamus (Lew et al., 1996). This is also confirmed by the study of McGregor *et al.* using [<sup>125</sup>I]βCIT data labelling of SERT in the dorsal raphe and the caudate-putamen (McGregor et al., 2003). Both of these studies used [<sup>125</sup>I]βCIT in the presence of DAT blockers for the detection of SERT binding sites. Also in line with those studies are the reductions in cortical and thalamic regions observed in the current study. Interestingly, Armstrong *et al.* reported significant reductions in the dorsal raphe using [<sup>3</sup>H]paroxetine to assess SERT density in MDMA- and vehicle-treated animals (Armstrong and Noguchi, 2004), but this finding could not be confirmed by any other study known to the author, including the [<sup>125</sup>I]βCIT and [<sup>3</sup>H]citalopram studies

## **Chapter 6 - Autoradiographic and micro-SPECT imaging of SERT depletion in rats using the radioligands [<sup>125</sup>I]βCIT and [<sup>125</sup>I]ADAM.**

presented here. However all the other data from the study of Armstrong and colleagues are consistent with the present findings using [<sup>3</sup>H]citalopram to label SERT, i.e. significant reductions in thalamic and cortical regions, the hippocampus and the caudate-putamen of MDMA-treated animals. While MDMA has been reported to be neurotoxic to the serotonergic system, no long-term effects were observed for the dopaminergic (Schmidt et al., 1986), or catecholaminergic system in general (O'Hearn et al., 1988). The present data using the highly specific DAT radioligand [<sup>3</sup>H]WIN 35, 428 is consistent with this. This is in contrast to the reductions detected by the less specific ligand [<sup>125</sup>I]βCIT (in the presence of fluoxetine to label DAT only). Armstrong *et al.* used [<sup>3</sup>H]mazindol to assess DAT and also showed a reduction in MDMA-treated animals (Armstrong and Noguchi, 2004). However, Battaglia *et al.* reported no change associated with MDMA-treatment using the same ligand, [<sup>3</sup>H]mazindol (Battaglia et al., 1987). Both [<sup>125</sup>I]βCIT (Neumeyer et al., 1996), and mazindol (Javitch et al., 1984), bind not only to DAT but also to NAT. Therefore the discrepancy between findings using [<sup>3</sup>H]WIN 35, 428, mazindol and [<sup>125</sup>I]βCIT may be due to the relative specificities of the ligands.

### **Comparisons between *in vitro* [<sup>125</sup>I]βCIT and the specific ligands, [<sup>3</sup>H]citalopram and [<sup>3</sup>H]WIN 35, 428.**

The specific ligands [<sup>3</sup>H]citalopram and [<sup>3</sup>H]WIN 35, 428 were used as “gold standard” measures of SERT and DAT respectively. There was a correlation of the absolute binding levels *in vitro* of [<sup>125</sup>I]βCIT, in the absence of any displacers, and [<sup>3</sup>H]citalopram. In addition, specific labelling of SERT, and DAT with [<sup>125</sup>I]βCIT in the presence of mazindol, or fluoxetine, respectively, is highly correlated with data from [<sup>3</sup>H]citalopram, and [<sup>3</sup>H]WIN 35, 428, the specific ligands for SERT and DAT. [<sup>125</sup>I]βCIT in the presence of mazindol only fails to detect significant differences between MDMA-treated and control rats, shown by [<sup>3</sup>H]citalopram binding, in the caudate-putamen, and the nucleus accumbens, 2 structures known to be rich in DAT. However, a higher rate of “false positive” binding, compared to [<sup>3</sup>H]WIN 35, 428, was detected when using [<sup>125</sup>I]βCIT in the presence of fluoxetine to label DAT. The data are indicative that *in vivo* SPECT with [<sup>125</sup>I]βCIT would provide a good estimate of SERT in the living animal.

## Chapter 6 - Autoradiographic and micro-SPECT imaging of SERT depletion in rats using the radioligands [<sup>125</sup>I]βCIT and [<sup>125</sup>I]ADAM.

### 6.5.2 *In vivo* SPECT imaging and *ex vivo* autoradiography.

#### ***In vivo* SPECT imaging with [<sup>125</sup>I]βCIT did not detect MDMA-induced changes in SERT availability.**

Despite the *in vitro* autoradiographic demonstration that MDMA treatment caused widespread reductions in SERT binding, [<sup>125</sup>I]βCIT SPECT was unable to detect this by means of *in vivo* SPECT.

*In vivo* [<sup>125</sup>I]βCIT SPECT images were good and consistent with our previous experience (Cain et al., 2009). Therefore the data acquisition and image analysis was relatively straightforward with good reproducibility of the analysis, which was performed 3 times. However, despite the good image quality, the results from the *in vitro* autoradiographic analysis of widespread reductions in [<sup>125</sup>I]βCIT binding to SERT in MDMA-treated rats was not confirmed. Moreover, the results of the current study were not the same as those from a previous rat *in vivo* [<sup>123</sup>I]βCIT SPECT study using the MDMA model of SERT depletion. While in the current study only a trend towards decreased binding ratios was observed in the thalamus, de Win *et al.* reported significant reductions in this structure when MDMA-treated animals were compared with vehicle controls. It is worth noting that in the de Win study animals received a scan before and after the MDMA treatments and so acted as their own controls. This contrasts with our design in which separate groups of animals were compared. De Win *et al.* used Wistar rats (compared to Sprague-Dawley rats used in this study) that were initially treated with the same MDMA regimen as described above. However, 2 out of 6 rats died, which led the authors to reduce the daily dose (de Win et al., 2004). This may reflect a different tolerance of this strain of rats to this SERT-depleting regimen. Indeed, in Dark Agouti rats, a single dose (10 - 15 mg/kg) of MDMA is sufficient to deplete cortical SERT by 30 - 50 % (for review see Easton *et al.* (Easton and Marsden, 2006)). Thus, a higher dose of MDMA may be required in Sprague-Dawley rats to yield similar levels of severity.

A recent human [<sup>123</sup>I]βCIT SPECT study that compared short-term MDMA users to MDMA-naïve controls showed no significant differences in thalamic and cortical SERT binding (de Win et al., 2008). However in heavy compared to non-MDMA users, significant effects on [<sup>123</sup>I]βCIT binding to the thalamus were reported. The participants in the de Win study classified as heavy users were estimated to have consumed a total of 322 ± 354 (mean ± SD) MDMA pills (de Win et al., 2008). Single doses of MDMA in

## **Chapter 6 - Autoradiographic and micro-SPECT imaging of SERT depletion in rats using the radioligands [<sup>125</sup>I]βCIT and [<sup>125</sup>I]ADAM.**

humans are estimated to be in the range of 75 - 125 mg. Interspecies neurotoxicity scaling has predicted that neurotoxicity of MDMA in humans results from consumption of 1.28 mg/kg which represents about 96 mg in a 75 kg human person. The interspecies neurotoxicity scaling also predicts 20 mg/kg of MDMA to be neurotoxic in rats (for review see Ricaurte *et al.* (Ricaurte et al., 2000)), and therefore in the present study the rats received 8 “neurotoxic doses”. The total amount taken, prior to scanning, by the heavy users described by de Win *et al.* ranged between 15 and 2000 pills (de Win et al., 2008). We observed a 60 % significant reduction in SERT density by means of [<sup>3</sup>H]citalopram binding to the thalamus in MDMA-treated vs. vehicle control animals. Compared to the human study, where up to 2000 neurotoxic doses were taken by the participants, a more severe SERT-depleting MDMA regimen may be necessary in order to be able to detect similar differences with SPECT in rats. Since our MDMA treatment regimen in rats was for only 4 days, representing a rather acute exposure to the drug, *in vivo* SPECT imaging might not be sensitive enough to detect these changes.

### ***Ex vivo* [<sup>125</sup>I]βCIT [<sup>125</sup>I]ADAM autoradiography did detect significant MDMA-induced changes in SERT availability.**

*Ex vivo* autoradiography for [<sup>125</sup>I]βCIT was able to detect differences between control and MDMA-treated groups in 6 out of the 25 structures examined, when ROI data was normalised to the cerebellum. This was then compared to absolute binding levels obtained from *in vitro* autoradiography data using [<sup>3</sup>H]citalopram, and [<sup>125</sup>I]βCIT in the absence of any displacers. Using [<sup>3</sup>H]citalopram 16 out of 26 structures were detected as significantly reduced due to MDMA treatment compared to vehicle, while using [<sup>125</sup>I]βCIT group differences were detected in 14 (out of 26) structures (both measurements were made with external standards). No “false positives” were present in the *ex vivo* [<sup>125</sup>I]βCIT data. However some structures which showed MDMA-induced reductions by *in vitro* [<sup>3</sup>H]citalopram autoradiography did not show differences when assessed by *ex vivo* [<sup>125</sup>I]βCIT autoradiography. One reason for the discrepancy may be the method of analysis, i.e. the normalisation of the ROI signal to that of the cerebellum. As *in vitro* [<sup>125</sup>I]βCIT autoradiography demonstrated (also [<sup>3</sup>H]citalopram), there was a reduction of 58 % [<sup>125</sup>I]βCIT binding (36 % for [<sup>3</sup>H]citalopram) in the MDMA-treated rats. Therefore using the cerebellum in a ratio means that the binding ratio is overestimated. Issues of using the cerebellum as a reference region are discussed below.

## Chapter 6 - Autoradiographic and micro-SPECT imaging of SERT depletion in rats using the radioligands [<sup>125</sup>I]βCIT and [<sup>125</sup>I]ADAM.

### ***In vivo* SPECT imaging with [<sup>125</sup>I]ADAM did not detect MDMA-induced changes in SERT availability.**

The major issue for [<sup>125</sup>I]ADAM was the poor quality of the SPECT images. This meant that the positioning of ROIs for measurements of ligand uptake could not be done with any degree of accuracy, as it was not possible to identify a semblance of brain structure within the images. Only the Harderian glands and the thyroid were judged to be reliable landmarks that could be identified on the images from each animal. However the anterior-to-posterior distance between these two anatomical structures is several millimetres and trying to use these to identify the relative position of the brain was extremely difficult. The uncertainty about whether the animal was lying straight within the scanner could have meant that the position of an ROI did not correspond to the real position of the structure. The tissue surrounding the brain, presumably muscles, had a much greater uptake of radioactivity compared to the brain. In the only other rat SPECT study of [<sup>125</sup>I]ADAM, uptake appeared to be restricted to the brain (Hwang et al., 2007). However it is not clear from that publication if postprocessing of their representative images might have been performed to maximise the brain signal in relation to the surrounding tissues. In comparison the quality of human [<sup>123</sup>I]ADAM SPECT images appears to be much better than those obtained from the rat with our SPECT scanner. Activity is much greater in the brain than in muscles around the eyes and jaws and coregistration with MRI and subsequent image analysis has been achieved (see for instance Oya *et al.*, Kauppinen *et al.*, Herold *et al.*, Frokjaer *et al.* and Yang *et al.* (Frokjaer et al., 2008, Herold et al., 2006, Kauppinen et al., 2005, Oya et al., 2000, Yang et al., 2008)). Biodistribution analysis of [<sup>125</sup>I]ADAM in the rat clearly indicates high uptake in muscles (Choi et al., 2000, Oya et al., 2000). Over the time course of our experiment, i.e. 120 min, with scan start 30 min p. i. and 90 min scan duration, Choi *et al.* reported muscle uptake of 21 %, 8 %, and 5 % of injected dose after 2, 60, and 120 min p. i., respectively while brain uptake was 8 %, 1 %, and 0.42 % at these 3 time points, respectively. Probably these values are pooled representing uptake into all body muscles, yet still these distribution data are informative and may go some way to explaining why the images were of such poor quality in the present study.

One possible reason why no SPECT images of the brain could be obtained would be that the [<sup>125</sup>I]ADAM had been metabolised so that no intact ligand was available for binding to SERT. However, at least for the 10 day maintenance rats, the finding that *ex vivo*

## **Chapter 6 - Autoradiographic and micro-SPECT imaging of SERT depletion in rats using the radioligands [<sup>125</sup>I]βCIT and [<sup>125</sup>I]ADAM.**

autoradiograms showed labelling of SERT-rich structures suggests that intact radioligand was present in the animals. However thyroid radioactivity uptake was high from the beginning of the scan indicating either high amounts of free injected [<sup>125</sup>I] present in the batch, or high *in vivo* metabolism, i.e. deiodination of [<sup>125</sup>I]ADAM. The main problem was that the structures, i.e. the midbrain and the cerebellum, could not be identified in the SPECT scans. There are another 2 small animal studies, in which [<sup>123</sup>I]ADAM SPECT appears to have successfully produced images. Hwang *et al.* used a combined SPECT/computed tomography device, with which structures could be defined on a structural brain computed tomography image acquired from the same animal in the same position (Hwang et al., 2007). This was not possible in the current study, where an MRI of a different rat, in a different bed position was used to define the ROIs and overlay them onto nonidentifiable [<sup>125</sup>I]ADAM SPECT structures. The other study used rabbits, which have substantially bigger brains on whose SPECT images the ROIs derived from MRI images could possibly more easily be overlaid (Ye et al., 2004).

### ***Ex vivo* [<sup>125</sup>I]ADAM autoradiography did not detect significant MDMA-induced changes in SERT availability.**

To the knowledge of the author, this was the first time that [<sup>123/125</sup>I]ADAM has been used to study a rat model of MDMA-induced SERT depletion. No significant differences between vehicle- and MDMA-treated rats were detected using *ex vivo* autoradiography in any group examined, i.e. 10 days and 30 days. This is surprising as both [<sup>3</sup>H]citalopram and [<sup>125</sup>I]βCIT *in vitro* autoradiography successfully detected widespread loss of SERT in MDMA-treated animals compared to vehicle controls. The only 2 structures that differed between groups were the superior colliculus and the dorsal raphe (-15 %, and +20 %, respectively), although these differences were non-significant. Also visual inspection of the [<sup>125</sup>I]ADAM autoradiographic images assured that there is a reasonable reduction in, for example, the superior colliculus. All other structures remained mainly unaffected by MDMA treatment. Visual comparison to [<sup>3</sup>H]citalopram autoradiographic images confirmed that [<sup>125</sup>I]ADAM bound to structures that are known to be rich in SERT, and that actually intact [<sup>125</sup>I]ADAM was present *in vivo*.

The reasons why despite the visually obvious reductions no statistical relevant differences were observed are unclear but may include the small numbers of animals in each group.

## Chapter 6 - Autoradiographic and micro-SPECT imaging of SERT depletion in rats using the radioligands [<sup>125</sup>I]βCIT and [<sup>125</sup>I]ADAM.

### Correlation between *in vivo* SPECT imaging and *ex vivo* autoradiography using [<sup>125</sup>I]βCIT.

Thalamic and caudate-putamen readings from [<sup>125</sup>I]βCIT *ex vivo* autoradiograms correlated well with *in vivo* SPECT data. Significant correlations were obtained for vehicle- and MDMA-treated animals, respectively, underpinning the above said with regard to impact of alignment accuracy. [<sup>125</sup>I]βCIT SPECT and MRI scans could be relatively easily aligned with each other, and therefore there was little uncertainty about the placement of the ROIs and this was shown by the reproducibility of the measurements taken in the 3 separate analyses.

### 6.5.3 Technical considerations.

#### [<sup>125</sup>I]ADAM stability issues.

Because of the poor [<sup>125</sup>I]ADAM SPECT image quality, i.e. no identifiable regions were present, correlations as done for *in vivo* [<sup>125</sup>I]βCIT SPECT vs. *ex vivo* autoradiography could not be performed with this tracer. In addition, problems occurred regarding the use of [<sup>125</sup>I]ADAM for *in vitro* autoradiography, and *in vivo* SPECT imaging that made analysis of the latter virtually impossible. A high thyroid uptake of [<sup>125</sup>I] was observed in the SPECT images. Good *in vivo* stability of a radioligand is indicated by low thyroid uptake over the course of an scanning experiment (Eersels et al., 2004). Choi *et al.* could recover over 90 % of [<sup>125</sup>I]ADAM from rat brain tissue of animals that were injected 120 min before with 0.37 MBq. Organ distribution showed a steady increase of activity in the thyroid over time, from 0.1 % (2 min p. i.) to 0.4 % (60 min p. i.) to 1.1 % (120 min p. i.) of the injected dose. This increase was accompanied by a loss of activity in the brain from 1.8 %, to 1 %, to 0.42 %, for 2, 60, and 120 min p. i., respectively (Choi et al., 2000). A similar biodistribution over time in rats was observed by Oya *et al.* (Oya et al., 2000). The time course of the scanning experiment presented in this study, i.e. a 90 min scan that was started 30 min p. i. of roughly 16 MBq [<sup>125</sup>I]ADAM, is within the time frame reported when thyroid activity uptake should have been lower than brain uptake, according to the data of Choi (Choi et al., 2000). However, thyroid activity uptake dominated the SPECT image, whose acquisition started 30 min p. i. from caudal to rostral, i.e. starting from the thyroid. No other structure was visible in an initially reconstructed SPECT scan image. High thyroid activity uptake that increases over the course of an experiment could indicate *in vivo* metabolism of the tracer, i.e. deiodination, of the compound (Quinlivan et al., 2003). Thyroid uptake was measured only at the start of the scanning session with the

## Chapter 6 - Autoradiographic and micro-SPECT imaging of SERT depletion in rats using the radioligands [<sup>125</sup>I]βCIT and [<sup>125</sup>I]ADAM.

MollyQ micro-SPECT which acquires images in a slice-by-slice fashion starting at the thyroid and moving rostrally (see below). In the 10 day maintenance experiment the *ex vivo* autoradiography images appeared to be of good quality indicating that there was brain uptake in regions known to be rich in SERT. The high thyroid uptake but good *ex vivo* autoradiographic images might suggest that the fraction of intact [<sup>125</sup>I]ADAM, was low while the amount of free [<sup>125</sup>I] in the injected dose was high, perhaps as a consequence of radioligand deiodination. However, Choi *et al.* reported a greater than 95 % purity of [<sup>125</sup>I]ADAM even after 2 months of storage (in 50 % ethanol) (Choi et al., 2000). In addition, the supplier (MAP, Finland) of [<sup>125</sup>I]ADAM for this study confirmed a stability of > 95 % after one month of storage. Although we have no definitive evidence of [<sup>125</sup>I]ADAM deiodination in our hands, the possibility cannot be discounted.

In this study, 4 different batches of [<sup>125</sup>I]ADAM were used. An initial attempt to establish an *in vitro* autoradiography protocol appeared promising using batch 2, however results could not be repeated with another batch (4) of radiolabelled ADAM. Batch 4 was used prior to the *in vitro* study for *in vivo* [<sup>125</sup>I]ADAM SPECT imaging of the 10 day maintenance animals. As mentioned above, the SPECT image quality was poor, however *ex vivo* autoradiograms were of good quality indicating uptake of [<sup>125</sup>I]ADAM to SERT-rich regions. *In vitro* autoradiography was carried out with the remainder of batch 4 in order to improve the autoradiographic protocol that was using batch 2 of [<sup>125</sup>I]ADAM. However the binding levels achieved were very different from those obtained using the batch 2. It is possible that free [<sup>125</sup>I] sticks to the walls of the vial it was kept in, which suggests that there was an exchange with the walls and the rest of the liquid in the vial. Amounts of activity used for autoradiography were checked with a scintillation counter, therefore it is possible that the activity measured was mainly free [<sup>125</sup>I]. Batch 3 was used for *in vivo* [<sup>125</sup>I]ADAM SPECT imaging of 30 day maintenance animals. A vehicle-treated animal was scanned with 13 MBq [<sup>125</sup>I]ADAM recovered from the vial by re-suspending remaining activity by adding a few 100 µl of saline to what was still in the vial (Fig. 6-27). When the *ex vivo* autoradiograms from this animal were compared to another vehicle-treated animal that was SPECT scanned 2 days before with the same, but not re-suspended batch (3), huge reductions of [<sup>125</sup>I]ADAM binding were observed in the superior colliculus, ventral tegmental area, substantia nigra and dorsal raphe.

**Chapter 6 - Autoradiographic and micro-SPECT imaging of SERT depletion in rats using the radioligands [<sup>125</sup>I]βCIT and [<sup>125</sup>I]ADAM.**

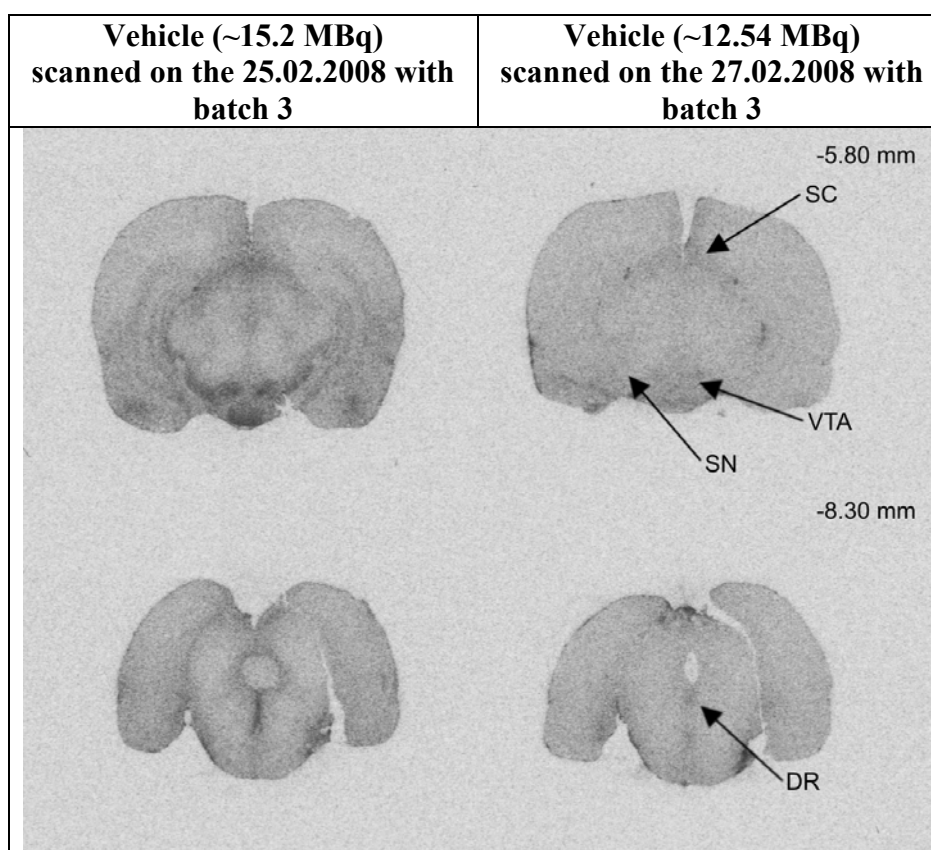


**Fig. 6-27. Evaluation of [<sup>125</sup>I]ADAM batch (3) in vehicle-treated animals of 30 day maintenance.**

Representative sections show vehicle-treated animals. Left: animal received ~15.2 MBq of [<sup>125</sup>I]ADAM i. v.. Right: animal received ~12.54 MBq of [<sup>125</sup>I]ADAM i. v.. Right animal finished off the batch. Few 100 µl of saline were added to the vial to re-suspend some of the activity that stuck to the vial walls. [<sup>125</sup>I]ADAM signal is clearly lower in right animal, i.e. in the superior colliculus (SC), ventral tegmental area (VTA), substantia nigra (SN), and dorsal raphe (DR). Animals were killed ~2 h p. i.. Note that film exposure duration was identical to sections presented in Fig. 6-12, however sections were apposed onto different films. Sections shown here in this figure were on separate sheets of film. Bregma level is indicated in top right corner.

**The cerebellum is an inappropriate reference region.**

In current SPECT imaging literature of SERT, it is common to use the cerebellum as reference region (Herold et al., 2006, Kauppinen et al., 2005, Lehto et al., 2008, Shang et al., 2007). An assumption that needs to be fulfilled in order to do so states that specific binding in the reference region should be negligible. It is clear from the *in vitro* autoradiography presented in the current study that there is specific SERT binding in the cerebellum. Moreover, this was reduced by MDMA treatment, as shown by *in vitro* autoradiography using either [<sup>3</sup>H]citalopram or [<sup>125</sup>I]βCIT. A reduction of SERT in the reference region would therefore overestimate *in vivo* binding measured by SPECT when expressed as the ratio region/cerebellum (Kish et al., 2005). This is indeed the case when

## Chapter 6 - Autoradiographic and micro-SPECT imaging of SERT depletion in rats using the radioligands [<sup>125</sup>I]βCIT and [<sup>125</sup>I]ADAM.

expressing our *in vitro* data from the [<sup>3</sup>H]citalopram and [<sup>125</sup>I]βCIT (in the absence of any displacers) experiments as a ratio to the cerebellum. Regions with a high SERT density (e.g. dorsal raphe, ventral tegmental area, caudate-putamen) were unaffected by MDMA treatment when absolute levels of binding were measured autoradiographically. However, when the data was expressed as a ratio of the cerebellum these structures showed large increases in binding ratio in the MDMA-treated group. This was more pronounced when using [<sup>3</sup>H]citalopram compared to [<sup>125</sup>I]βCIT, which could indicate differences in regional binding patterns of the two ligands. Differences between radioligand binding patterns were reported previously in a study in which Elfving *et al.* aimed to identify a suitable neuroimaging tracer amongst the compounds [<sup>3</sup>H]citalopram (S-enantiomer), [<sup>3</sup>H]paroxetine, and [<sup>123</sup>I]ADAM (Elfving *et al.*, 2007). [<sup>123</sup>I]ADAM, followed by [<sup>3</sup>H]paroxetine, were identified as the best ligands as both show high affinity for SERT, while SERT was not detectable using these in monkey cerebellar homogenates. [<sup>3</sup>H]citalopram showed less affinity compared to the aforementioned ligands, in addition to significant binding to the cerebellum, and was therefore discarded as an ideal candidate tracer for neuroimaging. Unfortunately, in this study [<sup>3</sup>H]citalopram was used as specific ligand for *in vitro* autoradiography along with [<sup>125</sup>I]βCIT to label SERT, both showing significant binding to the cerebellum that is affected by a SERT-depleting regimen using MDMA. In addition, with [<sup>125</sup>I]ADAM a promising ligand was at hand, that was shown not to bind to the cerebellum, however the *in vitro* autoradiography and *in vivo* SPECT imaging with this ligand was compromised by issues of ligand handling.

These findings indicate that the cerebellum is not a suitable reference region for assessing MDMA-induced depletion of SERT as it violates the requirement described above. In addition to issues involving the cerebellum as reference region, a bolus injection of any radioligand implies constantly changing radioligand concentrations *in vivo*, violating another assumption that states that SPECT measurements should be performed at steady state, i.e. when the blood plasma concentration of the radioligand and that of the tissue under examination are in equilibrium (Slifstein, 2008). Given all of these issues, kinetic modelling using arterial blood sampling may represent a better approach to *in vivo* [<sup>125</sup>I]βCIT SPECT imaging of the kind of experimental condition that depletes SERT.

## Chapter 6 - Autoradiographic and micro-SPECT imaging of SERT depletion in rats using the radioligands [<sup>125</sup>I]βCIT and [<sup>125</sup>I]ADAM.

### 6.6 Final conclusions.

This study demonstrated the validity of the model of MDMA-induced depletion of SERT by means of *in vitro* autoradiography with [<sup>3</sup>H]citalopram, [<sup>3</sup>H]WIN 35, 428, and [<sup>125</sup>I]βCIT. [<sup>3</sup>H]citalopram is binding to cerebellar SERT, so [<sup>3</sup>H]paroxetine might be a better choice to label SERT. [<sup>125</sup>I]βCIT in the presence or absence of mazindol provides excellent estimates of SERT densities *in vitro* compared to the specific SERT ligand [<sup>3</sup>H]citalopram. In contrast labelling of DAT with [<sup>125</sup>I]βCIT in the presence of fluoxetine is not very specific compared with the specific DAT ligand [<sup>3</sup>H]WIN 35, 428. No suggestions can be made on the basis of this study regarding [<sup>125</sup>I]ADAM labelling of SERT, neither in *in vitro*, *in vivo* nor *ex vivo*. However comparing [<sup>125</sup>I]βCIT SPECT data to those obtained from [<sup>125</sup>I]ADAM SPECT, [<sup>125</sup>I]βCIT is the better ligand based on this study. This is in contrast to publications that report successful use of [<sup>123</sup>I]ADAM as a specific SERT tracer with advantages over [<sup>123</sup>I]βCIT. The reasons why it was not possible to obtain good quality ADAM images could include methodological issues (perhaps the scanning procedure was not optimised) or issues relating to the stability of the radioligand. The data indicate that the cerebellum as reference region has significant limitations under the conditions of the type of experiment undertaken and therefore kinetic modelling would be more appropriate.

**Chapter 7 - General discussion.**

## Chapter 7 - General discussion.

In the presented thesis, state-of-the-art neuroimaging techniques were applied to study various diseases involving the serotonin system. For the first time, a mouse model of SERT-deficiency was investigated for changes in white matter composition and arborisation that could give rise to changes in DTI contrasts. As no convincing differences were found in this subtle condition, DTI was probed on a mouse model of severe white matter pathology, where it proved to reliably detect pathology confirmed by histopathology. Always speculated, but never specifically investigated by others, possible crosstalk between the serotonin system and white matter pathology was then explored using conventional autoradiography in the same mouse model. These data provide little evidence of white matter influencing the serotonergic system. Finally, SPECT imaging of SERT-depleted rats was performed to test the relative abilities of 2 different ligands to cope with this situation. Even though large reductions in SERT availability were confirmed with *post mortem* autoradiography, both ligands failed to reflect these changes *in vivo*.

Animal models of human diseases aim to simplify disease complexity in order to better understand a specific aspect of the disease and how pathophysiology develops and may be modulated. Genetically modified animals develop their defect in a stereotypic way, so that disease progression and severity is comparable from animal to animal. However highly inbred mice may also inherit traits that are not desirable and can vary from animal to animal, thus producing potential confounds to any results. This was demonstrated in the study of SERT KO mice in chapter 3 (page 98), where the callosal length of the strain of mice used (129S6 / SvEv) appeared to be influenced by some interactions at the genetic level that did likely not involve SERT deletion. The white matter organisation in SERT-KO appeared not to be altered compared to WT, while surprisingly the SERT-HT showed alterations in some DTI parameters. As these SERT-HT mice showed a 50 % reduction in SERT (Bengel et al., 1998), they have been suggested to represent a better genetic model for human depression, where apparently a SERT polymorphism predisposes to depression (Murphy and Lesch, 2008). It is worth recalling the DTI studies performed in human depressed patients that do not respond to antidepressant treatment. Compared to depressed patients that do respond, non-responders showed reduced FA in one study while in the other the FA was higher. In the former study the explanation was straightforward (Alexopoulos et al., 2008), in the latter the authors struggled to find a reason why. In searching for an explanation, Taylor and colleagues referred to an fMRI study showing that

cortical and limbic connectivity is functionally impaired in depression, and this connectivity may be strengthened through antidepressant treatment (Anand et al., 2005). Thus Taylor hypothesised that patients might respond better to antidepressants when structural abnormalities exist compared to their absence (Taylor et al., 2008). This explanation seems too far-fetched, and highlights a responsibility problem in the scientific literature. This hypothesis may suddenly become a believed myth, even if it is not supported by evidence. In addition, the disparity of these 2 studies raises the question whether the differences reported by other groups that compared healthy volunteers to depressed subjects are real and biologically relevant (Bae et al., 2006, Nobuhara et al., 2006, Yang et al., 2007a, Li et al., 2007a, Li et al., 2007b, Ma et al., 2007). These results, including the ones obtained from the SERT deficiency study (chapter 3, page 98), may indicate that at present the DTI technique is not mature enough yet and may lack the sensitivity to detect likely only subtle changes that potentially occur in the white matter of a depressed person. Nonetheless experimental studies such as the ones reported in this thesis are important in order to further improve DTI techniques for application in investigating the pathophysiology of psychiatric diseases. Such improvements certainly include probing the white matter integrity at much higher resolution: the water diffusion properties are given as an average in one voxel in a DTI parameter image. This voxel may include pieces of grey matter as a result of partial volume effects. Therefore, the higher the resolution, the smaller this effect will become. Also a better understanding of the interpretation of the DTI-derived parameters at the tissue level is warranted. Some contributions to the latter issue were provided in chapter 4 (page 158, discussed below).

Although DTI may currently lack sensitivity when applied to studies of specific genetic modifications, e.g. SERT-KO, or even to psychiatric diseases, this imaging technique has proved to be capable of detecting overt myelin and/or axonal pathology. This was demonstrated in a mouse model of PMD, which showed severe, widespread differences in DTI contrasts as compared to WT animals. The histopathological data indicated that myelin was already damaged at the time the animals were killed, so that no associations between FA and myelin status were observed. Nevertheless, previous developmental studies in humans and rats showed that an association between FA and myelin status exists (Jito et al., 2008, Saksena et al., 2008). In addition, individual tracts appeared to show different vulnerability to *Plp1* overexpression, however more data would need to be collected to support this notion. To summarise the relevance of the study described in chapter 4 (page 158), it was of supportive value to current knowledge on the interpretation

of FA, MD, and RD at the tissue level. However the structural correlate(s) of  $\lambda_1$  are by no means clear yet. A lot of speculative reports have been presented concerning the interpretation of this parameter in relation to the events occurring at the tissue level that may be associated with its change.  $\lambda_1$  was reported to be associated with axonal pathology (Song et al., 2002). In the absence of gliosis in a dysmyelinating condition,  $\lambda_1$  was suggested to remain unaltered by one group (Song et al., 2002), while another actually found an increase in the same mouse model (Tyszka et al., 2006). In a mouse model showing mild astrocytic hypertrophy,  $\lambda_1$  was reduced, while it was increased in the presence of massive gliosis (Harsan et al., 2007), and this was supported by the study of PLPOVR mice reported in this thesis. In addition,  $\lambda_1$  is consistently reduced in EAE models (Budde et al., 2008, DeBoy et al., 2007), in which gliosis also occurs thus indicating the different features within tissue that influence  $\lambda_1$  (Ahrens et al., 1998, Liedtke et al., 1998). In order to address the issues mentioned above, i.e. lack of correlation between FA and myelin changes, individual tract vulnerabilities, and uncertainty with respect to the tissue correlate of  $\lambda_1$ , more extensive studies of this type need to be conducted. Animal numbers were low for the single time point examined; but more importantly, only one time point during the progressive development of the white matter pathology in the PLPOVR mice was examined. Therefore future studies may include several time points, with larger numbers of animals. These additional studies are warranted in the light of previous observations, which showed that at P20, myelin is present in PLPOVR mice, although the sheaths are thinner compared to WT (dysmyelination) At P60, many axons are demyelinated but myelin is still present (Anderson et al., 1999). At P120, as shown in this thesis, virtually no myelin was present. Moreover, demyelination appears to be tract selective, however the study of Anderson *et al.* only examined the spinal cord, and not brain, further supporting the need to expand the present study (chapter 4, page 158) (Anderson et al., 1999). Examining the disease progression over time would also help to shed light onto what pathological features are reflected by changes in  $\lambda_1$ . Further studies could include the monitoring of the temporal onset of gene expression of markers relevant to axon outgrowth and maturation, as well as the assessment of histopathology using immunohistochemistry. In parallel, DTI data should be acquired in such a way that the individual parameters can be matched time wise to the histology data. It should be noted though that the breeding of WT and transgenic animals follows the Mendelian inheritance rule, stating that only 25 % of the offspring of hemizygous parent mice would have the desired genotype, i.e. either WT or PLPOVR, respectively. This

limited us technically in such a way that we were only able to obtain small animal numbers within the scope of this thesis.

It appears from the results presented in the current thesis, and from other preclinical studies available on imaging the SERT using SPECT, that animal SPECT is currently in the early phases of its development as a preclinical imaging tool compared to MRI technologies including DTI. There are only a few preclinical studies that have used SPECT to image SERT function. Even in human studies, the variability in test-retest SPECT studies is relatively high. Using [ $^{123}\text{I}$ ] $\beta\text{CIT}$ , for instance, which delivers high quality images of the SERT and DAT, a variability of 13 (healthy persons) - 17 % (Parkinson's disease) was observed for measurements made in the easily identifiable striatum (Seibyl et al., 1997). For [ $^{123}\text{I}$ ]ADAM SPECT in humans, this is surprisingly not much different. Variability in a test-retest setting was reported to range from 13 % to 22 % for the midbrain and medial temporal region, respectively (Catafau et al., 2005). In terms of reproducibility across lab reports disagree. Using [ $^{123}\text{I}$ ]ADAM SPECT in depressed humans, a reduction in midbrain binding has been reported by some (Newberg et al., 2005), while others find no differences compared to the control group (Catafau et al., 2006, Herold et al., 2006). In line with this discrepancy, it appears that the SERT, including all known mutations and polymorphisms, has been linked to a variety of diseases, such as depression, obsessive-compulsive disorder, autism, schizophrenia and so on. However, recent studies using [ $^{123}\text{I}$ ] $\beta\text{CIT}$  and SPECT give contrary reports on SERT density in, for instance, healthy subjects carrying different 5-HTTLPR polymorphisms. While in one it appears that SERT availability is reduced by 50 % in pooled s- compared to those that are homozygous long allele carriers (Fig. 1-11, page 33) (Heinz et al., 2000), another study could not find any differences in [ $^{123}\text{I}$ ] $\beta\text{CIT}$  binding in the brainstem region (l/l versus s/s carriers) (van Dyck et al., 2004).

SPECT imaging appears to be able to detect large reductions in tracer labelling of SERT such as occur during pharmacological blockade of the transporter (Erlandsson et al., 2005, Pirker et al., 1995). But even under conditions of significant transporter reductions, such as SERT depletion using MDMA, micro-SPECT using [ $^{125}\text{I}$ ] $\beta\text{CIT}$  appeared to struggle to detect a difference between control and treated rats as demonstrated in this thesis (chapter 6, page 242). If the same inter-scan variability of 13 - 17 %, as measured in human studies (Seibyl et al., 1997), is applied to the animal study reported here it is perhaps not surprising that a difference of 15 % in thalamic [ $^{125}\text{I}$ ] $\beta\text{CIT}$  binding (as measured using *ex vivo* autoradiography, normalised to the cerebellum) between MDMA- and vehicle-treated rats

could not be detected. Most of the studies mentioned referred to here used the cerebellum as reference region (Catafau et al., 2006, Herold et al., 2006, Newberg et al., 2005). This is probably one of the most problematic factors when using SPECT, as demonstrated by the *in vitro* autoradiography experiments. Therefore for future studies the application of the kinetic modelling approach cannot be stressed enough. Another major issue in SPECT imaging is the anatomical substrate. For highly specific SPECT ligands in a preclinical research setting that target the SERT, such as [<sup>125</sup>I]ADAM, it is essential to have a reliable anatomical image that has been acquired in the same animal position as the SPECT. Computed tomography-equipped SPECT tomographs exist mainly as clinical scanners, and only recently preclinical micro-SPECT scanners that include a computed tomography device were built. Despite the efforts in the right direction, computed tomography provides poor brain tissue contrast. Ideally, an MRI with a SPECT insert is necessary to acquire SPECT and high-resolution tissue contrast anatomical images at the same time. Only few prototype MRI/positron emission tomography cameras are available worldwide that, however, give promising results in coping with these issues (Judenhofer et al., 2007). It would also be of interest to measure, for instance, metabolite concentrations using magnetic resonance spectroscopy, under acute drug treatment of an animal, while SPECT is acquired in parallel.

In summary, it is the belief that the current technology for both DTI and SPECT imaging in small animals can give valuable information when large biological changes in either tissue structure (MRI) or availability of a neurotransmitter for radioligand binding (SPECT) are present. However, further technical improvements may be necessary if these techniques are to be applied to more subtle and complex pathological changes such as for instance in depression or other psychiatric disorders. Future SPECT imaging studies would also benefit from the application of methodologies such as kinetic modelling.

**References.**

**References.**

- ABRAMOFF, M. D., MAGELHAES, P. J. & RAM, S. J. (2004) Image Processing with ImageJ. *Biophotonics International*, 11, 36-42.
- ALEXANDER, A. L., LEE, J. E., LAZAR, M., BOUDOS, R., DUBRAY, M. B., OAKES, T. R., MILLER, J. N., LU, J., JEONG, E. K., MCMAHON, W. M., BIGLER, E. D. & LAINHART, J. E. (2007) Diffusion tensor imaging of the corpus callosum in Autism. *Neuroimage*, 34, 61-73.
- ALLEN, L. S. & GORSKI, R. A. (1992) Sexual orientation and the size of the anterior commissure in the human brain. *Proc Natl Acad Sci U S A*, 89, 7199-202.
- ALTAMURA, C., DELL'ACQUA, M. L., MOESSNER, R., MURPHY, D. L., LESCH, K. P. & PERSICO, A. M. (2007) Altered neocortical cell density and layer thickness in serotonin transporter knockout mice: a quantitation study. *Cereb Cortex*, 17, 1394-401.
- AMERICAN\_PSYCHIATRIC\_ASSOCIATION (2000) Diagnostic and statistical manual of mental disorders (Fourth edition---text revision (DSM-IV-TR). *American Psychiatric Association*. 4th ed. Washington, DC.
- ANAND, A., LI, Y., WANG, Y., WU, J., GAO, S., BUKHARI, L., MATHEWS, V. P., KALNIN, A. & LOWE, M. J. (2005) Antidepressant effect on connectivity of the mood-regulating circuit: an FMRI study. *Neuropsychopharmacology*, 30, 1334-44.
- ANDERSON, T. J., KLUGMANN, M., THOMSON, C. E., SCHNEIDER, A., READHEAD, C., NAVE, K. A. & GRIFFITHS, I. R. (1999) Distinct phenotypes associated with increasing dosage of the PLP gene: implications for CMT1A due to PMP22 gene duplication. *Ann N Y Acad Sci*, 883, 234-46.
- ANDERSON, T. J., SCHNEIDER, A., BARRIE, J. A., KLUGMANN, M., MCCULLOCH, M. C., KIRKHAM, D., KYRIAKIDES, E., NAVE, K. A. & GRIFFITHS, I. R. (1998) Late-onset neurodegeneration in mice with increased dosage of the proteolipid protein gene. *J Comp Neurol*, 394, 506-19.

- ANDREWS, H., WHITE, K., THOMSON, C., EDGAR, J., BATES, D., GRIFFITHS, I., TURNBULL, D. & NICHOLS, P. (2006) Increased axonal mitochondrial activity as an adaptation to myelin deficiency in the Shiverer mouse. *J Neurosci Res*, 83, 1533-9.
- ARCHIBALD, R., CHEN, K., GELB, A. & RENAUT, R. (2003) Improving tissue segmentation of human brain MRI through preprocessing by the Gegenbauer reconstruction method. *Neuroimage*, 20, 489-502.
- ARMSTRONG, B. D. & NOGUCHI, K. K. (2004) The neurotoxic effects of 3,4-methylenedioxymethamphetamine (MDMA) and methamphetamine on serotonin, dopamine, and GABA-ergic terminals: an in-vitro autoradiographic study in rats. *Neurotoxicology*, 25, 905-14.
- ASHBURNER, J. & FRISTON, K. J. (2000) Voxel-based morphometry--the methods. *Neuroimage*, 11, 805-21.
- AZMITIA, E. & GANNON, P. (1983) The ultrastructural localization of serotonin immunoreactivity in myelinated and unmyelinated axons within the medial forebrain bundle of rat and monkey. *J. Neurosci.*, 3, 2083-2090.
- BAE, J. N., MACFALL, J. R., KRISHNAN, K. R., PAYNE, M. E., STEFFENS, D. C. & TAYLOR, W. D. (2006) Dorsolateral prefrontal cortex and anterior cingulate cortex white matter alterations in late-life depression. *Biol Psychiatry*, 60, 1356-63.
- BAH, J., LINDSTROM, M., WESTBERG, L., MANNERAS, L., RYDING, E., HENNINGSSON, S., MELKE, J., ROSEN, I., TRASKMAN-BENDZ, L. & ERIKSSON, E. (2008) Serotonin transporter gene polymorphisms: effect on serotonin transporter availability in the brain of suicide attempters. *Psychiatry Res*, 162, 221-9.
- BASSER, P. J. & PIERPAOLI, C. (1996) Microstructural and Physiological Features of Tissues Elucidated by Quantitative-Diffusion-Tensor MRI. 111, 209.
- BATTAGLIA, G., YEH, S. Y., O'HEARN, E., MOLLIVER, M. E., KUCHAR, M. J. & DE SOUZA, E. B. (1987) 3,4-Methylenedioxymethamphetamine and 3,4-methylenedioxyamphetamine destroy serotonin terminals in rat brain: quantification of

- neurodegeneration by measurement of [3H]paroxetine-labeled serotonin uptake sites. *J Pharmacol Exp Ther*, 242, 911-6.
- BEAULIEU, C. (2002) The basis of anisotropic water diffusion in the nervous system - a technical review. *NMR Biomed*, 15, 435-55.
- BEAULIEU, C. & ALLEN, P. S. (1994) Water diffusion in the giant axon of the squid: implications for diffusion-weighted MRI of the nervous system. *Magn Reson Med*, 32, 579-83.
- BECK, S. G., PAN, Y. Z., AKANWA, A. C. & KIRBY, L. G. (2004) Median and dorsal raphe neurons are not electrophysiologically identical. *J Neurophysiol*, 91, 994-1005.
- BEHRENS, T. E., WOOLRICH, M. W., JENKINSON, M., JOHANSEN-BERG, H., NUNES, R. G., CLARE, S., MATTHEWS, P. M., BRADY, J. M. & SMITH, S. M. (2003) Characterization and propagation of uncertainty in diffusion-weighted MR imaging. *Magn Reson Med*, 50, 1077-88.
- BEN BASHAT, D., KRONFELD-DUENIAS, V., ZACHOR, D. A., EKSTEIN, P. M., HENDLER, T., TARRASCH, R., EVEN, A., LEVY, Y. & BEN SIRA, L. (2007) Accelerated maturation of white matter in young children with autism: a high b value DWI study. *Neuroimage*, 37, 40-7.
- BENVENISTE, H. & BLACKBAND, S. (2002) MR microscopy and high resolution small animal MRI: applications in neuroscience research. *Prog Neurobiol*, 67, 393-420.
- BERKE, J. (1960) The claustrum, the external capsule and the extreme capsule of *Macaca mulatta*. *The Journal of Comparative Neurology*, 115, 297-331.
- BESTER, M., HEESSEN, C., SCHIPPLING, S., MARTIN, R., DING, X. Q., HOLST, B. & FIEHLER, J. (2008) Early anisotropy changes in the corpus callosum of patients with optic neuritis. *Neuroradiology*, 50, 549-57.
- BIRD, T. D., FARRELL, D. F. & SUMI, S. M. (1978) Brain lipid composition of the shiverer mouse: (genetic defect in myelin development). *J Neurochem*, 31, 387-91.

- BONILHA, L., HALFORD, J. J., RORDEN, C., ROBERTS, D. R., RUMBOLDT, Z. & ECKERT, M. A. (2009) Automated MRI analysis for identification of hippocampal atrophy in temporal lobe epilepsy. *Epilepsia*, 50, 228-33.
- BREMNER, J. D., NARAYAN, M., ANDERSON, E. R., STAIB, L. H., MILLER, H. L. & CHARNEY, D. S. (2000) Hippocampal volume reduction in major depression. *Am J Psychiatry*, 157, 115-8.
- BROWN, P. & MOLLIVER, M. E. (2000) Dual Serotonin (5-HT) Projections to the Nucleus Accumbens Core and Shell: Relation of the 5-HT Transporter to Amphetamine-Induced Neurotoxicity. *J. Neurosci.*, 20, 1952-1963.
- CABRERA-VERA, T. M. & BATTAGLIA, G. (1998) Prenatal Exposure to Fluoxetine (Prozac) Produces Site-Specific and Age-Dependent Alterations in Brain Serotonin Transporters in Rat Progeny: Evidence from Autoradiographic Studies. *J Pharmacol Exp Ther*, 286, 1474-1481.
- CABRERA-VERA, T. M., GARCIA, F., PINTO, W. & BATTAGLIA, G. (1997) Effect of Prenatal Fluoxetine (Prozac) Exposure on Brain Serotonin Neurons in Prepubescent and Adult Male Rat Offspring. *J Pharmacol Exp Ther*, 280, 138-145.
- CAIN, S. M., RUEST, T., PIMLOTT, S., PATTERSON, J., DUNCAN, R., DEWAR, D. & SILLS, G. J. (2009) High resolution micro-SPECT scanning in rats using  $^{125}\text{I}$   $\beta$ -CIT: effects of chronic treatment with carbamazepine. *Epilepsia*, in press.
- CARHART-HARRIS, R. L., MAYBERG, H. S., MALIZIA, A. L. & NUTT, D. (2008) Mourning and melancholia revisited: correspondences between principles of Freudian metapsychology and empirical findings in neuropsychiatry. *Ann Gen Psychiatry*, 7, 9.
- CECCARELLI, A., ROCCA, M. A., VALSASINA, P., RODEGHER, M., PAGANI, E., FALINI, A., COMI, G. & FILIPPI, M. (2009) A multiparametric evaluation of regional brain damage in patients with primary progressive multiple sclerosis. *Hum Brain Mapp*.
- CHOI, S. R., HOU, C., OYA, S., MU, M., KUNG, M. P., SICILIANO, M., ACTON, P. D. & KUNG, H. F. (2000) Selective in vitro and in vivo binding of  $[(^{125}\text{I})\text{I}]\text{ADAM}$  to serotonin transporters in rat brain. *Synapse*, 38, 403-12.

COLEMAN, M. (2005) Axon degeneration mechanisms: commonality amid diversity. *Nat Rev Neurosci*, 6, 889-98.

CORDES, S. P. (2005) Molecular genetics of the early development of hindbrain serotonergic neurons. *Clin Genet*, 68, 487-94.

COURCHESNE, E. & PIERCE, K. (2005) Brain overgrowth in autism during a critical time in development: implications for frontal pyramidal neuron and interneuron development and connectivity. *Int J Dev Neurosci*, 23, 153-70.

CYR, M., CARON, M. G., JOHNSON, G. A. & LAAKSO, A. (2005) Magnetic resonance imaging at microscopic resolution reveals subtle morphological changes in a mouse model of dopaminergic hyperfunction. *Neuroimage*, 26, 83-90.

CZEH, B., MICHAELIS, T., WATANABE, T., FRAHM, J., DE BIURRUN, G., VAN KAMPEN, M., BARTOLOMUCCI, A. & FUCHS, E. (2001) Stress-induced changes in cerebral metabolites, hippocampal volume, and cell proliferation are prevented by antidepressant treatment with tianeptine. *Proc Natl Acad Sci U S A*, 98, 12796-801.

DAVIS, E., FENNOY, I., LARAQUE, D., KANEM, N., BROWN, G. & MITCHELL, J. (1992) Autism and developmental abnormalities in children with perinatal cocaine exposure. *J Natl Med Assoc*, 84, 315-9.

DE WIN, M. M., JAGER, G., BOOIJ, J., RENEMAN, L., SCHILT, T., LAVINI, C., OLABARRIAGA, S. D., DEN HEETEN, G. J. & VAN DEN BRINK, W. (2008) Sustained effects of ecstasy on the human brain: a prospective neuroimaging study in novel users. *Brain*.

DE WIN, M. M., JAGER, G., BOOIJ, J., RENEMAN, L., SCHILT, T., LAVINI, C., OLABARRIAGA, S. D., RAMSEY, N. F., HEETEN, G. J. & VAN DEN BRINK, W. (2008) Neurotoxic effects of ecstasy on the thalamus. *Br J Psychiatry*, 193, 289-96.

DE WIN, M. M. L., DE JEU, R. A. M., DE BRUIN, K., HABRAKEN, J. B. A., RENEMAN, L., BOOIJ, J. & DEN HEETEN, G. J. (2004) Validity of in vivo [<sup>123</sup>I][beta]-CIT SPECT in detecting MDMA-induced neurotoxicity in rats. 14, 185.

- DEBOY, C. A., ZHANG, J., DIKE, S., SHATS, I., JONES, M., REICH, D. S., MORI, S., NGUYEN, T., ROTHSTEIN, B., MILLER, R. H., GRIFFIN, J. T., KERR, D. A. & CALABRESI, P. A. (2007) High resolution diffusion tensor imaging of axonal damage in focal inflammatory and demyelinating lesions in rat spinal cord. *Brain*, 130, 2199-210.
- DREVETS, W. C., VIDEEN, T. O., PRICE, J. L., PRESKORN, S. H., CARMICHAEL, S. T. & RAICHEL, M. E. (1992) A functional anatomical study of unipolar depression. *J Neurosci*, 12, 3628-41.
- EASTON, N. & MARSDEN, C. A. (2006) Ecstasy: are animal data consistent between species and can they translate to humans? *J Psychopharmacol*, 20, 194-210.
- ELFVING, B., MADSEN, J. & KNUDSEN, G. M. (2007) Neuroimaging of the serotonin reuptake site requires high-affinity ligands. *Synapse*, 61, 882-8.
- ENNIS, C., KEMP, J. D. & COX, B. (1981) Characterisation of inhibitory 5-hydroxytryptamine receptors that modulate dopamine release in the striatum. *J Neurochem*, 36, 1515-20.
- ESAKI, T., COOK, M., SHIMOJI, K., MURPHY, D. L., SOKOLOFF, L. & HOLMES, A. (2005) Developmental disruption of serotonin transporter function impairs cerebral responses to whisker stimulation in mice. *Proc Natl Acad Sci U S A*, 102, 5582-7.
- EVANGELOU, N., KONZ, D., ESIRI, M. M., SMITH, S., PALACE, J. & MATTHEWS, P. M. (2001) Size-selective neuronal changes in the anterior optic pathways suggest a differential susceptibility to injury in multiple sclerosis. *Brain*, 124, 1813-20.
- FAN, J. B. & SKLAR, P. (2005) Meta-analysis reveals association between serotonin transporter gene STin2 VNTR polymorphism and schizophrenia. *Mol Psychiatry*, 10, 928-38, 891.
- FARDE, L., HALLDIN, C., MULLER, L., SUHARA, T., KARLSSON, P. & HALL, H. (1994) PET study of [<sup>11</sup>C]beta-CIT binding to monoamine transporters in the monkey and human brain. *Synapse*, 16, 93-103.

- FAVALE, E., RUBINO, V., MAINARDI, P., LUNARDI, G. & ALBANO, C. (1995) Anticonvulsant effect of fluoxetine in humans. *Neurology*, 45, 1926-7.
- FIELDS, R. D. (2008) White matter in learning, cognition and psychiatric disorders. *Trends Neurosci*, 31, 361-70.
- GARBERN, J. Y. (2007) Pelizaeus-Merzbacher disease: Genetic and cellular pathogenesis. *Cell Mol Life Sci*, 64, 50-65.
- GARDEN, G. A. & MOLLER, T. (2006) Microglia biology in health and disease. *J Neuroimmune Pharmacol*, 1, 127-37.
- GRIFFITHS, I., KLUGMANN, M., ANDERSON, T., THOMSON, C., VOUYIOUKLIS, D. & NAVE, K. A. (1998) Current concepts of PLP and its role in the nervous system. *Microsc Res Tech*, 41, 344-58.
- HAJSZAN, T., MACLUSKY, N. J. & LERANTH, C. (2005) Short-term treatment with the antidepressant fluoxetine triggers pyramidal dendritic spine synapse formation in rat hippocampus. *European Journal of Neuroscience*, 21, 1299-1303.
- HALLDIN, C., GULYAS, B., LANGER, O. & FARDE, L. (2001) Brain radioligands--state of the art and new trends. *Q J Nucl Med*, 45, 139-52.
- HARSAN, L. A., POULET, P., GUIGNARD, B., PARIZEL, N., SKOFF, R. P. & GHANDOUR, M. S. (2007) Astrocytic hypertrophy in dysmyelination influences the diffusion anisotropy of white matter. *J Neurosci Res*, 85, 935-44.
- HASAN, K. M., ALEXANDER, A. L. & NARAYANA, P. A. (2004) Does fractional anisotropy have better noise immunity characteristics than relative anisotropy in diffusion tensor MRI? An analytical approach. *Magn Reson Med*, 51, 413-7.
- HAZLETT, H. C., POE, M., GERIG, G., SMITH, R. G., PROVENZALE, J., ROSS, A., GILMORE, J. & PIVEN, J. (2005) Magnetic resonance imaging and head circumference study of brain size in autism: birth through age 2 years. *Arch Gen Psychiatry*, 62, 1366-76.

- HEILS, A., TEUFEL, A., PETRI, S., STOBER, G., RIEDERER, P., BENDEL, D. & LESCH, K. P. (1996) Allelic variation of human serotonin transporter gene expression. *J Neurochem*, 66, 2621-4.
- HEROLD, N., UEBELHACK, K., FRANKE, L., AMTHAUER, H., LUEDEMANN, L., BRUHN, H., FELIX, R., UEBELHACK, R. & PLOTKIN, M. (2006) Imaging of serotonin transporters and its blockade by citalopram in patients with major depression using a novel SPECT ligand [<sup>123</sup>I]-ADAM. *J Neural Transm*, 113, 659-70.
- HICKIE, I. B., NAISMITH, S. L., WARD, P. B., SCOTT, E. M., MITCHELL, P. B., SCHOFIELD, P. R., SCIMONE, A., WILHELM, K. & PARKER, G. (2007) Serotonin transporter gene status predicts caudate nucleus but not amygdala or hippocampal volumes in older persons with major depression. *J Affect Disord*, 98, 137-42.
- HOKFELT, T. & UNGERSTEDT, U. (1973) Specificity of 6-hydroxydopamine induced degeneration of central monoamine neurones: an electron and fluorescence microscopic study with special reference to intracerebral injection on the nigro-striatal dopamine system. *Brain Res*, 60, 269-97.
- HOPTMAN, M. J., NIERENBERG, J., BERTISCH, H. C., CATALANO, D., ARDEKANI, B. A., BRANCH, C. A. & DELISI, L. E. (2008) A DTI study of white matter microstructure in individuals at high genetic risk for schizophrenia. *Schizophr Res*.
- HORNAK, J. P. (1996-2008) The Basics of MRI.
- HUDSON, L. D. (2003) Pelizaeus-Merzbacher disease and spastic paraplegia type 2: two faces of myelin loss from mutations in the same gene. *J Child Neurol*, 18, 616-24.
- HUPPI, P. S., MAIER, S. E., PELED, S., ZIENTARA, G. P., BARNES, P. D., JOLESZ, F. A. & VOLPE, J. J. (1998) Microstructural development of human newborn cerebral white matter assessed in vivo by diffusion tensor magnetic resonance imaging. *Pediatr Res*, 44, 584-90.
- HWANG, L. C., CHANG, C. J., LIU, H. H., KAO, H. C., LEE, S. Y., JAN, M. L. & CHEN, C. C. (2007) Imaging the availability of serotonin transporter in rat brain with <sup>123</sup>I-ADAM and small-animal SPECT. *Nucl Med Commun*, 28, 615-21.

- J. MCAULIFFE, M., LALONDE, F. M., DELIA, M., GANDLER, W., CSAKY, K. & TRUS, B. L. (2001) Medical Image Processing, Analysis & Visualization in Clinical Research. *Proceedings of the Fourteenth IEEE Symposium on Computer-Based Medical Systems*. IEEE Computer Society.
- JAVITCH, J. A., BLAUSTEIN, R. O. & SNYDER, S. H. (1984) [3H]mazindol binding associated with neuronal dopamine and norepinephrine uptake sites. *Mol Pharmacol*, 26, 35-44.
- JITO, J., NAKASU, S., ITO, R., FUKAMI, T., MORIKAWA, S. & INUBUSHI, T. (2008) Maturational changes in diffusion anisotropy in the rat corpus callosum: Comparison with quantitative histological evaluation. *J Magn Reson Imaging*, 28, 847-854.
- JOHANSEN-BERG, H. & BEHRENS, T. E. J. (2009) *Diffusion MRI*, Academic Press.
- JOHNSON, V. P., CARPENTER, N. J. & KELTS, K. A. (1991) Pelizaeus-Merzbacher disease: clinical and DNA-linkage study of an extended family. *Am J Med Genet*, 41, 355-61.
- JONES, H. E., RUSCIO, M. A., KEYSER, L. A., GONZALEZ, C., BILLACK, B., ROWE, R., HANCOCK, C., LAMBERT, K. G. & KINSLEY, C. H. (1997) Prenatal stress alters the size of the rostral anterior commissure in rats. *Brain Res Bull*, 42, 341-6.
- JUDD, L. L., PAULUS, M. P., WELLS, K. B. & RAPAPORT, M. H. (1996) Socioeconomic burden of subsyndromal depressive symptoms and major depression in a sample of the general population. *Am J Psychiatry*, 153, 1411-7.
- JUDENHOFER, M. S., CATANA, C., SWANN, B. K., SIEGEL, S. B., JUNG, W. I., NUTT, R. E., CHERRY, S. R., CLAUSSEN, C. D. & PICHLER, B. J. (2007) PET/MR images acquired with a compact MR-compatible PET detector in a 7-T magnet. *Radiology*, 244, 807-14.
- KALUEFF, A. V., GALLAGHER, P. S. & MURPHY, D. L. (2006) Are serotonin transporter knockout mice 'depressed'? hypoactivity but no anhedonia. *Neuroreport*, 17, 1347-51.

- KANDEL, E. R., SCHWARTZ, J. H. & JESSELL, T. M. (2000) *Principles of Neural Science*, New York, McGraw-Hill.
- KELLER, T. A., KANA, R. K. & JUST, M. A. (2007) A developmental study of the structural integrity of white matter in autism. *Neuroreport*, 18, 23-7.
- KELLY, P. A., RITCHIE, I. M., QUATE, L., MCBEAN, D. E. & OLVERMAN, H. J. (2002) Functional consequences of perinatal exposure to 3,4-methylenedioxymethamphetamine in rat brain. *Br J Pharmacol*, 137, 963-70.
- KIES, M. W. (1985) Species-specificity and localization of encephalitogenic sites in myelin basic protein. *Springer Semin Immunopathol*, 8, 295-303.
- KIM, J. H., BUDDE, M. D., LIANG, H. F., KLEIN, R. S., RUSSELL, J. H., CROSS, A. H. & SONG, S. K. (2006) Detecting axon damage in spinal cord from a mouse model of multiple sclerosis. *Neurobiol Dis*, 21, 626-32.
- KISH, S. J., FURUKAWA, Y., CHANG, L. J., TONG, J., GINOVART, N., WILSON, A., HOULE, S. & MEYER, J. H. (2005) Regional distribution of serotonin transporter protein in postmortem human brain: is the cerebellum a SERT-free brain region? *Nucl Med Biol*, 32, 123-8.
- KOLBE, S., CHAPMAN, C., NGUYEN, T., BAJRASZEWSKI, C., JOHNSTON, L., KEAN, M., MITCHELL, P., PAINE, M., BUTZKUEVEN, H., KILPATRICK, T. & EGAN, G. (2009) Optic nerve diffusion changes and atrophy jointly predict visual dysfunction after optic neuritis. *Neuroimage*, 45, 679-86.
- KOSOFKY, B. E. & MOLLIVER, M. E. (1987) The serotonergic innervation of cerebral cortex: different classes of axon terminals arise from dorsal and median raphe nuclei. *Synapse*, 1, 153-68.
- KOVACEVIC, N., HENDERSON, J. T., CHAN, E., LIFSHITZ, N., BISHOP, J., EVANS, A. C., HENKELMAN, R. M. & CHEN, X. J. (2005) A three-dimensional MRI atlas of the mouse brain with estimates of the average and variability. *Cereb Cortex*, 15, 639-45.

- KUGAYA, A., SENECA, N. M., SNYDER, P. J., WILLIAMS, S. A., MALISON, R. T., BALDWIN, R. M., SEIBYL, J. P. & INNIS, R. B. (2003) Changes in human in vivo serotonin and dopamine transporter availabilities during chronic antidepressant administration. *Neuropsychopharmacology*, 28, 413-20.
- KUHLMANN, T., LINGFELD, G., BITSCH, A., SCHUCHARDT, J. & BRUCK, W. (2002) Acute axonal damage in multiple sclerosis is most extensive in early disease stages and decreases over time. *Brain*, 125, 2202-12.
- LAASONEN-BALK, T., KUIKKA, J., VIINAMAKI, H., HUSSO-SAASTAMOINEN, M., LEHTONEN, J. & TIIHONEN, J. (1999) Striatal dopamine transporter density in major depression. *Psychopharmacology (Berl)*, 144, 282-5.
- LAASONEN-BALK, T., VIINAMAKI, H., KUIKKA, J. T., HUSSO-SAASTAMOINEN, M., LEHTONEN, J. & TIIHONEN, J. (2004) 123I-beta-CIT binding and recovery from depression. A six-month follow-up study. *Eur Arch Psychiatry Clin Neurosci*, 254, 152-5.
- LAUKKA, J., MAKKI, M. & GARBERN, J. (2006) Diffusion Tensor Imaging Study of Pelizaeus-Merzbacher Disease. *ISMRM 14th SCIENTIFIC MEETING & EXHIBITION*. Seattle, Washington, USA.
- LEE, H. S., KIM, M. A., VALENTINO, R. J. & WATERHOUSE, B. D. (2003) Glutamatergic afferent projections to the dorsal raphe nucleus of the rat. *Brain Res*, 963, 57-71.
- LEW, R., SABOL, K. E., CHOU, C., VOSMER, G. L., RICHARDS, J. & SEIDEN, L. S. (1996) Methylenedioxymethamphetamine-induced serotonin deficits are followed by partial recovery over a 52-week period. Part II: Radioligand binding and autoradiography studies. *J Pharmacol Exp Ther*, 276, 855-865.
- LI, C., SUN, X., ZOU, K., YANG, H., HUANG, X., WANG, Y., LUI, S., LI, D., ZOU, L. & CHEN, H. (2007) Voxel based Analysis of DTI in Depression Patients. *International Journal of Magnetic Resonance Imaging*, 01, 043-048.

- LI, L., MA, N., LI, Z., TAN, L., LIU, J., GONG, G., SHU, N., HE, Z., JIANG, T. & XU, L. (2007) Prefrontal white matter abnormalities in young adult with major depressive disorder: a diffusion tensor imaging study. *Brain Res*, 1168, 124-8.
- LI, S., VARGA, V., SIK, A. & KOCSIS, B. (2005) GABAergic control of the ascending input from the median raphe nucleus to the limbic system. *J Neurophysiol*, 94, 2561-74.
- LIEDTKE, W., EDELMANN, W., CHIU, F. C., KUCHERLAPATI, R. & RAINE, C. S. (1998) Experimental autoimmune encephalomyelitis in mice lacking glial fibrillary acidic protein is characterized by a more severe clinical course and an infiltrative central nervous system lesion. *Am J Pathol*, 152, 251-9.
- LIM, K. O., WOZNIAK, J. R., MUELLER, B. A., FRANC, D. T., SPECKER, S. M., RODRIGUEZ, C. P., SILVERMAN, A. B. & ROTROSEN, J. P. (2008) Brain macrostructural and microstructural abnormalities in cocaine dependence. *Drug Alcohol Depend*, 92, 164-72.
- LIRA, A., ZHOU, M., CASTANON, N., ANSORGE, M. S., GORDON, J. A., FRANCIS, J. H., BRADLEY-MOORE, M., LIRA, J., UNDERWOOD, M. D. & ARANGO, V. (2003) Altered depression-related behaviors and functional changes in the dorsal raphe nucleus of serotonin transporter-deficient mice. 54, 960.
- LIU, H., LI, L., HAO, Y., CAO, D., XU, L., ROHRBAUGH, R., XUE, Z., HAO, W., SHAN, B. & LIU, Z. (2008) Disrupted white matter integrity in heroin dependence: a controlled study utilizing diffusion tensor imaging. *Am J Drug Alcohol Abuse*, 34, 562-75.
- LIVY, D. J., SCHALOMON, P. M., ROY, M., ZACHARIAS, M. C., PIMENTA, J., LENT, R. & WAHLSTEN, D. (1997) Increased axon number in the anterior commissure of mice lacking a corpus callosum. *Exp Neurol*, 146, 491-501.
- LIVY, D. J. & WAHLSTEN, D. (1991) Tests of Genetic Allelism between Four Inbred Mouse Strains with Absent Corpus Callosum. *J Hered*, 82, 459-464.
- LLEDO, P. M., ALONSO, M. & GRUBB, M. S. (2006) Adult neurogenesis and functional plasticity in neuronal circuits. *Nat Rev Neurosci*, 7, 179-93.

- LOENING, A. M. & GAMBHIR, S. S. (2003) AMIDE: a free software tool for multimodality medical image analysis. *Mol Imaging*, 2, 131-7.
- MA, Y., HOF, P. R., GRANT, S. C., BLACKBAND, S. J., BENNETT, R., SLATEST, L., MCGUIGAN, M. D. & BENVENISTE, H. (2005) A three-dimensional digital atlas database of the adult C57BL/6J mouse brain by magnetic resonance microscopy. *Neuroscience*, 135, 1203-15.
- MALBERG, J. E., EISCH, A. J., NESTLER, E. J. & DUMAN, R. S. (2000) Chronic Antidepressant Treatment Increases Neurogenesis in Adult Rat Hippocampus. *J. Neurosci.*, 20, 9104-9110.
- MALISON, R. T., MCCANCE, E., CARPENTER, L. L., BALDWIN, R. M., SEIBYL, J. P., PRICE, L. H., KOSTEN, T. R. & INNIS, R. B. (1998) [123I]beta-CIT SPECT imaging of dopamine transporter availability after mazindol administration in human cocaine addicts. *Psychopharmacology (Berl)*, 137, 321-5.
- MCGREGOR, I. S., CLEMENS, K. J., VAN DER PLASSE, G., LI, K. M., HUNT, G. E., CHEN, F. & LAWRENCE, A. J. (2003) Increased anxiety 3 months after brief exposure to MDMA ("Ecstasy") in rats: association with altered 5-HT transporter and receptor density. *Neuropsychopharmacology*, 28, 1472-84.
- MEYER, J. H. (2007) Imaging the serotonin transporter during major depressive disorder and antidepressant treatment. *J Psychiatry Neurosci*, 32, 86-102.
- MOELLER, F. G., HASAN, K. M., STEINBERG, J. L., KRAMER, L. A., DOUGHERTY, D. M., SANTOS, R. M., VALDES, I., SWANN, A. C., BARRATT, E. S. & NARAYANA, P. A. (2005) Reduced anterior corpus callosum white matter integrity is related to increased impulsivity and reduced discriminability in cocaine-dependent subjects: diffusion tensor imaging. *Neuropsychopharmacology*, 30, 610-7.
- MOELLER, F. G., STEINBERG, J. L., LANE, S. D., BUZBY, M., SWANN, A. C., HASAN, K. M., KRAMER, L. A. & NARAYANA, P. A. (2007) Diffusion tensor imaging in MDMA users and controls: association with decision making. *Am J Drug Alcohol Abuse*, 33, 777-89.

- MORIARTY, L. J. & BORGES, R. B. (2001) An oscillating extracellular voltage gradient reduces the density and influences the orientation of astrocytes in injured mammalian spinal cord. *J Neurocytol*, 30, 45-57.
- MURPHY, C. F., GUNNING-DIXON, F. M., HOPTMAN, M. J., LIM, K. O., ARDEKANI, B., SHIELDS, J. K., HRABE, J., KANELLOPOULOS, D., SHANMUGHAM, B. R. & ALEXOPOULOS, G. S. (2007) White-Matter Integrity Predicts Stroop Performance in Patients with Geriatric Depression. *Biol Psychiatry*, 61, 1007-10.
- MURPHY, D. L., LERNER, A., RUDNICK, G. & LESCH, K. P. (2004) Serotonin transporter: gene, genetic disorders, and pharmacogenetics. *Mol Interv*, 4, 109-23.
- MURPHY, D. L. & LESCH, K. P. (2008) Targeting the murine serotonin transporter: insights into human neurobiology. *Nat Rev Neurosci*, 9, 85-96.
- NAIR, G., TANAHASHI, Y., LOW, H. P., BILLINGS-GAGLIARDI, S., SCHWARTZ, W. J. & DUONG, T. Q. (2005) Myelination and long diffusion times alter diffusion-tensor-imaging contrast in myelin-deficient shiverer mice. 28, 165.
- NAISMITH, R. T., XU, J., TUTLAM, N. T., SNYDER, A., BENZINGER, T., SHIMONY, J., SHEPHERD, J., TRINKAUS, K., CROSS, A. H. & SONG, S. K. (2009) Disability in optic neuritis correlates with diffusion tensor-derived directional diffusivities. *Neurology*, 72, 589-594.
- NARAYANA, P. A., AHOBILA-VAJJULA, P., RAMU, J., HERRERA, J., STEINBERG, J. L. & MOELLER, F. G. (2009) Diffusion tensor imaging of cocaine-treated rodents. *Psychiatry Res*, 171, 242-51.
- NEUMEYER, J. L., TAMAGNAN, G., WANG, S., GAO, Y., MILIUS, R. A., KULA, N. S. & BALDESSARINI, R. J. (1996) N-substituted analogs of 2 beta-carbomethoxy-3 beta-(4'-iodophenyl)tropane (beta-CIT) with selective affinity to dopamine or serotonin transporters in rat forebrain. *J Med Chem*, 39, 543-8.
- NEWBERG, A. B., AMSTERDAM, J. D., WINTERING, N., PLOESSL, K., SWANSON, R. L., SHULTS, J. & ALAVI, A. (2005) 123I-ADAM binding to serotonin transporters in

- patients with major depression and healthy controls: a preliminary study. *J Nucl Med*, 46, 973-7.
- NICHOLS, T. E. & HOLMES, A. P. (2002) Nonparametric permutation tests for functional neuroimaging: a primer with examples. *Hum Brain Mapp*, 15, 1-25.
- NOBUHARA, K., OKUGAWA, G., SUGIMOTO, T., MINAMI, T., TAMAGAKI, C., TAKASE, K., SAITO, Y., SAWADA, S. & KINOSHITA, T. (2006) Frontal white matter anisotropy and symptom severity of late-life depression: a magnetic resonance diffusion tensor imaging study. *J Neurol Neurosurg Psychiatry*, 77, 120-2.
- NOLF, E. (2003) XMedCon - An open-source medical image conversion toolkit. *European Journal of Nuclear Medicine*, 30, 246.
- O'HEARN, E., BATTAGLIA, G., DE SOUZA, E. B., KUHAR, M. J. & MOLLIVER, M. E. (1988) Methylenedioxyamphetamine (MDA) and methylenedioxymethamphetamine (MDMA) cause selective ablation of serotonergic axon terminals in forebrain: immunocytochemical evidence for neurotoxicity. *J Neurosci*, 8, 2788-803.
- ONO, J., HARADA, K., MANO, T., SAKURAI, K. & OKADA, S. (1997) Differentiation of dys- and demyelination using diffusional anisotropy. *Pediatr Neurol*, 16, 63-6.
- ONO, J., HARADA, K., SAKURAI, K., KODAKA, R., SHIMIDZU, N., TANAKA, J., NAGAI, T. & OKADA, S. (1994) Mr Diffusion Imaging In Pelizaeus-Merzbacher Disease. *Brain & Development*, 16, 219-223.
- ONO, J., HARADA, K., TAKAHASHI, M., MAEDA, M., IKENAKA, K., SAKURAI, K., SAKAI, N., KAGAWA, T., FRITZ-ZIEROTH, B., NAGAI, T. & ET AL. (1995) Differentiation between dysmyelination and demyelination using magnetic resonance diffusional anisotropy. *Brain Res*, 671, 141-8.
- OSHIO, K., BINDER, D. K., YANG, B., SCHECTER, S., VERKMAN, A. S. & MANLEY, G. T. (2004) Expression of aquaporin water channels in mouse spinal cord. *Neuroscience*, 127, 685-93.

- PAXINOS, G. & FRANKLIN, K. B. J. (2001) *The Mouse Brain In Stereotaxic Coordinates*, Academic Press.
- PAXINOS, G. & WATSON, C. (1998) *The Rat Brain In Stereotaxic Coordinates*, Academic Press.
- PEREMANS, K., GOETHALS, I., DE VOS, F., DOBBELEIR, A., HAM, H., VAN BREE, H., VAN HEERINGEN, C. & AUDENAERT, K. (2006) Serotonin transporter and dopamine transporter imaging in the canine brain. *Nucl Med Biol*, 33, 907-13.
- PERSICO, A. M., BALDI, A., DELL'ACQUA, M. L., MOESSNER, R., MURPHY, D. L., LESCH, K. P. & KELLER, F. (2003) Reduced programmed cell death in brains of serotonin transporter knockout mice. *Neuroreport*, 14, 341-4.
- PIERPAOLI, C., BARNETT, A., PAJEVIC, S., CHEN, R., PENIX, L. R., VIRTA, A. & BASSER, P. (2001) Water diffusion changes in Wallerian degeneration and their dependence on white matter architecture. *Neuroimage*, 13, 1174-85.
- PIERPAOLI, C. & BASSER, P. J. (1996) Toward a quantitative assessment of diffusion anisotropy. *Magn Reson Med*, 36, 893-906.
- PIERPAOLI, C., JEZZARD, P., BASSER, P. J., BARNETT, A. & DI CHIRO, G. (1996) Diffusion tensor MR imaging of the human brain. *Radiology*, 201, 637-48.
- PIRKER, W., ASENBAUM, S., KASPER, S., WALTER, H., ANGELBERGER, P., KOCH, G., POZZERA, A., DEECKE, L., PODREKA, I. & BRUCKE, T. (1995) beta-CIT SPECT demonstrates blockade of 5HT-uptake sites by citalopram in the human brain in vivo. *J Neural Transm Gen Sect*, 100, 247-56.
- POGARELL, O., KOCH, W., SCHAAFF, N., POPPERL, G., MULERT, C., JUCKEL, G., MOLLER, H. J., HEGERL, U. & TATSCH, K. (2008) [123I] ADAM brainstem binding correlates with the loudness dependence of auditory evoked potentials. *Eur Arch Psychiatry Clin Neurosci*, 258, 40-7.
- POGARELL, O., POEPPERL, G., MULERT, C., HAMANN, C., SADOWSKY, N., RIEDEL, M., MOELLER, H. J., HEGERL, U. & TATSCH, K. (2005) SERT and DAT

- availabilities under citalopram treatment in obsessive-compulsive disorder (OCD). *Eur Neuropsychopharmacol*, 15, 521-4.
- POSENER, J. A., WANG, L., PRICE, J. L., GADO, M. H., PROVINCE, M. A., MILLER, M. I., BABB, C. M. & CSERNANSKY, J. G. (2003) High-dimensional mapping of the hippocampus in depression. *Am J Psychiatry*, 160, 83-9.
- QUINLIVAN, M., MATTNER, F., PAPAZIAN, V., ZHOU, J., KATSIFIS, A., EMOND, P., CHALON, S., KOZIKOWSKI, A., GUILLOTEAU, D. & KASSIOU, M. (2003) Synthesis and evaluation of iodine-123 labelled tricyclic tropanes as radioligands for the serotonin transporter. *Nucl Med Biol*, 30, 741-6.
- QUITKIN, F. M., MCGRATH, P. J., STEWART, J. W., TAYLOR, B. P. & KLEIN, D. F. (1996) Can the effects of antidepressants be observed in the first two weeks of treatment? *Neuropsychopharmacology*, 15, 390-4.
- READHEAD, C., SCHNEIDER, A., GRIFFITHS, I. & NAVE, K. A. (1994) Premature arrest of myelin formation in transgenic mice with increased proteolipid protein gene dosage. *Neuron*, 12, 583-95.
- RENEMAN, L., BOOIJ, J., HABRAKEN, J. B., DE BRUIN, K., HATZIDIMITRIOU, G., DEN HEETEN, G. J. & RICAURTE, G. A. (2002) Validity of [<sup>123</sup>I]beta-CIT SPECT in detecting MDMA-induced serotonergic neurotoxicity. *Synapse*, 46, 199-205.
- RICAURTE, G. A., YUAN, J. & MCCANN, U. D. (2000) (+/-)3,4-Methylenedioxymethamphetamine ('Ecstasy')-induced serotonin neurotoxicity: studies in animals. *Neuropsychobiology*, 42, 5-10.
- ROOSEDAAL, S. D., GEURTS, J. J., VRENKEN, H., HULST, H. E., COVER, K. S., CASTELIJNS, J. A., POWWELS, P. J. & BARKHOF, F. (2009) Regional DTI differences in multiple sclerosis patients. *Neuroimage*, 44, 1397-403.
- ROOT-BERNSTEIN, R. S. (1983) The structure of a serotonin and LSD binding site of myelin basic protein. 100, 373.

- ROOT-BERNSTEIN, R. S. & WESTALL, F. C. (1984) Serotonin binding sites. I. Structures of sites on myelin basic protein, LHRH, MSH, ACTH, interferon, serum albumin, ovalbumin and red pigment concentrating hormone. *Brain Res Bull*, 12, 425-36.
- RORDEN, C. & BRETT, M. (2000) Stereotaxic display of brain lesions. *Behav Neurol*, 12, 191-200.
- RUHE, H. G., OOTEMAN, W., BOOIJ, J., MICHEL, M. C., MOETON, M., BAAS, F. & SCHENE, A. H. (2008) Serotonin transporter gene promoter polymorphisms modify the association between paroxetine serotonin transporter occupancy and clinical response in major depressive disorder. *Pharmacogenet Genomics*.
- RUSCH, B. D., ABERCROMBIE, H. C., OAKES, T. R., SCHAEFER, S. M. & DAVIDSON, R. J. (2001) Hippocampal morphometry in depressed patients and control subjects: relations to anxiety symptoms. *Biol Psychiatry*, 50, 960-4.
- SAAKOV, B. A., KHORUZHAIA, T. A. & BARDAKHCH'IAN, E. A. (1977) [Ultrastructural mechanisms of serotonin demyelination]. *Biull Eksp Biol Med*, 83, 606-10.
- SACHER, J., ASENBAUM, S., KLEIN, N., GEISS-GRANADIA, T., MOSSAHEB, N., POETZI, C., ATTARBASCHI, T., LANZENBERGER, R., SPINDELEGGER, C., RABAS, A., HEINZE, G., DUDCZAK, R., KASPER, S. & TAUSCHER, J. (2007) Binding kinetics of <sup>123</sup>I[ADAM] in healthy controls: a selective SERT radioligand. *Int J Neuropsychopharmacol*, 10, 211-8.
- SACKEIM, H. A. (2001) The definition and meaning of treatment-resistant depression. *J Clin Psychiatry*, 62 Suppl 16, 10-7.
- SAKAI, K., SALVERT, D., TOURET, M. & JOUVET, M. (1977) Afferent connections of the nucleus raphe dorsalis in the cat as visualized by the horseradish peroxidase technique. *Brain Res*, 137, 11-35.
- SAKSENA, S., HUSAIN, N., DAS, V., PRADHAN, M., TRIVEDI, R., SRIVASTAVA, S., MALIK, G. K., RATHORE, R. K., SARMA, M., PANDEY, C. M. & GUPTA, R. K. (2008) Diffusion tensor imaging in the developing human cerebellum with histologic correlation. *Int J Dev Neurosci*, 26, 705-11.

SATEL, S. L., KRYSTAL, J. H., DELGADO, P. L., KOSTEN, T. R. & CHARNEY, D. S. (1995) Tryptophan depletion and attenuation of cue-induced craving for cocaine. *American Journal of Psychiatry*, 152, 778-783.

SCHMIDT, C. J., WU, L. & LOVENBERG, W. (1986) Methylenedioxymethamphetamine: a potentially neurotoxic amphetamine analogue. *Eur J Pharmacol*, 124, 175-8.

SCHMIERER, K., WHEELER-KINGSHOTT, C. A., BOULBY, P. A., SCARAVILLI, F., ALTMANN, D. R., BARKER, G. J., TOFTS, P. S. & MILLER, D. H. (2007) Diffusion tensor imaging of post mortem multiple sclerosis brain. *Neuroimage*, 35, 467-77.

SCHNABEL, J. A., RUECKERT, D., QUIST, M., BLACKALL, J. M., CASTELLANO SMITH, A. D., HARTKENS, T., PENNEY, G. P., HALL, W. A., LIU, H., TRUWIT, C. L., GERRITSEN, F. A., HILL, D. L. G. & HAWKES, D. J. (2001) A generic framework for non-rigid registration based on non-uniform multi-level free-form deformations. *Int. Conf. on Medical Image Computing and Computer-Assisted Intervention (MICCAI '01)*. Utrecht, NL.

SCHOEMAKER, R. C., VAN GERVEN, J. M. & COHEN, A. F. (1998) Estimating potency for the Emax-model without attaining maximal effects. *J Pharmacokinetic Biopharm*, 26, 581-93.

SCHWARTZ, E. D., COOPER, E. T., FAN, Y., JAWAD, A. F., CHIN, C. L., NISSANOV, J. & HACKNEY, D. B. (2005) MRI diffusion coefficients in spinal cord correlate with axon morphometry. *Neuroreport*, 16, 73-6.

SCHWARTZ, E. D., DUDA, J., SHUMSKY, J. S., COOPER, E. T. & GEE, J. (2005) Spinal cord diffusion tensor imaging and fiber tracking can identify white matter tract disruption and glial scar orientation following lateral funiculotomy. *J Neurotrauma*, 22, 1388-98.

SEGAL, M. (1975) Physiological and pharmacological evidence for a serotonergic projection to the hippocampus. *Brain Res*, 94, 115-131.

- SHANG, Y., GIBBS, M. A., MAREK, G. J., STIGER, T., BURSTEIN, A. H., MAREK, K., SEIBYL, J. P. & ROGERS, J. F. (2007) Displacement of serotonin and dopamine transporters by venlafaxine extended release capsule at steady state: a [<sup>123</sup>I]2beta-carbomethoxy-3beta-(4-iodophenyl)-tropane single photon emission computed tomography imaging study. *J Clin Psychopharmacol*, 27, 71-5.
- SHELIN, Y. I., SANGHAVI, M., MINTUN, M. A. & GADO, M. H. (1999) Depression duration but not age predicts hippocampal volume loss in medically healthy women with recurrent major depression. *J Neurosci*, 19, 5034-43.
- SHELIN, Y. I., WANG, P. W., GADO, M. H., CSERNANSKY, J. G. & VANNIER, M. W. (1996) Hippocampal atrophy in recurrent major depression. *Proc Natl Acad Sci U S A*, 93, 3908-13.
- SHERRIFF, F. E., BRIDGES, L. R. & SIVALOGANATHAN, S. (1994) Early detection of axonal injury after human head trauma using immunocytochemistry for beta-amyloid precursor protein. *Acta Neuropathol*, 87, 55-62.
- SHIGEMATSU, K., MCGEER, P. L., WALKER, D. G., ISHII, T. & MCGEER, E. G. (1992) Reactive microglia/macrophages phagocytose amyloid precursor protein produced by neurons following neural damage. *J Neurosci Res*, 31, 443-53.
- SIEGEL, G. J., ALBERS, R. W., BRADY, S. & PRICE, D. (2006) *Basic Neurochemistry: Molecular, Cellular and Medical Aspects*, Philadelphia, Lippincott–Raven.
- SIZONENKO, S. V., CAMM, E. J., GARBOW, J. R., MAIER, S. E., INDER, T. E., WILLIAMS, C. E., NEIL, J. J. & HUPPI, P. S. (2007) Developmental changes and injury induced disruption of the radial organization of the cortex in the immature rat brain revealed by in vivo diffusion tensor MRI. *Cereb Cortex*, 17, 2609-17.
- SLIFSTEIN, M. (2008) Revisiting an old issue: the discrepancy between tissue ratio-derived binding parameters and kinetic modeling-derived parameters after a bolus of the serotonin transporter radioligand <sup>123</sup>I-ADAM. *J Nucl Med*, 49, 176-8.

- SMERALDI, E., ZANARDI, R., BENEDETTI, F., DI BELLA, D., PEREZ, J. & CATALANO, M. (1998) Polymorphism within the promoter of the serotonin transporter gene and antidepressant efficacy of fluvoxamine. *Mol Psychiatry*, 3, 508-11.
- SMITH, S. M., JENKINSON, M., JOHANSEN-BERG, H., RUECKERT, D., NICHOLS, T. E., MACKAY, C. E., WATKINS, K. E., CICCARELLI, O., CADER, M. Z., MATTHEWS, P. M. & BEHRENS, T. E. (2006) Tract-based spatial statistics: Voxelwise analysis of multi-subject diffusion data. *Neuroimage*.
- SMITH, S. M., JENKINSON, M., WOOLRICH, M. W., BECKMANN, C. F., BEHRENS, T. E. J., JOHANSEN-BERG, H., BANNISTER, P. R., DE LUCA, M., DROBNJAK, I. & FLITNEY, D. E. (2004) Advances in functional and structural MR image analysis and implementation as FSL. *Mathematics in Brain Imaging*, 23, S208.
- SOLENOV, E. I., VETRIVEL, L., OSHIO, K., MANLEY, G. T. & VERKMAN, A. S. (2002) Optical measurement of swelling and water transport in spinal cord slices from aquaporin null mice. *J Neurosci Methods*, 113, 85-90.
- SONG, S.-K., YOSHINO, J., LE, T. Q., LIN, S.-J., SUN, S.-W., CROSS, A. H. & ARMSTRONG, R. C. (2005) Demyelination increases radial diffusivity in corpus callosum of mouse brain. 26, 132.
- SONG, S. K., SUN, S. W., RAMSBOTTOM, M. J., CHANG, C., RUSSELL, J. & CROSS, A. H. (2002) Dysmyelination revealed through MRI as increased radial (but unchanged axial) diffusion of water. *Neuroimage*, 17, 1429-36.
- STEJSKAL, E. O. & TANNER, J. E. (1965) Spin Diffusion Measurements: Spin Echoes in the Presence of a Time-Dependent Field Gradient. *The Journal of Chemical Physics*, 42, 288-292.
- SUN, S. W., LIANG, H. F., SCHMIDT, R. E., CROSS, A. H. & SONG, S. K. (2007) Selective vulnerability of cerebral white matter in a murine model of multiple sclerosis detected using diffusion tensor imaging. *Neurobiol Dis*, 28, 30-8.

- SUN, S. W., NEIL, J. J. & SONG, S. K. (2003) Relative indices of water diffusion anisotropy are equivalent in live and formalin-fixed mouse brains. *Magn Reson Med*, 50, 743-8.
- TAKAHASHI, M., HACKNEY, D. B., ZHANG, G., WEHRLI, S. L., WRIGHT, A. C., O'BRIEN, W. T., UEMATSU, H., WEHRLI, F. W. & SELZER, M. E. (2002) Magnetic resonance microimaging of intraaxonal water diffusion in live excised lamprey spinal cord. *Proc Natl Acad Sci U S A*, 99, 16192-6.
- TAUSCHER, J., PIRKER, W., DE ZWAAN, M., ASENBAUM, S., BRUCKE, T. & KASPER, S. (1999) In vivo visualization of serotonin transporters in the human brain during fluoxetine treatment. *Eur Neuropsychopharmacol*, 9, 177-9.
- TAYLOR, W. D., KUCHIBHATLA, M., PAYNE, M. E., MACFALL, J. R., SHELINE, Y. I., KRISHNAN, K. R. & DORAISWAMY, P. M. (2008) Frontal white matter anisotropy and antidepressant remission in late-life depression. *PLoS ONE*, 3, e3267.
- THEODORE, W. H. (2003) Does Serotonin Play a Role in Epilepsy? *Epilepsy Curr*, 3, 173-177.
- TRAPP, B. D. & NAVE, K. A. (2008) Multiple sclerosis: an immune or neurodegenerative disorder? *Annu Rev Neurosci*, 31, 247-69.
- TYSZKA, J. M., READHEAD, C., BEARER, E. L., PAUTLER, R. G. & JACOBS, R. E. (2006) Statistical diffusion tensor histology reveals regional dysmyelination effects in the shiverer mouse mutant. *Neuroimage*, 29, 1058-65.
- UPTON, A. L., RAVARY, A., SALICHON, N., MOESSNER, R., LESCH, K. P., HEN, R., SEIF, I. & GASPAR, P. (2002) Lack of 5-HT(1B) receptor and of serotonin transporter have different effects on the segregation of retinal axons in the lateral geniculate nucleus compared to the superior colliculus. *Neuroscience*, 111, 597-610.
- VARGA, V., KEKESI, A., JUHASZ, G. & KOCSIS, B. (1998) Reduction of the extracellular level of glutamate in the median raphe nucleus associated with hippocampal theta activity in the anaesthetized rat. *Neuroscience*, 84, 49-57.

- VERMA, R., MORI, S., SHEN, D., YAROWSKY, P., ZHANG, J. & DAVATZIKOS, C. (2005) Spatiotemporal maturation patterns of murine brain quantified by diffusion tensor MRI and deformation-based morphometry. *Proc Natl Acad Sci U S A*, 102, 6978-83.
- VOIGT, T. (1989) Development of glial cells in the cerebral wall of ferrets: direct tracing of their transformation from radial glia into astrocytes. *J Comp Neurol*, 289, 74-88.
- VONEIDA, T. J., VARDARIS, R. M., FISH, S. E. & REIHELD, C. T. (1981) The origin of the hippocampal commissure in the rat. *Anat Rec*, 201, 91-103.
- WAHLSTEN, D., CRABBE, J. C. & DUDEK, B. C. (2001) Behavioural testing of standard inbred and 5HT(1B) knockout mice: implications of absent corpus callosum. *Behav Brain Res*, 125, 23-32.
- WAHLSTEN, D., METTEN, P. & CRABBE, J. C. (2003) Survey of 21 inbred mouse strains in two laboratories reveals that BTBR T/+ tf/tf has severely reduced hippocampal commissure and absent corpus callosum. 971, 47.
- WANG, W., STEWARD, C. E. & DESMOND, P. M. (2008) Diffusion Tensor Imaging in Glioblastoma Multiforme and Brain Metastases: The Role of p, q, L, and Fractional Anisotropy. *AJNR Am J Neuroradiol*.
- WATANABE, Y., GOULD, E. & MCEWEN, B. S. (1992) Stress induces atrophy of apical dendrites of hippocampal CA3 pyramidal neurons. *Brain Res*, 588, 341-5.
- WHITAKER-AZMITIA, P. M. (2005) Behavioral and cellular consequences of increasing serotonergic activity during brain development: a role in autism? 23, 75.
- WILDE, E. A., BIGLER, E. D., HAIDER, J. M., CHU, Z., LEVIN, H. S., LI, X. & HUNTER, J. V. (2006) Vulnerability of the anterior commissure in moderate to severe pediatric traumatic brain injury. *J Child Neurol*, 21, 769-76.
- WOODS, R. P., GRAFTON, S. T., HOLMES, C. J., CHERRY, S. R. & MAZZIOTTA, J. C. (1998) Automated image registration: I. General methods and intrasubject, intramodality validation. *J Comput Assist Tomogr*, 22, 139-52.

- WORLD\_HEALTH\_ORGANISATION (2001) The World health report: 2001: Mental health: new understanding, new hope.
- XU, D., HAO, X., BANSAL, R., PLESSEN, K. J., GENG, W., HUGDAHL, K. & PETERSON, B. S. (2007) Unifying the analyses of anatomical and diffusion tensor images using volume-preserved warping. *J Magn Reson Imaging*, 25, 612-24.
- YANG, Q., HUANG, X., HONG, N. & YU, X. (2007) White matter microstructural abnormalities in late-life depression. *Int Psychogeriatr*, 19, 757-66.
- YANG, Y. K., YAO, W. J., YEH, T. L., LEE, I. H., CHEN, K. C. & LU, R. B. (2007) Association between serotonin transporter availability and hostility scores in healthy volunteers - a single photon emission computed tomography study with [(123)I] ADAM. *Psychiatry Res*, 154, 281-4.
- YE, X. X., HWANG, J. J., HSIEH, J. F., CHEN, J. C., CHOU, Y. T., TU, K. Y., WEY, S. P. & TING, G. (2004) In vivo quantification by SPECT of [123I] ADAM bound to serotonin transporters in the brains of rabbits. *Nucl Med Biol*, 31, 995-1003.
- YONG, V. W. (1998) Response of astrocytes and oligodendrocytes to injury. *Mental Retardation and Developmental Disabilities Research Reviews*, 4, 193-199.
- YU, Y. W., TSAI, S. J., CHEN, T. J., LIN, C. H. & HONG, C. J. (2002) Association study of the serotonin transporter promoter polymorphism and symptomatology and antidepressant response in major depressive disorders. *Mol Psychiatry*, 7, 1115-9.
- ZAIDI, H., RUEST, T., SCHOENAHN, F. & MONTANDON, M. L. (2006) Comparative assessment of statistical brain MR image segmentation algorithms and their impact on partial volume correction in PET. *Neuroimage*, 32, 1591-607.
- ZOU, K., HUANG, X., LI, T., GONG, Q., LI, Z., OU-YANG, L., DENG, W., CHEN, Q., LI, C., DING, Y. & SUN, X. (2008) Alterations of white matter integrity in adults with major depressive disorder: a magnetic resonance imaging study. *J Psychiatry Neurosci*, 33, 525-30.

**Appendices.**

**Appendices.****Mouse tissue processing.***Paraffin embedding for microtome cutting.*

<b>Station</b>	<b>Solution</b>	<b>Temp</b>	<b>Time</b>
1	70 % alcohol	35 °C	2 h
2	80 % alcohol	35 °C	2 h
3	96 % alcohol	35 °C	2 h
4	Absolute alcohol	35 °C	2 h
5	Absolute alcohol	35 °C	2 h
6	Absolute alcohol	35 °C	2 h
7	Absolute alcohol	35 °C	2 h
8	Xylene / absolute alcohol	35 °C	2 h
9	Xylene 1	35 °C	2 h
10	Xylene 2	35 °C	2 h
11	Paraffin wax 1	60 °C	2 h
12	Paraffin wax 2	60 °C	2 h
13	Paraffin wax 3	60 °C	2 h

*Resin embedding for electron microscopy.*

<b>Station</b>	<b>Solution</b>	<b>Temp</b>	<b>Time</b>
1	Isotonic cacodylate buffer	4 °C	50 min
2	1 % OsO <sub>4</sub> in cacodylate buffer	RT	2 h
3	Isotonic cacodylate buffer	RT	30 min
4	50 % alcohol	4 °C	5 min
5	50 % alcohol	4 °C	10 min
6	70 % alcohol	4 °C	5 min
7	70 % alcohol	4 °C	10 min
8	80 % alcohol	4 °C	5 min
9	80 % alcohol	4 °C	10 min
10	90 % alcohol	4 °C	5 min
11	90 % alcohol	4 °C	10 min
12	Absolute alcohol	4 °C	20 min
13	Absolute alcohol	4 °C	20 min
14	Propylene oxide	RT	15 min
15	Propylene oxide	RT	15 min
16	1:3 resin: propylene oxide	RT	13 h
17	1:1 resin: propylene oxide	RT	18 h
18	Resin	30 °C	6 h

**Preparation of slides for autoradiography and immunohistochemistry.**

***Immunohistochemistry: poly-L-lysine coated slides.***

Racked slides were placed in small tub filled with a 1:10 dilution of poly-L-lysine (Sigma) for 5 min, and then dried in an oven for an hour at 65 °C.

***Autoradiography: gelatine / chrome alum subbed slides.***

A 600 ml solution was prepared with 6 g of gelatine and 0.3 g of potassium chromium sulphate (chrome alum) filled up with distilled H<sub>2</sub>O. Subsequently, the solution was gently heated up to 60 °C until dissolved. The racked slides were then placed for ~5 min in small tubs filled with the gelatine/chrome alum mix and then dried overnight in an oven at 50 - 60 °C.

**Fixatives - Karnovsky's modified fixative for EM tissue preparation.**

***8 % paraformaldehyde.***

Add 20 g of PFA to 250 ml of distilled H<sub>2</sub>O and heat up to 65 °C. Add a few drops of 1 M NaOH to clear the solution and allow to cool.

***0.08 M cacodylate buffer.***

Dissolve 17.1224 g sodium cacodylate in 1 litre of distilled H<sub>2</sub>O and adjust to pH 7.2.

***Preparation of Karnovsky fixative (500 ml).***

250 ml 8 % PFA

100 ml 25 % EM grade glutaraldehyde

150 ml 0.08 M sodium cacodylate buffer

0.25 g calcium chloride

Add volumes, dissolve calcium chloride, adjust to pH 7.2, filter, and store at 4 °C.

**Reagents.**

***Araldite resin.***

30 g araldite CY212

25.2 g DDSA (dodecynyl succinic anhydride)

1.2 ml DMP 30 (2,4,6-tri(dimethylaminoethyl)phenol)

0.75 ml dibutylphthalate

***Reynold's lead citrate.***

(1.2 mM lead citrate, 1.8 mM sodium citrate, pH 12.0)

Solution A: dissolve 1.33 g lead nitrate in 15 ml distilled H<sub>2</sub>O before shaking vigorously for 1 min.

Solution B: dissolve 1.76 g sodium citrate in 15 ml distilled H<sub>2</sub>O and shake vigorously for 1 min.

Add solution A to B and equilibrate over 30 min with occasional shaking. Clear with 1 M NaOH and fill up with distilled H<sub>2</sub>O to an end volume of 50 ml.

***Saturated uranyl acetate.***

Dissolve uranyl acetate in excess in 50 % alcohol (store at 4 °C in the dark).